Pages 191 - 199

19 May 1967

NOTE: Per Terry Galloway letter dated 17 May 1967, pagination of thesis is incorrect. "Missing" pages 191 - 199 do not exist; no section has been left out, and the thesis is complete.

A STUDY ON THE MECHANISM OF MOLECULAR TRANSPORT WITH SYSTEMS OF GASEOUS PARAFFINS AND OF CONVECTIVE TRANSPORT FROM SINGLE CYLINDERS, SINGLE SPHERES, AND ARRAYS OF SPHERES INTO TURBULENTLY FLOWING STREAMS

thesis by

Terry Randolph Galloway

In Partial Fulfillment of the Requirements

For the Degree of

Doctor of Philosophy

California Institute of Technology
Pasadena, California
1967

(Submitted March 7, 1967)

ACKNOWLEDGEMENT

The encouragement and interest of my research advisor, Professor B. H. Sage, has been gratefully appreciated throughout all of this work. His patience and support in our studies of several new exploratory areas have been materially beneficial in maintaining the enthusiasm which the scope of these investigations, both theoretically as well as experimentally, constantly demanded.

The sincerely devoted and untiring efforts of the instrument makers, Willard DeWitt, who was a most essential part of the early development work and who died seeing half of the experimental program completed, and George Griffith, who carried out the majority of the ever-challenging and extremely demanding machine work, are most gratefully acknowledged.

Bill Lockwood, Ray Reed, and Bill Schuelke assisted materially in the construction and assembly of the numerous pieces of auxiliary equipment.

Henry Smith's persistant efforts in operating and controlling the Drop Apparatus Free Jet to the required degree of precision was most essential in the experimental program. Professor G. N. Richter kindly made available the facilities of the Student Laboratory for the early developmental studies and early experimental measurements with the 1.5 inch instrumented cylinder. Without the cooperation of Hollis Reamer much of the experimental work would not have been possible. J. M. Kendall, Sr. of the Jet Propulsion Laboratory is thanked for the use of his experimental model of a precision Silicon Oil Micromanometer.

The many untiring hours of the editors, Hilda Hager, Grace Fitzsimmons, and Florence Nash in the preparation of the many manuscipts associated with these investigations, as well as the many typists who accurately produced those finished copies, and of June Gray who so carefully prepared the some-one-hun-

dred illustrations and figures which were a most essential part of these manuscripts and this thesis, and of Virginia Berry, Shirley Homewood, Joan Jacobs, and Theresa Hubik who assisted in much of the numerical calculation, graphical work, and computer work are most sincerely acknowledged. Evelyn Anderson and Susan Davis so kindly assisted in the Xerographic reproduction.

To the Fluor Foundation for receipt of the Fluor Foundation Fellowship and to the California Institute for the research assistantship during the years of residence, the author is forever indebted.

ABSTRACT

PART I

Intermolecular pair potential functions for the Lennard-Jones ∞-6, 12-6, and 9-6 form, and of the three parameter forms of Morse and of Kihara for a spherical core, were used to fit new gas phase viscosity data at low pressure for the normal paraffins through n-decane. The intermolecular force parameters were obtained and found to be unique for the Morse and Kihara potentials. All potential models underestimated the temperature dependence of the viscosity, but the Kihara was found to be superior with deviations of several percent.

The Eucken relation for predicting the gas phase thermal conductivities of gaseous paraffins at low pressure proved to 18% low. Configurational thermal conductivities were calculated from experimental data, and a new form of conductivity excess above the configurational value was developed which produced a quantitative relationship to the heat capacity excess. This relation was compared with a number of theories and found to be in agreement, and it predicted the paraffin data within 4.9%.

Binary diffusion coefficient data were compiled and found to be in agreement with theoretical predictions, within the large experimental uncertainties associated with the data. Existing methods of prediction of viscosity and conductivity for binary mixtures of similar species were found to be inadequate for dissimilar systems and a more adequate but simple theoretical relation was shown to apply. Also the importance of the dense gas corrections involved in high pressure gas phase viscosities and conductivities are discussed.

PART II

Similarity solutions of the Blasius form to the problem of flow around a circular cylinder and sphere at moderately high Reynolds numbers were obtained for the general case of variable Prandtl (or Schmidt) groups. A dimensionless ratio referred to as the Frössling group" was obtained from these solutions which proved to be most useful in understanding the mechanism of transport from bluff bodies into turbulently flowing streams and into separated wake-flows. Quantitive experimental results were obtained for the influence of the level of turbulence in the main stream and effects of separation on the convective heat and mass transfer from cylinders and spheres. The Reynolds number was varied from 2,600 to 86,000 and free-stream turbulence from 0.013 to 0.25. These results were correlated in terms of the Frössling group and compared with available experimental data within 7.7% for cylinders and 8.8% for spheres.

The local Frössling group was found to be proportional to the product of the turbulence level and the square root of the Reynolds number in the laminar flow region and increased strongly with Reynolds number in the wake. The local effects of turbulence were uniform from 35% increases at the forward stagnation. The point of separation was strongly delayed by turbulence. The transition to supercritical flow was established from the heat transfer measurements and found to agree with drag measurements. The local pressure coefficient was measured with a small pitot tube in the surface, and remained as unity at the forward stagnation point, independent of turbulence variations, and was altered only slightly near and following separation by varying Reynolds number and turbulence during subcritical conditions. The dependence of the position of separation upon Reynolds number and free-stream turbulence level was established quantitatively.

PART III

The mechanism of local transport in regular packed arrays of uniform spheres was studied in the light of boundary layer theory and the established behavior from bluff bodies. Local measurements were made with a movable calorimeter on the surface of a sphere placed in a rhombohedral No. 6 array. The effective local velocity and turbulence level within the array were determined. This model was found to predict available data in packed, distended, and fluidized beds of all shaped particles within 9.8%, and 12% for columns irrigated with liquid.

Electrostatic reproductions of photography on pp. 132, 136, 220-221, 297-299, 308, 310, 368, 374, 376, 379, and 388 are not adequate.

TABLE OF CONTENTS

III. A Boundary Layer Model for the Mechanism of Fluid-Particle Transport in Packed, Distended, and Fluidized Beds of Uniform Spheres, Cylinders, and Commercial Packing.

LIST OF FIGURES

PART I

PART II

LIST OF TABLES

PART I

PART II

PART I

MOLECULAR TRANSPORT PROPERTIES OF THE GASEOUS PARAFFIN HYDROCARBONS*

INTRODUCTION

Prediction of transport properties of polyatomic molecules requires recognition of the internal structure of the individual molecular species and consequent effects on the mechanism of the inelastic collision process between these species. Simplified models for an intermolecular potential, though not exact, have been fairly satisfactory for molecules which can be represented as rigid spheres. Polyatomic molecules cannot be simply described by current intermolecular potential models, for the potential has to reflect too many of the effects of the complexity in internal structure of the molecule. The potential function is, therefore, a statistical average of the large variety of possible collision configurations and resulting internal excitations which result in the collision process.

Recently experimental data have become available which permit a deeper look at the molecular transport properties from a kinetic theory as well as molecular structure viewpoint. More accurate transport properties were badly needed in the evaluation of mass transfer from bluff bodies in turbulent fluid streams. Particularly, the normal paraffin hydrocarbon transport property data were previously extremely sparse, and methods of prediction applicable to much simpler molecular species were not sufficient. Consequently, the

---

* A portion of Part I has been accepted for publication by Chemical Engineering Science for the theoretical analysis portion and accepted by the Journal of Chemical and Engineering Data for the numerical portion. Permission has been granted by Pergamon Press to present a portion of the published article in Part I of this thesis.

homologous series of the normal paraffin hydrocarbons provided a very valuable systematic variation in molecular structure to develop a detailed analysis of the transport properties of these polyatomic molecules.

The molecular transport behavior of molecular species that can be characterized by a rigid sphere can be described by a one-parameter intermolecular pair potential model together with the Chapman-Enskög transport equations (1). Small molecules which can be represented as spherically symmetric but no longer completely rigid are fairly adequately described by the two-parameter Lennard-Jones potential. Large, spherically symmetric molecules have been adequately represented by the Kihara potential model, involving three parameters, which recognises the existence of a rigid and spherical molecular core of finite size, and they have been represented by the semi-empirical, three-parameter Morse potential. Molecules which deviate substantially from being spherically symmetric, such as those characterized as long cylinders, have been represented by the non-spherical core model of Kihara or the model of Corner as far as the intermolecular pair potential; however, for molecular transport the details of the necessary collision integrals have not been worked out.

PURE MOLECULAR SPECIES

The pure component molecular transport properties of shear viscosity and thermal conductivity are analyzed from the Chapman-Enskög kinetic theory of gases of rigid molecules in the dilute state , and these predictions are compared with the available experimental data. The intermolecular force constants evaluated from viscosity data using the Lennard-Jones 12-6 potential are then used to predict some equilibrium properties. The thermal conductivity data have been used to reveal information concerning the internal structure of the normal paraffins and its role in the collision mechanism.

VISCOSITY

Dilatational viscosity, which arises in shock phenomena or other processes where molecular kinetic velocities are exceeded and inelastic collisions are dominant, will not be considered; that is, only shear viscosity will be analyzed. For the normal gaseous paraffins, ranging from methane through decane, the experimental shear viscosity data (2-20) at the limit of low pressure have been shown in figure 1 for temperatures from 250° to 425° K.. From the viscosity data up to several atmospheres, the extrapolated values at the zero pressure limit were obtained (21). A comparison between the viscosity at atmospheric pressure and at the low pressure limit indicates the magnitude of gas non-idealities (21). A table of these values is given in Appendix A1 and in Appendix A2 the deviations of the data are given. This low pressure state, or "attenuation" (22), was selected to be sufficiently low so that gases remained dilute and binary collisions of molecules dominated and high enough to avoid the viscosity anomalies (23) associated with a high percentage of collisions with the walls of the viscometer. In this way, only the systematic variation of molecular structure should account for the varying temperature dependence of the viscosity.

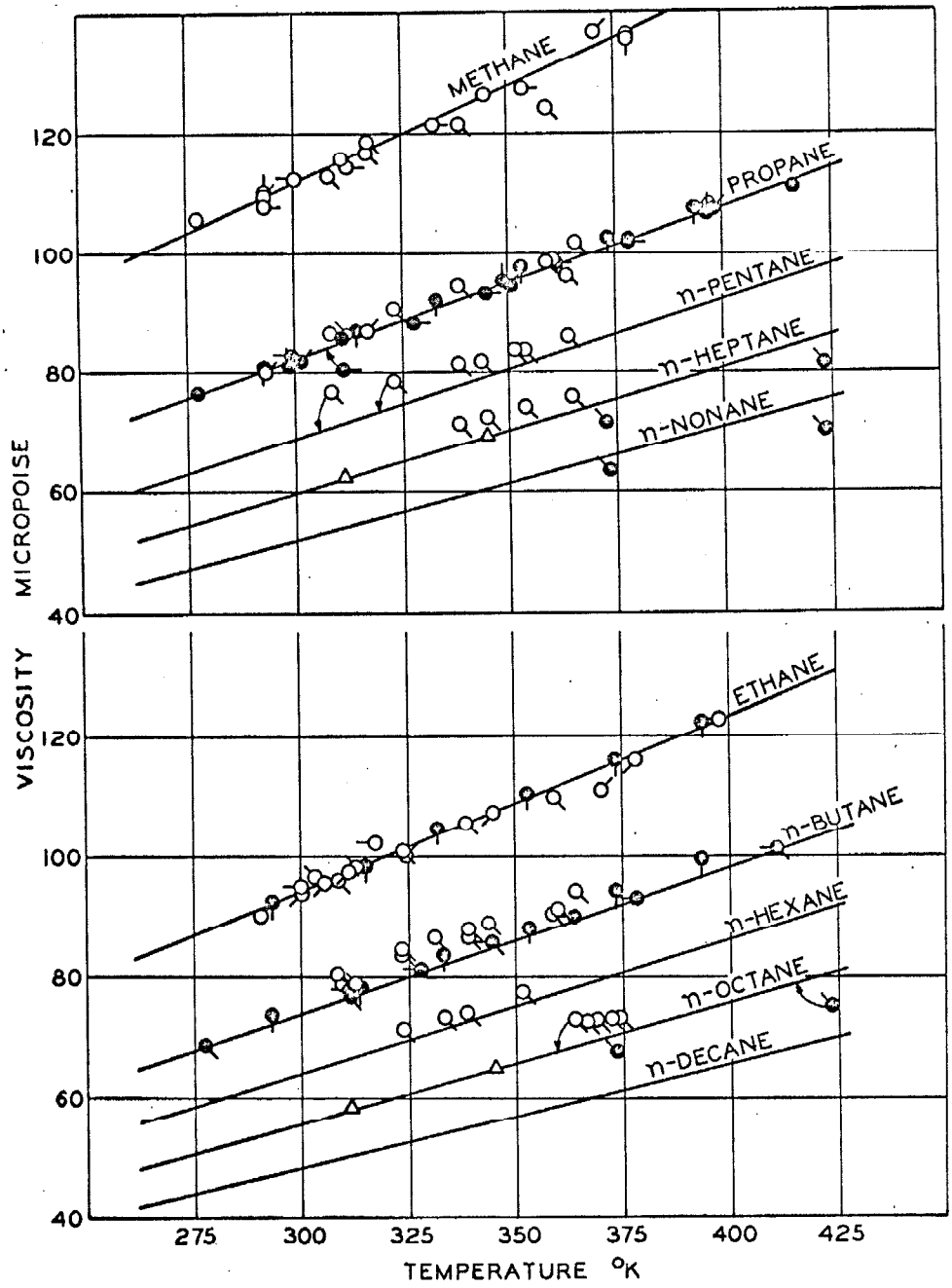

Carmichael (2)	Carmichael (8)	Sage (14)
Kestin (3)	Svehla (9)	Carmichael (15)
Trautz (4)	Senftleben (10)	Titani (16)
Kuss (5)	Carmichael (11)	Sage (18)
Lambert (6)	Bicher (12)	Melaven (19)
Sage (7)	Trautz (13)	Carmichael (20)

Fig. 1. Viscosity of the normal paraffin hydrocarbons at attenuation.

It is desirable, at first, to establish the validity of a law of corresponding states (1) between each of the species in the homologous series. Quantum mechanics suggests that the dominating attraction force exponent should be six. A reduced viscosity is formed for three potentials of the Lennard-Jones n-6 form using the relation of the force parameters to the experimental critical constants for the individual potential. This theoretical relationship for the reduced temperature dependence of the reduced viscosity has been shown in figure 2 as the solid curves. The available viscosity data (2-20) fall between the Sutherland model (00-6) and the Lennard-Jones 9-6 potential. It is clear that no single two-parameter intermolecular pair potential model of the Lennard-Jones n-6 form is adequate to describe the entire homologous series. The inadequacies of the well-established Lennard-Jones 12-6 model can best be illustrated by examining the computation of the force field parameters. Only for paraffins up through n-butane can a set of parameters be obtained directly by the well-established technique (1), and they depend strongly on temperatures that are chosen as the two experimental points. How much variation in the parameters would be required to represent the experimental data over the entire temperature range?

To answer this question the collision diameter, σ, and well depth, ϵ/k, were established approximately by current methods (1) from the Chapman-Cowling theory:

$$\eta_o^{(k)} = 26.693 \frac{\sqrt{M\,T}}{\sigma^2\,\Omega^{(2,2)*}}\, f_\eta^{(k)} \qquad (1)$$

The quantity in the denominator is the effective collision cross section for the Lennard-Jones 12-6 model and is slightly temperature dependent. To the kth approximation $f_\eta^{(k)}$ is also a weak function of the reduced temperature and is tabulated (1) for several potentials. For the conditions included in this study it did not deviate significantly from unity.

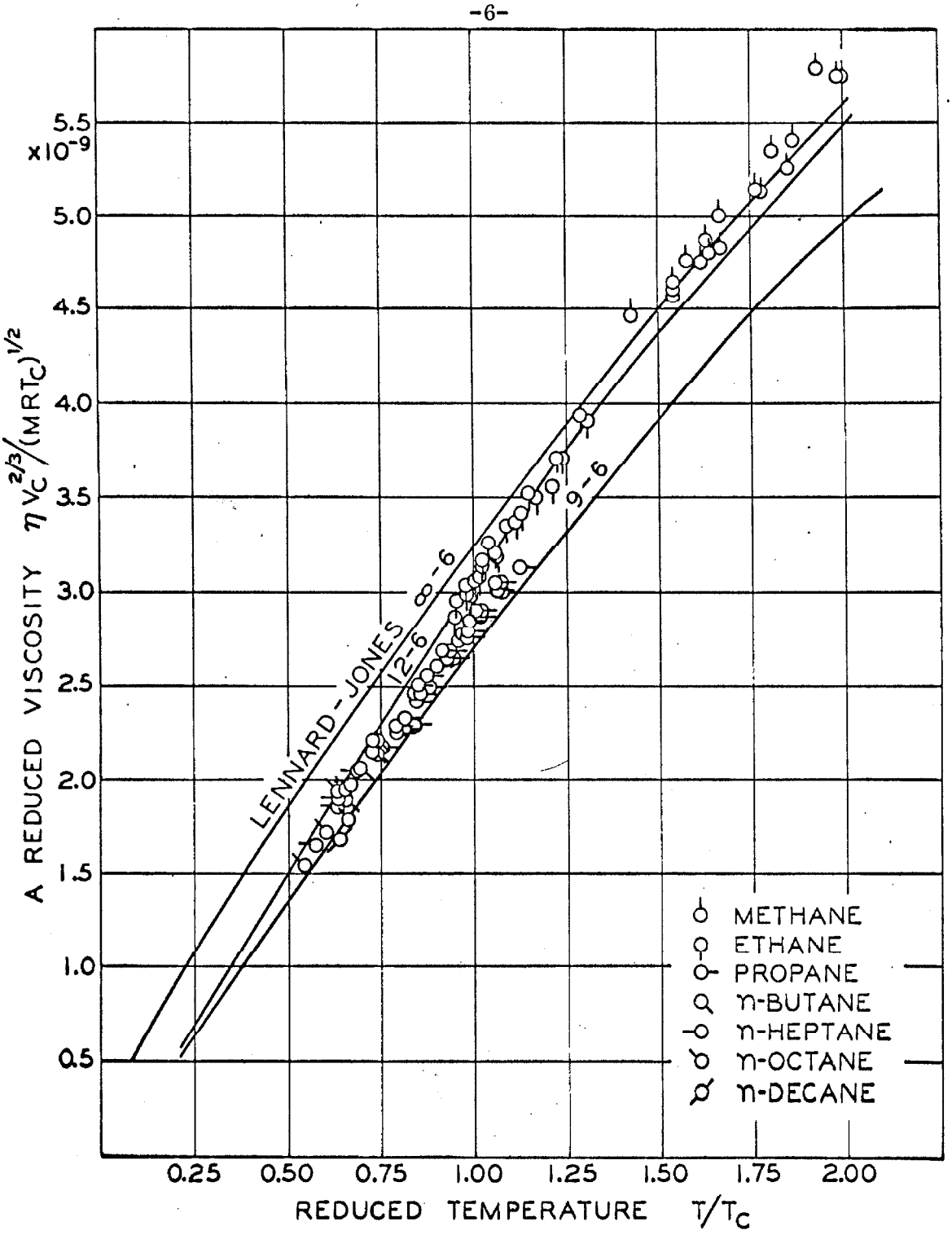

Fig. 2. A reduced viscosity prediction for various Lennard-Jones (n-6) potentials.

The second iteration involved obtaining the residual temperature dependence of the potential well depth, ϵ/k, for the collision diameter obtained in the first iteration. The proper collision diameter, statistically, is that which is associated with a potential well depth exhibiting a minimum temperature dependence. The solid curve presented in figure 3 is composed of such collision diameters and is compared to the values reported by Flynn and Thodos (25) for the paraffins and to the value presented by Hirschfelder for hydrogen (1). These compare closely in figure 4 to collision diameters obtained from the three-parameter potentials of Morse and of Kihara which will be discussed shortly. The resulting empirically determined, temperature dependent parameter ϵ/k is shown for the paraffins in figure 5. These results are intended to illustrate the magnitude of the parameter variation which is required to fit the data rather than to arrive at a molecularly significant result.

The inadequacy of the Lennard-Jones n-6 model for the paraffins increases with the molecular complexity involved and suggests that the molecular asymmetry and internal structure is important in viscosity. The mechanism of inelastic intermolecular collision of quasi-linear molecules depends upon the probability of various orientations. For such polyatomic molecules, the intermolecular pair potential is a statistical average of these various collision orientations. The net effect of this averaging is the observed narrowing and deepening of the potential well (26-28) compared to that for spherically symmetric molecules. It is likely (see proposition C) that the presence of molecular asymmetry and internal structure violates the very assumptions in the Chapman-Cowling theory itself.

The three parameter, spherical core model of Kihara (1, 29-31) and the empirically established Morse potential model (28, 32-35) have been useful in predicting a more realistic potential well shape for globular molecules, while Corner's "four center" model is particularly useful for linear molecules such as the normal paraffins. Unfortunately no collision integrals have been computed to date for the latter model. The three-parameter potentials of

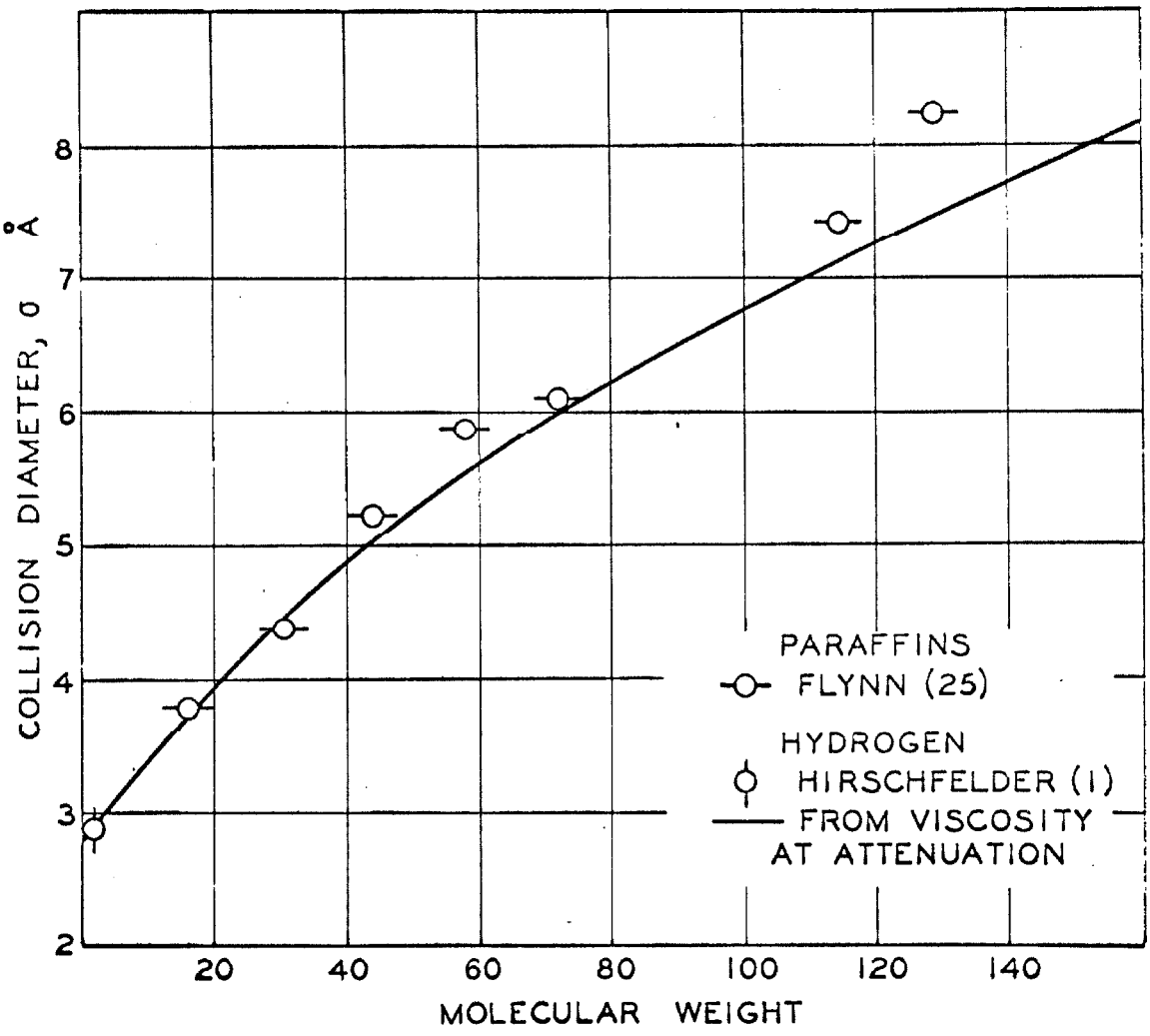

Fig. 3. Collision diameters for the Lennard-Jones 12-6 potential.

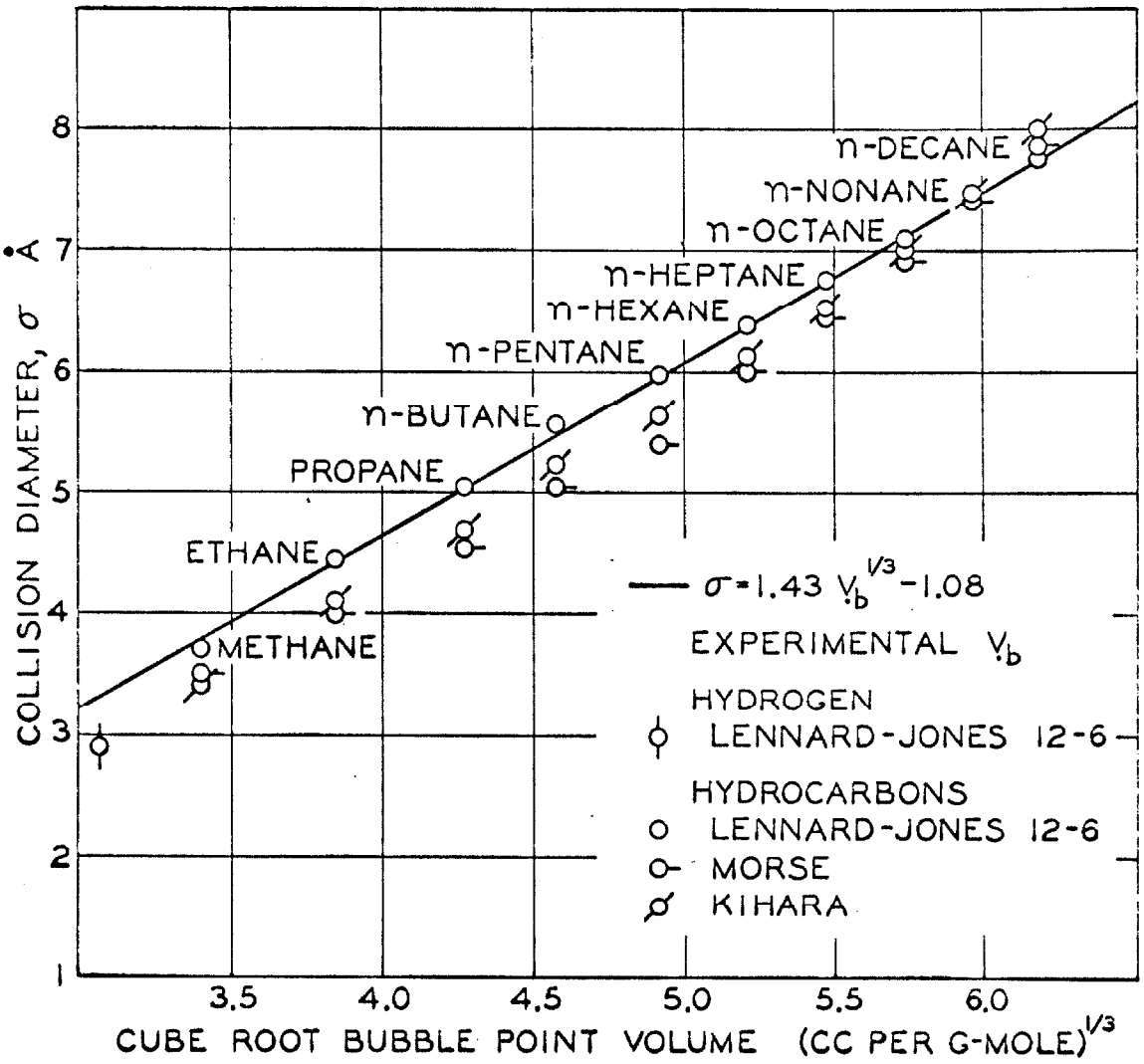

Fig. 4. Relation of collision diameter to bubble-point volume.

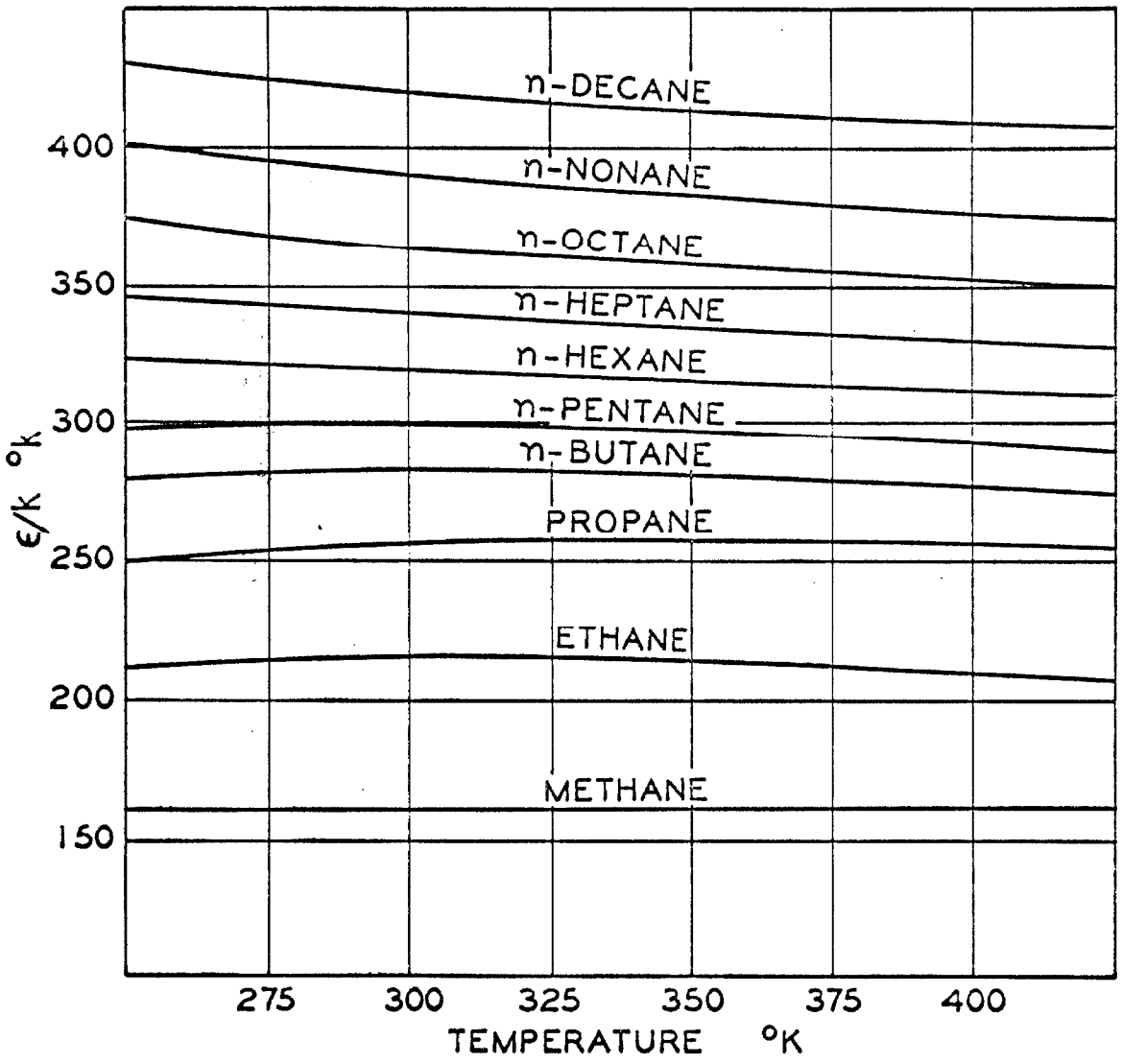

Fig. 5. Effect of temperature upon the "well-depth" of the Lennard-Jones 12-6 potential.

Kihara and Morse were used to predict the paraffin gas phase viscosities. The force constants were obtained by a non-linear regression technique similar to that used by Konowalow (28); however, the large quantity of more recent viscosity data (2-20) was included. The resulting force constants together with their individual confidence limits are presented in Table 1. Also shown in this table are the experimental standard deviations of the raw data about the graphically determined solid curves in figure 1, and the deviations of each particular potential from the solid curves of figure 1. The deviations of the Morse and Kihara potentials are greater than the deviation in the experimental data for all paraffins. The confidence limits in the individual force field parameters taken independently were obtained from the uncertainty in the parameters as a result of experimental scatter, as was expressed in the first column of table 1. For the heavier paraffin species the predicted temperature dependence was considerably low and the resulting inadequacy of the potential models is reflected in the larger confidence limits.

The Morse potential third parameter, C, is a measure of the potential curvature at its minimum, and empirically reflects the molecular asymmetry. The parameter, C, is approximately five for a number of spherically symmetric monatomic gases, such as neon, argon, krypton, and xenon. This parameter increases from 5.7 for methane to nearly 10. as asymmetry increases, and is simply related to the reduced latent heat of vaporization at the normal boiling point, as shown in figure 6. In the spherical core model of Kihara (1), the third parameter, γ, is the ratio of the core size to the collision diameter. For small, simple molecules which can be represented by the Lennard-Jones 12-6 potential model "γ" is zero. This parameter is also related to the reduced latent heat of vaporization as in figure 6. The third parameters, C and γ, are somewhat analogous to Pitzer's acentric factor (26-27) and a plot reveals a linear relationship. Apparently such a simple relationship can be derived theoretically (28). The energies of attraction, ϵ/k, in the Morse potential and, U_o/k, in the Kihara potential, are simply related to the normal boiling point as

TABLE 1. VISCOSITY FORCE CONSTANTS FOR MORSE AND KIHARA POTENTIALS

Component	Experimental Uncertainty	Morse Potential				Kihara Potential			
		δ (Å)	ϵ/k (°K)	C	Frac. Dev.	σ (Å)	U_o/k (°K)	γ	Frac. Dev.
Methane	2.0%	3.510	220.8	5.771	0.0023	3.411	260.0	0.194	0.0032
Ethane	1.4	3.986	383.0	6.010	0.0029	4.105	345.4	0.241	0.0040
Propane	1.9	4.542	475.6	6.481	0.0112	4.709	420.0	0.295	0.0093
n-Butane	2.8	5.045	579.2	7.236	0.0316	5.233	474.7	0.345	0.0220
n-Pentane	3.8	5.397	700.4	7.351	0.0419	5.630	530.	0.370	0.0296
n-Hexane	2.5	5.966	778.0	8.180	0.0528	6.109	575.	0.420	0.0390
n-Heptane	4.2	6.435	861.8	8.627	0.0599	6.517	675.	0.459	0.0483
n-Octane	4.7	6.91	952.	9.10	0.0651	6.996	716.	0.495	0.0561
n-Nonane	-	7.40	1035.	9.55	0.0665	7.46	795.	0.525	0.0612
n-Decane	-	7.87	1113.	9.83	0.0656	8.00	900.	0.55	0.0632
		Confidence Limits of Force Constants*							
Methane		0.001	0.3	0.022		0.026	13.	0.020	
Ethane		0.027	10.	0.32		0.024	14.	0.029	
Propane		0.043	35.	0.25		0.050	21.	0.050	
n-Butane		0.081	56.	0.32		0.125	30.	0.068	
n-Pentane		0.095	80.	0.35		0.152	83.	0.075	
n-Hexane		0.120	120.	0.62		0.120	84.	0.062	
n-Heptane		0.215	n.a.	1.20		0.235	185.	0.067	
n-Octane		0.26	n.a.	1.30		0.30	n.a.	n.a.	
n-Nonane		n.a.	n.a.	n.a.		n.a.	n.a.	n.a.	
n-Decane		n.a.	n.a.	n.a.		n.a.	n.a.	n.a.	

Experimental uncertainty defined by: $\left\{\sum_1^N [(\eta_e-\eta_s)/\eta_e]^2/(N-1)\right\}^{1/2}$, and fractional deviation by: $\left\{\sum_1^N [(\eta_s-\eta_p)/\eta_s]^2/(N-1)\right\}^{1/2}$

*Computed independently as a result of the experimental uncertainty in the data from the solid curves in Figure 1.

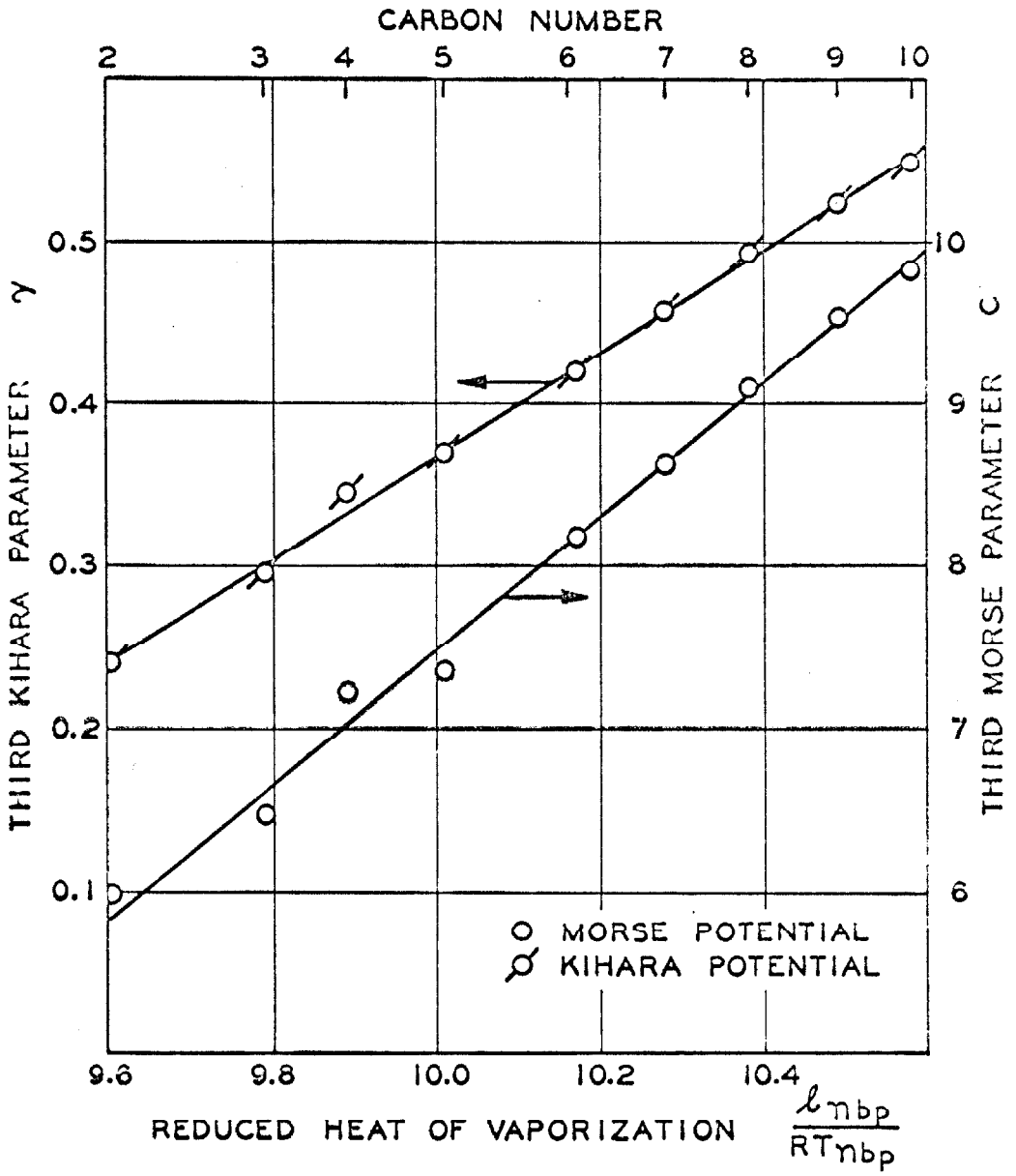

Fig. 6. Relation of the third parameters of the Morse and Kihara potentials to a reduced heat of vaporization.

shown in figure 7. Using the three potential parameters for the Morse and Kihara potentials given in figures 4, 6, and 7, t he deviations between the predicted viscosity at attenuation and the solid curves of figure 1 are presented as a function of temperature in figure 8.

Both the Morse and Kihara potentials fail to predict the correct temperature dependence of the normal paraffin viscosities. The fractional deviations of the viscosities are given in figure 8 as a function of temperature. For all the paraffins except methane, where the deviations are very small, the experimental temperature dependence is greater than that predicted by either model. The Kihara spherical core model is noticeably better at the higher temperatures where the repulsion forces become more important. Better overall predictions may be possible when the collisional integrals are obtained for the ellipsoidal core model of Kihara (1), or the Corner potential for linear molecules.

The potential parameters established from viscosity data for the Lennard-Jones 12-6 potential as shown in figures 3 and 5 have been used in the virial equation of state (1) to predict molal volumes for the saturated gas. The saturated liquid molal volumes were predicted by the Lennard-Jones Devonshire equation (1). A comparison between the predicted and experimental (36-50) molal volumes is shown in table 2 and indicates that the predicted molal gas volume is larger than experimental values for all paraffins and the predicted liquid molal volume becomes much larger than the experimental volume for the more complex paraffins. The differences in the predicted and experimental values for the gas can arise from molecular complexity. Perhaps there may be subtle differences in using second virial coefficient at equilibrium states and the non-equilibrium shear viscosity in order to establish the interaction parameters.

At elevated pressures dense gas corrections (1) become important in predicting gas phase viscosities and the subject is by no means simple. A formal kinetic theory of dense polyatomic fluids is not currently available. For molecular species which were sufficiently simple to be described by a two-parameter

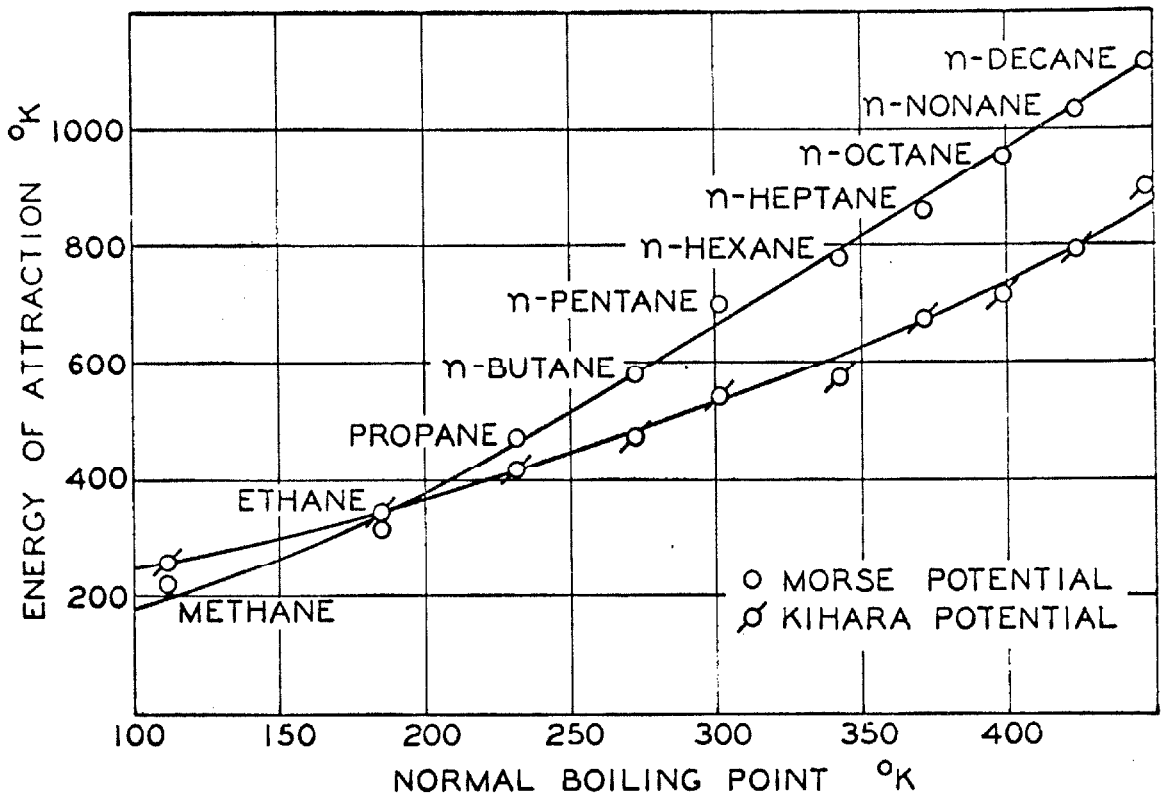

Fig. 7. Relation of the energies of attraction of the Morse and Kihara potentials to the normal boiling point.

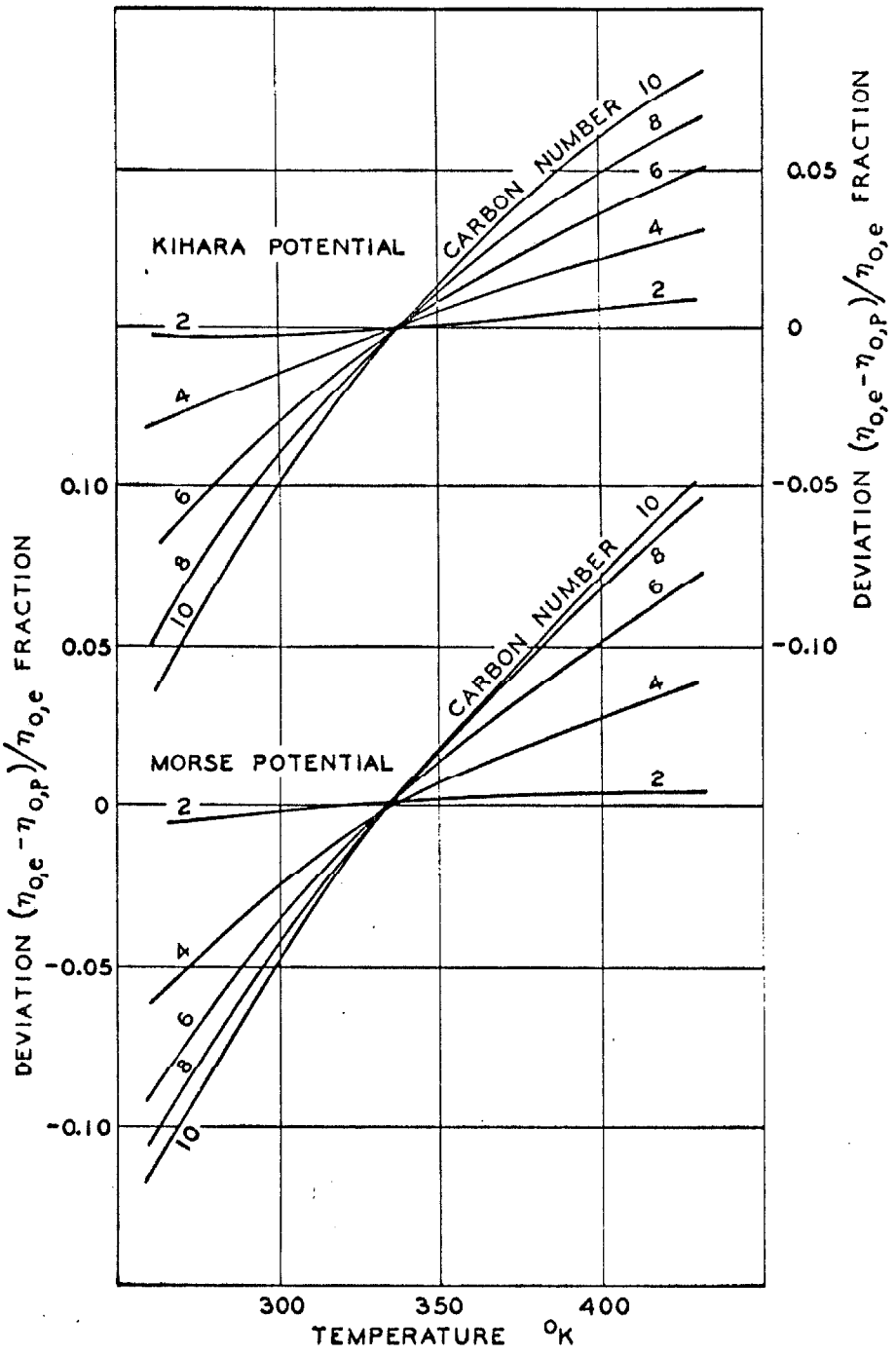

Fig. 8. Deviation of the viscosities predicted by the Morse and Kihara potentials from experimental values at attenuation.

TABLE 2. PREDICTION OF MOLAL VOLUMES OF SATURATED GAS AND LIQUID

Atmospheric Pressure

Component	VOLUME (cc/gmole) Dew Point		Bubble Point		Source
	Experimental	Predicted	Experimental	Predicted	
Methane	8830	8845	39.08	32.2	(36,37)
Ethane	14000	14746	56.56	58.5	(38,39)
Propane	18020	18460	77.10	87.1	(40)
n-Butane	21530	21789	95.51	117.2	(41)
n-Pentane	24270	24696	118.2	149.4	(42,43,44)
n-Hexane	26420	27288	140.4	183.3	(45,46)
n-Heptane	28770	29612	163.6	242.8	(42,47)
n-Octane	30630	31742	186.8	298.7	(42)
n-Nonane	32480	33653	211.0	344.2	(48)
n-Decane	34540	35361	234.3	349.5	(49,50)

intermolecular potential model, such as Lennard-Jones 12-6, the transport property behavior can be described (1) adequately at elevated pressures using the law of corresponding states. For the normal paraffin hydrocarbon homologous series no single intermolecular potential model, either of two- or three-parameters, were shown to be adequate. Consequently, a law of corresponding states as an approximation to first order behavior is described briefly.

Dense fluids were found by Enskög (1) to be described adequately by simple kinetic theory when two important dense gas corrections were recognised. Enskög noted that in dense fluids the assumptions of two-body collisional behavior and of the distance between molecules being large in comparison to molecular size are most certainly not valid. He was not able to relax the restriction of neglecting higher order collisions than two or of rigid spheres; however, he did consider effects of finite molecular size. As the result of finite molecular size there was a collisional transfer of momentum and energy as well as an increase in the rate of collisions. The increase, Y, in the rate of collision of molecules of finite size comparable to point particles was simply related to the equation of state:

$$\frac{PV}{RT} = 1 + \rho^* Y \tag{2}$$

where for rigid spheres:

$$Y = 1 + 0.6250\rho^* + 0.2869(\rho^*)^2 + 0.115(\rho^*)^3 \tag{3}$$

and:

$$\rho^* = b_o/V = \frac{2}{3}\pi N_o \sigma^3/V$$

The result of his rigid sphere analysis for viscosity is as follows:

$$\eta = \frac{1}{Y}\left[1 + \frac{4}{5}\rho^* Y + 0.761(\rho^* Y)^2\right]\eta_o \tag{4}$$

where η_o is the viscosity of the polyatomic gas at attenuation as given in figure 1 or equation 1. This can be rearranged as:

$$\frac{\eta-\eta_o}{\eta_o} = \frac{(0.8Y-0.6250)\rho^* + (0.761Y^2-0.2869)(\rho^*)^2 - 0.115(\rho^*)^3}{1+0.6250\rho^*+0.7869(\rho^*)^2+0.115(\rho^*)^3} \tag{5}$$

Since Y is a function of the reduced density, ρ^*, then this excess viscosity ratio is a function of the reduced density only for a rigid sphere:

$$\frac{\eta-\eta_o}{\eta_o} = f(\rho^*) \text{ only} \tag{6}$$

This expression is violated by nearly all available viscosity data which indicate $\eta-\eta_o$ to be a function of density alone. For example, even argon data show f to increase above that of equation 5 as the temperature is decreased. The argon viscosity data do, however, approach equation 5 asymptotically as the temperature exceeds 100° C. This result is not surprising since real molecules approach rigid sphere behavior at high temperature where the deficiency of intermolecular attractive forces is not so serious.

When the rigid sphere assumption is relaxed in the equation of state given in equation 2-3, a convenient alternative is the acentric factor approach (26-27) for dense polyatomic fluids:

$$\rho^* Y = (Z^{(o)}-1) + \omega Z^{(1)} + \omega^2 Z^{(2)} \tag{7}$$

For the limiting case of rigid spheres $Z^{(o)}-1$ is proportional to ρ^* and ω is zero. Since the function $Z^{(o)}-1$ was obtained from experimental data, the term $(Z^{(o)}-1)/\rho^*$ is not identical to equation 3. The excess viscosity ratio is strictly a function of the reduced density, reduced temperature, and acentric factor:

$$\frac{\eta-\eta_o}{\eta_o} = \varphi(\rho^*, T_R, \omega)$$

This can be rearranged into the form of equation 7:

$$\frac{\eta-\eta_o}{\eta_o} = \varphi^{(o)}(\rho^*, T_R, \omega)+\omega\varphi^{(1)}(\rho^*, T_R)+\ldots \tag{8}$$

where the dependence is nearly linear with ω and the functional dependence on T_R and ω is slight. It should be noted that this result was obtained from equation 4, which strictly applies only to rigid spheres, although equation 3 was corrected.

If equation 3 is replaced by the theoretically significant virial equation of state:

$$Y=B^*(T)+C^*(T)\rho^*+\ldots$$

then equation 4 becomes:

$$\frac{\eta-\eta_o}{\eta_o} = \frac{1+[B^*(T)+C^*(T)\rho^*](0.8\rho^*-1)+0.761\rho^{*2}[B^*(T)+C^*(T)\rho^*]^2}{B^*(T)+C^*(T)\rho^*} \tag{9}$$

Neither equation 8 or 9 predict argon viscosity as closely as equation 5. Apparently, recognising the attractive forces in the equation of state and not in the development of equation 4 presents an internal inconsistency. For example, over reasonable conditions the denominator of equation 9 remains

negative. Unless the Enskög theory for dense fluids can be developed recognising the attractive forces consistent with an equation of state, equation 5 will remain the only proper theoretical prediction which can be made of data, and is restricted to rigid sphere behavior.

It is intriguing to note an experimental fact that is apparent in the more precise viscosity measurements involving dense fluids (2,8,11,15) which indicates that $\eta-\eta_o$ is a function of density alone and that the functions, φ, depend nearly inversely on the square root of the absolute temperature. Equation 8 can be then empirically simplified to:

$$\frac{\eta-\eta_o}{\sigma^{-2}\sqrt{m\epsilon}} = \Phi_2^{(o)}(\rho^*,\omega) + \omega\Phi_2^{(o)}(\rho^*) + \ldots \qquad (10)$$

Currently* available experimental data for non-polar, dense fluids are being analyzed in terms of the following equation:

$$\frac{\eta-\eta_o}{\sigma^{-2}\sqrt{m\epsilon}} = f^{(o)}(\rho^*) + \omega_\eta f^{(1)}(\rho^*) \qquad (11)$$

This relation describes dense paraffins within the experimental accuracy and the preliminary results indicate that the empirical parameter, ω_η, is comparable to the acentric factor established from PVT data and that the function $f^{(o)}$ can be represented by the experimental data for argon. Careful analysis will be required to detect residual temperature dependence in the reduced viscosity excess in equation 11 as well as the theoretical basis for such a form.

---

* Shyne Yuan Wu is currently conducting such a study as partial requirements for the Doctor of Philosophy degree at the California Institute of Technology.

THERMAL CONDUCTIVITY

The thermal conductivity data (6, 9, 10, 20, 51-65) were reduced to the dilute state at low pressure (66) by using data available at various pressures up to three atmospheres. The differences between the conductivity at attenuation and atmospheric as well as the isothermal pressure derivative have been presented in Appendix A3. Figure 9 indicates the experimental thermal conductivity data at the limit of low pressure. The solid curves were established by graphical methods whereupon the deviations are presented in Appendix A4 and these curves are nearly identical to the curves established from a theoretical standpoint which will be described in the following section.

It is known that the vibrational and rotational energies and the exchange of translational-rotational energy contribute substantially to the molecular thermal conductivity of polyatomic molecules (1, 6, 24, 67-70). The "configurational conductivity" shall be denoted by $k_o^{(o)}$ and shall be the conductivity of a hypothetical polyatomic gas with all of its internal degrees of freedom "frozen". The configurational thermal conductivity will be identical to the experimental molecular thermal conductivity at low pressure only for a monatomic gas, which is spherically symmetric and without internal degrees of freedom. This reference conductivity, $k_o^{(o)}$, can be evaluated on the basis of the Chapman-Cowling theory with a knowledge of the intermolecular potential (1) as follows:

$$k_o^{(o)} = 1.9891 \times 10^{-4} \frac{\sqrt{T/M}}{\sigma^2 \Omega^{(2,2)*}} \tag{12}$$

The configurational thermal conductivity may also be obtained directly from measured viscosities at attenuation as:

$$k_o^{(o)} = \frac{15}{4} \frac{R}{M} \frac{f_k^{(k)}}{f_\eta^{(k)}} \eta_o \tag{13}$$

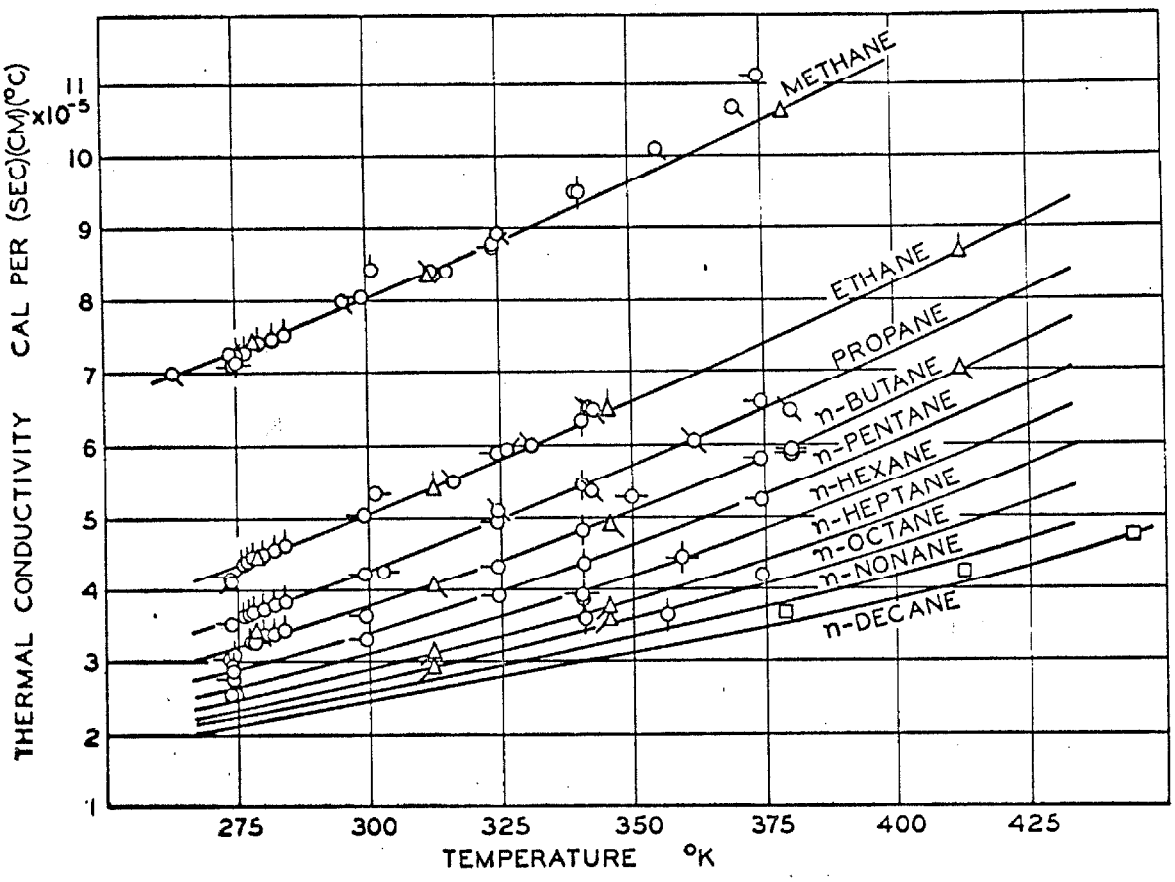

Moser (51)
Mann (52)
Keyes (53)
Svehla (9)
Johnston (54)
Kannuluik (55)
Lenoir (56)
Senftleben (10)
Lenoir (57)
Lambert (6)
Eucken (58)
Kramer (59)
Leng (60)
Lambert (61)
Carmichael (20)
Carmichael (62)
Carmichael (63)
Carmichael (64)
Carmichael (65)

Fig. 9. Thermal conductivity of the normal paraffin hydrocarbons at attenuation.

The configurational conductivity from Equation 13 is given in Appendix A3. The collision integral, $\Omega^{(2,2)*}$, included in equation 2 is known only for a limited number of intermolecular potential models with aspherical parameters (1, 29, 31, 35, 71), none of which has proved to be adequate, and in general will not be available for actual polyatomic molecules which one will commonly encounter. Consequently, to avoid idealized intermolecular pair potential models which cannot describe polyatomic molecules accurately, equation 13 was used to obtain the configurational thermal conductivity, $k_o^{(o)}$, from the experimental viscosity data at attenuation. The quantity, $f_k^{(k)}$, is a correction factor analogous to that discussed earlier in connection with viscosity and is near unity. The excess thermal conductivity from vibrational-rotational contributions for polyatomic molecules compared to the configurational conductivity is shown as $(k_o - k_o^{(o)})/k_o^{(o)}$ in figure 10. The solid curves were obtained directly from the curves shown in figures 1 and 9, using equation 13 for the configurational conductivity.

Eucken (58) has hypothesized that the thermal conductivity for a polyatomic gas can be represented by a sum of the contributions from the translational and the different internal degrees of freedom:

$$k_o = k_{o,tr} + k_{o,int} = [f_{tr} C_{v,o,tr} + f_{int} C_{v,o,int}] \eta_o / M \qquad (14)$$

The coefficients, f_{tr} and f_{int}, are the fractional contributions from the isochoric heat capacity corresponding to the translational and the internal degrees of freedom, respectively. The source of these polyatomic contributions to the conductivity comes about from the complex collision mechanism of the polyatomic species. As a warm molecule finds itself in a colder environment, the temperature characterizing the kinetic energy of the internal degrees of freedom is higher than that characterizing the translational degrees of freedom owing to the finite internal-translational relaxation time. This internal energy will then

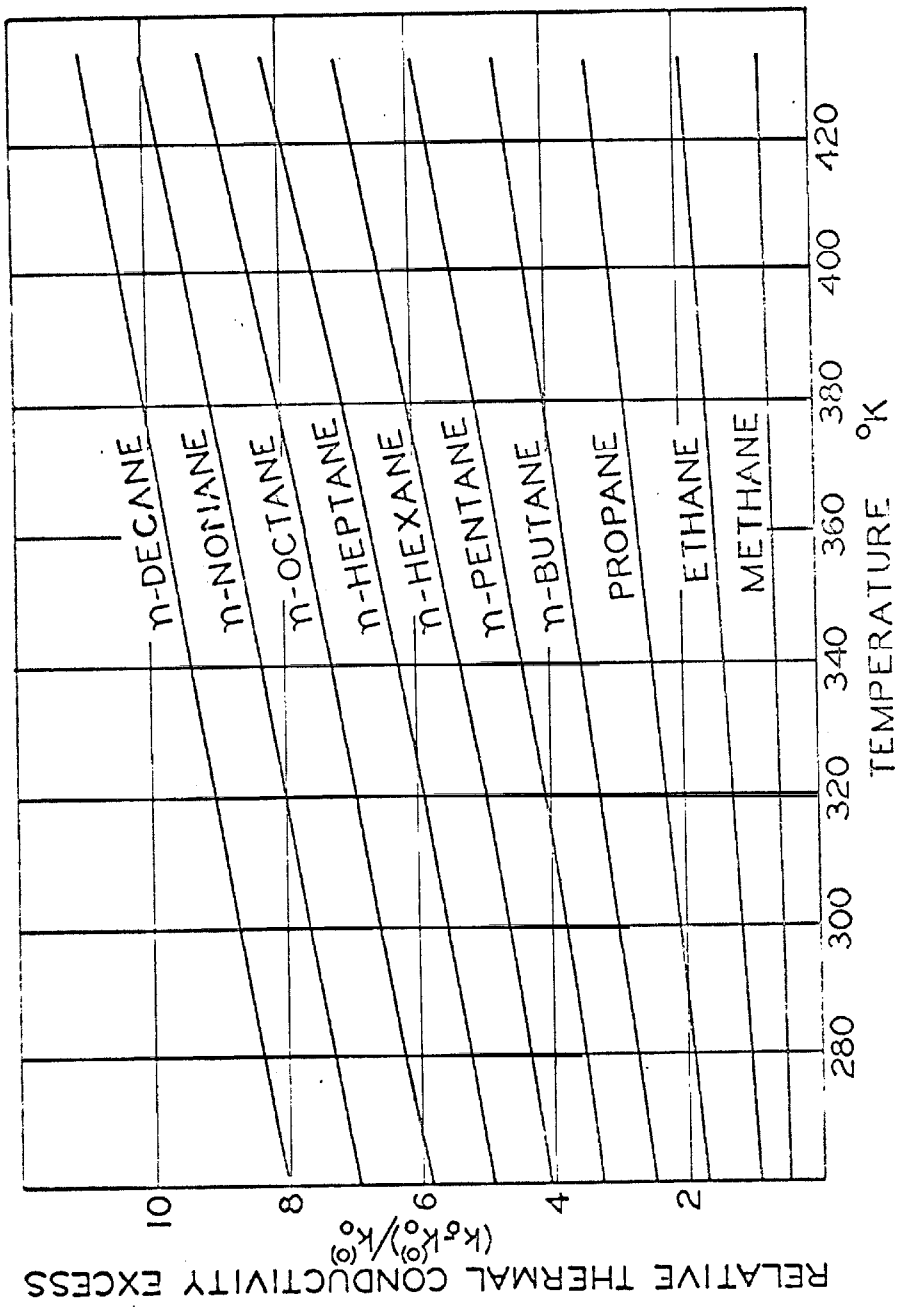

Fig. 10. Relative thermal conductivity excess for normal paraffin hydrocarbons.

"diffuse" into translational energy. The molecular relaxation time of this process depends upon the non-equilibrium distribution function and mechanism of collision. In actuality, there is a whole spectrum of relaxation times, since different types of internal degrees of freedom possess different characteristic relaxation times. By a simple unsteady state energy balance (69, 70, 72, 73) between conduction and diffusion, and a relaxation model for the change in internal to translational temperature, the contributions f_{tr} and f_{int} can be obtained. Various relaxation models are developed only from the intricacies of non-equilibrium statistical mechanics (73).

Recently, two models have been proposed (68, 69) which take into account the interactions described above between translational and rotational degrees of freedom which are important in polyatomic molecules. Mason and Monchick (68) have approximated the rigorous theory through the use of a single relaxation time, τ, to be approximated by ultrasonic absorption or shock tube experiments. Their results are:

$$f_{tr} = \frac{5}{2}\left[1 - \frac{5}{6}\left(1 - \frac{2}{5}\frac{1}{Sc_I}\right)\frac{C_{v,o,int}}{R}\frac{\eta}{P\tau}\right] \tag{15}$$

$$f_{int} = \frac{1}{Sc_I}\left[1 + \frac{5}{4}\left(1 - \frac{2}{5}\frac{1}{Sc_I}\right)\frac{\eta}{P\tau}\right] \tag{16}$$

The results are a first approximation and valid for large τ only. Saxena, Saksena, and Gambhir (69) used the Herzfeld theory of relaxation (74) to obtain the following results:

$$f_{tr} = \frac{5}{2}\left\{1 - \frac{C_{v,o,int}}{C_{v,o}}\left[1 - \exp\left(-\frac{1}{Z}\frac{C_{v,o}}{C_{v,o,tr}}\right)\right]\right\} \tag{17}$$

$$f_{int} = \frac{1}{Sc_I}\left\{1 + \frac{C_{v,o,tr}}{C_{v,o}}\left[1 - \exp\left(-\frac{1}{Z}\frac{C_{v,o}}{C_{v,o,tr}}\right)\right]\right\} \tag{18}$$

In these expressions, τ is the relaxation time, Z is the average number of collisions during time τ, and Sc_I is the Schmidt number characterizing the internal-translational diffusion process which can be estimated (68) from $5\Omega^{(1,1)*}/6\Omega^{(2,2)*}$. These results in equations 15-18 are particularly satisfactory for large relaxation times. Cowling (70) has illustrated the differences in their relaxation models.

To obtain a result which had been established empirically by the author (66) earlier, the relaxation time between f_{tr} and f_{int} was eliminated from equations 15 and 16 and f_{tr} substituted into equation 14 to obtain:

$$\frac{k_o - k_o^{(o)}}{k_o^{(o)}} = \frac{4}{15}\left[f_{int} + \frac{5}{2}\left(1 - f_{int}Sc_I\right)\right]\left(\frac{C_{P,0}}{R} - \frac{5}{2}\right) \qquad (19)$$

Repeating this procedure by eliminating the exponential term in equations 17 and 18, the same relation as in equation 19 was obtained. If the "Eucken Assumption" (58) of $f_{tr}=5/2$, $f_{int}=1$, and $Sc_I=1$ is made for rigid spheres and no internal-translational exchange is considered, the following simple relation is obtained:

$$\frac{k_o - k_o^{(o)}}{k_o^{(o)}} = 0.266\left(\frac{C_{P,0}}{R} - \frac{5}{2}\right) \qquad (20)$$

Hirschfelder (72, 75) treated the internal energy as a single quantum state and neglected any internal-translational exchange to obtain $f_{tr}=5/2$, and $f_{int}=1/Sc_I$. From the Buckingham and Lennard-Jones 12-6 potentials, Hirschfelder obtained an average value of $Sc_I=1.3275$. From equation 17 this corresponds to:

$$\frac{k_o - k_o^{(o)}}{k_o^{(o)}} = 0.354\left(\frac{C_{P,0}}{R} - \frac{5}{2}\right) \qquad (21)$$

It has been established (6, 68, 69, 73) that the approximation of $f_{tr}=5/2$ is too high and $f_{int}=1/Sc_I$ is too low. To obtain better estimates for these factors, a detailed knowledge of the relaxation time in the translational-internal exchange process is necessary. Experimental determinations of the relaxation times for the paraffins heavier than methane are quite uncertain and involve considerable extrapolation (76-78). For methane, however, reliable data exist (68, 76). From the data given by Mason (68), values of the ratio $(k_o-k_o^{(o)})/(k_o^{(o)}((C_{P,0}/R)-5/2))$ of 0.320, 0.326, 0.328, and 0.333 were obtained for temperatures of 300°, 350°, 400°, and 450° K., respectively. From the times given by Herzfeld (76), the foregoing ratio values of 0.331 and 0.316 for 109° C. and 15° C., respectively, were obtained. These results indicate that translational-rotational exchange is an important mode of excitation, as rotational relaxation times are shorter (76) than vibration relaxation times for normal cases. However, when free internal rotation is involved, as in the normal paraffins, there is some uncertainty (76) as to their relative sizes.

From an empirical basis, the following relationship was established earlier (66), and is further supported by the theoretical analysis above:

$$\frac{k_o-k_o^{(o)}}{k_o^{(o)}} = 0.3267\left(\frac{C_{P,0}}{R}-\frac{5}{2}\right) \qquad (22)$$

Extensive data for the actual isobaric heat capacity at attenuation of the paraffin hydrocarbons are available (21). The utility of equation 22, together with equations 20 and 21, is shown in figure 11. The range of temperatures and the standard errors of estimate for each of the ten normal paraffins (6, 9, 10, 20, 52-65) are shown in Table 3. The overall relative standard error of estimate was 3.16 percent. As a matter of interest, a few inorganic diatomic and monatomic molecular species (21, 79) have been included, and they also agree with the predictions of Equation 22, as may be seen in Figure 11.

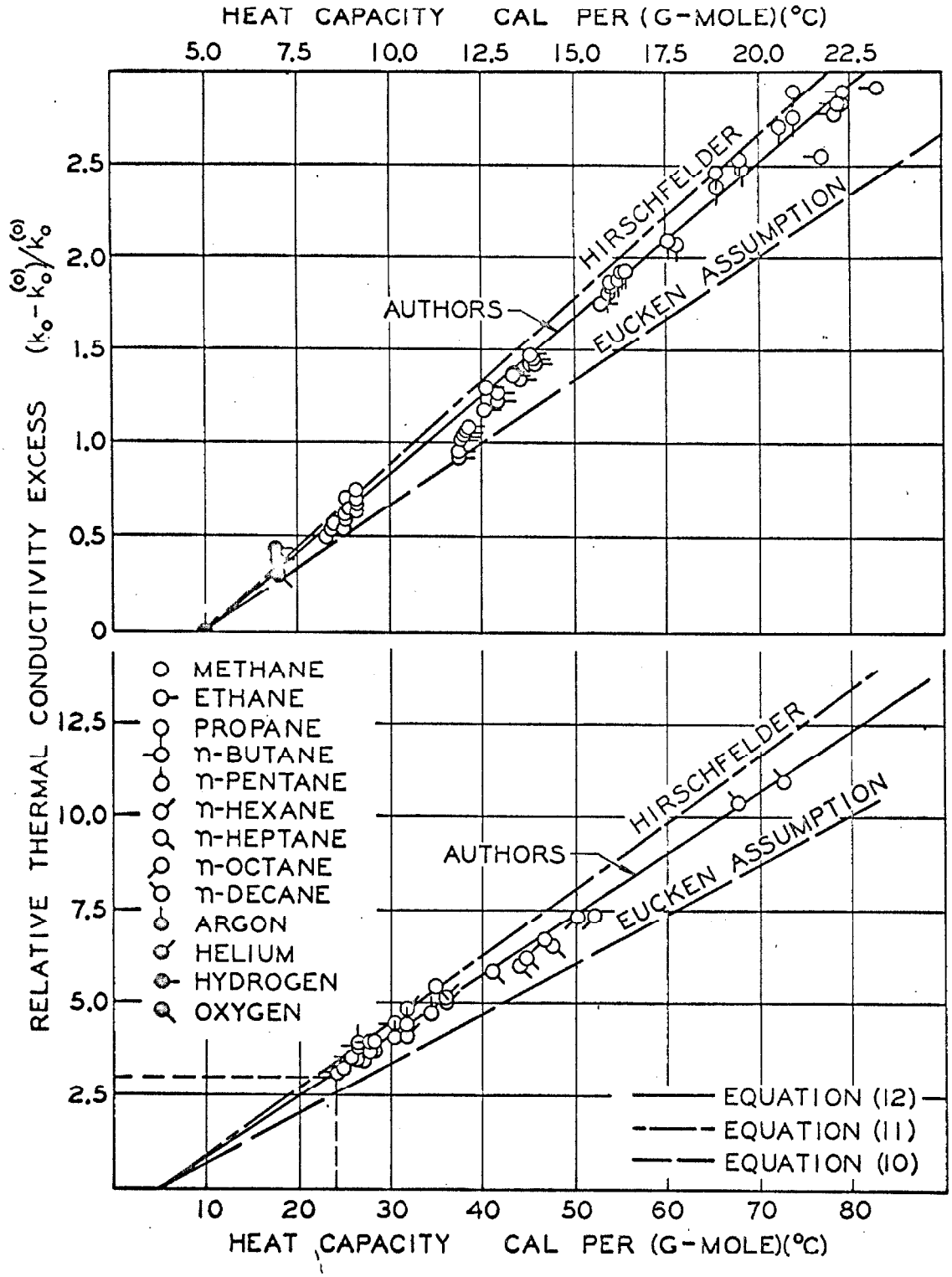

Fig. 11. Effect of heat capacity upon relative thermal conductivity excess.

TABLE 3. DEVIATIONS OF THERMAL CONDUCTIVITY AT LOW PRESSURE

Component	Number of Points	Temperature, °K. Lower	Upper	Deviation Average	Standard	Source
Methane	27	263	378	2.07%	2.48%	(6, 9, 10, 52-58, 62)
Ethane	21	273	411	3.11	4.08	(6, 9, 10, 52, 53, 57, 58, 60, 63)
Propane	16	273	379	2.29	2.96	(6, 9, 10, 52, 60)
n-Butane	16	273	411	2.67	3.76	(6, 10, 52, 59, 64)
n-, iso-Pentane	7	273	373	3.30	4.55	(6, 10, 51, 52)
n-Hexane	4	273	339	3.85	4.66	(6, 51, 52, 61)
n-Heptane	5	273	373	4.82	6.08	(6, 51, 52, 61)
n-Octane	3	311	355	2.53	3.58	(6, 20)
n-Nonane	0	-	-	-	-	
n-Decane	3	378	444	4.94	4.92	(65)

Correlation equation: $(k_o - k_o^{(o)})/k_o^{(o)} = 0.3267\left(\frac{C_{P,0}}{R} - \frac{5}{2}\right)$

Average fractional deviation deviation defined by: $\left[\sum_1^n \left| (k_c - k_p)/k_e \right| \right]_o / N$

Fractional standard deviation defined by: $\left\{\sum_1^N \left[(k_e - k_p)/k_e\right]_o^2 / (N-1)\right\}^{1/2}$

The rigorous theory of polyatomic gases by deBoer (73) can be utilized to develop a rigorous equation for the excess conductivity, although currently there are no quantitative means of evaluating the numerous coefficients. Again the theoretical quantities are reduced by their rigid sphere values which define the coefficients β_{tt} and β_{ii}:

$$a_{tt} = 4\,\Omega^{(t)} + \frac{11}{2}\,\Omega^{(\tau)} = \beta_{tt}\,4\,\Omega^{(2,2)} \tag{23}$$

$$a_{ii} = 4\,\Omega^{(i)} + \frac{3}{2}\,\Omega^{(\tau)} = \beta_{ii}\,4\,\Omega^{(1,1)}\,\frac{C_{v,o,int}}{R} \tag{24}$$

$$a_{it} = -\frac{5}{2}\,\Omega^{(\tau)} \tag{25}$$

The symbols $\Omega^{(t)}$, $\Omega^{(i)}$, and $\Omega^{(\tau)}$ represent collision integrals of non-equilibrium states involving translation, internal motion, and relaxation mechanisms, and currently have not been evaluated. The conductivity as an excess ratio can be expressed as:

$$\frac{k_o - k_o^{(o)}}{k_o^{(o)}} = \frac{1}{\beta_{tt} + \dfrac{a_{it}^{\,2}\,R}{16\beta_{ii}\Omega^{(1,1)}\Omega^{(2,2)}C_{v,o,int}}} \left\{ \frac{4}{25}\,\frac{\beta_{tt}\Omega^{(2,2)}}{\beta_{ii}\Omega^{(1,1)}} + \right.$$

$$\left. \frac{R}{C_{v,o,int}} \left[(1-\beta_{tt}) - \frac{1}{5}\,\frac{a_{it}}{\beta_{ii}\Omega^{(1,1)}} \left(1 - \frac{5}{16}\,\frac{a_{it}R}{\beta_{tt}\Omega^{(2,2)}C_{v,o,int}}\right)\right] \right\} \left(\frac{C_{P,0}}{R} - \frac{5}{2}\right) \tag{26}$$

For very large polyatomic molecules ($C_{v,int} \gg R$, and $\beta_{ii} \simeq \beta_{tt}$) there results:

$$\frac{k_o - k_o^{(o)}}{k_o^{(o)}} = \frac{8}{25}\,\frac{\Omega^{(2,2)*}}{\beta_{tt}\,\Omega^{(1,1)*}} \left(\frac{C_{P,0}}{R} - \frac{5}{2}\right) \tag{27}$$

From the empirical coefficient in equation 22, the order of magnitude of the

quantity β_{tt} can be estimated at T*=1.0; thereby obtaining an estimate for $\Omega^{(\tau)}$ as around 0.07. To date no theoretical computations have been made for this collision integral. Equation 25 indicates that all terms of Equation 26 involving a_{it}^2 will be around three orders of magnitude less than the remaining terms, so that Equation 26 can be simplified for polyatomic molecules as:

$$\frac{k_o - k_o^{(o)}}{k_o^{(o)}} = \left\{ \frac{8\Omega^{(2,2)*}}{25\beta_{tt}\Omega^{(1,1)*}} + \frac{R}{C_{v,o,int}} \left[(1-\beta_{tt}) - \frac{1}{5} \frac{a_{it}}{\beta_{ii}\Omega^{(1,1)}} \right] \right\} \left(\frac{C_{P,0}}{R} - \frac{5}{2} \right) \qquad (28)$$

Equation 28 differs from Equation 27 by 0.2% for typical conditions covered in this investigation. These results would indicate that the linear relationship shown in Figure 11 would actually be very slightly (0.25%) concave downward. Therefore, the useful near-linear relationship shown in Figure 11 has, indeed, sound theoretical justification from various models of relaxation as in Equations 15-21, and 26.

The thermal conductivity for dense polyatomic fluids at higher pressures can be estimated from the Enskög theory (1) analogous to that discussed for viscosity. For rigid spheres the result is:

$$\frac{k - k_o}{k_o} = \frac{(1.2Y - 0.6250)\rho^* + (0.755Y^2 - 0.2869)(\rho^*)^2 - 0.115(\rho^*)^3}{1 + 0.6250\rho^* + 0.7869(\rho^*)^2 + 0.115(\rho^*)^3} \qquad (29)$$

Correcting the error in the earlier development (1)*, the quantity k_o is the thermal conductivity of a polyatomic gas at low pressure (or "attenuation") from Equation 22. Again Y is a function of the reduced density as in Equation 3, and the excess conductivity ratio for rigid spheres becomes a function of the reduced density alone:

$$\frac{k-k_o}{k_o} = f_2(\rho^*) \text{ only} \tag{30}$$

The use of Pitzer's acentric factor or the virial equation of state results in an equation analogous to Equations 8 and 9. Again the behavior of real gases are expected to asymptotically approach Equation 29 as the temperature is increased. For thermal conductivity also precise experimental measurements (62-64) indicate that $k-k_o$ is very nearly invariant with temperature, which suggests a result analogous to Equation 10:

$$\frac{k-k_o}{\sigma^{-2}\sqrt{m\epsilon}} = \breve{\Phi}_3^{(0)}(\rho^*, \omega) + \omega\, \breve{\Phi}_3^{(1)}(\rho^*) + \ldots \tag{31}$$

No work has been done to date in investigating the utility of such a relationship, but it is expected to be as successful as the corresponding relation for viscosity at moderate densities. At the higher densities, however, the internal degrees of freedom will become more restricted and contribute proportionately less to the conductivity.

---

* See Proposition E for correction of this error.

BINARY MIXTURES

Simple monatomic, diatomic and triatomic non-polar molecules in binary mixtures have been adequately studied (1), and methods of prediction from statistical mechanics have been adequate. Simple cases of polar species have also been treated (1). However, for binary mixtures including one polyatomic specie with a simple second component such as a diatomic, the methods of prediction have not been extensively tested. The transport properties of molecular diffusion, viscosity, and thermal conductivity in binary mixtures of a paraffin hydrocarbon and a diatomic molecule are analyzed.

MOLECULAR DIFFUSION

The data for gaseous binary diffusion coefficients of the paraffins with other gaseous species are limited (80-85), and examples are shown in Figure 12 for a pressure of one atmosphere. Data available (80-84) for binary molecular diffusion of a paraffin with an inorganic, diatomic molecule such as nitrogen, oxygen, or less exactly for air, are tabulated in Table 4 and in Appendix A5 in Engineering units. The solid curves were established from the Chapman-Cowling theory (1) for diffusion as follows:

$$[\mathcal{D}_{12}]_o^{(k)} = 2.6280 \times 10^{-3} f_{\mathcal{D}}^{(k)} \frac{T^3 (M_1+M_2)/2M_1M_2}{P\sigma_{12}^2 \Omega^{(1,1)*}} \qquad (32)$$

The quantity, $\Omega^{(1,1)*}$, was evaluated from the Lennard-Jones 12-6 potential. The binary collision diameter was taken as the arithmetic mean of the component collision diameters obtained from measurements of viscosity at attenuation. For the energy of attraction, the deviation from the geometric mean (1) was taken to be a function of the product of the molecular weights and the absolute temperature, and is illustrated in Figure 13. Binary mixtures of hydrogen,

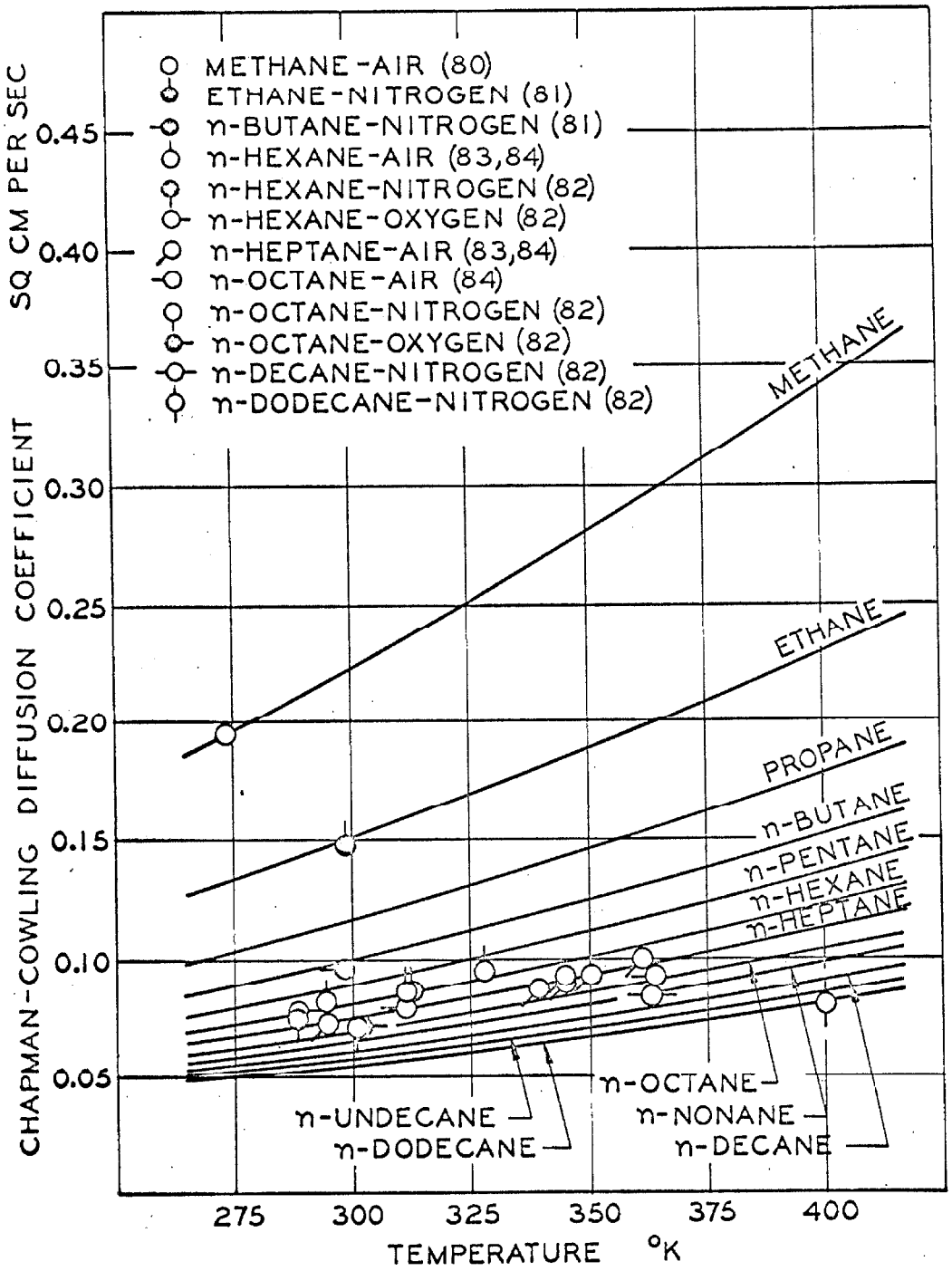

Fig. 12. Chapman-Cowling diffusion coefficients for binary systems at one atmosphere.

TABLE 4. GASEOUS BINARY DIFFUSION COEFFICIENTS

Atmospheric Pressure

Component 1	Component 2	Temperature °C.	σ_{12} · A	ϵ_{12}/k °K.	$\mathcal{D}_{12}$ cm^2/sec	Source
Air	Methane	0.	3.663	106.4	0.196	(80)
Air	n-Hexane	20.9	4.998	111.2	0.0803	(83)
		37.6	4.998	130.1	0.0843	(83)
		37.8	4.998	130.1	0.0862	(84)
		54.5	4.998	126.6	0.0933	(83)
Air	n-Heptane	20.9	5.188	132.2	0.0710	(83)
		37.6	5.188	139.6	0.0775	(83)
		65.6	5.188	144.2	0.0870	(84)
		71.0	5.188	145.2	0.0917	(83)
		71.1	5.188	145.3	0.0912	(84)
		76.7	5.188	147.2	0.0938	(84)
		87.8	5.188	151.1	0.0986	(83)
Air	n-Octane	90.6	5.358	152.2	0.0932	(84)
Nitrogen	Ethane	25.	4.066	128.5	0.148	(81)
Nitrogen	n-Butane	25.	4.620	148.3	0.0960	(81)
Nitrogen	n-Hexane	15.	5.030	126.4	0.0757	(82)
Nitrogen	n-Octane	30.	5.390	121.3	0.0710	(82)
Nitrogen	n-Decane	90.	5.720	129.2	0.0841	(82)
Nitrogen	n-Dodecane	126.	6.030	173.7	0.0813	(82)
Oxygen	n-Hexane	15.	4.906	125.8	0.0753	(82)
Oxygen	n-Octane	30.	5.266	121.7	0.0705	(82)

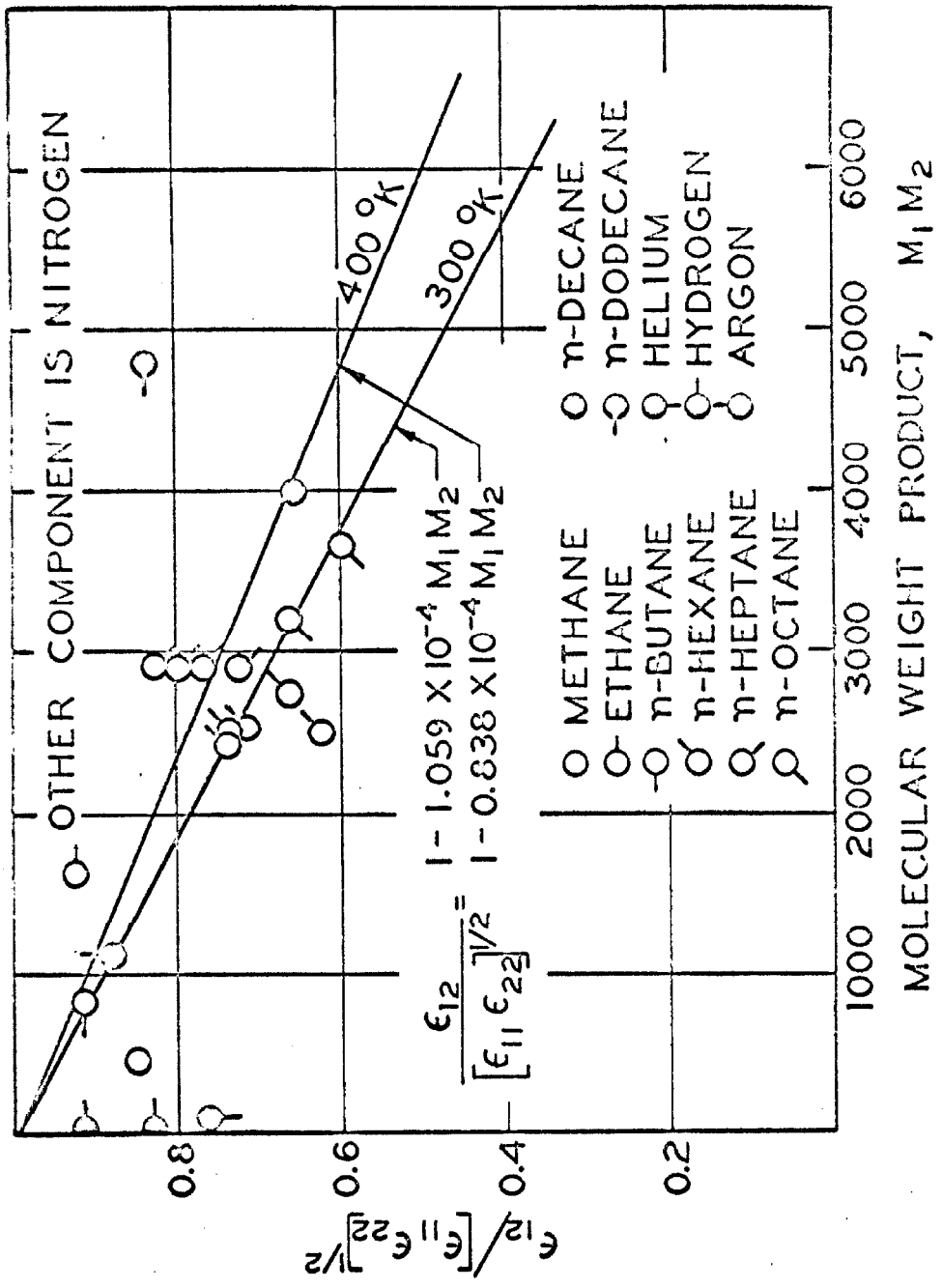

Fig. 13. The "well depth" of the Lennard-Jones 12-6 potential.

helium, and argon with nitrogen are included for comparison. Although the scatter is considerable, some trends are apparent. It is noted (1) that the Lennard-Jones 12-6 collision integrals are only a weak function of the energy of attraction; therefore, these energies need to be evaluated only approximately. A reduced plot of the experimental binary diffusion data shown in Figure 12 is shown in Figure 14 to illustrate that the Lennard-Jones 12-6 potential is useful in predicting molecular diffusion when the energy of attraction, ϵ/k, is treated as temperature dependent. More complete diffusion coefficient data are necessary before a meaningful analysis using the Morse and Kihara potentials is feasible.

The composition dependence for the binary system nitrogen-heptane at 310.9° K. was calculated by the procedure set forth by Hirschfelder (1). The diffusion coefficient was found to go through a weak maximum near 30 mole percent nitrogen which was 0.5 percent higher than the value for 100 percent nitrogen. The value for 0 mole percent nitrogen was 0.1 percent above the 100 percent nitrogen value. This dependence should be negligible for most transport studies.

The effects of pressure on the binary diffusion coefficient for dense polyatomic fluids are not well established experimentally. Enskög's theory (1) for dense fluids composed of rigid, spherical molecules indicates that:

$$\frac{P\mathcal{D}_{12} - (P\mathcal{D}_{12})_o}{(P\mathcal{D}_{12})_o} = \rho_1^* \left(\frac{\sigma_1/4 + \sigma_2}{\sigma_1 + \sigma_2}\right) + \rho_2^* \left(\frac{\sigma_2/4 + \sigma_1}{\sigma_1 + \sigma_2}\right) + \ldots \qquad (33)$$

This relation has not been compared with experimental data.

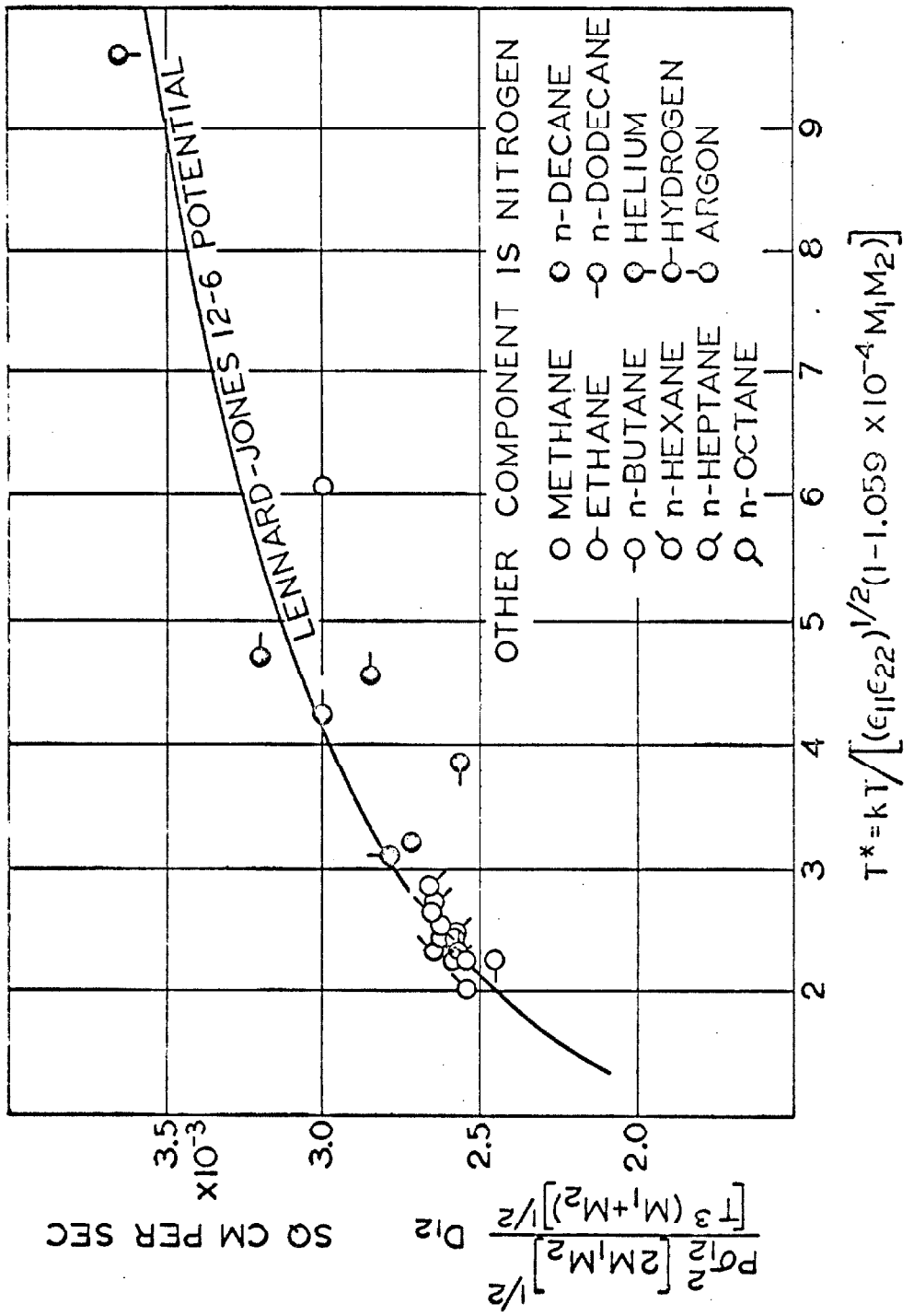

Fig. 14. The Chapman-Cowling diffusion coefficient.

VISCOSITY

Experimental measurements are available for the binary system, nitrogen-heptane, at 344.3° K. at a pressure below 0.15 atmosphere (20). The experimental results are shown in Figure 15 along with the viscosity of pure n-heptane (20) and nitrogen (79). The solid curves were calculated from a mixing rule of the Chapman-Cowling form of (1, Eqn. 8.2-22) with empirical coefficients:

$$\frac{\beta_\eta}{\eta_{mix}} = \frac{x_1^2}{\eta_{11}} + \frac{2x_1x_2}{\eta_{12}} + \frac{x_2^2}{\eta_{22}} \tag{34}$$

Since β_η is commonly near unity (1), the functional dependence upon composition can be represented empirically for a limited temperature range by the following simple expression:

$$\beta_\eta = 1 + C_\eta x_1 x_2 \tag{35}$$

The calculated viscosities presented in Figure 15 were obtained by taking η_{12} and C_η as empirical coefficients. For the nitrogen-heptane system, the empirical value of β_η at a mole fraction of 0.50 nitrogen was found to be 1.0137 and η_{12} was 99.58 micropoise. A value of η_{12} of 92.2 micropoise was obtained from Equation 1, utilizing the harmonic mean molecular weight, arithmetic mean collision diameter, and geometric mean energy of attraction. A harmonic mean of the pure component viscosities yielded a value of 102.6 micropoises for the system of nitrogen-heptane. A quantity α_η can be taken as a constant for all similar systems as follows:

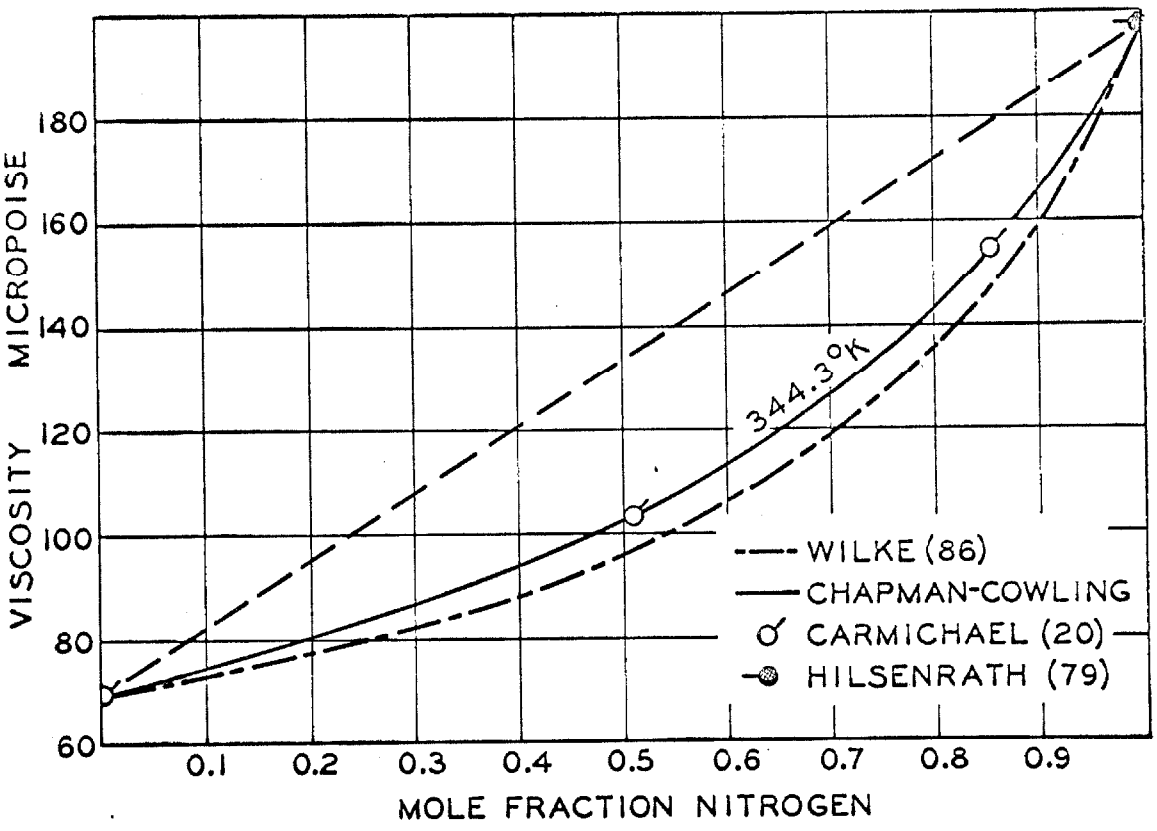

Fig. 15. Viscosity of nitrogen-n-heptane system at attenuation.

$$\alpha_\eta = \frac{\eta_{12}(\eta_{11} + \eta_{22})}{\eta_{11}\,\eta_{22}} = 1.9390 \qquad (36)$$

The numerical value of 1.9390 for α_η was obtained from the empirical coefficients of Equation 18 for the nitrogen-heptane system.

The binary viscosity parameter, η_{12}, is also of value in the prediction of the binary diffusion coefficient from the following in which A* may be computed by the method of Hirschfelder (1):

$$\mathcal{D}_{12} = \frac{3}{5}\,\frac{M_1 + M_2}{M_1 M_2}\,\frac{A_{12}^{*}\,RT}{P}\,\eta_{12} \qquad (37)$$

In the nitrogen-heptane binary system at 344.3° K., this relation predicted 0.0864 cm^2/sec which compared with an experimental value for air-heptane of 0.09121 shown in Figure 12. Also shown for comparison in Figure 15 is the prediction of binary viscosity by the method proposed by Wilke (86), which is significantly lower than the experimental data (20).

THERMAL CONDUCTIVITY

As an example of thermal conductivity measurements for mixtures of a diatomic and a polyatomic gas, the measurements of the nitrogen-heptane system at a pressure of 0.15 atmosphere are shown in Figure 16 (4,13). Owing to the internal degrees of freedom of the polyatomic molecule, the prediction of thermal conductivity at attenuation is more difficult. The following relation given by Hirschfelder (1),

$$k_{mix} = \frac{15}{4} \left(\frac{R}{x_1 M_1 + x_2 M_2} \right) \eta_{mix} \tag{38}$$

was not useful even when a correction for a polyatomic molecule was made on the basis of Figure 11. A comparison is shown in Figure 16 with the empirical method of Lindsay and Bromley (87) as well as with the semi-empirical results of Mason (88). Both of these methods of prediction yield values lower than the experimental results. A more satisfactory approach appears to involve a theoretical relation based on the form of Equation 24 (1, Eqn. 8.2-36):

$$\frac{\beta_k}{k_{mix}} = \frac{x_1^2}{k_{11}} + \frac{2x_1x_2}{k_{12}} + \frac{x_2^2}{k_{22}} \tag{39}$$

The quantity, β_k, was approximated from a relation of the form of Equation 25. For the data in Figure 16, the value for β_k at a composition of 0.5 mole fraction nitrogen was 1.1943 and k_{12} was 3.1433×10^{-5} cal/sec-cm-° C. The quantity, α_k, in the following equation may be of utility in approximating the thermal conductivity of other similar binary systems at attenuation:

$$\alpha_k = \frac{k_{12}(k_{11} + k_{22})}{k_{11}k_{22}} = 1.272 \tag{40}$$

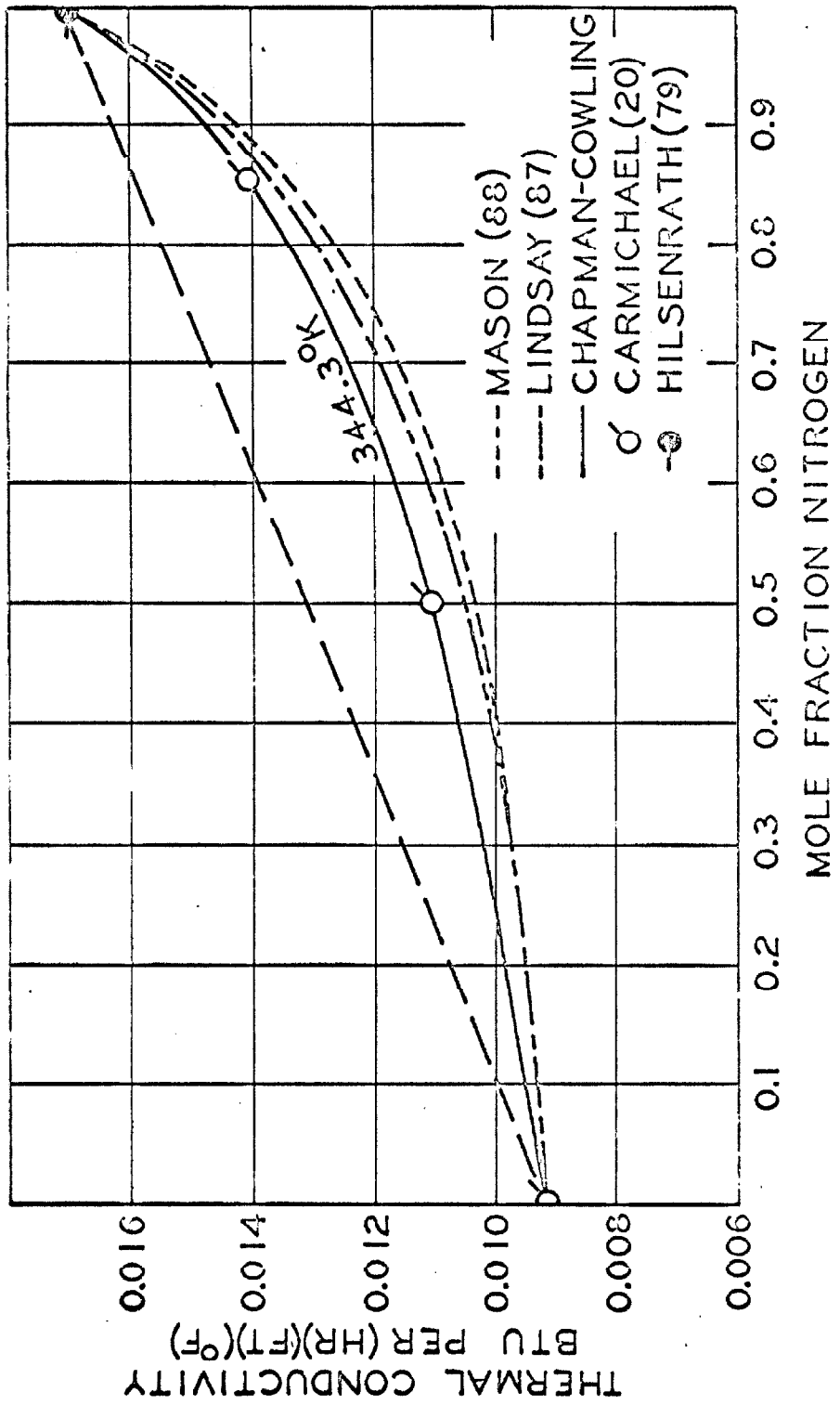

Fig. 16. Thermal conductivity of nitrogen-n-heptane system at attenuation.

The numerical value of α_k of 1.272 was based upon the empirical coefficients of Equation 29 for the nitrogen-heptane system. It will be necessary to obtain further experimental data for binary polyatomic systems in order to permit the utility of Equations 39 and 40 to be established.

REFERENCES

1. HIRSCHFELDER J. O., CURTISS C. F. and BIRD R. B., Molecular Theory of Gases and Liquids, Second Printing, John Wiley & Sons, Inc., New York 1964.
2. CARMICHAEL L. T., BERRY VIRGINIA and SAGE B. H., J. Chem. Eng. Data 1965 10 57.
3. KESTIN J. and LEIDENFROST W., Physica 1959 25 1033.
4. TRAUTZ MAX and SORG K. G., Ann. Physik 1931 Ser. 5, 10 81.
5. KUSS E., Z. Angew. Phys. 1952 4 203.
6. LAMBERT J. D., COTTON K. J., PAILTHORPE M. W., ROBINSON A. M., SCRIVINS J., VALE W. R. F. and YOUNG R. M., Proc. Roy. Soc. (London) 1955 231 A 280.
7. SAGE B. H. and LACEY W. N., Trans. AIME 1938 127 118.
8. CARMICHAEL L. T. and SAGE B. H., J. Chem. Eng. Data 1963 8 94.
9. SVEHLA R. A., N.A.S.A. Tech. Rep. R-132, 1962.
10. SENFTLEBEN HERMANN and GLADISCH HEINZ, Z. Physik 1949 125 653.
11. CARMICHAEL L. T., BERRY VIRGINIA M. and SAGE B. H., J. Chem. Eng. Data 1964 9 411.
12. BICHER L. B. Jr., and KATZ D. L., Industr. Engng. Chem. 1943 35 754.
13. TRAUTZ MAX and KURZ FRIEDRICH, Ann. Physik 1931 Ser. 5, 9 981.
14. SAGE B. H. and LACEY W. N., Industr. Engng. Chem. 1938 30 829.
15. CARMICHAEL L. T. and SAGE B. H., J. Chem. Eng. Data 1963 8 612.
16. TITANI TOSHIZO, Bull. Chem. Soc. Japan 1929 4 277.
17. TITANI TOSHIZO, Bull. Chem. Soc. Japan 1930 5 98.

18. SAGE B. H., YALE W. D. and LACEY W. N., Industr. Engng. Chem. 1939 31 223.

19. MELAVEN R. M. and MACK EDWARD Jr., J. Am. Chem. Soc. 1932 54 888.

20. CARMICHAEL L. T. and SAGE B. H., A.I.Ch.E.J. 1966 12 559.

21. Am. Petroleum Inst. Res. Project 44, Chemical Thermodynamic Properties Center, Texas A & M Univ. Selected Values of Properties of Hydrocarbons and Related Compounds.

22. SAGE B. H., Thermodynamics of Multicomponent Systems, pp. 147-148, Reinhold Publishing Corp., New York 1965.

23. DUSHMAN SAUL, Scientific Foundations of Vacuum Technique, pp. 43-53. John Wiley & Sons, Inc., New York 1962.

24. CHAPMAN SYDNEY and COWLING T. G., Mathematical Theory of Non-Uniform Gases, Cambridge Univ. Press, New York 1939.

25. FLYNN L. W. and THODOS GEORGE, A.I.Ch.E.J. 1962 8 362.

26. PITZER K. S., J. Am. Chem. Soc. 1955 77 3427.

27. PITZER K. S., LIPPMANN D. Z., CURL R. F. Jr., HUGGINS C. M. and PETERSEN D. E., J. Am. Chem. Soc. 1955 77 3433.

28. KONOWALOW D. D., Phys. Fluids 1966 9 23.

29. BARKER J. A., FOCK W. and SMITH F., Phys. Fluids 1964 7 897.

30. O'CONNELL J. P. and PRAUSNITZ J. M., Advances in Thermophysical Properties at Extreme Temperatures and Pressures, pp. 19-32 ASME, 1965.

31. O'CONNELL J. P. and PRAUSNITZ J. M., Amer. Documen. Inst., Washingt D. C., Document No. 8432, 1965.

32. KONOWALOW D. D., TAYLOR M. H. and HIRSCHFELDER J. O., Phys. Fluids 1961 4 622.

33. KONOWALOW D. D. and HIRSCHFELDER J. O., Phys. Fluids 1961 4 629.

34. KONOWALOW D. D. and SERGIO CARRA, Phys. Fluids 1965 8 1585.

35. LOVELL S. E. and HIRSCHFELDER J. O., Theoretical Chemistry Laboratory, University of Wisconsin, Report WIS-AF-19, Series 5, Dec. 20, 1961.

36. OLDS R. H., REAMER H. H., SAGE B. H. and LACEY W. N., Industr. Engng. Chem. 1943 35 922.

37. CORCORAN W. H., BOWLES R. R., SAGE B. H. and LACEY W. N., Industr. Engng. Chem. 1945 37 825.

38. REAMER H. H., OLDS R. H., SAGE B. H. and LACEY W. N., Industr. Engng. Chem. 1944 36 956.

39. BARKELEW C. H., VALENTINE J. L. and HURD C. O., Chem. Engng. Progr. 1947 43 25.

40. REAMER H. H., SAGE B. H. and LACEY W. N., Industr. Engng. Chem. 1949 41 482.

41. OLDS R. H., REAMER H. H., SAGE B. H. and LACEY W. N., Industr. Engng. Chem. 1944 36 282.

42. YOUNG SYDNEY, Sci. Proc. Roy. Dublin Soc. 1909-10 12 374-443.

43. SAGE B. H. and LACEY W. N., Industr. Engng. Chem. 1942 34 730.

44. KOZICKI WILLIAM and SAGE B. H., J. Chem. Eng. Data 1960 5 331.

45. STEWART D. E., SAGE B. H. and LACEY W. N., Industr. Engng. Chem. 1954 46 2529.

46. HUISMAN JOHN and SAGE B. H., J. Chem. Eng. Data 1964 9 223.

47. NICHOLS W. B., REAMER H. H. and SAGE B. H., Industr. Engng. Chem. 1955 47 2219.

48. CARMICHAEL L. T., SAGE B. H. and LACEY W. N., Industr. Engng. Chem. 1953 45 2697.

49. COUCH H. T., KOZICKI WILLIAM and SAGE B. H., J. Chem. Eng. Data 1963 8 346.

50. REAMER H. H., OLDS R. H., SAGE B. H. and LACEY W. N., Industr. Engng. Chem. 1942 34 1526.

51. MOSER, Dissertation (Berlin) 1913, Chemical Engineer's Handbook, Third Edition, John H. Perry, Ed., McGraw-Hill Book Co., 1950, p. 461.

52. MANN W. B. and DICKINS B. G., Proc. Roy. Soc. (London) 1931 134 Series A, 77.

53. KEYES F. G., Trans. Amer. Soc. Mech. Engrs. 1954 76 809.

54. JOHNSTON H. L. and GRILLY E. R., J. Chem. Phys. 1946 14 233.

55. KANNULUIK W. B. and DONALD H. B., Austral. J. Sci. Res. 1950 3 417.

56. LENOIR J. M. and COMINGS E. W., Chem. Engng. Progr. 1951 47 223.

57. LENOIR J. M., JUNK W. A. and COMINGS E. W., Chem. Engng. Progr. 1953 49 539.

58. EUCKEN A., Physik Z. 1913 14 324.

59. KRAMER F. R. and COMINGS E. W., J. Chem. Eng. Data 1960 5 462.

60. LENG D. E. and COMINGS E. W., Industr. Engng. Chem. 1957 49 2042.

61. LAMBERT J. D., STAINES E. N. and WOODS S. D., Proc. Roy. Soc.(London) 1950 A200 262.

62. CARMICHAEL L. T., REAMER H. H. and SAGE B. H., J. Chem. Eng. Data 1966 11 52.

63. CARMICHAEL L. T., BERRY VIRGINIA and SAGE B. H., J. Chem. Eng. Data 1963 8 281.

64. CARMICHAEL L. T. and SAGE B. H., J. Chem. Eng. Data 1964 9 511.

65. CARMICHAEL L. T. and SAGE B. H., "Thermal Conductivity of n-Decane," Calif. Inst. Tech., to be published.

66. GALLOWAY T. R. and SAGE B. H., "Transport Properties of the Normal Paraffins at Attenuation," accepted by Chemical Engineering Science.

67. SAXENA S. C., SAKSENA M. P., GAMBHIR R. S. and GANDHI J. M., Physica 1965 31 333.

68. MASON E. A. and MONCHICK L., J. Chem. Phys. 1962 36 1622.

69. SAXENA S. C., SAKSENA M. P. and GAMBHIR R. S., Brit. J. Appl. Phys. 1964 15 843.

70. COWLING T. G., Brit. J. Appl. Phys. 1964 15 959-962.

71. SMITH J. J. and MUNN R. J., J. Chem. Phys. 1964 41 3560.

72. HIRSCHFELDER J. O., J. Chem. Phys. 1957 26 282.

73. DE BOER J. and UHLENBECK G. E., Studies in Statistical Mechanics, North-Holland Pub. Co., Amsterdam, 1964.

74. HERZFELD K. F., Thermodynamics and Physics of Matter, F. D. Rossini, Ed., Section H, Princeton University Press, N. J. 1955.

75. HIRSCHFELDER J. O., J. Chem. Phys. 1957 26 274.

76. HERZFELD K. F. and LITOVITZ T. A., Absorption and Dispersion of Ultrasonic Waves, Academic Press, 1959.

77. MASON W. P., (Edit.), Physical Acoustics - Principles and Methods, Vol. II, Part A, Academic Press, 1965.

78. NOZDREV V. F., The Use of Ultrasonics in Molecular Physics, Pergamon Press Ltd., 1965.

79. HILSENRATH J. et al., Tables of Thermal Properties of Gases, Natl. Bur. Std. (U.S.) Circ. No. 564, 1955.

80. COWARD H. F. and GEORGESON E. H. M., J. Chem. Soc. (London) 1937 Part II, 1085.

81. BOYD C. A., STEIN NORMAN, STEINGRIMSSON VIRGINIA and RUMPEL W. F., J. Chem. Phys. 1951 19 548.

82. CUMMINGS G. A. Mc. D. and UBBELOHDE A. R., J. Chem. Soc. (London) 1953 Part 4 3751.

83. SCHLINGER W. G., REAMER H. H., SAGE B. H. and LACEY W. N., "Diffusion Coefficients in Hydrocarbon Systems. n-Hexane and n-Heptane in Air," Fundamental Research on Occurrence and Recovery of Petroleum, 1952-1953, Am. Petroleum Inst., pp. 70-106.

84. REAMER H. H. and SAGE B. H., "Total Schmidt Numbers in Turbulent Material Transport," Calif. Inst. Tech., to be published.

85. International Critical Tables, Vol. V, p. 62, McGraw-Hill Book Co., Inc., New York, 1929.

86. WILKE C. R., J. Chem. Phys. 1950 18 517.

87. LINDSAY A. L. and BROMLEY L. A., Industr. Engng. Chem. 1950 42 1508.

88. MASON E. A. and SAXENA S. C., Phys. Fluids 1958 I 361-369.

NOMENCLATURE

a_{ii} = deBoer interaction coefficients (see text Eqn. 24)

a_{it} = deBoer interaction coefficients (see text Eqn. 25)

a_{tt} = deBoer interaction coefficients (see text Eqn. 23)

A^* = Ratio of collision integrals $\Omega^{(1,1)^*}/\Omega^{(2,2)^*}$

b_o = Molecular co-volume $= \frac{2}{3}\pi N_o \sigma^3$ (cc/gmole)

B = Second virial coefficient (cc/gmole)

B^* = Reduced Second virial coefficient $= B/b_o$

C = Third parameter of the Morse potential

C = Empirical coefficient

C = Third Virial coefficient $(cc^2/gmole^2)$

C^* = Reduced third virial coefficient $= C/b_o^2$

$C_{P,0}$ = Isobaric heat capacity at low pressure limit (cal/gmole-° C.)

$C_{V,0}$ = Isochoric heat capacity at low pressure limit (cal/gmole-° C.)

$\mathfrak{D}$ = Binary diffusion coefficient (from Chapman-Cowling) (cm^2/sec)

f = Correction factor, function of reduced temperature T^*

f = Fractional contribution to thermal conductivity, defined in Eqn. 4

k = Boltzman's constant (erg/gmole-° K.)

k = Thermal conductivity (cal/sec-cm-° C.)*

k_o = Thermal conductivity at the low pressure limit (cal/sec-cm-° C.)

$k_o^{(o)}$ = Configurational thermal conductivity at the low pressure limit (cal/sec-cm-° C)

l = Heat of vaporization (cal/gmole)

m = Molecular mass $= M/N_o$ (gm/molecule)

M = Molecular weight (gm/gmole)

N = Number of points

N_o = Avagadro's number (molecules/gmole)

P = Total pressure (atmos. or dynes/cm^2)

R = Universal gas constant (cal/gmole-° K.)

Sc_I = Schmidt number for the internal-translational diffusion process

T = Absolute temperature (° K.)

T_c = Critical temperature (° K.)

T_R = Reduced temperature = T/T_c

T^* = Reduced temperature = kT/ϵ

U_o = Energy of attraction (potential well depth) for Kihara potential (erg/gmole-°K)

V = Molal volume (cc/gmole)

V_b = Bubble point volume (cc/gmole)

x = Mole fraction

Y = Rate of collision increase (dimensionless)

Z = Average number of collisions during time, τ

$Z^{(n)}$ = Pitzer's compressibility factor, n=0, 1, 2, ... (see text Eqn. 7)

GREEK

α = Measure of deviation from geometric mean

β = Molecular disparity function (see text Eqns. 34, 39)

β_{tt} = Dimensionless deBoer translational interaction coefficient = $a_{tt}/4\ \Omega^{(2,2)}$

β_{ii} = Dimensionless deBoer internal interaction coefficient = $a_{ii}/4\ \Omega^{(1,1)} C_{v,o,int}/R$

γ = Ratio of Kihara core diameter to collision diameter

δ = Collision diameter for Kihara potential

ϵ = Energy of attraction (potential well depth) for Lennard-Jones (n-6) and Morse potentials (erg/gmole-°K.)

η = Viscosity (shear) (micropoise)

η_o = Viscosity at the low pressure limit (micropoise)

τ = Molecular internal-translational relaxation time (microseconds)

ρ^* = Reduced density = $b_o/V = \frac{2}{3}\pi N_o \sigma^3$ (dimensionless)

σ = Collision diameter for Lennard-Jones (n-6) or Morse potentials (Å)

$\Omega^{(t)}$ = Non-equilibrium collision integral involving translation

$\Omega^{(i)}$ = Non-equilibrium collision integral involving internal motion

$\Omega^{(\tau)}$ = Non-equilibrium collision integral involving relaxation phenomena

$\Omega^{(1,1)*}$ = Collision integral, reduced by rigid sphere value

$\Omega^{(2,2)*}$ = Collision integral, reduced by rigid sphere value

ω = Pitzer's acentric factor (see text Eqn. 7)

SUBSCRIPTS

1 = for component 1

2 = for component 2

$\mathcal{D}$ = for diffusion

int = for internal degrees of freedom

k = for thermal conductivity

mix = for a binary mixture

nbp = at the normal boiling point

p = predicted

s = smoothed (solid curves in Figure 1)

tr = for translational degrees of freedom

η = for viscosity

o = at the low pressure ("attenuation")

SUPERSCRIPTS

(o) = configurational quantity

(k) = kth approximation

* = value normalized by reference to rigid sphere quantity

---

* The symbol, k, corresponds to the symbol, λ, widely used in international scientific literature for thermal conductivity.

PART I

APPENDICES

APPENDIX A 1

In the following table are included the smoothed values of the viscosity obtained from a plot of viscosity as a function of temperature and pressure. At the zero pressure limit, extrapolated graphically, the viscosity is presented at "attenuation" as well as the approximate isothermal derivative of viscosity with pressure. A value of viscosity is also given at either one atmosphere pressure or at the dew point, whichever is lower.

APPENDIX A1

VISCOSITY OF THE NORMAL PARAFFINS

Temperature °F.	Vapor Pressure P.S.I.A.	$(d\eta/dP)_{T,P=0}$	Viscosity, Micropoise — Attenuation	Atmospheric	Dew Point
		Methane			
40	-	0.003[a]	104.10	104.14	-
70	-	0.006	108.65	108.74	-
100	-	0.011	115.20	115.36	-
130	-	0.015	120.68	120.89	-
160	-	0.019	126.17	126.44	-
190	-	0.021	131.65	131.96	-
220	-	0.024	137.25	137.61	-
250	-	0.028	142.82	143.27	-
280	-	0.032	148.24	148.71	-
		Ethane			
40	385.0	0.004	88.00	88.05	-
70	558.3	0.008	92.88	93.00	-
100		0.014	97.77	97.97	-
130		0.018	103.08	103.35	-
160		0.023	107.39	107.73	-
190		0.027	112.27	112.66	-
220		0.031	117.18	117.64	-
250		0.037	122.12	122.66	-
280		0.042	126.99	127.60	-

TABLE I. (Cont.)

Temperature °F.	Vapor Pressure P.S.I.A.	$(d\eta/dP)_{T,P=0}$	Viscosity, Micropoise — Attenuation	Atmospheric	Dew Point
		Propane			
40	79.0	0.004	76.37	76.43	-
70	125.1	0.010	80.64	80.79	-
100	188.7	0.016	84.91	85.15	-
130	273.5	0.022	89.30	89.62	-
160	383.8	0.027	93.71	94.11	-
190	524.8	0.032	97.87	98.34	-
220		0.038	102.03	102.59	-
250		0.044	106.17	106.82	-
280		0.051	110.31	111.06	-
		n-Butane			
40	17.7	0.005	68.76	68.83	-
70	31.3	0.012	72.74	72.91	-
100	51.5	0.019	76.72	76.99	-
130	80.6	0.025	80.91	81.28	-
160	120.6	0.031	85.11	85.57	-
190	173.3	0.038	89.23	89.79	-
220	241.2	0.045	93.15	93.81	-
250	327.7	0.052	97.19	97.96	-
280	436.0	0.060	101.24	102.13	-

TABLE I. (Cont.)

Temperature °F.	Vapor Pressure P.S.I.A.	$(d\eta/dP)_{T,P=0}$	Viscosity, Micropoise		
			Attenuation	Atmospheric	Dew Point
		n-Pentane			
40	4.3	0.006	64.00	-	64.02
70	8.6	0.013	67.95	-	68.06
100	15.7	0.021	71.90	72.21	-
130	25.8	0.028	75.74	76.15	-
160	42.5	0.036	79.58	80.10	-
190	64.0	0.043	83.44	84.07	-
220	94.9	0.052	87.31	88.07	-
250	134.5	0.060	91.15	92.04	-
280	186.6	0.070	95.00	96.02	-
		n-Hexane			
40	1.11	0.006	59.73	-	59.73
70	2.46	0.014	63.27	-	63.28
100	4.95	0.024	66.91	-	67.03
130	9.16	0.032	70.57	-	70.86
160	15.82	0.040	74.24	74.83	-
190	25.76	0.049	78.12	78.84	-
220	39.87	0.059	82.00	82.86	-
250	59.24	0.067	85.51	86.49	-
280	84.93	0.078	89.01	90.16	-

TABLE I. (Cont.)

Temperature °F.	Vapor Pressure P.S.I.A.	$(d\eta/dP)_{T,P=0}$	Viscosity, Micropoise — Attenuation	Atmospheric	Dew Point
		n-Heptane			
40	0.32	0.007	55.30	-	55.30
70	0.73	0.016	58.85	-	58.85
100	1.58	0.026	62.40	-	62.40
130	2.62	0.035	65.90	-	65.91
160	6.11	0.044	69.40	-	69.67
190	10.63	0.054	74.70	-	75.27
220	17.48	0.066	76.41	77.37	-
250	27.36	0.076	79.85	80.97	-
280	40.96	0.088	83.30	84.59	-
		n-Octane			
40	0.08	0.007	51.40	-	51.40
70	0.22	0.016	54.80	-	54.80
100	0.52	0.027	58.20	-	58.21
130	1.19	0.036	61.55	-	61.59
160	2.50	0.045	64.90	-	65.01
190	4.49	0.056	68.20	-	68.45
220	7.57	0.068	71.50	-	72.01
250	12.93	0.084	74.98	-	76.07
280	20.33	0.097	78.00	79.43	-

TABLE I. (Cont.)

Temperature °F.	Vapor Pressure P.S.I.A.	$(d\eta/dP)_{T,P=0}$	Viscosity, Micropoise — Attenuation	Atmospheric	Dew Point
		n-Nonane			
40	0.006	0.008	48.00	-	48.00
70	0.044	0.019	51.09	-	51.10
100	0.179	0.031	54.19	-	54.20
130	0.438	0.042	57.29	-	57.30
160	0.961	0.052	60.40	-	60.45
190	1.92	0.065	63.50	-	63.62
220	3.57	0.079	66.61	-	66.89
250	6.23	0.092	69.80	-	70.37
280	10.28	0.108	73.00	-	74.11
		n-Decane			
40	0.004	0.009	44.70	-	44.70
70	0.019	0.021	47.55	-	47.55
100	0.073	0.034	50.40	-	50.40
130	0.168	0.045	53.35	-	53.35
160	0.40	0.057	56.30	-	56.32
190	0.83	0.071	59.15	-	59.21
220	1.59	0.086	62.00	-	62.14
250	3.04	0.100	65.00	-	65.30
280	5.08	0.116	68.00	-	68.65

[a] Values of $d\eta/dP$ expressed in micropoise/P.S.I.A.

APPENDIX A2

The range of experimental conditions, the number of experimental points, the deviations about the smoothed curve presented in Figure 1, and the source of the individual hydrocarbon data are given in the following table. The measurements of the heavier paraffins are less numerous and considerably more scattered than the lighter. The more precise experimental measurements of viscosity usually involve experimental uncertainties around 3%. The overall agreement of the data with the smoothed curves presented was 2.6 % and in most cases well within the experimental uncertainties involved.

APPENDIX A2

RANGE OF CONDITIONS FOR VISCOSITY

Component	Temperature Lower	Temperature Upper	Maximum Pressure (psia)	Number Points	Deviation Average	Deviation Standard	Source
Methane	40. °F.	220. °F.	19	18	1.4%	2.0%	(6,28,31,32,46,53,56)
Ethane	63.	256.	34	23	1.0	1.4	(7,32,51,53,56)
Propane	40.	290.	50	34	1.4	1.9	(3,8,32,47,51,53,56,57)
n-Butane	32.	280.	60	26	2.4	2.8	(9,32,48,51,55)
n-Pentane	122.	195.	0	6	3.4	3.8	(32)
n-Hexane	122.	172.	0	4	2.1	2.5	(32)
n-Heptane	100.	303.	0.8	8	3.4	4.2	(10,32,39)
n-Octane	100.	304.	0.3	9	3.8	4.7	(10,32,39)
n-Nonane	212.	303.	0.3	2	5.8	n.a.	(39)
n-Decane	-	-	-	-	-	-	n.a.

APPENDIX A3

The values of the smoothed thermal conductivity obtained from the graphically determined curves of Figure 9 have been tabulated below as a function of temperature and pressure. At the low pressure limit, or "attenuation" the thermal conductivity is given in engineering units (for the convenience of the engineering minded users) together with the associated isothermal pressure derivative. This derivative was found to be very nearly invariant with temperature. From plots of the conductivity with pressure, the values of conductivity at one atmosphere pressure or dew point, whichever is lower, is also presented.

The configurational thermal conductivity for each of the normal paraffins has been calculated from Equation 13 using the experimental viscosities that were presented in Figure 1. In convenient units Equation 13 can be written:

$$k_o^{(o)} = 0.745361 \times 10^{-5} \frac{\eta_o}{M}$$

where $k_o^{(o)}$ is the configurational conductivity in cal/sec-cm-° C., η_o is the viscosity at low pressure in micropoise (10^{-6} poise), and M is the molecular weight. The quantity $k_o^{(o)}$ is presented in Table 2 of this appendix.

APPENDIX A3

THERMAL CONDUCTIVITY OF NORMAL PARAFFINS

Temperature °F.	Vapor Pressure P.S.I.A.	Thermal Conductivity, Btu/(sec)(ft)(°F) Attenuation	Atmospheric	Dew Point
		Methane		
		$(dk/dP)_{T,P=0} = 0.0016 \times 10^{-6}$		
40	-	4.917×10^{-6}	4.942×10^{-6}	-
70	-	5.275	5.296	-
100	-	5.633	5.650	-
130	-	5.994	6.014	-
160	-	6.356	6.378	-
190	-	6.724	6.745	-
220	-	7.128	7.144	-
250	-	7.531	7.548	-
280	-	7.947	7.968	-
		Ethane		
		$(dk/dP)_{T,P=0} = 0.0018 \times 10^{-6}$		
40	385.0	3.008×10^{-6}	3.038×10^{-6}	-
70	558.3	3.323	3.353	-
100	-	3.639	3.667	-
130	-	4.003	4.033	-
160	-	4.367	4.394	-
190	-	4.714	4.742	-
220	-	5.061	5.083	-
250	-	5.404	5.426	-
280	-	5.748	5.771	-

TABLE I. (Cont.)

Temperature °F.	Vapor Pressure P.S.I.A.	Thermal Conductivity, Btu/(sec)(ft)(°F) Attenuation	Atmospheric	Dew Point
		Propane		
		$(dk/dP)_{T,P=0} = 0.0021 \times 10^{-6}$		
40	79.0	2.492×10^{-6}	2.517×10^{-6}	-
70	125.1	2.799	2.818	-
100	188.7	3.106	3.119	-
130	273.5	3.439	3.457	-
160	383.8	3.772	3.794	-
190	524.8	4.115	4.137	-
220		4.458	4.480	-
250		4.815	4.835	-
280		5.180	5.207	-
		n-Butane		
		$(dk/dP)_{T,P=0} = 0.0024 \times 10^{-6}$		
40	17.7	2.217×10^{-6}	2.253×10^{-6}	-
70	31.3	2.483	2.519	-
100	51.5	2.750	2.786	-
130	80.6	3.017	3.054	-
160	120.6	3.306	3.342	-
190	173.3	3.661	3.697	-
220	241.2	4.022	4.056	-
250	327.7	4.479	4.511	-
280	436.0	4.911	4.951	-

TABLE I. (Cont.)

Temperature °F.	Vapor Pressure P.S.I.A.	Thermal Conductivity, Btu/(sec)(ft)(°F) Attenuation	Atmospheric	Dew Point
		n-Pentane		
	$(dk/dP)_{T,P=0} = 0.0026 \times 10^{-6}$			
40	4.4	2.000×10^{-6}	-	2.011×10^{-6}
70	8.6	2.236	-	2.261
100	15.7	2.472	2.511×10^{-6}	-
130	25.8	2.764	2.806	-
160	42.5	3.056	3.106	-
190	64.0	3.369	3.414	-
220	94.9	3.683	3.722	-
250	134.5	4.061	4.099	-
280	186.6	4.414	4.460	-
		n-Hexane		
	$(dk/dP)_{T,P=0} = 0.0029 \times 10^{-6}$			
40	1.17	1.844×10^{-6}	-	1.847×10^{-6}
70	2.46	2.061	-	2.070
100	4.95	2.278	-	2.294
130	9.16	2.520	-	2.548
160	15.82	2.778	2.817×10^{-6}	-
190	25.76	3.069	3.108	-
220	39.87	3.361	3.400	-
250	59.24	3.711	3.760	-
280	84.93	4.042	4.088	-

TABLE I. (Cont.)

Temperature °F.	Vapor Pressure P.S.I.A.	Thermal Conductivity, Btu/(sec)(ft)(°F) Attenuation	Atmospheric	Dew Point
		n-Heptane		
		$(dk/dP)_{T,P=0} = 0.031 \times 10^{-6}$		
40	0.32	1.722×10^{-6}	-	1.722×10^{-6}
70	0.73	1.919	-	1.923
100	1.58	2.117	-	2.125
130	2.62	2.325	-	2.336
160	6.11	2.550	-	2.567
190	10.63	2.803	-	2.830
220	17.48	3.056	3.094×10^{-6}	-
250	27.36	3.364	3.409	-
280	40.96	3.650	3.707	-
		n-Octane		
		$(dk/dP)_{T,P=0} = 0.0034 \times 10^{-6}$		
40	0.08	1.630×10^{-6}	-	1.630×10^{-6}
70	0.22	1.805	-	1.807
100	0.52	1.980	-	1.983
130	1.19	2.184	-	2.185
160	2.50	2.389	-	2.397
190	4.49	2.601	-	2.620
220	7.57	2.814	-	2.844
250	12.93	3.063	-	3.107
280	20.33	3.298	3.360×10^{-6}	-

TABLE I. (Cont.)

Temperature °F.	Vapor Pressure P.S.I.A.	Thermal Conductivity, Btu/(sec)(ft)(°F) Attenuation	Atmospheric	Dew Point
		n-Nonane		
		$(dk/dP)_{T,P=0} = 0.0036 \times 10^{-6}$		
40	0	1.533×10^{-6}	-	1.533×10^{-6}
70	0.44	1.800	-	1.800
100	0.179	1.867	-	1.867
130	0.438	2.045	-	2.044
160	0.961	2.225	-	2.228
190	1.92	2.415	-	2.421
220	3.57	2.600	-	2.614
250	6.23	2.825	-	2.845
280	10.28	3.034	-	3.058
		n-Decane		
		$(dk/dP)_{T,P=0} = 0.0039 \times 10^{-6}$		
40	0.004	1.464×10^{-6}	-	1.464×10^{-6}
70	0.019	1.618	-	1.618
100	0.073	1.772	-	1.772
130	0.168	1.932	-	1.933
160	0.40	2.092	-	2.094
190	0.83	2.250	-	2.261
220	1.59	2.408	-	2.419
250	3.04	2.596	-	2.611
280	5.08	2.754	-	2.785

APPENDIX A3

TABLE 2. CONFIGURATIONAL THERMAL CONDUCTIVITY

$k_o^{(o)} \times 10^5$ (cal/sec-cm-°C.)

Temp. (°C)	Methane	Ethane	Propane	n-Butane	n-Pentane	n-Hexane	n-Heptane	n-Octane	n-Nonane	n-Decane
-10.	4.6167	2.0750	1.2276	0.83584	0.62572	0.48634	0.38828	0.31698	0.26267	0.22117
0.	4.7682	2.1473	1.2716	0.86713	0.65000	0.50536	0.40405	0.33016	0.27377	0.23049
10.	4.9252	2.2205	1.3154	0.89829	0.67396	0.52482	0.41974	0.34321	0.28470	0.23950
20.	5.0790	2.2933	1.3588	0.92997	0.69824	0.54420	0.43536	0.35639	0.29545	0.24846
30.	5.2323	2.3657	1.4024	0.96138	0.72231	0.56366	0.45106	0.36951	0.30643	0.25768
40.	5.3857	2.4386	1.4450	0.99254	0.74617	0.58277	0.46690	0.38256	0.31747	0.26674
50.	5.5404	2.5107	1.4888	1.0236	0.77066	0.60180	0.48252	0.39567	0.32857	0.27570
60.	5.6946	2.5833	1.5319	1.0550	0.79514	0.62117	0.49822	0.40866	0.33944	0.28497
70.	5.8479	2.6560	1.5755	1.0862	0.81859	0.64046	0.51347	0.42184	0.35008	0.29414
80.	6.0013	2.7284	1.6186	1.1180	0.84297	0.65975	0.52953	0.43469	0.36135	0.30310
90.	6.1555	2.8010	1.6617	1.1491	0.86694	0.67895	0.54515	0.44794	0.37204	0.31216
100.	6.3098	2.8744	1.7050	1.1802	0.89090	0.69850	0.56093	0.46079	0.38303	0.32112
110.	6.4631	2.9465	1.7488	1.2117	0.91528	0.71744	0.57699	0.47410	0.39395	0.33013
120.	6.6173	3.0191	1.7919	1.2429	0.93946	0.73690	0.59254	0.48728	0.40470	0.33940
130.	6.7716	3.0917	1.8355	1.2742	0.96342	0.75610	0.60838	0.50046	0.41569	0.34836
140.	6.9230	3.1636	1.8782	1.3054	0.98760	0.77521	0.62400	0.51345	0.42655	0.35752
150.	7.0726	3.2360	1.9215	1.3369	1.0119	0.79407	0.63962	0.52656	0.43748	0.36669

APPENDIX A4

In the following table are presented the range of experimental conditions, the number of experimental points, the deviations of the points from the graphically determined curves of figure 9, and the sources of the individual paraffin data. The experimental uncertainty in the more precise measurements was around 3%, and in all cases, except n-hexane, the standard deviation was well within the experimental uncertainty. The overall deviation was 2%.

APPENDIX A4

RANGE OF CONDITIONS FOR THERMAL CONDUCTIVITY

Component	Temperature Lower	Temperature Upper	Maximum Pressure (psia)	Number Points	Average	Standard	Source
Methane	13°F.	220. °F.	18.	26	1.2%	1.7%	(13, 19, 25, 27, 29, 32, 35, 36, 38, 51, 53)
Ethane	32.	280.	18.	21	1.3	2.0	(11, 19, 29, 32, 34, 36, 38, 51. 53)
Propane	32.	222.	15.	16	0.9	1.3	(32, 34, 38, 51, 53)
n-Butane	32.	280.	17.	17	1.4	2.1	(12, 30, 32, 38, 51)
n-Pentane	32.	212.	4.	7	2.1	3.2	(32, 38, 40, 51)
n-Hexane	32.	185.	7.	5	3.5	5.4	(32, 33, 38, 40)
n-Heptane	32.	212.	0.4	5	1.5	2.5	(10, 32, 40)
n-Octane	100.	178.	0.1	3	0.7	1.0	(10, 32)
n-Nonane	-	-	-	0	-	-	n.a.
n-Decane	378.	444.	0.1	3	n.a.	n.a.	(65)

APPENDIX A5

The individual binary diffusion coefficient data at one atmosphere pressure for the available normal paraffins are presented in the following table for each of the temperatures. The values have been presented in engineering units. The individual sources have been included also, and it can be noted that the majority of data have not been readily available in the literature. The deviations of this data from the graphically determined curves of Figure 12 have been given, and in all cases the standard deviation was considerably less than the experimental uncertainties that would be anticipated in the measurements.

APPENDIX A5

BINARY DIFFUSION COEFFICIENTS AT ATMOSPHERIC PRESSURE

System	Temperature °F.	$\mathscr{D}_{12}$ (ft^2/sec)	Source
Methane-Air	32.	182.09×10^{-4}	Jost (26)
Ethane-Nitrogen	77.	137.50	Boyd (5)
n-Butane-Nitrogen	77.	89.19	Boyd (5)
n-Hexane-Air	70.	86.44	Schlinger (50)
	100.	90.72	Schlinger (50)
	100.	92.80	Reamer (45)
	130.	100.40	Schlinger (50)
n-Hexane-Nitrogen	59.	70.33	Cummings (18)
n-Hexane-Oxygen	59.	69.96	Cummings (18)
n-Heptane-Air	70.	76.46	Schlinger (50)
	100.	83.36	Schlinger (50)
	150.	93.64	Reamer (45)
	160.	98.70	Schlinger (50)
	160.	98.18	Reamer (45)
	170.	100.95	Reamer (45)
	190.	106.07	Schlinger (50)
n-Octane-Air	195.	100.27	Reamer (45)
n-Octane-Nitrogen	86.	65.96	Cummings (18)
n-Octane-Oxygen	86.	65.50	Cummings (18)
n-Decane-Nitrogen	194.	78.13	Cummings (18)
n-Dodecane-Nitrogen	259.	75.53	Cummings (18)
Average Deviation		1.4%	
Standard Deviation		1.7%	

PART TWO

PART II

HEAT AND MASS TRANSPORT FROM SINGLE CYLINDERS AND SPHERES INTO TURBULENT FLUID STREAMS*

INTRODUCTION

Boundary layer flow adjacent to a surface owes its very existence to the net effect of the molecular collisions of the molecules in the flowing fluid against the surface. The mean speed of the molecular velocities is characterized by and depend directly upon the thermodynamic temperature. The component velocity normal to the surface which a molecule of point mass possesses upon impact with the surface results in a transfer of momentum normal to the surface. This rate of change of momentum as the molecules collide and rebound back into the main fluid stream imparts a force exerted upon the surface area. The normal pressure acting upon the surface is the sum of this force arising from molecular motions per unit area as well as the intermolecular forces which act upon the surface. The component velocity acting parallel to the surface gives rise to shear forces adjacent to the surface. It is here that a shear law must be imposed. It was Stokes hypothesis that the viscous stress is directly proportional to the rate of deformation of the fluid, which is valid only for Newtonian fluids.

Molecular interpretation of convective transport immediately reveals that treating averaged properties (macroscopic approach) can only be valid when the

---

* A portion of Part II is being published in three parts: "Local and Macroscopic Transport from a 1.5 inch Cylinder in a Turbulent Air Stream," accepted by A. I. Ch. E. Journal, "Thermal and Material Transport from Spheres. Prediction of Macroscopic Thermal and Material Transfer," and "Thermal and Material Transport from Spheres. Prediction of Local Transport," transmitted to Int. J. Heat Mass Transfer. Permission has been granted by A. I. Ch. E. and Pergamon Press to present a portion of the published articles in Part II of this thesis.

fluid can be represented as a continuum; with physical properties changing insignificantly over distances comparable to molecular mean free paths. Continuum mechanics are invalid when there are shock fronts or when the fluid is at very low pressure such that the mean free path is no longer much smaller than physical dimensions.

Transport processes are by their very nature dependent upon deviations from an equilibrium velocity distribution. When the deviations are small, first order perturbation theory can be applied for solution of the Boltzman equation. Using continuum mechanics, Newtonian shear laws, and first order perturbations, the equations of conservation of mass, momentum, and energy result. The Navier-Stokes equations result from the conservation of momentum when the normal and shear forces acting on the surface are separated. An order of magnitude analysis of each term in these equations reveal that ce rtain terms are insignificant when the boundary layer flow adjacent to the surface is thin. Keeping only the largest terms the famous "Boundary Layer Equations" result. Although in actual practice the fluid mainstream is always turbulent to some degree or the molecular velocity distribution is complicated and depends upon the history of the flow, the boundary layer equations can be used very successfully in understanding the first order behavior -- as in "Laminar Flow".

Heat and mass transfer from single spheres and cylinders has been studied for over fifty years and little incite has emerged concerning the molecular mechanism of transport between a solid boundary or interface and a turbulent fluid stream. The concept of a laminar boundary layer forming at the stagnation point of a bluff body and developing in extent as the flow proceeds around the body has proven to be most useful. Theoretical similarity solutions to the equations of motion in the immediate vicinity of the forward stagnation point agree satisfactorily with experimental measurements at the lower flow rates.

Velocities of fluids past bluff bodies in the range of practical interest introduce two very major complications -- in the vicinity of 100° in angle from the forward stagnation point the boundary layer separates from the surface as a result of an increasing adverse pressure gradient in the direction of flow, which creates a very complicated flow process in the wake of the bluff body, and also the free stream itself introduces small perturbations on the laminar boundary layer through the action of small turbulent eddies ever present in the mainstream. The vortices of the wake which form and detach from the rear of the bluff body alter the velocity profile in the region of the laminar boundary layer in the frontal region which interacts with the boundary layer and complicates the mechanism of transport through this layer. The action of the wake together with natural instabilities in the flow contribute to fluctuations in the forward stagnation point, where the laminar boundary layer is constantly being created. Each of these secondary effects contributes in an important way to the detailed mechanism of transport from a bluff body in a turbulent fluid stream which cannot be handled by current theoretical techniques.

The overall mechanism of transport depends on the net effect of the various local mechanisms around the bluff body. The action of free stream turbulence on the laminar boundary layers and the Reynolds number dependence of the transport in the separated wake flow regime have been the subject of considerable uncertainty in the past, typified by transport rates which depended on the Reynolds number more strongly than as the classical square root dependence. Experimental measurements described here were carried out particularly to reveal these complicating factors in the mechanism of transport, where previous theoretical analysis has failed. Intermediate flow rates were selected so that the Reynolds number limit corresponds to conditions such that the wake-flow transport represents a very small portion of the overall transport and the upper limit such that the laminar boundary layer just becomes turbulent before separation at the lower free stream turbulence levels. In this flow regime the

the mechanism of free-stream turbulence and wake-flow transport are most interesting and particularly revealing. It is unfortunate that so few experimental studies were carried quantitatively in this flow regime.

A THEORETICAL BACKGROUND

An experimental study of transport by forced convection from bluff bodies can be augmented to a surprising degree by theoretical considerations, even though not one of them is sufficient to completely solve the problem. Theoretical treatment of idealized cases is particularly valuable in guiding in the proper experimental quantities and range of conditions to be studied. The Frössling group which emerges from theoretical analysis has proved to be just such an experimental variable, useful in revealing the inadequacies of theory as well as indicating the complexity of the basic mechanism of transport as first order behavior. The range of experimental conditions from initial formation of a sizable wake to the transition region is suggested from a theoretical background to be most profitable in studying effects of free stream turbulent perturbations on the flow and on transport as well as of the presence of the separated wake-flow region.

Statistical mechanics of molecular motions has dictated under what conditions transport mechanisms can be treated on a macroscopic level, as aluded to in the introduction. In addition to the requirements of continuum mechanics, Stokes hypothesis concerning the shear law must be valid,and the rate of transport sufficiently low so that the first order perturbation theory can be used to obtain the solution to the Boltzmann equation. When the normal and shear forces are separated this solution reduces (1) to the Navier-Stokes equations:

$$\rho\left(\frac{\partial u}{\partial t} + u\frac{\partial u}{\partial x} + v\frac{\partial v}{\partial y} + w\frac{\partial u}{\partial z}\right) = X - \frac{\partial P}{\partial x} + \frac{\partial}{\partial x}\left(\mu\frac{\partial u}{\partial x}\right) + \frac{\partial}{\partial y}\left(\mu\frac{\partial u}{\partial y}\right) + \frac{\partial}{\partial z}\left(\mu\frac{\partial u}{\partial z}\right) \tag{1}$$

$$\rho\left(\frac{\partial v}{\partial t} + u\frac{\partial v}{\partial x} + v\frac{\partial v}{\partial y} + w\frac{\partial v}{\partial z}\right) = Y - \frac{\partial P}{\partial y} + \frac{\partial}{\partial x}\left(\mu\frac{\partial v}{\partial x}\right) + \frac{\partial}{\partial y}\left(\mu\frac{\partial v}{\partial y}\right) + \frac{\partial}{\partial z}\left(\mu\frac{\partial v}{\partial z}\right) \tag{2}$$

$$\rho\left(\frac{\partial w}{\partial t} + u\frac{\partial w}{\partial x} + v\frac{\partial w}{\partial y} + w\frac{\partial w}{\partial z}\right) = Z - \frac{\partial P}{\partial z} + \frac{\partial}{\partial x}\left(\mu\frac{\partial w}{\partial x}\right) + \frac{\partial}{\partial y}\left(\mu\frac{\partial w}{\partial y}\right) + \frac{\partial}{\partial z}\left(\mu\frac{\partial w}{\partial z}\right) \tag{3}$$

where x, y, and z are component coordinants, t is time, X, Y, and Z represent any external body forces, and the component velocities are u, v, and w(t,x,y,z), and ρ is density and μ absolute viscosity. The conservation of mass is:

$$\frac{\partial \rho}{\partial t} + \frac{\partial(\rho u)}{\partial x} + \frac{\partial(\rho v)}{\partial y} + \frac{\partial(\rho w)}{\partial z} = 0 \tag{4}$$

and the equation of state:

$$\frac{Pv}{RT} = 1 + B^*(T)\rho^* + C^*(T)(\rho^*)^2 + \ldots \tag{5}$$

where ρ^* is reduced density and B*, C*, ... are the second, third, and higher virial coefficients respectively that have been introduced in Part I. The conservation of energy and of molecular species can be written in full generality, however, in the interest of brevity simplifications will be made first.

In general, when there is transport of heat there will be a temperature gradient across the boundary layer. Since the absolute viscosity in Equations 1 - 3 depends on the temperature, this property will vary from point to point. However, the Von Missis (1) transformation is useful here, which transforms a similarity variable, discussed later, in such a way that the constant property solution is valid when property variation is treated as a ratio across the boundary layer. Fluids which are incompressible can be represented by constant density. Also for fluids where no body forces are acting (i.e. buoyant forces such as natural convection in a gravitational field, or electrical or magnetic forces) the body forces, X, Y, and Z vanish. When unsteady fluctuations of component velocities in time are small in comparison to the component velocity, the instantaneous velocities u, v, and w can be composed (1) of a time averaged velocity U, V, and W plus a time fluctuating contribution u', v', and w' such as:

$$u = U + u' \tag{6}$$

The instantaneous temperature and molecular specie concentration can be similarly represented. Making the boundary layer simplifications (1) on the conservation of mass, momentum, energy, and molecular specie in addition to the restrictions enumerated above, Equations 1-4 together with the conservation of energy and molecular species (1) are greatly simplified. For bluff bodies, such as cylinders and spheres, two coordinates are sufficient: the distance along the surface, x, and distance normal to the surface, y, as shown in Figure 1. The simplified equations follow:

Continuity

two-dimensional:

$$\frac{\partial U}{\partial x} + \frac{\partial V}{\partial y} = 0 \tag{7}$$

axially symmetric:

$$\frac{\partial (Ur)}{\partial x} + \frac{\partial (Vr)}{\partial y} = 0 \tag{8}$$

Motion:

$$U\frac{\partial U}{\partial x} + V\frac{\partial U}{\partial y} = -\frac{1}{\rho}\frac{dP}{dx} + \nu\frac{\partial^2 U}{\partial y^2} - \frac{\partial}{\partial y}\overline{(u'v')} \tag{9}$$

Energy:

$$U\frac{\partial T}{\partial x} + V\frac{\partial T}{\partial y} = \alpha\frac{\partial^2 T}{\partial y^2} - \frac{\partial}{\partial y}\overline{(v'T')} - \frac{\overline{u'v'}}{C_P}\frac{\partial U}{\partial y} + \frac{\nu}{C_P}\left(\frac{\partial U}{\partial y}\right)^2 \tag{10}$$

Binary diffusion:

$$U\frac{\partial C_A}{\partial x} + V\frac{\partial C_A}{\partial y} = \mathcal{D}_{AB}\frac{\partial^2 C_A}{\partial y^2} - \frac{\partial}{\partial y}\overline{(v'c')} \tag{11}$$

The algebraic details of these simplifications need not be discussed since Schlicting (1) has discussed these points in detail. For incompressible fluids the fluctuating components of the pressure are shown to be insignificant; however, for compressible fluids little has been done. In the energy equation the inter-

TWO-DIMENSIONAL

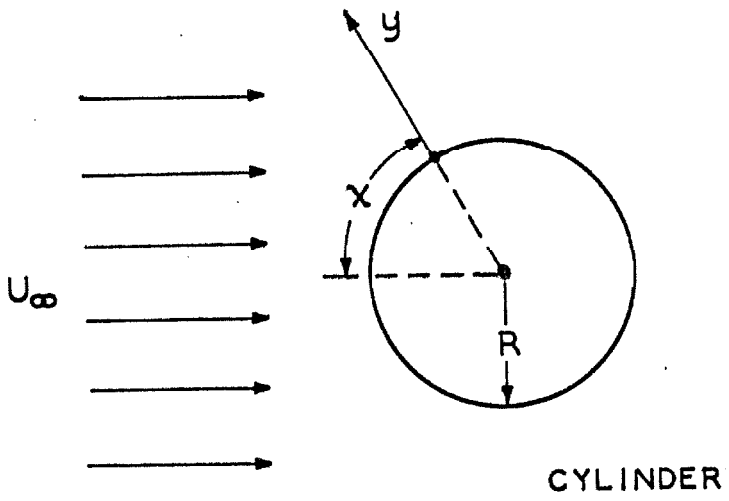

Figure 1. System of Coordinates

diffusion of the species and the Dufour effect have been neglected, since commonly the species in transport studies are not grossly dissimilar in nature. In the diffusion equation the additional flux of mass from pressure gradients, body forces, and large thermal gradients have been neglected. Normally these second order effects are considerably less than the first order effects under study.

Eddy coefficients of viscosity, thermal conductivity, and diffusivity are defined (1,2,3) by comparing Equations 9-11 to their laminar analog with the viscosity, conductivity, or diffusivity coefficient augmented by a corresponding eddy coefficient in the following equations:

$$U\frac{\partial U}{\partial x} + V\frac{\partial U}{\partial y} = -\frac{1}{\rho}\frac{dP}{dx} + \frac{\partial}{\partial y}\left[(\nu + \epsilon_m)\frac{\partial U}{\partial y}\right] \tag{12}$$

$$U\frac{\partial T}{\partial x} + V\frac{\partial T}{\partial y} = \frac{\partial}{\partial y}\left[(\alpha + \epsilon_h)\frac{\partial T}{\partial y}\right] + \frac{\nu + \epsilon_m}{C_P}\left(\frac{\partial U}{\partial y}\right)^2 \tag{13}$$

$$U\frac{\partial C_A}{\partial x} + V\frac{\partial C_A}{\partial y} = \frac{\partial}{\partial y}\left[(\mathcal{D}_{AB} + \epsilon_d)\frac{\partial C_A}{\partial y}\right] \tag{14}$$

There results the following definitions:

$$\epsilon_m = -\frac{\overline{u'v'}}{\partial U/\partial y} \tag{15}$$

$$\epsilon_h = -\frac{\overline{v'T'}}{\partial T/\partial y} \tag{16}$$

$$\epsilon_d = -\frac{\overline{v'C'}}{\partial C/\partial y} \tag{17}$$

These definitions, which emerge directly from the boundary layer equations

written for small fluctuations, state that turbulent eddy fluxes of momentum, heat, and concentration are directly proportional to the local driving force. The turbulent Prandtl and Schmidt groups may be defined in terms of the appropriate eddy coefficients as follows:

$$Pr_t = \epsilon_m / \epsilon_h \tag{18}$$

$$Sc_t = \epsilon_m / \epsilon_d \tag{19}$$

The use of the eddy coefficients will be discussed later.

The important analogy defeat between heat and mass transfer, as seen by comparing Equations 13 and 14, remains as the viscous dissipation term. This indicates that the heat flux is no longer proportional to the temperature difference between the free stream and the wall. This effect becomes important at the higher flow rates and is certainly present in turbulent flow, which possesses characteristically large velocity gradients near the wall. This frictional heat which is localized near the wall (ϵ_m reaches a maximum a short distance from the wall) raises the temperature of the stream above that of the free stream, which is denoted by the "adiabatic wall temperature:"

$$T_a = T_\infty + r(Pr) \frac{U_\infty}{2gC_p} \tag{20}$$

For laminar flow the recovery factor, r, is a function of the Prandtl group, Pr, and is given closely by the following for the lower Prandtl numbers:

$$r(Pr) = Pr^{0.5} \tag{21}$$

For transition to the turbulent regime the recovery factor is always larger than the square root of the Prandtl number. For flat plates parallel to flowing air streams it has been found (1) that the experimental recovery factor increases from the square root of the Prandtl number to an asymptote of about 0.89.

Thermal measurements in the flow of air past cylinders (5) for Reynolds numbers about 10^5 indicate that the recovery factor at low turbulence level decreases steadily from 1.0 at stagnation to zero at 140° and goes negative thereafter, resulting in a reverse heat flux. While for higher turbulence levels it reached 0.32 at 140° and remained such. Thus, the new driving force for transport will be $T_o - T_a$ instead of $T_o - T_\infty$. Therefore, when the Nusselt group is defined in terms of the overall driving force, $T_o - T_\infty$, the solution must be of the form:

$$Nu = C_1 \frac{T_o - T_a}{T_o - T_\infty} Re^n Pr^{1/3} \tag{22}$$

For laminar flow of air at 100 fps past a flat plate ($C_1 = 0.664$, $n = 1/2$) this correction term amounts to about 1%. The viscous dissipation effect rapidly becomes important for high velocity flow of gases with larger Prandtl numbers. The solution of Equation 13 can be carried out by neglecting this dissipation term and then correcting the result as in Equation 22. The numerous effects complicating the treatment and analysis of transport from bluff bodies, such as separation, free stream turbulence, tunnel blockage, local velocity, blowing boundary layer, natural convection, and variable properties, will be discussed later.

The exact solution of the basic equation of 7, 8, and 12-14 for variable Prandtl or Schmidt groups, subcritical flow, negligible free stream turbulence, and no interfacial blowing velocity can be obtained and is most informative in interpreting and analyzing experimental results. The system of coupled equations to be solved are:

Continuity

two-dimensional:

$$\frac{\partial U}{\partial x} + \frac{\partial V}{\partial y} = 0 \tag{23}$$

axially-symmetric:

$$\frac{\partial(Ur)}{\partial x} + \frac{\partial(Vr)}{\partial y} = 0 \tag{24}$$

Motion:

$$U\frac{\partial U}{\partial x} + V\frac{\partial V}{\partial y} = -\frac{1}{\rho}\frac{dP}{dx} + \nu\frac{\partial^2 U}{\partial y^2} \tag{25}$$

Energy:

$$U\frac{\partial T}{\partial x} + V\frac{\partial T}{\partial y} = \alpha\frac{\partial^2 T}{\partial y^2} \tag{26}$$

Mass:

$$U\frac{\partial C_a}{\partial x} + V\frac{\partial C_A}{\partial y} = \mathcal{D}_{AB}\frac{\partial^2 C_A}{\partial y^2} \tag{27}$$

The associated boundary conditions are:

$$y=0 \qquad U, V=0 \qquad T=T_o \qquad C_A = C_{A,0} \tag{28}$$

$$y=\infty \qquad U=U_1(x) \qquad \frac{\partial U}{\partial y}=0 \qquad \frac{\partial^2 U}{\partial y^2} \tag{29}$$

where U_1 is the velocity immediately outside the boundary layer, and the subscript ∞ denotes in the free stream, far from the boundary layer and o at the surface of the bluff body. In general, the solution to Equation 27 used the boundary conditions:

$$y=0 \qquad U=0 \qquad V=V_o \tag{30}$$

which arises from the fact that there is mass transfer occurring between the interface and the free stream. These solutions have been carried out and will be discussed later. The solutions to Equations 26-27 will consequently be analogous when $v_o = 0$.

TWO-DIMENSIONAL CASE

First, the exact solution to the Equations of 23, 25, and 26 for the two-dimensional case will be determined; then for the axially-symmetric case. The solution to Equation 23 outside the boundary layer, $y=\infty$, for an inviscid fluid in irrotational flow (often termed "potential flow") is:

$$U_1 = 2\, U_\infty \sin(x/R) \tag{31}$$

for the two-dimensional boundary layer as for a circular cylinder. Using Equation 25 outside the boundary layer:

$$U_1 \frac{dU_1}{dx} = -\frac{1}{\rho}\frac{dP}{dx} \tag{32}$$

obtains the pressure profile:

$$\frac{P_o - P_\infty}{\frac{1}{2}\rho U_\infty^2} = 1 - 4\sin^2(x/R) \tag{33}$$

The dimensionless quantity on the left of Equation 33 is referred to as the "pressure coefficient" and denoted C_P.

The stream function $\Psi(x,y)$ will be used which satisfies the continuity equation 23 so that there results:

$$U = \frac{\partial \Psi}{\partial y} \qquad \text{and} \qquad V = -\frac{\partial \Psi}{\partial x} \tag{34}$$

Substituting the velocities into the equation of motion as 25 there obtains:

$$\frac{\partial \Psi}{\partial y}\frac{\partial^2 \Psi}{\partial x \partial y} - \frac{\partial \Psi}{\partial x}\frac{\partial^2 \Psi}{\partial y^2} = U_1 \frac{dU_1}{dx} + \nu \frac{\partial^3 \Psi}{\partial y^3} \tag{35}$$

The properties of similarity are useful in determining the solution to Equation 35, since by similarity all velocity profiles become identical when the local velocity is scaled by the velocity outside the boundary layer, U_1, and when the distance normal to the surface is scaled by the distance $\nu x/U_1$. Thus, there results:

$$\frac{U}{U_1} = F(y\ U_1/\nu x) = F(\eta) \tag{36}$$

In the region of the stagnation point Equation 31 becomes:

$$U_1 = 2\ U_\infty x/R \tag{37}$$

The similarity variable η becomes:

$$\eta = \frac{y}{R}\sqrt{\frac{2U_\infty R}{\nu}} \tag{38}$$

The stream function is then chosen near the stagnation point to be represented by the first term in the Blasius series (1):

$$\Psi = \sqrt{\frac{2U_\infty \nu}{R}}\ x\ f(\eta) \tag{39}$$

From Equation 34 the component velocities are then obtained:

$$U = 2U_\infty \frac{x}{R} f'(\eta) \tag{40}$$

$$V = \sqrt{\frac{2U_\infty \nu}{R}}\ f(\eta) \tag{41}$$

Calculating the derivative $U_1 dU_1/dx$ from Equation 37 and the derivatives of

the stream function of Equation 39 as $\partial\Psi/\partial x$, $\partial^2\Psi/\partial x\partial y$, $\partial\Psi/\partial y$, $\partial^2\Psi/\partial y^2$, and $\partial^3\Psi/\partial y^3$ an ordinary differential equation results:

$$\frac{4U_\infty^2 x}{R}\left[(f')^2 - ff' - 1 - f'''\right] = 0$$

or

$$(f')^2 - ff'' - f''' - 1 = 0 \tag{42}$$

with the transformed boundary conditions:

$$y=0,\ \eta=0 \qquad U=0 \qquad f(0)=0 \tag{43}$$

$$V=0 \qquad f'(o)=0 \tag{44}$$

The value of the similarity transformation is now obvious as the second order, partial differential Equation of 25 with variable coefficients has now been transformed to the ordinary differential Equation of 42.

A power series solution to Equation 42 can be obtained about $\eta=0$ in the following form:

$$f(\eta) = \sum_{i=0}^{7} C_i \eta^i \tag{45}$$

An asymptotic expansion solution about $\eta=\infty$:

$$f = \eta - \beta + f_2 \tag{46}$$

is necessary in order to satisfy the third boundary condition:

$$y=\infty,\ \eta=\infty \qquad f'(\infty) = 1 \tag{47}$$

The two solutions as Equations 45 and 46 are then pieced together at some appropriate η, matching all derivatives, obtaining f for all η. Since an exact analytic form of solution is required for variable Prandtl or Schmidt groups and precise numerical results were not necessary, the boundary condition at infinity was satisfied by choosing η sufficiently large so that $f'(\infty) \approx 1$ but sufficiently small so that the power series was convergent. The solution of Equation 45 was evaluated by noting that from Equations 43 and 44 respectively the coefficients $C_o=0$ and $C_1=0$ and by computing the derivatives f', f'', f''', $(f')^2$, and ff' and equating equal powers of η, the coefficients were obtained as:

$$\begin{aligned} C_2 &= \text{free} \\ C_3 &= -1/6 \\ C_4 &= 0 \\ C_5 &= C_2^2/30 \\ C_6 &= C_2 C_3/30 = -C_2/180 \\ C_7 &= C_3^2/70 = 1/2520. \end{aligned} \tag{48}$$

The free coefficient, C_2, was then evaluated as 0.6169 . The resulting equations for $f(\eta)$ and $f'(\eta)$ were:

$$f(\eta) = 0.6169\eta^2 - 0.1666\eta^3 + 0.01269\eta^5 - 0.00343\eta^6 + 0.000397\eta^7 \tag{49}$$

$$f'(\eta) = 1.2338\eta - 0.5000\eta^2 + 0.06345\eta^4 - 0.02058\eta^5 + 0.002779\eta^7 \tag{50}$$

A comparison of $f'(\eta)$ with that tabulated by Schlicting (1), obtained by using an asymptotic expansion and higher terms in the Blasius series, has been shown in Table 1 and the agreement is remarkable.

The fluid mechanics of the problem, which are now solved, can be used directly in the energy equation 26. First, a series expansion of the Blasius

TABLE 1

TWO-DIMENSIONAL VELOCITY DISTRIBUTION COMPARISON

η	$f'(\eta)$ Tifford	$f'(\eta)$ The Author
0.00	0.0000	0.0000
0.20	0.2266	0.2266
0.40	0.4145	0.4152
0.60	0.5663	0.5671
0.80	0.6859	0.6869
1.00	0.7779	0.7794
1.40	0.8968	0.9030
2.00	0.9732	1.0000

type for the dimensionless temperature is employed:

$$\theta = \frac{T - T_\infty}{T_o - T_\infty} = \theta_o(\eta) + \xi\,\theta_1(\eta) + \xi^2\,\theta(\eta) + \ldots \tag{51}$$

where $\xi = x/2R$. The energy equation 26 simplifies to:

$$U\frac{\partial\theta}{\partial x} + V\frac{\partial\theta}{\partial y} = \alpha\,\frac{\partial^2\theta}{\partial y^2} \tag{52}$$

Computing the derivatives, $\partial\theta/\partial y$, $\partial\theta/\partial x$, and $\partial^2\theta/\partial y^2$ and using the component velocities from Equations 40 and 41, substitution into Equation 52 yields a set of ordinary differential equations, the first of which is:

$$\theta_o'' = -f(\eta)\ \mathrm{Pr}\ \theta_o' \tag{53}$$

The second equation for θ_1 vanishes since by symmetry $\partial T/\partial\xi = 0$ at $\xi = 0$, and similarly all equations involving odd subscripts also vanish. Only equations for even subscripted quantities of θ remain. In order to obtain all the terms in these higher equations, correspondingly higher terms must be carried in the Blasius series, Equation 39. Their solution is most difficult; carried out only by Frössling (5) for specific values of the Prandtl number only. Equation 53 shall be solved exactly for variable Prandtl number and higher terms in Equation 51 carried for indicating the form of the result.

The general solution to Equation 53 is:

$$\theta_o = A_o \int_0^\eta \exp\left(-\int_0^\eta \mathrm{Pr}\ f\,d\eta\right)d\eta + B \tag{54}$$

with the boundary conditions on θ:

$$\begin{array}{llll} \eta = 0 & \text{all } \xi & \theta_o = 1 & \theta_1, \theta_2, \ldots = 0 \\ \eta = \infty & \text{all } \xi & \theta_o = 0 & \theta_1, \theta_2, \ldots = 0 \end{array} \tag{55}$$

The coefficient A_o can be obtained from:

$$-1 = A_o \int_0^{\infty} \exp(-Pr \int_0^{\eta} f(\eta) d\eta) d\eta \tag{56}$$

If τ is defined as:

$$\tau = Pr \int_0^{\eta} f(\eta) d\eta \tag{57}$$

then Equation 56 becomes:

$$-1 = A_o \int_0^{\eta} e^{-\tau} \left(\frac{d\eta}{d\tau}\right) d\tau \tag{58}$$

The quantity τ can be obtained by integrating f in Equation 57:

$$\frac{\tau}{Pr} = 0.2057\eta^3 - 0.04166\eta^4 + 0.002115\eta^6 - 0.000490\eta^7 + 0.0000496\eta^8 \tag{59}$$

To invert this equation for η, the first term can be used as an approximation for the higher terms with an error of the order of τ^8:

$$\eta \approx 1.693(\tau/Pr)^{1/3}$$

In this manner Equation 59 can be solved for η^3. The cube root is then extracted by means of the binomial theorem to obtain:

$$\eta = 1.693\left[\left(\frac{\tau}{Pr}\right)^{1/3} + 0.114\left(\frac{\tau}{Pr}\right)^{2/3} - 0.0130\left(\frac{\tau}{Pr}\right) + 0.0080\left(\frac{\tau}{Pr}\right)^{4/3} + 0.0101\left(\frac{\tau}{Pr}\right)^{5/3} + 0.0012\left(\frac{\tau}{Pr}\right)^{2}\right] \tag{61}$$

Taking the derivatives of this series with respect to τ, substituting into Equation 58, and integrating, the coefficient A_o is obtained as:

$$A_o = -0.662\ Pr^{1/3}\left[\frac{1}{1 + \Phi(Pr)}\right] \tag{62}$$

where:

$$\Phi(Pr) = \frac{0.114}{Pr^{1/3}} - \frac{0.0146}{Pr^{2/3}} - \frac{0.0106}{Pr} + \frac{0.0170}{Pr^{4/3}} + \frac{0.0048}{Pr^{5/3}}$$

To obtain the Nusselt group the following relations apply:

$$Nu_\infty = \frac{hd}{k_\infty} = \frac{q\,d}{k_\infty (T_o - T_\infty)} = \frac{k_\infty (\partial T/\partial y)_{y=o}\ d}{k_\infty (T_o - T_\infty)}$$

or:

$$Nu_\infty = \left[-\partial\theta/\partial y\right]_{y=0} d = -d\left[\partial\theta/\partial\eta\right]_{\eta=0}\sqrt{\frac{2U_\infty}{\nu\ R}}$$

But since R=d/2 the Nusselt group becomes:

$$Nu_\infty = 2\sqrt{\frac{U_\infty d}{\nu}}\ \left[-\partial\theta/\partial\eta\right]_{\eta=0} \tag{63}$$

From Equations 51, 54, and 62 and noting that $Re_\infty = U_\infty d/\nu$, the result is:

$$\frac{Nu_\infty}{Re_\infty^{1/2} Pr_{m,\infty}^{1/3}} = 1.324\ (1 - A_2' \xi^2 - A_4' \xi^4 - \ldots)\left[\frac{1}{1 + \Phi(Pr)}\right] \tag{64}$$

This is an exact result using series solutions for the numerical evaluation. The quantity on the left of Equation 64 remains constant as first order behavior. This useful form of the result immediately suggests that this grouping would be a most valuable quantity to study experimentally. For this reason it has been termed the "Frössling group" in recognition for Nils Frössling's (5, 6) great contributions in this area:

$$Fs_{\infty} = \frac{Nu_{\infty}}{Re_{\infty}^{1/2} \, Pr_{m,\infty}^{1/3}} \tag{65}$$

and the corresponding group for mass transfer, with negligible interfacial velocity is:

$$Fs_{\infty} = \frac{Sh_{\infty}}{Re_{\infty}^{1/2} \, Sc_{m,\infty}^{1/3}} \tag{66}$$

These groups remain invariant with varying Prandtl or Schmidt numbers at large values of Prandtl or Schmidt numbers. The small variation of the bracketed term of Equation 64 with Prandtl or Schmidt numbers has been shown in Table 2 in the form of the Frössling number at the forward stagnation point. The coefficients A'_2, A'_4, ... may be very slightly dependent upon the Prandtl group. The quantity in parenthesis in Equation 64 yields the angular dependence of the Frössling group from stagnation. Nils Frössling (5) has calculated this dependence at high Reynolds numbers (19,000) using an experimental velocity distribution for two special cases: solving the equations with a single value of the Schmidt number and solving with a flat velocity profile. His results have been shown in Figure 2 together with experimental data taken by the author for comparable Reynolds numbers. Squire (7) carried an exact solution through at the stagnation point, and this has been shown here. Also shown in Figure 2 with $A'_2=0.524$ there are the results of this work which have been obtained for unrestricted variable Prandtl or Schmidt numbers and for varying angle from stagnation, although the numerical evaluation is not as refined as Frössling's specific cases. Also this analysis has relaxed the restriction of Frössling flat velocity profile for the higher values of the Schmidt number, which have gone as high as 15,000. The solution obtained in this work lies between Frössling's two cases. All the exact theoretical solutions fall between the experimental data for low (2660) and moderate (23,000) Reynolds numbers.

TABLE 2

FLOW ABOUT A CIRCULAR CYLINDER

PRANDTL NUMBER DEPENDENCE OF STAGNATION POINT HEAT TRANSFER

Pr	$\bar{\Phi}$(Pr)	Fs
0.7	0.132	1.168
1.0	0.146	1.158
2.0	0.083	1.222
5.0	0.061	1.248
50.0	0.0299	1.284
200.0	0.0195	1.300

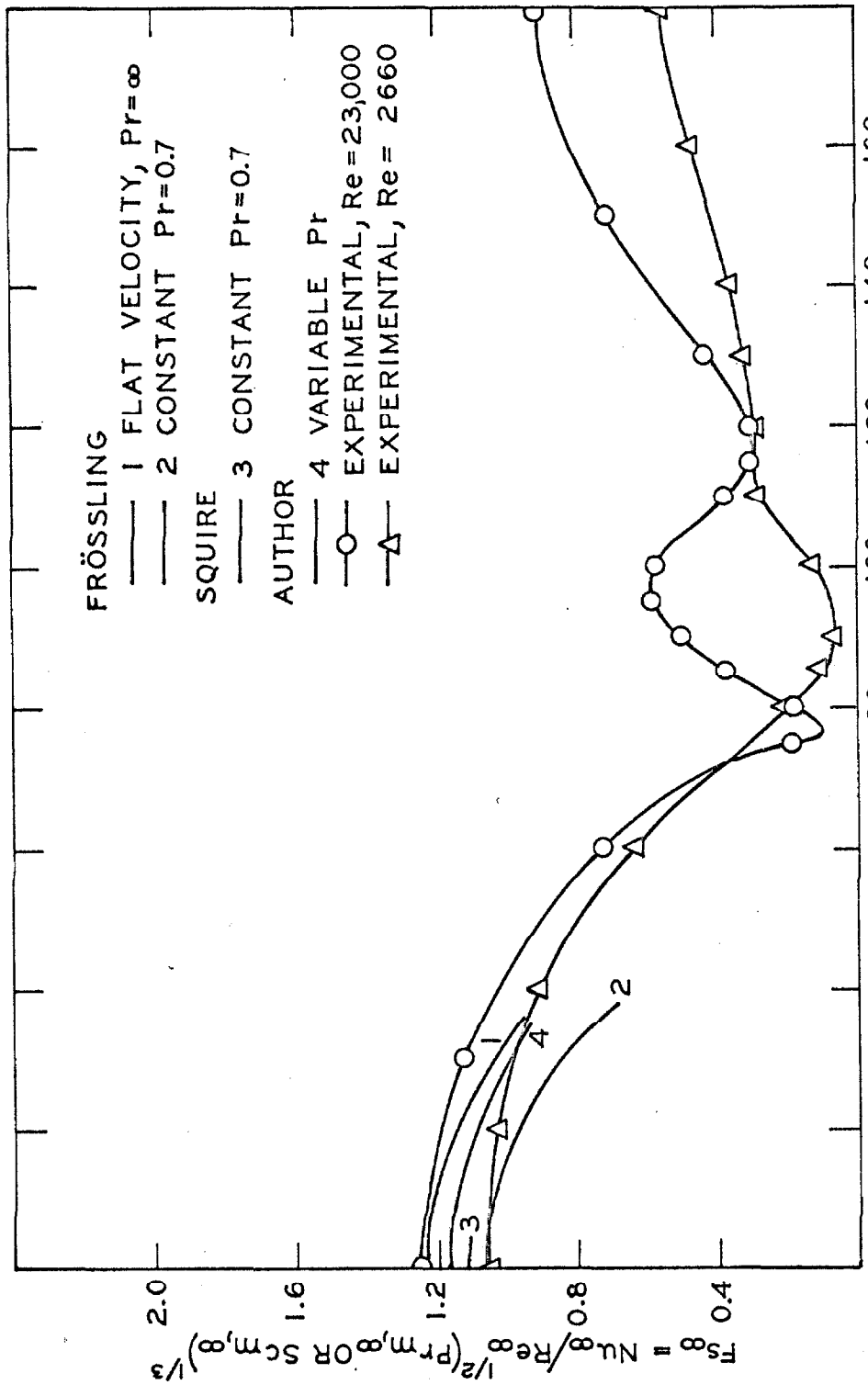

Figure 2. Frössling Number and Local Transfer from a Cylinder.

AXIALLY-SYMMETRIC CASE

The axially-symmetric geometry considered in this section is that of a sphere, whereupon the solution to Equation 24 is:

$$U_1 = \frac{3}{2} U_\infty \sin(x/R) \tag{67}$$

By applying Equation 25 outside the boundary layer, Equation 32 is obtained which produces the pressure profile, with the aid of Equation 67:

$$\frac{P_o - P_\infty}{\frac{1}{2}\rho_\infty U_\infty} = 1 - \frac{9}{4}\sin^2(x/R) \tag{68}$$

The stream function for the axially-symmetric geometry differs from the two-dimensional case owing the different continuity Equation 24, which depends on the radius change from the axis of symmetry as shown in Figure 3. For a sphere the radius generator is:

$$r - R \sin(x/R) \tag{69}$$

From the equation of continuity 24, the velocity components can be expressed in terms of the stream function:

$$U = \frac{1}{r}\frac{\partial(\psi r)}{\partial y} = \frac{\partial \psi}{\partial y} \tag{70}$$

$$V = -\frac{1}{r}\frac{\partial(\psi r)}{\partial x} = -\frac{\partial \psi}{\partial x} - \frac{1}{r}\frac{dr}{dx}\psi$$

Using these velocity components in Equation 25, the following equation is obtained:

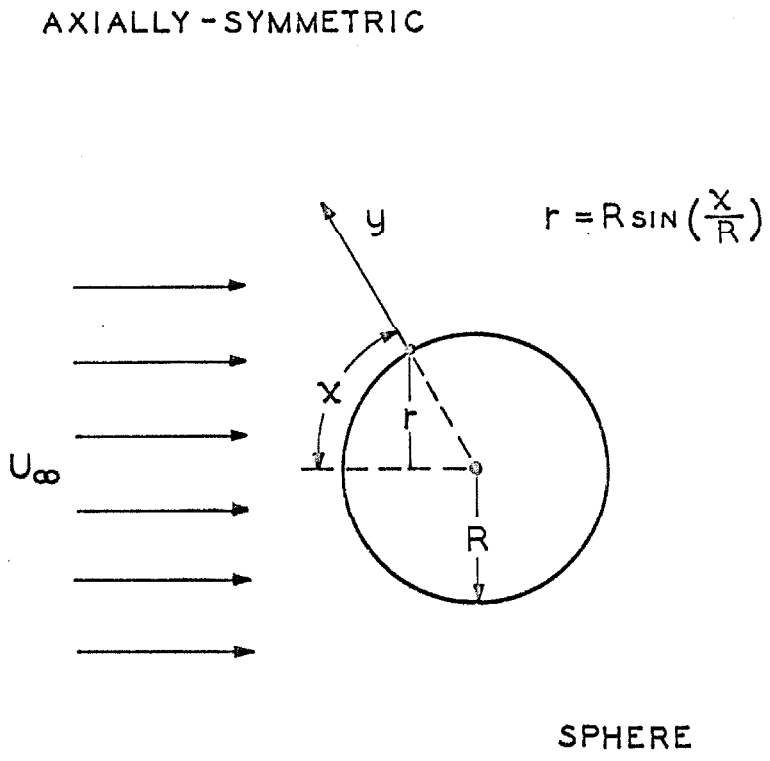

Figure 3. System of Coordinates.

$$\frac{\partial \psi}{\partial y}\frac{\partial^2 \psi}{\partial x \partial y} - \left(\frac{\partial \psi}{\partial x} + \frac{1}{r}\frac{dr}{dx}\psi\right)\frac{\partial^2 \psi}{\partial y^2} = U_1 \frac{dU_1}{dx} + \nu \frac{\partial^3 \psi}{\partial y^3} \tag{72}$$

For a region in the immediate vicinity of the forward stagnation (small x), the following simplifications result:

$$\frac{1}{r}\frac{dr}{dx} = \frac{R\cos(x/R)}{R^2 \sin(x/R)} \approx \frac{1}{x} \tag{73}$$

and:

$$U_1 \frac{dU_1}{dx} = \frac{9\, U_\infty^2}{4\, R\nu}\, x \tag{74}$$

By the same procedure as for the two-dimensional case a set of similarity variables is chosen to reduce Equation 72 to an ordinary differential equation and these variables were found to be:

$$\eta = \frac{y}{R}\sqrt{\frac{3\, U_\infty R}{\nu}}\,,$$

with the first term in the Blasius series as:

$$\Psi = \frac{1}{2}\sqrt{\frac{3U_\infty \nu}{R}}\; x\, f(\eta) \tag{76}$$

The component velocities become:

$$U = \frac{3}{2} U_\infty \frac{x}{R}\, f'(\eta) \tag{77}$$

$$V = \frac{1}{2}\sqrt{\frac{3U_\infty \nu}{R}}\; f(\eta) \tag{78}$$

Calculating the required derivatives of the stream function of Equation 76, $\partial\Psi/\partial x$, $\partial^2\Psi/\partial x\partial y$, $\partial\Psi/\partial y$, $\partial^2\Psi/\partial y^2$, and $\partial^3\Psi/\partial y^3$, Equation 72 reduces to:

$$\frac{9U_\infty^2}{4R^2 x}\left[(f')^2 - 2 ff'' - 2 f''' - 1 \right] = 0$$

or:

$$(f')^2 - 2 ff' - 2 f''' - 1 = 0 \tag{79}$$

with the transformed boundary conditions given in Equations 43 an d 44.

A power series solution to Equation 79 was obtained in a manner exactly analogous to the two-dimensional case as Equations 45-48. A new set of coefficients was obtained as:

$$\begin{aligned} C_2 &= \text{free} \\ C_3 &= -1/12 \\ C_4 &= 0 \\ C_5 &= 0 \\ C_6 &= C_2/720 \\ C_7 &= -1/20160 \\ C_8 &= 0 \end{aligned} \tag{80}$$

The free coefficient C_2 was found to be 0.4637 and the resulting equations for $f(\eta)$ and $f'(\eta)$ were:

$$f(\eta) = 0.4637\eta^2 - 0.0834\eta^3 + 0.000644\eta^6 - 0.0000496\eta^7 \tag{81}$$

$$f'(\eta) = 0.9274\eta - 0.2502\eta^2 + 0.003864\eta^5 - 0.0003472\eta^6 \tag{82}$$

$f'(\eta)$ has been compared in Table 3 with that presented by Schlicting (1), using asymptotic expansions and higher order terms in the Blasius series. The agreement is very close.

TABLE 3

AXIALLY-SYMMETRIC VELOCITY DISTRIBUTION

COMPARISON

η	$f'(\eta)$ Frössling	$f'(\eta)$ The Author
0.00	0.0000	0.0000
0.20	0.1755	0.1755
0.40	0.3311	0.3311
0.60	0.4669	0.4666
0.80	0.5833	0.5832
1.00	0.6811	0.6808
1.40	0.8258	0.8268
2.00	0.9422	0.9564
3.00	0.9949	1.315

Again a series solution as in Equation 51 can be used for the temperature Equation 52 with the aid of the component velocities given in Equations 77 and 78. The transformation works, and the ordinary differential equation identical to Equation 53 is obtained. Again only the even subscripted terms in the temperature series remain. The same results as in Equations 54-58 apply, therefore.

Performing the integration indicated by Equation 57, there yields the series:

$$\frac{\tau}{Pr} = 0.1546\eta^3 - 0.0208\eta^4 + 0.0000920\eta^7 - 0.0000620\eta^8 \qquad (83)$$

This equation is then inverted by the procedure described earlier, to obtain the expression for η:

$$\eta = 1.864\left[\left(\frac{\tau}{Pr}\right)^{1/3} + 0.08407\left(\frac{\tau}{Pr}\right)^{2/3} - 0.00705\left(\frac{\tau}{Pr}\right) + 0.000994\left(\frac{\tau}{Pr}\right)^{4/3} - 0.002410\left(\frac{\tau}{Pr}\right)^{5/3} + 0.000707\left(\frac{\tau}{Pr}\right)^{6/3}\right] \qquad (84)$$

Taking the derivative of η with respect to τ, substituting into Equation 58, and carrying out the integrating, the coefficient A_o results:

$$A_o = -0.601\ Pr^{1/3}\left[\frac{1}{1 - \Phi_2(Pr)}\right] \qquad (85)$$

where:

$$\Phi_2(Pr) = \frac{0.0840}{Pr^{1/3}} - \frac{0.00790}{Pr^{2/3}} + \frac{0.001325}{Pr} - \frac{0.00406}{Pr^{4/3}} + \frac{0.00317}{Pr^{5/3}}$$

The Nusselt group is then obtained as in the previous case, noting, however, that it is for convection only:

$$Nu_{\infty, c} = -d\left[\frac{\partial\theta}{\partial\eta}\right]_{\eta=o} \sqrt{\frac{3U_\infty}{\nu R}} \qquad (86)$$

$$Nu_{\infty,c} = 6\sqrt{\frac{U_\infty d}{\nu}}\left[-\frac{\partial\theta}{\partial\eta}\right]_{\eta=0} \tag{87}$$

$$Nu_{\infty,c} = 6\ Re_\infty^{1/2}\left[-A_o-\xi^2A_2-\xi^4A_4\right] \tag{88}$$

Normally the Nusselt group is presented for spheres which includes the stagnant, steady state conduction limit of 2. This limit has been studied quite early both experimentally (8) and theoretically (9), and it is well documented in the literature discussed later. It is simply derived by solving Equation 52 for U, V=0.

When the solution for A_o in Equation 62 is used in Equation 88, the result is obtained:

$$\frac{Nu_\infty - 2}{Re_\infty^{1/2} Pr_{m,\infty}^{1/3}} = 1.471(1 - A_2'\xi^2 + A_4'\xi^4)\left[\frac{1}{1+\Phi_2(Pr)}\right] \tag{89}$$

The group on the left of this equation for spheres is analogous to that for cylinders in Equation 64 and is again termed the "Frössling group":

$$Fs_\infty = \frac{Nu_\infty - 2}{Re_\infty^{1/2} Pr_{m,\infty}^{1/3}} \tag{90}$$

The corresponding group for mass transfer is:

$$Fs_\infty = \frac{Sh_\infty - 2}{Re_\infty^{1/2} Sc_{m,\infty}^{1/3}} \tag{91}$$

The few minor analogy defeats will be discussed later. The Frössling group remains invariant with the Prandtl or Schmidt group at high values of the

Prandtl or Schmidt number, however, it varies very slightly at the lower values as indicated in Table 4 for the Frössling number at the forward stagnation point. The quantity in Equation 64 in parenthesis produces the angular dependence of the Frössling group from the stagnation point of the sphere. Nils Frössling (5) also calculated the angular dependence for a sphere at a single Schmidt number of 2.532 in order to compare with his experimental evaporation rates of a napthalene sphere (6). Frössling used the experimental velocity distributions based on Re_{∞}=157,200. He did not complete his corresponding calculations involving the flat profile for a sphere for variable Schmidt number. In Figure 4 is shown the angular dependence predicted by the author for A_2'=0.441 for variable Prandtl or Schmidt numbers, together with Frössling's calculations for a Schmidt number of 2.532 and his stagnation limit for his flat velocity profile approximation. Again the solution from this work lies between Frössling's two cases. Also included in Figure 4 is Sibulkin's exact solution (10) for a Prandtl number of 0.7. Also shown here are smoothed experimental data from the 1-inch silver sphere at a Reynolds number of 3700 and low turbulence level of 0.013 and the agreement is satisfactory considering the experimental uncertainties near stagnation.

There is a variety of other theoretical techniques used to solve the systems of equations, mostly of the momentum-integral form and of the integral-energy equation. The details of both exact and approximate solutions for bluff bodies are outlined in detail by Rosenhead (11). A realistic solution for the sphere was done recently by Brown, Pitts, and Leppert (12), using approximate methods, and excellent agreement with experiments were obtained.

BOUNDARY LAYER DETACHMENT:

The techniques presented above for the exact solution to the equations of motion and conservation of energy (or species) predict the local transfer from

TABLE 4

FLOW ABOUT A SPHERE

PRANDTL NUMBER DEPENDENCE OF STAGNATION POINT HEAT TRANSFER

Pr	Φ_2(Pr)	Fs
0.7	0.0863	1.357
1.0	0.0765	1.368
2.0	0.0615	1.386
5.0	0.0464	1.408
50.0	0.0228	1.439
200.0	0.0144	1.450

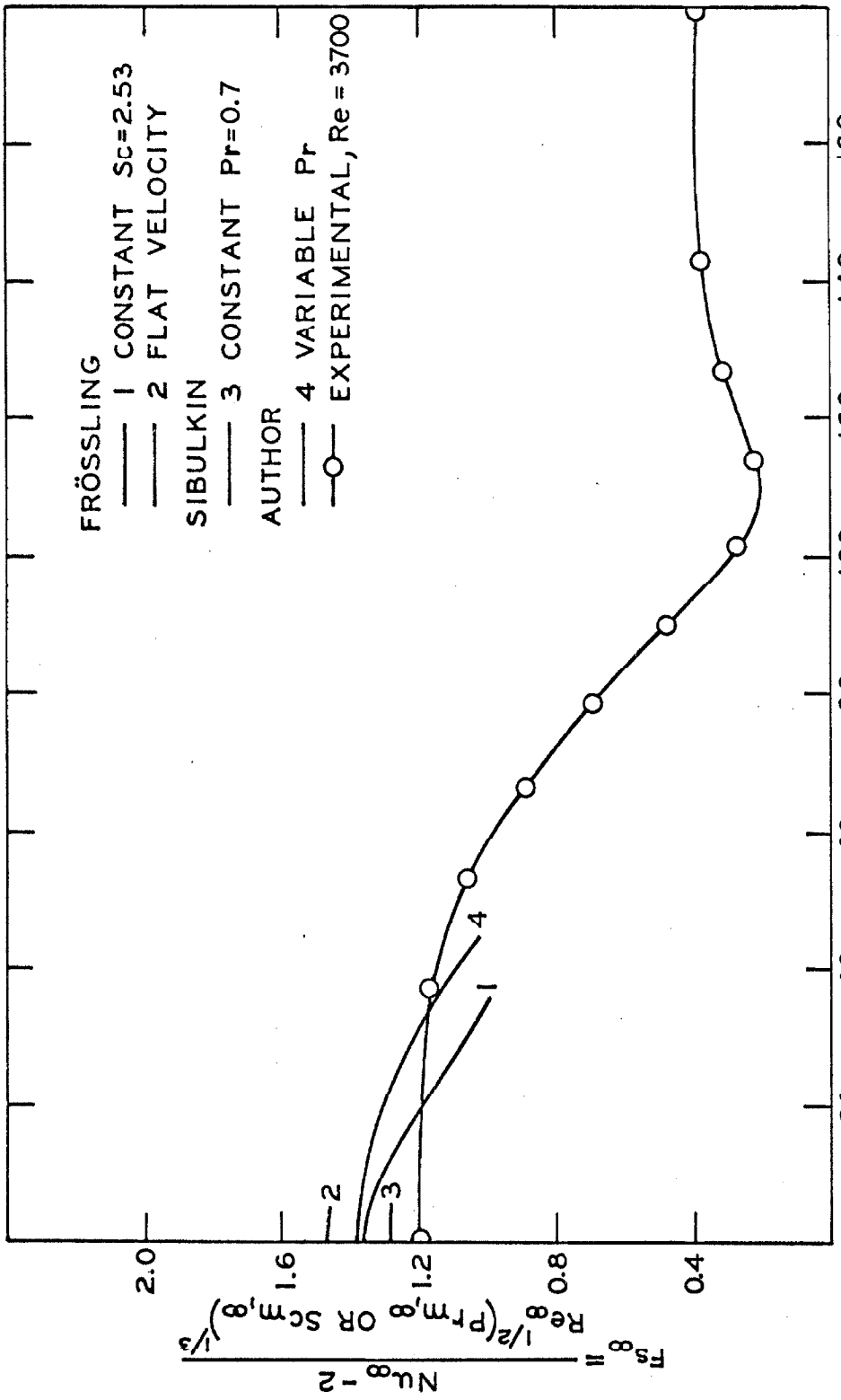

Figure 4. Frössling Number and Local Transfer From a Sphere.

the bluff body as a function of angle from the forward stagnation. Frössling's analysis (5) has predicted the angular dependence of the transport as far from the forward stagnation point as a Blasius series solution permits, short of fantastic labor in extending the series. The fluid mechanics alone, however, can be solved more accurately by carrying many Blasius terms. For example, carrying eleven terms (1), the velocity profile can be obtained with an accuracy sufficient to predict the position of detachment.

Detachment or separation of the momentum boundary layer arises when intermolecular shearing forces near the surface reduce the kinetic energy of the fluid molecules as they are accelerated away from the forward stagnation point, which is in the region of decreasing pressure. Later the pressure increases again (see Figure 5) as the particles move toward the latter half of the bluff body and are decelerated accordingly. The molecules near the surface do not possess sufficient kinetic energy to surmount this pressure barrier, and they stop and reverse direction. At this point the shear forces vanish and also the velocity gradient at the surface. This point is called the "point of separation". As a result, the molecules farther away from the surface possess more energy and overtake those which were closer to the surface, resulting in a vortex. The occurence of this vortex results in a wake behind the bluff body which drastically alters the entire picture of both the fluid mechanics and heat and mass transport.

A comparison between the potential flow pressure distribution around a circular cylinder and that measured by the author for both low (5700) and high (86,000) Reynolds numbers for low turbulence of 1.3% is shown in Figure 5. The inviscid model is only close to experimental measurements in the region of the forward stagnation point. The experimental point of separation was observed to occur about 75°; using eleven terms in the Blasius series, a point of 108.8° was predicted (1). The severe alteration of the pressure profile as a result of the detachment of the boundary layer is certainly apparent. Blockage effects

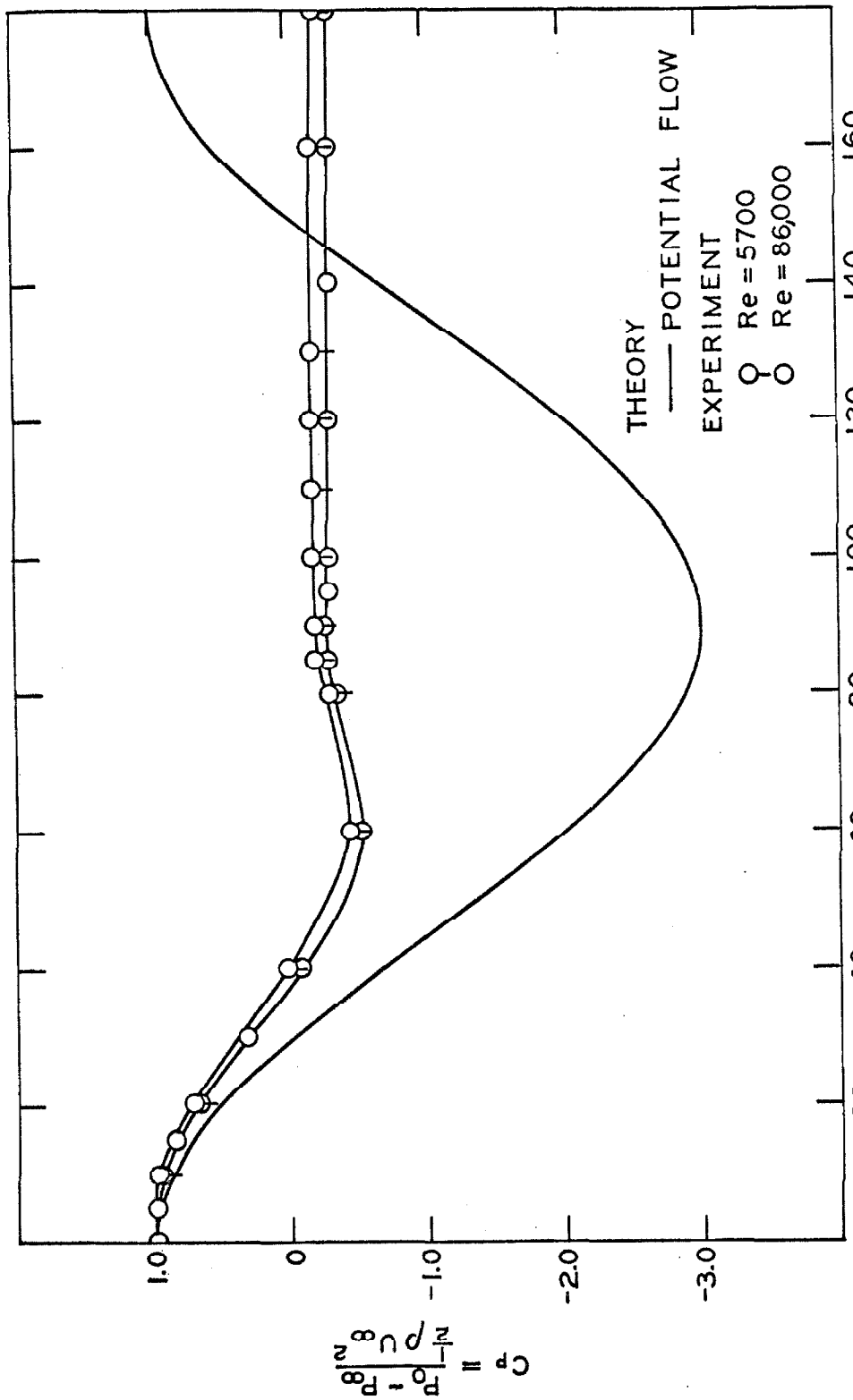

Figure 5. Pressure Coefficient of a Cylinder.

(discussed in detail later), which undoubtedly exist, tend to accentuate the difference in profiles. Increasing free stream turbulence lessens the difference, owing to the additional kinetic energy which is stored in the fluid as it is accelerated in the boundary layer.

For the case of a sphere an identical situation is observed. A point of separation of 109.6° is predicted (1) for a sphere when seven terms in the Blasius series are used. Experimentally a point of separation about 95° was found. Jet blockage was probably less for the 0.5 to 1.5 inch spheres than the 1.5 inch cylinder, which was mounted above a 3 x 12 inch jet. Further work needs to be done theoretically in predicting the point of separation when the velocity profile outside the boundary layer differs from potential flow, as the presence of the wake acts to alter this profile as if the cylinder were non-circular or the sphere an ellipsoid.

TURBULENT CONVECTIVE TRANSPORT:

The problem of turbulent transport originates in two different ways: from the transition of the laminar boundary layer which is formed following the forward stagnation point into a turbulent boundary layer before separation and from the perturbing action of free stream turbulence on the laminar boundary layer in the region of stagnation. The first problem arises only at very high velocities (for cylinders $Re_\infty = 3.0 \times 10^5$ and for spheres $Re_\infty = 2.8 \times 10^5$). The turbulent boundary layer can only be treated when the eddy profiles are known, $\epsilon_m(x,y)$, $\epsilon_h(x,y)$, and $\epsilon_d(x,y)$, in conjunction with Equations 7 or 8 and 12-14. Unfortunately, little work has been done in this area for bluff bodies.

Free stream turbulence interacts with the laminar boundary layer, as will be shown later, in a very complicated way such that the rate of transport from a surface is increased. Our experimental work tends to indicate that effects

of free stream turbulence are analogous to a "tuning phenomenon" within the laminar boundary layer involving unstable oscillations next to the surface and which apparently are ever-present. Such a phenomenon is not well understood and not currently amenable to rigorous theoretical treatment. An approximate stochastic model which involves finite eddy coefficients in the region of the surface and uses an empirical representation for the shear has been presented as Proposition D. Eckert and Drake (3, pg. 221) mention that there are some experimental measurements which indicate that a certain amount of turbulence exists right up to the surface. It is clear that much more work has to be done in this area. A valuable technique would be to make temperature traverses into the calorimeter and compute the eddy profiles.

TUNNEL BLOCKAGE:

A mainstream, parallel and infinite in extent, in which to carry out transport studies is not feasible experimentally. One must settle for finite fluid streams where the body under investigation may be only a few times smaller in diameter than the mainstream. Blockage is referred to as the ratio of the area of the body under study to the area of the mainstream. Blockage in a wind tunnel acts in such a way as to increase the velocity outside the boundary layer above that which would occur in an infinite mainstream. Effects of finite free jet width are more complicated but in general the streamlines are divergent, the velocity outside the boundary layer is reduced, and the wake is altered. However, in free jets the effect is not large.

Blockage effects in wind tunnels can be divided into two contributions: "solid blockage" which is responsible for the increase of the velocity as a result of the reduction in flow cross section and "wake blockage" which results in wake distortion. Solid blockage can be predicted from an increase in velocity outside the boundary layer. A first order prediction of this velocity increase can

be expressed in terms of the effective increase in velocity as resulting from geometrical considerations alone:

cylinders:
$$\frac{U_{1,eff}}{U_1} = \frac{WL}{WL - d \sin \Psi L} = \frac{W/d}{W/d - \sin \Psi} \tag{92}$$

spheres:
$$\frac{U_{1,eff}}{U_1} = \frac{\pi W^2/4}{\frac{\pi W^2}{4} - \frac{\pi d^2}{4} \sin^2 \Psi} = \frac{(W/d)^2}{(\frac{W}{d})^2 - \sin^2 \Psi} \tag{93}$$

where W is the tunnel width and d is the diameter of the bluff body. The effective increase in velocity is illustrated for spheres in Figure 6. The effective increase in the Frössling group correlation, A and B, are also shown. Such a correction was also made by Brown et. al. (12). This first order correction for solid blockage should be used to correct the experimental Reynolds number at each of the angles. Or for prediction purposes, use the free stream Reynolds number and correct the coefficients A and B, which are discussed later. For the average transport this result must be integrated over the entire surface:

$$\frac{A(W/d)}{A(\infty)} = \frac{B(W/d)}{B(\infty)} = \left[\int_0^{180°} \frac{(W/d)^2 \sin \Psi \, d\Psi}{(W/d)^2 - \sin^2 \Psi}\right]^{1/2} \tag{94}$$

This correction for the overall transport has been shown in Figure 7. It is expected from these geometrical considerations alone, which will underestimate the effect very slightly, that the blockage must be kept under 2% for errors in the Frössling number to be under 1%. Typical measurements which will be discussed later ranged in blockage ratio from 4 to 18%.

Wake blockage is considerably more complicated and does not lend itself to simplified analysis (13). The net effect in tunnel blockage seems to be a reduction in wake volume (14, 15) and increased stability. The drag coef-

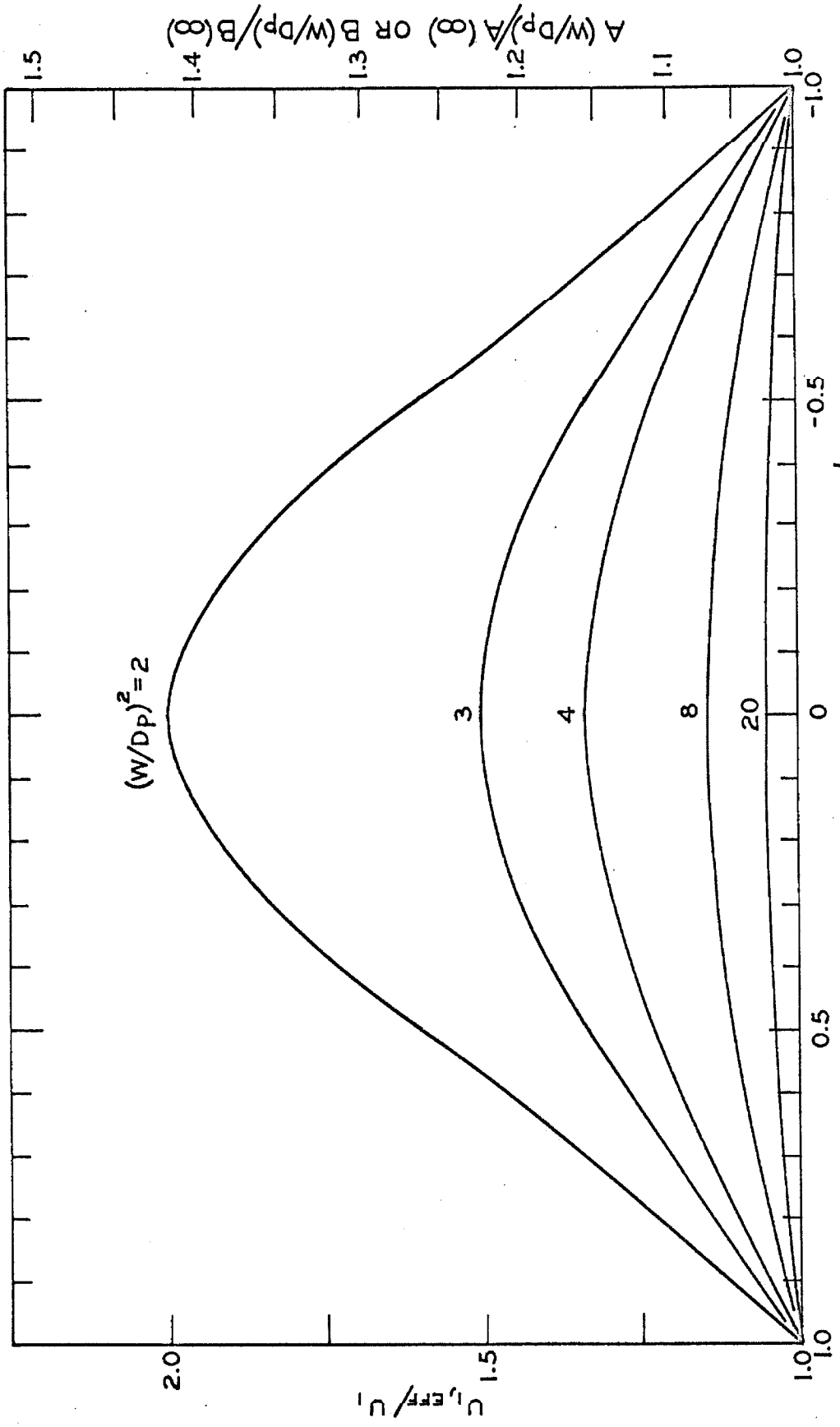

Figure 6. Local Blockage

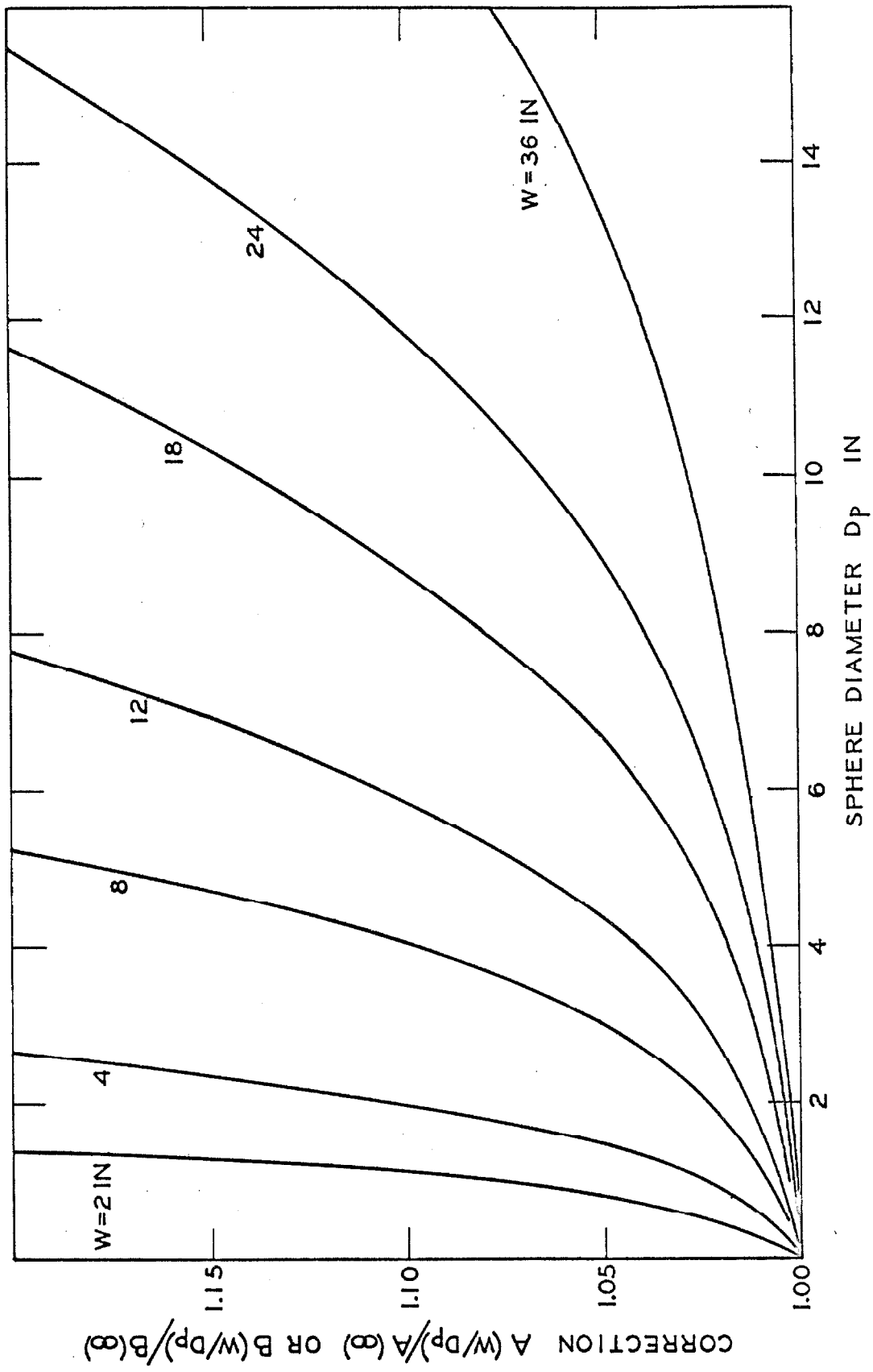

Figure 7. Overall Blockage.

ficient and the critical Reynolds number are increased with increased wake blockage (14, 15) and blockage effects move the point of separation forward slightly. Pope (15. 5) developed a useful relationship as follows:

$$\frac{U_{1,eff}}{U_1} = 1 + 0.822\ (d/W)^2 + \frac{C_D}{4}(d/W)$$

from conformal mapping techniques using potential flow. The second order term represents solid blockage, and the third term wake blockage. The solid blockage predicted by Pope compares within a few percent to that of Equation 94.

In free jets the effects of finite duct width are found to be opposite to those found in wind tunnels. Once the flow passes out of the confined walls of the duct and impinges upon a bluff body, the streamlines rapidly diverge. Limited pitot tube traverses in the wake made by the author indicate qualitatively that the volume of the wake is somewhat expanded. The diverging streamlines apparently result in a decrease in the velocity just outside the boundary layer. In Figure 8 are shown experimental results from this work of the velocity profile outside the boundary layer for cylinders under varying degrees of free jet extent calculated from the solution to Equation 3:

$$\frac{U_1}{U_\infty} = \sqrt{1 - C_p} \tag{95}$$

These experimental results were chosen since they represent the lower and upper Reynolds numbers investigated; furthermore, the intermediate Reynolds number tests also fall on this same profile. The point of separation for these tests was found from heat transfer measurements to vary from 75° to 82° , and is also apparent from these velocity profiles. In Figure 8 are also shown the measurements of Cuffel (16) for $Re_{\infty} = 3500.$ and Yuge (17) for $Re_{\infty} = 40,000.$,

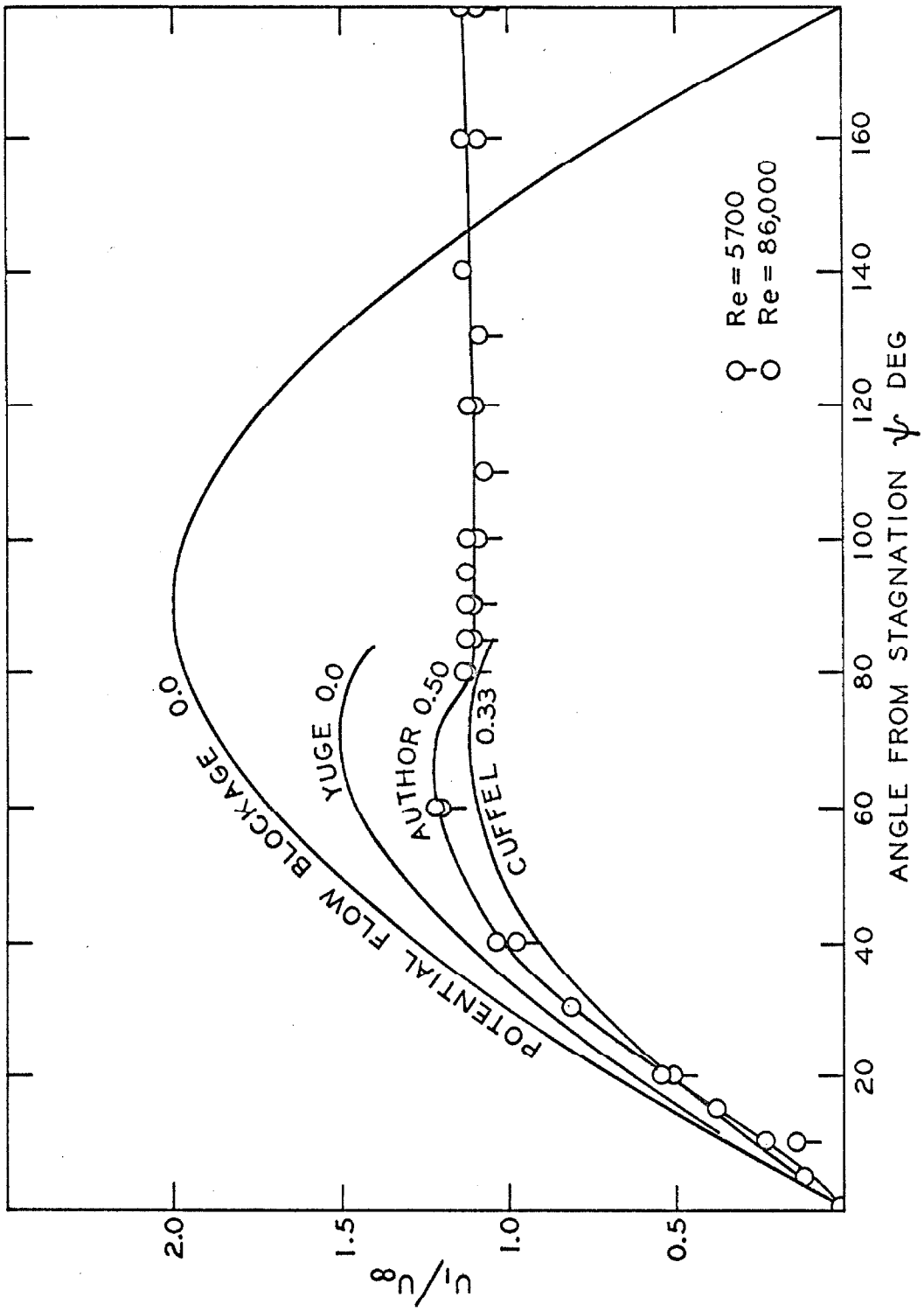

Figure 8. Local Velocity Outside the Boundary Layer on a Cylinder.

which involved blockage ratios of 0.33 and 0.0 respectively. The results of this work fall between Cuffel and Yuge, indicating that the effects of finite free jet width are not nearly as severe as for wind tunnel studies. More detailed experimental studies will be required in order to quantitatively study blockage in free jets

LOCAL VELOCITY:

The velocity which characterizes momentum, energy and mass transport is the free stream velocity, U_∞, in Equations 39-41, 63, and 87. The velocity outside the boundary layer, U_1, is scaled directly by U_∞. The free stream velocity is that velocity which would be measured in the free stream had the bluff body not been present. It is not correct to use an average velocity across the duct (such as based on the mass flow rate) as this will be considerably less than the centerline velocity for a free jet with a flat working section. The free stream velocity, U_∞, can easily be measured with a pitot tube located a half inch or so upstream of the bluff body and then retracted during heat transfer studies. This was done in all the experimental studies reported here.

INTERFACIAL VELOCITY:

The effects of a finite velocity normal to the bluff body surface, V_o, can be predicted theoretically. The boundary condition in Equation 30 must be used instead of that in Equation 28. For this case $f(\eta)$ at the surface becomes

$$f(0) = -\frac{V_o}{U_\infty} Re_\infty^{1/2} \tag{96}$$

The fluid mechanics have been solved for the two- and three-dimensional stagnation points. Rosenhead (11, pp. 242-244, 332-335) presents the solutions for suction and blowing at the interface, $-5 < f(o) < 5$, and suction was found to delay separation. The solution to the energy equation has not been carried out for finite f(0); however, the thermal transport solution at the three-dimensional stagnation point for a finite interfacial velocity is available (18,19). For the measurements involving spheres presented here, the quantity $f(0) \simeq 0.04$, and the Frössling group would be lower by about 7%. A comparison of this theory with experimental results will be presented later.

NATURAL CONVECTION EFFECTS:

In a gravitational field, driving forces of either temperature or concentration across the boundary layer give rise to bouyant forces which effect the conservation of momentum. The viscous term in the equation of motion (Equation 25) must be augmented by a body force which linearly involves the driving force, such as:

$$\beta g\ (T-T_{\infty}) = \theta \frac{\nu^2}{d^3}\ Gr \qquad (97)$$

which applies to a vertical section of a bluff body where β is the isobaric thermal expansion coefficient, $\frac{1}{V}(\frac{\partial V}{\partial T})_P$, Gr, the Grashof group, $gd^3\beta\ (T_o - T_{\infty})/\nu^2$ and θ, the dimensionless temperature defined in Equation 51.

Numerous theoretical works have been done for vertical flat plates and vertical cylinders (1); however, only two exact theoretical solutions have been carried out for horizontal cylinders and spheres. Hermann(1) obtained the dependence of the average Nusselt group on the Grashof group for a horizontal cylinder placed in air (Pr=0.7) as:

$$Nu^* = 0.372\ Gr^{1/4} \tag{98}$$

and Shell (1) computed the average Nusselt group for a sphere surrounded by air as:

$$Nu^* = 2 + 0.429\ Gr^{1/4} \tag{99}$$

For variable Prandtl number, the solutions involve the product of the Grashof and the Prandtl groups instead of Grashof alone. Both of these theoretical solutions agree within several percent with experimental data (1). There were no exact solutions found for local transport by natural convection from cylinders and spheres.

The combined action of forced convection with natural convection has been treated by Yuge (20) and Klyachko (21). For Reynolds numbers above 400, natural convective transport at moderate driving forces is negligible compared to forced convection. For Reynolds numbers below 400, in counter-flow, where the action of forced and natural convection oppose each-other, the net transport passes through a minimum. In parallel or cross-flow there is a smooth transition between the two mechanisms of transport. Separating the two effects of forced and natural convection is not easy. Extrapolating the Nusselt numbers to zero temperature difference can be done for a given Reynolds number, removing natural convective effects for both parallel and counter-flow; however, this procedure requires very accurate data. When flow is parallel the natural convection (and other effects such as end-effect conduction and radiation losses) can be removed by varying the driving force once, at zero Reynolds number, and subtracting this directly from the measurements at finite Reynolds number at a particular flow rate. The second method is valid only for parallel flow and for the lower driving forces. It is

also difficult to separate the effects of natural convection from variable properties in forced convection when the driving force is independently varied.

VARIABLE PROPERTIES:

Transport measurements involving real fluids suffer from the disadvantage that physical properties change with temperature, pressure, and composition. Two independent problems arise from this unfortunate fact. First, the Frössling, Reynolds, Prandtl, and Schmidt groups must be evaluated at some convenient and reproducable experimental condition. Secondly, the actual variation of the properties through the boundary layer must be taken into account, since the variation differs considerably between real fluids (i.e. air, water, oil, mercury, etc.). Since the transport coefficient is defined by the ratio of the flux to the driving force, the coefficient must certainly not depend on the driving force. In fact, the solution should not involve any function of the driving force at all. For example, the ratio of the temperature of the free stream to that of the interface should not strictly be allowed (as one may occasionally find in the literature). The solution must only involve fluid and flow properties.

When the thermal conductivity in the Nusselt number and kinematic viscosity in the Reynolds number are evaluated at different locations, as was done previously for the 0.5 and 1 inch silver and porous spheres, a dependence on the temperature driving force by necessity must result. A plot of $(Nu_o-2)/Re_\infty^{1/2}$ is found to decrease strongly (30%) with increasing temperature driving force (-40° to 120° F.) while a plot of $(Nu_\infty-2)/Re_o^{1/2}$ is found to increase strongly (40%) with driving force. Here the "o" has been used to denote that the properties were evaluated at surface conditions. However, a plot of $(Nu_\infty-2)/Re_\infty^{1/2}$ increased only slightly (7%) with driving force.

Evaluating all physical properties in the Frössling, Reynolds, Prandtl, and Schmidt groups at the free stream is especially convenient compared to reference states at the interface or at mean conditions in that the free stream conditions are usually well established and reproducable. Now that a reference state is set, the problem still remains to account for variation in properties across the boundary layer. Here is where a theoretical analysis serves as a guide.

For the general case of variable properties the Navier-Stokes equations can be simplified with the boundary layer assumptions as:

Continuity

Two-dimensional:

$$\frac{\partial(\rho U)}{\partial x} + \frac{\partial(\rho V)}{\partial y} = 0 \tag{100}$$

Axially-symmetric

$$\frac{\partial(\rho U r)}{\partial x} + \frac{\partial(\rho V r)}{\partial y} = 0 \tag{101}$$

Motion:

$$\rho\left(U\frac{\partial U}{\partial x} + V\frac{\partial U}{\partial y}\right) = -\frac{dP}{dx} + \frac{\partial}{\partial y}\left(\mu\,\frac{\partial U}{\partial y}\right) \tag{102}$$

Energy:

$$\rho C_p\left(U\frac{\partial T}{\partial x} + V\frac{\partial T}{\partial y}\right) = \frac{\partial}{\partial y}\left(k\frac{\partial T}{\partial y}\right) \tag{103}$$

Specie:

$$U\frac{\partial C_A}{\partial x} + V\frac{\partial C_A}{\partial y} = \frac{\partial}{\partial y}\left(\mathcal{D}_{AB}\,\frac{\partial C_A}{\partial y}\right) \tag{104}$$

These equations can be reduced to ordinary differential equations by applying the famous Von Misses transformation (1):

$$d\zeta = \frac{\rho}{\rho_\infty} d\eta \tag{105}$$

The ordinary differential equation for two-dimensional boundary layers of Equation 42 becomes:

$$(f')^2 - ff'' - \frac{d}{d\zeta}\left[\frac{\rho\mu}{\rho_\infty \mu_\infty} f''\right] - 1 = 0 \tag{106}$$

where the prime denotes differentiation with respect to ζ . For the axially-symmetric case Equation 79 becomes:

$$(f')^2 - 2ff'' - 2\frac{d}{d\zeta}\left[\frac{\rho\mu}{\rho_\infty \mu_\infty} f''\right] - 1 = 0 \tag{107}$$

The energy equation (Eqn. 53) becomes:

$$\frac{d}{d\zeta}\left[\frac{\rho k}{\rho_\infty \mu_\infty} \theta'\right] = - f(\zeta)\, Pr_\infty \left(\frac{C_P}{C_{P,\infty}}\right) \theta' \tag{108}$$

and the diffusion equation becomes:

$$\frac{\rho}{\rho_\infty}\frac{d}{d\zeta}\left[\frac{\rho \mathcal{D}_{AB}}{\rho_\infty \mathcal{D}_{AB,\infty}} G_A'\right] = - f(\zeta)\, Sc_\infty\, G_A' \tag{109}$$

where G_A is the dimensionless specie concentration, $\frac{C_A - C_{A,\infty}}{C_{A,o} - C_{A,\infty}}$, analogous to Θ.

A most interesting consequence of the Von Misses transformation is that for the following special case of fluid property variation:

$$\rho\mu = \text{const} \tag{110}$$

$$\rho k = \text{const} \tag{111}$$

$$C_P = \text{const} \tag{112}$$

$$\mathcal{D}_{AB} = \text{const} \tag{113}$$

the Equations 106-108 reduce to the constant property case, replacing the similarity variable η with ζ. From Part I of this thesis it can be seen that Equations 110-113 are very nearly correct. For example Equation 110 actually is:

$$\rho\mu \approx \frac{1}{T^{1/2}\Omega^*(T^*)\ (1 + B^*(T^*)\rho^* + C^*(T^*)\rho^{*2})} \tag{114}$$

which is constant for a small range in temperature. For a polyatomic gas Equation 111 depends somewhat more strongly on temperature than in Equation 114. Equation 109 can not be simplified readily under such a transformation, short of ρ= const and $\mathcal{D}_{AB}$=const; therefore, the Von Misses transformation is worthless for diffusion. This reveals another analogy defeat between heat and mass transfer, in that property variation of ρk and $\rho\mathcal{D}$ is quite different through the boundary layer.

An exact analytic solution of transport with variable properties is extremely difficult. To obtain significant property variation large driving forces are required, which creates significant natural convection. Sparrow and Gregg (22) solved the problem of natural convection with variable properties numerically using six cases for fluid property variation. The six cases varied from Equations 110-112 to empirically fully describing the actual properties of air and liquid mercury. These authors used the concept of a reference temperature where properties can be evaluated, such that the constant property solutions are valid. The problem of combined forced and natural convection with variable properties is exceedingly complex and has not been treated to date.

In this work a useful empirical fact has been used to simplify the problem, with the underlying philosophy of placing the uncertainties of molecular property variation in a term which will do the least harm. Using the molecular theory of transport properties presented in Part I, the following approximation can be made:

$$\left(\frac{\nu_\infty}{\nu}\right)^{1/3} \approx \frac{\rho\,\mu}{\rho_\infty \mu_\infty} \approx \frac{\rho\,k}{\rho_\infty k_\infty} \approx \frac{\rho^2 \mathcal{D}_{AB}}{\rho_\infty^2 \mathcal{D}_{AB,\infty}} \tag{115}$$

The variation in Frössling number from molecular property variation can be empirically represented by:

$$Fs_\infty \propto (\nu_\infty/\nu_o)^n , \tag{116}$$

where n is taken to be an empirical exponent.

EXPERIMENTAL BACKGROUND

The experimental work described herein has been strongly guided by the theoretical background described in the previous section. The Frössling group which has emerged from the exact theoretical solution has been used throughout in studying experimentally the local variation of transport around cylinders and spheres, the effects of separation, the perturbing action of free-stream turbulence, and variable properties. The overall transport can then be treated from the direct knowledge of the local behavior. The Reynolds number ranged from 2,600 to 86,000, the turbulence level of the free-stream from 0.013 to 0.25, and the scale of turbulence from 0.3 to 1.1 inches. The experimental results were then compared and correlated with all other known transport data from cylinders and spheres.

CYLINDERS

One of the most significant and extensive contributions to local transport, both experimentally as well as theoretically, was the work of Frössling (5, 6). This investigator suspended liquid drops over an air jet and measured the change in radius by photomicrography. The drop radii varied from 0.1 to 0.9 mm and the air velocity from 0.2 to 7 m/sec, corresponding to a Reynolds number, as defined in the Nomenclature, from 2 to 800 for the evaporation of nitrobenzene, aniline, and water. Local convective rates were determined by measuring the pointwise variation in the radius of a solid napthalene sphere in a free jet stream of air. Frössling (5, 6) analyzed these results for spheres theoretically and excellent agreement was obtained, and he carried out the same theoretical analysis for cylinders. Both of these exact theoretical solutions were discussed in the previous section and compared with experimental data.

LITERATURE:

Shortly before Frössling undertook his experimental program involving local transport in a free jet, increases in the overall heat transfer with turbulence were observed as early as 1925 (23). Subsequent to that time, a number of systematic studies of turbulence have been made (24-32). Churchill and co-workers (33,24) carried out heat transfer measurements on cylinders and correlated the results of numerous other investigations. Perkins and Leppert (35) studied forced thermal convection from cylinders to a stream of water and to ethylene glycol up to a Reynolds number of 100,000, and varied the Prandtl number from 1 to 300. The turbulence level was 1.08%. Their results reflect, for the most part, behavior characteristic of transport in the wake involving gaseous streams. Richardson (36,37) has reviewed a substantial amount of data and concluded that the Reynolds number dependence of transport in the laminar portion and in the turbulent wake portion can be represented separately. Grafton (38) concludes that in the laminar region the local Frössling number is independent of the Reynolds number, whereas in the wake it is not.

In the analysis of the available data for both cylinders and spheres, it was found in confirmation with the exact theory presented in the previous section that the Frössling group is a useful transport parameter for both thermal and material transfer from bluff bodies. Empirically the Frössling number appears to be a complicated function of the angle measured from the forward stagnation point, the Reynolds number, turbulence level of the free-stream, and weakly dependent upon scale of turbulence and the molecular properties of the fluid. Although an exact theoretical treatment of the effects of free stream turbulence on the laminar boundary layer formed on a bluff body is not to be found at this time, the procedure has been outlined in the previous section. If one believes that the perturbing action of free stream

turbulence can be explained by a tuning mechanism creating unstable oscillations near the surface, then a model such as that developed in Proposition D might be useful. Regardless of the theoretical model employed, the following form of an empirical expression for either macroscopic or local Frössling numbers is intuitively correct:

$$Fs_{\infty} = A \left(\frac{\nu_{\infty}}{\nu_{o}}\right)^{n} + \left[B \frac{Z_t}{Z_t + C} + D\right] Re_{\infty}^{1/2} (Pr \text{ or } Sc)_{m,\infty}^{m} \qquad (117)$$

The Frössling numbers for heat and mass transfer are equivalent when the Lewis number (Le=Sc/Pr) is near unity. The analogy breaks down at high mass transfer rates with large associated interfacial velocities normal to the surface, and at high driving forces when molecular property variation across the boundary layer is large. These points were discussed in the previous section.

EXPERIMENTAL APPARATUS:

In Figure 9 is shown the 1.5 inch copper cylinder equipped with a small solid copper calorimeter 0.100 inch in diameter at the surface, supported by a thin bakelite disk. The lower portion of the figure shows an enlargement of the calorimeter and disk. A photograph of the unwired copper calorimeter and its position in the finished cylinder is given in Figure 10. Double glass covered, Advance wire 0.005 inch in diameter was wound into the spiral groove within the calorimeter. A stainless steel radiation shield was mounted on the outside of the calorimeter which was fitted into the small well in the main cylinder. In operation, the calorimeter heater current was adjusted by means of voltage dividers until the temperature difference between the calorimeter surface and the surface of the copper cylinder was reduced to less than 0.02° F. The actual schematic of the electronic circuit is pre-

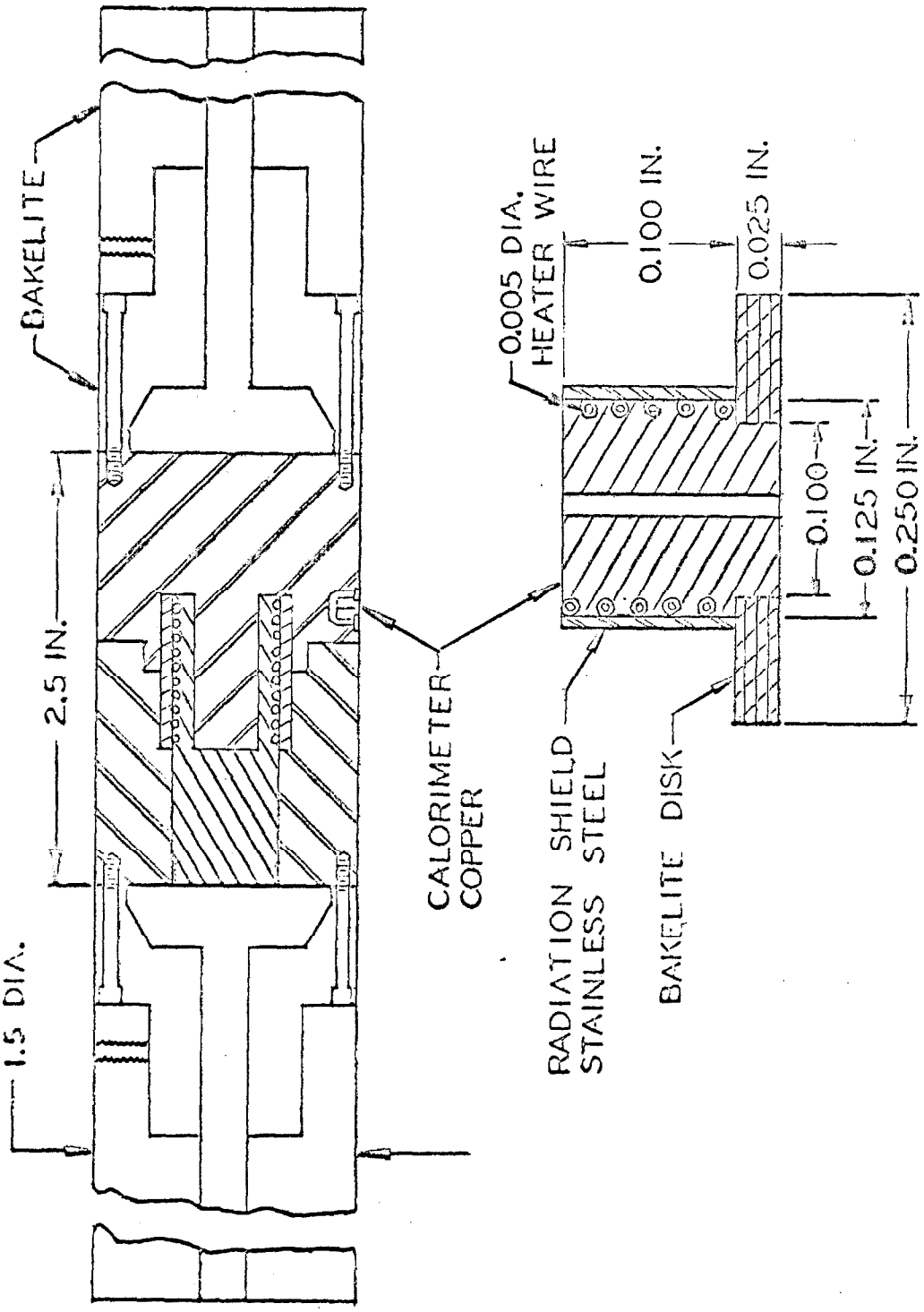

Fig. 9 1.5 inch copper cylinder and calorimeter

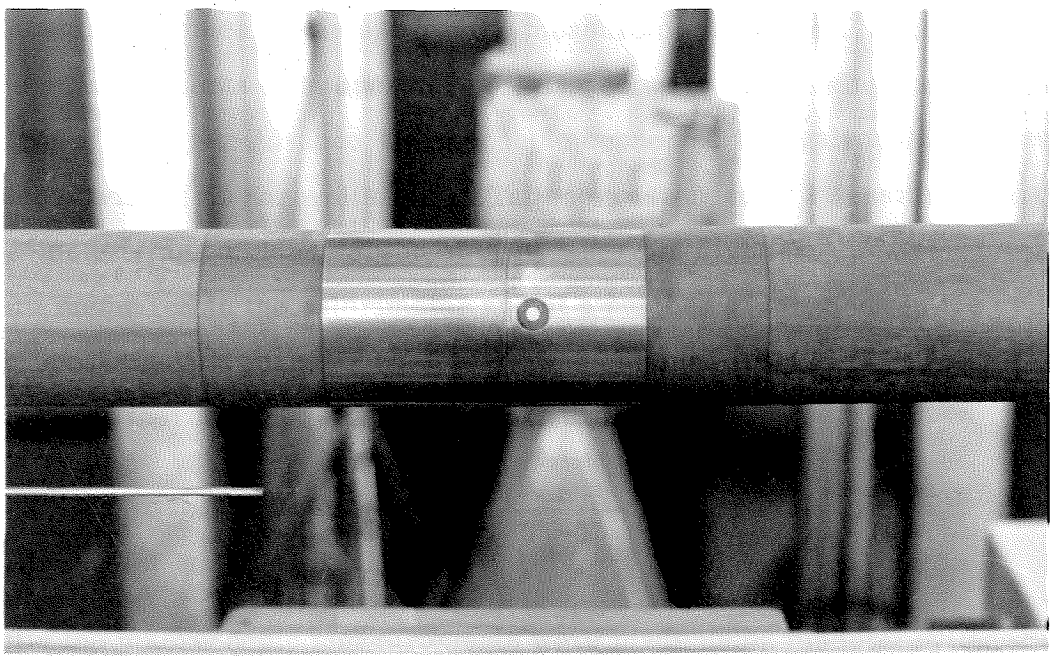

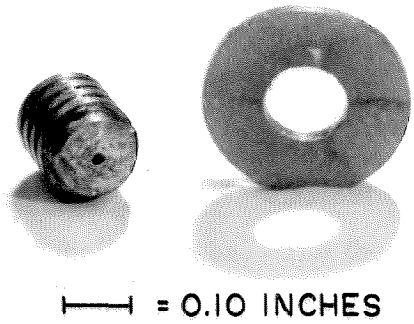

Figure 10. Photograph of the 1.5 inch Cylinder and Calorimeter.

sented later, since it was used in the measurements of the 1.5 inch sphere. The measurements of temperature difference were made using the potential output of a copper-Advance thermocouple connected to a galvanometer having a sensitivity of 50 nanovolts/mm. This corresponded to a sensitivity on the one-meter ground glass screen of 0.001° F./mm division. Temperatures were measured in the calorimeter and at a number of locations in the cylinder. The local thermal transfer coefficient was obtained from local values of the measured thermal flux and temperature difference:

$$h = \frac{q}{T_o - T_\infty} \tag{118}$$

while the macroscopic measurements were made using the total cylinder thermal flux and the average temperature difference. The heat flux was obtained from the electrical energy dissipated in the cylinder heater at a particular air velocity and was decreased by the energy dissipated at the same driving force at no flow as a result of energy losses arising from phenomena other than forced convection:

$$Nu^* = 5.2131 \frac{(i^2R)^*_{Re} - (i^2R)^*_{Re=0}}{k\,(T_o - T_\infty)} \tag{119}$$

where the electrical energy is in watts, thermal conductivity in Btu/hr-ft-° F., and temperature in Fahrenheit degrees. The theoretical aspects of separating fully forced convection from other mechanisms was discussed earlier. The local Nusselt numbers were best obtained from the macroscopic Nusselt numbers, which were of greater accuracy, in the following way:

$$Nu_\infty = \frac{(i^2R)_{Re} - (i^2R)_{Re=0}}{\frac{1}{180}\int_0^{180}\left[(i^2R)_{Re} - (i^2R)_{Re=0}\right]d\psi}\, Nu^*_\infty \tag{120}$$

The local energy dissipated from sources other than forced convection was measured at no flow, as in the macroscopic case, as a function of the temperature driving force and angle from stagnation. Equation 120 insures that the local results will integrate to the accurately measured macroscopic Nusselt number and also will tend to normalize out any systematic errors, such as uncertainties in the effective calorimeter area.

The cylinder was mounted at the top of a 3 by 12 inch rectangular duct as shown in Figure 11. An 8-foot, 12 by 12 inch damping section was used which was then reduced to the section size of the rectangular jet. A photograph of the entire installation used for the 900 series tests at the working section of the jet is shown in Figure 12, illustrating, from left to right, the thermocouple ice bath, the cylinder mounted atop the jet, the calorimeter balancing network, and the one-inch kerosine micromanometer. The remaining electronics are hidden in the photographs. The installation used for the 600 series tests employing the identical duct geometry, but different instrumentation and air supply system, is described later.

The longitudinal turbulence level was reduced to 1.3% at the working section of the jet as a result of the flow acceleration achieved by the converging section. Damping screens of 0.1 inch square mesh were employed before and after the eight-foot damping section. Various turbulence levels were generated. as shown in Figure 11, by varying the downstream distance of the cylinder from both a "punched plate grid" which was constructed similarly to that described by van der Hegge Zijnen as his grid "27/7" (39), and from a "circular-hole grid" patterned after Davis (40,41). The measurements of van der Hegge Zijnen and Davis were used to establish the longitudinal turbulence level and to estimate the integral scale as a function of the downstream position from the grid. The evaluation of the level of turbulence as a function of downstream position from a grid has been analyzed critically in an excellent and comprehensive treatment by Couch (42). He presents

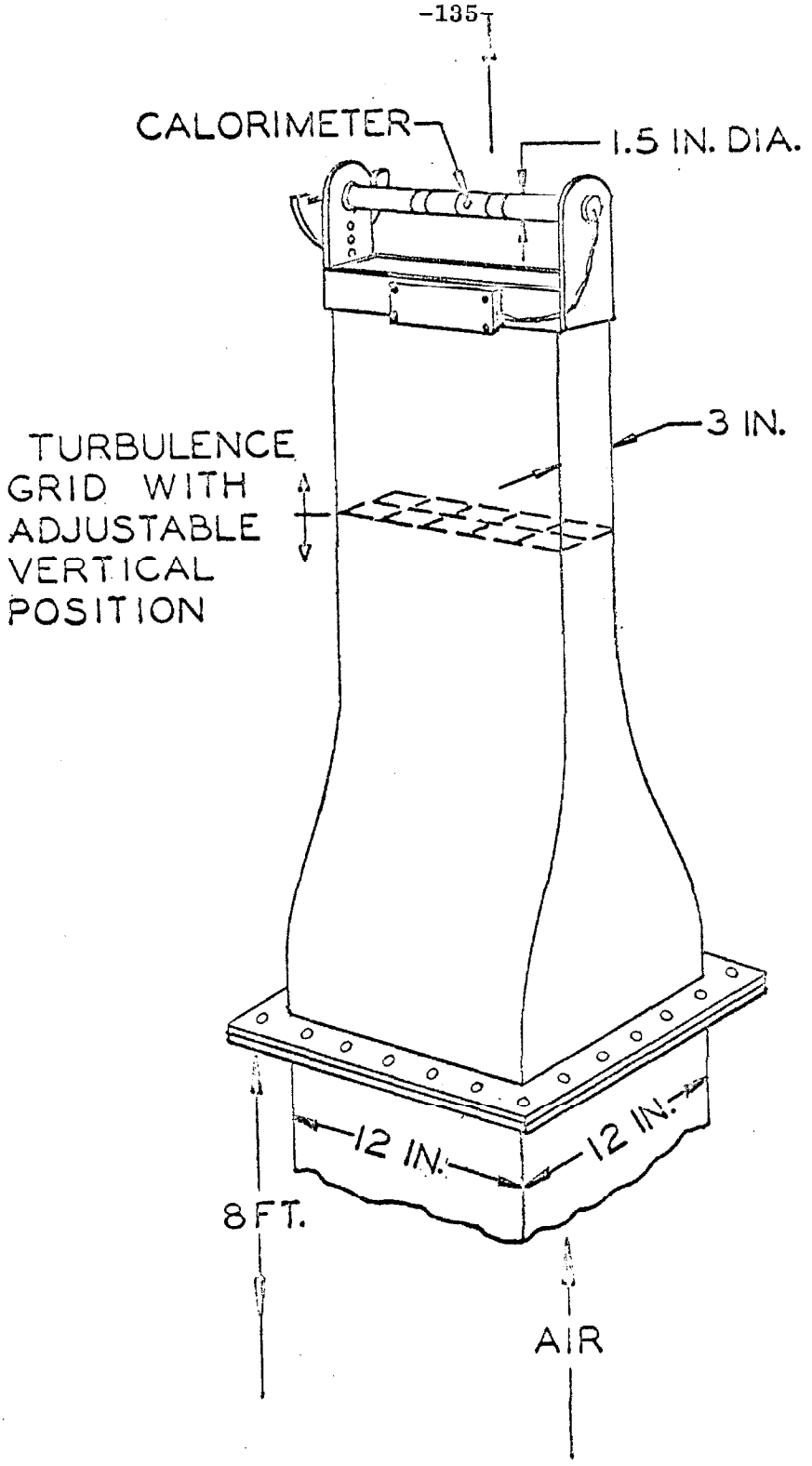

Fig. 11. Arrangement of cylinder and duct

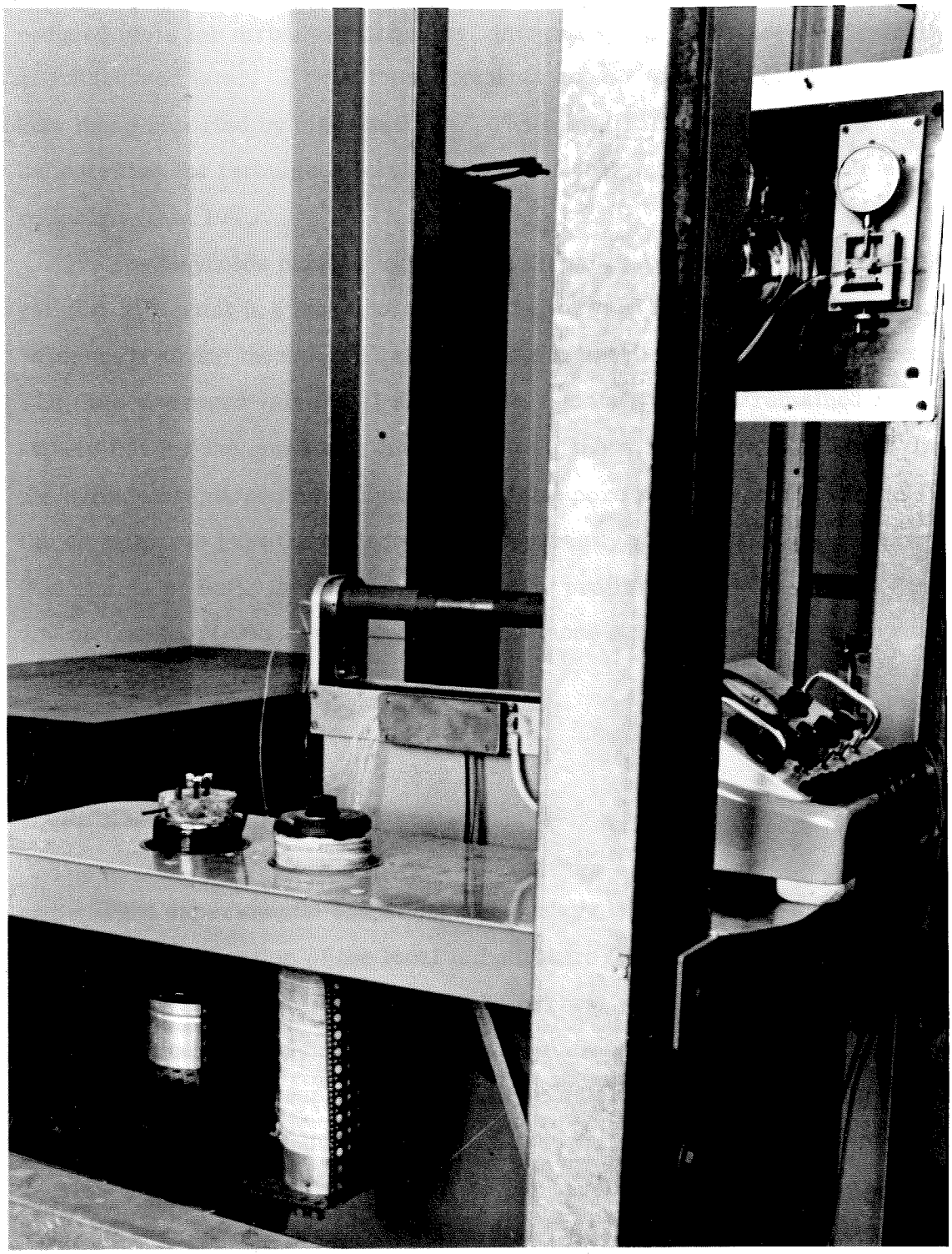

Figure 12. Photograph of Installation at Working Section.

reduced plots for turbulence intensity, integral scale, and microscale which are discussed later. Davis' measurements appear to be somewhat lower than those reported by other authors. The results of Couch's analysis indicate that the turbulence level downstream from grids can be predicted reliably within 10%.

The Reynolds number was evaluated from the measured free stream velocity at a point 0.5 inch upstream of the forward stagnation point in accordance with the theoretical restrictions enumerated in the previous section. The time-averaged velocity at the working section of the jet remained relatively flat for the conditions investigated as shown in Figure 13. At all times the cylinder remained entirely within the flat portion of the profile; however, the streamlines past the cylinder were apparently somewhat slightly divergent. The effects of finite jet width on the velocity profile outside the boundary layer and on transport were evaluated in the previous section, and they were not found to be large.

EXPERIMENTAL RESULTS:

The experimental end effect of boundary layer separation is best shown in the alteration of the local temperature field about a cylinder (16) in Figure 14 from the field which can be currently predicted from theoretical grounds. The form of the temperature field alone is responsible for the thermal transport discussed theoretically earlier and now presented as experimental measurements. In Figure 14 the variation in the density of isotherms near the cylinder surface at angles beyond around 90° is of particular interest.

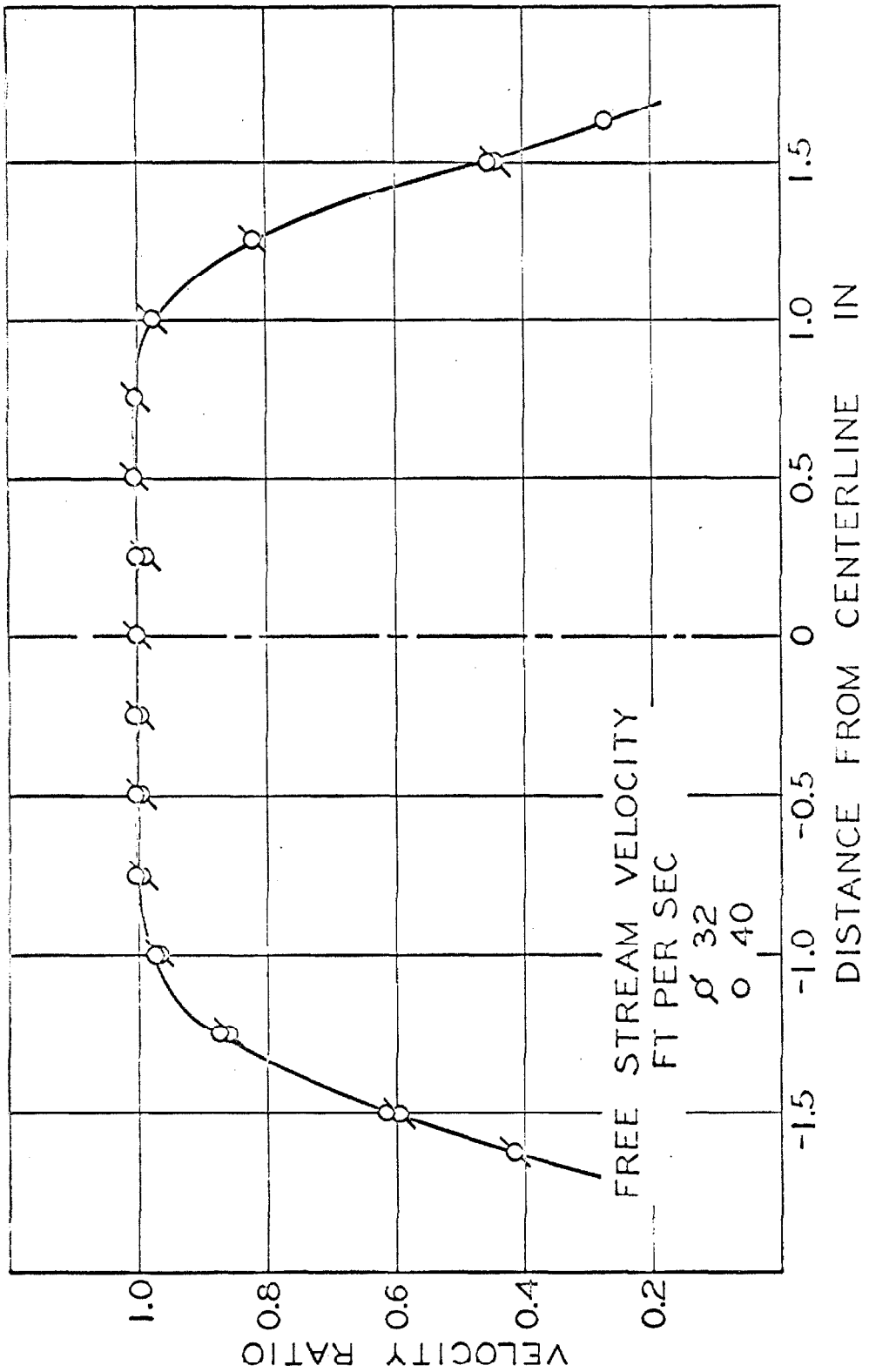

Fig. 13. Velocity ratio as function of position

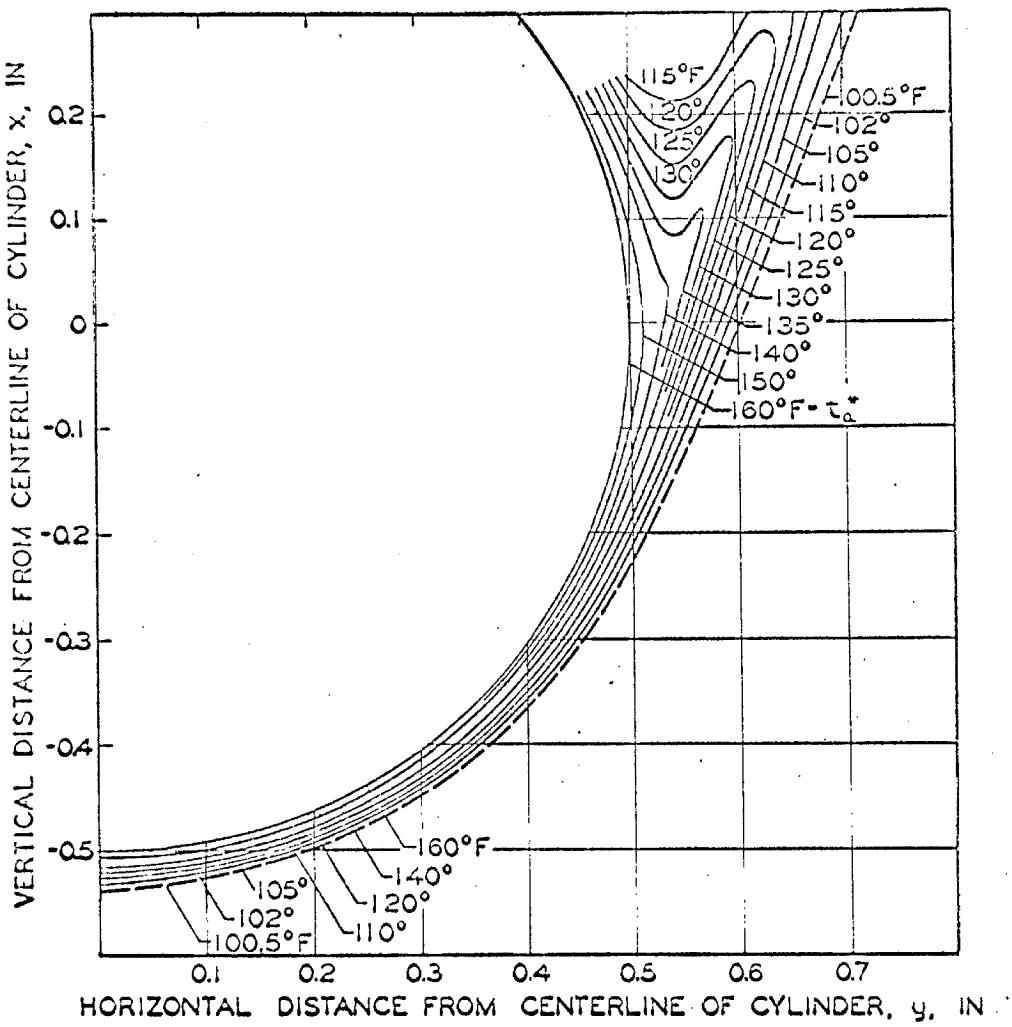

Air Stream: Flow in Positive Vertical Direction
U_∞ = 7.81 ft/sec
t_∞ = 100° F

Cylinder: r_o = 0.4997 in.
t_c = 160° F
$Re_{c,\infty}$ = 3500

FIGURE 14. Temperature Contours in the Nonisothermal Boundary Flow about a Cylinder

The measurements of overall thermal transport, which is the net effect of the entire temperature field, about the 1.5 inch cylinder are recorded in Table 5, and Figure 15 illustrates the Frössling number as a function of the lower Reynolds numbers with level of turbulence as a parameter. The empirical coefficients of Equation 117 for the overall Frössling number in subcritical flow were evaluated by nonlinear regression techniques utilizing the data in Table 5. The resulting equation is:

$$Fs_{\infty} = 0.4763\left(\frac{\nu_{\infty}}{\nu_o}\right)^{0.16} + \left[\frac{0.007162 Z_t}{Z_t + 0.1300} + 0.001226\right] Re_{\infty}^{1/2} (Pr \text{ or } Sc)_{m,\infty}^{1/6} \quad (121)$$

The standard error of estimate of the experimental points from the curves, which are based on Equation 121 and shown in Figure 15, was 3.39%. The average error was 0.11%, and the experimental reproducibility was 0.9%. For the majority of measurements recorded in Table 5 the integral turbulence scale varied from 0.3 to 0.5 inch with decreases in turbulence level. The scale of the turbulence was estimated from the geometry of the grid employed and the measurements of van der Hegge Zijnen (39).

Figure 16 shows the macroscopic Frössling number for several investigations (25-29, 31, 32, 35, 39, 43, 44), using the kinematic viscosity ratio, ν_{∞}/ν_o, for the variations in the kinematic viscosity across the boundary layer. The basis and limitations for this ratio were discussed earlier. In order to plot Equation 121, the effect of kinematic viscosity ratio in the turbulent contribution was neglected. The solid curves were for subcritical flow as given by Equation 121 while the graphically determined dashed curves in the lower portion of the figure represent the transition to supercritical flow. The upper portion is merely an enlargement of the lower Reynolds number transport. The dashed curves in the upper portion of Figure 16 will be discussed shortly. Although the range of Prandtl numbers treated was 0.6-300 and Schmidt was 0.6-1.8, the coefficient of 1/6 in Equation 121 possesses a large uncertainty

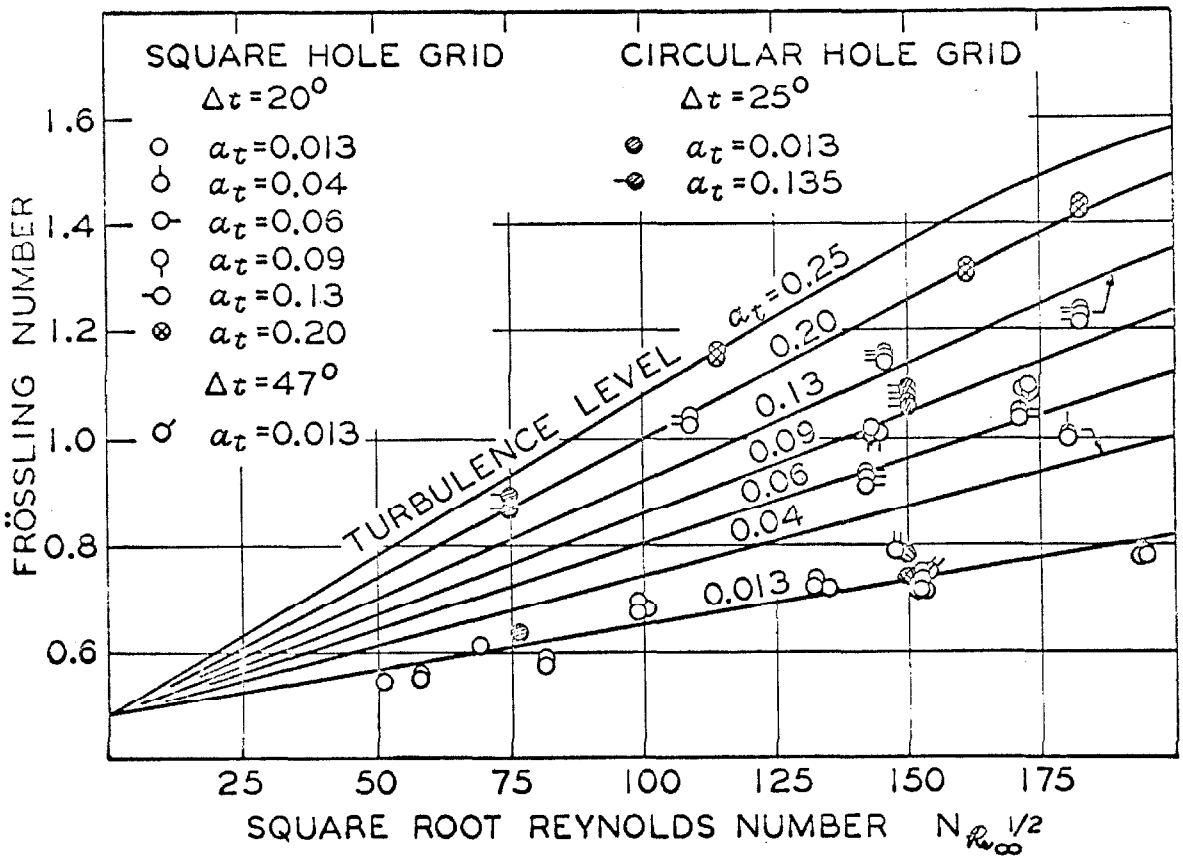

Fig. 15. Effect of turbulence on macroscopic thermal transport

TABLE 5. EXPERIMENTAL RESULTS FOR MACROSCOPIC THERMAL TRANSPORT*

Test Number	Reynolds Number	Level of Turbulence+	Temperature, °F. Airstream	Temperature, °F. Interface	Viscosity Ratio±	Total Thermal Flux Btu/Sec	Nusselt Number	Frössling Number§
			Square Hole Grid (39)					
919	2667	0.013	90.62	103.17	0.9623	0.890 x 10^{-3}	25.29	0.5499
918	3382	0.013	93.07	108.44	0.9839	1.256	29.03	0.5604
917	4879	0.013	95.03	112.27	0.9481	1.879	38.83	0.6244
916	6706	0.013	94.14	113.33	0.9434	2.307	42.66	0.5851
915	10406	0.013	92.78	109.94	0.9489	2.938	60.87	0.6868
936	11966	0.222	84.08	106.25	0.9334	6.204	100.98	1.0354
935	13147	0.256	85.05	106.73	0.9349	7.148	118.68	1.1609
913	17570	0.013	92.30	103.90	0.9654	2.816	86.37	0.7312
910	18254	0.013	82.90	105.80	0.9316	5.523	87.58	0.7277
929	20364	0.090	88.91	104.98	0.9516	5.892	131.19	1.0267
928	20365	0.060	88.42	106.09	0.9464	5.830	118.22	0.9296
930	21305	0.139	89.19	103.46	0.9577	5.977	149.99	1.1529
927	21893	0.046	87.71	107.37	0.9411	5.745	104.84	0.7949
932	23329	0.013	91.19	138.01	0.9655	13.400	102.02	0.7500
931	23403	0.013	90.16	110.39	0.9394	5.586	98.61	0.7234
934	25942	0.210	85.54	106.48	0.9370	11.065	190.08	1.3236
925	29483	0.052	85.76	102.44	0.9550	7.424	160.00	1.0456
924	29958	0.079	85.62	100.86	0.9544	7.166	169.13	1.0963
923	32536	0.041	87.86	104.09	0.9515	7.319	161.70	1.0059
926	33422	0.120	83.01	97.74	0.9549	8.155	200.08	1.2278
933	33456	0.188	84.75	103.28	0.9445	12.038	234.12	1.4361
914	38160	0.013	89.63	104.15	0.9564	5.382	136.88	0.7852

Test Number	Reynolds Number	Level of Turbulence+	Temperature, °F. Airstream	Temperature, °F. Interface	Viscosity Ratio*	Total Thermal Flux Btu/Sec	Nusselt Number	Frössling Number§
			Circular Hole Grid (40,41)					
641	5791	0.013	99.06	128.99	0.9608		43.21	0.6380
642A	5677	0.135	99.02	126.72	0.9635		58.49	0.8723
642B	5673	0.135	99.06	125.95	0.9645		60.54	0.9032
643A	22676	0.135	99.44	123.86	0.9676		147.08	1.0975
643B	22678	0.135	99.40	123.94	0.9675		144.22	1.0761
643C	22675	0.135	99.40	123.94	0.9675		142.83	1.0658
643D	21678	0.135	99.31	123.73	0.9676		142.03	1.0839
644A	22527	0.013	99.36	130.80	0.9590		104.99	0.7860
644B	22519	0.013	99.53	132.23	0.9575		100.09	0.7495
644C	22465	0.013	99.61	132.05	0.9578		100.08	0.7503
645A	85967	0.013	99.40	122.62	0.9692		266.77	1.0224
645B	85967	0.013	99.40	122.62	0.9692		271.10	1.0390
646A	72557	0.135	99.57	116.68	0.9773		370.15	1.5441
646B	72557	0.135	99.57	116.68	0.9773		372.84	1.5554
646C	73924	0.135	99.57	116.68	0.9773		369.41	1.5267

* See Notation for definition of terms

\+ Level of longitudinal turbulence defined by:

$$\alpha_t = [\overline{(u')^2}]^{1/2}/U_\infty$$

The integral scale of turbulence was estimated (21) to vary from 0.3 to 0.5 inch

* Viscosity ratio defined by: ν_∞/ν_o

§ Prandtl number used in calculations varied between 0.7060 and 0.7085 and between 0.7048 and 0.7049 for data taken with the square hole and circular hole grids respectively

and more high Schmidt number data at high turbulence levels will be required in order to refine this dependence. Consequently this uncertain dependence has been left out of the abscissa. There is a large body of data available from investigations which did not systematically vary or report the turbulence level and these have been reviewed by Douglas and Churchill (34). Qualitatively the trends they report are comparable to those shown in Figure 16, suggesting that much of the scatter they show could be explored by variations in turbulence level.

Recorded in Table 6 is the standard error of estimate of each set of experimental data by author from the curves shown in Figure 16, as well as the values of the average error for each source of experimental data. It is apparent that there is some bias between one set of measurements and another. In the lower part of the table is shown the average value of the standard error of estimate of all of the data.

The dashed curves of Figure 16 representing the transition to supercritical flows were based on the data of Kestin (29), Giedt (28), Seban (31), and of this work for the highest values of turbulence and Reynolds number. The point of transition was established from pressure distributions. Giedt (28) noted that the macroscopic Nusselt number was affected less by turbulence at the critical Reynolds number than in subcritical flow, owing to large decreases in the pressure coefficient in the wake corresponding to transition of the laminar boundary layer to turbulent before separation. The initial formation of the supercritical region shown by a linear dashed curve varies with the turbulence level. The critical Reynolds numbers where subcritical flow first begins to pass into a transition region to supercritical are indicated by the large dashed line labeled "transition". The effects of turbulence on this critical Reynolds number are shown in Figure 17. The points taken from Figure 16 compare very favorably with the data of Fage (45). The uncertainty

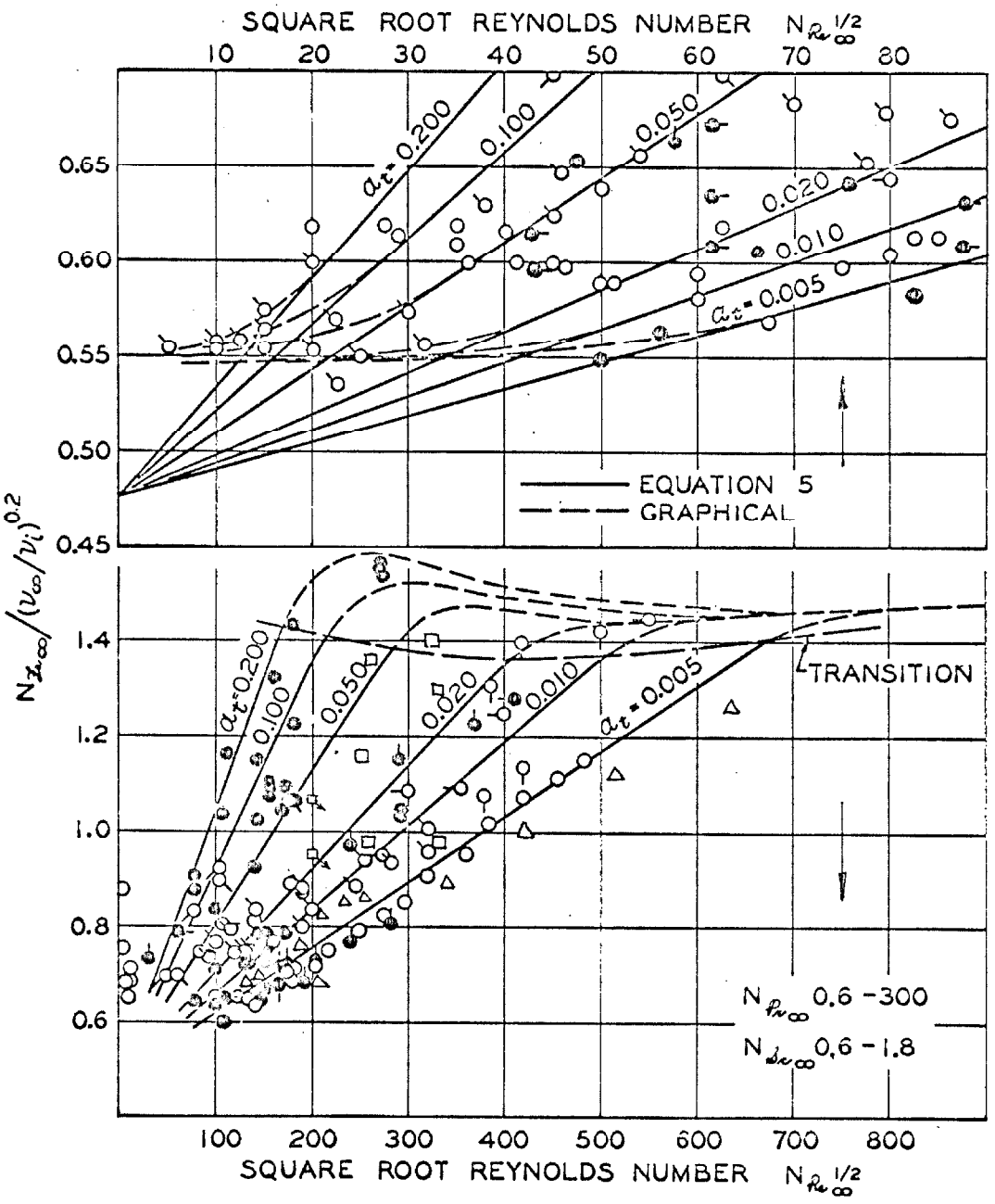

	Turbulence Intensity	Turbulence Scale
Authors	0.013-0.25	0.4
Couch (44)	0.013-0.14	0.3
Van der Hegge Zijnen (30)	0.02, 0.05, 0.12	1.0
Seban (4)	0.014	0.15
Schnautz (32)	0.005, 0.025	
Hilpert (43)	0.009	
Zapp (2)	0.009, 0.03, 0.115	
Maisel (26,27)	0.16	varied
Comings (25)	0.03, 0.07	
Kestin (29)	0.01, 0.03	0.06-0.23
Maisel (26,27)	0.24	varied
Geidt (28)	0.01, 0.04	0.15
Perkins (35)	0.011	
Schmidt (2)	0.005	

Fig. 16. Macroscopic Frössling Number from several investigators

TABLE 6

COMPARISON OF RESULT FOR MACROSCOPIC TRANSPORT

Reference	Number Points	Turbulence Level Minimum	Turbulence Level Maximum	Deviation Average	Deviation Standard
Authors	34	0.013	0.25	2.70%	4.57%
Comings (25)	4	0.03	0.07	1.57	1.98
Couch (44)	10	0.013	0.14	5.67	7.09
Giedt (28)	4	0.01	0.04	8.82	12.2
Hilpert (43)	27	0.009	0.009	6.59	8.54
Kestin (29)	5	0.01	0.03	3.78	4.58
Maisel (26,27)	4	0.24	0.24	12.9	13.5
Perkins (17)	37	0.011	0.011	9.3	15.5
Schmidt (2)	11	0.005	0.005	4.2	5.4
Schnautz (32)	13	0.005	0.025	4.31	5.61
Seban (4)	1	0.014	0.014	1.10	1.10
Van der Hegge Zijnen (30)	3	0.02	0.12	10.2	10.6
Zapp (2)	8	0.009	0.115	5.6	9.7
Overall	161	0.005	0.25	6.07	7.78

Average deviation defined by: $\sum_{1}^{N} \left| (Fs_e - Fs_p)/Fs_e \right| /N$

Standard deviation defined by: $\left\{ \sum_{1}^{N} [(Fs_e - Fs_p)/Fs_e]^2/(N-1) \right\}^{1/2}$

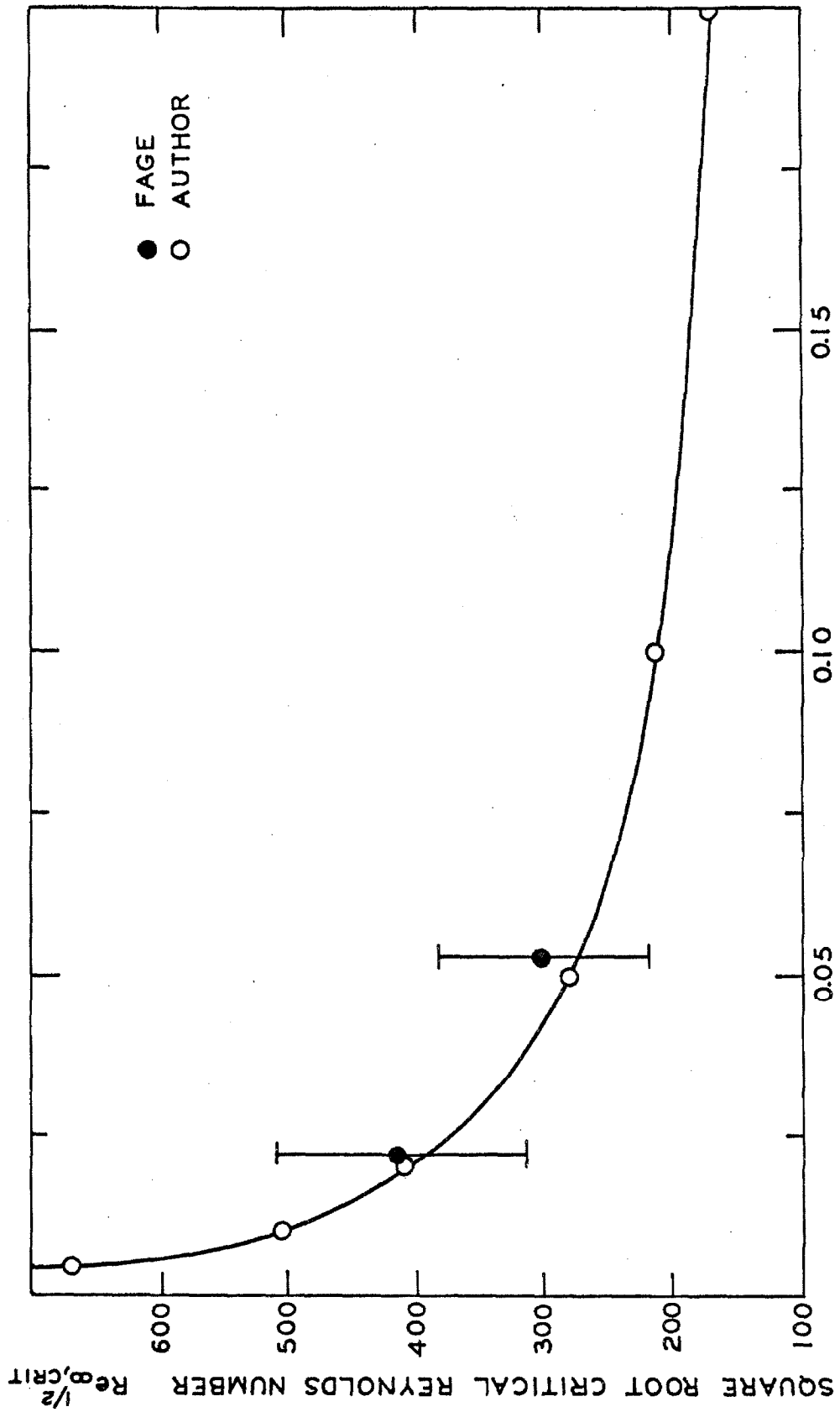

Figure 17. Effects of Turbulence on Critical Reynolds Number.

in Fage's points represents the range of critical Reynolds numbers which were observed from pressure distributions. This transitional behavior for cylinders is typical of transport from spheres, which will be illustrated later.

It should be noted that at Reynolds numbers below 25, there is a tendency for most of the data to yield much larger values of the Frössling group than would be predicted directly from measured values of the Reynolds group. This may result from the increasing importance of residual conduction and natural convection as the forced convective influences become smaller at the lower Reynolds numbers. Also, the concept of a turbulence threshold in this region may prove useful and has been indicated by dashed curves in the upper portion of Figure 16. Assuming that the action of free-stream turbulence on a laminar boundary with an associated pressure gradient is the result of the amplification of small residual perturbations as a consequence of instabilities in the system, a Reynolds number threshold or initial point of instability amplification is apparent below which variation in free-stream turbulence does not significantly affect the laminar boundary. It would have been desirable, if possible, to correct this information shown in Figure 16 for the other authors by deleting any natural convective and possible other influences; however, the published information in these cases was not sufficient.

The effect of level of turbulence as predicted from Equation 121 is shown directly in Figure 18. As would be expected from earlier studies (25,28,31,38), the effect of turbulence is most pronounced at the lower levels. These curves do not converge to a single value in the limit of no turbulence, owing to the varying contribution of the wake.

Utilizing the calorimeter described earlier, together with a small surface pitot tube, the local thermal transport and several pressure coefficients from the cylinder were established. These detailed local experimental

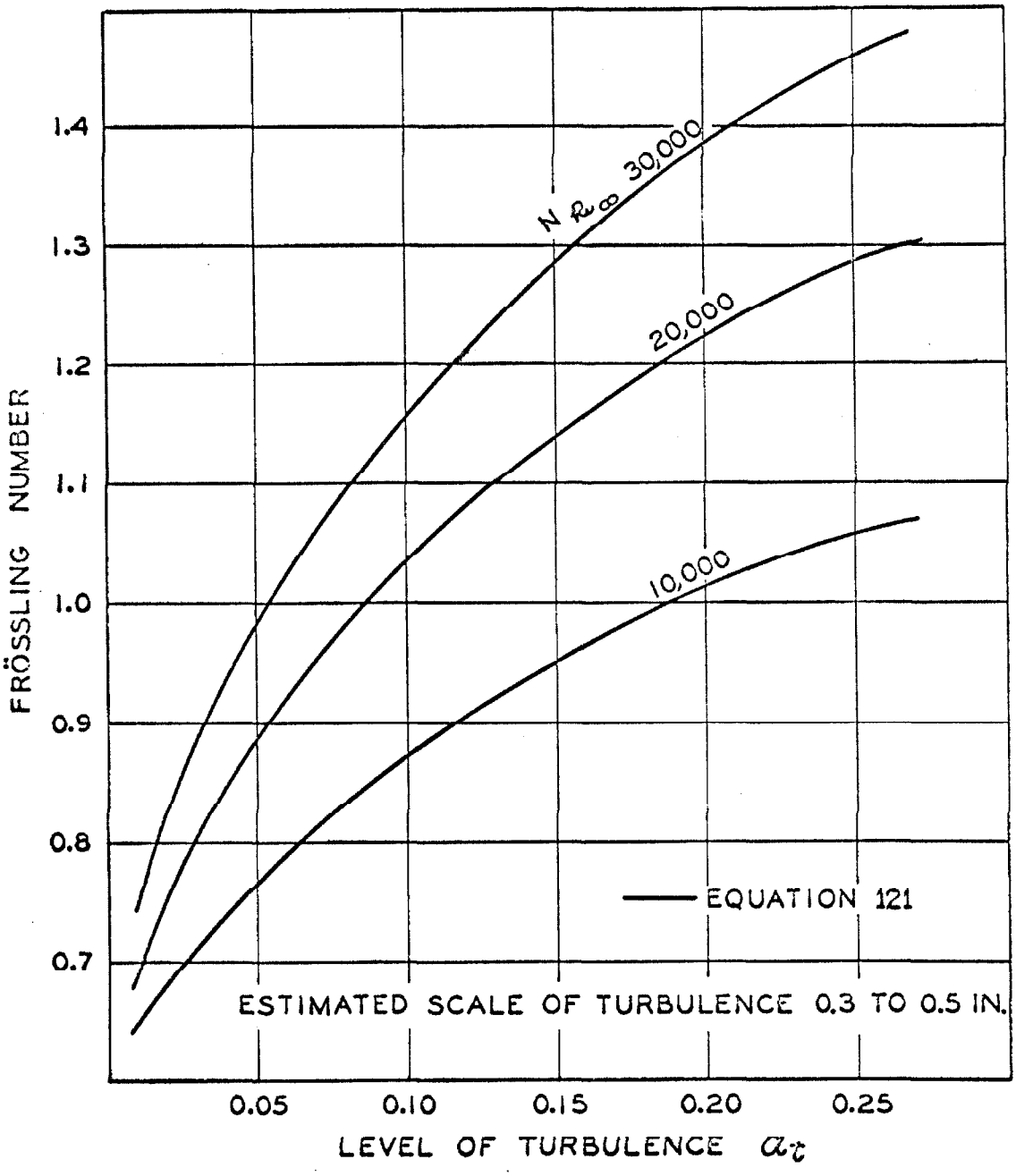

Fig. 18. Effect of level of turbulence upon macroscopic thermal transport

results are presented in Table 7 for both the 600 series and the 900 series tests. As an illustration of the complicated behavior encountered, the local thermal transport expressed in terms of the Frössling number for Reynolds numbers of 12,000, 22,000, and 33,000 is shown in Figure 19 as a function of angle from stagnation, with the level of turbulence generated by the grid of van der Hegge Zijnen (39) as a parametric variable. The apparently anomalous behavior at the stagnation point for the higher turbulence levels and Reynolds numbers may be due to the random fluctuations of the forward stagnation point (46,47). Figure 20 shows the results for the local pressure and thermal transport distribution at low free-stream turbulence. There is an indication of a small anomaly in the thermal transfer near the forward stagnation that is symmetric with respect to angle. The calorimeter, which was described in Figure 9 and was used to measure the local thermal transport, indicated low frequency fluctuations near the forward stagnation as well as near separation that evidently affects the heat transfer. The pressure distribution near the forward stagnation, however, followed accepted theory (1) for moderate Reynolds numbers, and there were no anomalies. The reduction in the pressure coefficient, C_p, for a Reynolds number of 86,000 suggests that the boundary layer became turbulent before separation, as is expected in supercritical flow. Such behavior is also reflected in the thermal transfer results. The results compare favorably with those of Giedt (28) and Seban (31).

The introduction of the "circular-hole grid" patterned after Davis (40, 41) produced a longitudinal turbulence level of 0.135 at 6 mesh diameters downstream, with nearly the same scale of turbulence as the square grid used earlier (39). The anomaly near stagnation and the low-frequency fluctuation in thermal transfer vanished, as is shown in Figure 21. These results suggest that the apparent stagnation anomaly in thermal transfer is the result of local fluctuations near stagnation rather than turbulence anisotropy. Such

TABLE 7

EXPERIMENTAL RESULTS FOR LOCAL TRANSPORT

USING SQUARE HOLE GRID (39)

Angle[+] Degrees	Thermal Flux[≠] Btu/Sec	Nusselt Number	Frössling Number	$\frac{N_{Nu\infty}}{N^{*}_{Nu\infty}}$	Thermal Flux[≠] Btu/Sec	Nusselt Number	Frössling Number	$\frac{N_{Nu\infty}}{N^{*}_{Nu\infty}}$
	Test 919				Test 918			
0	2.947×10^{-6}	47.95	1.043	1.896	4.156×10^{-6}	55.27	1.067	1.904
20	2.920	47.54	1.034	1.880	4.012	53.36	1.030	1.838
40	2.597	42.28	0.919	1.672	3.534	47.00	0.907	1.619
60	1.818	29.59	0.643	1.170	2.525	33.59	0.648	1.157
80	0.622	10.12	0.219	0.400	0.581	7.72	0.149	0.266
85	0.315	5.11	0.111	0.202	0.174	2.32	0.0448	0.0779
90	0.108	3.29	0.0715	0.130	0.292	3.89	0.0751	0.134
100	0.369	5.99	0.130	0.237	0.835	11.09	0.214	0.382
110	0.838	13.63	0.296	0.539	1.206	16.02	0.309	0.552
120	0.887	14.44	0.314	0.571	1.191	15.85	0.306	0.546
130	0.928	15.10	0.328	0.597	1.244	16.55	0.319	0.570
140	1.059	17.22	0.374	0.681	1.557	20.70	0.399	0.713
160	1.339	21.80	0.474	0.862	2.024	26.91	0.519	0.927
180	1.586	25.82	0.561	1.021	2.483	33.01	0.637	1.137

Angle[+] Degrees	Thermal Flux[+] Btu/Sec	Nusselt Number	Frössling Number	N_{Nuco}/N^{*}_{Nuco}	Thermal Flux[+] Btu/Sec	Nusselt Number	Frössling Number	N_{Nuco}/N^{*}_{Nuco}
		Test 917				Test 916		
0	6.058×10^{-6}	73.62	1.184	1.896	8.162×10^{-6}	82.33	1.129	1.930
20	5.811	70.59	1.135	1.818	7.666	77.34	1.061	1.813
40	5.090	61.86	0.995	1.593	6.711	67.70	0.928	1.587
60	3.575	43.45	0.698	1.119	4.774	48.16	0.661	1.129
70					2.735	27.60	0.378	0.647
75					1.699	17.15	0.235	0.402
80	0.595	7.22	0.116	0.186	0.709	7.17	0.0983	0.168
85	0.395	4.81	0.0774	0.124	0.656	6.61	0.0907	0.155
90	0.764	9.28	0.149	0.239	1.439	14.50	0.199	0.340
95					2.290	23.08	0.316	0.541
100	1.863	22.64	0.364	0.583	2.906	29.31	0.402	0.687
105					2.693	27.17	0.373	0.637
110	2.005	24.35	0.391	0.627	2.622	26.45	0.363	0.620
115					2.318	23.38	0.321	0.548
120	1.373	16.66	0.268	0.429	1.791	18.04	0.247	0.423
125					1.833	18.47	0.253	0.433
130	1.538	18.68	0.300	0.481	2.006	20.66	0.277	0.474
140	1.993	24.23	0.389	0.624	2.726	27.52	0.377	0.645
160	3.302	40.11	0.645	1.033	4.042	40.78	0.559	0.956
180	4.025	48.92	0.787	1.260	5.169	52.13	0.715	1.222

Angle[+] Degrees	Thermal Flux[≠] Btu/Sec	Nusselt Number	Frössling Number	$\frac{N_{Nu}}{N^{*}_{Nu_\infty}}$	Thermal Flux[≠] Btu/Sec	Nusselt Number	Frössling Number	$\frac{N_{Nu}}{N^{*}_{Nu_\infty}}$
	Test 915				Test 936			
0	8.448×10^{-6}	111.64	1.259	1.834	16.081×10^{-6}	167.63	1.718	1.660
20	7.778	102.81	1.160	1.689	16.277	169.65	1.739	1.680
40	6.566	86.80	0.979	1.426	15.122	157.63	1.616	1.561
60	4.314	57.03	0.643	0.937	12.583	131.17	1.345	1.299
70	2.180	28.79	0.325	0.473				
80	0.489	6.45	0.0728	0.106	6.299	65.64	0.673	0.650
85	0	0	0	0	4.274	44.53	0.457	0.441
90	2.706	35.79	0.404	0.588	3.619	37.66	0.386	0.373
95	3.536	46.75	0.527	0.768	4.119	42.92	0.440	0.425
100	3.885	51.37	0.579	0.844	5.332	55.54	0.569	0.550
105	3.689	48.76	0.550	0.801				
110	3.029	40.05	0.452	0.658	6.760	70.48	0.723	0.698
115	2.536	33.54	0.378	0.551				
120	1.954	25.81	0.291	0.424	6.409	66.85	0.685	0.662
125	2.030	26.84	0.303	0.441				
130	2.482	32.81	0.370	0.539				
135					5.160	53.82	0.551	0.533
140	3.283	43.40	0.490	0.713				
145					5.476	57.05	0.585	0.565
160	5.218	68.96	0.778	1.133	7.619	79.37	0.813	0.786
170					9.112	95.02	0.947	0.941
180	6.568	86.80	0.979	1.426	9.502	99.06	1.016	0.981

Angle+ Degrees	Thermal Flux≠ Btu/Sec	Nusselt Number	Frössling Number	$\frac{N_{Nu\infty}}{N^*_{Nu\infty}}$	Thermal Flux≠ Btu/Sec	Nusselt Number	Frössling Number	$\frac{N_{Nu\infty}}{N^*_{Nu\infty}}$
	Test 935				Test 913			
0	17.358×10^{-6}	181.94	1.779	1.533	6.384×10^{-6}	132.49	1.122	1.534
10	17.748	188.46	1.843	1.588				
20	17.751	188.46	1.843	1.588	6.179	128.17	1.085	1.484
40	16.805	178.49	1.746	1.504	5.362	111.24	0.942	1.288
60	13.988	148.59	1.453	1.252	3.512	72.81	0.616	0.843
75					0.561	11.66	0.0987	0.135
80	8.561	90.91	0.889	0.766	0.987	20.47	0.173	0.237
90	4.966	52.69	0.515	0.444	3.205	66.42	0.562	0.769
95	4.771	50.68	0.496	0.427				
100	5.563	59.10	0.578	0.498	3.727	77.30	0.654	0.895
105	7.368	78.21	0.765	0.659				
110					2.571	53.38	0.452	0.618
115	8.854	93.99	0.919	0.792				
120					2.444	50.70	0.429	0.587
125	8.090	85.92	0.840	0.724				
130					3.193	66.25	0.561	0.767
140	6.226	66.10	0.647	0.557				
150	6.612	70.26	0.687	0.592	4.429	91.90	0.778	1.064
160	8.555	90.91	0.889	0.766				
170	10.853	115.24	1.127	0.971				
180	11.272	119.75	1.171	1.009	6.054	125.58	1.063	1.454

Angle[+] Degrees	Thermal Flux[≠] Btu/Sec	Nusselt Number	Frössling Number	$\frac{N_{Nu_\infty}}{N^*_{Nu_\infty}}$	Thermal Flux[≠] Btu/Sec	Nusselt Number	Frössling Number	$\frac{N_{Nu_\infty}}{N^*_{Nu_\infty}}$
	Test 910				Test 929			
0	14.744×10^{-6}	114.92	1.264	1.736	15.983×10^{-6}	226.43	1.772	1.726
20					15.232	215.68	1.688	1.644
30	13.194	102.81	1.130	1.553				
40					13.628	192.98	1.510	1.471
60	8.583	66.86	0.735	1.010	10.755	152.31	1.192	1.161
75	2.282	17.74	0.195	0.268	6.373	90.26	0.706	0.688
80	2.293	17.87	0.196	0.270	4.469	63.30	0.495	0.482
85	4.393	34.22	0.376	0.517	3.492	49.46	0.387	0.377
90	5.887	45.88	0.504	0.693	4.092	57.98	0.454	0.442
95	6.794	52.89	0.582	0.799	5.815	82.39	0.645	0.628
100	6.754	52.63	0.579	0.795	7.183	101.67	0.796	0.775
105					7.521	106.53	0.834	0.812
110	4.422	34.49	0.379	0.521				
115	3.625	28.67	0.311	0.427	7.264	102.85	0.805	0.784
120	3.654	28.47	0.313	0.430				
125					5.831	82.52	0.646	0.629
130	5.087	39.65	0.436	0.599				
135					5.427	76.88	0.602	0.586
145					5.887	83.44	0.653	0.636
150	8.326	64.88	0.713	0.980				
160					7.860	111.25	0.871	0.848
180	10.588	82.48	0.907	1.246	9.348	132.37	1.036	1.009

Angle[+] Degrees	Thermal Flux[∓] Btu/Sec	Nusselt Number	Frössling Number	$\frac{N_{Nu_\infty}}{N^*_{Nu_\infty}}$	Thermal Flux Btu/Sec	Nusselt Number	Frössling Number	$\frac{N_{Nu_\infty}}{N^*_{Nu_\infty}}$
		Test 928				Test 930		
0	15.860×10^{-6}	198.49	1.561	1.679	14.524×10^{-6}	238.33	1.832	1.589
20	15.456	193.53	1.522	1.637	14.111	231.58	1.780	1.544
40	13.390	167.64	1.318	1.418	12.946	212.38	1.632	1.416
60	9.815	122.83	0.966	1.039	10.482	172.04	1.322	1.147
75	4.263	53.44	0.420	0.452				
80	2.586	32.39	0.255	0.274	5.767	94.64	0.727	0.631
85	3.089	38.66	0.304	0.327	4.418	72.44	0.557	0.483
90	4.842	60.65	0.477	0.513	3.892	63.90	0.491	0.426
95					4.866	79.79	0.613	0.532
100	6.837	85.59	0.673	0.724	6.800	111.59	0.858	0.744
105					7.983	130.94	1.006	0.873
110	7.005	87.72	0.689	0.742	8.432	138.29	1.063	0.922
120	6.232	78.02	0.613	0.660	7.543	123.74	0.951	0.825
130	5.551	69.51	0.547	0.588				
135					5.685	93.29	0.717	0.622
140	7.389	92.57	0.728	0.783				
150					6.033	98.84	0.759	0.659
160	9.764	122.24	0.961	1.034				
170					9.038	148.34	1.140	0.989
180	10.837	135.72	1.067	1.148	9.515	156.14	1.200	1.041

Angle[+] Degrees	Thermal Flux[‡] Btu/Sec	Nusselt Number	Frössling Number	$\frac{N_{Nuc}}{N^{*}_{Nuc}}$	Thermal Flux[‡] Btu/Sec	Nusselt Number	Frössling Number	$\frac{N_{Nuc}}{N^{*}_{Nuc}}$
	Test 927				Test 932			
0	16.554 x 10^{-6}	182.00	1.379	1.736	38.914 x 10^{-6}	165.37	1.216	1.621
20	15.962	175.50	1.331	1.674	38.137	162.11	1.192	1.589
40	13.957	153.48	1.163	1.464	33.115	140.68	1.034	1.379
60	9.779	107.56	0.816	1.026	23.310	99.06	0.728	0.971
70					11.443	48.66	0.358	0.477
75	3.690	40.57	0.308	0.387	7.842	33.36	0.245	0.327
77					7.520	31.93	0.235	0.313
80	2.635	28.94	0.219	0.276	9.406	39.99	0.294	0.392
85	3.778	41.52	0.315	0.396				
90	4.985	54.83	0.416	0.523	17.372	72.86	0.543	0.724
100	5.856	64.37	0.488	0.614	17.762	75.49	0.555	0.740
110	5.782	63.53	0.482	0.606				
115					12.204	51.83	0.381	0.508
120	5.621	103.69	0.468	0.989				
130	6.702	73.70	0.559	0.703	16.144	68.66	0.505	0.673
150	8.756	96.24	0.729	0.918				
155					26.368	112.02	0.823	1.098
170	10.379	114.06	0.865	1.088				
180	10.382	114.17	0.866	1.089	29.036	123.34	0.907	1.209

Angle[+] Degrees	Thermal Flux[‡] Btu/Sec	Nusselt Number	Frössling Number	$\frac{N_{Nu_\theta}}{N^*_{Nu_\infty}}$	Thermal Flux[‡] Btu/Sec	Nusselt Number	Frössling Number	$\frac{N_{Nu_\theta}}{N^*_{Nu_\infty}}$
		Test 931				Test 934		
0	15.823 x 10^{-6}	163.20	1.197	1.655	26.651 x 10^{-6}	272.38	1.896	1.433
20	15.510	159.94	1.173	1.622	27.539	281.51	1.960	1.481
40	13.492	139.14	1.021	1.411	25.866	283.41	1.841	1.391
60	9.107	93.88	0.688	0.952	21.876	223.72	1.558	1.177
70	4.188	43.19	0.317	0.438				
75	2.684	27.71	0.203	0.281				
80	3.632	37.37	0.274	0.379	16.062	164.23	1.143	0.864
90	7.200	74.25	0.545	0.753	12.182	124.50	0.867	0.655
95					10.275	105.11	0.732	0.553
100	6.869	70.80	0.519	0.718	10.471	107.02	0.745	0.563
105					12.459	127.35	0.887	0.670
115	4.463	46.05	0.338	0.467	16.753	171.26	1.192	0.901
120					17.167	175.44	1.222	0.923
130	6.142	63.31	0.464	0.642	15.724	160.81	1.119	0.846
145					12.305	125.83	0.876	0.662
155	10.439	107.58	0.789	1.091	11.906	121.65	0.847	0.640
160					12.765	130.58	0.909	0.687
165					14.443	147.69	1.028	0.777
175					16.883	172.59	1.202	0.908
180	11.543	119.02	0.873	1.207	17.839	182.29	1.269	0.959

Angle[+] Degrees	Thermal Flux[‡] Btu/Sec	Nusselt Number	Frössling Number	$\frac{N_{Nuc}}{N^{*}_{Nuc}}$	Thermal Flux[‡] Btu/Sec	Nusselt Number	Frössling Number	$\frac{N_{Nuc}}{N^{*}_{Nuc}}$
		Test 925				Test 924		
0	18.732 x 10^{-6}	253.76	1.658	1.586	17.608 x 10^{-6}	261.30	1.694	1.545
20	18.284	249.28	1.618	1.548	16.965	251.83	1.632	1.489
40	16.742	226.88	1.483	1.418	15.196	225.45	1.461	1.333
60	12.954	175.52	1.147	1.097	12.512	185.70	1.204	1.098
70					10.353	153.74	0.996	0.909
80	4.946	66.88	0.437	0.418	7.276	107.90	0.699	0.638
85	4.256	57.60	0.376	0.360	5.369	79.66	0.516	0.471
90	6.040	81.76	0.534	0.511	4.740	70.34	0.456	0.416
95					6.251	92.85	0.602	0.549
100	10.453	141.60	0.925	0.885	8.994	133.44	0.865	0.789
105	10.690	144.80	0.946	0.905	11.028	163.72	1.061	0.968
110	10.260	138.88	0.907	0.868	11.848	175.73	1.139	1.039
115					11.235	166.76	1.081	0.986
120	8.778	118.88	0.777	0.743	10.434	154.92	1.004	0.916
125					9.464	140.55	0.911	0.831
130	7.126	96.48	0.630	0.603	8.394	124.65	0.808	0.737
135	7.092	96.00	0.627	0.600	7.572	112.47	0.729	0.665
140	7.351	99.52	0.650	0.622	7.293	108.24	0.702	0.640
145					7.056	104.69	0.679	0.619
150	8.865	120.16	0.785	0.751				
160	10.710	145.12	0.948	0.907	9.438	140.04	0.908	0.828
170	12.326	167.04	1.091	1.044				
180	12.867	174.32	1.139	1.090	11.771	174.71	1.132	1.033

Angle+ Degrees	Thermal Flux+ Btu/Sec	Nusselt Number	Frössling Number	$N_{Nu_\infty} / N^*_{Nu_\infty}$	Thermal Flux+ Btu/Sec	Nusselt Number	Frössling Number	$N_{Nu_\infty} / N^*_{Nu_\infty}$
		Test 923				Test 926		
0	19.117 x 10^{-6}	262.76	1.634	1.625	19.460 x 10^{-6}	296.32	1.818	1.481
20	18.360	252.41	1.570	1.561	19.305	293.92	1.804	1.469
40	16.207	222.82	1.386	1.378	17.823	271.51	1.666	1.357
60	12.304	169.14	1.052	1.046	14.830	225.89	1.386	1.129
70	7.791	107.04	0.666	0.662				
75	5.039	69.21	0.430	0.428				
80	3.808	52.39	0.326	0.324	10.136	154.26	0.947	0.771
85	5.020	69.04	0.429	0.427				
90	7.468	102.68	0.639	0.635	7.566	115.25	0.707	0.576
95	9.149	125.80	0.782	0.778	7.032	107.04	0.657	0.535
100	10.085	138.58	0.862	0.857	8.381	127.65	0.783	0.638
105	9.965	136.96	0.852	0.847				
110	9.545	131.14	0.816	0.811	12.504	192.48	1.169	0.952
115	8.769	120.47	0.749	0.745	13.735	209.28	1.284	1.046
120	8.158	112.06	0.697	0.693	13.303	202.68	1.244	1.013
125	7.504	103.16	0.642	0.638				
130	7.193	98.80	0.615	0.611	10.771	163.86	1.006	0.819
135	7.408	101.87	0.634	0.630				
140	7.892	108.50	0.675	0.671	8.856	134.85	0.827	0.674
150	10.282	141.32	0.879	0.874	8.324	126.85	0.778	0.634
160	11.760	161.54	1.005	0.999	9.926	151.26	0.928	0.756
170					12.402	163.26	1.002	0.816
180	13.423	184.50	1.148	1.141	13.673	208.28	1.278	1.041

Angle+ Degrees	Thermal Flux ≠ Btu/Sec	Nusselt Number	Frössling Number	$\frac{N_{Nu\infty}}{N^{*}_{Nu\infty}}$	Thermal Flux ≠ Btu/Sec	Nusselt Number	Frössling Number	$\frac{N_{Nu\infty}}{N^{*}_{Nu\infty}}$
	Test 933				Test 914			
0	27.480 x 10^{-6}	320.51	1.966	1.369	12.966 x 10^{-6}	217.91	1.250	1.592
20	27.796	324.02	1.987	1.384	12.198	204.91	1.175	1.497
40	26.162	305.06	1.871	1.303	11.099	186.43	1.069	1.362
60	21.869	254.96	1.564	1.089	7.592	127.57	0.732	0.932
75					2.851	47.91	0.275	0.350
80	16.994	198.06	1.215	0.846	4.201	70.63	0.405	0.516
85					5.693	95.68	0.549	0.699
90	13.971	162.95	0.999	0.696	6.140	103.21	0.592	0.754
95	13.117	152.88	0.938	0.653	5.365	90.48	0.519	0.661
100	11.977	139.54	0.856	0.596	5.054	84.86	0.487	0.620
105	12.849	149.84	0.919	0.640				
110					4.406	74.05	0.425	0.541
115	17.110	199.47	1.223	0.852				
120					4.967	83.50	0.479	0.610
125	18.196	212.21	1.301	0.906				
135	16.142	188.23	1.155	0.804				
140					7.152	120.18	0.689	0.878
150	13.077	152.41	0.935	0.651				
160	13.399	156.16	0.958	0.667	9.128	153.44	0.880	1.121
170	15.762	183.78	1.127	0.785				
180	18.618	217.03	1.331	0.927	10.515	176.71	1.014	1.291

* See Notation for definition of terms

\+ Angle measured from stagnation

≠ The thermal flux is associated with an area of 0.077993 sq.ft.

TABLE 7

EXPERIMENTAL RESULTS FOR LOCAL TRANSPORT

USING CIRCULAR HOLE GRID (40,41)

Angle+ Degrees	Nusselt Number	Frössling Number	Pressure Coefficient
	Test 641		
0	76.39	1.1279	-
0	75.69	1.1175	-
10	75.99	1.1220	0.979
20	73.80	1.0896	0.731
40	65.09	0.9610	0.022
60	47.66	0.7037	-0.427
80	14.76	0.2179	-0.275
85	13.36	0.1972	-0.180
90	19.71	0.2910	-0.191
100	30.77	0.4543	-0.169
110	28.66	0.4231	-0.157
120	24.11	0.3559	-0.191
130	25.20	0.3721	-0.180
160	39.47	0.5828	-0.191
180	49.53	0.7313	-0.191

Angle+ Degrees	Nusselt Number	Frössling Number	Pressure Coefficient
	Test 642		
0	110.16	1.6431	1.028
20	-	-	0.623
40	92.89	1.3856	0.101
60	75.28	1.1229	-0.492
80	37.17	0.5545	-0.405
90	19.20	0.2864	-0.333
100	23.50	0.3506	-0.275
110	23.54	0.3512	-0.289
120	25.19	0.3669	-0.275
130	29.25	0.4363	-0.289
160	53.49	0.7978	-0.289
180	73.69	1.0991	-0.261

Angle+ Degrees	Nusselt Number	Frössling Number	Pressure Coefficient
	Test 643		
0	242.07	1.8164	-
10	238.31	1.7882	0.7731
20	233.66	1.7533	0.5578
40	208.38	1.5636	-0.1122
60	173.16	1.2994	-0.9183
80	97.76	0.7336	-0.8792
90	72.03	0.5405	-0.7369
100	116.50	0.8742	-0.7143
110	102.24	0.7672	-0.5713
130	91.36	0.6856	-0.4787
150	97.38	0.7307	-0.4682
180	136.50	1.0243	-0.4554

Angle+ Degrees	Nusselt Number	Frössling Number	Pressure Coefficient
	Test 644		
0	158.13	1.1845	1.0094
20	155.16	1.1622	0.6767
40	138.04	1.0340	-0.0419
60	99.09	0.7423	00.5937
80	44.67	0.3346	-0.3626
90	75.32	0.5642	-0.3492
100	83.92	0.6286	-0.3641
120	63.50	0.4757	-0.3821
140	85.74	0.6422	-0.3851
160	102.32	0.7664	-0.3746
180	119.02	0.8915	-0.3880

Angle+ Degrees	Nusselt Number	Frössling Number	Pressure Coefficient
	Test 645		
-10	358.83	1.3743	0.9455
-5	361.38	1.3841	0.9896
-5	361.19	1.3834	0.9986
0	350.79	1.3436	1.0186
0	350.30	1.3417	1.0178
5	350.35	1.3419	0.9858
5	352.77	1.3511	1.0081
10	363.87	1.3937	0.9431
15	351.86	1.3477	0.8463
20	349.73	1.3395	0.6940
30	332.25	1.2726	0.3165
40	310.46	1.1891	-0.0858
60	218.89	0.8384	-0.5021
80	168.78	0.6464	-0.2724
85	163.71	0.6270	-0.2750
90	177.52	0.6799	-0.2812
95	179.88	0.6889	-0.2819
100	194.13	0.7436	-0.2832
120	217.75	0.8340	-0.2859
140	252.59	0.9675	-0.2927
160	293.79	1.1252	-0.2944
180	319.30	1.2229	-0.3051

Angle+ Degrees	Nusselt Number	Frössling Number	Pressure Coefficient
	Test 646		
0	532.32	2.2138	1.0215
5	535.17	2.2257	0.9841
10	529.43	2.2018	0.8897
15	515.63	2.1444	0.7457
20	503.69	2.0947	0.5589
30	475.55	1.9777	0.0965
40	447.33	1.8603	-0.4055
60	391.60	1.6286	-1.3208
80	319.33	1.3280	-1.7407
90	264.42	1.0996	-1.5953
95	263.89	1.0975	-1.4328
100	273.39	1.1369	-1.2297
110	418.19	1.7391	-0.7779
120	414.22	1.7226	-0.4761
130	321.26	1.3360	-0.3645
140	249.99	1.0397	-0.3323
150	234.09	0.9735	-0.3225
160	282.14	1.1734	-0.3202
170	336.35	1.3988	-0.3187
180	367.54	1.5285	-0.3178

* See Nomenclature for definition of terms.

+ Angle measured from stagnation.

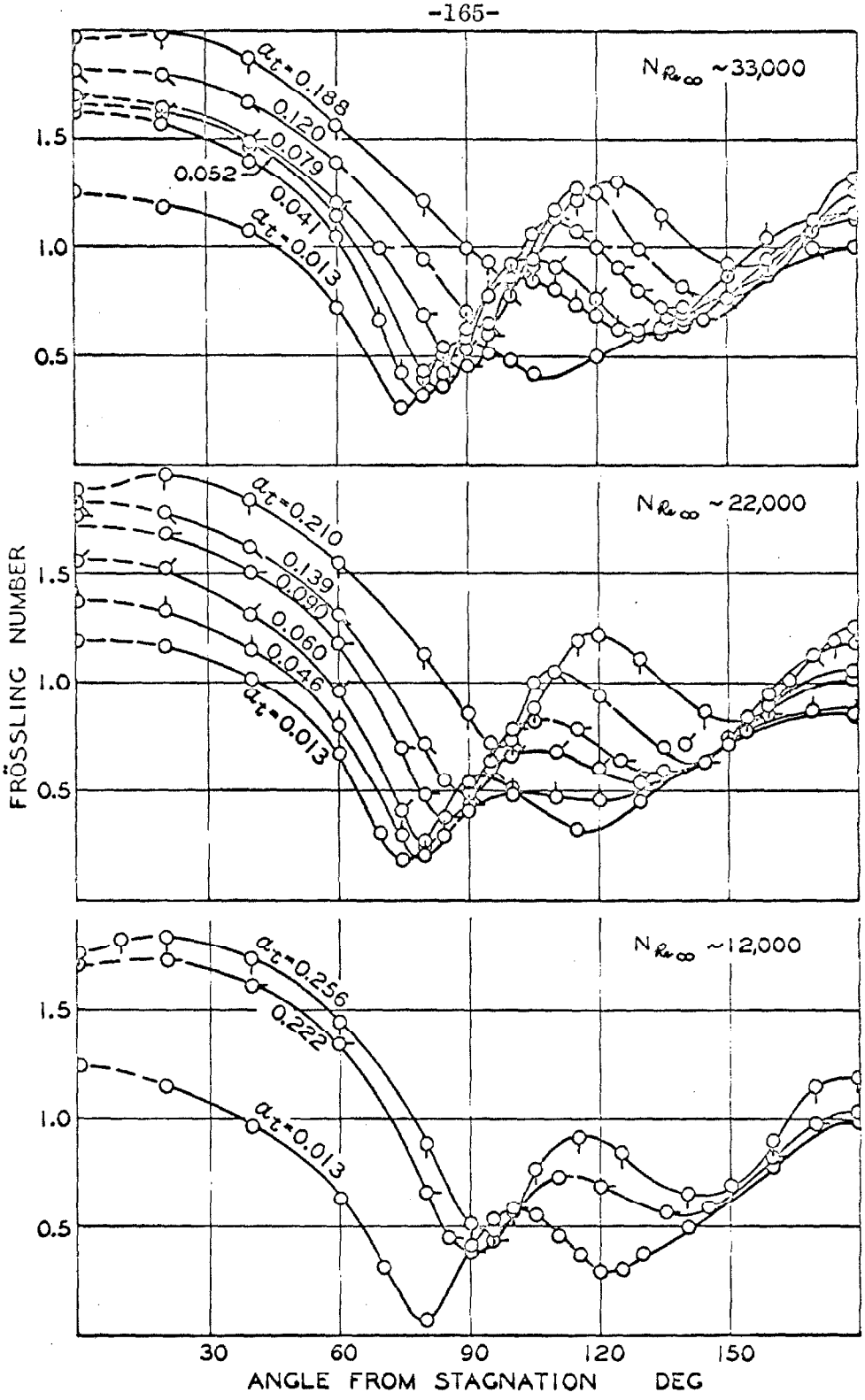

Fig. 19. Effect of level of turbulence upon local thermal transport

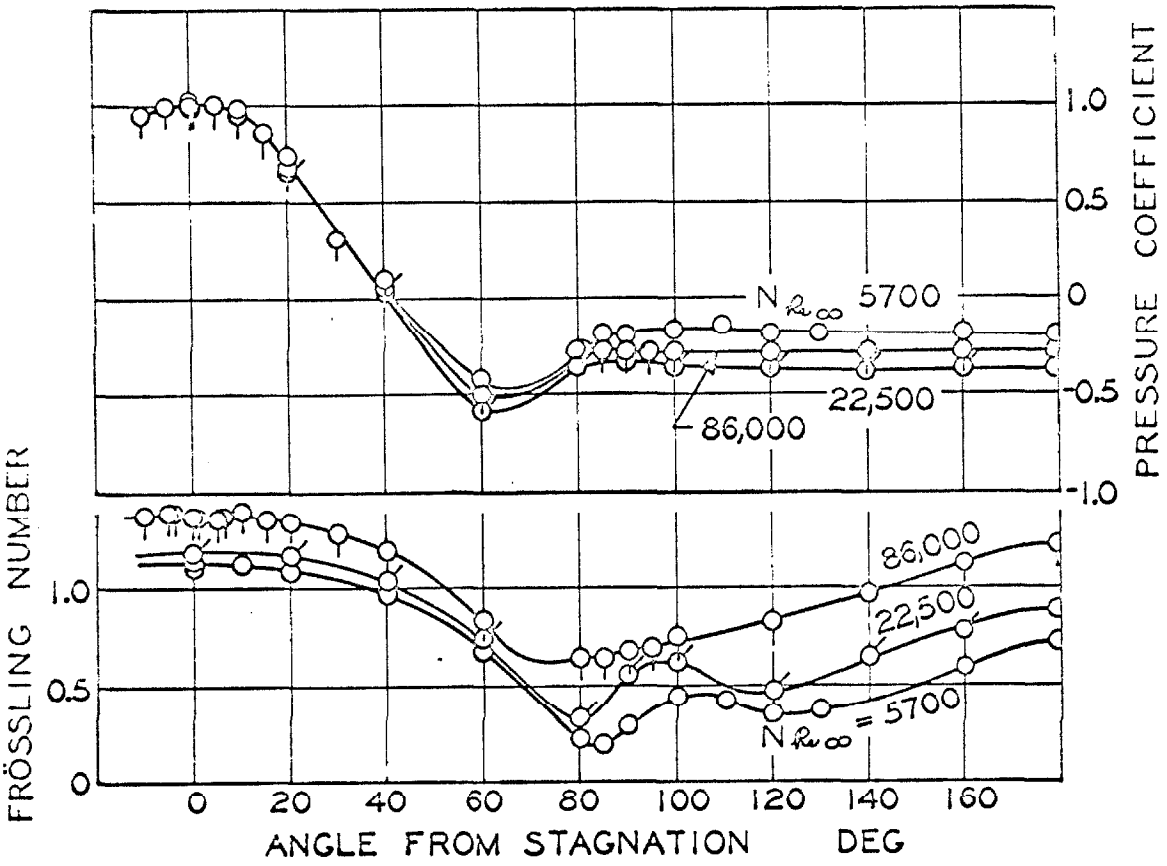

Fig. 20. Variation in Frössling Number and pressure coefficient at a turbulence level of 0.013

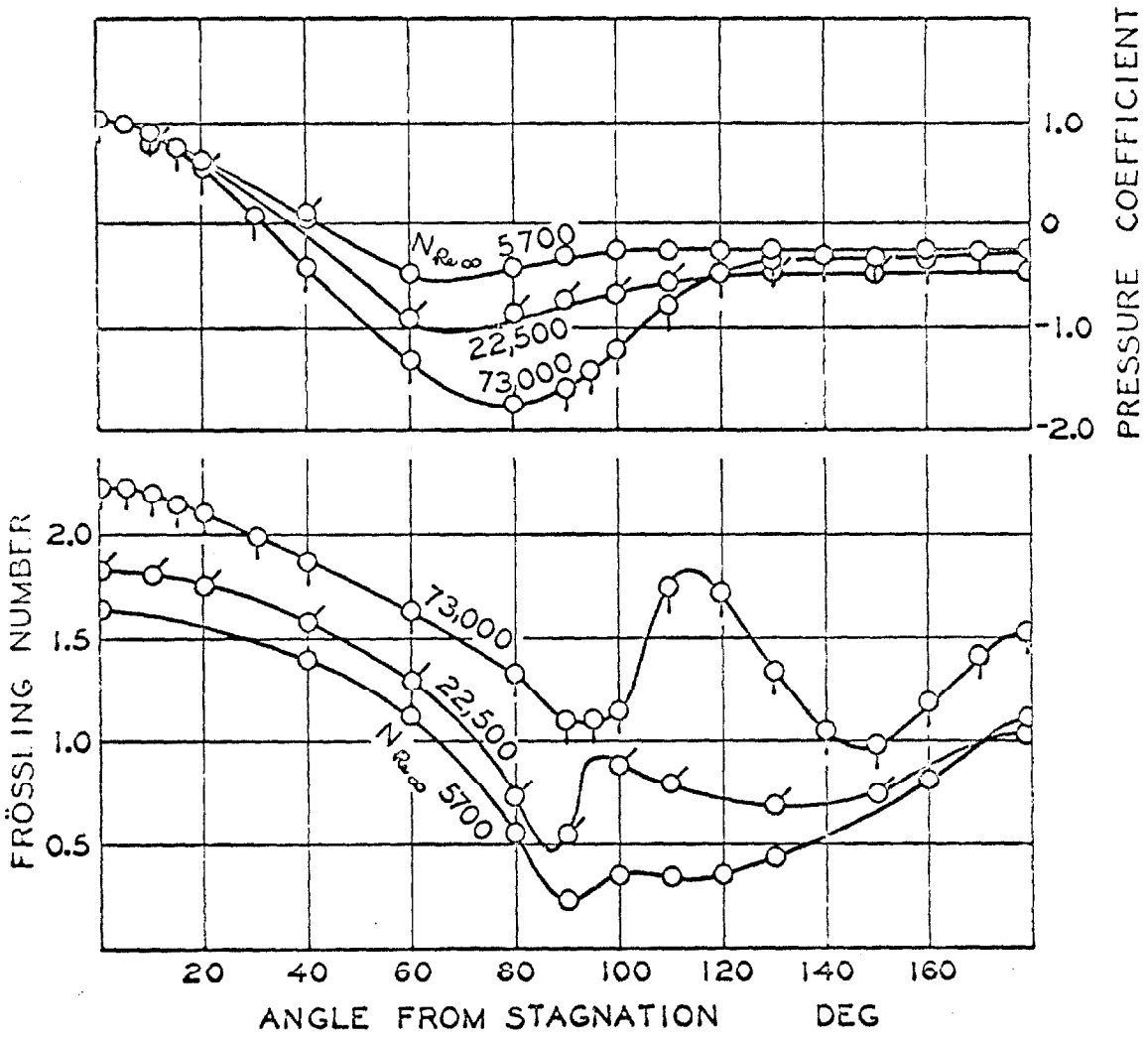

Fig. 21. Variation in Frössling Number and pressure coefficient at a turbulence level of 0.135

fluctuations are in agreement with the turbulence amplification found near stagnation by Kuethe, et. al. (47).

Figure 22 illustrates the effects of turbulence for a Reynolds number of 22,500 on the pressure coefficient and heat transfer. The effects of turbulence are larger when the pressure gradient is greater. This is to be expected from the effects of turbulence on a flat plate with a superimposed pressure gradient (48). The results shown in Figures 20-22 for the "circular-hole grid" (40,41) compare quantitatively within a few percent to those measured using a square mesh grid patterned after van der Hegge Zijnen (39). The turbulence influences the momentum boundary layer to a lesser degree than the thermal boundary layer, as can be seen in Figures 20-22 from the invariance with turbulence of the pressure coefficient near the forward stagnation point. The influence of Reynolds number for a level of turbulence corresponding to that of the free stream of 0.013 is shown in Figure 23, where the local Frössling number is presented as a function of the angle from stagnation with the Reynolds number as a parameter. These results suggest that a systematic mechanism of local transport is responsible for the displacement of these curves.

The local effects of Reynolds number and turbulence level on the Frössling number are shown at each angle in Figures 24-40. The behavior from angles 0° to 80° is simply what is expected for direct augmentation of transport by turbulent perturbations on a laminar layer. At 80° there are the first signs of a larger increase in Frössling number at low turbulence level as the result of instabilities, which were measurable near separation. Following 85° until 105° the effects of turbulence sharply decrease, the intercept falls to zero and the Frössling number depends strongly on the Reynolds number which means that the Nusselt number varies with theReynolds number to the first power. This stronger dependence upon the Reynolds

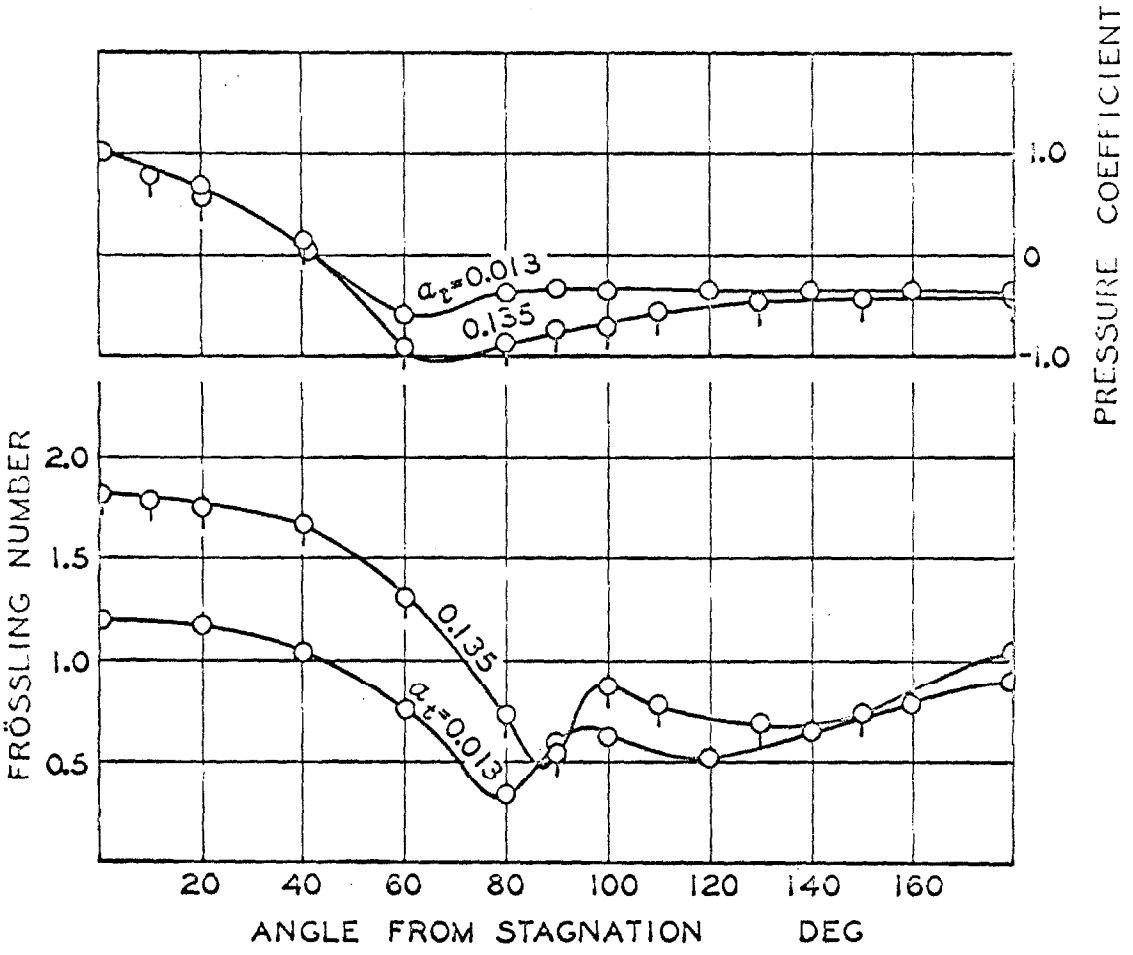

Fig. 22. Comparison of effect of turbulence level upon Frössling Number and pressure coefficient at a Reynolds Number of 22,500

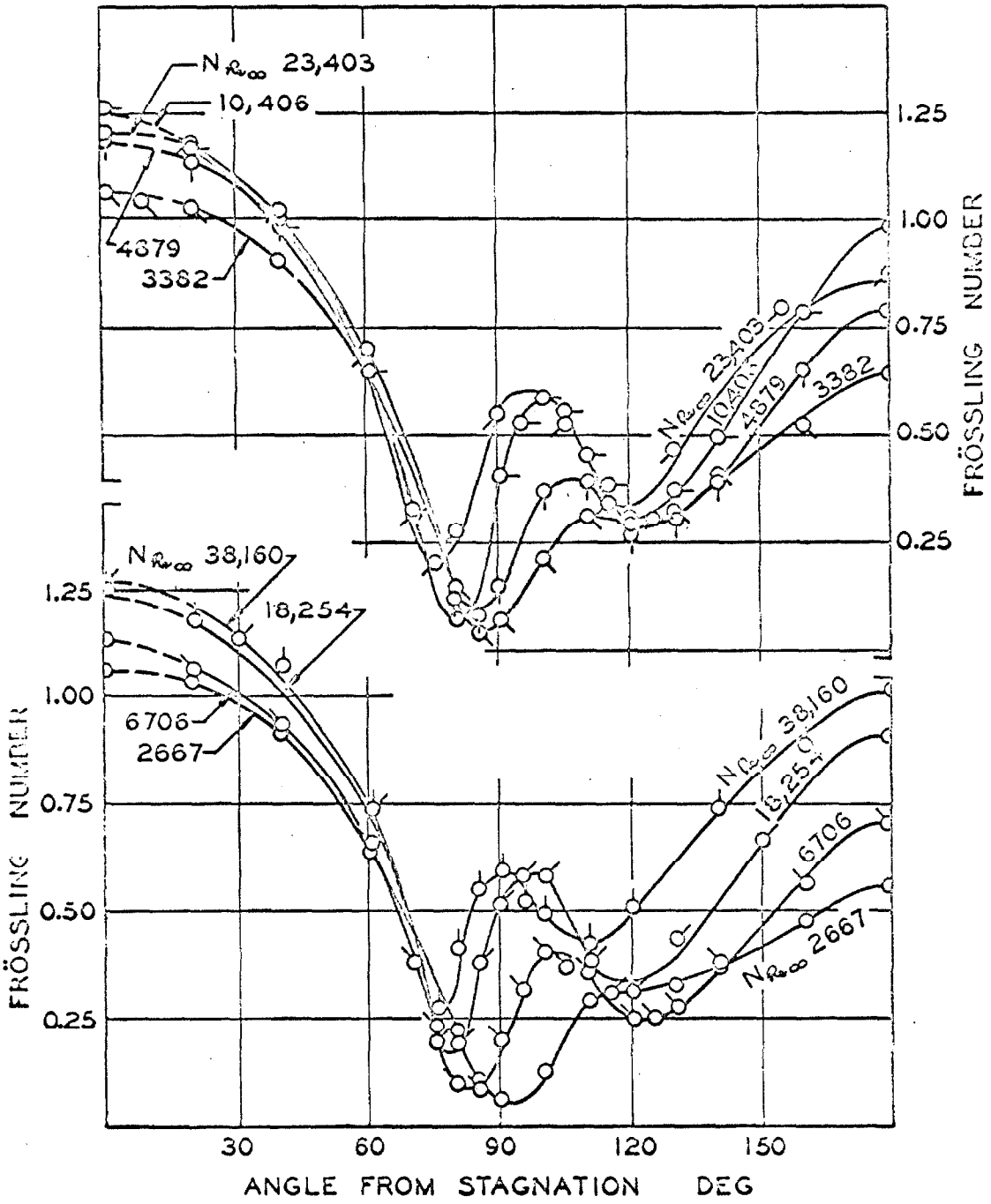

Fig. 23., Effect of Reynolds Number upon local thermal transport for a turbulence level of 0.013

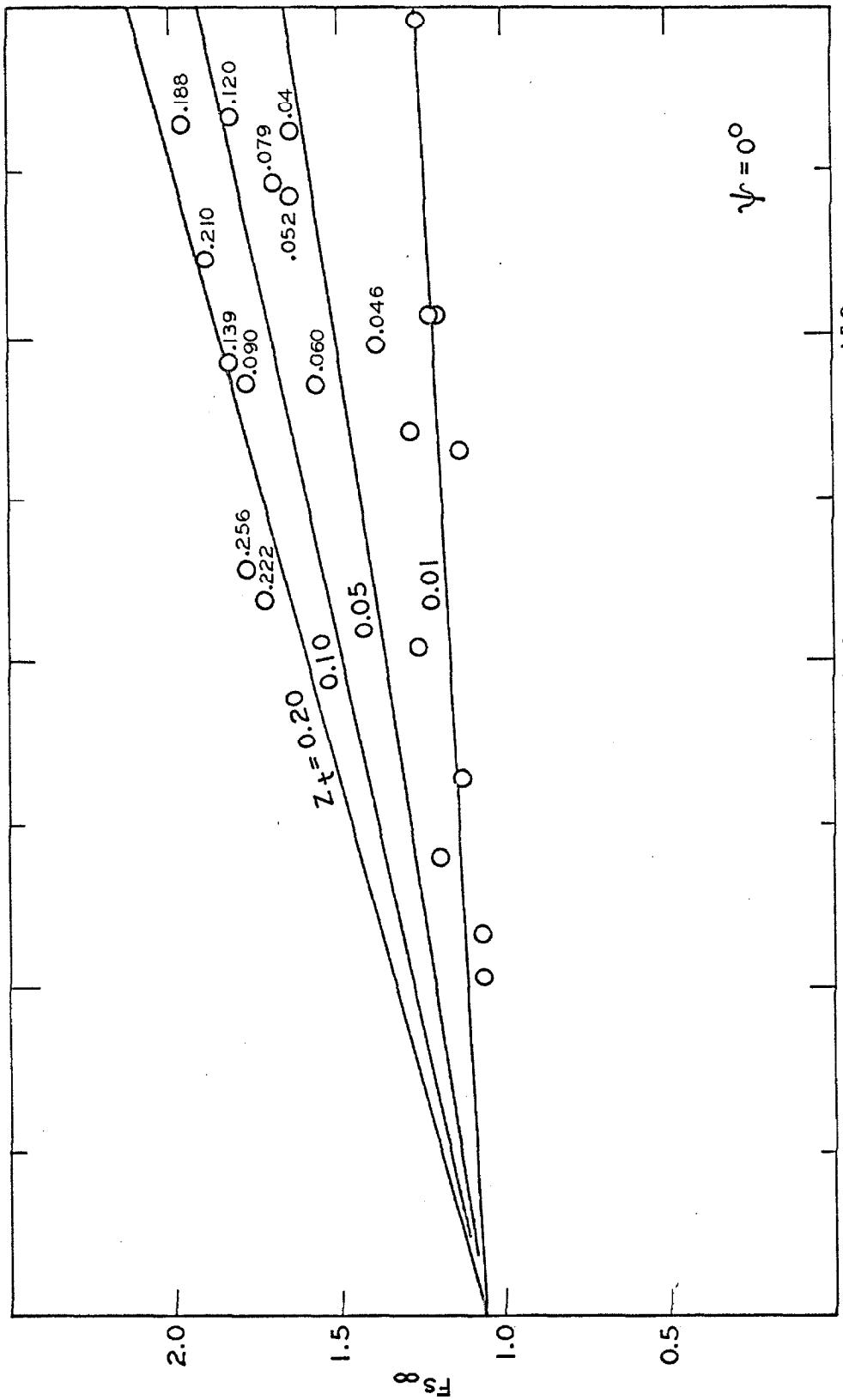

Figure 24. Local Effects of Reynolds Number and Turbulence Level on Frössling Number at 0°.

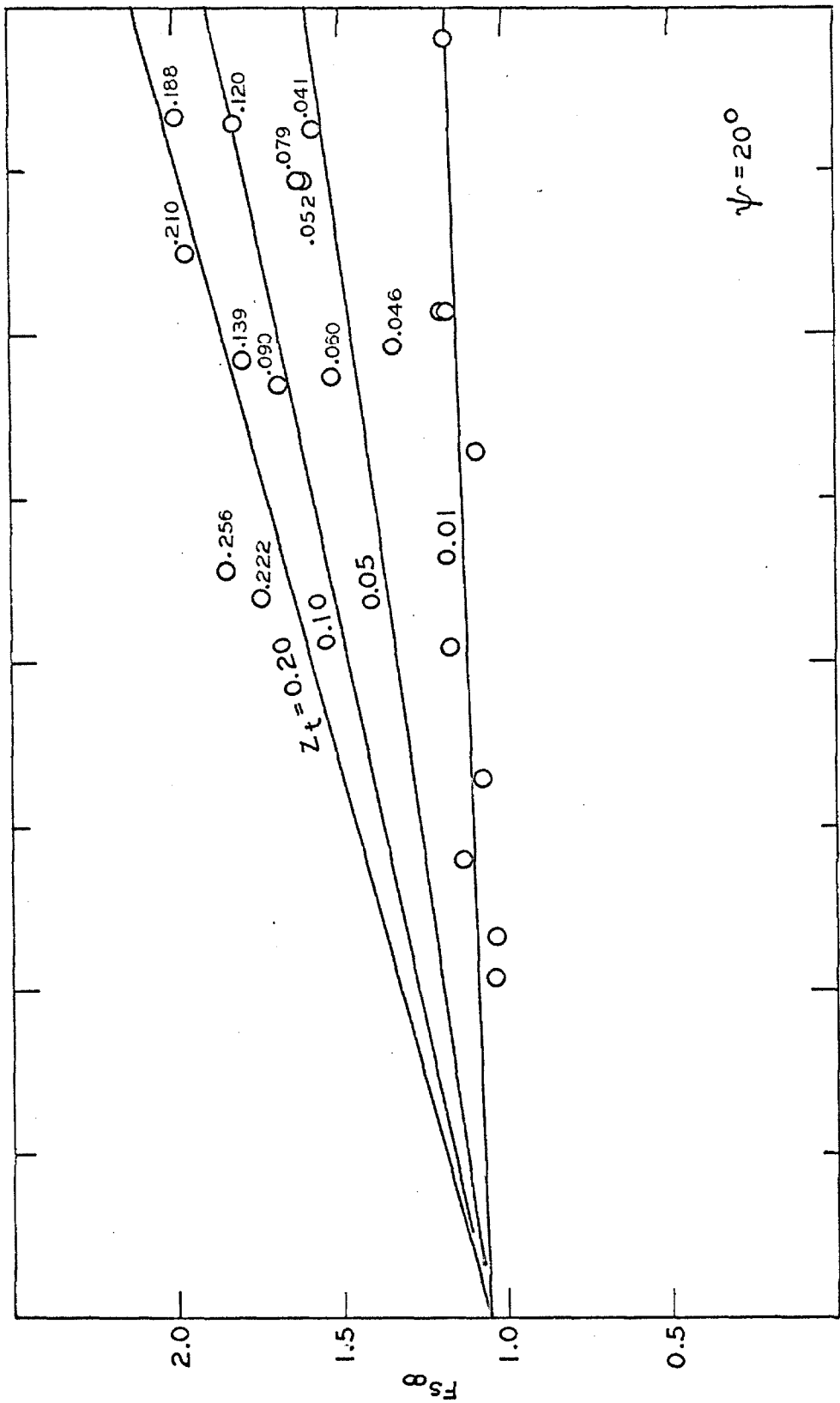

Figure 25. Local Effects of Reynolds Number and Turbulence Level on Frössling Number at 20°.

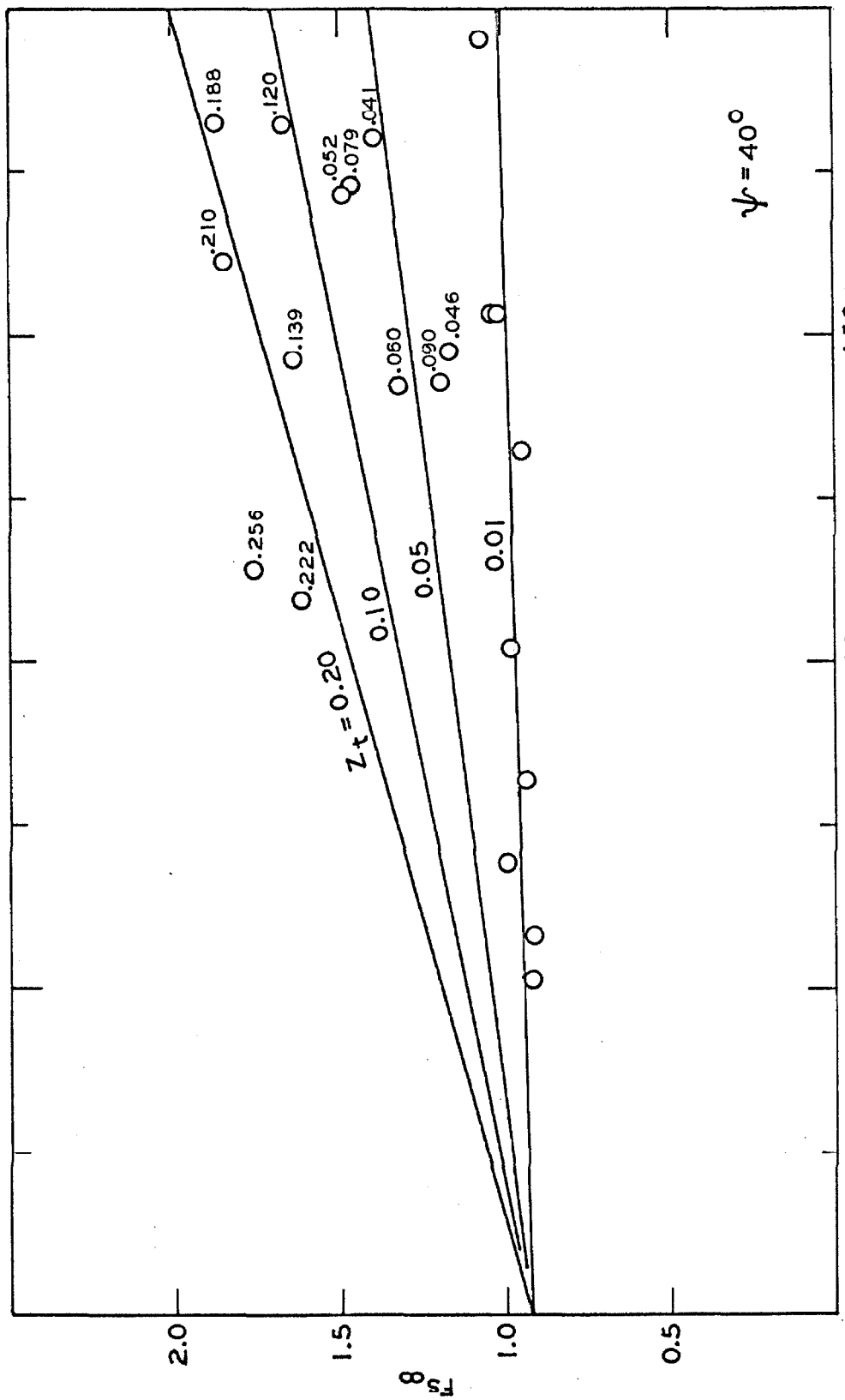

Figure 26. Local Effects of Reynolds Number and Turbulence Level on Frössling Number at 40°.

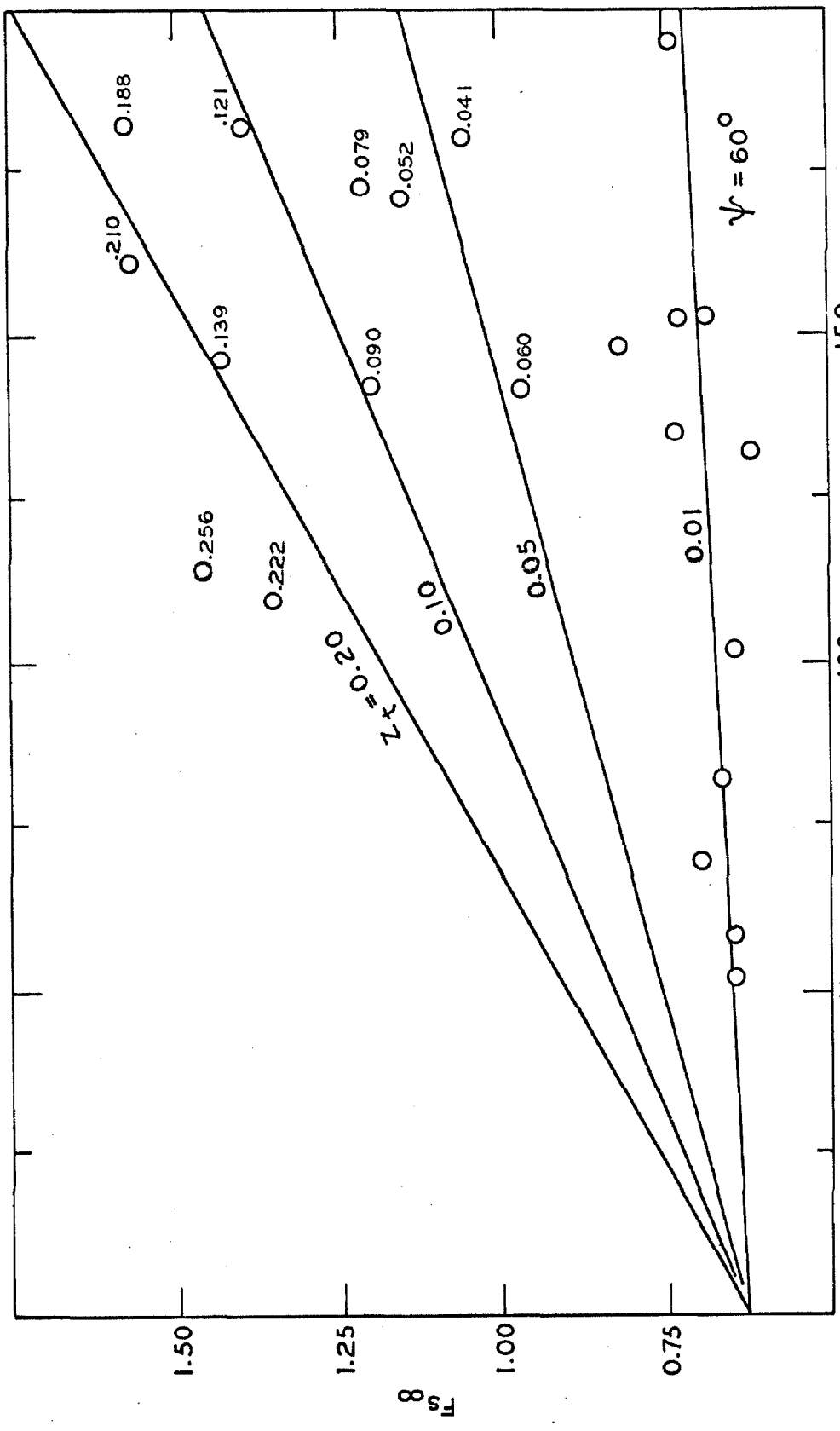

Figure 27. Local Effects of Reynolds Number and Turbulence Level on Frössling Number at 60°.

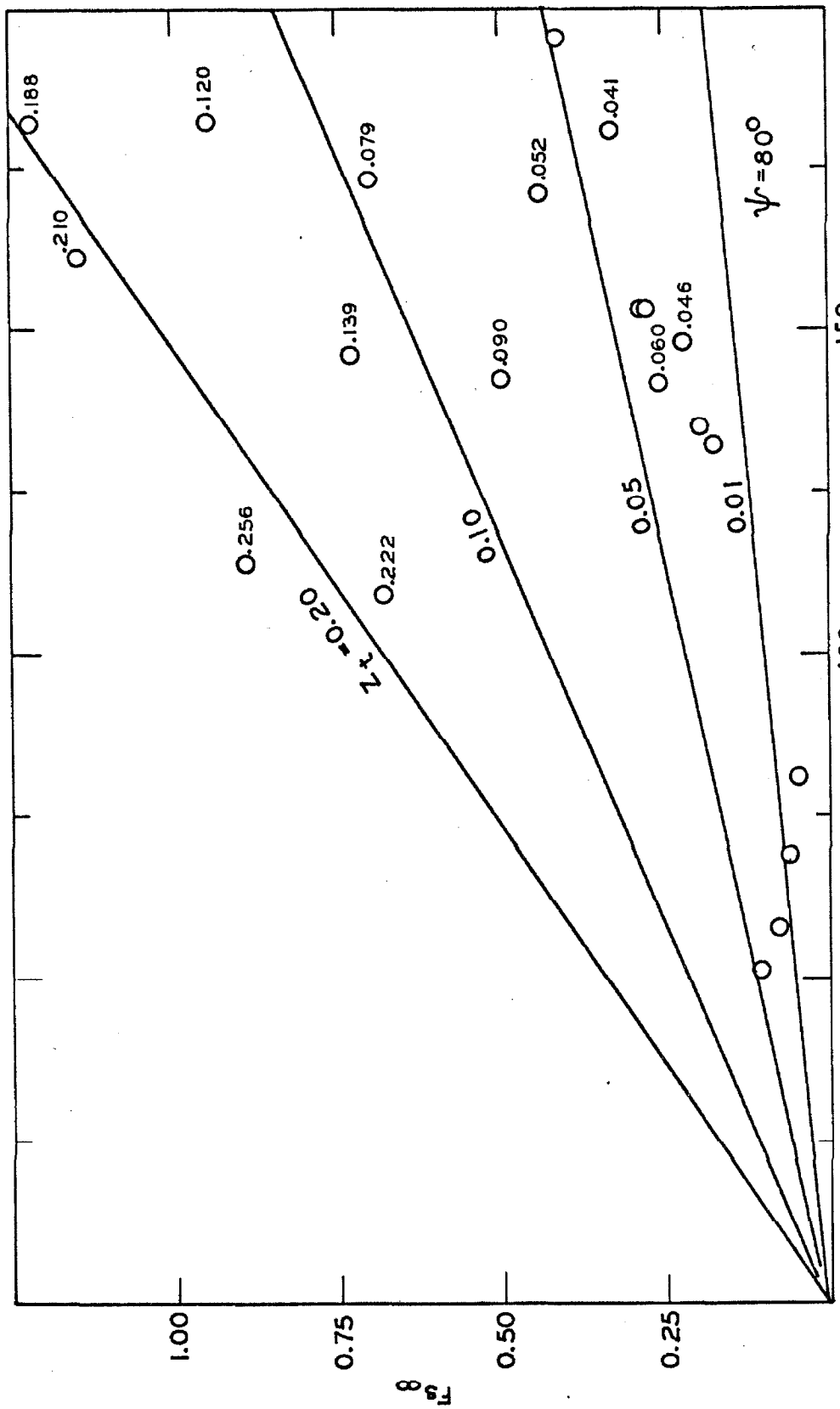

Figure 80. Local Effects of Reynolds Number and Turbulence Level on Frössling Number at 80°.

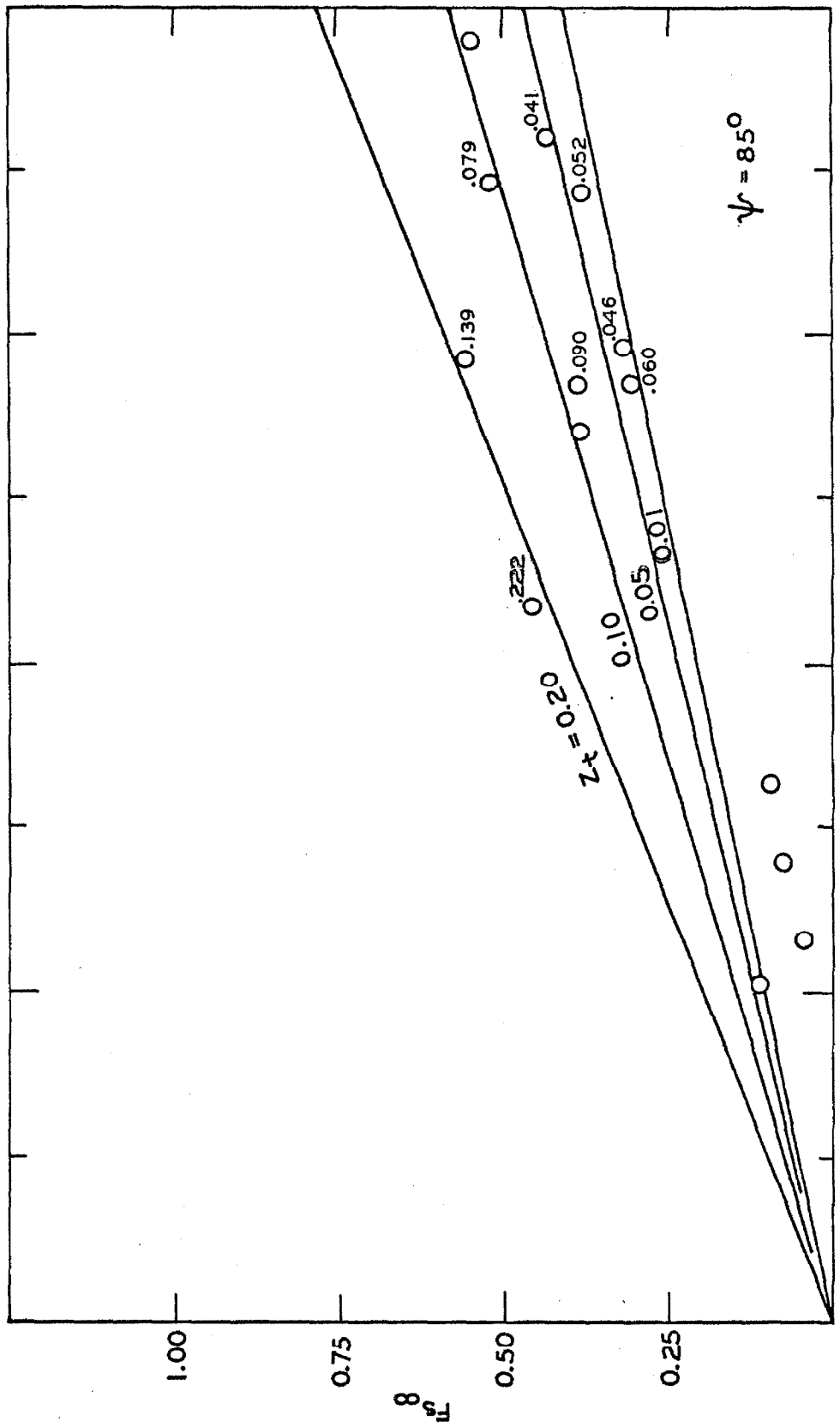

Figure 29. Local Effects of Reynolds Number and Turbulence Level on Frössling Number at 85°.

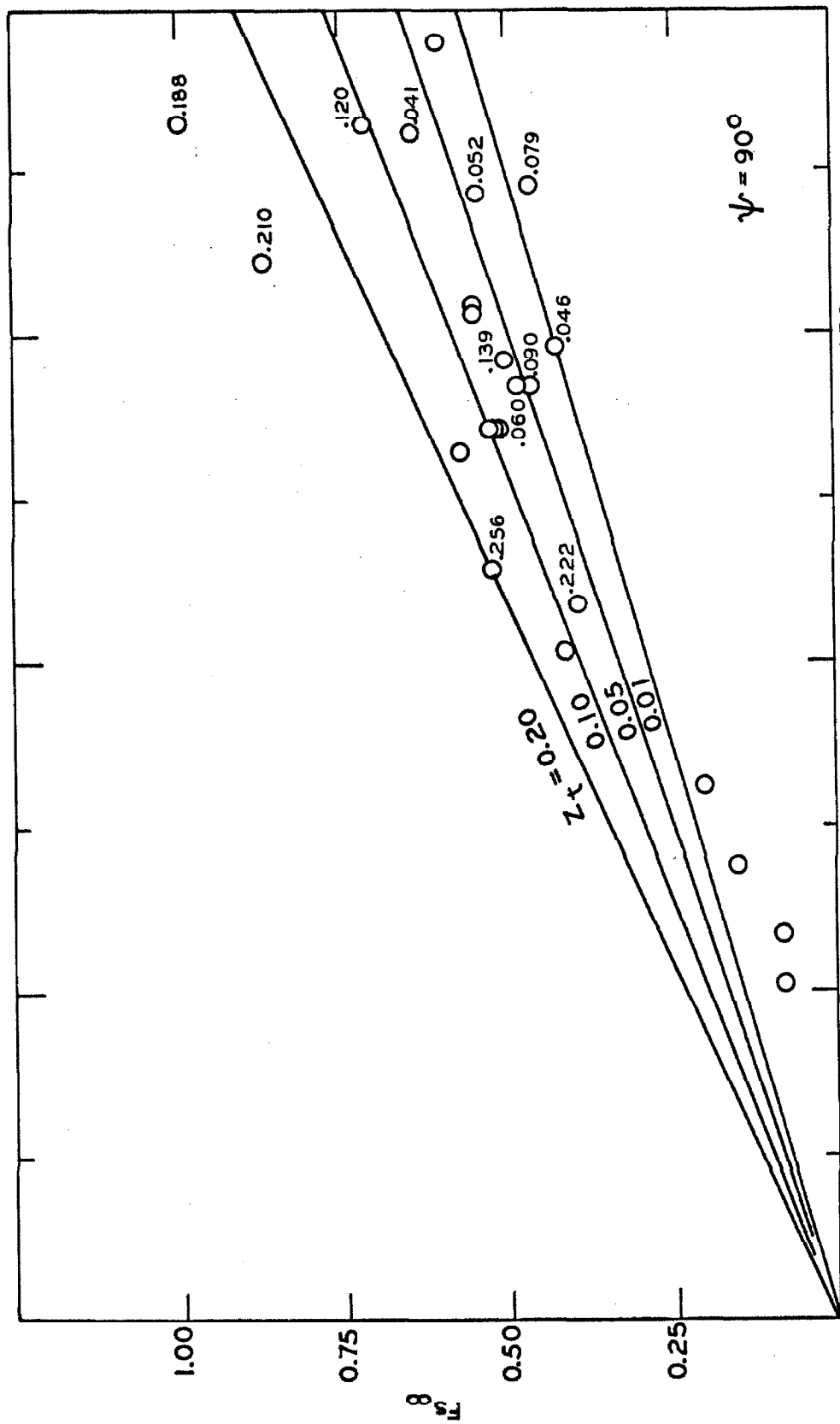

Figure 30. Local Effects of Reynolds Number and Turbulence Level on Frössling Number at 90° .

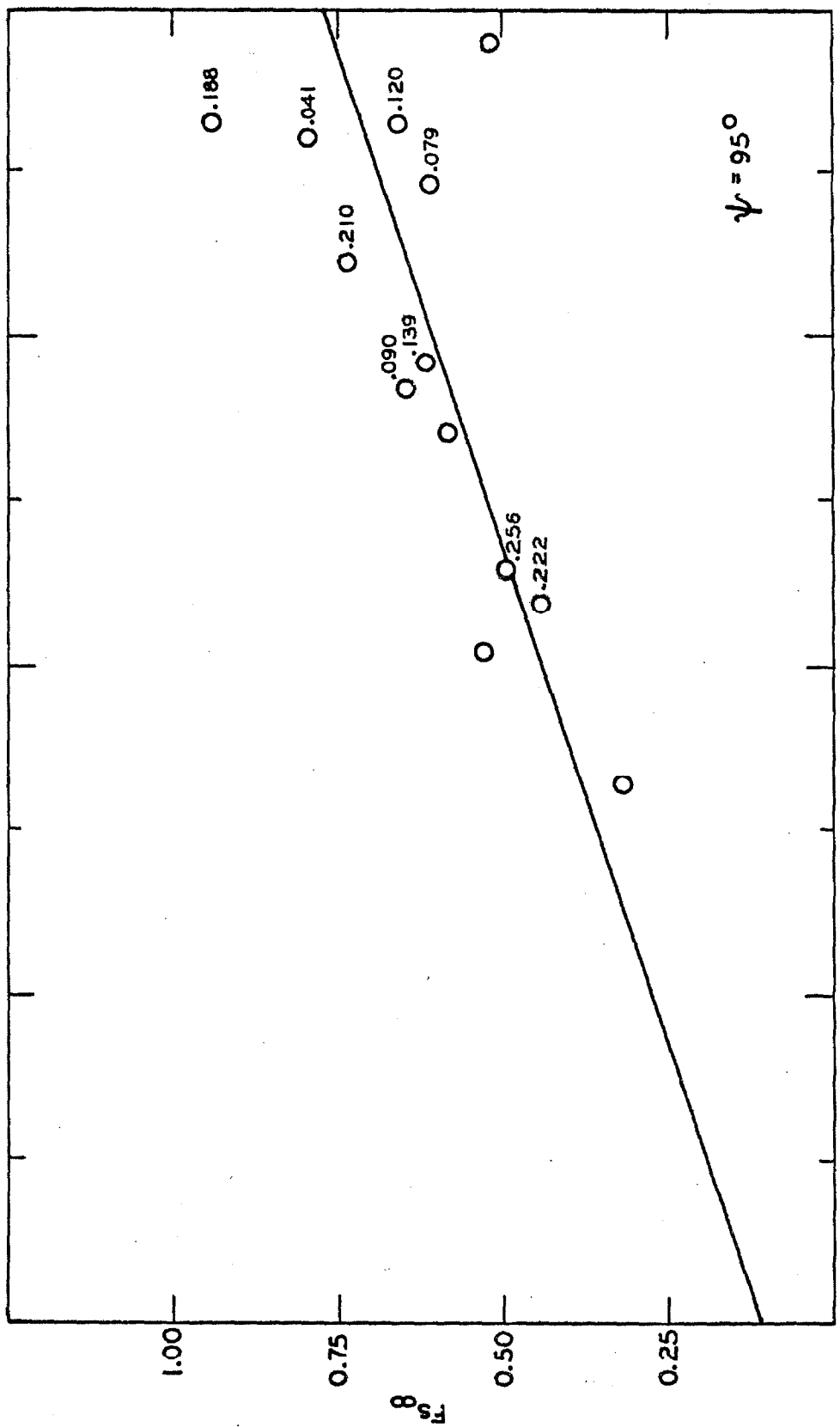

Figure 31. Local Effects of Reynolds Number and Turbulence Level on Frössling Number at 95°.

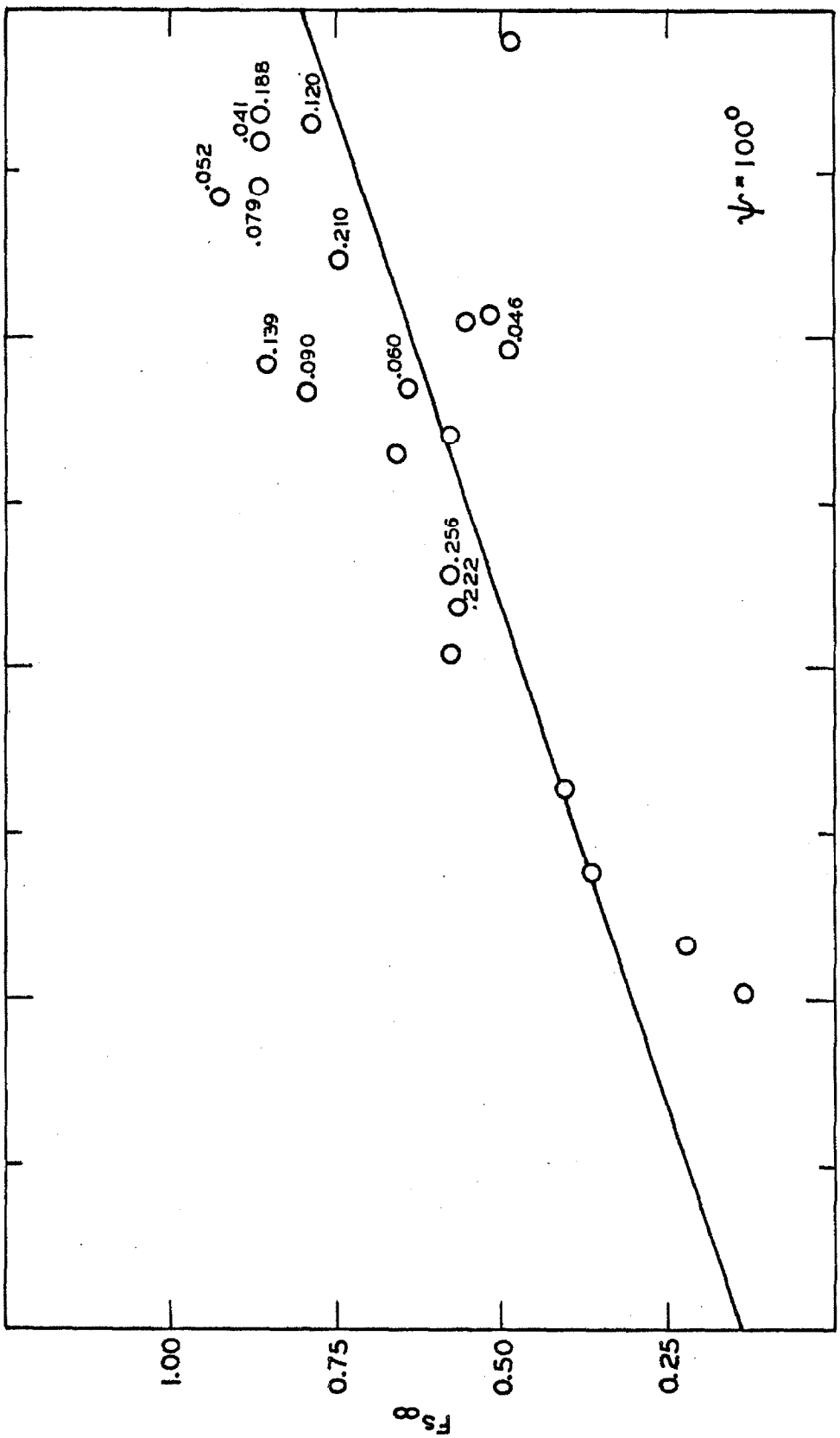

Figure 32. Local Effects of Reynolds Number and Turbulence Level on Frössling Number at 100°.

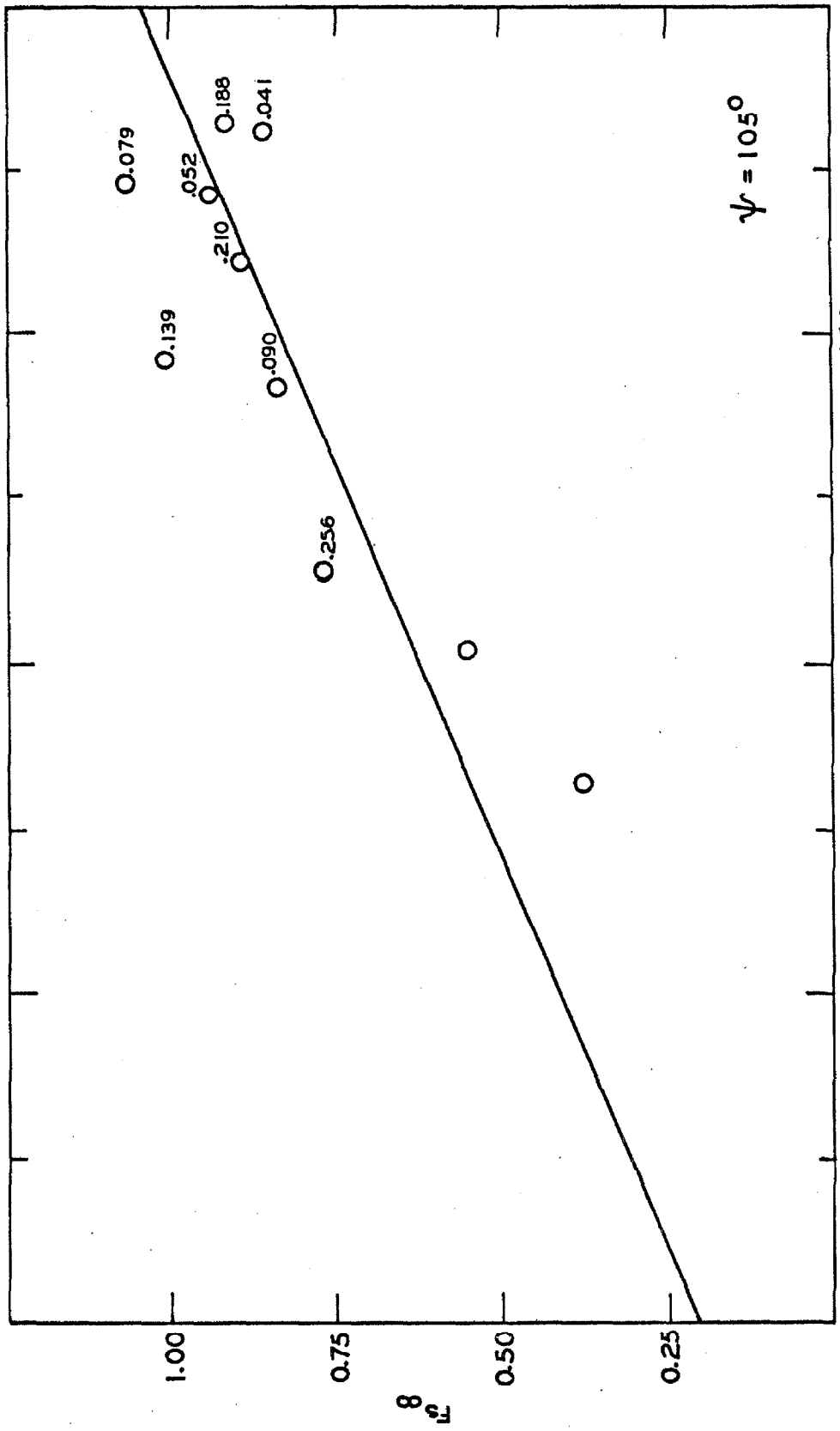

Figure 33. Effects of Reynolds Number and Turbulence Level on Frössling Number at 105°.

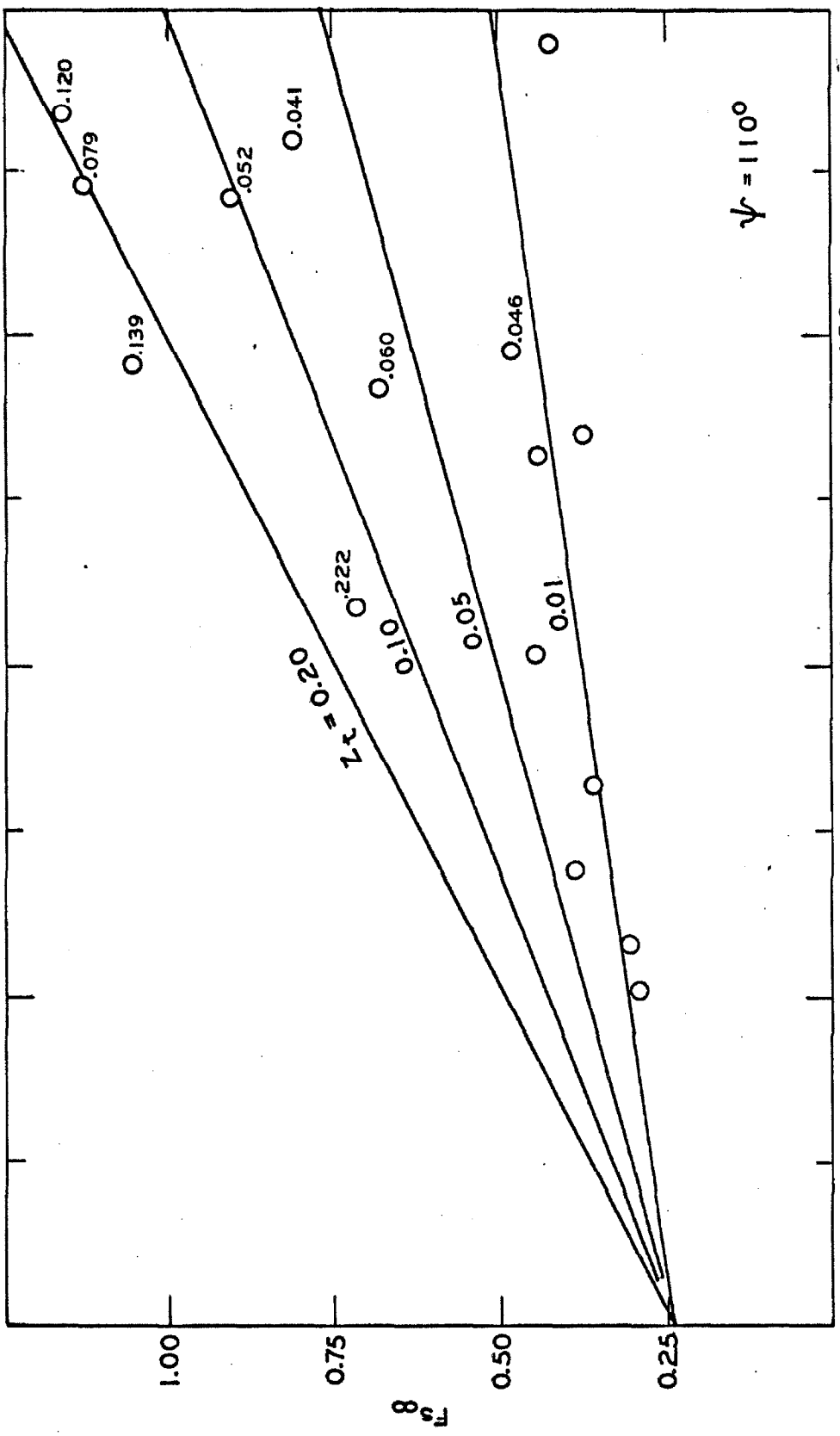

Figure 34. Local Effects of Reynolds Number and Turbulence Level on Frössling Number at 110°.

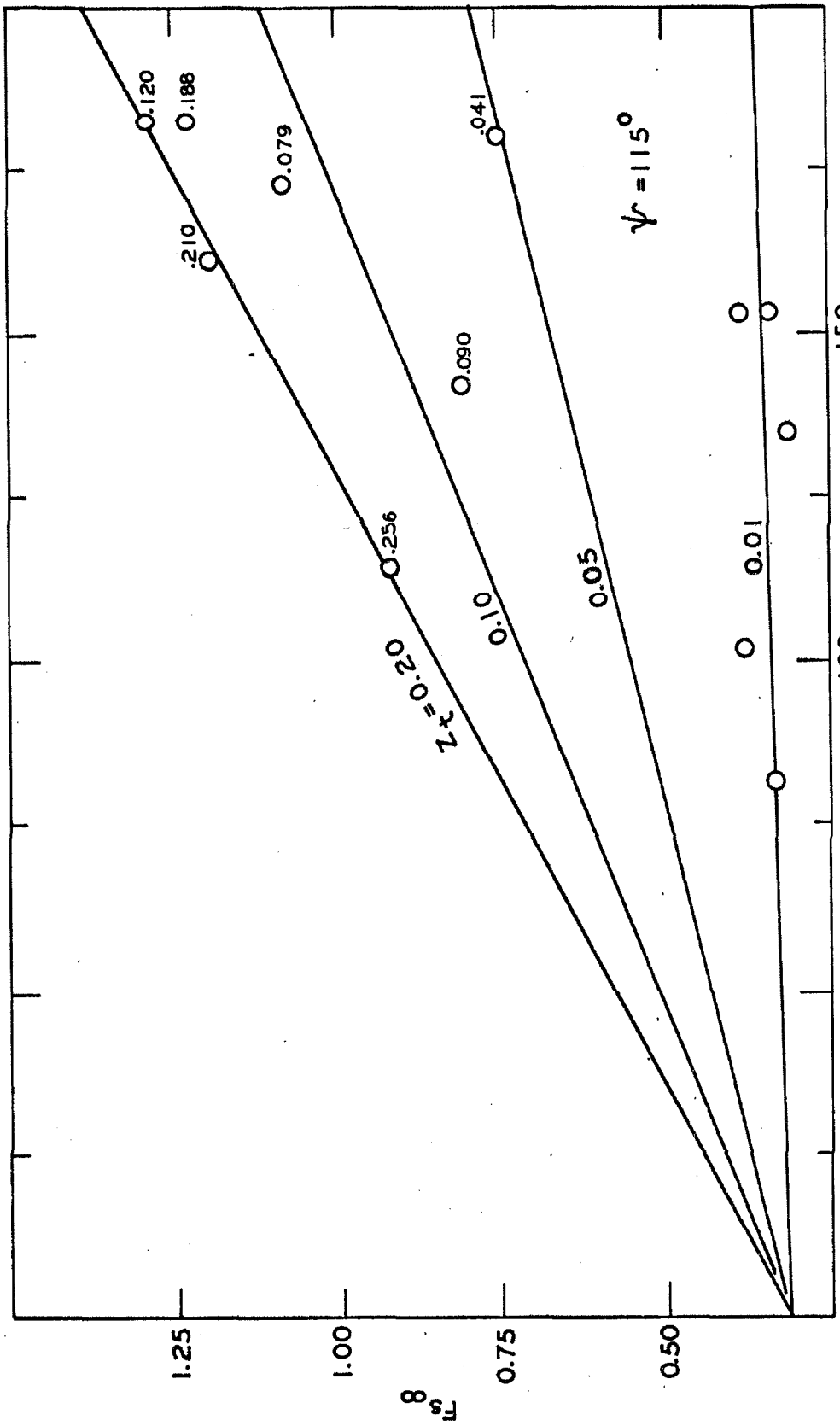

Figure 35. Local Effects Of Reynolds Number and Turbulence Level on Frössling Number at 115°.

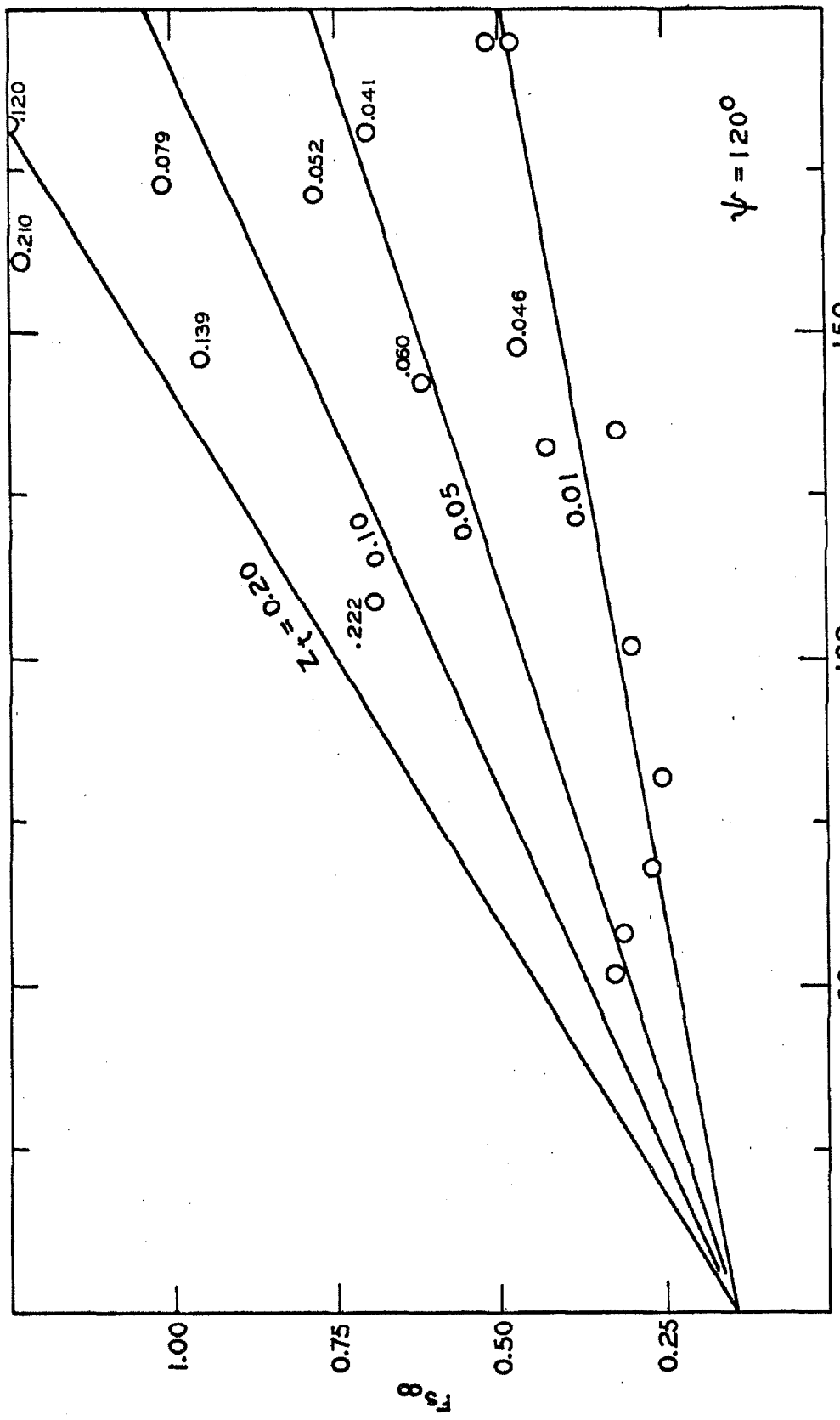

Figure 36. Local Effects of Reynolds Number and Turbulence Level on Frössling Number at 120°.

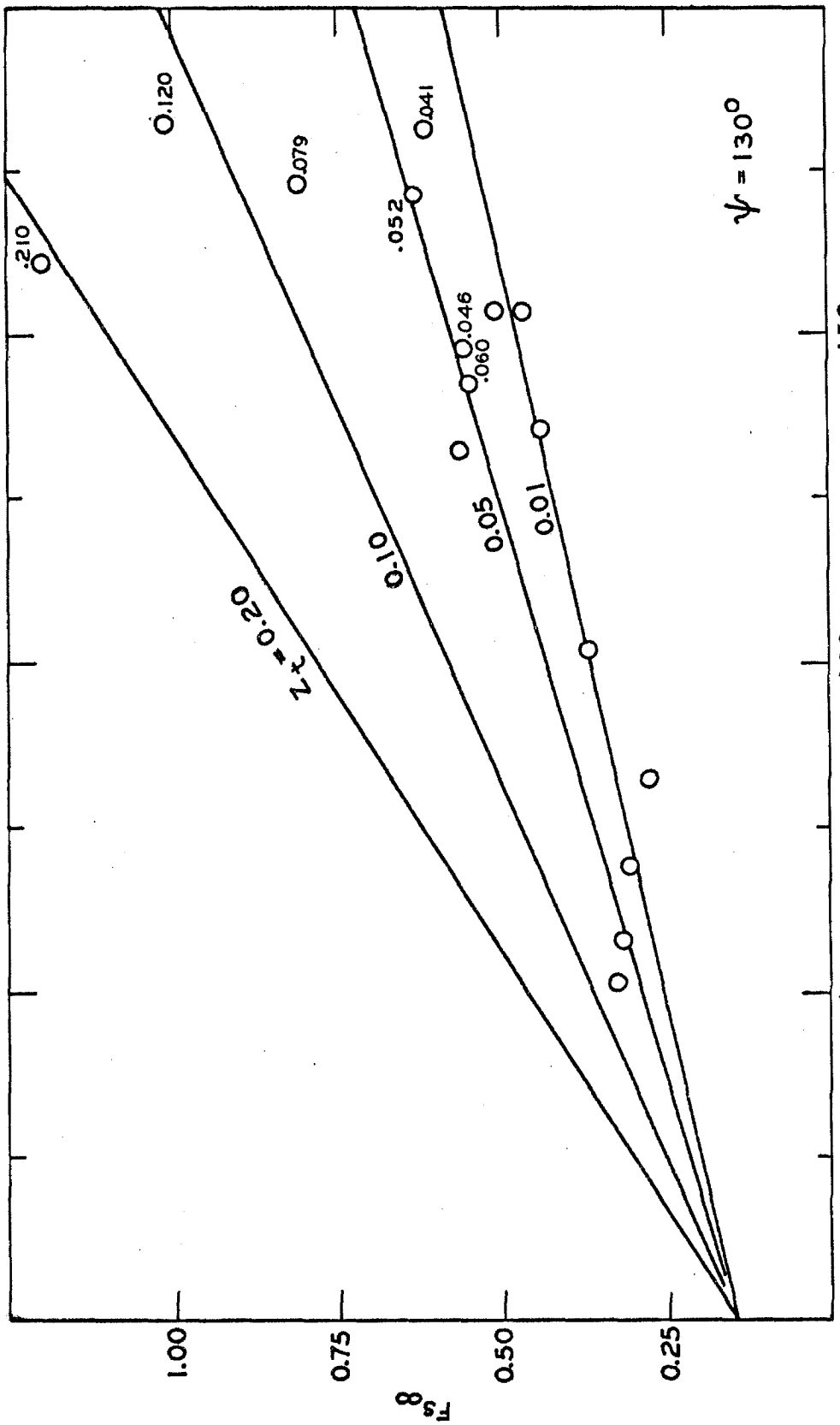

Figure 37. Local Effects of Reynolds Number and Turbulence Level on Frössling Number at 130°.

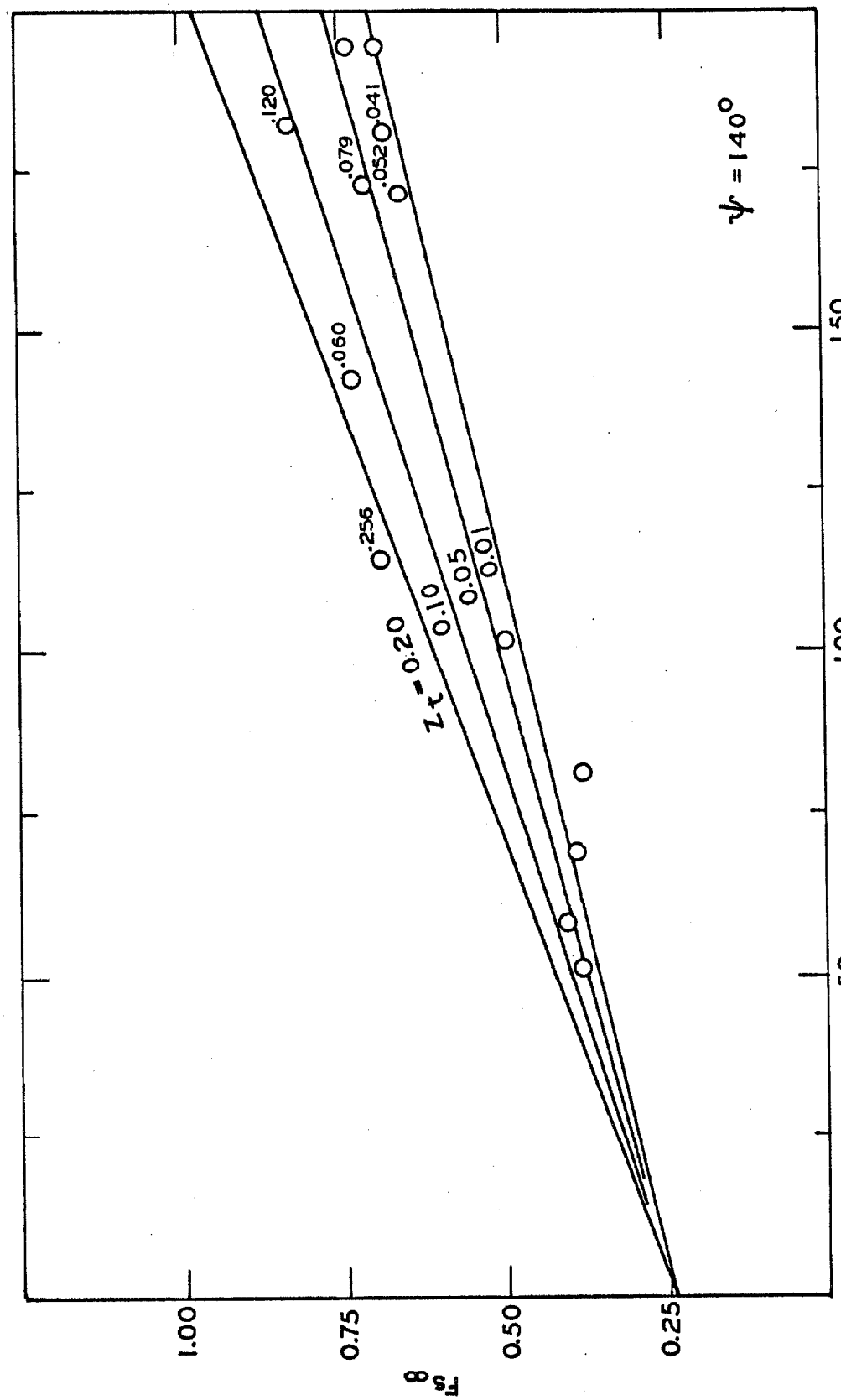

Figure 38. Local Effects of Reynolds Number and Turbulence Level on Frössling Number at 140°.

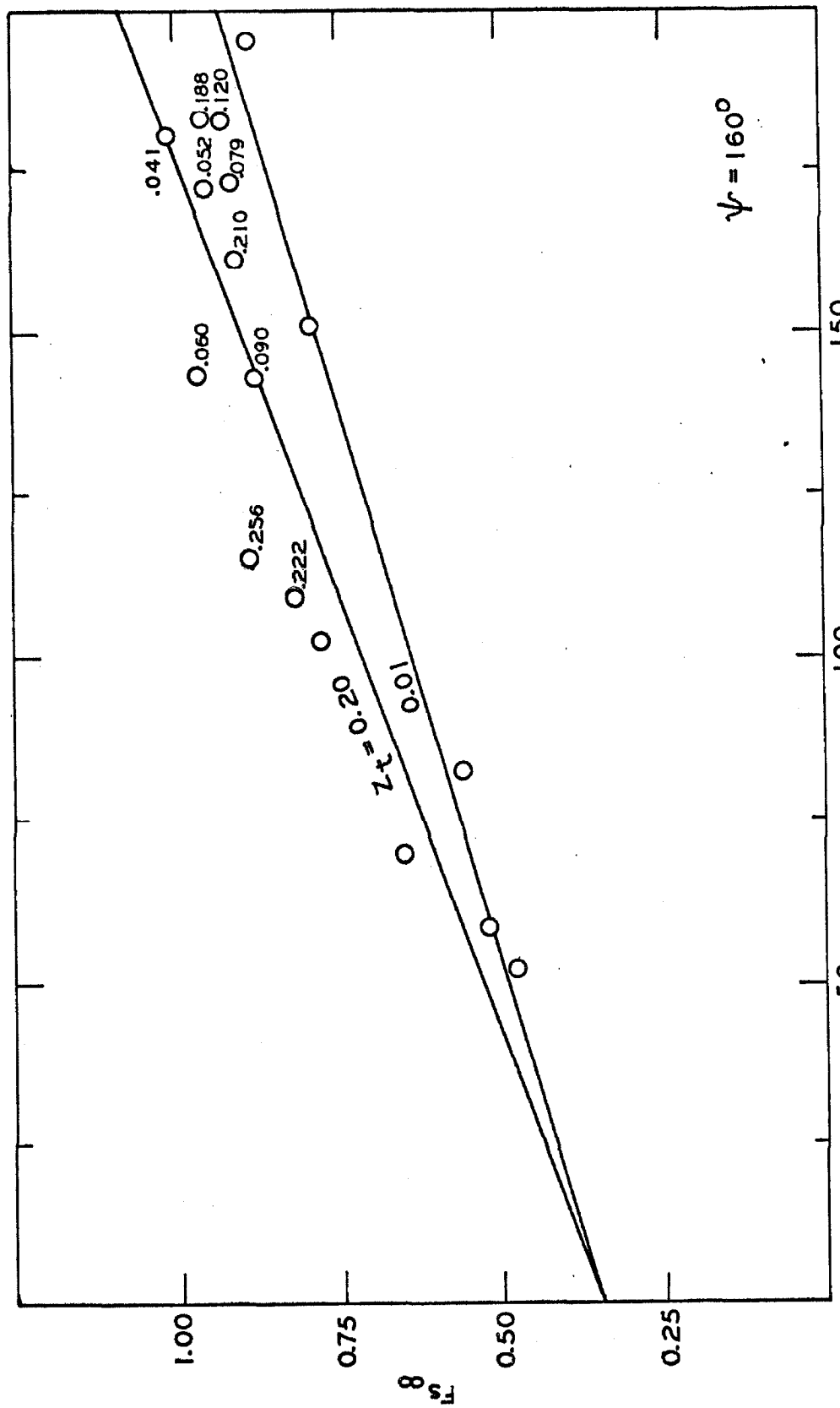

Figure 39. Local Effects of Reynolds Number and Turbulence Level on Frössling Number at 160°.

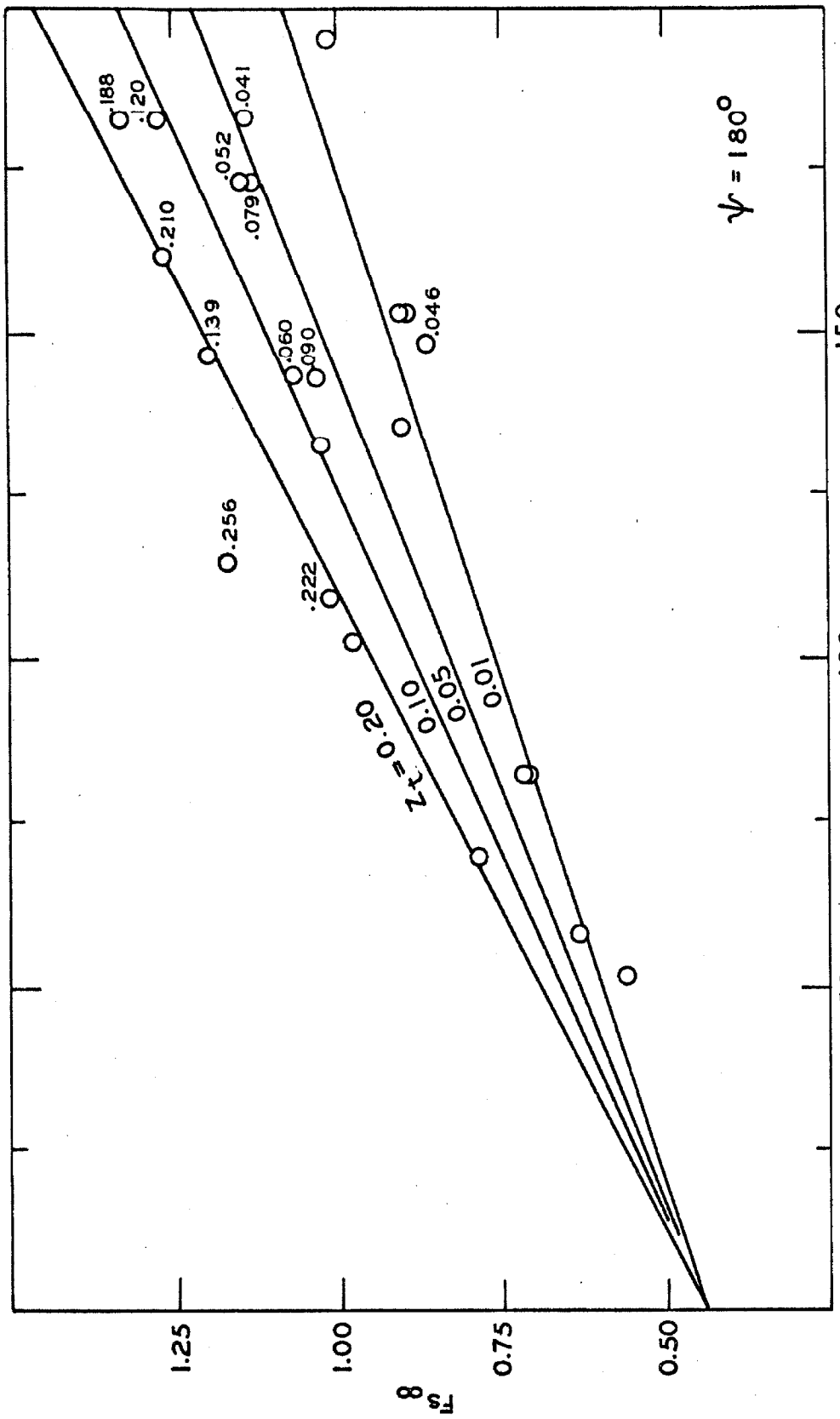

Figure 40. Local Effects of Reynolds Number and Turbulence Level on Frössling Number at 180°.

number and negligible effect of turbulence which occurs in this region of separated flow are characteristic of a turbulent boundary layer. Beginning at 95° the intercept begins to increase again, suggesting some rudimentary form of a laminar boundary layer in the process of formation as a result of backflow; however, on the top of this is still the characteristically turbulent layer, judging from the high dependence on Reynolds number. Shortly before 110° the laminar boundary layer has fully reattached in backflow and depends on Reynolds number and turbulence level in exactly the same way as the laminar layer did near the forward stagnation point. Near the rear stagnation point the effects of turbulence decrease again, suggesting a slight separation process as the two backflow laminar layers begin to converge. These figures (Figs. 24-40) have been particularly informative in regard to the local mechanism of transport.

If Equation 121 is considered as describing the local transport at a particular angle from stagnation as a function of Reynolds number and level of turbulence, it is possible to show the behavior for the different types of flow at various positions around the cylinder. This has been done in Figure 41, where each of the four coefficients is shown as a function of angle from stagnation. Coefficient A represents local transport completely free of effects of turbulence and turbulent boundary layers. Coefficient B reflects the degree to which turbulence effects the transport. C merely describes the non-linearity of the effects of turbulence. D represents the stronger dependence of the Frössling number upon Reynolds number in regions of a turbulent boundary layer or separated flow. The finite value of D in the laminar region suggests coupling of this region to action in the wake (such as changing wake length) by means of alteration in the velocity profile outside the boundary layer.

The data which have been accumulated confirm the results of earlier investigators and indicate the complicated flow pattern that exists beyond

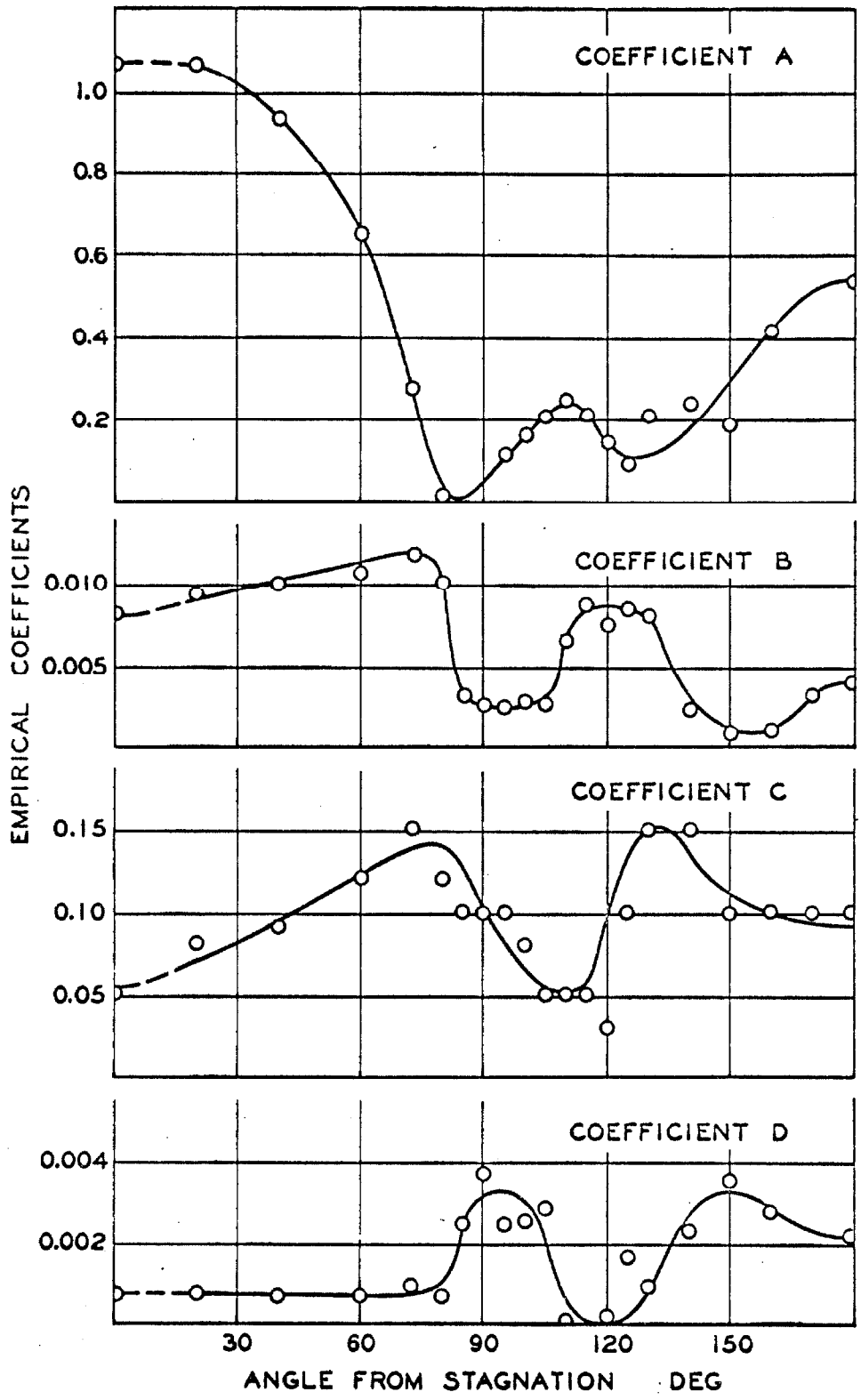

Fig. 41. Effect of angle of stagnation upon coefficients of Equation 5

separation in the wake. In Figure 42 is shown the local Nusselt number established from the present data as a function of angle for selected Reynolds numbers, for a level of longitudinal turbulence of approximately 0.013. Also included for comparison are the data of Giedt (28) and Seban (31) for a level of turbulence of 0.015.

The information available concerning local thermal transport permits an evaluation of the influence of the level of turbulence of the free stream and of Reynolds number upon the angle of separation. These results are shown in Figure 43. It is apparent that at the lower Reynolds numbers, the limited data available indicate a rather small change in the angle of separation with free-stream turbulence level. However, at Reynolds numbers above 12,000, the angle of separation increases rapidly with an increase in the level of turbulence. Such behavior is substantiated by measurements of Giedt (28) and Grove (49).

Pages 191 - 199

19 May 1967

NOTE: Per Terry Galloway letter dated 17 May 1967, pagination of thesis is incorrect. "Missing" pages 191 - 199 do not exist; no section has been left out, and the thesis is complete.

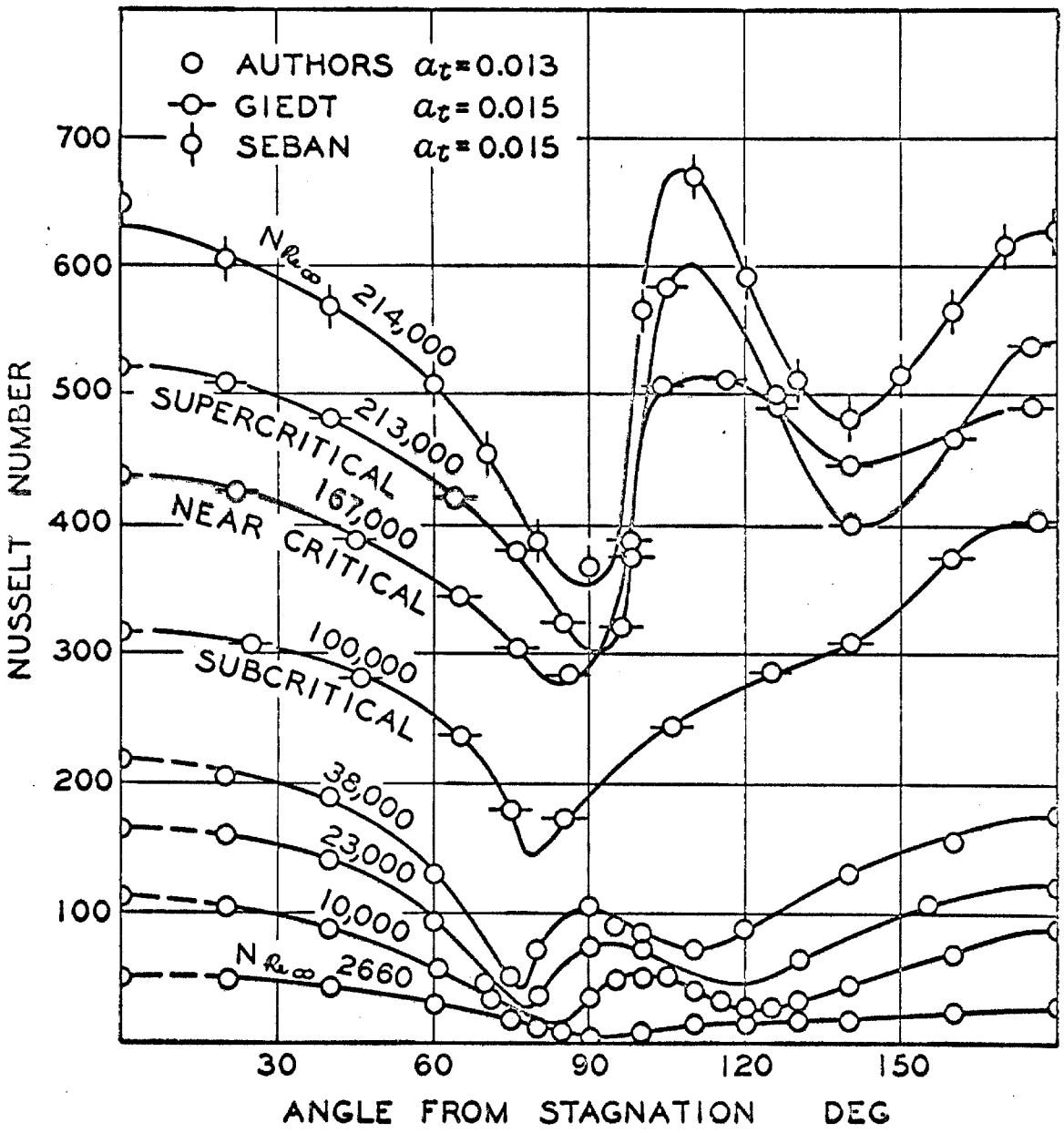

Fig. 42. Effect of angle from stagnation upon local thermal transport

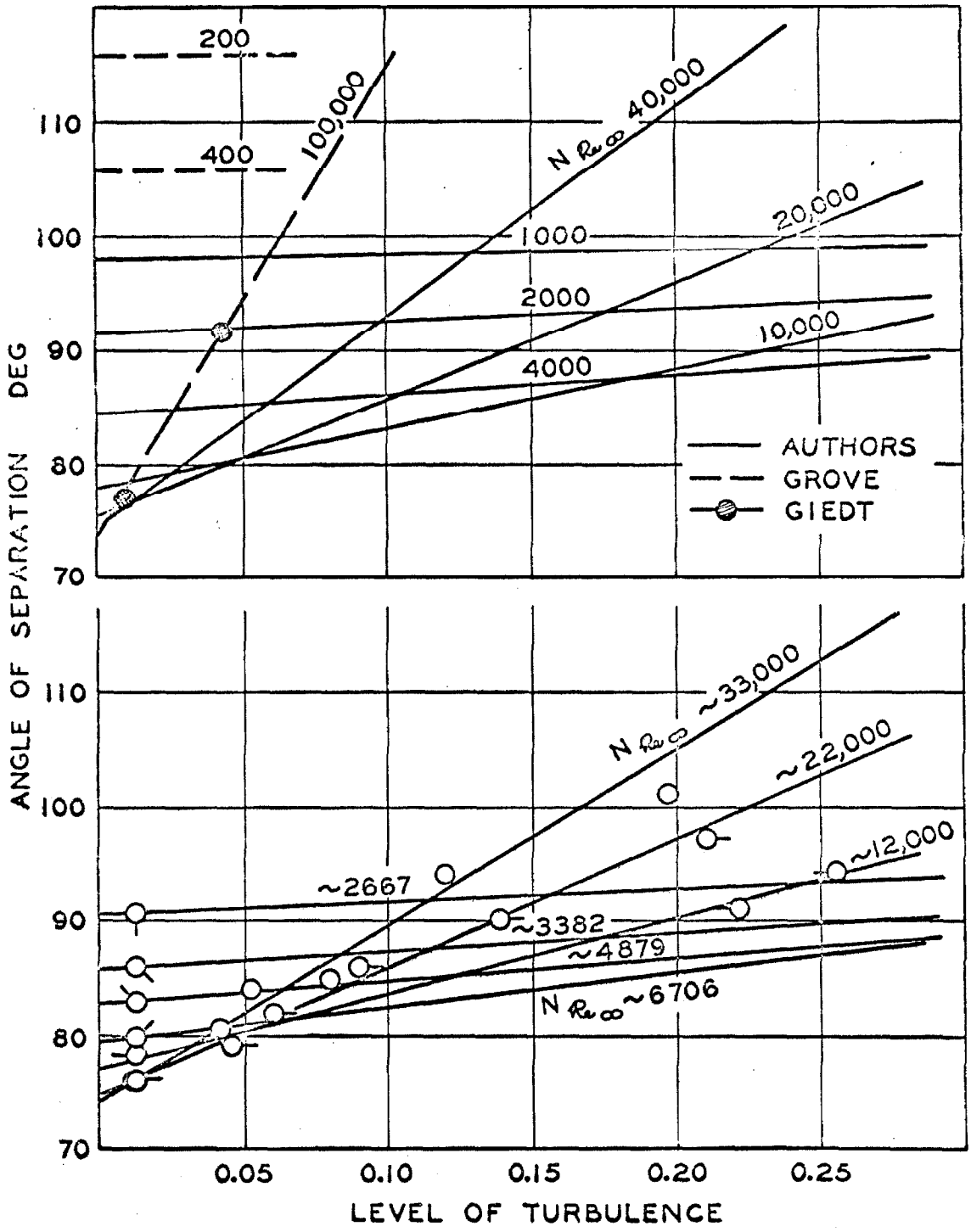

Fig. 43. Effect of flow conditions upon angle of separation

SPHERES

LITERATURE -- MACROSCOPIC TRANSPORT:

During the past decade there has been a marked increase in interest in local transport from spheres. Most of the more recent work brings to light the complex nature of the transport. A background for this work began in 1910 when Morse (50) sublimed small iodine spheres into air and noted that the rate of evaporation was quite accurately proportional to the sphere radius. Langmuir (51) utilized the data of Morse to describe the transport processes from small spheres, and recognised and illustrated the existence of the stagnant limit of 2 for a group of terms later to be referred to as the "Sherwood number". Fuchs (52) also treated the early problem of material transport from spheres into stagnant air.

Frössling (5, 6) was the first to analyze the transport processes involving forced convection from spheres both experimentally and theoretically, resulting in the following empirical solution for the Sherwood number:

$$Sh = 2 + 0.552 Re^{1/2} Sc_m^{1/3} \qquad (122)$$

R. W. Powell (53) then carried out his investigation of the evaporation of water by forced convection from an assortment of geometric shapes. His data were the first to show clearly the non-linear aspects of the problem, part of which is believed to have been related to the elevated free-stream turbulence in his equipment. Kramers (54) carried out work involving the energy transport from small spheres at low Reynolds numbers with a large variety of fluids in order to investigate the influence of the Prandtl number. Although his data

appear to have been quite seriously influenced by natural convection effects, the dependency on the Prandtl group was successfully demonstrated. Later, Ranz and Marshall (55) varified Kramers trends and extended this work to energy transport in the low Reynolds number region, 0 to 200. Tang , Duncan, and Schweyer (56) investigated in the range of Reynolds number from 50 to 3000; however, their Nusselt number results were about 50 percent lower than those of Ranz and Marshall. Ingebo (57) carried out similar transport studies from drops of various liquids. Hsu, Sato, and Sage (58) studied the evaporation of drops of n-heptane in turbulent airstreams.

Maisel and Sherwood (26) showed the complexities of the transport process involving fluid streams of elevated turbulence, resulting in increases of the Nusselt number with free-stream turbulence for Reynolds numbers around 10,000. Loitzianski and Schwab (59) had carried out similar work at Reynolds numbers around 100,000 involving energy transport and found similar increases, although for much lower turbulence levels. Later, Sage and co-workers (60-64) showed identical trends for heat and mass transfer from 0.5 and 1.0 inch spheres over a range of Reynolds numbers of 800 to 7,500, varying the turbulence level from 1 to 15 percent, and spanning the range of flow rates of Loitzianski (59).

In the 1950's, the aerodynamic studies of the cooling of heated spheres were given considerable attention, relative to the local tranfer around the surface of the sphere at air velocities in the critical and supercritical regions. Typical of this work are the measurements of Lautman (65), Xenakis (66), Amerman (67), Cary (68), and Wadsworth (69). The quality of the experimental work varied considerably, but the local behavior was demonstrated. An analysis of their data clearly illustrates the increased dependence of the Nusselt group on the Reynolds number in the wake. In the case of the work of Wadsworth (69), the influence of the turbulence of the free stream on transport was severely

complicated by the coupling of the variation of turbulence with the Reynolds group.

Klyachko (70) recently analyzed the problem of combined forced and free convection and indicated the problems in experimental measurements. Yuge (71) carried out extensive counter-flow measurements in the region of comparable forced and free convection from spheres, and verified the minimum in the Reynolds dependent Nusselt number data previously reported. The forced convection data of Klyachko (70) and Yuge (71) above Reynolds numbers of 10 are in agreement with the work of Sage and coworkers (60-64), and also indicate the higher Reynolds dependence at higher flow rates owing to the wake effect.

The qualitative properties of the wake of a sphere were discussed by Torobin and Gauvin (72) in a semitheoretical light, and their representation suggests that this higher Reynolds dependence is logical. Pasternak and Gauvin (73) correlated transport from spheres together with transport from approximately 20 geometric shapes, all at elevated turbulence intensities of about 10 percent. The effects of systematically varying the turbulence level were neglected in their work.

Subsequent to the work of Kramers (54), Griffith (74) extended the measurements to mass transfer studies by systematically varying the fluid in forced convection from drops, bubbles and rigid spheres to establish the influence of the Schmidt group as the cube root. Linton and Sutherland (75) completed work on the local mass transfer from benzoic acid spheres in a water tunnel. Their results compare well with those involving both heat and mass transfer from spheres. Vliet and Leppert (76) extended the use of the water tunnel to a range of Reynolds numbers up to 50,000 by employing an electrical induction-heated sphere. By systematically varying the sphere surface temperature, the effects of variable properties were investigated.

Their work varified the cube root of the Prandtl number, using the film conditions for all properties and a viscosity ratio of the surface and free stream.

Thodos and coworkers (77-79) carried out investigations involving simultaneous heat and mass transfer utilizing single spheres, in order to explain data of spheres in a multiple-body array. Simultaneous heat and mass transfer employing single spheres was carried out by Sage and coworkers (61, 63, 64). The recent measurements of Keey and Glen (80) concerning the material transfer from spheres indicated the inadequacies of simple relationships describing the changes in the Sherwood group, Reynolds group, and Schmidt group, as suggested by the earlier data.

The problem of maintaining uniform energy dissipation within a heated sphere is complicated by the transport behavior of a spherical surface, as illustrated by the nearly isothermal measurements of Vliet and Leppert (76) and the nonisothermal measurements of Kramers (54). The material transfer from nearly isothermal solid spheres was discussed by Garner and coworkers (81-84) who indicated that the Sherwood number for Reynolds numbers greater than 250, is a function of $Re^{1/2}$ and $Sc^{1/3}$, and that for lower Reynolds numbers the material forced convection is severly complicated by the combined presence of free convection effects, which air the total transport in upflow while suppressing transport in downflow. They also demonstrated the migration of the point of separation in the region between Stokes and boundary layer flows.

The turbulent field near the stagnation point of blunt bodies of revolution was considered in some detail by Kuethe, Willmarth, and Crocker (47). Their results illustrated the utility of a turbulent perturbation penetration model describing the influence of free-stream turbulence which was subseqently elucidated by Harriot (85). All of these results reveal that near the surface the Reynolds dependency involves a complex influence of turbulence, in addition to its established effect upon separation and strongly nonlinear effects in the

wake-flow. The earlier measurements of Kramers (54), Lautman (65), Cary (68), and Xenakis (66), which were primarly of a macroscopic nature, demonstrated these turbulent perturbation and nonlinear wake effects rather strikingly. Büyüktür (48) has shown experimentally, on flat plates, the coupling effects of pressure changes and turbulent perturbations of the boundary layer.

The influence of the blockage ratio of the sphere area within the wind tunnel upon the effective velocity in thermal transfer complicated the interpretation of the measurements of Cary (68), Xenakis (66), and Wadsworth (69). A similar set of investigations involving cylinders is available for comparison. Kestin (29) and Seban (31) indicated the importance of increased free-stream turbulence, which was generated behind a screen, upon the local heat transfer from cylinders, while Comings (25), utilizing parallel dowels, and Giedt (28), using a cord net, reported similar information of the local heat transfer from cylinders as a function of the increased turbulence level of the incident stream.

The influence of Reynolds number and level of turbulence upon the macroscopic thermal and material transport from spheres was recently evaluated by the authors (86). As was indicated in this recent publication, the nonlinear effects of level of turbulence and sphere diameter appeared to be significant, currently shown to enter as the Reynolds number. The diameter dependence suggests the increasing importance of the wake at higher Reynolds numbers. Some of the work carried out in water tunnels, such as that of Brown, Pitts, and Leppert (12), and the work of Wadsworth (69) with wind tunnels, was under such conditions that the effect of blockage was appreciable and perhaps may have accounted for a small amount of the influence of scale previously indicated (86). However, the effect of size of sphere and of level of turbulence was large enough to make it worthwhile to investigate these effects upon local transport.

There was some evidence that the effects of diameter (in the form of the Reynolds number) in the wake flow region were large compared to those in the forward hemisphere, and that the interrelation of these two effects was further complicated by the change in the point of separation with the level of turbulence, as discussed by Lin (87). Skelland and Cornish (88) investigated the effect of oblation of the spheres and these authors varied the importance of the laminar as compared to the separated region. The results showed no strong or unreasonable trends with degree of oblation. Grafton (89) carried out a theoretical analysis of the importance of the laminar and wake flow regions relative to the overall transport, and illustrated that the data for lower Reynolds numbers can be explained by treating both regions individually. Richardson (26,37) reviewed turbulent separated flows, and concluded that separated flows should be considered as an individual class with a characteristic Reynolds dependency described by the two-thirds power of the Reynolds number. This higher dependence of the sphere wake on the Reynolds number with increasing flow rate was shown by Kinard, Manning, and Manning (90), Keey and Glen (80),and Galloway and Sage (86), and was expressed in empirical form describing extensive data. The latter work considered effects of free-stream turbulence while the former did not.

LOCAL TRANSPORT LITERATURE:

A knowledge of the local transport from spheres significantly enhances the understanding of flow and transport dynamics associated with blunt bodies. One of the earliest analyses of local transport from spheres was the work of Frössling (6). In addition to the rather complete theoretical analysis, which was discussed earlier in Part II, as well as some experimental work involving macroscopic transport to an air stream from drops of different hydrocarbons, the local transport from a naphthalene sphere subliming into an air stream by forced convection was measured. Frössling verified experimentally the predicted Sherwood number at stagnation. Frössling's data for Reynolds numbers up to 100 show the locus of separation and the strong effect of Reynolds number upon transport in the wake.

Garner and coworkers (81, 82, 84) carried out measurements of local transport, using solid spheres of benzoic and adipic acids in a water tunnel. In addition to local material transport, Garner studies the effect of Reynolds number on the locus of separation from the aft stagnation point to a position 104° from the forward stagnation at a Reynolds number of 500. The magnitude of the Sherwood numbers reported by Garner appears to be about 40 percent higher than many other values; such behavior possibly being attributed to elevated free-stream turbulence in Garner's water tunnel. Linton and Sutherland (75) extended local material transport studies in a water tunnel up to a Reynolds number 7580, and found good agreement with the earlier work of Frössling (6). Linton (75) also indicated the possibility of effects of free-stream turbulence on material transport.

Effects of free-stream turbulence intensity on the local thermal transport were first systematically investigated with cylinders by Giedt (29) and

later by Seban (31), revealing a modest increase in thermal transfer in the forward area with small increases in free-stream turbulence. Such measurements were extended to spheres by Wadsworth (69). The latter measurements indicated the complicated behavior in the wake, and the displacement of the region of separation with increases in free-stream turbulence since the scale of turbulence was much smaller than the diameter of the sphere. Other investigators (65-68) have measured local transport employing spheres, and of these the work of Xenakis (66) is worthy of note. His work involved measurements well into the supercritical region at Reynolds numbers as high as 1.6×10^6; however, he did not treat the effects of free-stream turbulence in his measurements.

Local thermal transfer from spheres with artificially increased free-stream turbulence was studied by Venezian and coworkers (64), using a silver sphere 1.0 inch in diameter. The experimental measurements were made in a rectangular air jet 3 by 12 inches. The local heat transfer coefficient was established from the measured interfacial temperature gradient in the boundary layer normal to the surface. By use of a perforated plate, the free-stream longitudinal turbulence was varied from 0.05 to 0.15. The longitudinal turbulence without a perforated plate was measured with a Shubauer probe and found to be 0.013. Similar studies were reported by Short (62) and Brown (63) for a 0.5 inch sphere. Recently, Brown, Pitts, and Leppert (12) measured the local heat transfer coefficients from a 1.5 inch sphere in a water tunnel. They varied the Prandtl number from 2.2 to 6.8 for Reynolds numbers varying from 500 to 480,000. Their results demonstrated the marked effect of Reynolds number upon transport in the wake region, as well as the influence of variable properties of the fluid in the boundary layer.

Qualitative aspects of the flow aft of separation were illustrated by Hsu (58), who measured the time averaged, local temperature profiles with a thermocouple about a 0.5 inch silver sphere, and these results are illustrated

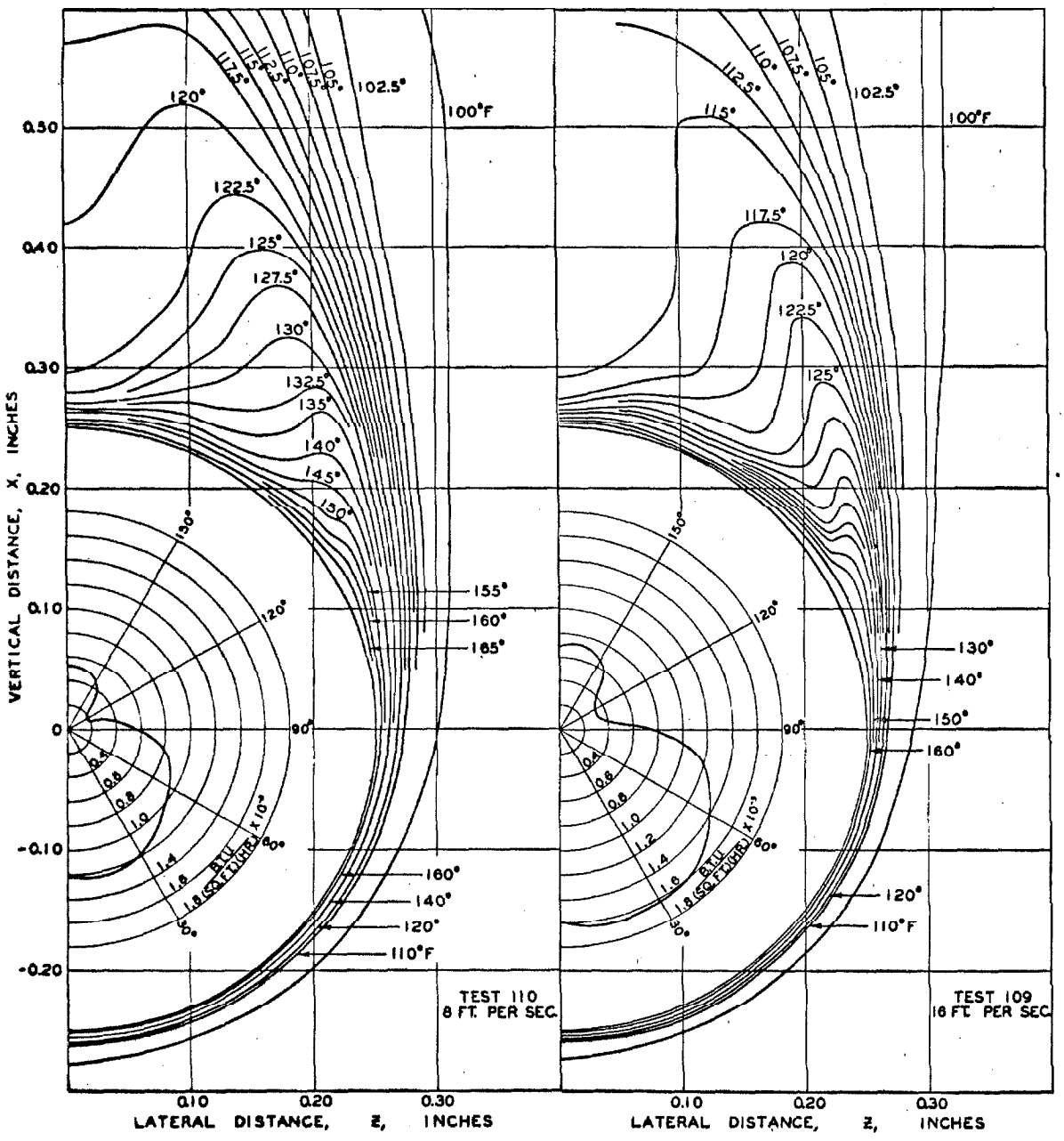

Figure 44. Local Temperature Profiles About a 0.5-inch Silver Sphere.

in Figure 44 together with the angular variation in the thermal flux. As theoretically discussed in detail in the earlier section, a separation of the thermal boundary layer results around 100° in agreement with experiment. The effect of velocity in the wake region is qualitatively shown in this two-part figure also. Torobin and Gauvin (72) and Lee and Barrow (91) have also described the qualitative aspects of wake flow aft of a sphere. Richardson (36, 37) sought to empirically describe separated flows as characterized by the Reynolds number to the two-thirds power. The determination of the quantitative effect of Reynolds number and free-stream turbulence level on the local heat and mass transfer from spheres will be the subject of the following sections.

EQUIPMENT:

The instrumented sphere was 1.4666 ± 0.0007 inches in diameter and constructed out of high purity copper. The sphere is divided into two halves as shown in Figure 45. The larger half is fixed to the stem, while the smaller half rotated The two halves are separated by a 0.0002 inch thick hard chrome plate. The rotating half is driven with a ring bevel gear by the outer sleeve with respect to the stem. The inner-most sleeve always rotates together with the outer sleeve to prevent moving the numerous electrical leads. The entire sphere can then be rotated about the stem axis by rotating all the sleeves together. The main heater is annular and is fitted about the axis of rotation of the movable sphere section. It has been designed so as to conduct equally to both halves. A small calorimeter 0.100 inches in diameter is located in the movable portion of the sphere and is equipped with a small heater. Photographs of the individual parts are given in Appendix A6.

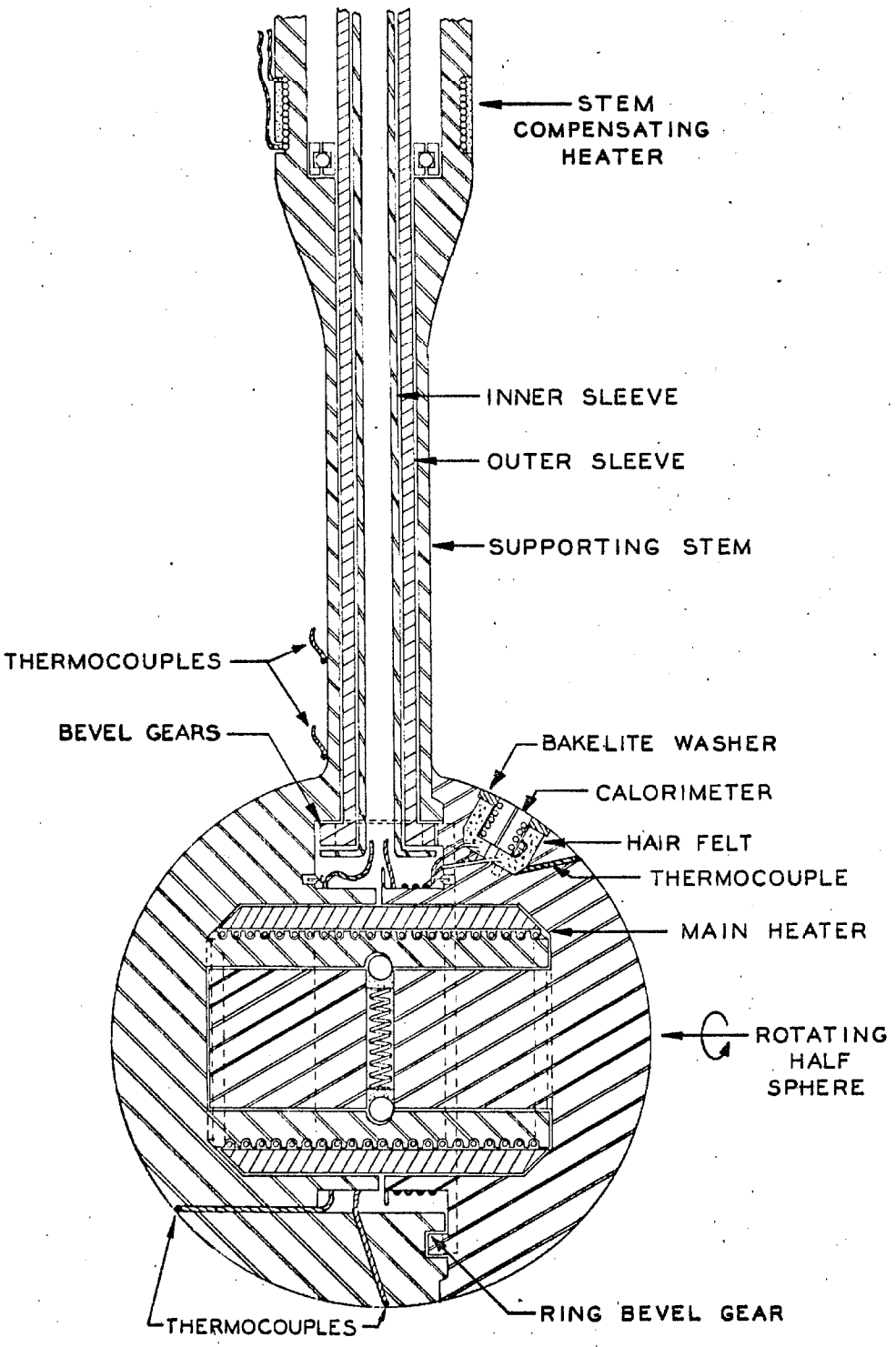

Fig. 45. Details of Instrumented Sphere

Both these heaters together with the stem heater were prepared by winding small diameter, epoxy-coated, glass insulated Advance wire into spiral grooves and sealing them in place with epoxy. The main heater and stem heater wire were number 30 gauge (B. S.), 0.010 inch in diameter, with an insulation outer diameter of 0.0142 inches and resistance of 2.989 ohms per foot. The calorimeter heater wire was number 36 gauge (B.S.), 0.005 inch in diameter, with an outer diameter at the insulation of 0.0092 inch and a resistance of 12.03 ohms per foot. The excess epoxy remaining from gluing the wires into the grooves was removed on the lathe. A copper sleeve was then shrunk fit outside these spiral grooves of the main heater and a stainless steel shield pressed on the outside of the calorimeter heater and the stem heater.

In the operation of the instrumented sphere at a particular Reynolds number current is applied to the main heater until the desired surface temperature is achieved; then the current to the stem compensating heater is adjusted to eliminate any conduction into the stem (the area of which was 1.13% that of the sphere) at the junction to the sphere. With the proper manipulation of the stem and interior sleeves the calorimeter can be positioned at almost every point on the surface. At a particular position of the calorimeter the current supplied to the calorimeter heater is adjusted so that the difference between the calorimeter surface and the main body of the sphere is reduced below 0.02° F. as a null measurement. From the calorimeter current and the average temperature driving force, the local Nusselt number was obtained directly.

The schematic of the electrical circuit employed for carrying out these precision measurements is shown in Figure 46. The circuit can be divided into three regions of operational functions as denoted by the long dotted lines.

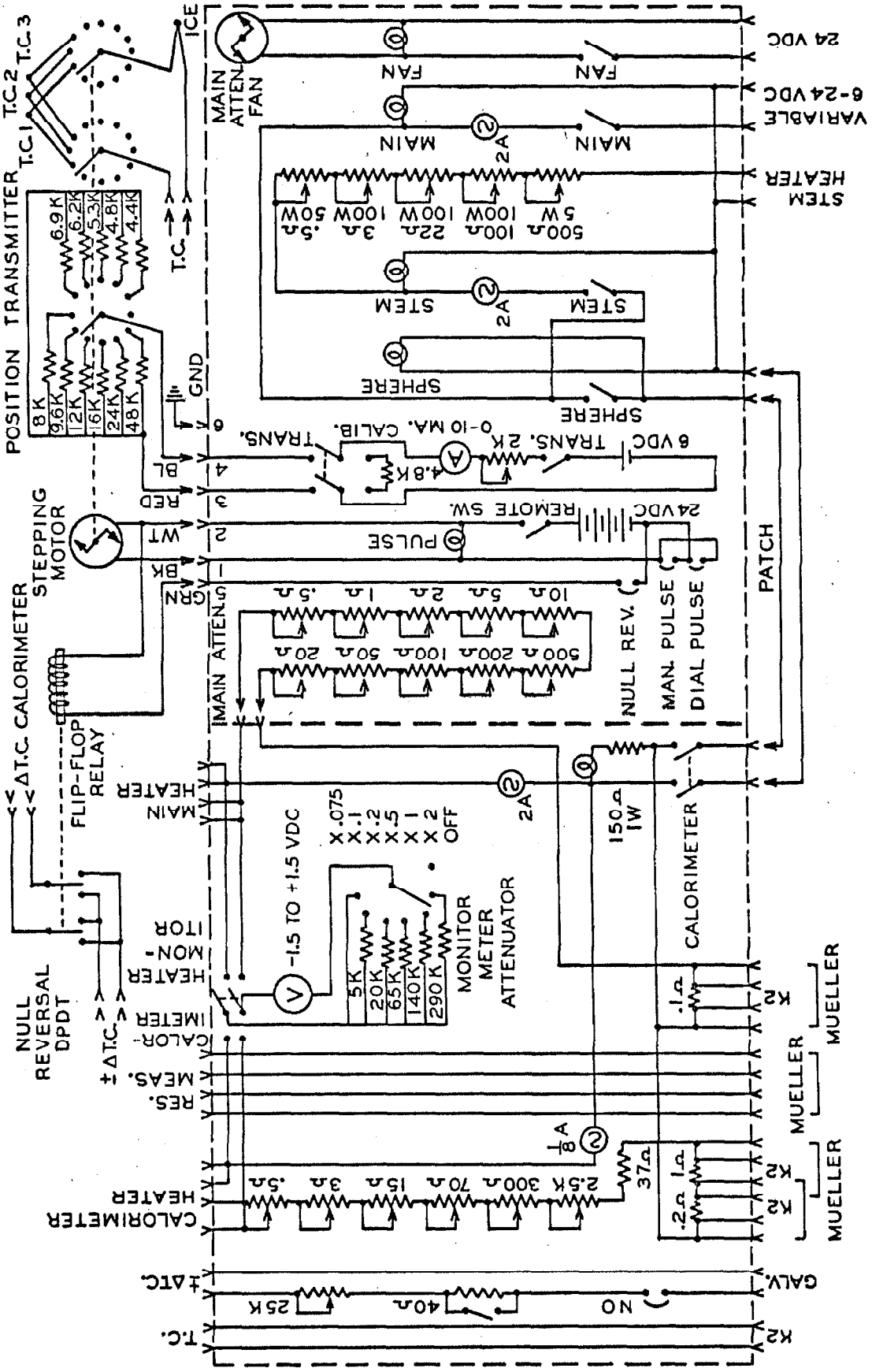

Figure 46. Schematic of Electrical Circuit.

The left hand square is the calorimeter balancing network, the right hand square is the main heater and stem heater voltage dividers and remote servo operated controls, and above the upper dotted line are the remote devices located at the test section used in the sphere measurements. In the operation of the 1.5 inch copper cylinder only the calorimeter balancing network and main heater attenuator were used, and since the measuring instruments in the laboratory housing the cylinder test section were in close proximity to the test section no remote devices were necessary.

The calorimeter balancing network consists of temperature reading connections, voltage divider and monitoring devices, reading from left to right. The output of various copper-Advance thermocouples (T.C.) is measured by a White dual potentiometer. The individual thermocouples to be read are selected by a rotary switch with silver contacts that is immersed in high thermal conductivity, multiply filtered transformer oil within a closed heavy brass cylinder. The brass cylinder is suspended within a long dewar at the end of two long concentric bakelite shafts, one of which is for support, and the other for driving the switch. This dewar is located at the test section, and the motion of the rotary switch is actuated by a stepping servo motor with position readout described later.

The differential thermocouple between the calorimeter and the main body ($\pm\Delta$T.C.) is connected to a high precision Leeds and Northrup galvanometer with a sensitivity of 50 nanovolts per millimeter at 1 meter, corresponding to a resolution on the ground glass screen of 0.001° F./mm division. Variable sensitivity (25K), critical coil damping (40Ω), and push-button operation is provided. The output of this differential thermocouple is quickly reversed by a remote flip-flop relay at the test section, located as close to the sphere as possible. The precision with which this null detection was made was very important in adjusting the current in the calorimeter. Owing to the great distance (by wire) and number of plugboards and solder joints between the test

section and measuring instruments, stray potentials and contact potentials in the plugs and solder joints in the leads were ever-present. These potentials in the leads were isolated out by reversing the output of the differential thermocouple at the source; thus, these unwanted potentials only appeared as a constant deflection in one direction (changing slowly in time). The reversible differential thermocouple output consequently appeared superimposed on top of the constant deflection, adding and then subtracting as the differential thermocouple output was reversed. These reversals had to be made quickly in order to avoid detecting the slow drifts in the constant deflection from the leads. These reversals could be made with the galvanometer connected even at full sensitivity without large transients.

The calorimeter voltage divider consisted merely of a variable resistance (38.2 to 2800 ohms) in series with the heater. These resistances consisted of high wattage Ohmite rheostats (up to 150 watts). The large contact area helped avoid contact resistance variations with current. Two standard resistors (0.2 to 1.0 ohms) were used in series in order to measure the current over the range of levels. The voltage drop across these standard resistors was measured with a Leeds and Northrup K2 potentiometer. The small size of the sphere and the required flexibility in the leads necessitated using two smaller current leads and then measuring the heater resistance as a function of temperature. The resistance measurement was made by plugging the four-wire heater leads into a Mueller bridge. The main sphere heater current is measured in this section by a series 0.1 ohm standard resistor. The main heater attenuator is not contained in this section as discussed later. Both voltages applied to the calorimeter and main sphere heater are monitored by a calibrated meter at various attenuations during start-up and for reference.

The standard resistors were carefully constructed in order to minimize the thermal effects of heavy current flow. The manganin coils were located above two parallel brass plates (1/8 x 1 x 1 inch), and the individual ends

soldered in the individual plates. These plates were separated by a thin polyethylene film (around 0.001 inch thick) to assure that both plates were at the same temperature. The double leads were then attached directly to these plates. The plates were mounted on a thin sheet of bakelite about 4 inches square and it was inturn mounted on a thick (1/4 inch) brass plate 10 inches by 6 inches for a heat sink. These standard resistors were located within this calorimeter balancing network section. The calibration of these standard resistors was checked by voltage drop measurements and found to be very nearly independent of the current level.

The next section (dotted square on the right) of Figure 46 contained the main sphere heater attenuators. This variable resistance (0.1 to 888.6 ohms) was constructed from Manganin wire of varying diameters formed in coils, and each of the coils were suspended in a high velocity constant temperature air stream supplied by a D.C. motor-driven fan with low electrical noise. The fan was arranged so as to suck the air through the resistors to avoid any thermal convection currents from the D.C. motor itself. Each of the coils were tapped in positions, 30 in number. Ten heavy, leaf-type rotary switches with 28 positions were used to select the tap location. Each of the switches was mounted in heavy blocks to insure that all taps were at the same temperature. Ball bearing detents were constructed to center each of the leaf-assemblies accurately over the heavy silver contacts.

The differential thermocouple d.p.d.t. reversing switch was constructed out of gold plated silver contacts and driven by the flip-flop relay. This type of actuation was preferred since only a brief pulse of low current was transmitted in the laboratory (by shielded cable isolated far from the instrument leads) and did not remain on for a length of time sufficient to create heating effects near the thermocouple leads. At no time were there any effects of these current pulses detected on the differential thermocouple galvanometer held on highest sensitivity. The reversal was actuated by a push-button located at the instruments and could be carried out extremely rapidly.

The next portion of the circuit shown in Figure 46 moving to the right in this section consisted of means to generate the pulses that were used to operate the remote thermocouple selector switch. Again it was felt that short pulses would create less interference with precision measurements than would constant currents with their associated heating effects. The stepping servo motor consisted of a Ledex rotary solenoid-operated ratchet which actuated stepwise both the position transmitter and the silver contact, selector switch. The position transmitter consisted of a set of individual resistors which were individually switched in series with an ammeter and battery. The ammeter indicated directly the number of the thermocouple being read. To check against voltage drifts in the battery a standard resistor could be switched in and the meter recalibrated using a series 2K potentiometer. A fixed scale was attached to the rotary switch in order to indicate the position as a check against mechanical failures. The pulses were generated by two means. Single pulses could be sent by a normal pushbutton, or the actual thermocouple could be selected by a telephone dial which was modified to send a number of position-going pulses corresponding to the number indicated by the position transmitter.

The rest of the circuit consisted of indicating lights, power switches, and protective fuses, as well as the sphere stem compensating heater attenuator. The current in the stem heater was adjusted until the lower portion of the stem was at a temperature equal to that of the copper sphere. This voltage divider consisted of a variable resistance from 0.5 to 625.5 ohms made of high wattage Ohmite potentiometers for current stability. The entire installation of the instruments is shown in the photograph of Figure 47. The plugboards off to the left of the photograph were used to plug in the various measuring instruments and made connections to the test section. The slots below the plugboard contained the ground glass screens upon which were projected the images from numerous galvanometers that were used. The first instrument on the left is the calorimeter balancing network and on its right the main heater and associated

balancing network, and auxilary circuits. The physical layout of the controls is well represented in the schematic diagram of Figure 46.

These circuits were used to adjust the current supplied to the calorimeter, main heater, and stem compensating heater. From these currents and heater resistances the total heat could be computed. Any residual thermal losses such as conduction or radiation were measured as a function of driving force and polar angle at no flow and subtracted off directly as a heat flux. The validity of this procedure has been analyzed in detail in the theoretical discussion. Owing to the greater precision of the average transfer obtained from the main heater, the calorimeter heat flux was determined with respect to the average heat flux, which was then expressed as the ratio of the local Nusselt number to the average. This tended to compensate for any systematic errors in local measurements. Also in the calorimeter well passing through the bakelite disk was a very small pitot tube for measuring the local pressure In operation, however, it was plugged with stoppages in the small lines.

The 1.5 inch instrumented sphere is installed immediately above a 6 by 6 inch square jet with the forward stagnation point level with the top edge of the jet as shown in Figure 48. The square 6 x 6 inch duct is 20 inches long and can be fitted with a punched hole turbulence grid with 7/8 inch holes set in a square array on 1 inch centers, patterned after Davis (40,41). This grid, shown in Figure 49, can be raised and lowered within this duct to achieve various artificially generated turbulence levels at positions corresponding to the forward stagnation point of the sphere. In this way the turbulence level could be varied from 0.038 to 0.25, with the turbulence level of the free stream about 0.013 (92). The converging section had a constraction ratio of 4. Upstream of the entrance to the column was an eight foot, twelve inch square, vertical damping section equipped with sets of one-quarter inch mesh damping screens. The superficial mass flow rate was measured by Hershel-type venturi meters and the air temperature was controlled to $100.0 \pm 0.1°$ F. with platinum resistance

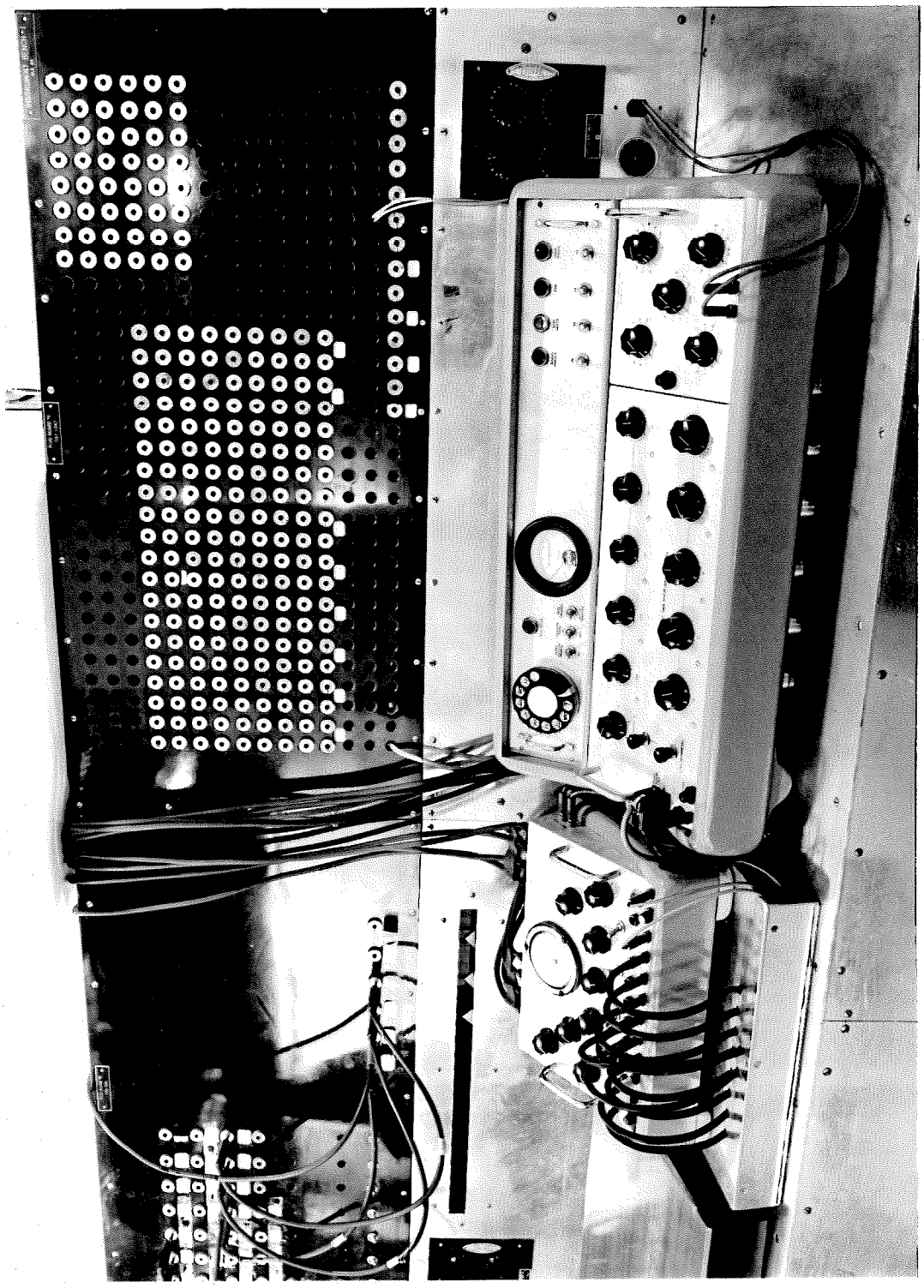

Figure 47. Photograph of Sphere Calorimeter and Main Heater Balancing Networks.

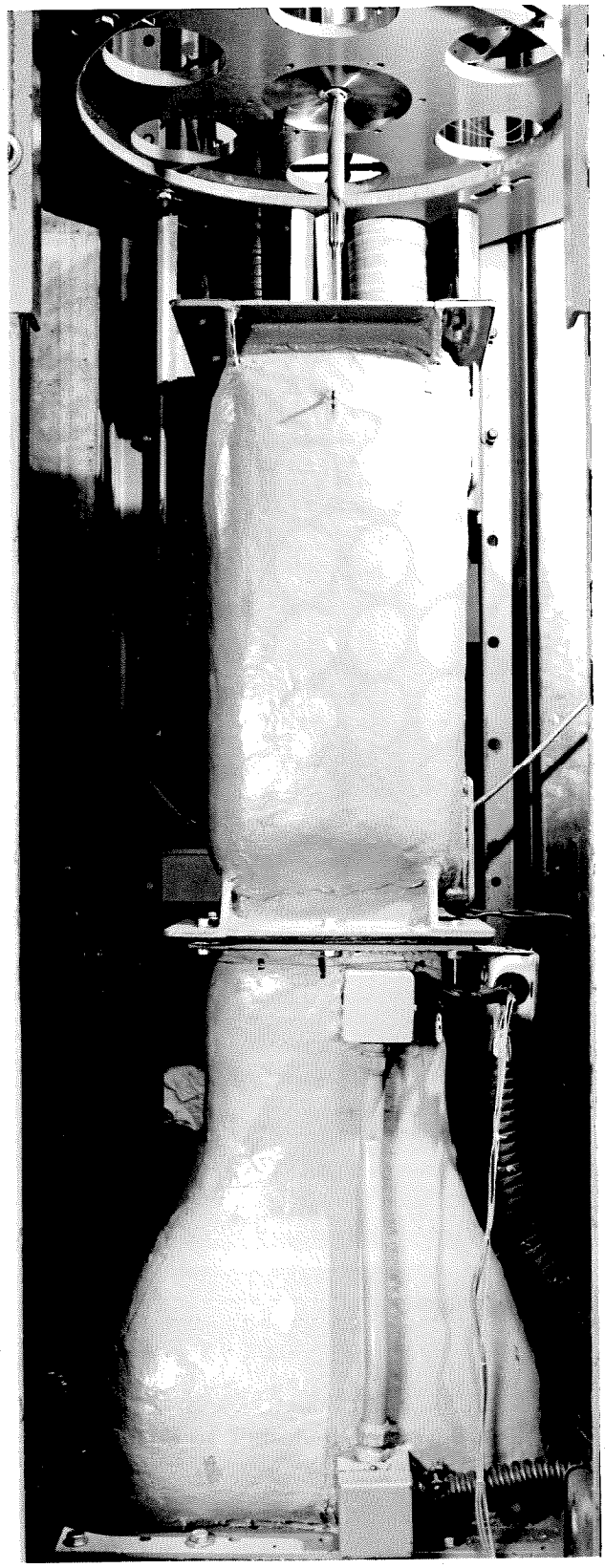

Figure 48. Photograph of Sphere Suspende in the 6 x 6 Jet.

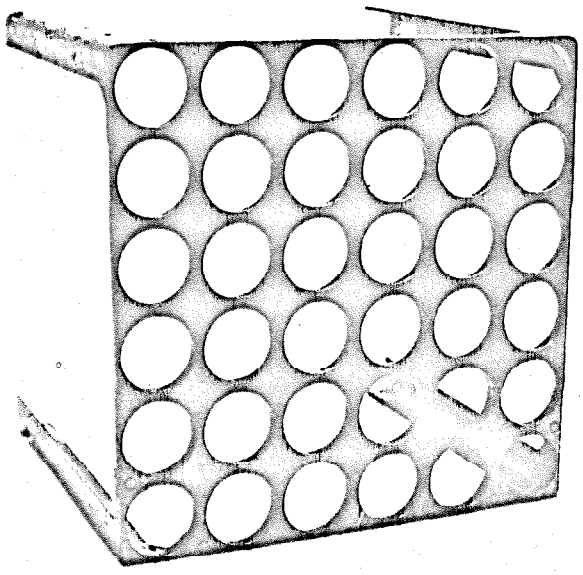

Figure 49. Photograph of Punched Plate, 6 x 6 inch Turbulence Grid.

thermometers. The air was supplied by two 2000 cfm centrifugal, squirrel cage blowers arranged in series, the rate of rotation of which was controlled by comparison with a 100 KHZ quartz crystal oscillator frequency standard, which maintained a constant mass flow rate within 0.2%. The velocity measurements in the working section of the jet were made with a pitot tube in conjunction with a production prototype of a model of a eight-inch silicon oil micromanometer (93) shown as Figure 3 in Appendix A6 and with a six-inch Kerosine micromanometer instrument, shown in Figure 4 in Appendix A6, which is currently under developmental study.

ANALYSIS

Theoretical analysis presented earlier has shown the importance of the dimensionless ratio termed the "Frössling group",

$$Fs = \frac{Nu - 2}{Re^{1/2} Pr^{1/3}} \tag{122}$$

for thermal transport and

$$Fs = \frac{Sh - 2}{Re^{1/2} Sc^{1/3}} \tag{123}$$

for mass transport. The entire temperature field, as was illustrated in Figure 44, is basic to thermal transport. The temperature gradient at the surface of the sphere is the quantity which is responsible for thermal transport and the heat transfer coefficient is merely a useful phenomenalogical concept which has been extremely useful in expressing both theoretical and experi-

mental results. The thermal boundary layer thickness also reflects the shape of the temperature field near the surface and can be thought of as a region possessing resistance to thermal transfer. Typical variation in thermal boundary thickness with angle from the forward stagnation point has been presented in Figure 50 for two widely different velocities, that of Bathish (94) for Re=4000 and of Wadsworth (69) for Re=240,000. Lower values of the thickness reflect large heat transfer coefficients and hence larger Nusselt numbers. Figure 50 also shows the first order result that heat transfer increases with increasing Reynolds number and decreases away from the forward stagnation point, achieving a minimum near 100°, corresponding to separation. Small increases at stagnation represent a possible anomaly as discussed for the cylinder. Following separation thethickness is difficult to define; however, Wadsworth (69) noted that for certain conditions the boundary layer thickness reattaches to the surface and decreases local heat transfer in the wake region. The thermal thickness involves a knowledge of the entire temperature field and is exceedingly difficult to establish experimentally.

The measured variation of the Frössling number with polar angle is feasible experimentally and is illustrated in Figure 51 for a number of other investigators (62-64, 66, 69) for longitudinal turbulence levels below 0.05. A more complicated behavior in the wake at Reynolds numbers above 2×10^5 is characteristic of nearly all measurements. Transition to supercritical flow alters the flow in the wake, which is qualitatively indicated in Figure 51.

The earlier experimental data for local transfer (62-64), corrected for radiant transport, were subjected to an integral restraint applied graphically to insure consistency with the measured macroscopic transport. The macroscopic measurements involving the direct determination of the total transport under the same conditions of flow were of greater precision and accuracy than the local values. The local values of Nusselt number were constrained in the graphical analysis to satisfy the following integral expression involving

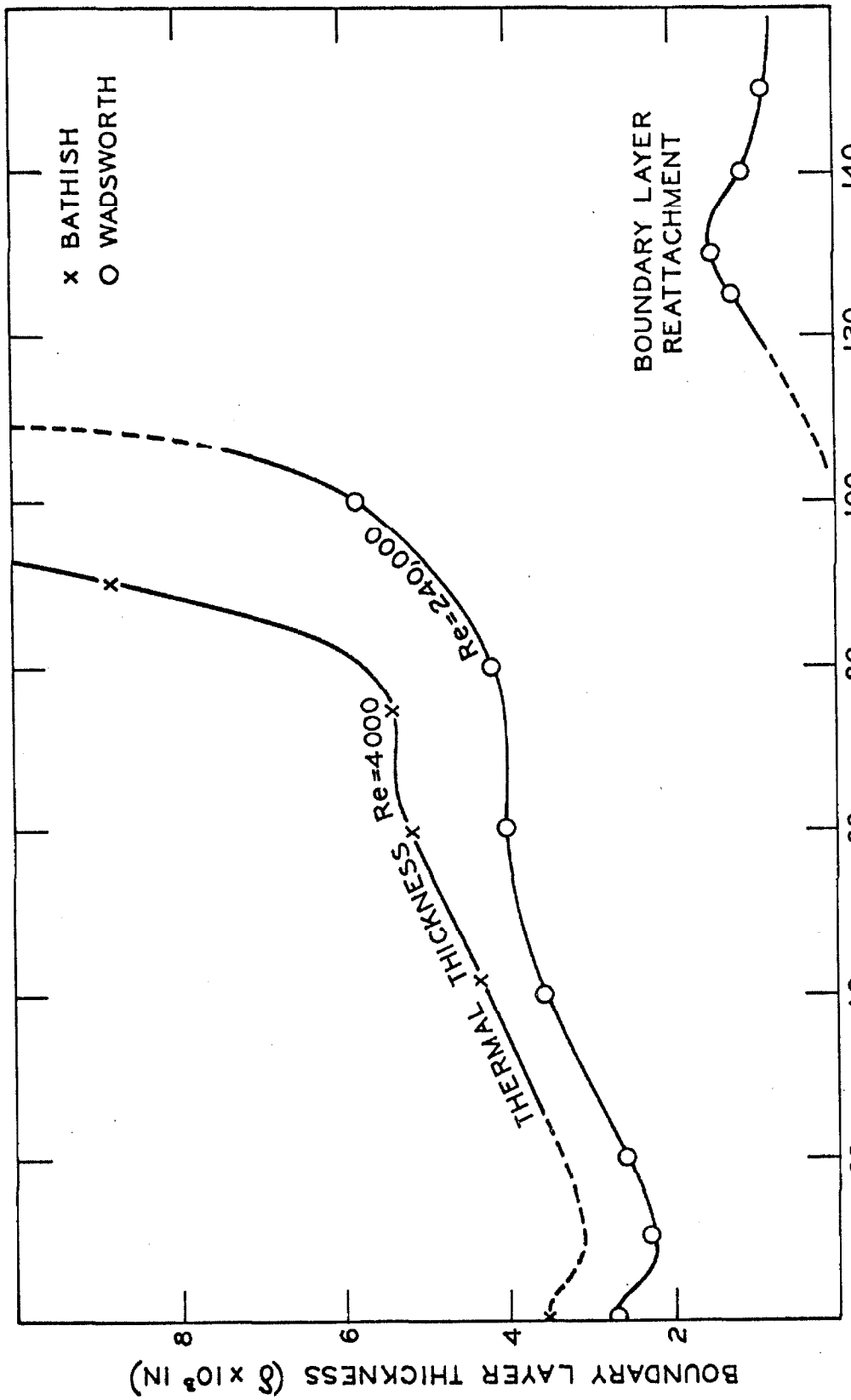

Figure 50. Angular Variation of the Thermal Boundary Layer Thickness.

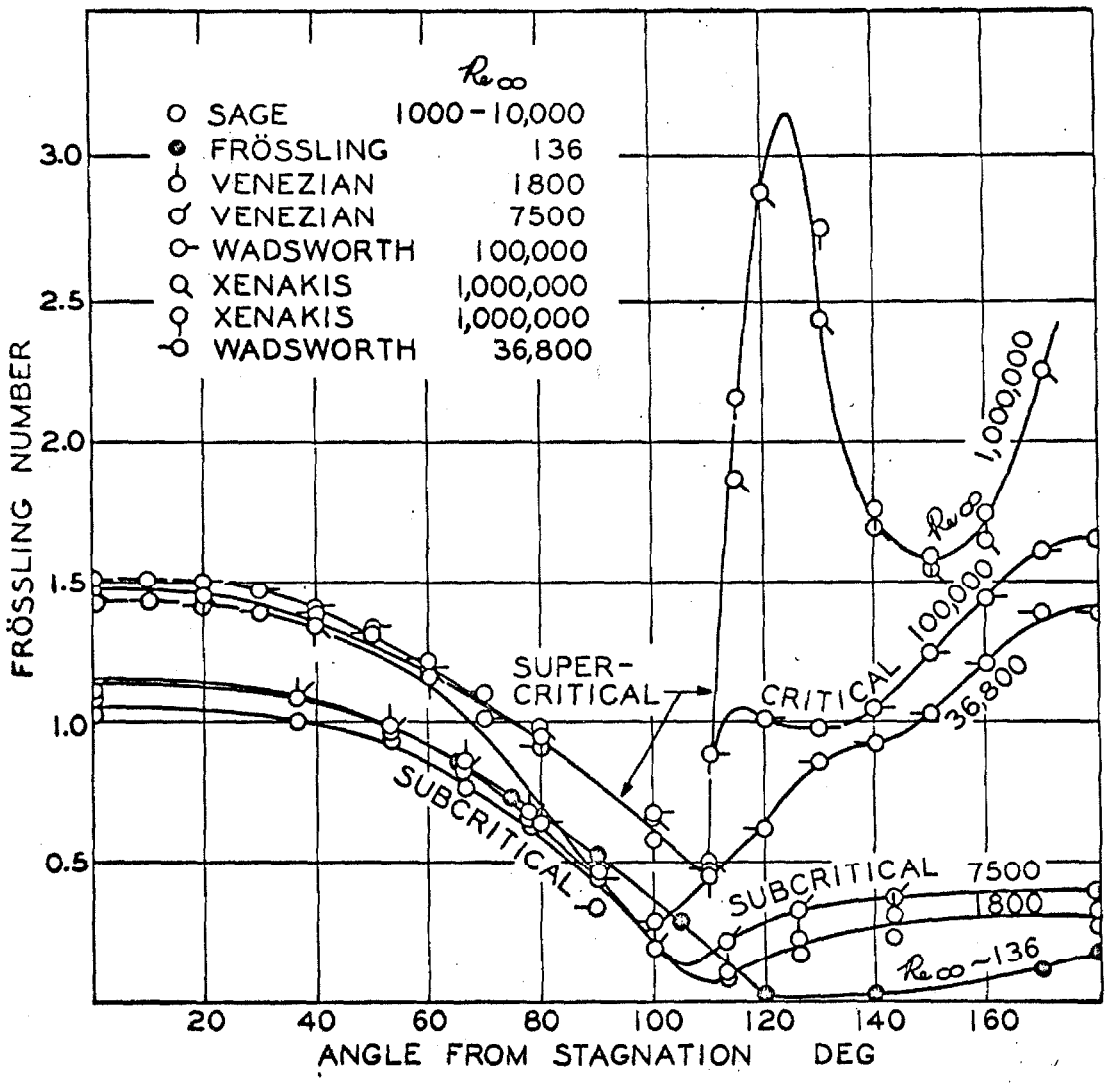

Fig. 51. Effect of polar angle upon local Frössling number.

the macroscopic data:

$$\int_0^{180°} \left(\frac{Nu}{Nu^*}\right) \sin\psi d\psi = 2 \tag{124}$$

Transport rates at even values of the cosine of the polar angle were determined. The detailed local results together with the integral macroscopic values, as well as the average and standard deviations of the experimental data (62-64) from the smoothed curves, are presented in Tables 8-10 for the 0.5 inch porous sphere and the 0.5 inch and 1.0 inch silver spheres.

At levels of turbulence below 0.02, the following empirical relation (82) has been used in the past to approximate the behavior for local thermal transfer:

$$Nu = 2 + C(\psi) Re^m Pr^{1/3} \tag{125}$$

The coefficient "C" and the exponent "m" are functions of polar angle, ψ. To illustrate the inadequacies of Equation 125, the variation of the empirical exponent "m" with polar angle is shown in Figure 52. Furthermore, in the region of separation this exponent depends upon the Reynolds number.

The effects of free-stream turbulence are of importance. The earlier experimental data for spheres (62-64) indicate an influence of turbulence similar to that obtained for cylinders by Giedt (28), Seban (31), and that presented earlier for the 1.5 inch instrumented cylinder of the author. There has been some uncertainty in establishing quantitatively the turbulence level associated with the rectangular 3 by 12 inch punched plate grid patterned by Davis (40,41) which was used in the earlier work (62-64). The authors (62-64) previously chose to indicate this uncertainty in referring to the turbulence level as "apparent" level of longitudinal turbulence. In this work a larger

TABLE 8 Experimental results for 0.5 inch porous sphere

Polar angle Deg	Cos ψ	Test number 165,291	121	290	107	108	98	99	101	100
Turbulence level, α_t		0.013	0.013	0.013	0.056	0.052	0.094	0.088	0.148	0.135
Reynolds number, Re_∞		891	1809	3613	1811	3649	1815	3642	1808	3671
Macroscopic Nusselt number, Nu^*_∞		16.36	25.67	32.75	24.35	35.56	24.68	36.94	31.34	43.06
0	1.0	32.43	52.13	60.99	45.05	67.06	48.27	70.83	59.95	80.61
36.87	0.8	31.62	50.64	59.81	44.72	66.20	47.80	68.54	58.01	76.27
53.13	0.6	28.84	46.65	54.13	41.76	61.32	43.71	61.47	53.34	69.51
66.42	0.4	23.94	38.65	46.02	35.79	51.32	35.24	50.64	44.54	58.94
78.46	0.2	18.03	30.10	36.69	26.84	38.76	26.43	38.26	34.47	47.31
90.00	0.0	11.75	21.04	26.25	17.69	26.75	18.09	27.31	24.54	34.52
101.54	-0.2	6.06	12.88	16.07	10.12	15.55	10.86	16.99	15.26	21.78
113.58	-0.4	6.06	8.53	12.10	6.35	13.45	6.61	12.59	9.40	14.91
126.87	-0.6	8.74	10.49	16.52	11.68	18.77	11.27	20.25	14.10	22.83
143.13	-0.8	9.17	12.90	17.97	15.64	21.32	14.39	23.01	17.88	26.11
180.00	-1.0	9.23	14.44	18.56	17.10	22.03	15.37	24.08	18.26	26.93
$\int (Nu_\infty / Nu^*_\infty) \sin\psi \, d\psi$		2.002	2.001	2.000	1.996	1.999	1.999	1.998	1.999	2.006
Average deviation[a]		-0.030	-0.003	0.031	-0.049	-0.030	0.042	-0.057	0.074	-0.080
Standard deviation[b]		0.120	0.060	0.151	0.059	0.039	0.149	0.083	0.134	0.140
Weighting factor[c]		0.083	0.167	0.066	0.170	0.112	0.067	0.121	0.075	0.071

[a] Average deviation defined by

$$s = \frac{\sum_1^{N_p} (Nu_{\infty,e} - Nu_{\infty,c}) / Nu_{\infty,e}}{N_p}$$

[b] Standard deviation defined by

$$\sigma = \left[\frac{\sum_1^{N_p} [(Nu_{\infty,e} - Nu_{\infty,c}) / Nu_{\infty,e}]^2}{N_p - 5} \right]^{1/2}$$

[c] Normalized weighting factor used in regression analysis only, and defined by

$$w = 1/(100\,\sigma)$$

TABLE 9 Experimental results for 0.5 inch silver sphere

Polar angle Deg	Cos ψ	Test number 161	160	92	110	109	89	90	93	91
Turbulence level, α_t		0.013	0.013	0.146	0.054	0.051	0.094	0.088	0.146	0.135
Reynolds number, Re_∞		909	3643	1807	1806	3638	1808	3640	1808	3641
Macroscopic Nusselt number, Nu^*_∞		18.18	35.55	27.56	25.86	36.15	26.34	37.62	27.55	41.13
0	1.0	32.22	67.48	52.44	47.07	65.67	49.80	68.69	66.69	74.37
36.87	0.8	31.19	67.24	51.08	45.97	65.78	49.29	66.13	51.33	72.11
53.13	0.6	29.52	61.35	46.23	43.12	62.24	45.01	59.04	47.83	65.11
66.42	0.4	24.78	51.16	39.24	36.54	53.41	37.94	50.37	41.54	55.03
78.46	0.2	19.93	39.38	31.93	28.78	42.06	29.77	40.15	33.17	43.79
90.00	0.0	14.59	25.61	23.49	21.16	29.91	20.88	29.84	22.34	32.07
101.54	-0.2	9.19	12.29	14.18	13.54	15.66	11.94	18.36	9.71	20.91
113.58	-0.4	6.57	8.75	8.08	9.32	9.68	8.28	13.25	6.97	16.34
126.87	-0.6	9.62	13.67	12.14	12.64	14.06	12.21	19.67	12.21	23.60
143.13	-0.8	12.25	17.58	16.91	14.73	20.55	14.98	24.81	18.15	29.35
180.00	-1.0	13.38	18.92	18.29	14.98	24.45	15.87	25.89	21.57	30.49
$\int (Nu_\infty / Nu^*_\infty) \sin\psi \, d\psi$		1.98	2.004	1.997	2.001	1.98	2.002	1.998	2.032	1.999
Average deviation[a]		-0.011	0.030	-0.0047	0.006	-0.008	-0.035	-0.084	0.043	-0.131
Standard deviation[b]		0.294	0.061	0.045	0.062	0.038	0.065	0.143	0.077	0.201
Weighting factor[c]		0.034	0.164	0.223	0.161	0.263	0.154	0.070	0.130	0.050

[a] Average deviation defined by

$$s = \frac{\sum_1^{N_\psi} (Nu_{\infty,e} - Nu_{\infty,c}) / Nu_{\infty,e}}{N_\psi}$$

[b] Standard deviation defined by

$$\sigma = \left[\frac{\sum_1^{N_\psi} [(Nu_{\infty,e} - Nu_{\infty,c}) / Nu_{\infty,e}]^2}{N_\psi - 5} \right]^{1/2}$$

[c] Normalized weighting factor used in regression analysis only, and defined by

$$w = 1/(100\,\sigma)$$

TABLE 10 Experimental results for a 1.0 inch silver sphere

Polar angle Deg	Cos ψ	Test number 176A,177	176B	174,175	185	186	183	184	182	181	179	180	178
Turbulence level, a_t		0.013	0.013	0.013	0.051	0.054	0.067	0.064	0.091	0.086	0.143	0.132	0.151
Reynolds number, Re_∞		1880	3730	7500	7480	3715	3740	7530	3720	7430	3720	7490	1880
Macroscopic Nusselt number, Nu^*_∞		24.1	34.2	48.6	51.1	35.4	34.9	52.5	36.2	52.7	41.9	63.8	27.3
0	1.0	43.92	65.15	87.99	97.18	67.62	67.75	100.53	68.18	105.02	78.69	121.14	50.44
36.87	0.8	43.88	63.81	86.19	95.64	65.54	67.12	96.75	67.17	103.97	76.56	115.08	50.79
53.13	0.6	40.40	58.02	78.04	88.49	59.87	61.05	87.29	62.57	94.53	70.31	102.96	47.83
66.42	0.4	35.59	48.74	66.68	76.41	50.61	50.36	74.27	53.33	77.82	59.80	87.95	41.52
78.46	0.2	28.90	37.78	52.84	58.51	39.96	37.64	57.83	39.96	59.21	46.68	71.16	33.07
90.00	0.0	19.92	26.14	35.36	37.65	28.89	25.38	40.60	26.19	40.44	32.81	52.08	23.74
101.54	-0.2	9.91	15.17	18.40	42.65	17.22	14.07	25.27	14.57	21.87	19.95	32.36	12.45
113.58	-0.4	6.26	12.26	19.42	14.83	14.15	12.86	19.07	11.41	15.45	14.37	22.21	6.92
126.87	-0.6	11.03	16.92	27.53	23.16	16.83	16.87	26.89	16.59	21.24	21.50	32.74	10.03
143.13	-0.8	13.79	20.28	31.08	29.00	17.97	19.14	31.52	20.58	25.94	25.85	42.38	13.25
180.00	-1.0	14.51	21.10	31.71	30.33	18.14	20.05	32.19	21.88	27.73	27.15	46.21	14.18
$\int (Nu_\infty / Nu^*_\infty) \sin\psi \, d\psi$		1.997	1.998	1.997	1.995	1.998	1.998	2.002	1.997	2.004	2.010	2.003	1.998
Average deviation[a]		-0.067	-0.014	0.0027	-0.033	0.003	-0.002	0.005	-0.0007	0.032	0.051	0.0067	-0.012
Standard deviation[b]		0.078	0.036	0.089	0.085	0.063	0.017	0.080	0.012	0.162	0.169	0.097	0.052
Weighting factor[c]		0.129	0.278	0.112	0.118	0.159	0.589	0.126	0.834	0.062	0.059	0.103	0.192

[a] Average deviation defined by

$$s = \frac{\sum_1^{N_p} (Nu_{\infty,e} - Nu_{\infty,c}) / Nu_{\infty,e}}{N_p}$$

[b] Standard deviation defined by

$$\sigma = \left[\frac{\sum_1^{N_p} [(Nu_{\infty,e} - Nu_{\infty,c}) / Nu_{\infty,c}]^2}{N_p - 5} \right]^{1/2}$$

[c] Normalized weighting factor used in regression analysis only, and defined by

$$w = 1/(100\,\sigma)$$

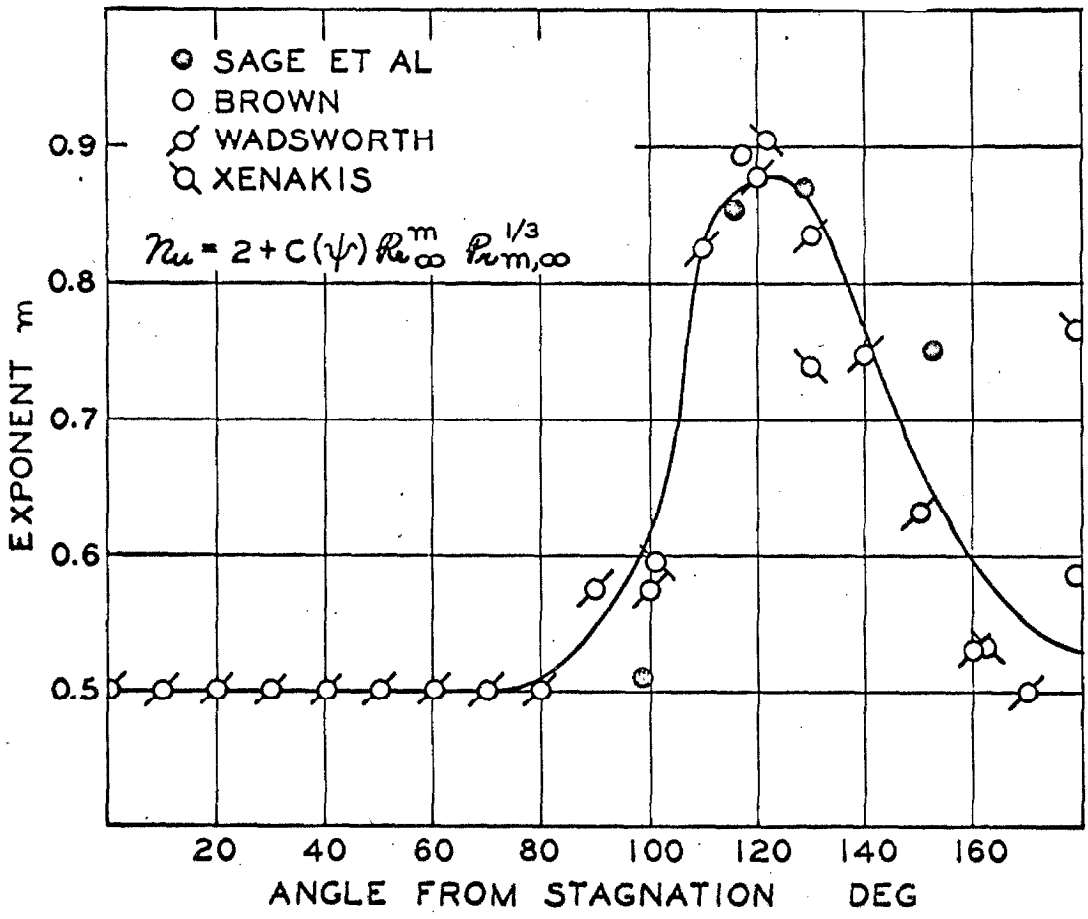

Fig. 52. Variation of exponent of Equation 125 with Polar Angle.

grid, 6 inches across was used which is more nearly comparable to that of Davis (40,41) and is amenable to analysis by recent techniques (39, 95-101). Couch (42) has made a careful analysis of the available data and current theoretical techniques for the prediction of the decay of turbulence behind punched plate grids, and his results have been used in this work for the 6 by 6 inch grid. The longitudinal level of free stream turbulence is shown for this grid as a function of the distance downstream in Figure 53. The turbulence is essentially isotropic except for close proximity to the grid, such as within 5 inches. The corresponding integral turbulence scale is shown in Figure 54.

Regression analysis of the data presented in Tables 8-10 has indicated that in the region of the forward stagnation point the Frössling number is linearly proportional to the square root of the Reynolds number as shown in Figure 55. The kinematic viscosity ratio has been used here as suggested by the earlier theoretical discussion for the variation of molecular properties through the boundary layer. A cross plot of these results with the "apparent" turbulence level is given in Figure 56. The standard errors of estimate in the Frössling number for the experimental data (62-64) used to establish the full curves of both these figures has been shown in both. Differences between the 0.5 inch porous sphere and the 0.5 inch and 1.0 inch spheres are not statistically significant in these figures. Within the uncertainty of measurement, the Frössling number can be expressed as linear with the square root of the Reynolds number and as a second order polynomial with the "apparent" longitudinal turbulence level, α_t, as follows for the forward hemisphere:

$$Fs = A\left(\frac{\nu_\infty}{\nu_o}\right)^{0.16} + B\alpha_t(\alpha_t + C)Re^{1/2} \qquad (126)$$

A comparison of this "apparent longitudinal level " with that quoted by Hsu (102) and Short (62) which was based on measurements of Davis (40,41)

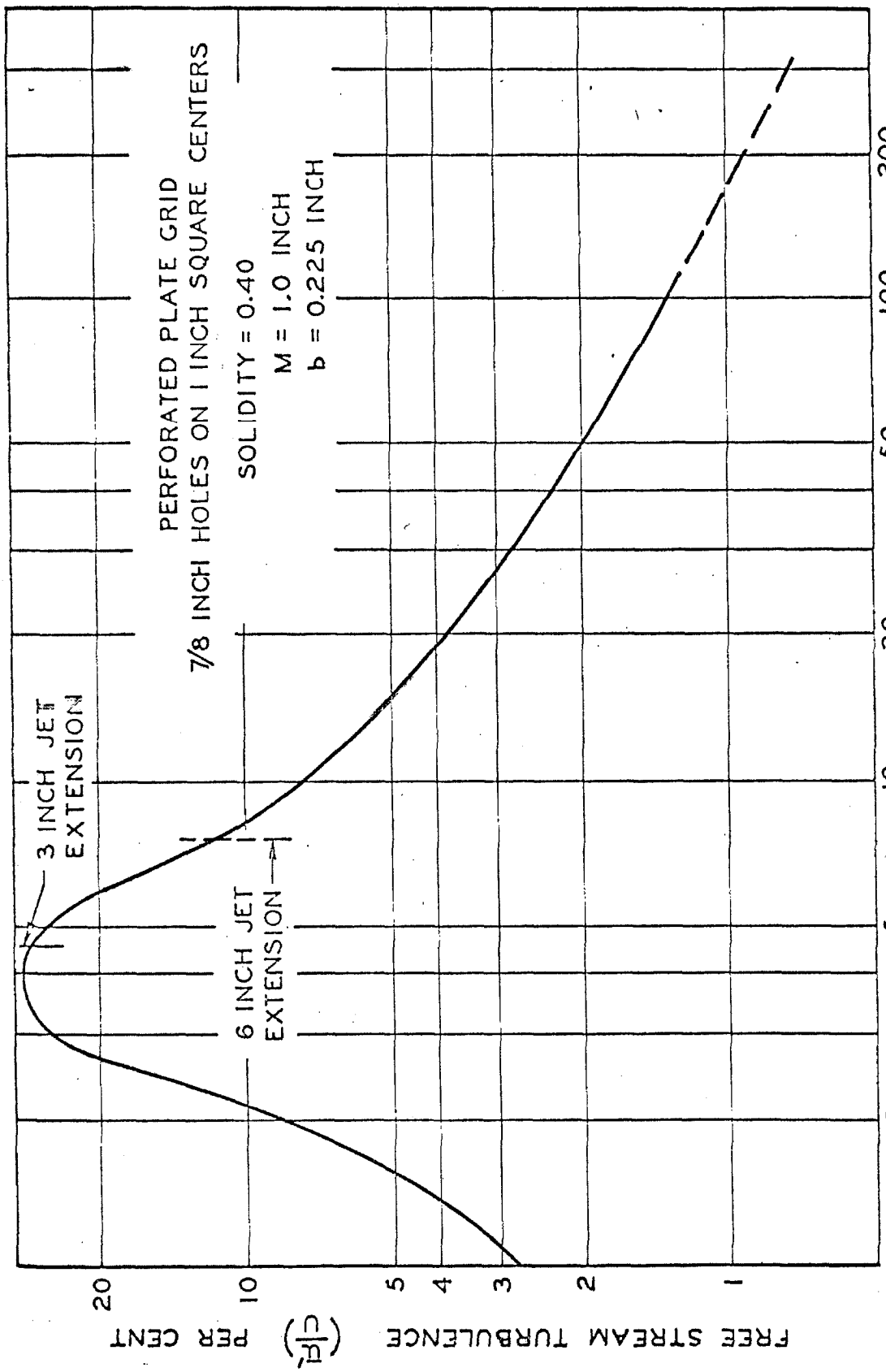

Figure 53. Longitudinal Level of Turbulence Downstream of the Perforated Grid.

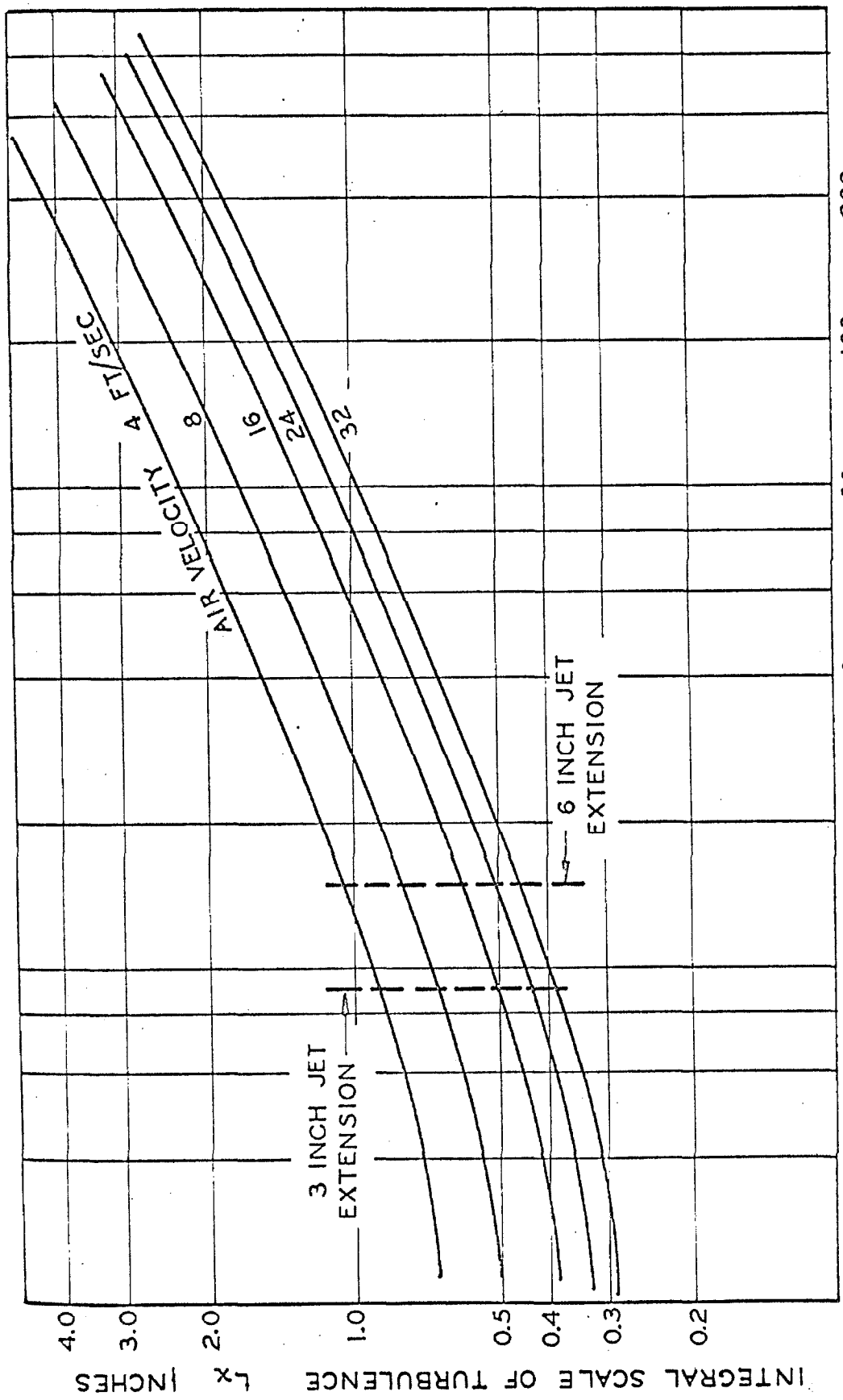

Figure 54. Integral Scale of Turbulence Downstream of the Perforated Grid.

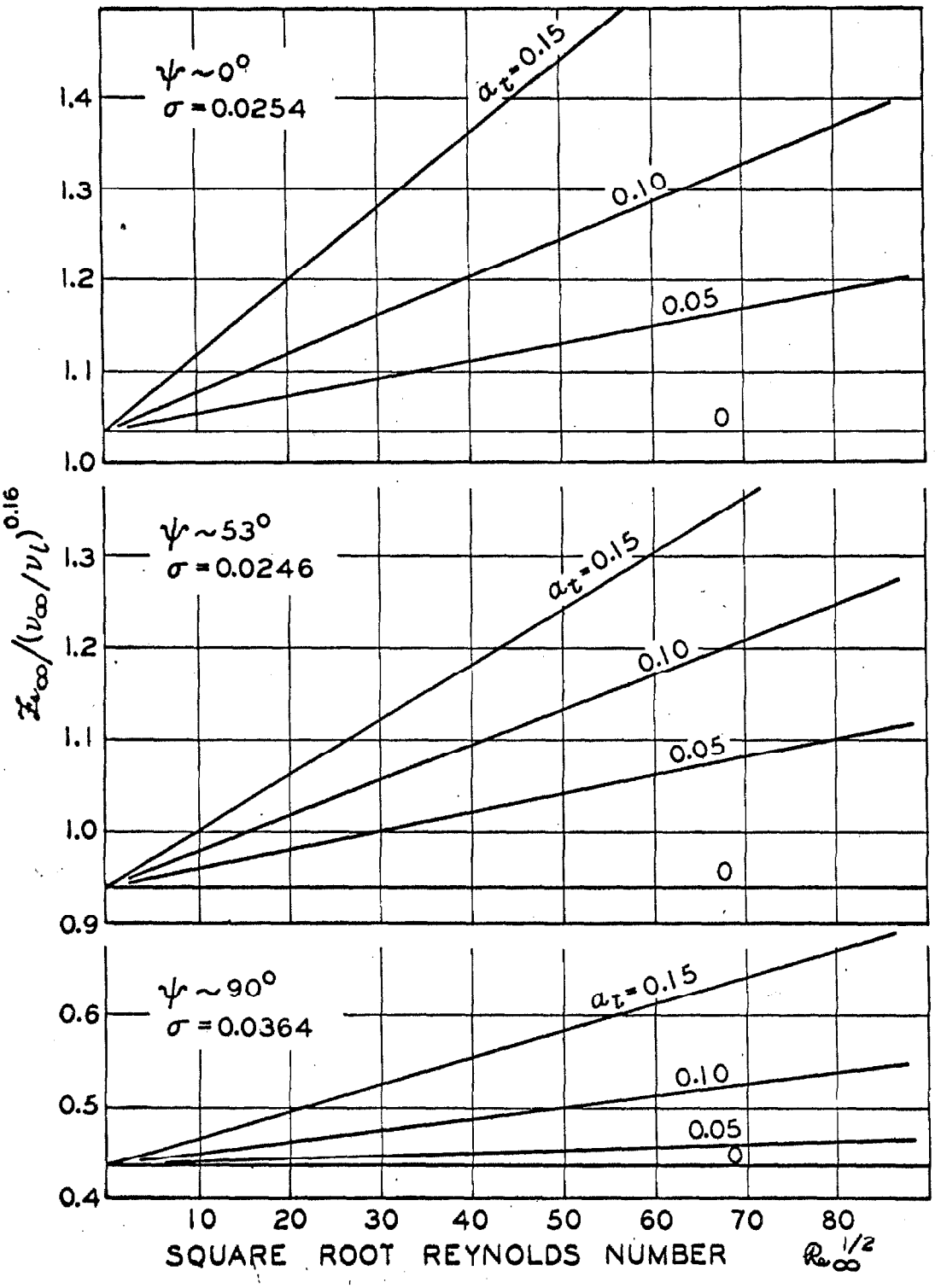

Fig. 55. Variation of local Frössling number with Reynolds number.

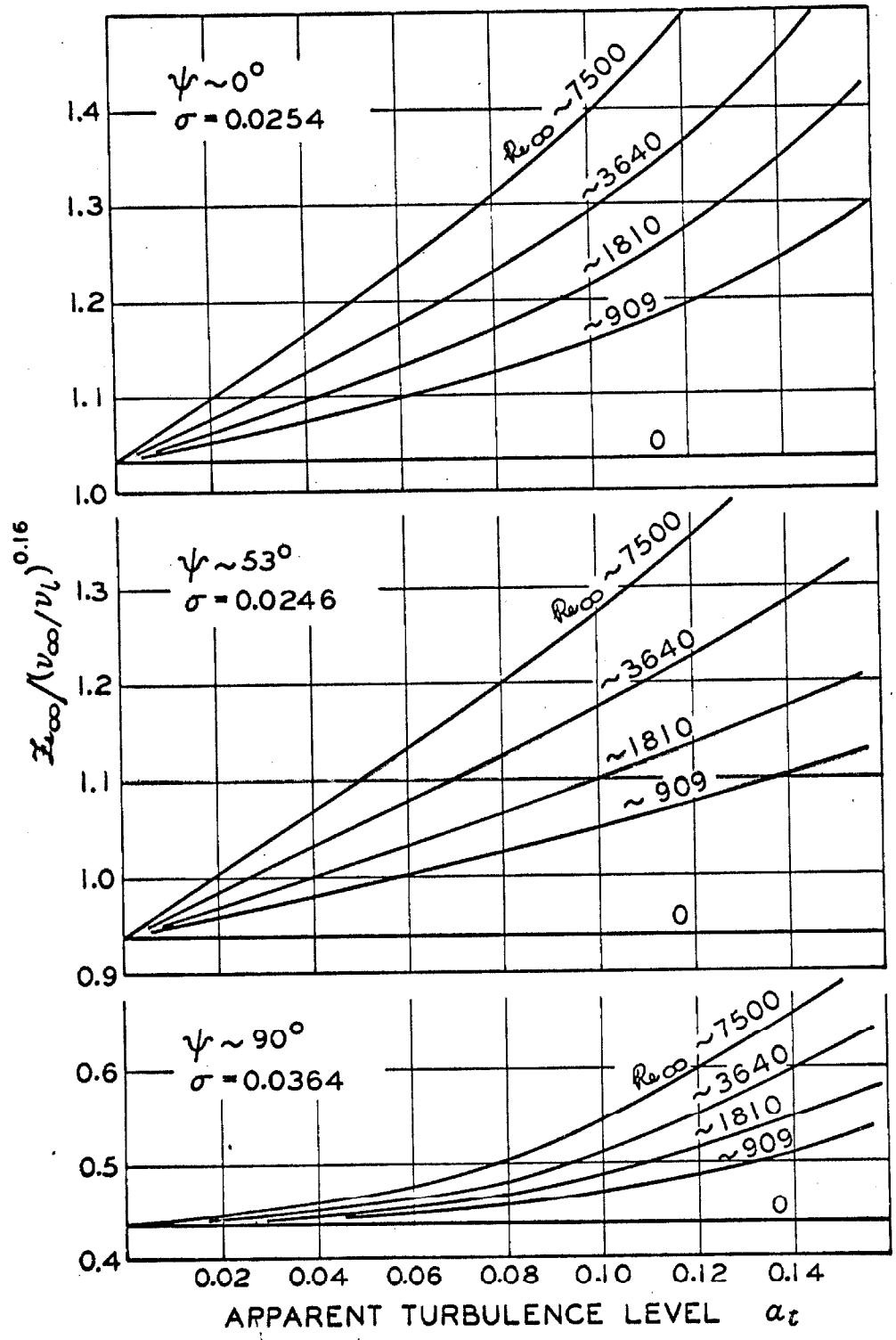

Fig. 56. Effect of level of turbulence upon local Frössling number.

indicates substantial agreement with Figure 53 for downstream distances in excess of 8 inches. Only for the shorter distances is the "apparent" value low, and furthermore this is a region where anisotropy is prevalent.

In the region of separated flow, which is encountered primarily in the aft hemisphere, the nature of the transport is different from that in the forward hemisphere. Figure 57 shows results in the aft hemisphere for thermal transport obtained from 0.5 inch and 1.0 inch silver spheres (62, 64) and thermal with simultaneous material transport from a 0.5 inch porous sphere (63). In the turbulent, separated wake no large effect from the level of turbulence was observed. From this separated flow data (62-64) and that of Wadsworth (69) and Xenakis (66), the following relation is suggested:

$$Fs = A\left(\frac{\nu_\infty}{\nu_o}\right)^{0.16} + DRe^{1/2} \qquad (127)$$

The earlier data for local transport (62-64), together with those available from others (6, 12, 66, 69, 75, 82), are shown for thermal and for material transport with the level of turbulence as a parameter in Figures 58 and 59 for selected angles. The behavior exhibited for the numerous angles in the vicinity of those which are shown in these figures is well typified by the selected angles in Figures 58 and 59. The range of conditions of the experimental data used in the regression analysis has been indicated in Table 11. The molecular transport properties developed in Part I of this thesis were necessary for analysis of this data.

In the turbulent, separated flow region of the wake, the local Frössling number can be characterized as independent of the level of free-stream turbulence and may be described by Equation 127. Two distinct possible mechanisms of transport were recognised in the wake, that characterized by a laminar and that associated with a turbulent boundary layer. Near 108° from stagnation the laminar layer separated, and the region downstream was

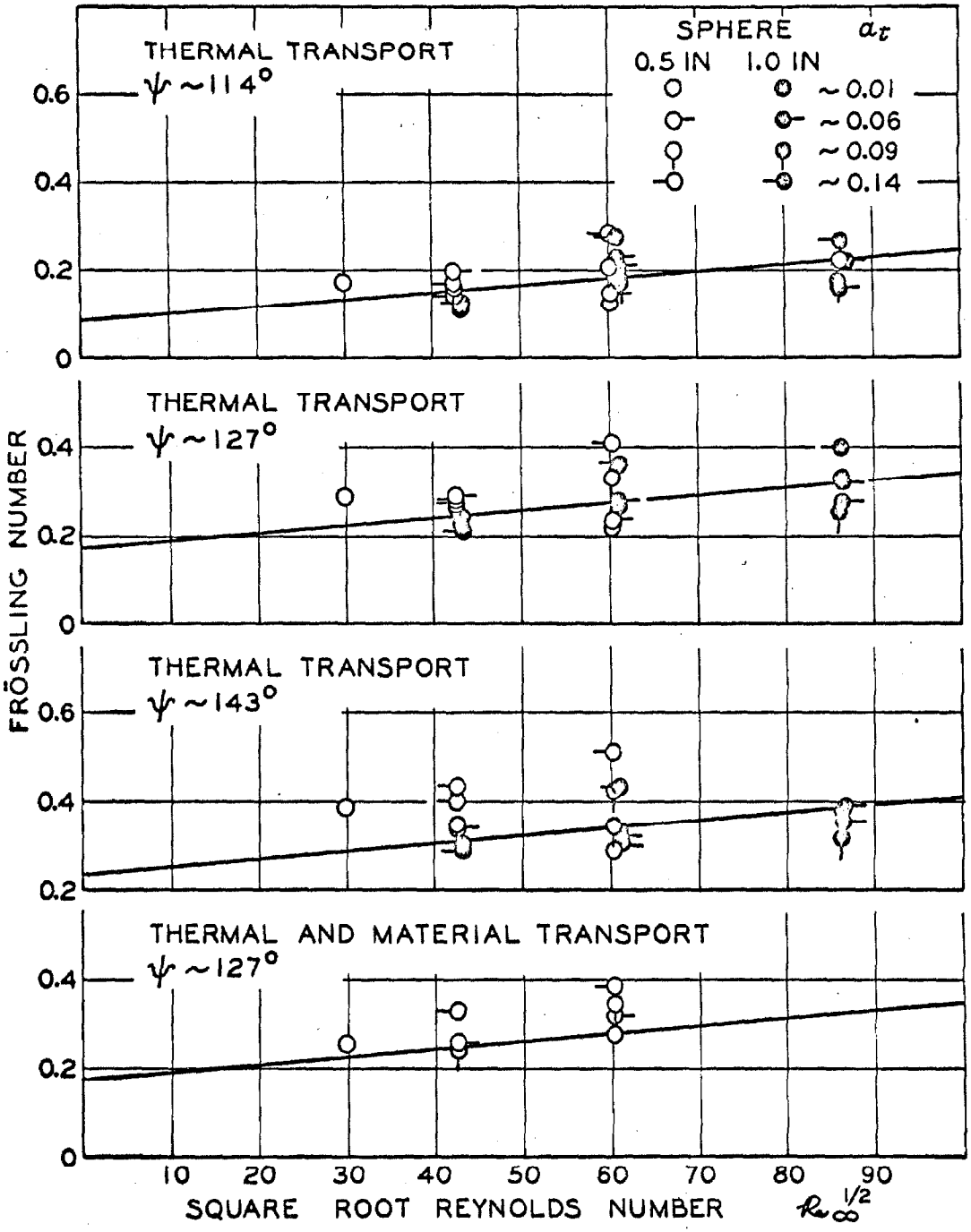

Fig. 57. Effect of Reynolds number in subcritical flow on local transport in aft hemisphere.

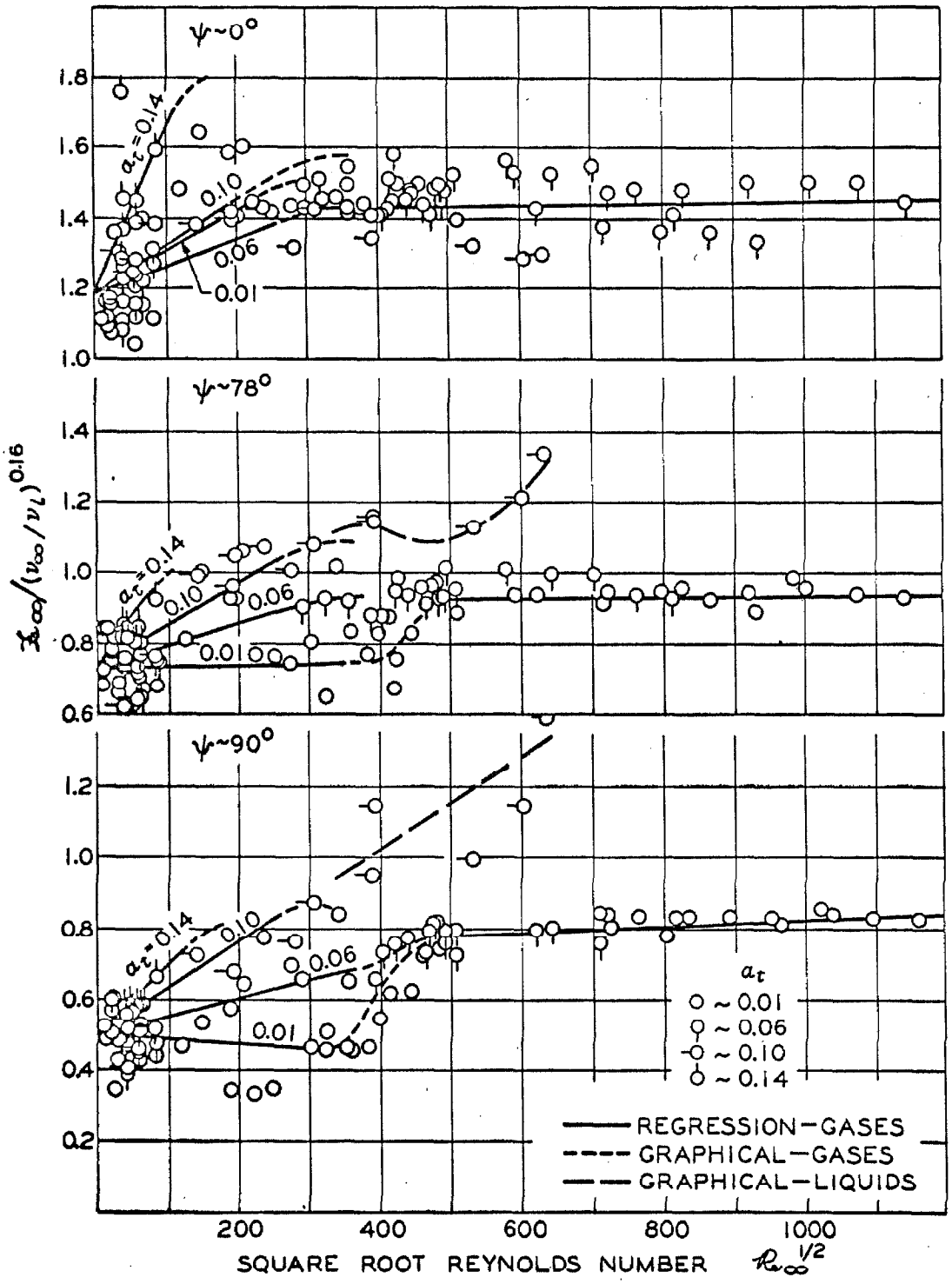

Fig. 58. Effect of Reynolds number on local transport in forward hemisphere.

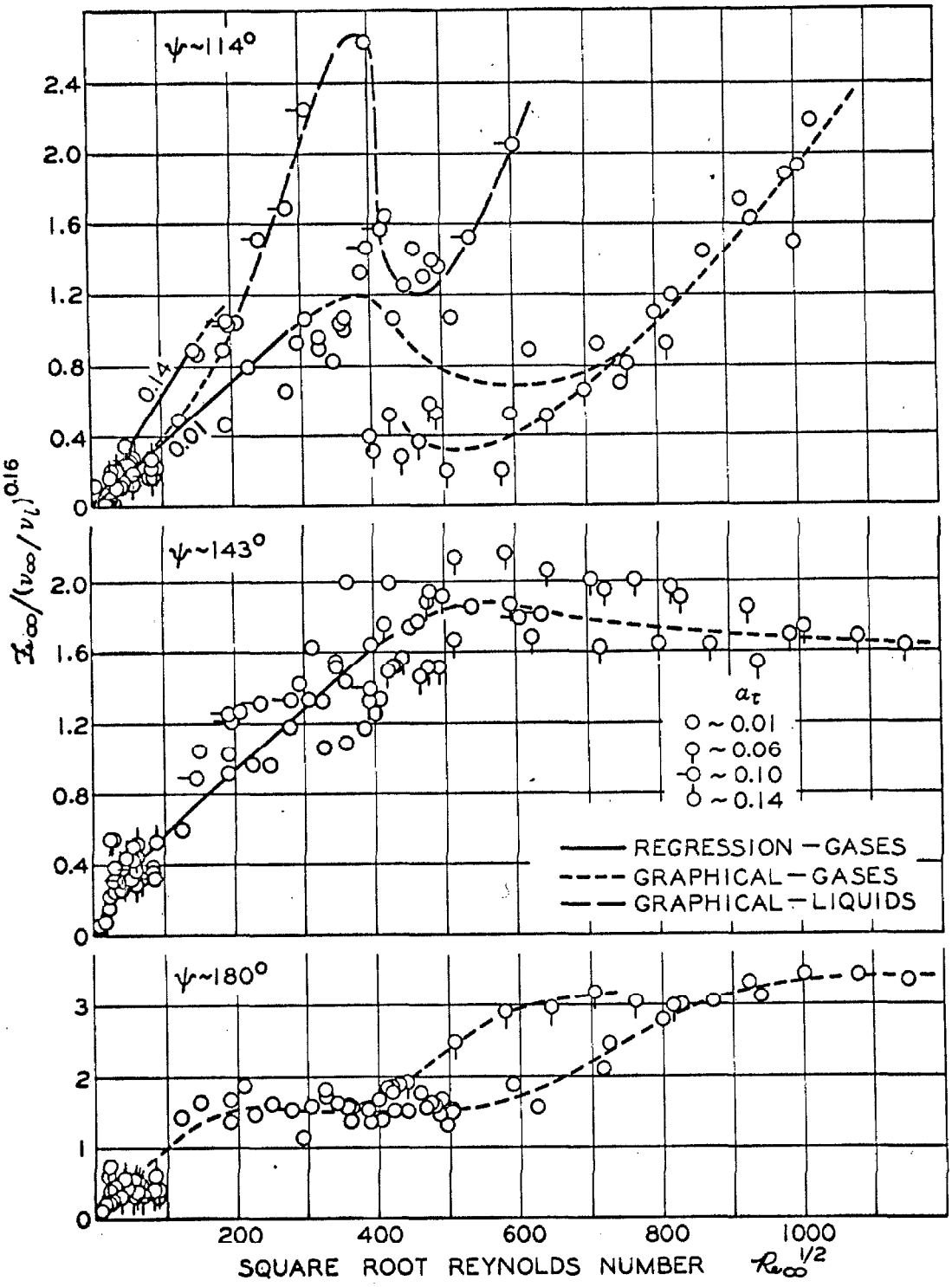

Fig. 59. Effect of Reynolds number on local transport in aft hemisphere.

Table 11

Summary of experimental conditions for data employed[a]

Description of sphere material	diameter[c]	Number of points	Turbulence level minimum	maximum	Prandtl Number minimum	maximum	Schmidt Number minimum	maximum	Viscosity ratio[b] minimum	maximum	Range of data: Reynolds Number minimum	maximum	Nusselt or Sherwood Number minimum	maximum	Remarks
porous ceramic	0.5	99	0.013	0.15	-	-	1.2		1.36	1.38	800	7300	16	67	air jet
silver	0.5	99	0.013	0.15	0.7		-	-	0.67	0.84	900	7300	18	41	air jet
silver	1.0	132	0.013	0.15	0.7		-	-	0.835	0.837	1800	7500	24	64	air jet
naphthalene	0.02	66	-	-	-	-	0.6	2.8	1.0		50	1000	7	30	jet
benzoic acid	0.38	11	low		-	-	1210		-	-	490	7500	150	430	water tunnel
benzoic acid	0.75	18	high		-	-	1210		-	-	100	800	80	300	water tunnel
copper	1.5	30	0.01		2.2	6.8	-	-	1.0	2.7	5	480,000	0	1500	water tunnel
copper	4.	340	0.02	0.07	0.7		-	-	0.94		1800	200,000	90	700	wind tunnel
copper	6.	88	0.02		0.7		-	-	-	-	87,000	667,000	300	800	wind tunnel
copper	9.	88	0.02		0.7		-	-	-	-	130,000	1,000,000	314	1000	wind tunnel
copper	12.	88	0.02		0.7		-	-	-	-	177,000	1,200,000	800	1500	wind tunnel
benzoic acid	0.5	-[d]	high		-	-	819	1389	-	-	20	800	71	232	water tunnel
benzoic and adipic acids	0.38-0.75	-[d]	high		-	-	1340	1525	-	-	100	700	70	320	water tunnel

[a] See nomenclature for definition of terms

[b] Kinematic ratio defined as ν_∞ / ν_i

[c] Sphere diameter expressed in inches

[d] Data not used in evaluation of coefficients

treated as turbulent. In the turbulent wake, vortex formation may result in the creation of a laminar back-flow. Thus, some laminar regions in the wake may be described by Equation 126, while the turbulent portions are represented by Equation 127. When the effects of the turbulent separated wake and the free-stream turbulence are treated as being independent. Equations 126 and 127 can be combined linearly to obtain a relation applicable to any position on the surface, with the coefficients angularly dependent. The equation for subcritical flow used for the regression analysis was therefore taken to be:

$$Fs = A\left(\frac{\nu_\infty}{\nu_o}\right)^n + \left[B\, Z_t(Z_t + C) + D\right] Re^{1/2} (Pr \text{ or } Sc)^m \qquad (128)$$

The qualitative nature of the functional dependence of the turbulence level, Z_t, and the exponent m taken to be 1/6 is in agreement with current stochastic, random eddy penetration model such as described by Harriot (85) or by Proposition E herein. The exponent n was found to be 0.16 from analysis of overall transport data which will be discussed later. The solid curves of Figures 58 and 59 were predicted from Equation 128 for subcritical flow and by the following equation for supercritical flows:

$$Fs = A\left(\frac{\nu_\infty}{\nu_o}\right)^{0.16} + D_t\, Re^{1/2} (Pr \text{ or } Sc)^{1/6} \qquad (129)$$

The short dotted lines were graphically determined in the transition region from subcritical to supercritical flows. Equation 128 and 129 are difficult to show graphically because of the kinematic viscosity ratio term. As a first order approximation for these graphical purposes the ordinant was taken to be $Fs/(\nu_\infty/\nu_o)^{0.16}$. The Prandtl or Schmidt numbers were not included in the abscissa in order to illustrate the differences between the transport involving liquids from those of gases. The liquid data is noticeably higher for many

angles and the transition occurs somewhat earlier. The additional Prandtl or Schmidt group dependence is a first approximation to such behavior and additional data are required to refine these minor differences.

The increases in Frössling number with increasing free-stream turbulence are strongest near stagnation and decrease continuously up to separation. The marked effect of polar angle upon the behavior is evident. The effects of transition begin to appear at a polar angle of about 70° . Instabilities in the flow appear as the Reynolds number is increased up to the critical value, above which the instabilities dissappear. In the transition region, the characteristic instabilities become greater as the polar angle is increased. Much of the scatter of the experimental data may well result from the fluctuations in the position of the locus of separation. The relative absence of the effect of level of turbulence upon the local Frössling number is evident in Figures 58 and 59 for the wake-flow region.

The effect of the scale of turbulence on the local transport from spheres has not been investigated in detail. Maisel and Sherwood (26,27) studied the effects of the intensity and of the scale of turbulence on the overall thermal transport from spheres. The foregoing measurements indicated no effect of the scale of turbulence on the overall thermal transport. The negative result may have been due to the fact that the int egral scale of turbulence was only a fraction of the diameter of the spheres investigated. Van der Hegge Zijnen (30) carried out a similar experimental investigation involving cylinders and the scale of turbulence was varied over a wide range. These studies suggest that the effects of turbulence on the local Frössling number may be largest when the scale of turbulence is comparable to the diameter of the sphere. The quantitative effects of scale on the overall transport are discussed later.

The results of this regression analysis of the available local transport data from spheres (6, 12, 62-64, 66, 69, 75, 82) can be expressed as semi-empirical relations derived from theoretical background for prediction of local heat and mass transfer from spheres for liquids and gases as a function of

polar angle, Reynolds number, free-stream turbulence, the molecular properties of the fluid in the free stream, and the variation of such properties through the boundary layer. The coefficients to Equation 128 for subcritical flow are presented as a function of angle in Figure 60. The angular variation of the laminar and turbulent contributions for subcritical flow are evident. The larger Reynolds number dependence of the transport in the wake is in qualitative agreement with results from cylinders. The behavior of the turbulent contributions near the forward stagnation is somewhat complicated by the presence of instabilities and motion of this point. The data near separation were scattered and the effects of turbulence in this region are undoubtedly coupled to the migration of the position of separation.

The statistical analysis as well as the individual numerical coefficients for this regression analysis is given in Table 12 for both subcritical and supercritical flow. The last part of this table involves an identical analysis involving entirely the data of Sage and coworkers (62-64) and the results are indeed comparable. These coefficients were used to predict the solid curves of Figures 58 and 59.

OVERALL TRANSPORT FROM SPHERES:

The detailed local mechanism of transport from a sphere was shown in the discussion above to vary considerably from point to point along the surface. The overall transport is namely an average of each of these mechanisms over the entire surface. Having established a modest knowledge of the local behavior which can be described by either Equation 128 or 129, the overall transport must also be described by the same functional dependence with the local coefficients averaged over the surface. The more important physical factors which give rise to the variation of the Frössling number with conditions

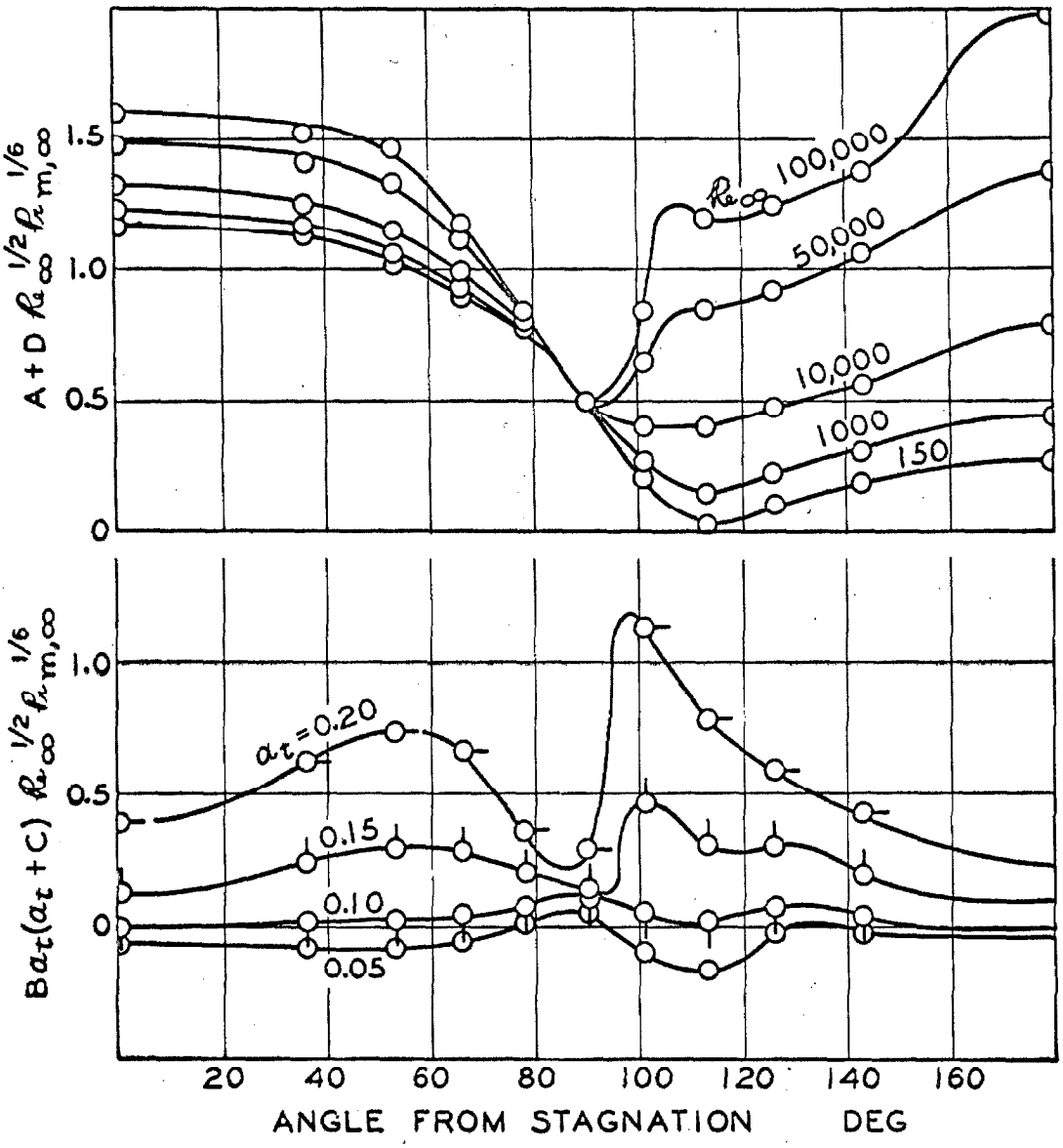

Fig. 60. Coefficients of Equation 7 as a function of polar angle.

TABLE 12

EMPIRICAL COEFFICIENTS FOR EQUATIONS 128 AND 129

Polar angle Deg	Cos ψ	Number data points Used	Rejected[b]	Coefficient A	B	C	D	Deviation, fraction Average[c]	Standard[d]
				Subcritical flow					
0	1.0	58	3	1.1849	0.2122	-0.1072	0.001317	0.00172	0.0453
36.9	0.8	59	2	1.1425	0.3001	-0.09403	0.001199	0.00209	0.0493
53.1	0.6	58	1	1.0143	0.3436	-0.09264	0.001466	0.00277	0.0556
66.4	0.4	63	1	0.8964	0.2859	-0.08356	0.0009623	0.000229	0.0498
78.5	0.2	59	2	0.7351	0.09017	-0.006822	0.0002934	0.00477	0.0748
90.0	0.0	54	5	0.5010	-0.03257	-0.4449	-0.0002787	0.0000618	0.0933
101.5	-0.2	55	3	0.2123	0.5087	-0.08828	0.001968	0.00214	0.180
113.6	-0.4	56	5	0.02280	0.3618	-0.09168	0.003743	0.0229	0.219
126.9	-0.6	61	4	0.1162	0.2351	-0.06142	0.003598	0.0344	0.182
143.1	-0.8	60	5	0.1882	0.1734	-0.07295	0.003797	0.0162	0.112
180.0	-1.0	61	2	0.2713	0.2333	-0.2001	0.005223	0.0570	0.243
				Supercritical flow					
0	1.0	42	1	1.4155	-0.09410	-0.09114	-0.00003900	0.000573	0.0243
36.9	0.8	44	0	1.3463	-0.01841	-0.1244	-0.00005591	0.000432	0.0206
53.1	0.6	26	0	1.3427	-0.006833	-0.4064	-0.0002765	0.000445	0.0216
66.4	0.4	38	0	1.0616	0.07020	-0.06481	0.0001322	0.000973	0.0318
78.5	0.2	42	1	0.9264	0.1043	-0.06476	0.00006054	0.000724	0.0294
90.0	0.0	29	1	0.4163	0.06141	-0.004980	0.0005782	0.00325	0.0633
101.5	-0.2	45	0	0.9220	0.4920	-0.08459	-0.00009771	0.0661	0.249
113.6	-0.4	38	2	0.8437	0.7592	-0.08504	0.0008995	0.0842	0.377
126.9	-0.6	39	0	1.3385	-0.2332	-0.1029	0.001379	0.0106	0.109
143.1	-0.8	39	0	1.1039	-0.2108	-0.02139	0.0005497	0.00480	0.0748
180.0	-1.0	31	0	0.09682	0.9612	-0.06214	0.003739	0.00374	0.0704

Polar angle Deg	Cos ψ	Number data points Used	Rejected[b]	Coefficient A	B	C	D	Deviation, fraction Average[c]	Standard[d]
				Sage et al, combined (60-64)					
0	1.0	28	2	1.0339	0.4447	-0.05925	0.003302	0.000592	0.0254
36.9	0.8	29	1	1.0041	0.2912	-0.04042	0.003246	0.000268	0.0243
53.1	0.6	28	2	0.9402	0.2284	-0.02158	0.002463	0.00139	0.0246
66.4	0.4	27	3	0.7726	0.2376	-0.03904	0.002429	0.00190	0.0256
78.5	0.2	26	4	0.6288	0.2964	-0.08141	0.001782	0.000119	0.0287
90.0	0.0	26	4	0.4372	0.2554	-0.08688	0.0009740	0.000312	0.0364
101.5	-0.2	27	3	0.1940	0.1618	-0.08770	0.001196	0.00287	0.0624
113.6	-0.4	30	0	0.08346	0.01362	0.09413	0.001591	0.00481	0.0806
126.9	-0.6	26	4	0.1711	0.06447	-0.02732	0.001687	0.0000293	0.0400
143.1	-0.8	24	6	0.2353	0.1543	-0.05513	0.001751	0.000865	0.0341
180.0	-1.0	26	4	0.2632	0.1691	-0.04860	0.001588	0.00151	0.0423

[a] Coefficients for equations

$$Fs_\infty = A\,(v_\infty / v_i)^{0.16} + [B\alpha_t(\alpha_t + C) + D]\, Re_\infty^{1/2}\, Pr_{m,\infty}^{1/6}$$

$$Fe_\infty = A\,(v_\infty / v_i)^{0.16} + [B\alpha_t(\alpha_t + C) + D]\, Re_\infty^{1/2}\, Sc_{m,\infty}^{1/6}$$

[b] Statistically rejected when deviation exceeds 4σ

[c] Average deviation defined by

$$s = \frac{\sum_1^{N_p} \{ w\,[(Fs_{\infty,e} - Fs_{\infty,c}) / Fs_{\infty,e}] \}}{N_p}$$

[d] Standard deviation defined by

$$\sigma = \left[\frac{\sum_1^{N_p} \{ w\,[(Fs_{\infty,e} - Fs_{\infty,c}) / Fs_{\infty,e}]^2 \}}{N_p - N_c} \right]^{1/2}$$

of flow appear to be the greater dependence of the transport upon the Reynolds number in the region of separated flow, the free-stream turbulent perturbation of the laminar boundary layer, migration of the point of separation, the influence of the integral scale of turbulence, and the transition to supercritical flow.

The two most important local effects, that of the effects of turbulence and that of wake-flow transport, are well exhibited in Figure 61. These effects are supported by six independent sets of measurements (58, 60-64). The residual dependence of the Frössling number on Reynolds number at very low turbulence arises from wake-flow contributions, and the effects of free-stream turbulence in the forward hemisphere augment this dependence to a degree which increases with the magnitude of turbulence level. All data points shown in Figure 61 are raw data points corrected for radiative transport and conductive losses in the supports where necessary, involving molecular transport properties established in Part I, and have not been smoothed in any way. These raw data have been tabulated for drops, porous spheres, and silver spheres in Tables 13 to 16 respectively. The solid curves were obtained by regression analysis using Equation 128 upon the individual sets of data with equal weight for every one of the data points. The coefficients of these regressions together with the associated statistics are shown in Table 16. The differences between the various spheres or drops are not statistically significant in most cases. The 0.5 inch silver sphere is somewhat higher undoubtedly from eddy shedding behind the horizontal tubes passing from each side of the equator of the sphere. The data involving the 0.5 inch porous spheres appeared somewhat low and were associated with considerably larger experimental uncertainties and systematic errors. The data obtained from the 1.0 inch sphere were believed to be the most reliable.

In Figure 62 is shown a comparison of Equations 128-129 with the experimental data available from other investigators for varying turbulence

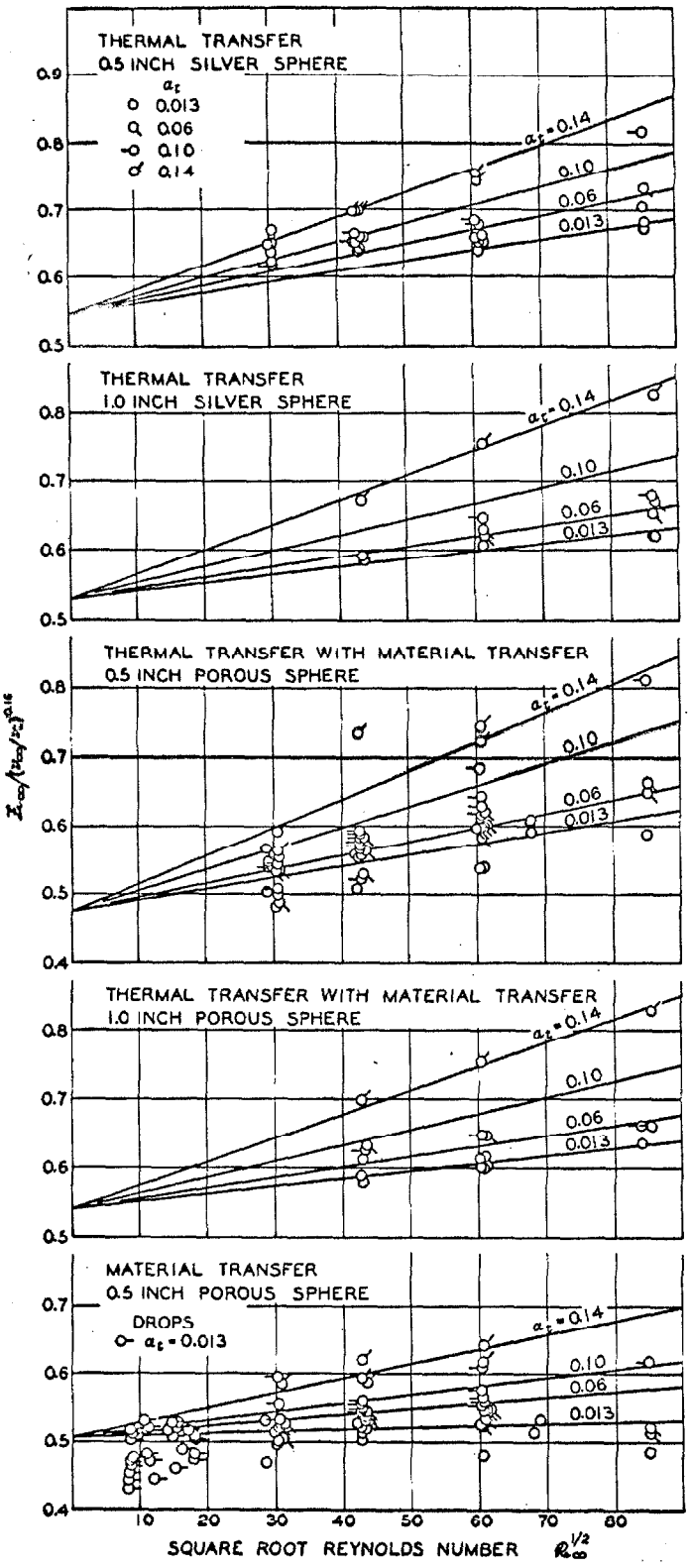

Fig. 61. Macroscopic Frössling Number for several levels of turbulence.

TABLE 13

MACROSCOPIC TRANSPORT FROM n-HEPTANE DROPS

Test number	Air temperature °F	Turbulence level	Mole fraction air	Reynolds number	Interface temperature °F	Evaporation $10^6 \times$ lb/sec	Viscosity ratio[b]	Sherwood number
42d	100.0	0.013	0.9510	66.2	65.35	0.13220	1.3568	7.70
40d	100.0	0.013	0.9507	67.9	65.14	0.13220	1.3578	6.81
38d	100.0	0.013	0.9529	68.0	63.60	0.13220	1.3519	6.95
45d	100.0	0.013	0.9511	69.4	65.32	0.13220	1.3567	7.13
39.1d	100.0	0.013	0.9542	73.5	62.65	0.15378	1.3441	7.95
39.2d	100.0	0.013	0.9542	73.5	62.65	0.15378	1.3441	7.85
39d	100.0	0.013	0.9542	73.8	62.65	0.15378	1.3441	7.95
43d	100.0	0.013	0.9510	74.7	65.00	0.15378	1.3584	7.52
46d	100.0	0.013	0.9515	74.9	64.78	0.15378	1.3596	7.49
41d	100.0	0.013	0.9528	75.7	63.70	0.15378	1.3518	6.62
44d	100.0	0.013	0.9542	81.0	62.66	0.18377	1.3441	8.23
47d	100.0	0.013	0.9520	81.8	64.35	0.18377	1.3486	7.85
28d	100.0	0.013	0.9495	114.6	66.07	0.13220	1.3536	8.98
25d	100.0	0.013	0.9522	116.8	64.33	0.13220	1.3489	9.75
26d	100.0	0.013	0.9523	122.4	62.33	0.15378	1.3452	9.82
24d	100.0	0.013	0.9548	126.6	64.15	0.15378	1.3496	9.16
27d	100.0	0.013	0.9509	140.4	65.12	0.18377	1.3578	9.13
34d	100.0	0.013	0.9536	192.6	63.16	0.18377	1.3499	11.68
32d	100.0	0.013	0.9552	204.0	61.63	0.21525	1.3484	12.18
32.1d	100.0	0.013	0.9552	205.7	61.63	0.21525	1.3484	12.18
36d	100.0	0.013	0.9544	206.0	62.73	0.20362	1.3436	12.24
32.2d	100.0	0.013	0.9552	209.4	61.63	0.21525	1.3484	12.08
30d	100.0	0.013	0.9548	227.9	61.88	0.24301	1.3474	12.66

TABLE 13 (cont.)

Test number	Air temperature °F	Turbulence level	Mole fraction air	Reynolds number	Interface temperature °F	Evaporation lb/sec	Viscosity ratio[b]	Sherwood number
31d	100.0	0.013	0.9547	228.5	61.92	0.25976	1.3476	12.77
37d	100.0	0.013	0.9536	233.4	63.27	0.24301	1.3495	11.50
48d	100.0	0.013	0.9526	279.7	62.26	0.24301	1.3456	13.04
51d	100.0	0.013	0.9542	291.5	62.64	0.24301	1.3441	13.64
49d	100.0	0.013	0.9548	302.8	62.22	0.27899	1.3458	14.14
50.1d	100.0	0.013	0.9548	315.5	62.20	0.27899	1.3460	14.14
55d	100.0	0.013	0.9522	316.9	62.26	0.27899	1.3492	13.40
50.2d	100.0	0.013	0.9548	318.7	62.20	0.27899	1.3460	14.13
50d	100.0	0.013	0.9548	321.7	62.20	0.27899	1.3460	13.68

[a] See nomenclature for definition of terms

[b] Viscosity ratio defined as: ν_∞ / ν_o

[c] Schmidt number for this data averaged was $Sc_\infty = 2.1302$

TABLE 14

MACROSCOPIC TRANSPORT FROM 0.5 INCH POROUS SPHERE

Test number	Air temperature °F	Turbulence level	Mole fraction air	Reynolds number	Interface temperature °F	Evaporation rate lb/sec	Thermal flux Btu/sec	Viscosity ratio[b]	Nusselt number	Sherwood number
45	99.9	0.013	0.94882	822	64.11	2.494×10^{-6}	0.3164×10^{-3}	1.3809	15.54	20.27
48	100.1	0.013	0.94930	822	64.11	2.721	0.3135	1.3631	17.23	22.65
50	100.2	0.013	0.94904	889	64.08	2.720	0.3512	1.3639	17.57	22.73
49	100.2	0.013	0.94970	1760	63.77	3.795	0.4968	1.3649	23.95	32.03
46	99.6	0.013	0.94942	1802	63.76	3.777	0.4968	1.3627	24.40	31.62
52	100.1	0.013	0.94966	1807	63.76	3.807	0.5001	1.3642	24.17	32.16
51a	100.1	0.013	0.94956	4599	64.97	6.049	0.8142	1.3590	40.72	50.80
51b	100.1	0.013	0.94956	4599	64.97	6.037	0.8126	1.3590	40.64	50.70
47	100.1	0.013	0.94933	4602	64.98	5.850	0.7907	1.3590	39.56	49.10
104.4	100.1	0.055	0.94973	3649	63.89	5.564	0.7408	1.3634	35.94	46.88
104.1	100.1	0.058	0.94966	911	63.88	2.761	0.3524	1.3634	17.09	23.24
104.7	100.1	0.058	0.95014	1813	63.52	3.911	0.5100	1.3650	25.18	33.30
104.5	100.1	0.059	0.94965	3649	63.91	5.604	0.7463	1.3634	36.22	47.06
104.8	100.1	0.063	0.95014	1813	63.51	3.937	0.5134	1.3650	25.36	33.52
104.6	100.1	0.064	0.94966	3649	63.95	5.624	0.7493	1.3632	36.39	47.22
104.2	100.1	0.067	0.94964	911	63.85	2.781	0.3545	1.3635	17.18	23.41
104.3	100.1	0.068	0.94974	911	63.83	2.789	0.3555	1.3637	17.22	23.52
104.9	100.1	0.068	0.95014	1813	63.51	3.942	0.5140	1.3650	25.39	33.57
106.7	100.1	0.071	0.94929	3642	64.00	5.654	0.7530	1.3628	36.65	47.44
106.1	100.1	0.075	0.94959	912	63.81	2.785	0.3550	1.3637	17.19	23.73
106.4	100.1	0.075	0.95004	1803	63.50	3.951	0.5155	1.3650	24.74	33.58
106.8	100.1	0.078	0.94914	3642	64.08	5.719	0.7624	1.3624	37.18	47.85
106.2	100.1	0.083	0.94958	912	63.79	2.802	0.3569	1.3641	17.27	23.62
106.5	100.1	0.083	0.95004	1803	63.50	4.000	0.5221	1.3650	25.05	34.01
106.9	100.1	0.087	0.94906	3642	64.14	5.796	0.7724	1.3667	37.73	48.41
106.3	100.1	0.093	0.94958	912	63.78	2.823	0.3595	1.3641	17.39	23.80
106.6	100.1	0.093	0.94997	1803	63.55	4.035	0.5263	1.3647	25.30	34.25
105.7	100.1	0.097	0.94893	3645	64.29	5.890	0.7848	1.3652	38.50	49.06
105.1	100.1	0.106	0.94963	914	63.75	2.883	0.3670	1.3641	17.73	26.34
105.4	100.1	0.106	0.94922	1810	63.61	4.056	0.5921	1.3647	25.48	34.37
105.8	100.1	0.111	0.94943	3645	64.47	6.179	0.8259	1.3650	40.73	51.95
105.2	100.1	0.123	0.94971	914	63.72	2.914	0.3722	1.3643	17.97	24.74
105.5	100.1	0.123	0.94975	1810	63.72	4.232	0.5257	1.3643	25.38	35.81
105.9	100.1	0.130	0.94834	3645	64.73	6.631	0.8888	1.3643	44.15	54.53
105.3	100.1	0.146	0.94971	914	63.71	3.051	0.3881	1.3643	18.73	25.90
105.6	100.1	0.146	0.94944	1810	63.92	4.483	0.4881	1.3635	23.71	37.69

TABLE 14 (cont.)

Test number	Air temperature °F	Turbulence level	Mole fraction air	Reynolds number	Interface temperature °F	Evaporation rate lb/sec	Thermal flux Btu/sec	Viscosity ratio[b]	Nusselt number	Sherwood number
201a	100.03	0.013	0.94898	911	64.05	2.708×10^{-6}	0.3279×10^{-3}	1.3628	16.10	22.56
201b	100.03	0.013	0.94924	1768	63.77	3.671	0.4514	1.3641	21.99	30.69
198	100.10	0.013	0.94887	3657	64.12	4.807	0.6104	1.3628	29.97	39.89
200	100.04	0.013	0.94868	3662	64.12	4.985	0.6617	1.3621	32.54	41.33
199	100.25	0.013	0.94658	7251	65.78	7.261	0.9548	1.3562	48.90	57.80
209	100.15	0.060	0.94571	7240	66.42	7.840	1.0401	1.3773	54.46	61.27
208	100.06	0.065	0.94904	3647	63.91	5.389	0.7173	1.3637	35.04	44.89
207b	100.06	0.070	0.94951	1823	63.45	3.917	0.4853	1.3654	23.42	32.98
207a	100.06	0.071	0.94890	909	63.85	2.736	0.3218	1.3639	15.70	22.79
210	100.04	0.078	0.94540	7244	66.71	8.000	1.0625	1.3763	54.98	62.16
205	100.85	0.087	0.94889	3634	64.14	5.448	0.6972	1.3653	33.51	45.15
206b	99.85	0.092	0.94926	1812	63.53	3.802	0.4669	1.3645	22.72	31.88
206a	99.85	0.094	0.94903	916	63.74	2.767	0.3230	1.3636	16.35	23.14
204b	100.85	0.116	0.94496	7222	67.25	9.497	1.2798	1.3731	67.16	73.18
204a	100.85	0.143	0.94746	3642	64.93	6.114	0.7952	1.3616	39.05	49.51
203b	100.92	0.147	0.94870	1806	63.96	4.142	0.5177	1.3675	24.69	34.36
203a	100.92	0.151	0.94917	922	63.72	2.887	0.3421	1.3684	16.22	24.01
291	100.09	0.013	0.94867	870	64.05	2.737	0.3512	1.3628	17.14	24.44
165	100.00	0.013	0.94914	913	64.06	2.528	0.3200	1.3628	15.58	22.40
121	100.06	0.013	0.94889	1809	63.77	3.784	0.4979	1.3628	25.67	31.58
290	100.17	0.013	0.94843	3613	64.12	4.756	0.6315	1.3627	32.45	39.71
289	100.15	0.013	0.94867	3615	64.12	4.756	0.6319	1.3627	30.89	39.38
108	100.07	0.052	0.94953	3649	63.88	5.515	0.7325	1.3631	35.56	45.72
107	100.01	0.056	0.95004	1811	63.52	3.888	0.5068	1.3652	24.35	32.84
99	100.07	0.088	0.94906	3642	64.15	5.681	0.7552	1.3621	36.94	47.34
98	100.1	0.094	0.94983	1815	63.55	3.931	0.5137	1.3652	24.68	33.75
100	100.07	0.135	0.94990	3671	64.80	6.467	0.8650	1.3590	43.06	52.01
101	100.07	0.148	0.94950	1808	63.94	4.371	0.6267	1.3632	31.34	36.26

TABLE 14 (cont.)

MACROSCOPIC TRANSPORT FROM 1.0 INCH POROUS SPHERE

Test number	Air temperature °F	Turbulence level	Mole fraction air	Reynolds number	Interface temperature °F	Thermal flux Btu/sec	Viscosity ratio[b]	Nusselt number
303	100.15	0.013	0.97755	1822	79.94	0.5762 x 10^{-3}	1.1847	25.04
310	100.15	0.013	0.97753	1824	79.91	0.5992	1.1770	26.00
328	100.11	0.013	0.97742	1825	79.81	0.5716	1.1774	24.74
322	100.15	0.013	0.97740	3620	79.50	0.8248	1.1786	35.09
307	100.17	0.013	0.97750	3621	79.37	0.8400	1.1793	35.49
326	100.02	0.013	0.97734	3624	78.92	0.8169	1.1767	35.27
327	100.07	0.013	0.97744	3625	78.89	0.8458	1.1770	35.10
305	100.13	0.013	0.97748	3625	79.12	0.8577	1.1781	35.88
306	100.13	0.013	0.97753	3625	79.39	0.8451	1.1793	35.80
309	100.15	0.013	0.97756	3626	79.60	0.8349 x 10^{-3}	1.1782	35.71
311	100.13	0.013	0.97735	7056	79.39	1.2049	1.1793	51.05
318	100.11	0.065	0.97720	7294	79.41	1.2691	1.1789	53.87
316	100.07	0.067	0.97745	3632	79.69	0.8799	1.1777	37.93
317	100.15	0.071	0.97741	1823	80.63	0.5950	1.1742	26.79
312	100.63	0.087	0.97733	7092	79.21	1.2671	1.1808	53.22
314	100.15	0.092	0.97735	3615	79.56	0.8839	1.1783	37.71
313	100.11	0.094	0.97745	1852	80.37	0.5998	1.1752	26.70
319	100.11	0.133	0.97730	7299	79.40	1.5768	1.1789	66.91
321	100.15	0.147	0.97749	3613	79.67	1.0169	1.1779	43.62
320	100.13	0.149	0.97750	1822	80.51	0.6546	1.1748	29.32

a See nomenclature for definition of terms

b Viscosity ratio defined as z_∞ / z_i

c The Prandtl and Schmidt numbers used in the calculations varied between 0.7045 and 0.7048 and 2.129 and 2.130, respectively

d Evaporating fluid, n-heptane

e Evaporating fluid, n-octane

TABLE 15

MACROSCOPIC TRANSPORT FROM SILVER SPHERES[a]

Test number	Air temperature °F	Turbulence level	Reynolds number	Interface temperature °F	Thermal flux Btu/sec	Viscosity ratio[b]	Nusselt number
			0.5 in. silver sphere[c]				
60	100.2	0.013	909	205.1	1.094×10^{-3}	0.7384	18.70
64	100.1	0.013	909	175.9	0.783	0.8004	18.53
68	100.2	0.013	914	245.1	1.533	0.6678	18.97
80	100.1	0.013	1805	245.9	2.085	0.6666	25.64
69	100.1	0.013	1814	205.9	1.531	0.7366	25.94
66	100.0	0.013	1815	154.4	0.783	0.8491	25.82
61	99.8	0.013	1819	176.6	1.093	0.8126	25.53
70	100.0	0.013	3654	178.2	1.533	0.7950	35.15
71	100.1	0.013	3655	205.5	2.086	0.7374	35.49
73	100.1	0.013	3657	243.8	2.856	0.6696	35.64
79	100.0	0.013	7220	243.0	4.155	0.6706	52.10
75	100.1	0.013	7264	199.5	2.856	0.7497	51.51
74	100.0	0.013	7265	173.1	2.086	0.8060	51.18
85	100.1	0.080	7248	167.3	2.087	0.8200	55.70
86	100.0	0.086	3657	173.3	1.533	0.8058	37.50
88	100.0	0.092	914	177.7	0.783	0.7960	18.08
87	100.1	0.092	1814	175.7	1.094	0.8009	25.95
84	100.1	0.120	7225	160.2	2.087	0.8358	62.27
83	100.1	0.129	3647	167.7	1.533	0.8185	40.66
82	99.8	0.144	911	174.6	0.784	0.8001	18.80
81	100.0	0.145	1806	171.1	1.094	0.8107	27.48

Test number	Air temperature °F	Turbulence level	Reynolds number	Interface temperature °F	Thermal flux Btu/sec	Viscosity ratio[b]	Nusselt number
			0.5 in. silver sphere[c]				
161	100.13	0.013	909	177.01	0.7972×10^{-3}	0.7977	18.18
160	100.06	0.013	3643	206.64	2.1247	0.7352	35.55
109	100.06	0.051	3638	175.23	1.5617	0.8021	36.15
110	100.06	0.054	1806	175.45	1.1146	0.8017	25.86
90	100.06	0.088	3640	173.39	1.5616	0.8060	37.62
89	100.06	0.094	1806	175.41	1.1146	0.8017	26.34
91	100.06	0.135	3641	167.14	1.5621	0.8203	41.13
92	100.06	0.146	1807	171.48	1.1146	0.8104	27.56
93	100.03	0.146	1808	171.08	1.1148	0.8110	27.55
			1.0 in. silver sphere[c]				
176a	100.54	0.013	1880	160.03	2.3371×10^{-3}	0.8372	24.2
177	100.54	0.013	1884	160.03	1.632	0.8372	24.0
176b	99.98	0.013	3730	160.03	2.3371	0.8363	34.2
175	100.02	0.013	7500	160.25	3.3356	0.8363	48.6
174	100.02	0.013	7500	160.25	3.3179	0.8363	48.6
185	100.15	0.051	7480	160.03	3.4785	0.8367	51.1
186	100.00	0.054	3715	160.25	2.4155	0.8359	35.4
184	100.13	0.064	7530	160.16	3.5811	0.8363	52.5
183	99.81	0.067	3740	159.98	2.3821	0.8358	34.9
181	100.09	0.086	7430	160.26	3.6016	0.8355	52.7
182	100.09	0.091	3720	160.17	2.4659	0.8357	36.2
180	100.19	0.132	7490	160.30	4.3481	0.8364	63.8
179	100.04	0.143	3720	160.19	2.8578	0.8355	41.9
178	100.11	0.151	1880	160.02	1.8557	0.8367	27.3

TABLE 16

COEFFICIENTS OF EQUATION 128 FOR SMALL SPHERES

Nature of transport and sphere type	Number data points Used	Rejected[a]	Coefficients A	B	C	D	Deviation fraction Average	Standard
Thermal								
0.5 in. silver sphere	30	0	0.5445	0.08206	0.03970	0.001579	0.0000475	0.0105
1.0 in. silver sphere	14	0	0.5270	0.1548	-0.02429	0.001229	0.000128	0.0173
Thermal and material								
0.5 in. porous sphere	57	7	0.4748	0.2357	-0.03464	0.001909	0.000295	0.0255
1.0 in. porous sphere	20	0	0.5401	0.1290	0.005893	0.001182	0.000121	0.0141
Material								
0.5 in. porous sphere	56	7	0.5037	0.06256	0.06240	0.0002396	0.000104	0.0188

[a] Point was statistically rejected when standard deviation exceeded 5σ

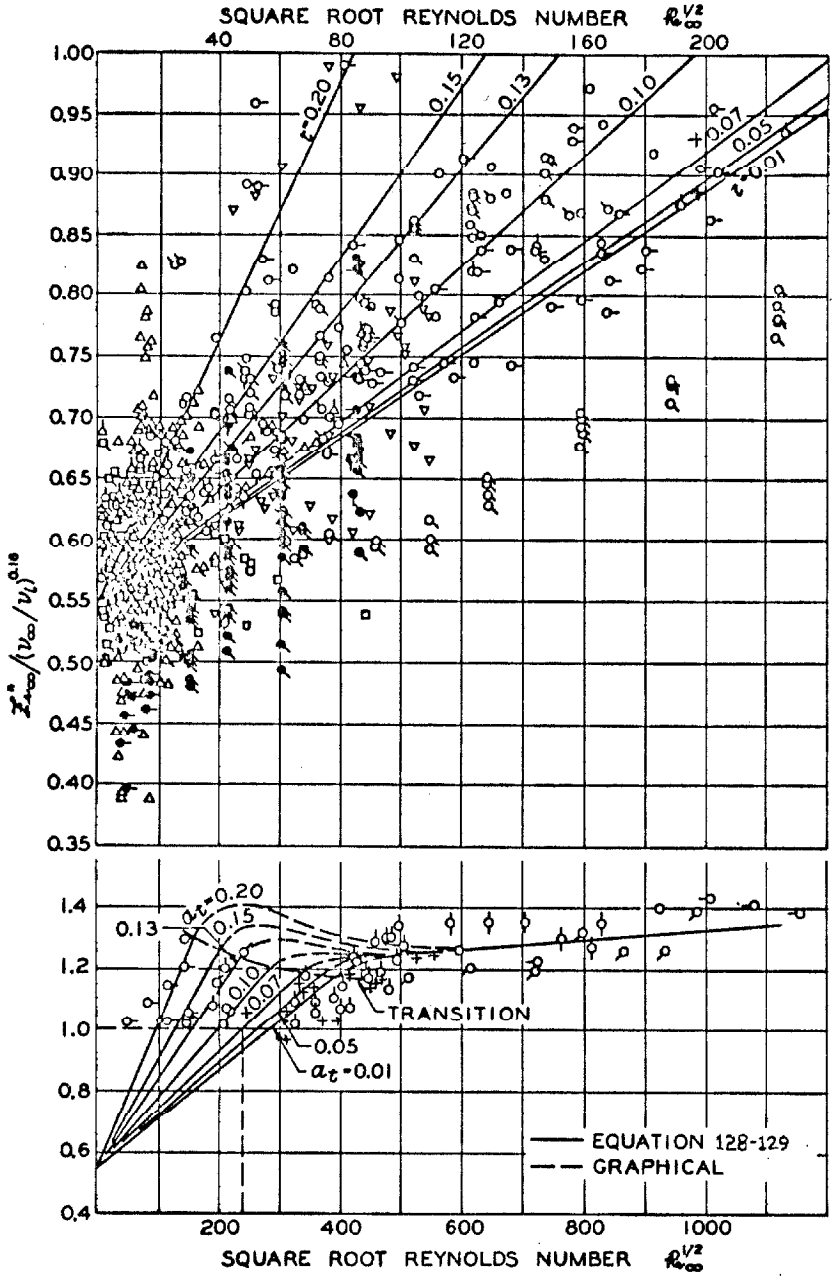

Authors	z_t=0.013-0.15	Maisel (27)	z_t=0.03-0.23	Evnochides (77)	~0.01
Hsu (58)	0.013	Vliet (76)	~0.01	Kramers (54)	~0.05
Brown (61,63)	0.013-0.15	Pasternak (73)	0.10	Skelland (88)	~0.01
Venezian (64)	0.013-0.15	Steele (104)	~0.01	Ranz (55)	0.02
Sato, Short (60,62)	0.013-0.15	Wadsworth (69)	0.02-0.12	Linton (75)	~0.01
Venezian (64)	0.013-0.15	Powell (53)	~0.15	Frössling (6)	—
Garner (81,82)	~0.15	Rowe (105)	~0.01	Loitzianski (59)	0.004-0.04

Fig. 62. Macroscopic Frössling Number from several investigators

levels (12,26,66,69,73,76,81,103-105) for heat and mass transfer involving gases and liquids. The upper portion of the figure shows as an enlarged portion of the lower where there is the great abundance of data at low Reynolds numbers. The turbulence levels for each of the data points could not be indicated in this figure. The lower portion shows the region of the onset of transition to supercritical flow, the transition region itself (as dotted curves), and the supercritical flow (single solid line). Again several liberties were taken in this plot in the ordinant and abscissa as explained previously. The range of experimental conditions covered by each set of data has been enumerated in Table 17. Four cases were used in the regression analysis of the subcritical data with Equation 128 as shown in Table 18. Thermal, thermal with simultaneous material, and material transport were treated independently, and then all the data were combined. The solid cirves shown in Figure 62 as subcritical are for the three types of transport combined. The supercritical data was analyzed separately. Table 18 shows the statistical analysis of the regression as well as the individual range of conditions. There were no statistically significant differences between the various types of transport. A comparison with the results involving the 1.5 inch instrumented cylinder is indeed apparent. As in Figure 62 for spheres there are sufficient data in the supercritical region to establish the curve with sufficient accuracy.

The effects of the integral scale of turbulence are shown in Figure 63. It can be seen from the trends shown that,although Maisel and Sherwood (26) did vary the integral scale of turbulence, the maximum scale, L, was so much smaller than the diameter of the sphere, d, that the influence of turbulence was small. The Frössling number is around 0.55 for very low turbulence levels and the increase with turbulence depends on the scale parameter, d/L. The points shown were obtained for both data involving spheres (26, 60-64) and cylinders (30), and the results are comparable. This plot indicates that the effects of turbulence are greatest when the integral scale of turbulence are comparable to the diameter of the bluff body under study.

Table 12

Range of experimental conditions[a]

Description	Number of points	Turbulence level minimum	Turbulence level maximum	Prandtl Number minimum	Prandtl Number maximum	Schmidt Number minimum	Schmidt Number maximum	Viscosity ratio[b] minimum	Viscosity ratio[b] maximum	Range of data: Reynolds Number minimum	Range of data: Reynolds Number maximum	Range of data: Nusselt or Sherwood Number minimum	Range of data: Nusselt or Sherwood Number maximum	Source	Remarks
n-heptane drops	33		0.013				2.130	1.34	1.36	66	322	6	11	(58)	air jet
0.5 in. porous sphere	65	0.013	0.151	0.7045	0.7048	2.129	2.130	1.36	1.38	900	7,200	15	73	(61,63)	air jet
1.0 in. porous sphere	20	0.013	0.149	0.7045	0.7047	2.129	2.130	1.175	1.185	18	7,300	24	67	(64)	air jet
0.02 in. naphthalene drops	99	-				0.6	2.2	1.0		50	1,000	17	30	(6)	air jet
0.38 in. benzoic acid spheres	14	low				1210				490	7,500	150	430	(75)	water tunnel
0.50 in. benzoic acid spheres	13	high				1210				100	800	80	300	(81)	water tunnel
0.75 in. benzoic acid spheres	15	high				1210				100	700	70	320	(82)	water tunnel
0.5 in. benzoic, cinnamic acid and 2-naphthol spheres	13	low				1200				600	140,000	36	360	(104)	water tunnel
0.04 in. water drops	78	0.02				1.2		1.0		0	200	2	9	(55)	air jet
2.0 in. naphthalene spheroids	16	low		1.0126		2.5		1.0		200	6,000	5	70	(88)	wind tunnel
1.0-1.4 in. porous spheres	56	0.03	0.23			0.6	1.7	1.157		3,000	4,000	40	400	(28)	wind tunnel
0.8-6.1 in. porous spheres	17	high				0.6		1.0		0	5,000	0	50	(53)	wind tunnel
0.2-0.5 in. celite spheres	16	0.10				-				1,000	4,000	30	60	(73)	wind tunnel
1.4-2.0 in. celite spheres	30	low		0.7		0.6	1.8	0.8		1,400	12,000	90	600	(77)	air jet
0.5 in. benzoic acid, naphthalene and copper spheres	171	low		0.7	7.3	2.5	2100	1.0		10	10,000	9	265	(105)	water trough & tunnel
0.5 in. silver sphere	29	0.013	0.151	0.7045	0.7047			0.67	0.84	900	7,300	18	62	(60,67,84)	air jet
1.0 in. silver sphere	14	0.013	0.151	0.7046	0.7047			0.835	0.837	1,800	7,500	24	64	(63)	air jet
0.87 in. copper sphere	62	low		2.5	7			1.0	2.7	1,000	50,000	20	400	(76)	water tunnel
4.0 in. copper sphere	30	0.02	0.12	0.7				0.936		1,800	200,000	90	700	(69)	wind tunnel
1.5 in. copper sphere	4	1		2.2	6.8			1.0	2.7	5	480,000	0	1,500	(12)	water tunnel
6.0 in. copper sphere	8	0.02		0.7						87,000	667,000	300	800	(66)	wind tunnel
9.0 in. copper sphere	8	0.02		0.7						130,000	1,000,000	314	1,000	(86)	wind tunnel
12.0 in. copper sphere	8	0.02		0.7						177,000	1,200,000	800	1,500	(66)	wind tunnel
0.28-0.50 in. steel spheres	79	-		0.7	380					200	1,500	10	30	(54)	wind & water tunnel
0.125-0.625 in. spheres	.c	-	-		0.7	-	-	-	-	50	3,000	4	13	(56)	glass tube
2.8-5.9 in. nickel plated copper spheres	.c	0.004	0.028		0.7	-	-	-	-	30,000	300,000	145	610	(59)	wind tunnel
9.0 in. copper sphere	.c	0.02			0.7	-	-	-	-	130,000	1,000,000	630	2,000	(65)	wind tunnel
5.0 in. iron sphere	.c	-	-		0.7	-	-	-	-	44,000	150,000	150	300	(68)	fan
0.38-2.5 in. steel and brass spheres	.c	-	-		0.7	-	-	-	-	10	100,000	3	700	(71)	wind tunnel
0.02-0.06 in. spheres	.c	-	-	-	-	127	1400	-	-	4	100	4	57	(74)	water tunnel
0.271 in. sphere	.c	low		-	-	0.5	2.7	0.7	1.0	800	5,700	19	40	(57)	jet

[a] See nomenclature for definition of terms

[b] Viscosity ratio defined as μ_∞/μ_s

[c] Data not used in evaluation of coefficients

TABLE 18

RECOMMENDED COEFFICIENTS FOR EQUATIONS 128 AND 129[a]

	Nature of transport									
	Thermal		Thermal and material		Material		Combined		Thermal	
	minimum	maximum	minimum	maximum	minimum	maximum	minimum	maximum	minimum	maximum
Applicable range	Subcritical flow[b]								Supercritical flow[c]	
Sphere diameter, in.	0.25	12.0	0.02	2.0	0.02	2.0	0.02	12.0	4.0	12.0
Reynolds Number	1.2	300,000	2.1	119,500	2.1	48,300	1.2	300,000	250,000	1,330,000
Turbulence level, fraction	0.005	0.15	0.01	0.15	0.005	0.23	0.005	0.23	0.005	0.07
Prandtl or Schmidt Number	0.70	380.	0.697	0.721	0.593	1210.	0.593	1210.	0.708	
Viscosity ratio	0.66	2.7	1.00	1.36	1.00	1.37	0.66	2.7	1.00	
Nusselt or Sherwood Number	6.9	543.	2.89	78.6	2.58	198.	2.89	543.	550.	1418.
Number of data points Used	388		143		436		947		22	
Rejected[d]	5		3		4		11		2	
Recommended coefficients A	0.5747		0.5604		0.5454		0.5483		1.171	
B	0.1674		0.3988		0.09904		0.1212			
C	-0.05628		-0.1110		-0.0004096		-0.04595			
Deviation, fraction D	0.001449		0.002073		0.001362		0.001656		0.000159	
Average[e]	0.00652		0.00162		0.00693		0.00630		0.0102	
Standard[f]	0.0786		0.0543		0.102		0.0881		0.0477	

a See nomenclature for definition of terms

b Subcritical flow

$$\mathcal{F}^*_{s,\infty} = A\,(\nu_\infty/\nu_i)^{0.16} + [B\,\alpha_t(\alpha_t + C) + D]\,Re_\infty^{1/2}\,(Pr_{m,\infty} \text{ or } Sc_{m,\infty})^{1/6}$$

c Supercritical flow

$$\mathcal{F}^*_{s,\infty} = A\,(\nu_\infty/\nu_i)^{0.16} + D\,Re_\infty^{1/2}\,Pr_{m,\infty}^{1/6}$$

d Points statistically rejected when deviation exceeds 5σ

e Average deviation defined by:

$$s = \left\{\sum_1^{N_p} w\,[(\mathcal{F}^*_{s,\infty,e} - \mathcal{F}^*_{s,\infty,c})/\mathcal{F}^*_{s,\infty,e}]\right\}/N_p$$

f Standard deviation defined by:

$$\sigma = \left[\left\{\sum_1^{N_p} w\,[(\mathcal{F}^*_{s,\infty,e} - \mathcal{F}^*_{s,\infty,c})/\mathcal{F}^*_{s,\infty,e}]^2\right\}/(N_p - N_c)\right]^{1/2}$$

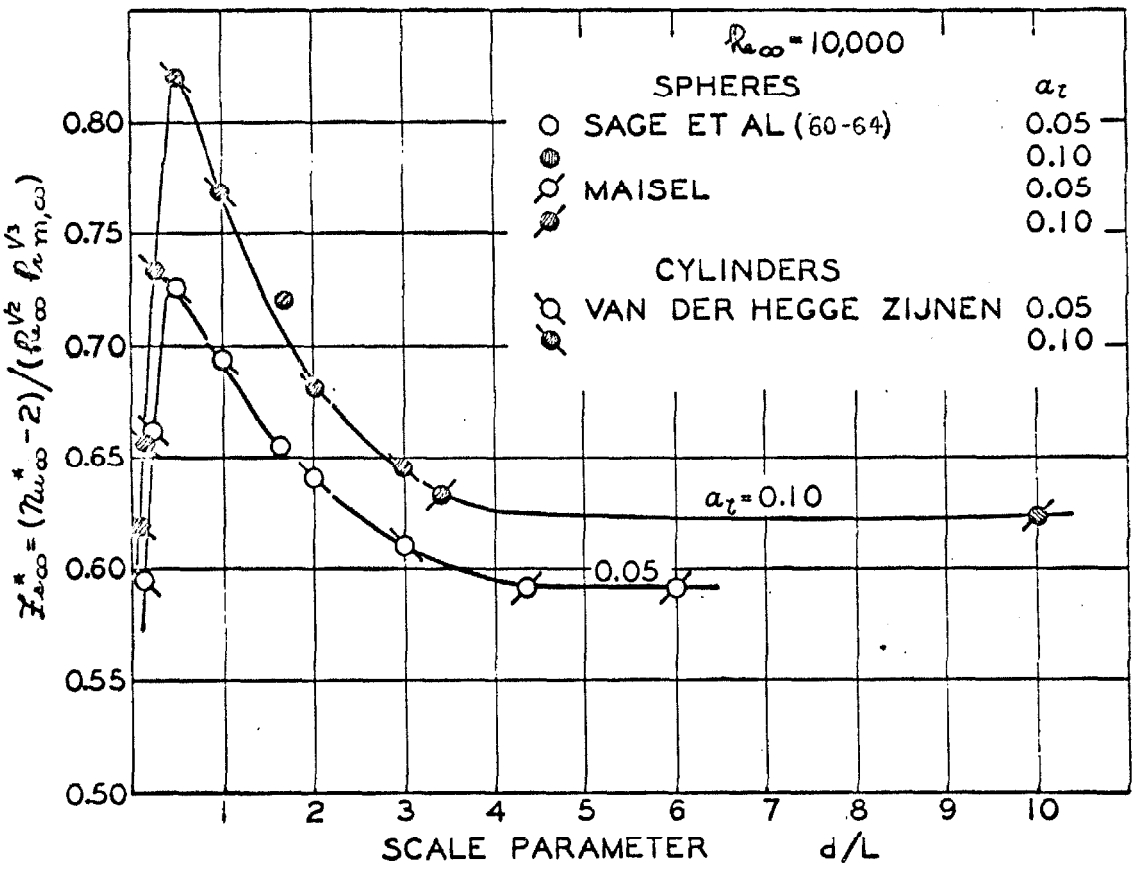

Fig. 63. Macroscopic Frössling Number as function of conditions of flow

The transition of the laminar boundary layer into a turbulent layer before separation, as in supercritical flow, is shown by the gradual change in the slope of the Frössling number with Reynolds number in Figure 62. Such curves appear as dotted, and the dashed curve labeled transition is the first outset of this transition. The transition Reynolds number for this initial onset established in Figure 62 depends strongly on the free-stream turbulence level as given in Figure 64. For comparison, the transition Reynolds number obtained from the drag measurements of Dryden (100) is included, and the agreement is excellent. For Reynolds numbers below the transition Reynolds number Equation 128 applies.

The variation in molecular transport properties through the boundary layer should be accounted for by using only molecular properties. A form of solution for subcritical flow allowing for variable molecular properties might utilize the ratio of kinematic viscosities of the free stream and of interfacial conditions on the surface as discussed earlier. All other molecular and flow properties are then evaluated at conditions prevailing in the free stream. The validity of such an approach using transport from spheres can be seen in Figure 65 from data using air (60-64) and water (76). Such a procedure, when data at all Reynolds numbers and levels of turbulence are considered in a regression analysis, yields a flat minimum in the standard error at a value of the exponent of 0.16. The full curves are obtained from the equations shown while the points are experimental values. The data for water are higher, owing to the increased nonlinear wake effect encountered at the higher molecular Prandtl numbers. Without a detailed knowledge of the variation of the properties throughout the boundary layer, the use of effective molecular properties is, at best, only a fair approximation.

There are a number of secondary effects which were discussed in the theoretical analysis that are important in the experimental transport measurements from spheres. For Reynolds numbers greater than 400, natural

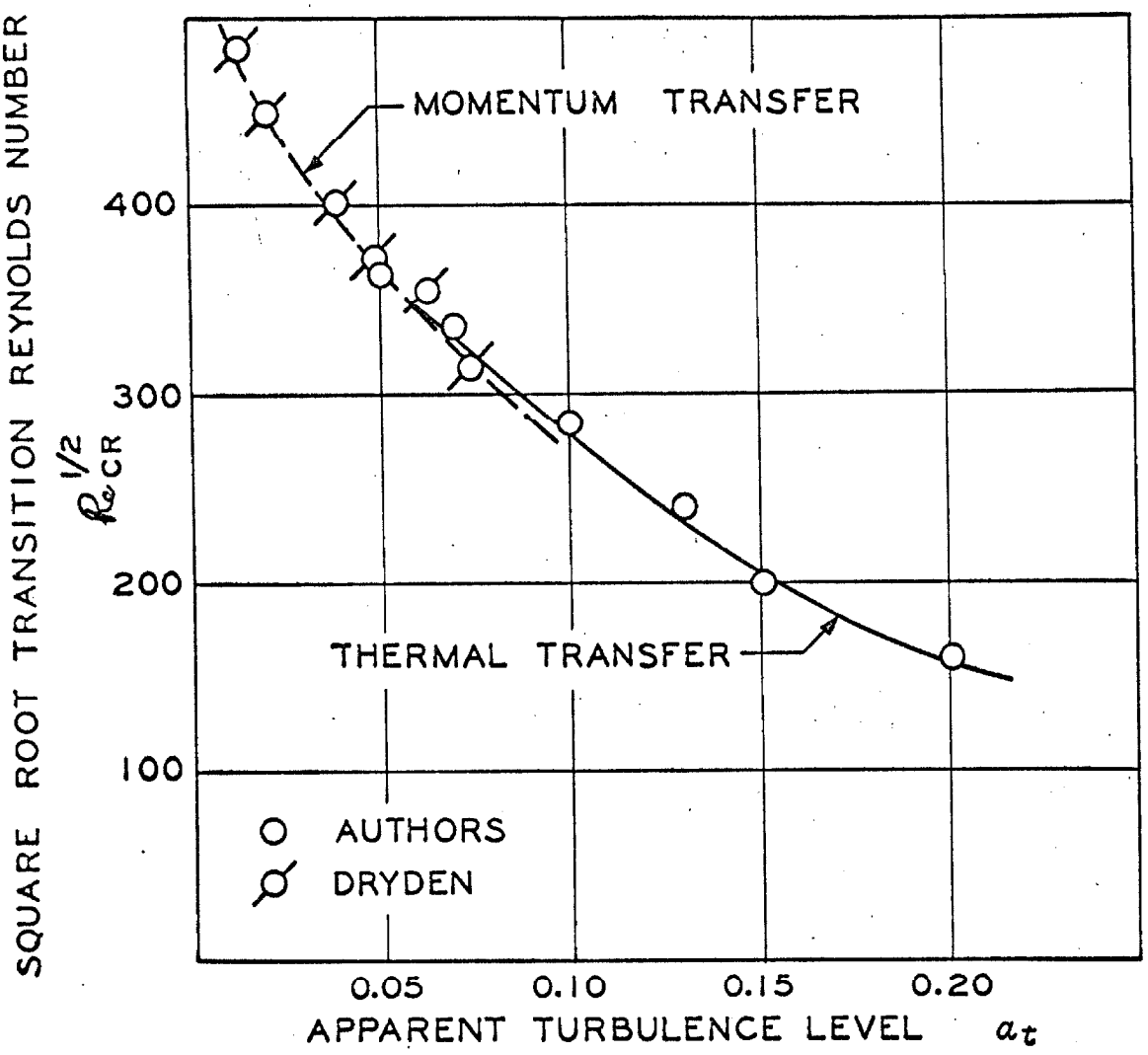

Fig. 64. Influence of level of turbulence upon transition Reynolds Number

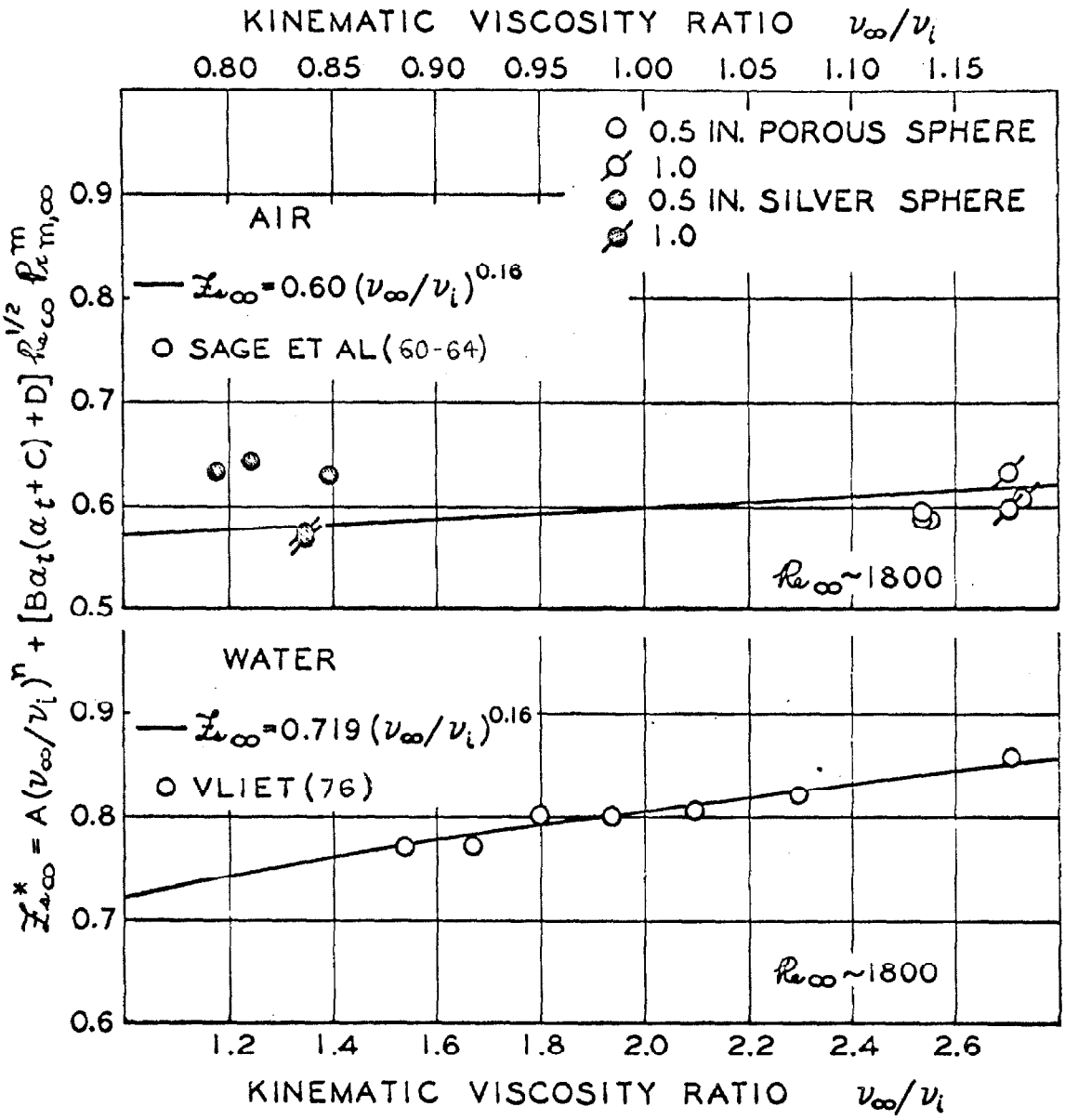

Fig. 65. Effect of kinematic viscosity ratio upon macroscopic Frössling Number

convection is usually negligible compared to forced convection. The magnitude of natural convection becomes more pronounced for large temperatures or concentration gradients. An excellent experimental procedure was to vary the driving force and extrapolate the Nusselt or Sherwood numbers to zero driving force. A simpler method which is adequate for measurements involving small driving forces (eg. $\Delta T=20^\circ$ F.) is to subtract previously measured natural convective transfer rates for the same corresponding driving force. The validity of this technique was established in the theoretical analysis. It is also desirable to recognise effects of local surface temperature variation in evaluating the effective driving force, which is possible only by experimentally measuring this variation around the sphere.

An often neglected effect is a finite momentum velocity normal to the interface associated with mass transfer. The "blowing velocity" yields smaller temperature and concentration gradients by increasing the boundary layer thickness, thus decreasing the heat or mass transfer coefficient. Such effects for spheres have been estimated by analytical methods (18,19) which were discussed earlier. Figure 66 illustrates the effect of the blowing parameter, which is a dimensionless velocity normal to the surface, on the ratio of the heat transfer coefficient with mass transfer to that without. For the measurements involving the porous spheres (61-64) the theoretical analysis predicted a 7 percent decrease in heat transfer. The single experimental point represents the average of data obtained for the 0.5 inch and 1.0 inch silver and porous spheres (60-64) corresponding to a blowing parameter of 0.1. An effect of this magnitude has also occurred in the work of other investigators (26, 53, 74, 75-84, 88, 89) carried out in wind tunnels (65-69). When the area of the sphere cross section is comparable to the area of the tunnel working section, the average velocity past the sphere is increased by the amount of reduction in tunnel area or "solid blockage" and the wake is distorted somewhat, resulting in "wake blockage". Corrections for both these effects were described

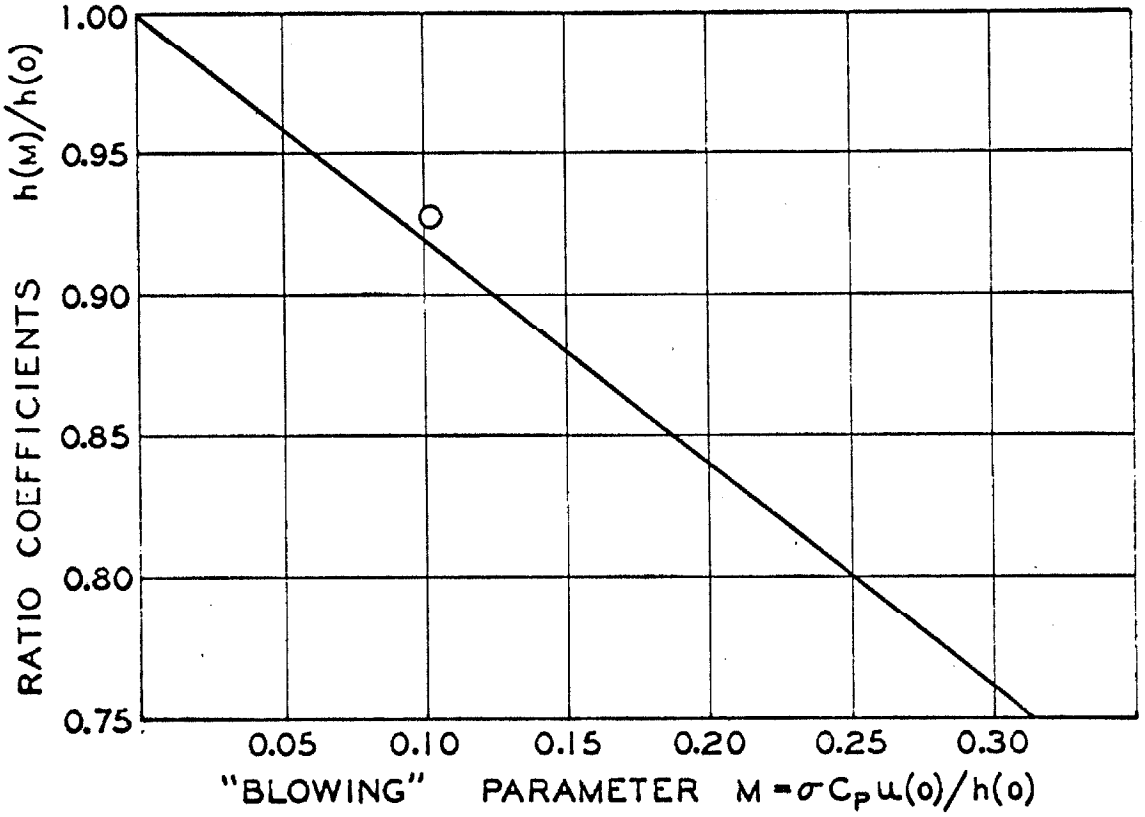

Fig. 66. Effect of "blowing parameter" upon material transport

earlier, and only for the data of Wadsworth (69) were they necessary. In addition, these exists a slight alteration of the velocity profile as the free-stream turbulence is varied, emphasizing that corrections for local velocity can be made accurately only from a detailed knowledge of the actual velocity profile prevailing at the time of measurement.

RECENT MEASUREMENTS FROM THE 1.5 INCH INSTRUMENTED SPHERE

Detailed local measurements were made with the calorimeter-instrumented sphere, described in the design section, particularly to refine the local mechanism of transport more precisely in the areas of interest and to check out the operation of this equipment for its use in the packed array of spheres, described in Part III. The analysis of local macroscopic transport from spherical surfaces presented in the previous section was completed several years before the 1.5 inch instrumented sphere was completed in the Instrument Shop, after having been delayed for about one and a half years. The presentation herein is, therefore, understandably brief and shall represent a survey of particular areas of interest in local transport. This study will be continued in considerably more detail by another graduate student.

The first experimental work to be carried out involving the 1.5 inch copper sphere was to calibrate all of the internal thermocouple junctions and the differential thermocouple junction in situ over the necessary range of temperature, 65° - 110° F. The calibration standard was a platinum-resistance thermometer (#1019), placed in a well insulated enclosure with the sphere. The room temperature was varied over a period of several days to allow sufficient time for steady-state conditions to be reached and each of the junction potentials was recorded.

The thermal losses in the form of conduction through the stem, radiation away from the heated sphere to the colder surroundings, and natural convection transport from the spherical surface were measured directly. The conduction through the supporting stem could, indeed, be reduced to negligible limits by carefully adjusting the stem compensating heater so that the temperature gradient in the stem where it joins the spherical surface just exactly vanishes. Three thermocouples were attached to the stem;

arranged at two locations on the stem one-half inch apart near the point of stem juncture with the sphere and at the stem compensating heater. The thermal loss measurements in the Heat Transfer Laboratory were found to be substantially influenced by residual air currents in the room and from the 6 x 6 jet duct. These prevailing convective effects were estimated and subtracted from the thermal losses.

The velocity profile at the working section of the 6 x 6 jet was measured over the range of Reynolds number from 5200 to 68,000 at the low turbulence prevailing in the free jet, which was estimated (92) to be 0.013, and is shown in Figure 67. The working section of the profile remained flat over a distance greater than twice the sphere diameter. At the higher velocities a small decrease was observed just upstream of the sphere by about one-half inch. The characteristic velocity was taken to be that velocity prevailing at the working section without the effects of the presence of the sphere or the confining effects of the jet walls. At the highest turbulence level of 0.256 small inhomogenieties in velocity across the jet were observed which could be explained from the proximity of the punched-plate grid.

The overall Frössling number was calculated from the heat loss from the main sphere heater after having subtracted off the measured stagnant heat loss at the corresponding temperature driving force. Corrections were made for the stem area and calorimeter area which were unavailable for transport. Also the average over the surface area of the five surface thermocouples was calculated and used in obtaining the effective driving force for the overall transport. The average variation in surface temperature was about 0.4° F., with the rotating half of the sphere remaining somewhat warmer. This surface temperature variation remained invariant with the conditions of flow and thermal flux.

The experimentally determined Frössling numbers are shown in Figure 68 as a function of the square root of the Reynolds number and turbulence level of the free-stream. The detailed measurements are given in

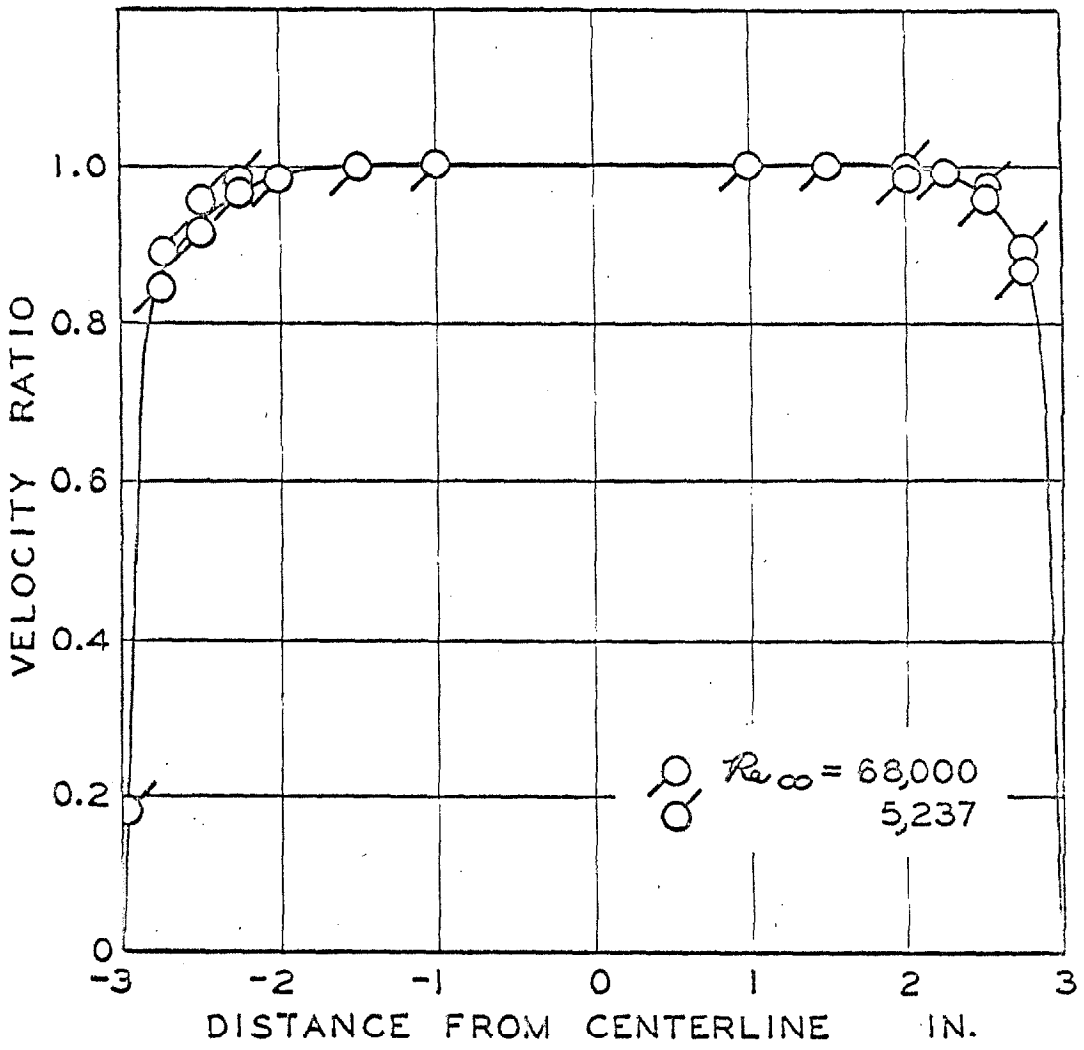

Figure 67. Velocity Profile Across the 6 x 6 inch Free Jet.

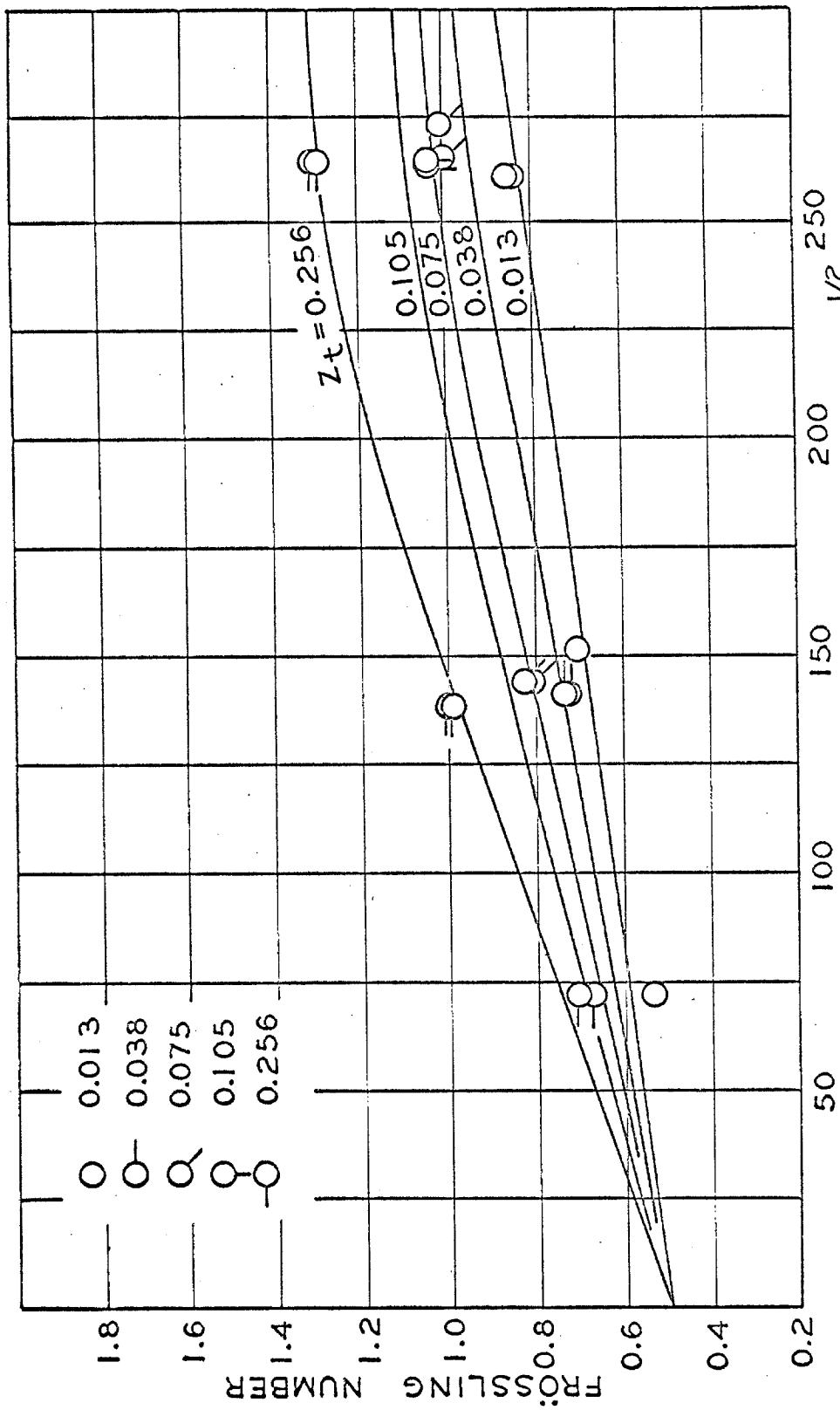

Figure 68. Effect of Reynolds Number upon the Overall Frössling Number from the 1.5-inch Sphere.

Table 19. As in the measurements from the 1.5 inch cylinder the experimental reproduceability was about 0.9%, remaining somewhat greater for measurements involving small temperature driving forces or low flow rates. The average temperature driving force used in these measurements was 10° F. The trends of Figure 68 compare almost exactly to those presented earlier for the 1.5 inch cylinder, with the effects of turbulence somewhat smaller, as well as to measurements of Vliet (76), Linton (75), and Sage and coworkers (58, 60-64) discussed earlier and shown in Figure 62. The solid curves shown in the latter figure appear somewhat higher than these recent data from the 1.5 inch sphere, however, these least square, regression curves were greatly biased by the large mass of data at the lower Reynolds numbers ($Re_\infty < 4000$) which were undoubtedly affected by residual natural convection. These data in Figure 68 together with that of recent authors begin to establish the quantitative effects of turbulence with considerably more certainty. A cross plot of Figure 68 shows the effects of turbulence to be nearly linear, and the influence is found to increase strongly with increased Reynolds number.

The local transport measurements from the 1.5 inch calorimeter-instrumented sphere are particularly interesting. As shown in Figure 70 in terms of the Frössling number and the cosine of the polar angle measured from the forward stagnation point, the data reveal a surprising degree of finer detail than was possible from the previous data analyzed in the preceding section. These results are shown for the three Reynolds numbers studied as a function of the free-stream turbulence level. There are several important points to note from this figure. The Frössling number is substantially increased in the region of the laminar boundary layer prevailing on the surface of the forward hemisphere with increases in the turbulence level of the free stream outside the boundary layer. The point of boundary layer separation is definitely delayed as a result of increased turbulence and the

TABLE 19: EXPERIMENTAL RESULTS FOR LOCAL AND MACROSCOPIC TRANSPORT FROM THE 1.5 INCH SPHERE.

		Test	654	655	656	657	658
		Nu*	34.308	45.59	122.59	105.41	92.39
		Re_∞	5237.6	5237.8	19,266.9	20886.2	19967.9
		Z_t	0.013	0.256	0.256	0.075	0.038
		Fs*	0.5326	0.7077	0.9925	0.8196	0.7348
Polar Angle	Cos γ	ν_∞/ν_o	0.9836	0.9877	0.9881	0.9863	0.9847
36.87	0.8	Fs=	-	1.0391	1.3595	1.1525	1.1261
45.57	0.7		0.8718	1.0269	1.3109	1.1045	1.0600
53.13	0.6		0.8614	-	1.2861	1.0567	1.0138
60.00	0.5		0.7750	1.0323	1.2448	0.9906	0.9534
66.42	0.4		0.7508	-	1.1865	0.9364	0.8891
72.54	0.3		-	0.8767	1.1189	0.8441	0.7765
78.46	0.2		0.5906	-	1.0402	0.7073	0.6277
84.26	0.1		-	0.6938	0.9230	0.5323	0.4617
90.00	0.0		0.3526	0.5997	0.7892	0.4132	0.3539
95.74	-0.1		0.2876	0.4608	0.6793	0.4188	0.3871
101.54	-0.2		0.2972	0.4022	0.6640	0.5348	0.4404
107.46	-0.3		0.3368	0.4054	0.7660	0.6359	0.4725
113.58	-0.4		0.3464	0.4548	0.8952	0.7048	0.5304
120.00	-0.5		0.3457	0.4820	0.9219	0.7033	0.5554
126.87	-0.6		0.3426	0.4815	0.8597	0.6793	0.5422
134.43	-0.7		0.3338	0.4648	0.7666	0.7191	0.5758
143.13	-0.8		0.3451	0.5439	0.7525	0.8562	0.7236
150.00	-0.86602		0.3587	0.6618	0.8435	0.9908	0.8949

TABLE 19: (Cont.)

		Test	659	660	661	662	663
		Nu*	95.16	197.30	238.07	241.59	302.06
		Re_∞	22953.8	67788.7	70240.4	69872.7	69939.4
		Z_t	0.013	0.013	0.075	0.105	0.256
		Fs*	0.7058	0.8513	1.0094	1.0270	1.2835
Polar Angle	Cos γ	ν_∞/ν_o	0.9843	0.9841	0.9865	0.9879	0.9911
36.87	0.8	Fs=	1.1020	1.1554	1.2285	1.3109	1.5320
45.57	0.7		1.0470	1.1386	1.1873	1.2595	1.5028
53.13	0.6		0.9956	1.0971	1.1270	1.2137	-
60.00	0.5		0.9446	1.0210	1.0861	1.1625	1.4420
66.42	0.4		0.8891	0.8940	1.0351	1.1218	-
72.54	0.3		0.7771	0.7474	0.9778	1.0576	1.3321
78.46	0.2		0.6245	0.5401	0.9110	0.9928	-
84.26	0.1		0.4664	0.4955	0.7914	0.9003	1.2012
90.00	0.0		0.3418	0.4858	0.6577	0.7594	1.1296
95.74	-0.1		0.3748	0.5238	0.5546	0.6283	1.0620
101.54	-0.2		0.4606	0.5597	0.6163	0.6078	1.0323
107.46	-0.3		0.4978	0.6569	1.0003	0.8104	1.0780
113.58	-0.4		0.4981	0.7312	1.2124	1.1175	1.2458
120.00	-0.5		0.4762	0.7981	1.2285	1.1961	1.3464
126.87	-0.6		0.4694	0.8164	1.1178	1.0933	1.2972
134.43	-0.7		0.5142	0.8597	1.0005	0.9409	1.2082
143.13	-0.8		0.6428	0.9911	0.9407	0.8233	1.0569
150.00	-0.86602		0.7857	1.1426	1.0011	0.8653	1.1163

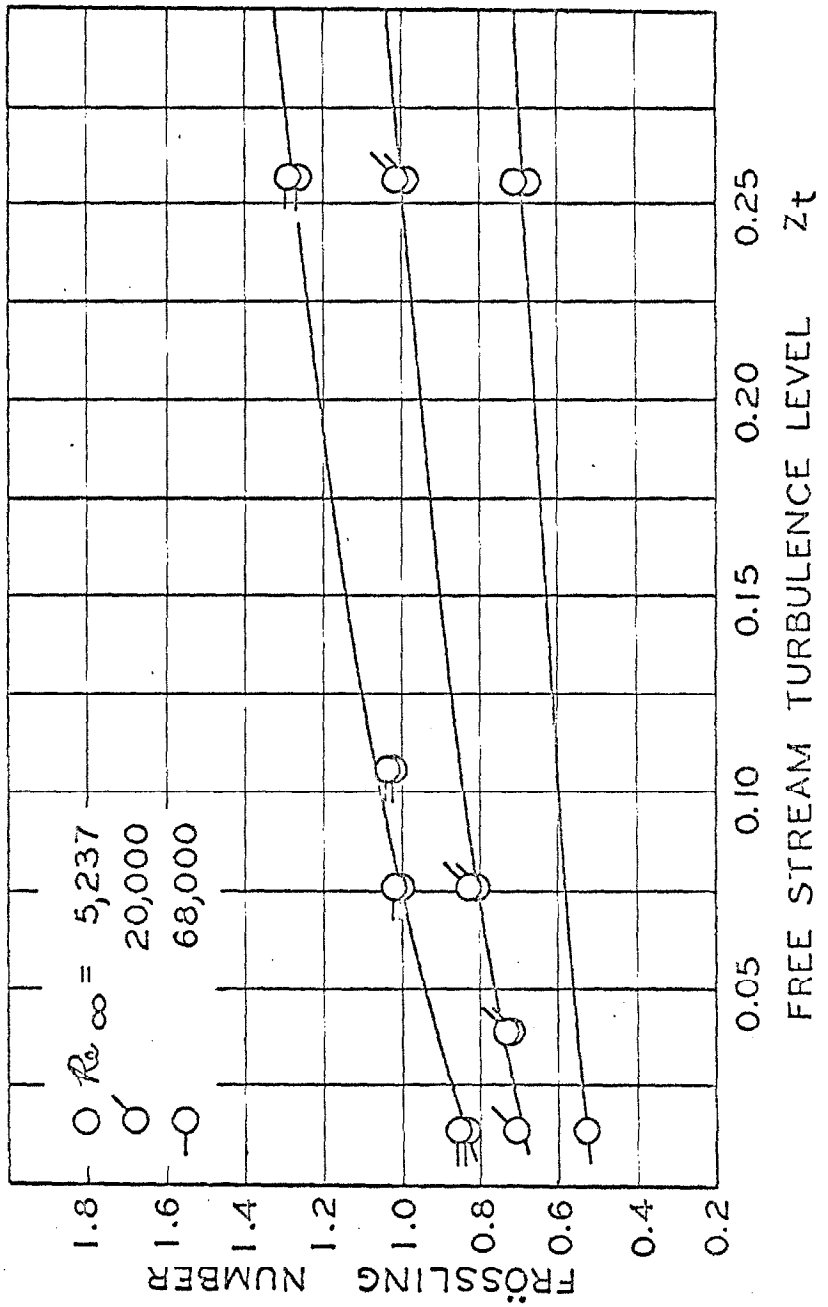

Figure 69. Effect of Turbulence Level on the Overall Frössling Number.

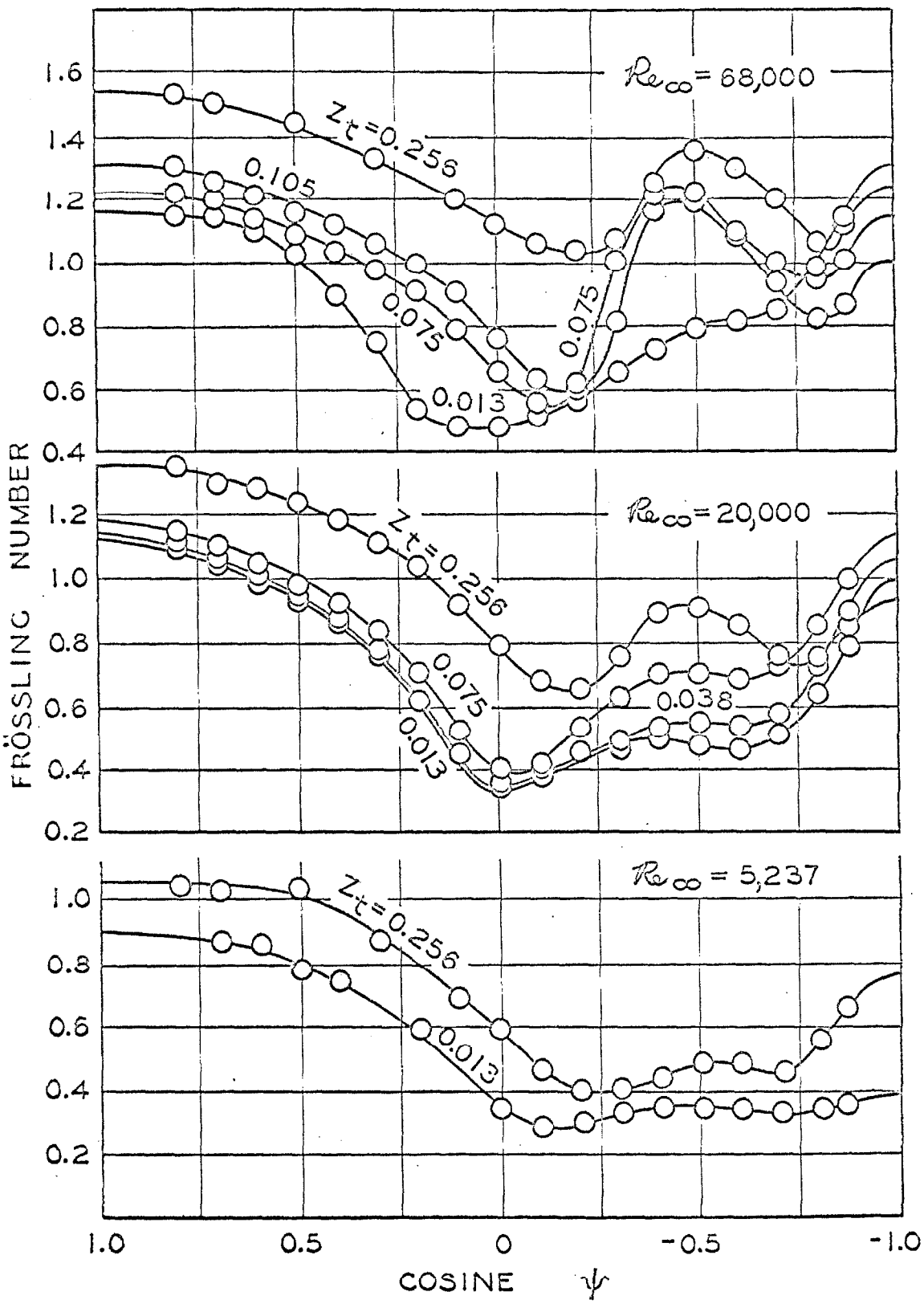

Figure 70. Local Transport From the 1.5-inch Sphere at Several Reynolds Numbers.

boundary layer reattaches in the rear hemisphere at about 120° . This reattached boundary layer then separates at about 135° . There are two regions of separated, wake-flow and two regions with an attached boundary layer. The primary point of separation is definitely moved forward as a result of the adverse pressure gradient increasing with increasing Reynolds number.

The direct effect of Reynolds number on the mechanism of local transport is best illustrated in Figure 71 at the low and high turbulence levels. At high turbulence there appears to be a uniform net increase with very little remaining variations. At low turbulence the Frössling number in the region of the forward stagnation point increases with Reynolds number. This increase, as in the cylinder case also, is believed to be from the alteration of the velocity profile with the movement of the position of separation and the increase in wake length. The local results for a Reynolds number of 68,000 are nearly symmetric and agree more closely with the theoretical predictions discussed earlier. This agreement, however, may be fortuitous in that one would expect better agreement for moderately low Reynolds numbers. Experimental verification of the theoretical limit has yet to be established precisely. One can only note here that experimentally the Frössling number at stagnation is lower than theory.

The sensitivity of the point of laminar boundary layer separation on the free-stream turbulence and Reynolds number is obvious from Figure 72. Separation is always delayed with increasing turbulence and is advanced with increased Reynolds numbers at moderate Reynolds numbers. The point of separation is again delayed at the combined conditions of high turbulence- and high Reynolds number-flows. This experimentally verified migration of separation is fundamental to the entire transport mechanism over the spherical surface as discussed in detail earlier on theoretical grounds. These experimental results agree very closely with those obtained from the 1.5 inch cylinder, and again suggest that the mechanisms are indeed completely analogous.

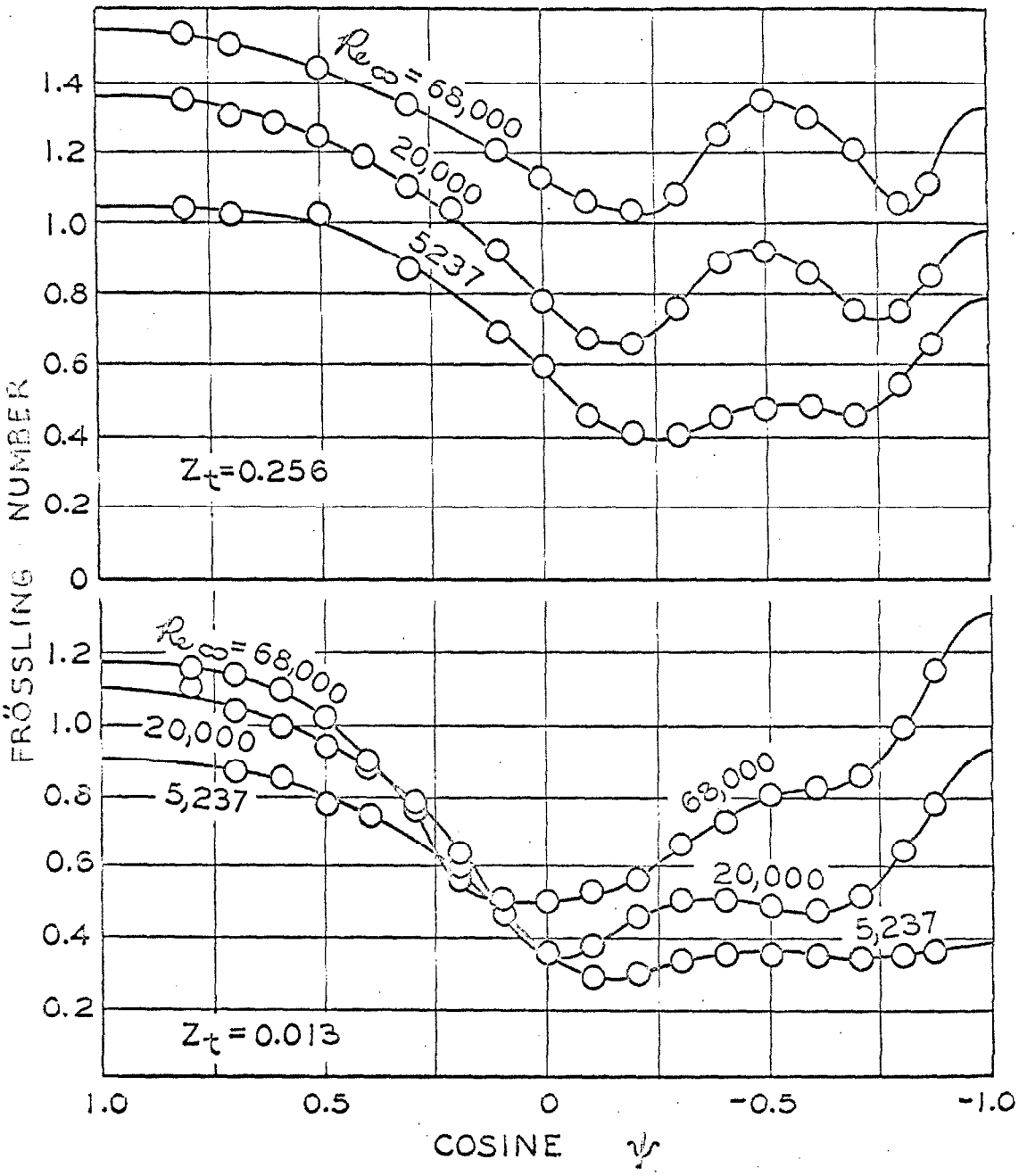

Figure 71. Local Transport From the 1.5-inch Sphere at Low and High Turbulence.

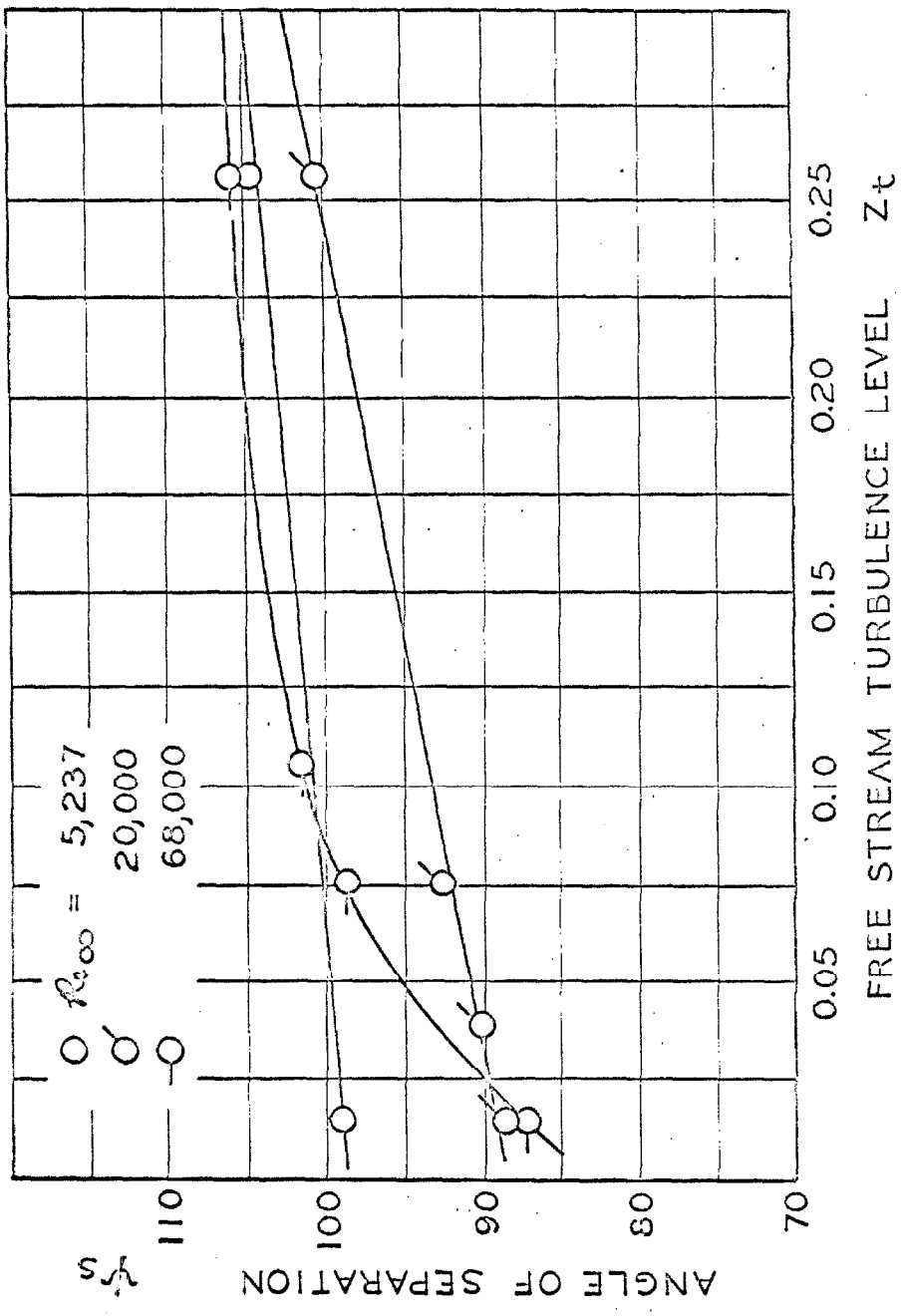

Figure 72. The Migration of the Point of Separation.

CONCLUSIONS

The major conclusions concerning transport from cylinders and spheres in turbulently flowing streams developed in Part II of this thesis shall be enumerated as follows:

1. A useful dimensionless group, termed the Frössling group, has been developed from similarity solutions to the equations of motion and of energy.
2. The local Frössling number at the forward stagnation point of both cylinders and spheres was measured experimentally and found to increase uniformly with the turbulence level of the free-stream.
3. The laminar boundary was found to separate around 100° and then reattach to the surface at about 120° and again separate near 140° .
4. The point of separation was found to depend systematically on the Reynolds number and the turbulence level of the flowing fluid stream.
5. As a result of the migration of separation the separated wake transport depended to a greater degree on the Reynolds number than did the transport in the laminar boundary layer.
6. The Frössling number was found to increase slightly with Reynolds number near the stagnation points of cylinders and spheres, and it is expected to be a result of an alteration in velocity profile.
7. The local pressure coefficient was measured for the cylinder and found to remain unity at the forward stagnation and was unaffected by turbulence. Alteration with flow conditions occurred in the region of separation.
8. The transition to supercritical flow was established from correlating the heat transfer measurements with Frössling number, and the effect of turbulence on the transition Reynolds number was found to agree with drag measurements for both cylinders and spheres.

LIST OF REFERENCES

1. Schlicting, H., Boundary Layer Theory, translated by Dr. J. Kestin (McGraw-Hill, N. Y., 1960) 4th edition, 647 pp.
2. Knudsen, J. G., and D. L. Katz, Fluid Dynamics and Heat Transfer, (McGraw-Hill, N.Y., 1958), 576 pp.
3. Eckert, E. R. G., and R. M. Drake, Heat and Mass Transfer, (Mc Graw-Hill, N. Y., 1959), 530 pp.
4. Seban, R. A., "The Influence of Free Stream Turbulence on the Local Heat Transfer From Cylinders," Trans. A.S. M.E., J. Heat Transfer 82, 101-107 (1960)
5. Frössling, Nils, "Evaporation, Heat Transfer, and Velocity Distribution in Two-Dimensional and Rotationally Symmetric Laminar Boundary Layer Flow," NACA TM 1432 (1958).
6. Frössling, Nils, "On the Evaporation of Falling Drops," Gerlands, Beitrage zur Geophysik, Band 52, Heft 1/2, 170-216 (1938).
7. Squire, H. B., "Heat Transfer Calculations for Aerofoils," ARC Reports and Memoranda, No. 1986, Nov. 1942.
8. Morse, H. W., "On Evaporation From the Surface of a Solid Sphere," Proc. Am. Acad. Arts and Sci., 363-367 (1910).
9. Langmuir, I., "The Evaporation of Small Spheres," Phys. Rev. 12, 368-370 (1918).
10. Sibulkin, M, "Heat Transfer Near the Forward Stagnation Point of a Body of Revolution," J. Aero. Sci. 19, 570-571 (1952).
11. Rosenhead, L., Laminar Boundary Layers, (Oxford at the Clarendon Press, 1963), 687 pp.
12. Brown, W. S., C. C. Pitts, and G. Leppert, "Forced Convection Heat Transfer from a Uniformly Heated Surface," Trans. A. S. M. E.,

J. Heat Transfer 84, 133-140 (1962).

13. Maskell, E. C., "A Theory of the Blockage Effects on Bluff Bodies and Stalled Wings in a Closed Wind Tunnel," Royal Aircraft Establishment, Rpt. No. Aero. 2685, Nov. 1963.

14. Grove, A. S., F. H. Shair, E. E. Petersen, Andreas Acrivos, "An Experimental Investigation of the Steady Separated Flow Past a Circular Cylinder," J. Fluid Mech. 19, 60-80 (1964).

15.5 Pope, A., Wind Tunnel Testing, (New York: Wiley & Sons, 1954), 2nd edition.

15. Shair, F. H., A. S. Grove, E. E. Petersen, and Andreas Acrivos, "The Effect of Confining Walls on the Stability of the Steady Wake Behind a Circular Cylinder," J. Fluid Mech. 17, 546-550 (1963).

16. Cuffel, R. F., Ph.D. Thesis, California Institute of Technology, Pasadena, California (1964).

17. Yuge, T., "Theory of Distributions of the Coefficients of Heat Transfer of Two-Dimensional Bodies of Various Shapes," Reports of the Institute of High Speed Mechanics, Tohoku University, (Sendai, Japan), Vol. 6, No. 58, pp. 153-173 (1956)

18. Short, W. W., "Heat Transfer and Sublimation at a Stagnation Point in Potential Flow", J. Appl. Mech. 27, 613-616 (1960).

19. Sage, B. H., and P. A. Longwell, Comments on: "Heat Transfer and Sublimation at a Stagnation Point in Potential Flow," J. Appl. Mech. 28, 471-473 (1961).

20. Yuge, T., "Experimental on Heat Transfer From Spheres Including Combined Natural and Forced Convection," Trans. A. S. M. E., J. Heat Transfer 82, 214-220 (1960).

21. Klyachko, L. S., "Heat Transfer Between a Gas and a Spherical Surface with the Combined Action of Free and Forced Convection," Trans. A. S. M. E., J. Heat Transfer, 85, 355-357 (1963).

22. Sparrow, E. M., and J. L. Gregg, "The Variable Fluid-Property Problem in Free Convection," Trans. A. S. M. E. 80, 879-886 (1958).

23. Reiher, H., VDI Forsch. Gebiete Ingenieurw, Heft. 269 (1925)

24. Goukhman, A., V. Joukovsky, and L. G. Loitzianski, Tech. Phys. (U. S. S. R.) 1, 221 (1934).

25. Comings, E. W., J. T. Clapp, and J. F. Taylor, "Air Turbulence and Transfer Processes -- Flow Normal to Cylinders," Ind, and Eng. Chem. 40, 1076-1082 (1948).

26. Maisel, D. S., and T. K. Sherwood, "Evaporation of Liquids into Turbulent Gas Streams ," Chem. Eng. Progr. 46, 131-138 (1950).

27. Maisel, D. S., and T. K. Sherwood, "Effect of Air Turbulence on Rate of Evaporation of Water," Chem. Eng. Progr. 46, 172-175 (1950).

28. Giedt, W. H., "Effect of Turbulence Level of Incident Air Stream on Local Heat Transfer and Skin Friction on a Cylinder," J. Aero. Sci. 18 , 725-730, 760 (1951).

29. Kestin, J., and R. F. Maeder, "Influence of Turbulence on Transfer of Heat from Cylinders, " NACA TN 4018 (1957).

30. Van der Hegge Zijnen, B. C., "Heat Transfer from Horizontal Cylinders to a Turbulent Air Flow," Appl. Sci. Res. 7A, 205-223 (1958).

31. Seban, R. A., "The Influence of Free Stream Turbulence on the Local Heat Transfer From Cylinders," Trans. A. S. M. E., J. Heat Transfer 82, 101-107 (1960).

32. Schnautz, J. A., "Effect of turbulence Intensity on Mass Transfer from Plates, Cylinders, and Spheres in Air Streams," Ph. D. Thesis, 1958, Oregon State College, Corvallis (Univ. Microfilm No. 33920).

33. Churchill, S. W., and J. C. Brier, "Convective Heat Transfer from a Gas Stream at High Temperature to a Circular Cylinder Normal to the Flow," Chem. Eng. Progr. Symp. Ser. 51, No. 17, 57-66 (1955).

34. Douglas, W. J. M., and S. W. Churchill, "Recorrelation of Data for Convective Heat Transfer Between Gases and Single Cylinders with Large Temperature Difference," Chem. Eng. Progr. Symp. Series, 52, 23-28 (1956).

35. Perkins, H. C., and G. Leppert, "Forced Convection Heat Transfer from a Uniformly Heated Cylinder," Trans A. S. M. E., J. Heat Transfer, 84, 257-261 (1962).

36. Richardson, P. D., "Estimation of the Heat Transfer From the Rear of an Immersed Body to the REgion of Separated Flow," Aeron. Res. Lab., Office of Aerospace Res., USAF, AD No. 290339, ARL 62-423 (1962).

37. Richardson, P. D. "Heat and Mass Transfer in Turbulent Separated Flows," Chem. Eng. Sci. 18, 149-155 (1963).

38. Grafton, R. W., "Prediction of Mass Transfer from Spheres and Cylinders in Forced Convection," Chem. Eng. Sci. 18, 457-466 (1963).

39. Van der Hegge Zijnen, B. G., "Measurements of the Intensity, Integral Scale, and Microscale of Turbulence Downstream of Three Grids in a Stream of Air", Appl. Sci. Res 7A, 149-174 (1957).

40. Davis, Leo, 'Measurements of Turbulence Level Behind a Set of Square-Mesh Grids and Correlation with Grid Pressure Loss," Rept. 3-22, Jet Propulsion Laboratory, Calif. Inst. of Technology, 1950.

41. Davis, Leo, "Measurement of Turbulence Decay and Turbulent Spectra Behind Grids," Rept. 3-17, Jet Propulsion Laboratory, Calif. Inst. of Technology, 1952.

42. Couch, H. T., Proposition 5, Ph. D. Thesis, Calif. Inst. of Technology 1966.

43. Hilpert, R., "Warmeabgabe von Geheigten Drähten und Rohren im Luftstrom," Forsch. Gebiete Ingenieurw, 4, 215-244 (1933).

44. Couch, H. T., "Part II: Heat and Mass Transfer from a Cylinder Placed in a Turbulent Air Stream -- Sherwood and Frössling Numbers as a Function of Free Stream Turbulence Level and Reynolds Number," Ph.D. Thesis, Calif. Inst. of Technology, 1966.

45. Fage, A., "On *Reynolds Numbers of Transition*," Brit. AEro. Comm. Research and Memoranda 1765 (1936).

46. Sutera, S. P., "Vorticity Amplification in Stagnation-Point Flow and Its Effect on Heat Transfer," J. Fluid Mech. 21, 513-534 (1965).

47. Kuethe, A. M., W. W. Willmarth, and G. H. Crocker, "Turbulence Field Near the Stagnation Point on Blunt Bodies of Revolution," Proc. Heat Tranfer Fluid Mech. Inst. 1961, Stanford Univ. Press, pp. 10-22 (1961).

48. Büyüktür, A. R., J. Kestin, and P. F. Maeder, "Influence of Combined Pressure Gradient and Turbulence on the Transfer of Heat from a Plate," Int. J. Heat Mass Transfer 7, 1175-1185 (1964).

49. Grove, A. S., F. H. Shair, E. E. Petersen, and Andreas Acrivos, "An Experimental Investigation of the Steady Separated Flow Past a Circular Cylinder," J. Fluid. Mech. 19, 60-80 (1964).

50. Morse, H. W., "On Evaporation From the Surface of a Solid Sphere," Proc. Am Acad. Arts and Sci., 45, 363-367 (1910).

51. Langmuir, I., "The Evaporation of Small Spheres," Phys. Rev. 12, 368-370 (1918).

52. Fuchs, N., "Concerning the Velocity of Evaporation of Small Droplets in a Gas Atmosphere," NACA TM 1160 (1947).

53. Powell, R. W., "Further Experiments on the Evaporation of Water from Saturated Surfaces," Trans. Inst. Chem. Engrs. (London), 18, 36-55 (1940).

54. Kramers, H., "Heat Transfer from Sphers to Flowing Media," Physica 12, 61-80 (1946).

55. Ranz, W. E., and W. R. Marshall, "Evaporation from Drops", Parts I and II, Chem. Eng. Progr. 48, 141-146, 173-180 (1952).

56. Tang, Y. S., J. M. Duncan, and H. E. Schweyer, "Heat and Momentum Transfer Between a Spherical Particle and Air Streams," NACA TN 2867 (1951).

57. Ingebo, R. D., "Vaporization Rates and Heat-Transfer Coefficients of Pure Liquid Drops," NACA TN 2368 (1951).

58. Hsu, N. T., K. Sato, and B. H. Sage, "Effect of Shape on Evaporation of Drops," Ind. and Eng. Chem. 46, 870-876 (1954).

59. Loitzianski, L. G., and B. Schwab, "The Thermal Scale of Turbulence," Tech. Phys. (U.S.S.R.) II, 414-430 (1935).

60. Sato, K., and B. H. Sage, "Thermal Transfer in Turbulent Gas Streams -- Effect of Turbulence on Macroscopic Transport from Spheres," Trans. A. S. M. E. 80, 1380-1386 (1958).

61. Brown, R. A. S., K. Sato, and B. H. Sage, "Material Transfer in Turbulent Gas Streams. Effect of Turbulence on Macroscopic Transport from Spheres," J. Chem. and Eng. Data 3, 263-272 (1958).

62. Short, W. N., R. A. S. Brown, and B. H. Sage, "Thermal Transfer in Turbulent Gas Streams, Effect of Turbulence on Local Transport from Spheres," 27, 393-402 (1960).

63. Brown, R.A.S., and B. H. Sage, "Material Transfer in Turbulent Gas Streams. Effect of Turbulence on Local Transport From Spheres," J. Chem. and Eng. Data, 6, 355-359 (1961).

64. Venezian, E., M. J. Crespo, and B. H. Sage, "Thermal and Material Transfer in Turbulent Gas Streams, One-Inch Spheres," A.I. Ch. E. J. 8, 383-388 (1962).

65. Lautman, L. G., and W. C. Droege, "Thermal Conductances about a Sphere Subjected to Forced Convection," Air Materiel Command, Serial No. AIRL A6118 50-15-3, 1950.

66. Xenakis, G., A. E. Amerman, and R. W. Michelson, "An Investigation of the Heat Transfer Characteristics of Spheres in Forced Convection," Wright Air Develop. Center, Wright-Patterson Air Force Base, Ohio, WADC Tech. Rept. 53-117, 1953.

67. Amerman, A. E., "An Investigation of the Heat-Transfer Characteristics of Spheres in Forced Convection," Wright Air Develop. Center, Wright-Patterson Air Force Base, Ohio, WADC Tech. Rept. 53-117, Suppl. 1, 1953.

68. Cary, J. R., "The Determination of Local Forced-Convection Coefficients for Spheres," Trans. A. S. M. E. 75, 483 (1953).

69. Wadsworth, J., "The Experimental Examination of the Local Heat Transfer on the Surface of a Sphere when Subjected to Forced Convection Cooling," Nat. Res. Council Can., Div. Mech. Eng., Rpt. No. MT-39, 1958.

70. Klyachko, L. S., "Heat Transfer Between a Gas and a Spherical Surface With the Combined Action of Free and Forced Convection," Trans. A.S.M.E., J. Heat Transfer 85, 355-357 (1963).

71. Yuge, T., "Experiments on Heat Transfer from Spheres Including Combined Natural and Forced Convection," Trans. A.S.M.E., J Heat Transfer 82, 214-220 (1960).

72. Torobin, L.B., and W. H. Gauvin, "Fundamental Aspects of Solids-Gas Flow, Part II: The Sphere Wake in Steady Laminar Flows," Canad. J. Chem. Eng. 37, 167-176 (1959).

73. Pasternak, I.S., and W. H. Gauvin, "Turbulent Heat and Mass Transfer from Stationary Particles," Canad. J. Chem. Eng. 38, 35-42 (1960).

74. Griffith, R. M., "Mass Transfer from Drops and Bubbles," Chem. Eng. Sci. 12, 198-213 (1960).

75. Linton, W.H., and K. L. Sutherland, "Transfer from a Sphere into a Fluid in Laminar Flow," Chem. Eng. Sci. 12, 214-229 (1960).

76. Vliet, G. C., G. Leppert, "Forced Convection Heat Transfer from an Isothermal Sphere to Water," Trans. A.S.M.E., J Heat Transfer 83, 163-175 (1961).

77. Evnochides, S., and G. Thodos, "Simultaneous Mass and Heat Transfer in the Flow of Gases Past Single Spheres," A.I.Ch.E. J. 7, 78-80 (1961).

78. Gupta, A., and G. Thodos, "Mass and Heat Transfer in the Flow of Fluids Through Fixed and Fluidized Beds of Spherical Particles," A.I.Ch.E. J. 8, 608-610 (1962).

79. McConnachie, J. T. L., and G. Thodos, "Transfer Processes in the Flow of Gases Through Packed and Distended Beds of Spheres," A.I.Ch.E. J. 9, 6-64 (1963).

80. Keey, R. B., and J. B. Glen, "Mass Transfer from Solid Spheres," Canad. J. Chem. Eng. 42, 227-232 (1964).

81. Garner, F. H., and R. W. Grafton, "Mass Transfer in Fluid Flow from a Solid Sphere," Proc. Roy. Soc., Ser. A, 224, 64-82 (1954).

82. Garner, F. H., and R. B. Keey, "Mass Transfer from Single Solid Spheres -- I. Transfer at Low Reynolds Numbers," Chem. Eng. Sci. 9, 119 (1958).

83. Garner, F. H., and R. B. Keey, "Mass-Transfer from Single Solid Spheres -- II. Transfer in Free Convection," Chem. Eng. Sci., 9, 218-224 (1959).

84. Garner, F. H., and R. D. Suckling,"Mass Transfer from a Soluble Solid Sphere," A.I.Ch.E. J. 4, 114-124 (1958).

85. Harriot, P., "A Random Eddy Modification of the Penetration Theory," Chem.Eng. Sci. 17, 149-154 (1962).

86. Galloway, T. R., and B. H. Sage, "Thermal and Material Transfer in Turbulent Gas Streams -- A Method of Prediction for Spheres," Int. J. Heat Mass Transfer 7, 283-291 (1964).

87. Lin, C. C., editor, High Speed Aerodynamics and Jet Propulsion, Vol. 5,

Turbulent Flows and Heat Transfer, (Princeton Univ. Press, N.Y., 1959) 549 pp.

88. Skelland, A. H. P., and A. R. H. Cornish, "Mass Transfer from Spheroids to an Air Stream," A.I.Ch.E. J. 9, 73-76 (1963).

89. Grafton, R. W., "Prediction of Mass Transfer from Spheres and Cylinders in Forced Convection," Chem. Eng. Sci., 18, 457-466 (1963).

90. Kinnard, G. E., F. S. Manning, and W. P. Manning, "A New Correlation for Mass Transfer from Single Spheres," Brit. Chem. Eng. 8, 326-327 (1965).

91. Lee, K., and H. Barrow, "Some Observations on Transport Processes in the Wake of a Sphere in Low Speed Flow," Int. J. Heat Mass Transfer 8, 403-409 (1965).

92. Chen, S.S., "Mass Transfer From a Cylinder to an Air Stream in Axisymmetrical Flow (An Experimental Study)," Ph.D. Thesis, Calif. Inst. of Technology, pg. 26, 1966.

93. Kendall, J. M., "The Design and Performance of Precision Oil Micromanometers," U.S. Naval Ordinance Laboratory, NAVORD Rpt. 6803, June 29, 1961.

94. Bathish, L. N., and B. H. Sage, "Thermal Transfer in Turbulent Gas Streams: Temperature Distribution in Boundary Flow About Spheres," A.I. Ch. E. J. 6, 693-697 (1960).

95. Baines, W. D., and E. G. Peterson, "An Investigation of Flow Through Screens," Trans. A.S.M.E. 73, 467-480 (1951)

96. Batchelor, G. K., and A. A. Townsend, "Decay of Vorticity in Isotropic Turbulence, " Proc. Roy. Soc. (London) Ser. A, 190, 534-550 (1947).

97. Batchelor, G. K., and A. A. Townsend, "Decay of Isotropic Turbulence in the Initial Period," Proc. Roy Soc. (london). Ser. A, 193, 539-558 (1948)

98. Batchelor, G.K., and A. A. Townsend, "Decay of Turbulence in the Final Period," Proc. Roy. Soc. (London) Ser. A, 194, 527-543 (1948).

99. Dryden, H. L., and G. B. Schubauer, "The Use of Damping Screens for the Reduction of Wind Tunnel Turbulence," J. Aero. Sci. 14, No. 4, 221-228 (1947).

100. Dryden, H. H., and G. B. Schubauer, W. C. Mock, and H. K. Scramstad, "Measurements of Intensity and Scale of Wind Tunnel Turbulence and Their Relation to the Critical Reynolds Number of Spheres," NACA No. 581 (1937).

101. Hall, A. A., "Measurements of the Intensity and Scale of Turbulence," Aero. Res. Comm. Research and Memoranda No. 1842 (London), 1938.

102. Hsu, N. T., and B. H. Sage, "Thermal and Material Transfer in Turbulent Gas Streams: Local Transport from Spheres," A. I. Ch. E. J. 3, 405-410 (1957).

103. Powell, R. W., "Further Experiments on the Evaporation of Water from Saturated Surfaces," Trans. Inst. Chem. Engrs. (London) 18, 36-55 (1940).

104. Steele, L. R., and C. J. Geankoolis, "Mass Transfer from a Solid Sphere to Water in Highly Turbulent Flow," A. I. Ch. E. 5, 178-181 (1959).

105. Rowe, P. N., K. T. Claxton, and J. B. Lewis, "Heat and Mass Transfer from a Single Sphere in an Extensive Flowing Fluid," Trans. Inst. Chem. Engrs. (London) 43, T14-31 (1965).

NOMENCLATURE

A = Empirical coefficient in Equation 117 for cylinders and Equation 126 for spheres.

A = Cross sectional area (ft^2)

A_o = Coefficient of Equation 54

b_o = Molecular covolume = $\frac{2}{3} \pi N_o \sigma^3$ (cc/gmole)

B = Coefficient of Equation 54

B = Second virial coefficient (cc/gmole)

B = Empirical coefficient of Equation 117 for cylinders and Equation 126 for spheres

B^* = Reduced second virial coefficient = B/b_o

C_i = Coefficient in Equation 45, $i=0,1,\ldots,\infty$

C = Third virial coefficient ($cc^2/gmole^2$)

C = Empirical coefficient in Equation 117 for cylinders and Equation 126 for spheres.

C^* = Reduced third virial coefficient = C/b_o^2

C = Time averaged concentration (lbs specie/ft^3)

C_D = Drag coefficient

C_P = Isobaric heat capacity (cal/gmole-°C. or Btu/lbmole-°F.)

C_p = Pressure coefficient = $(P_o - P_\infty)/(\frac{1}{2} \rho_\infty U_\infty^2)$

c = Instantaneous concentration (lbs specie/ft^3)

c' = Concentration fluctuation about C (lbs specie/ft^3)

D = Empirical coefficient in Equation 117 for cylinders and Equation 126 for spheres.

D_t = Empirical coefficient in Equation 129 for spheres

$\mathcal{D}$ = Binary diffusion coefficient (from Chapman-Cowling) (ft^2/sec)

d = Diameter of body (ft)

Fs = Frössling group defined by Equations 65 and 66 for cylinders and Equations 122 and 123 for spheres

f = Blasius function defined by Equation 31 or Equation 76

G = Dimensionless concentration = $(C-C_\infty)/(C_o-C_\infty)$

Gr = Grashoff group = $gd^3\beta(T_o-T_\infty)/\nu^2$

g = Local acceleration of gravity (ft/sec^2)

h = Heat transfer coefficient = $q/kA(T_o-T_\infty)$

i = Current flow (amps)

k = Thermal conductivity (cal/sec-cm-°C. or Btu/sec-ft-°F.)

Le = Lewis group = Sc/Pr

N_o = Avagadro's number (molecules/gmole)

Nu = Nusselt group = hd/k

n = Empirical exponents in Equation 117

m = Empirical exponents in Equation 117

Pr = Prandtl group = $\mu C_P/k$

P = Total pressure (atmospheres)

q = Local heat flux (Btu/ft^2-sec)

R = Universal gas constant (cal/gmole-°K. or ft^3-atmos./lbmole-°R.)

R = Electrical resistance (ohms)

Re = Reynolds group = $U_\infty d/\nu$

r, R = Radial coordinate (ft)

r = Recovery factor, defined by Equation 20

Sc = Schmidt group = $\nu/\mathfrak{D}$

Sh = Time averaged Sherwood group = $hd/\mathfrak{D}$

T = Absolute temperature (°K. or °R.)

t = Instantaneous absolute temperature (°K. or °R.)

T' = Temperature fluctuations about T (°K. or °R.)

t = Time (seconds)

U = Time averaged velocity in the x direction (ft/sec)

U_1 = Velocity in the x direction immediately outside the boundary layer (ft)

u = Instantaneous velocity in the x direction (ft/sec)

u' = Velocity fluctuations about U (ft/sec)

V = Time averaged velocity in the y direction (ft/sec)

V = Molal volume (cc/gmole)

v = Instantaneous velocity in the y direction (ft/sec)

v' = Velocity fluctuations about V (ft/sec)

W = Width of wind tunnel or free jet (ft)

W = Time averaged velocity in the z direction (ft/sec)

w = Instantaneous velocity in the z direction (ft/sec)

w' = Velocity fluctuations about W (ft/sec)

X = External body force in the x direction (lbf/ft^3)

x = Component coordinate (ft)

Y = External body force in the y direction (lbf/ft^3)

y = Component coordinate (ft)

Z = External body force in the z direction (lbf/ft^3)

z = Component coordinate (ft)

Z_t = Longitudinal turbulence level of the free stream = $\sqrt{\overline{(u')^2}}/U_\infty$

GREEK

α = Thermal diffusivity (ft^2/sec)

β = Isobaric thermal expansion coefficient = $\frac{1}{V}\left(\frac{\partial V}{\partial T}\right)_P$ $(°F.)^{-1}$

ϵ = Eddy coefficient (ft^2/sec)

η = Dimensionless similarity variable = $y\sqrt{U_1/\nu x}$

θ = Dimensionless temperature = $(T-T_\infty)/(T_o-T_\infty)$

μ = Viscosity of the media at position x, y, z (lbm/ft-sec)

ν = Kinematic viscosity = μ/ρ (ft^2/sec)

Φ = Functional relation defined in Equation 66 for cylinders

Φ_2 = Functional relation defined in Equation 85 for spheres.

Ψ = Stream function defined by Equation 34

ζ = Von Misses variable defined by Equation 105

ξ = Dimensionless distance = x/2R = x/d

τ = Dimensionless variable defined by Equation 57

ρ = Density of the media at position x, y, z (lbm/ft^3)

ρ^* = Reduced density = $b_o/V = \frac{2}{3}\pi N_o \sigma^3/V$

σ = Collision diameter for Lennard-Jones (n-6) or Morse potentials (Å)

Ω = Collision integral, see Part I

SUBSCRIPTS

A = Molecular specie A

a = Adiabatic wall temperature

B = Molecular specie B

d = of diffusion

eff = Effective quantity

h = of heat

m = of momentum

m = Quantity based on molecular properties

t = Quantity based on turbulent eddy coefficients (i.e. Equations 18 and 19)

o = at the surface

1 = at a position immediately outside the boundary layer

∞ = in the free stream

SUPERSCRIPTS

$\overline{(\quad)}$ = Time averaged quantity

* = Surface average of the local values

APPENDIX A6

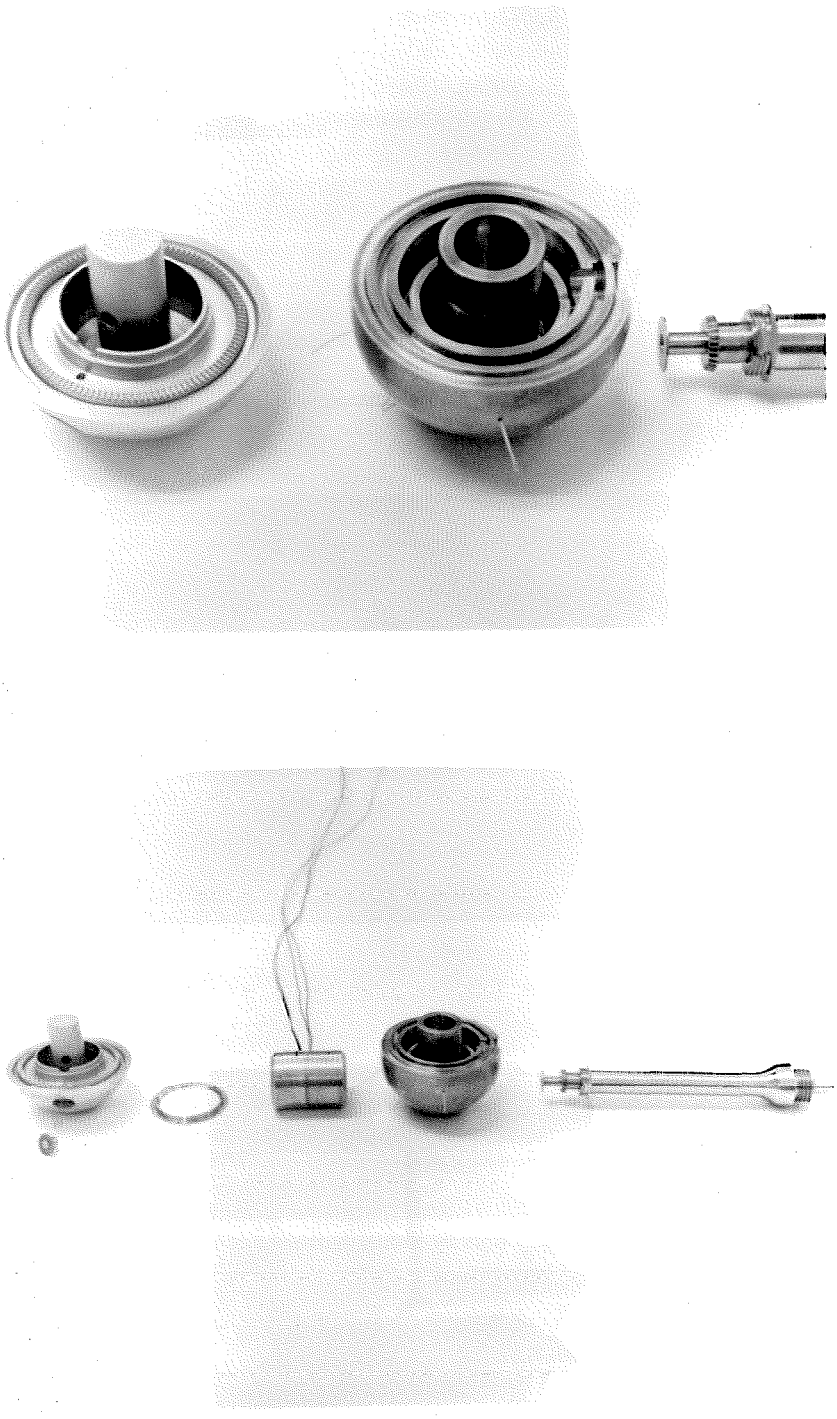

Figure 1. The 1.5 inch Sphere -- Disassembled.

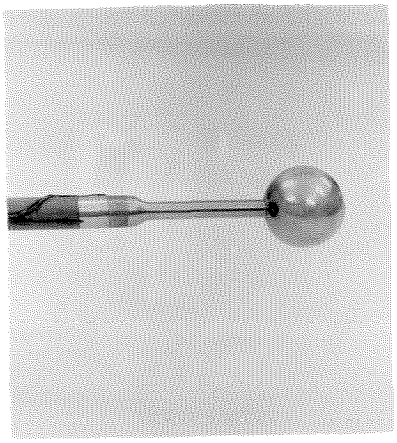

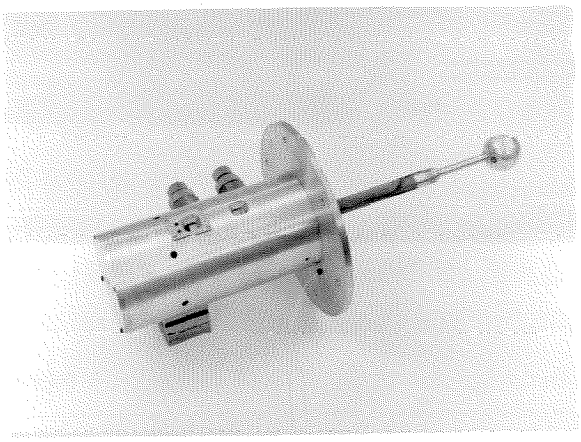

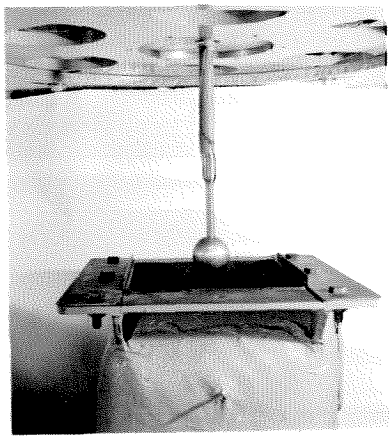

Figure 2. Three Views of the Assembled Sphere.

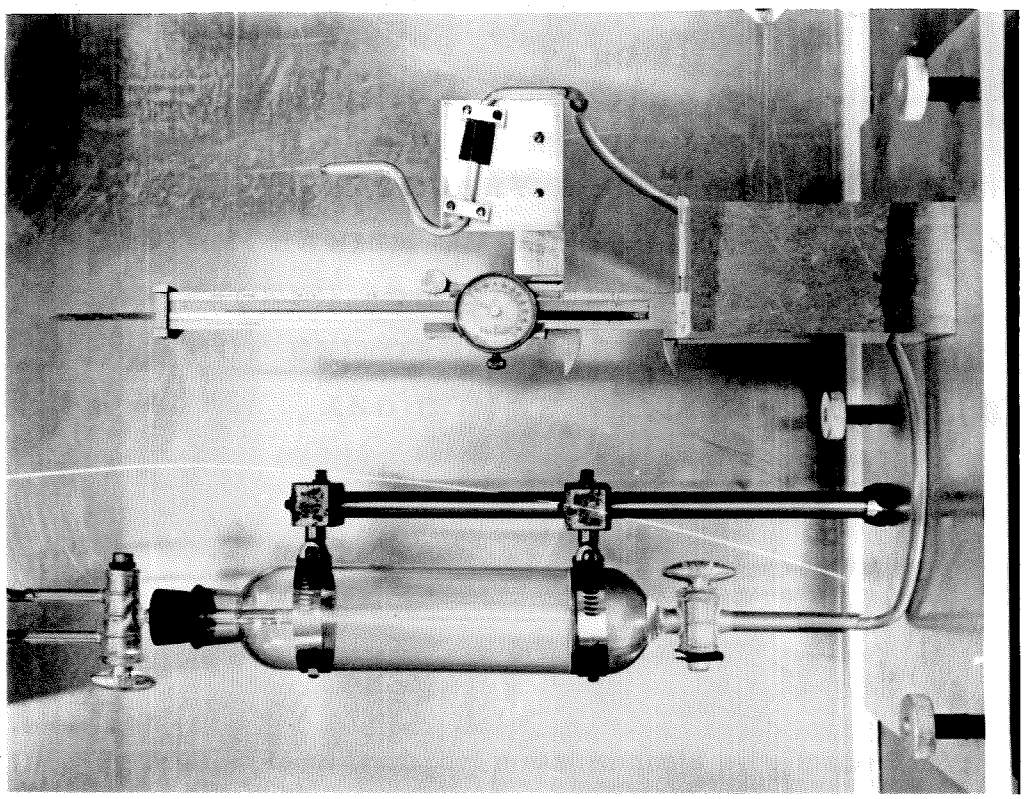

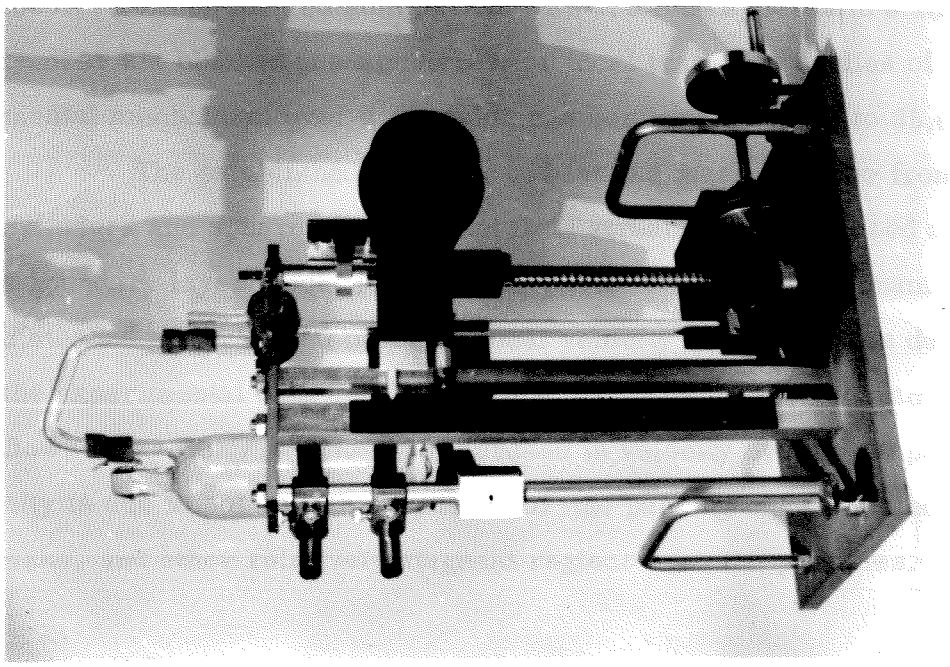

Figure 3. Two Micromanometers.

PART III

A BOUNDARY LAYER MODEL FOR THE MECHANISM OF FLUID-PARTICLE TRANSPORT IN PACKED, DISTENDED AND FLUIDIZED BEDS OF UNIFORM SPHERES, CYLINDERS, AND COMMERCIAL PACKING

SUMMARY

Detailed local transport measurements were made from a 1.5 inch diameter, calorimeter instrumented sphere placed in a turbulently flowing stream, where the effects of Reynolds number and artificially induced free-stream turbulence were studied. This sphere was placed in a 12 inch diameter, 20 inch long column packed with 1.5 inch spheres in a rhombohedral number six blocked passage array for local transport studies of the fundamental mechanism over a Reynolds number range of 9850 to 35,600.

The established behavior of heat and mass transfer from single cylinders and spheres in turbulent fluid streams has been used as a basis for a boundary layer model for the fluid-particle transport mechanism in packed, distended and fluidized beds. A local velocity in the array is determined from the experimental data and is used in a Reynolds number characterizing the flow, $Re'_{\infty}=Re_{\infty}/(\epsilon-\epsilon_b)$. The increase in velocity over the superficial velocity is due to not only the presence of the packing but also to boundary layer, wake, and other relatively stagnant regions near the particles. A chacteristic

turbulence intensity within the flow passage was obtained from available experimental data and found to agree with measured values. A single analytic equation was found to represent transport involving single spheres, packed arrays of spheres, short cylinders, and commerical packing; distended beds of spheres and fluidized beds of spherical particles. The overall standard deviation was 8.8% for single spheres and 9.8% for various types of packed arrays. This model predicted the height of a transfer unit in packed colums being irrigated with liquid within 12% for twelve cases involving both absorption and vaporization.

INTRODUCTION

The overall mechanism of fluid-particle transport in packed beds depends upon the local flow behavior in the interstices of the array of particles. Accurate methods of predicting transport in fixed and fluidized beds are becoming more necessary for developing more refined catalytic reactors, nuclear reactors, absorption towers, and the wide variety of fixed and fluidized bed operations. To improve the accuracy of current methods it is necessary to inquire into the basic mechanism of the local behavior with the aid of some fundamental model.

In the past, variations in the capillary flow model for porous solids have been used. In this analysis a model for the flow around a bluff body in a turbulent free stream is used for the heat and mass transport within the array of particles. Such a model involves the local velocity and free stream turbulence within the flow regions between the particles.

There has been an extensive background (1-26) of experimental work done in the past on transport in packed and distended arrays of various geometries as well as in fluidized beds. These data, emphasizing the very little local transport data (7, 16, 20, 23), have been most useful in developing this model.

This analysis of the mechanism of transport in packed beds was begun in 1963. During this work it was necessary to study the molecular transport properties of polyatomic gases and the effects of turbulence on the forced convective transport involving single spheres (27-28) and cylinders (29) in considerably more detail than previously in order to better understand the transport in a regular array of spheres and other shapes. The early results in comparison to single particle behavior have suggested the action of intensities of turbulence in excess of 10% upon the thermal boundary layers about

surfaces in the void space of the array and indicated that the effective local velocity was considerably higher than predicted by the quotient of the superficial velocity and the particle voidage. These early results are presented in Appendix A7. Recently Mickley, Smith, and Korchak (30) have made rather detailed measurements in the interstices of a rhombohedral number three array (31) of the local velocity profile and properties of local turbulence. They found turbulence intensities of 15% near the wall which increased to about 50% in the center of the void and apparently very little, if any, eddy shedding behind the particles.

There have been several theoretical and semi-theoretical predictions worthy of note for pressure drop through packed beds (7,31-34) which have been most successful; however, analogies to transfer of heat or mass (35,36) have, for the most part, not been satisfactory. The most successful theoretical work in multiple particle systems has been in the limit of low velocity. The "Free Surface" model involving flow in the envelope between concentric spheres has been useful in predicting pressure drop (37) and heat and mass transport (38) at low Reynolds number. Also at low flow Galerkin's error distribution method has been used to predict friction factors in packed beds in cubic arrays within 5%. For higher Reynolds numbers (less than 1000) Carberry (39) used a boundary layer model in a fixed bed, which postulated the formation of a boundary layer which was repeatedly developed and destroyed through the array. Kusik and Happel (40) combined the boundary layer model and free surface model to predict fixed bed transport for Reynolds numbers above 100. This practical model predicted the proper magnitude of the transport but too little dependence upon Reynolds number.

This part of the thesis is intended to reveal, as a boundary layer model, a possible mechanism for transport of both liquids and gases in arrays of particles in the form of packed, distended, or fluidized beds through some detailed local heat transfer measurements in the rhombohedral number six

array with a blocked passage. An extensive analysis of all known data is made over a wide range of Prandtl, Schmidt, and Reynolds numbers for a large variety of packing configurations and voidage in order to present a method of prediction which can be relied upon.

EXPERIMENTAL

The packed column consisted of a 12 inch diameter tube 20 inches in length as in Figure 1. The packing was made up of selected celluloid table tennis spheres, 1.4656 inches in diameter, with an average (from 135 measurements) variation in diameter of 0.0041 inches, from asphericity as well as variation from sphere to sphere. The best spheres were selected for the array around the instrumented sphere. The celluloid spheres were glued together with a drop of polystyrene cement at the twelve points of contact in a rhombohedral number six blocked passage array. The geometry of such an array as well as other possible geometries has been described by Martin and McCabe (31). The flow was normal to the basal plane of the typical hexagonal cell. Partial spheres were used at the wall to fill out the array and reduce the wall effects. These partial spheres were filled with polyurethane foam and then cut to fit the curvature of the column wall. This was done in order to prevent distortion of the partial spheres at the higher flow rates.

The instrumented sphere was 1.4666 ± 0.0007 inches in diameter and constructed out of high purity copper. The sphere is divided into two halves as shown in Figure 45 in the previous section. The larger half is fixed to the stem, while the smaller half rotates. The rotating half is driven by the outer drive sleeve in the stem with respect to the stem. The inner-most sleeve always rotates together with the stem. The entire sphere can then be rotated about the stem axis by rotating all the sleeves together. The main heater is annular and is fitted about the axis of rotation of the movable sphere section. It has been designed so as to conduct equally to both halves. As described earlier a small calorimeter 0.100 inches in diameter is located in the movable

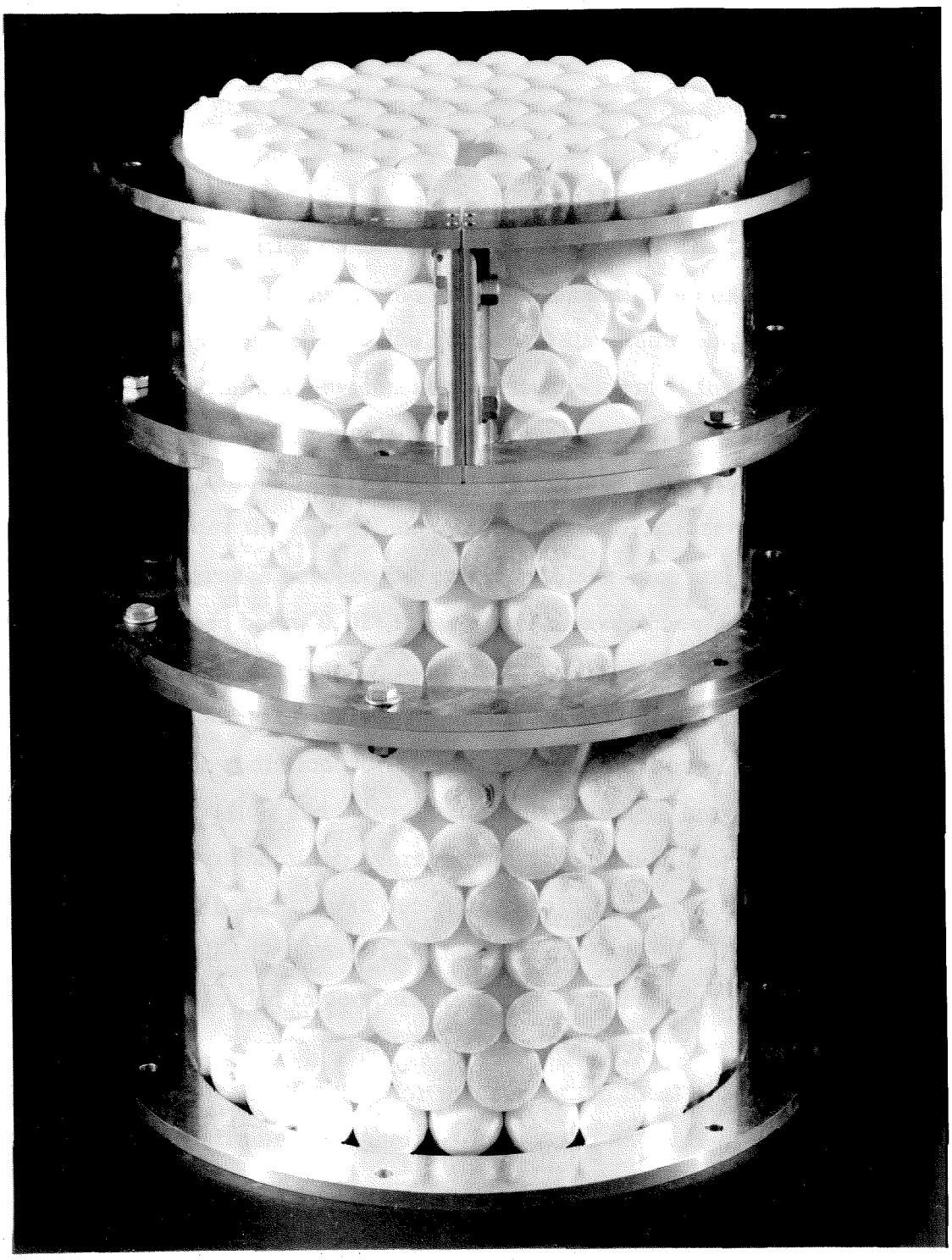

Figure 1. The Rhombohedral No. 6 Blocked Passage Array in the 12-inch Diameter Column.

portion of the sphere and is equipped with a small heater. Both heaters were prepared by winding small diameter, epoxy-coated, glass insulated wire into spiral grooves and sealing them in place with epoxy. The excess epoxy was removed on the lathe. A sleeve was then shrunk fit outside these spiral grooves.

In the operation of the instrumented sphere, at a particular Reynolds number, current is applied to the main heater until the desired surface temperature is achieved; then the current to the stem compensating heater is adjusted to eliminate any conduction into the stem at the junction to the sphere. With the proper manipulation of the stem sleeves the calorimeter can be positioned at almost every point on the surface. At a particular position of the calorimeter the current supplied to the calorimeter heater is adjusted so that the difference between the calorimeter surface and the main body of the sphere is reduced below 0.02° F. as a null measurement. From the calorimeter current and the average temperature driving force the local Nusselt number was obtained directly. As described earlier any residual losses such as conduction or radiation were measured as a function of driving force and polar angle at no flow and subtracted off directly as a heat flux. Owing to the greater precision of the average transfer obtained from the main heater, the calorimeter heat flux was determined with respect to the average heat flux, which was then expressed as the ratio of the local Nusselt number to the average. This tended to compensate for any systematic errors in local measurements. Also in the calorimeter well passing through the bakelite disk is a very small pitot tube for measuring the local pressure profile.

The instrumented sphere is inclined at an angle of 35.26° from the vertical as in Figure 2a. Spheres were then assembled around the stem to complete the array. The passages exposed to the instrumented sphere in the lower half plane of the array are shown in Figure 2b. There were twelve layers upstream and five downstream of the instrumented sphere in order to

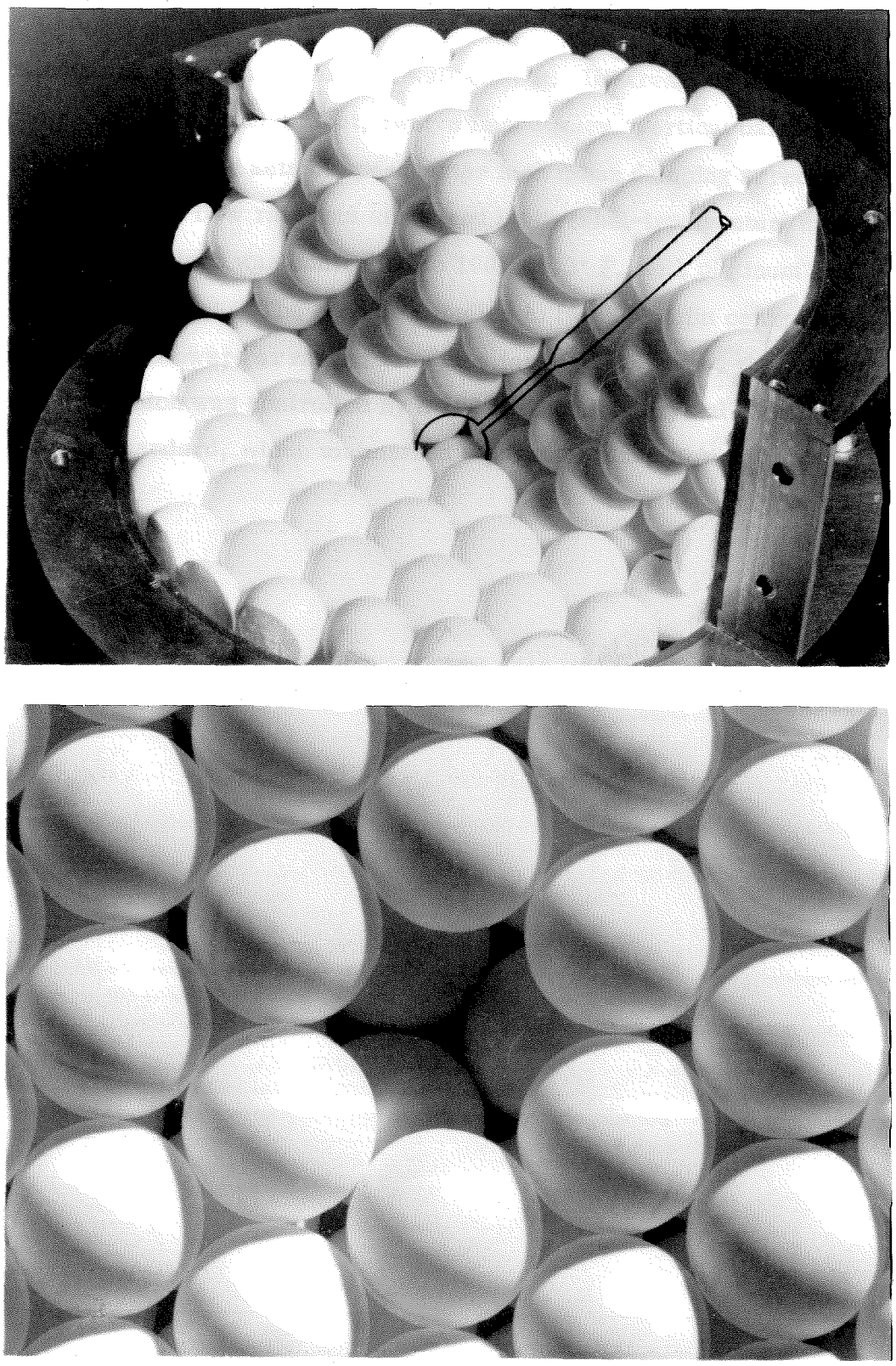

Figure 2. The Location of the Instrumented Sphere.

eliminate end effects and residual wall effects. Upstream of the entrance to the column was an eight foot, twelve inch square, vertical damping section equipped with sets of one-quarter inch mesh damping screens. The superficial mass flow rate was measured by Hershel-type venturi meters and the temperature was controlled to 100.0±0.1° F. with platinum resistance thermometers. The air was supplied to two 2000 cfm centrifugal, squirrel cage blowers arranged in series for high pressure, the rate of rotation of which was controlled by a 100 KHZ quartz crystal oscillator frequency standard, which maintained a constant mass flow rate within 0.2%.

ANALYSIS

The mechanism of transport within a system of multiple particles must not deviate drastically from transport from bluff bodies. As the flow impinges upon a surface, a boundary layer must be formed; although it is complicated by the acceleration and deceleration of the flow in the flow passages between particles. The velocity that characterizes the boundary layer is therefore not simply related to the superficial velocity which is based on the empty tower. The first problem is to obtain the proper velocity. Apparently, there is some critical bed voidage where wakes will be formed behind the particles. Kusik (40) assumed a voidage of 0.2 for this value, which is lower than that for tightest possible packing configuration for all particle configurations. Thus, a reasonable critical voidage must be taken into account.

At the beginning of this analysis of packed beds in 1963 (see Appendix A7) high effective turbulence intensities were apparent from the considerably higher transport rates that were observed compared to those suggested by a laminar boundary layer model. From the known action of free-stream turbulence upon boundary layer described earlier, such a characteristic turbulence intensity within the bed passages can be obtained. The action of turbulence in the complicated mechanism of transport in a fluidized bed is particularly important.

BOUNDARY LAYER MODEL:

The thermal and concentration boundary layer is formed and developed when flow impinging in the bed forms jets of flow which in turn impinge

on another particle about the passage. As the flow proceeds around the particle it is divided into various regions owing to the presence of the surrounding particles. Each of these regions then form jets of flow to impinge on another particle. This mechanism is repeated up through the column. As the jets impinge on the particle they mix and as they flow around the particle they are isolated again into regions of flow, which in turn individually mix with other surrounding jets. This process of radial dispersion comes about from the geometric configuration of the array of particles.

In this process of jet formation and splitting the flow along the adjacent surfaces it develops a boundary layer that controls the rate of transport from the particles. The complex mixing process, which occurs as these various jets of flow impinge into eachother and create various size eddies, is essential. This vorticity is transported to the region of the boundary layer where it interacts in much the same way as free-stream turbulence perturbs the laminar boundary region of a bluff body in a wind tunnel or free jet.

In arrays of particles possessing a high degree of voidage, the particles will be sufficiently far apart so that the adverse pressure gradient will cause the boundary layer to separate, with the consequent formation of a wake. The vorticity in these wakes will then be transported to the laminar boundary layer on the next downstream particle and interact in a perturbing fashion as the vorticity does in the mixing jets in a more closely packed bed.

In this way there are two plausible mechanisms which can generate turbulence in an array of particles. The generation of turbulence in a distended array of particles is expected to arise from predominantly the wake mechanism; whereas, in the packed array turbulence may be generated by predominantly the mixing process. The turbulence levels in both arrays would consequently be expected to be rather high. As the voidage of the array

approaches unity in the limit of a single particle in an infinite media the turbulence level must decay off to the residual level of the free stream which should be of the order of a few percent. The actual experimental data support this intuitive reasoning quite closely.

NUSSELT AND SHERWOOD NUMBERS IN AN ARRAY OF PARTICLES:

The available data on packed, distended and fluidized beds of spheres (1-26) were converted from J-factors, heights of transfer units, etc. to conventional Nusselt numbers for heat transfer and Sherwood numbers for mass transfer and are shown in Figures 3 and 4, respectively, using the superficial Reynolds number. Note how much higher the data appear above the line which represents transport from single spheres at a high free-stream turbulence of 15%. The legend for Figures 3 and 4 is given on page 329.

These results also show the magnitude of the minimum Nusselt and Sherwood numbers. At the beginning of this work the minimum Nusselt and Sherwood numbers were derived from the iso-concentration surface model suggested by Zabrodsky (41) as:

$$Nu_{min} \text{ or } Sh_{min} = \frac{2}{1 - (1-\varepsilon)^{1/3}} \qquad (1)$$

Zabrodsky concludes that a value of $Nu_{min}=8.6$ is closer to the "minimum true value of the Nusselt number for particles of any diameter". Recently this same derivation was published in a note by Rowe (42) and was criticized for departing from experimental data (43). Frantz (43) made an extensive survey of transport in fluidized beds and showed that Nusselt numbers below 2 were obtained by fourteen authors. The range of the minimum Nusselt

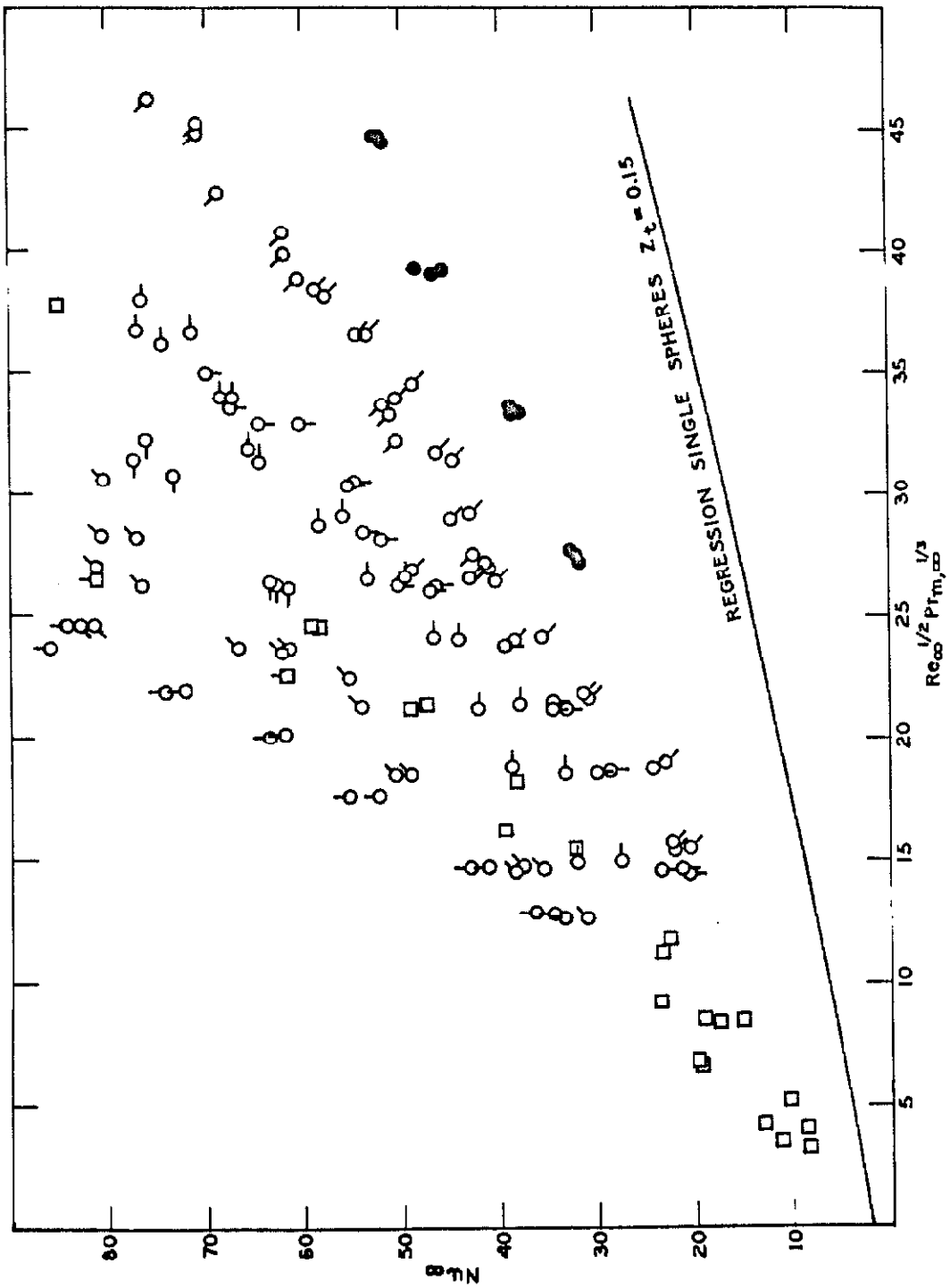

Figure 3. Heat Transfer in Packed and Distended Beds of Spheres.

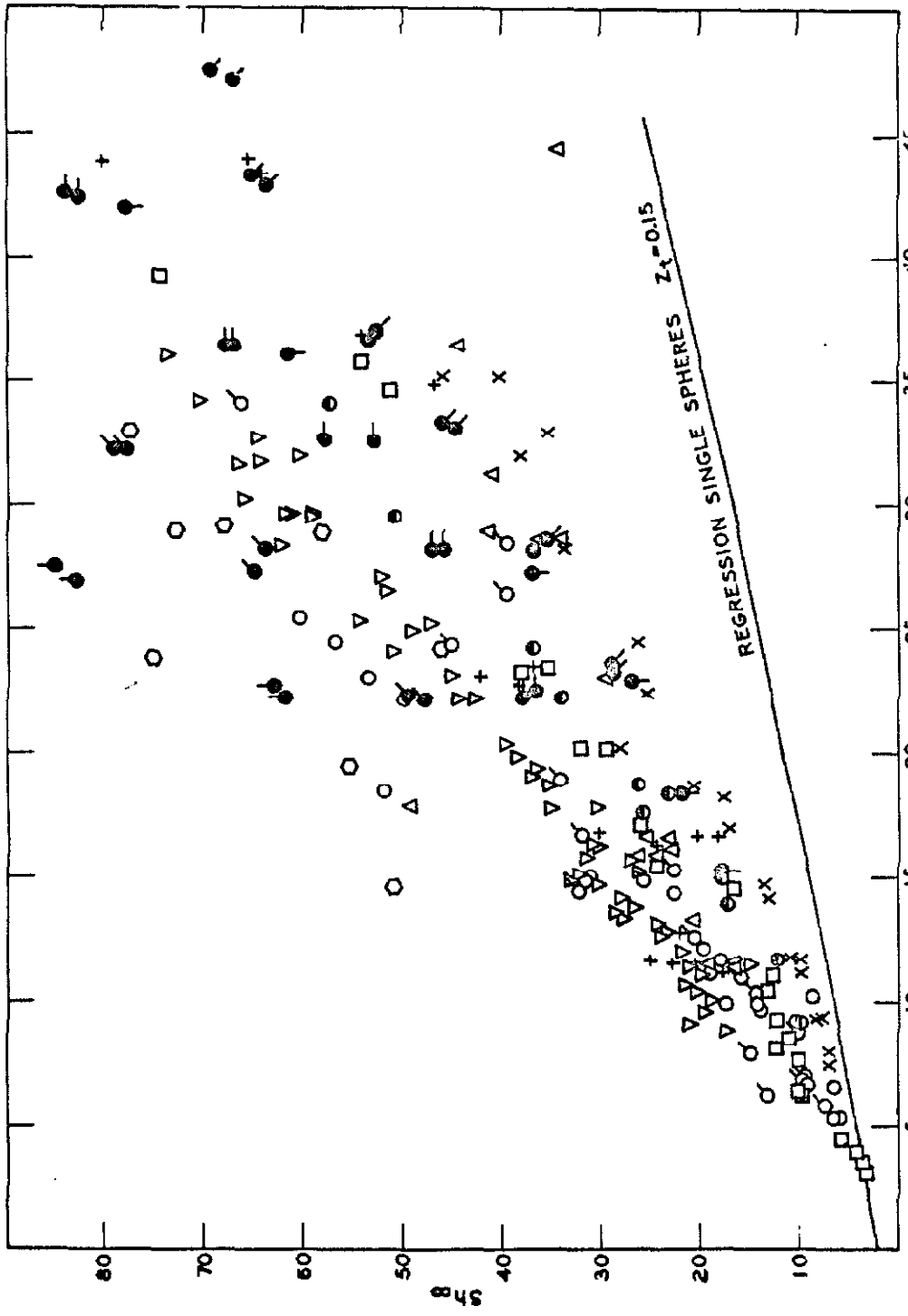

Figure 4. Mass Transfer in Packed and Distended Beds of Spheres.

number was from 5×10^{-5} to 5.5 (five orders of magnitude!) for particles of diameters from 360 to 1000 microns. There is undoubtedly a difficulty experimentally in evaluating the proper temperature driving force; however, detailed analysis (10) of the temperature distribution has revealed no anomalies and additional data still indicate a strong decrease in the stagnant limit, Nu_{min}, with particle diameter or with particle surface area per unit bed volume. This diameter dependence is a very real effect. For particles smaller than 50 microns, effects of interparticle adhesive forces on fluidization and heat transfer are well substantiated. This molecular, interparticle force, arising from the attractive "London" component of Van der Waals forces effective up to 100 Å, cause agglomeration (43.5).

Cornish (44) has discussed the problem of determining the thermal conductivity of the surrounding heterogeneous bed (involving the fluid and particles) and of the use of the driving force between the particle surface and the sink. This difficulty in evaluating the conductivity arises when the instrumented sphere is surrounded by spheres at the same surface temperature, since the temperature gradient at the surface becomes less steep. With the Nusselt group defined with the driving force between the surface and the sink, the experimental value will approach zero as the instrumented sphere becomes surrounded with sources. This hypothesis would presumably apply to all particle diameters; however, such an effect is only experimentally observed for particles of diameter less than one-sixteenth of an inch. Until the cause of the anomalously low values of the Nusselt number for small particle diameters and its strong dependence on diameter is isolated for fluidized beds of micron size particles, the lower limit of particle diameters amenable to this boundary layer model will be restricted to one-sixteenth of an inch.

Experimental data shown in Figures 3 and 4 indicate that for particles of diameter from 1/16 to 4 inches with various fractions of the bed acting as

sources and sinks the minimum Nusselt or Sherwood number is two or less. It is also apparent that the transport cannot be characterized by a superficial Reynolds number and that the linear variation with square root of the Reynolds number is doubtful.

LOCAL VELOCITY:

There have been a number of attempts to determine the proper local velocity to characterize the transport behavior by using modified Reynolds numbers and J-factors or a combination thereof (3, 6, 9, 11, 13, 14, 16, 19, 21, 22, 25, 35, 36). The most common of these modifications use the hydraulic diameter $\epsilon d/(1-\epsilon)$ and local velocity U_o/ϵ. Neither one of these hypotheses is applicable to a single particle, boundary layer model. The concept of a hydraulic diameter of a flow passage does not apply to a single particle in an infinite stream. The local velocity U_o/ϵ will always be too low, owing to the violation of the plug flow assumption.

The presence of the boundary layer developing along the particle surface in a flow passage slows the flow in this region and accelerates the flow outside the boundary layer. As discussed earlier it is the velocity outside the boundary layer which is the proper velocity to characterize transport through this layer (the momentum, thermal, and concentration layers being taken as equivalent for this discussion). Any additional stagnant regions in the bed also contribute to this acceleration of velocity in the flow passages. The volume fraction of the bed occupied by boundary layer regions or other relatively stagnant regions will be represented by ϵ_b. Accordingly, the proper local velocity to characterize the transport would be:

$$U_o/(\epsilon-\epsilon_b) \qquad (2)$$

The ratio of the proper local Reynolds number to the superficial Reynolds number is consequently:

$$\frac{Re'_{\infty}}{Re_{\infty}} = \frac{1}{\epsilon - \epsilon_b} \tag{3}$$

The quantity, ϵ_b, was evaluated experimentally and the resulting ratio is shown in Figure 5 for three groups of packing configuration. Kusik (40), using intuitive arguments developed a relation similar to Equation 3:

$$\frac{Re'_{\infty}}{Re_{\infty}} = \frac{1}{\epsilon - [0.75(1-\epsilon)(\epsilon-0.2)]} \tag{4}$$

which is also shown in Figure 5 and is quite low. If a projected area model is hypothesized for the increase in velocity, the following ratio is obtained for a rhombohedral number six array:

$$\frac{Re'_{\infty}}{Re_{\infty}} = \frac{1}{1 - \frac{\pi}{2\sqrt{3}}\left[\frac{6}{\pi\sqrt{2}}(1-\epsilon)\right]^{2/3}} \tag{5}$$

and for a cubic array:

$$\frac{Re'_{\infty}}{Re_{\infty}} = \frac{1}{1 - \frac{\pi}{4}\left[\frac{6}{\pi}(1-\epsilon)\right]^{2/3}} \tag{6}$$

These two relations are also shown in Figure 5 and compare only qualitatively to the experimental curves.

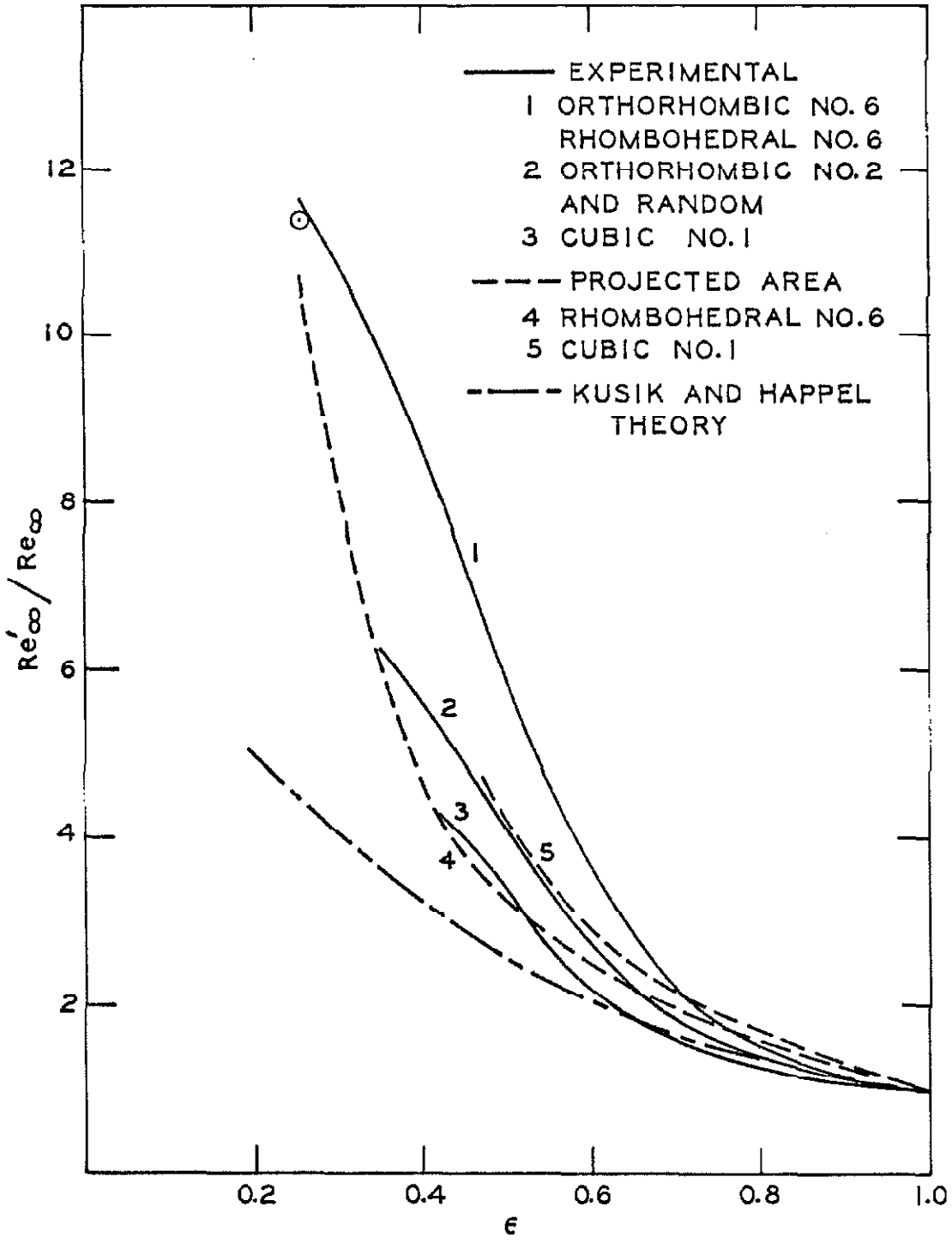

Figure 5. The Interstitial Reynolds Number.

The single experimental point shown in Figure 5 was obtained directly from measurements in the rhombohedral No. 6, blocked passage array taken by means of a small pitot tube. Eight measurements were made in the flow passages for each of the modified Reynolds numbers, Re'_∞=10,000, 19,200, and 35,500, with the pitot tube located in the center of the passage (as shown in Figure 2) at the top of the array. There are two types of flow passages which open to the top of the array, shown in Figure 2, one being a single sphere deep and the other two spheres deep. The incomplete and finite nature of the array at the location of the pitot tube was compensated for by averaging the measurements made in both types of passages opening to the top. Clearly, however, deep in the bed all passages are identical, and in these passages this is the velocity which is desired by this method. The ratio of the interstitial Reynolds number to the superficial value decreased from 11.5 to 9.8 for Re'_∞ from 10,000 to 35,000. Since most of the experimental data analyzed to obtain the solid curve labeled "1" were for the lower Reynolds numbers (around 3,000) the value obtained for Re'_∞ = 10,000 was shown. For comparable Reynolds numbers the comparison is expected to be nearly exact.

The characteristic voidage of the stagnant boundary regions, ϵ_b, obtained from these velocity measurements varied from 0.1715 to 0.1574 for Re'_∞ from 10,000 to 35,000. This slight variation is to be expected, since the relatively stagnant regions will tend to be more completely swept out of the vicinity near the points of contact at the higher velocity. The solid point shown later in Figure 6 was obtained from the lowest velocity measurements. The pressure drop measured through the array at low velocity agreed within a few percent with Ergun (33).

LOCAL HEAT TRANSFER MEASUREMENTS:

The nature of the local velocity field in the flow passages of the array characterizes the local heat transfer completely. Where a high velocity jet impinges on the surface of the calorimeter-instrumented sphere, the heat trans-

fer is the greatest, analogous to the forward stagnation point of a single sphere. Tables of the detailed experimental measurements in the array are presented in Appendix A8. The bottom portion of Figure 2 illustrates clearly the flow passages exposed to the instrumented sphere, where this sphere has been removed from the center. The local heat transfer variation around the surface resulting from the interaction of these flow passages is shown in Figure 5.5 for the three modified Reynolds numbers. The parameter, ϕ, is the angle measured from the vertical, clockwise about the center flow passage shown in the lower portion of Figure 2. Detailed measurements were also made for ϕ=40 and 60°, and they are typified by those selected angles in Figure 5.5.

The three different points of contact are shown by the heavy arrows for the regions of the instrumented sphere near the forward stagnation, the equator, and the rear stagnation. For angles of ϕ between these points of contact, the curves were found to be merely logical combinations of the appropriate curves shown. Note that the angle of symmetry is 60° for the rhombohedral No. 6 array.

From Figure 5.5 clearly the mechanism of transport at the forward stagnation point is analogous to stagnation point transport at the forward point on a single sphere placed in a stream of highly elevated turbulence. The magnitude of the Frössling number compares closely to that measured with the single 1.5-inch sphere at the forward stagnation point for 25.6% turbulence in the free-stream. In the region near the equator in the packed array, transport is characterized by somewhat lower levels of turbulence. The overall transport is characterized by a 16% effective interstitial turbulence level in the array as shown later in Figure 8. These results of Figure 5.5 for the local transport at the forward stagnation point of a sphere in the rhombohedral No. 6, blocked passage array assert that a boundary layer is formed which grows in thickness very rapidly along the surface as a result of the rapid deceleration in the flow as it immerges from the forward flow passage and proceeds around the sphere. This is reflected directly in the sharp decrease in the Frössling number away from stagnation.

The twelve points of contact have a profound effect on the heat transfer.

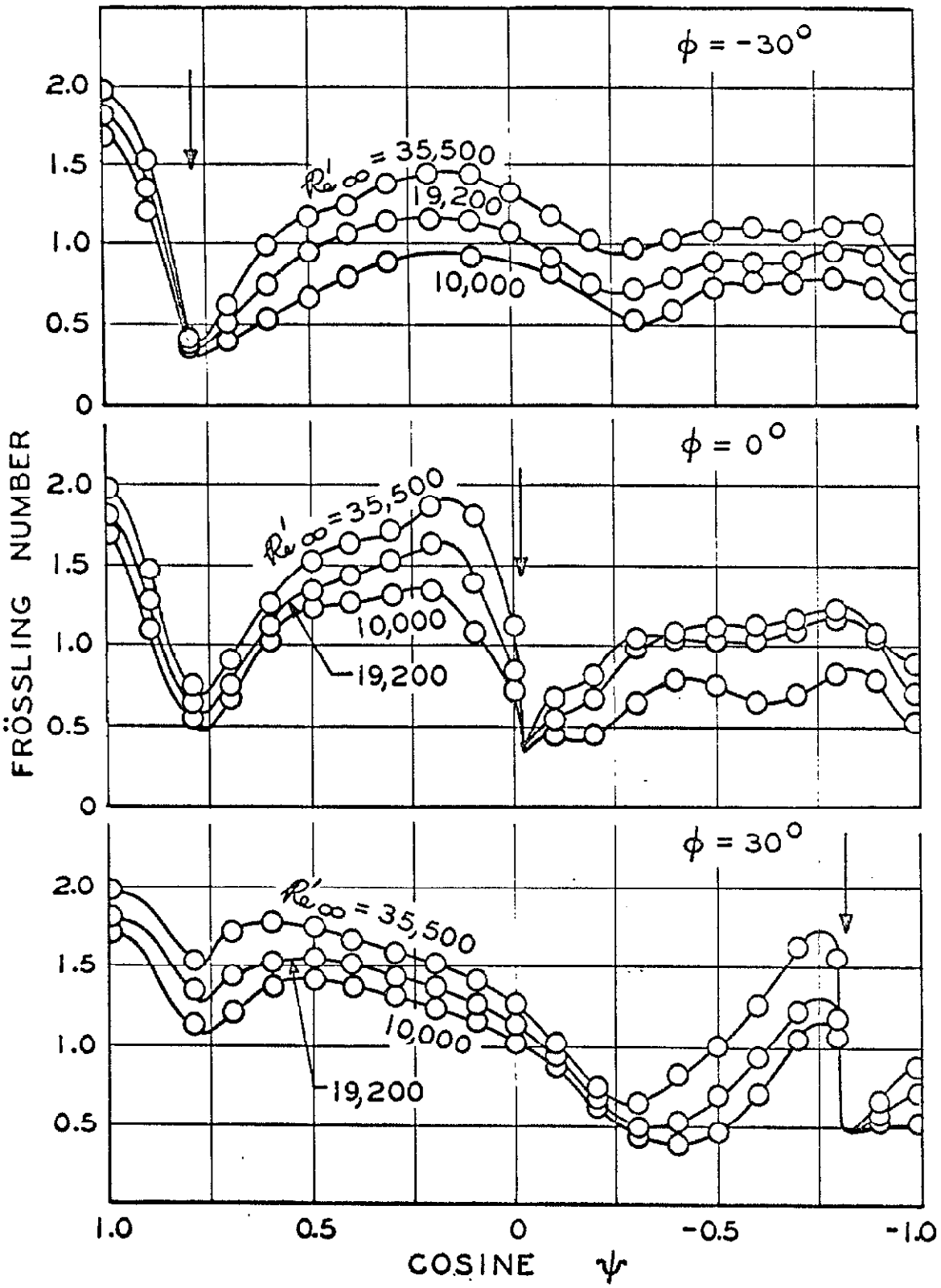

Figure 5.5 Local Thermal Transfer in the Rhombohedral No. 6 Array.

This is in agreement with measurements made by others (7,20,23) in different arrays. Within the 60° lune of interest in this rhombohedral array, they occur at γ, ϕ: 35.2646, -30; 90, 0; 144.7354, 30. The remaining nine points are obvious from conditions of symmetry. The first sharp dip in the transfer shown in Figure 5.5 at cosine γ=0.8, or 35°, results from the proximity of the first layer of spheres. It is most pronounced at ϕ=-30° for the point of contact and least at ϕ=30°. (Figure 2 will aid in visualization). The increase in transport following this first layer results from the backflow of a vortex next to the surface and its associated boundary layer. At ϕ=30° this vortex exists for cos γ=0.8 to 0.6, after which the jet from the flow passage creates another boundary layer along the surface from cos γ=0.6 to 0.3. In this last region (for ϕ=30°) the boundary layer then separates just as it does on the single sphere. The characteristic shift of the point of separation forward with increasing Reynolds number can even be seen for ϕ=30° at about cos γ=0.3. For other regions which are not in line with a jet but behind another sphere the decrease in heat transfer following cos γ=0.8 is not nearly so rapid, owing to more complicated, multiple vortex action. For ϕ=0 and -30° probably three vortices exist, with the middle one being the smallest. Following the contact point in the second layer of spheres (at ϕ=0°, γ=90°), there are at least six vortices coupled to form the various boundary layer regions from cos γ=0 to -1.0. Similarly for ϕ=-30°, there are at least four. For ϕ=30° near cos γ=-0.7 there is undoubtedly a very intense vortex just before the point of contact as a result of three converging flow passages. The mechanism of local transport developed above is in agreement with that postulated by Rhodes and Peebles (23) for local mass transfer in two completely different array configurations and lends support to the analysis.

These results indicate that the mechanism for transport in an array of multiple particles is that of the action of a primary boundary layer arising from flow adjacent to the surface as well as of a secondary boundary layer arising from the backflow of a vortex. The individual mechanisms are analogous to those of a single sphere and suggests the Frössling group to characterize the transport.

FRÖSSLING NUMBER AND TURBULENCE:

Studies of the influence of free-stream turbulence level on the transport from single spheres (27,28) and cylinders (29) have indicated that the Frössling number depends rather simply on the turbulence level, particularly near the forward stagnation point, and on the Reynolds number in the flow regime, Re_∞=100 to 40,000. The Frössling number is linearly related to the square root of the Reynolds number and the slope increases with increasing turbulence level. At vanishingly low turbulence intensities the slope is small but still finite owing to the stronger dependence of wake-flow transport on the Reynolds number. For transport from single spheres the following relation (27) has predicted results within 8.8% for 958 data points involving a wide range of conditions:

$$Fs_\infty = A(v_\infty/v_o)^n + [B\,Z_t(Z_t+C)+D]Re_\infty^{1/2}(Pr_{m,\infty} \text{ or } Sc_{m,\infty})^m \qquad (7)$$

This equation for the Frössling number is the basis of the boundary layer model for packed, distended, and fluidized beds. For this early discussion the empirical exponents will be taken as zero, since these terms contribute very little even to the single sphere prediction. All available transport data for beds of particles with diameters in excess of one-sixteenth of an inch are converted to the Frössling number, which is then plotted with the square root of the superficial Reynolds number. The large quantity of data can be described very well by the relation:

$$Fs_\infty = A' + S'Re_\infty^{1/2} \qquad (8)$$

The adequacies of such a relation can be analyzed most critically by exam-

ining the parameters A' and S'. From the intercept A' the ratio of the local Reynolds number to the superficial Reynolds number is thus obtained:

$$\frac{Re'_{\infty}}{Re_{\infty}} = (A'/A)^2 = \frac{1}{\epsilon - \epsilon_b} \tag{9}$$

From the slope S' the apparent interstitial turbulence level is obtained:

$$B Z_t (Z_t + C) + D = S' (\epsilon - \epsilon_b) \tag{10}$$

Equation 7 can now be rewritten into a useful form, where the constants A, B, C, and D are well established (27) from overall transport from single spheres involving both liquids and gases and both heat and mass transfer and the result is:

$$Fs_{\infty}(\epsilon - \epsilon_b)^{1/2} = Fs'_{\infty} = 0.5483(\nu_{\infty}/\nu_o)^n + [0.1212 Z_t (Z_t - 0.04595) + 0.01656](Re'_{\infty})^{1/2}(Pr_{m,\infty} \text{ or } Sc_{m,\infty})^m \tag{11}$$

where n was found to be 0.16 and m to be 1/6. The solid curves in Figure 5 were obtained directly from Equation 9. The experimental volume fractions ϵ_b of the boundary layers and stagnant regions in the bed were obtained from Equation 9 and are shown in Figure 6. The data fall into three groups of bed configuration. The maxima in the curves may correspond to the generation of wakes after the particles, creating relatively large stagnant eddying regions unavailable for flow. The solid point is from the author's measurements.

The apparent interstitial turbulence levels obtained from this model are shown in Figure 7. They fall into two groups, depending on the bed con-

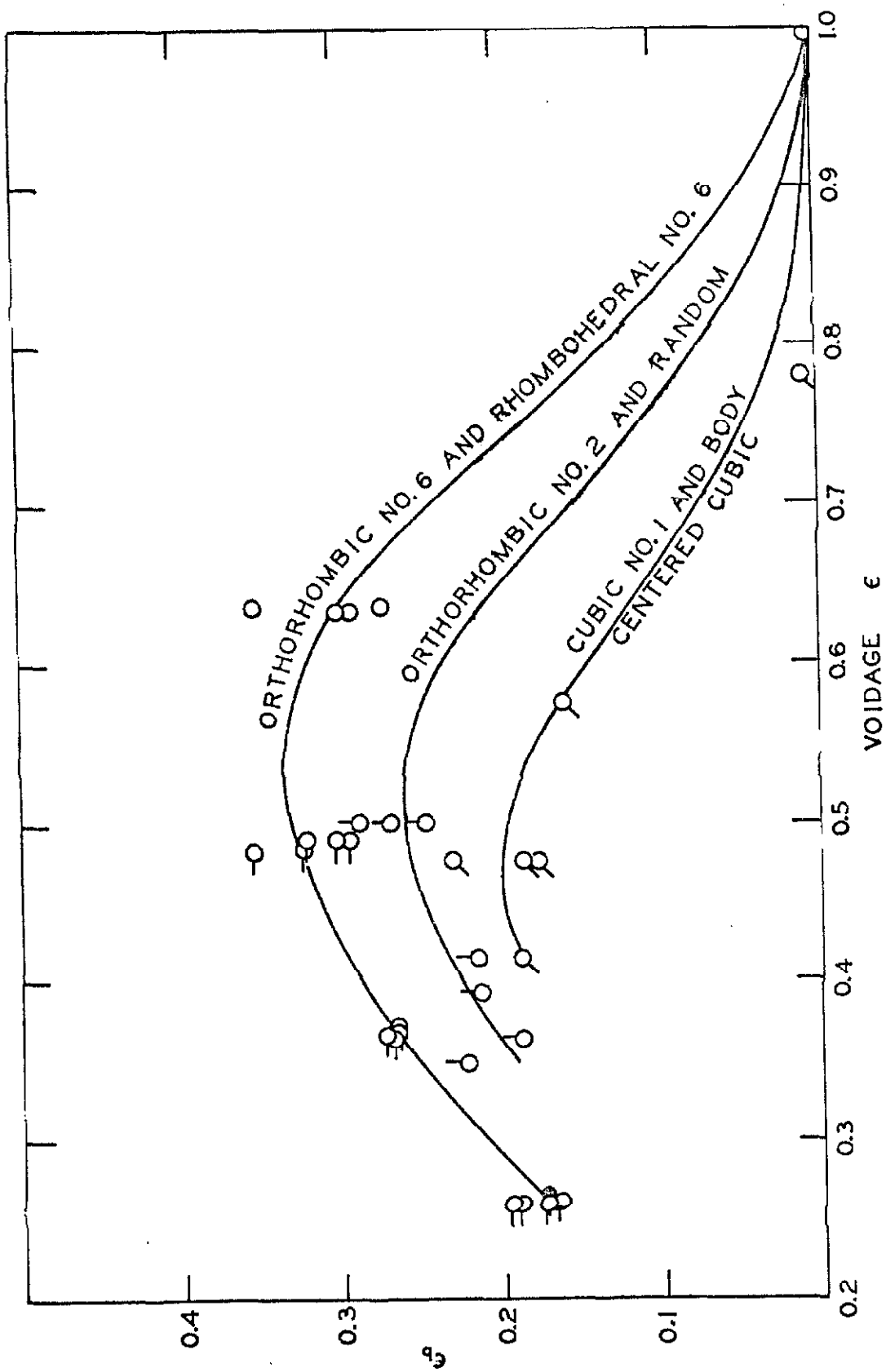

Figure 6. Voidage of the Stagnant Boundary Regions.

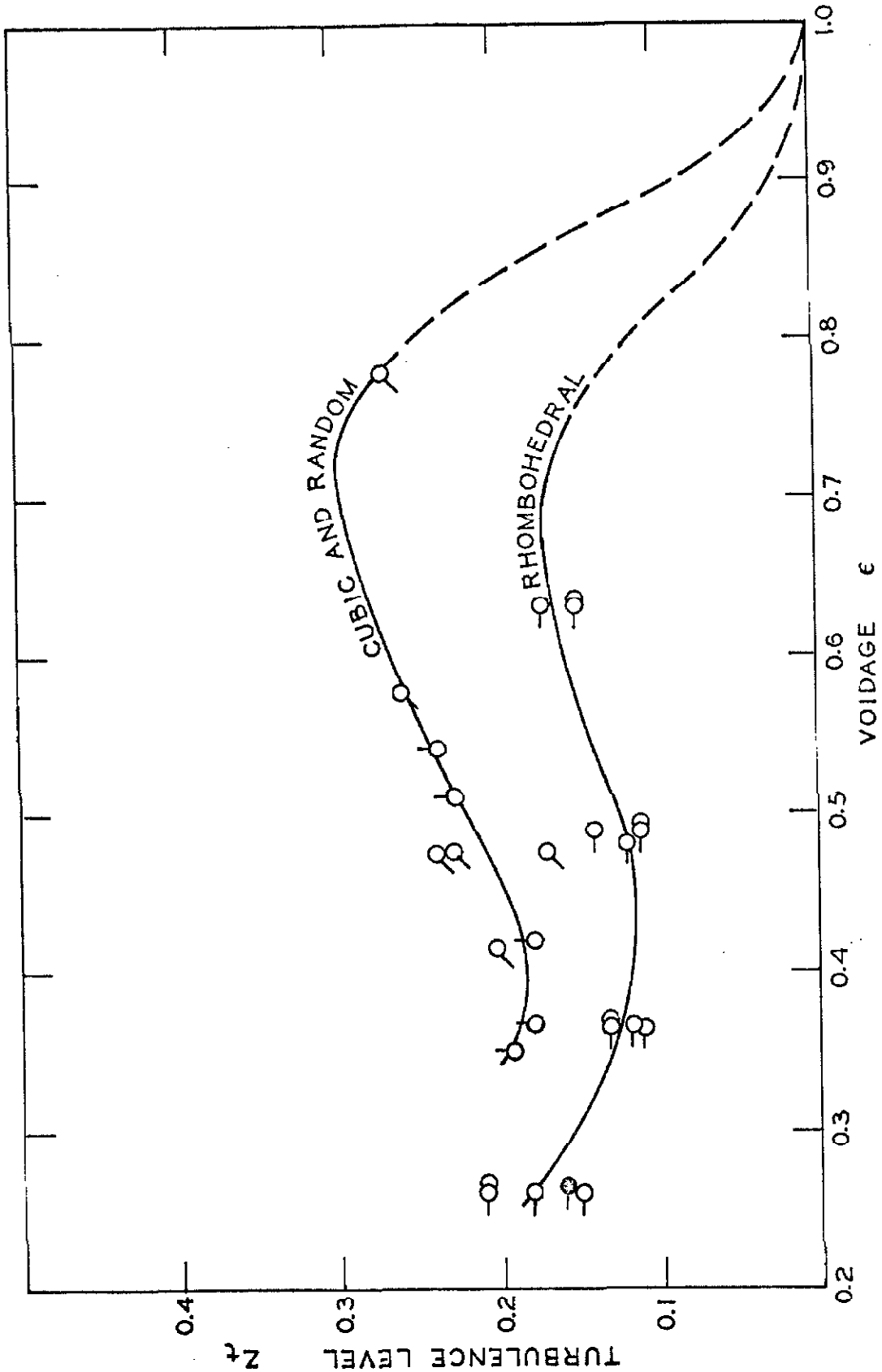

Figure 7. Apparent Interstitial Turbulence in Packed and Distended Beds of Spheres.

figuration. The solid point shown was obtained from the overall transport taken by the author. Cubic and random geometries apparently create either more mixing of the flow passages, or more wake flow, or both. The cubic and random curves compare very closely to that obtained from the analysis to follow of fluidized bed data. Mickley, Smith, and Korchak (24) measured the turbulence level in the flow passage of a number three rhombohedral array of 1.50 inch diameter spheres. The level varied from 15% near the particle surface to 47% near the center of the void space. These results suggest turbulence levels around 20% are reasonable acting outside the boundary layer on the particle surfaces. The individual parameters and range of conditions for each author has been tabulated in Table 1.

The Frössling number based on the local velocity, Fs'_{∞}, is then plotted with the square root of the local Reynolds number, Re'_{∞}, in Figure 8. In such a plot the spread of the data has been reduced by a factor of six. The data at high Schmidt number show sharp increases in Frössling number at the low Reynolds numbers owing to residual effects of natural convection. Gaffney and Drew (6) in particular, have shown these effects to be from natural convection by varying the Grashof number. The data shown here are those for both packed and distended beds of spheres as well as those data for fluidized beds. The fluidized bed data provide a wide range of bed voidage from densely packed to nearly infinitely expanded (ϵ=1).

As superficial Reynolds number is increased in a fluidized bed, the bed will expand lowering both the local velocity as well as the rate of transport. When the Frössling number is based on the local velocity, the spread of data is reduced very considerably. The fluidized bed data appear at a nearly constant local Reynolds number and the residual variation in Fs'_{∞} is from changes in interstitial turbulence level. The resulting apparent interstitial turbulence in fluidized beds is shown in Figure 9 and compares closely to the cubic and random curve in Figure 7 for fixed beds. Effects of turbulence in fluidized beds have been suggested before. Ziegler and Holmes (25)

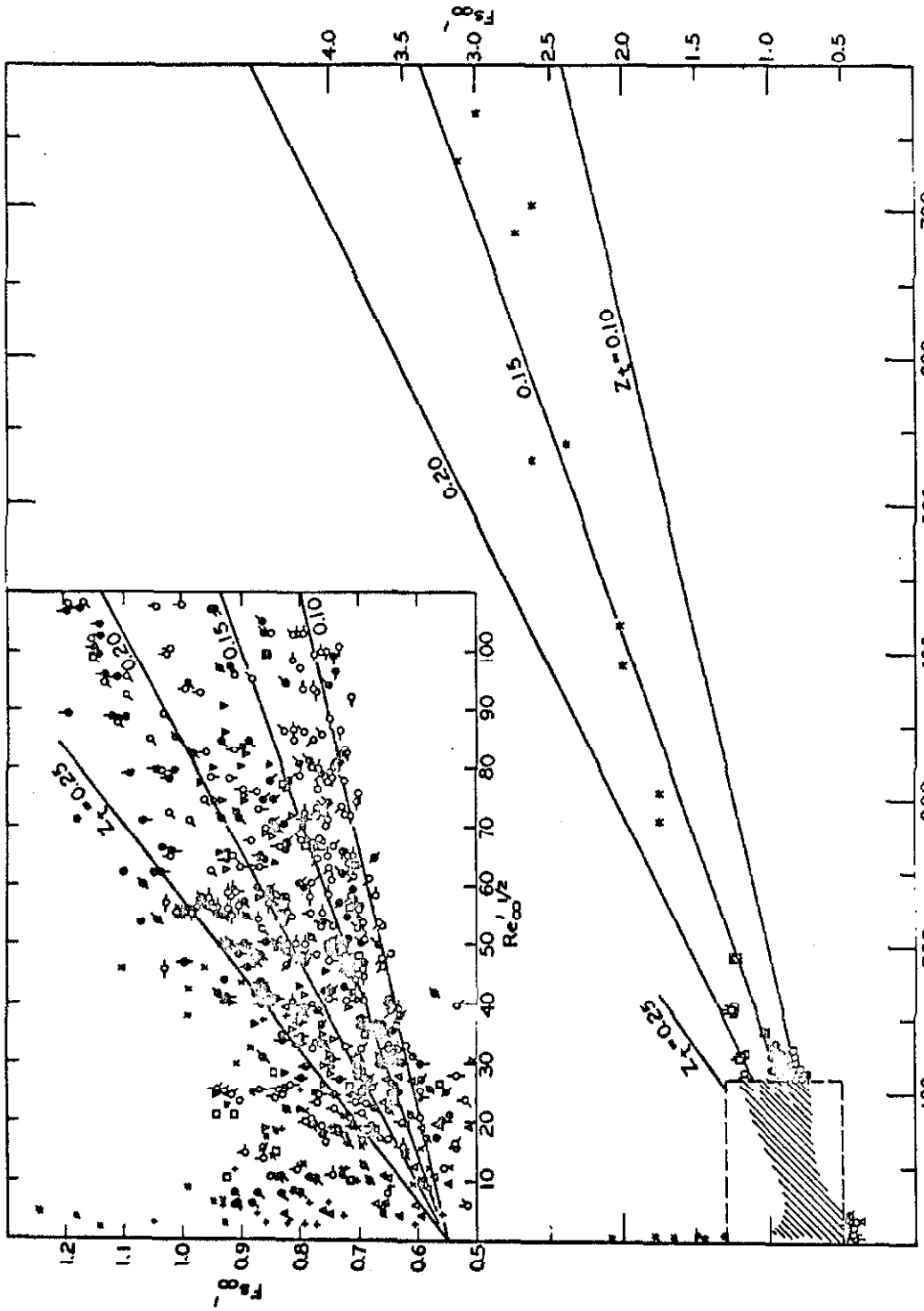

Figure 8. Heat and Mass Transfer in Packed, Distended, and Fluidized Beds of Spheres.

LEGEND FOR FIGURE 8

FIXED BEDS

■	The author	ϵ=0.2595	Pr=0.704
+	Gaffney and Drew	0.50	Sc=380
✳	Gaffney and Drew	0.50	Sc= 10,000
△	Gaffney and Drew	0.50	Sc= 165
○	Chu, Kalil, and Wetteroth	0.38	Sc= 2.57
□	DeAcetis and Thodos	0.48	Pr= 0.718
□	DeAcetis and Thodos	0.48	Sc= 0.607
▽	Gamson, Thodos, & Hougan	0.42	Sc= 0.615
⌀	McCune and Wilhelm	0.37	Sc= 1400
×	McConnachie	0.778	Sc= 0.617
◓	McConnachie	0.576	Sc= 0.617
⊘	McConnachie	0.416	Sc= 0.617
⚲	Rowe	0.260	Pr= 0.73
⚲	Rowe	0.365	Pr= 0.73
⚲	Rowe	0.488	Pr= 0.73
⚲	Rowe	0.632	Pr= 0.73
⚲	Rowe	0.476	Pr= 0.73
⚲	Rowe	0.260	Pr= 7.0
⚲	Rowe	0.365	Pr= 7.0
⚲	Rowe	0.488	Pr= 7.0
⚲	Rowe	0.632	Pr= 7.0
⚲	Rowe	0.260	Sc= 2.54
⚲	Rowe	0.365	Sc= 2.54
⚲	Rowe	0.632	Sc= 2.54
⚲	Rowe	0.476	Sc= 2.54
⚲	Rowe	0.260	Sc= 1400
⚲	Rowe	0.365	Sc= 1400
⚲	Rowe	0.488	Sc= 1400
⚲	Rowe	0.632	Sc=1400
⚲	Rowe	0.476	Sc= 1400
✳	Wadsworth	0.260	Pr= 0.71
⚲	Meek	0.35	Pr= 0.70

FLUIDIZED BEDS

⚲	Rowe	D_p=0.250"	ϵ=0.41-0.64	Sc=1400
⚲	McCune and Wilhelm	0.189	0.5 - 0.9	Sc=1200
⚲	McCune and Wilhelm	0.125	0.5 - 0.9	Sc=1200
⚲	McCune and Wilhelm	0.0494	0.5 - 0.9	Sc=1200
⚲	McCune and Wilhelm	0.0814	0.5 - 0.9	Sc=1200
⚲	McCune and Wilhelm	0.25L	0.5 - 0.9	Sc=1200
⚲	McCune and Wilhelm	0.25s	0.5 - 0.9	Sc=1200

TABLE 1: PACKED BEDS OF SPHERES
PACKING PARAMETERS AND RANGE OF CONDITIONS

Author	Geometry	D_p (in.)	Pr or Sc	Re	ϵ	ϵ_b	Z_t
Galloway	Cubic	0.673	0.718	160-1100	0.476	n.a.	n.a.
Galloway	Cubic	0.673	0.609	160-1100	0.476	n.a.	n.a.
Galloway	Rhombo	0.673	0.718	260-1300	0.3954	n.a.	n.a.
Galloway	Rhombo	0.673	0.609	260-1300	0.3954	n.a.	n.a.
Galloway	Rhombo	0.673	0.718	155-1100	0.2595	n.a.	n.a.
Galloway	Rhombo	0.673	0.609	155-1100	0.2595	n.a.	n.a.
Gaffney	Random	.25-.50	400	1.9-383	.494-.526	.246	.23
Gaffney	Random	.25-.50	12,000	0.8-124	.461-.550	.289	n.a.
Gaffney	Random	.25-.50	160	8.3-753	.509-.570	.270	.24
Chu	Random	.028-.077	2.57	16-340	.38 - .64	.209	.15
DeAcetis	Rhombo	0.627	0.607	13-2136	0.482	.354	.12
Gamson	Random	.09-.456	0.615	110-1780	.404-.430	.214	.18
Hobson	Random	0.370	800	3.3-35	.475-.538	n.a.	n.a.
McCune	Random	.125-.250	1200	14-1765	.355-.375	.187	.18
McConnachie	Cubic	0.61	0.617	43-1600	0.416	.188	.20
McConnachie	Cubic	0.61	0.617	120-2100	0.576	.160	.26
McConnachie	Cubic	0.61	0.617	53-1700	0.778	≈ 0	.27
Rowe	Rhombo	1.50	0.73	202-748	0.260	.174	.18
Rowe	Rhombo	1.50	0.73	196-1510	0.365	.272	.13
Rowe	Rhombo	1.50	0.73	275-1780	0.488	.323	.11
Rowe	Rhombo	1.50	0.73	294-1810	0.632	.351	.15
Rowe	Cubic	1.50	0.73	261-1505	0.476	.232	.17
Rowe	Rhombo	1.50	7.0	165-967	0.260	.232	.21
Rowe	Rhombo	1.50	7.0	189-954	0.365	.272	.11
Rowe	Rhombo	1.50	7.0	214-1059	0.488	.293	.11
Rowe	Rhombo	1.50	7.0	211-1025	0.632	.292	.15
Rowe	Rhombo	1.50	2.54	275-1086	0.260	.165	.21
Rowe	Rhombo	1.50	2.54	261-1754	0.365	.261	.13
Rowe	Rhombo	1.50	2.54	274-1923	0.488	.321	n.a.
Rowe	Rhombo	1.50	2.54	294-2003	0.632	.300	.17
Rowe	Cubic	1.50	2.54	127-1526	0.476	.176	.24
Rowe	Rhombo	1.50	1400	236-1227	0.260	.192	n.a.
Rowe	Rhombo	1.50	1400	228-1174	0.365	.272	.12
Rowe	Rhombo	1.50	1400	246-1174	0.488	.301	.14
Rowe	Rhombo	1.50	1400	141-946	0.632	.272	.24
Rowe	Cubic	1.50	1400	241-1101	0.476	.176	.23
Wadsworth	Rhombo	4.00	0.71	6900-50,000	0.260	.174	.15
Meek	Random	0.394	7.0	677-2983	0.350	.220	.19
The Author	Rhombo	1.50	0.70	950-3700.	0.260	.171	.16
OVERALL	Rhmb-cubic	.02-4	.6-13300	.8-50000	.26-.80	0-.35	.1-.3

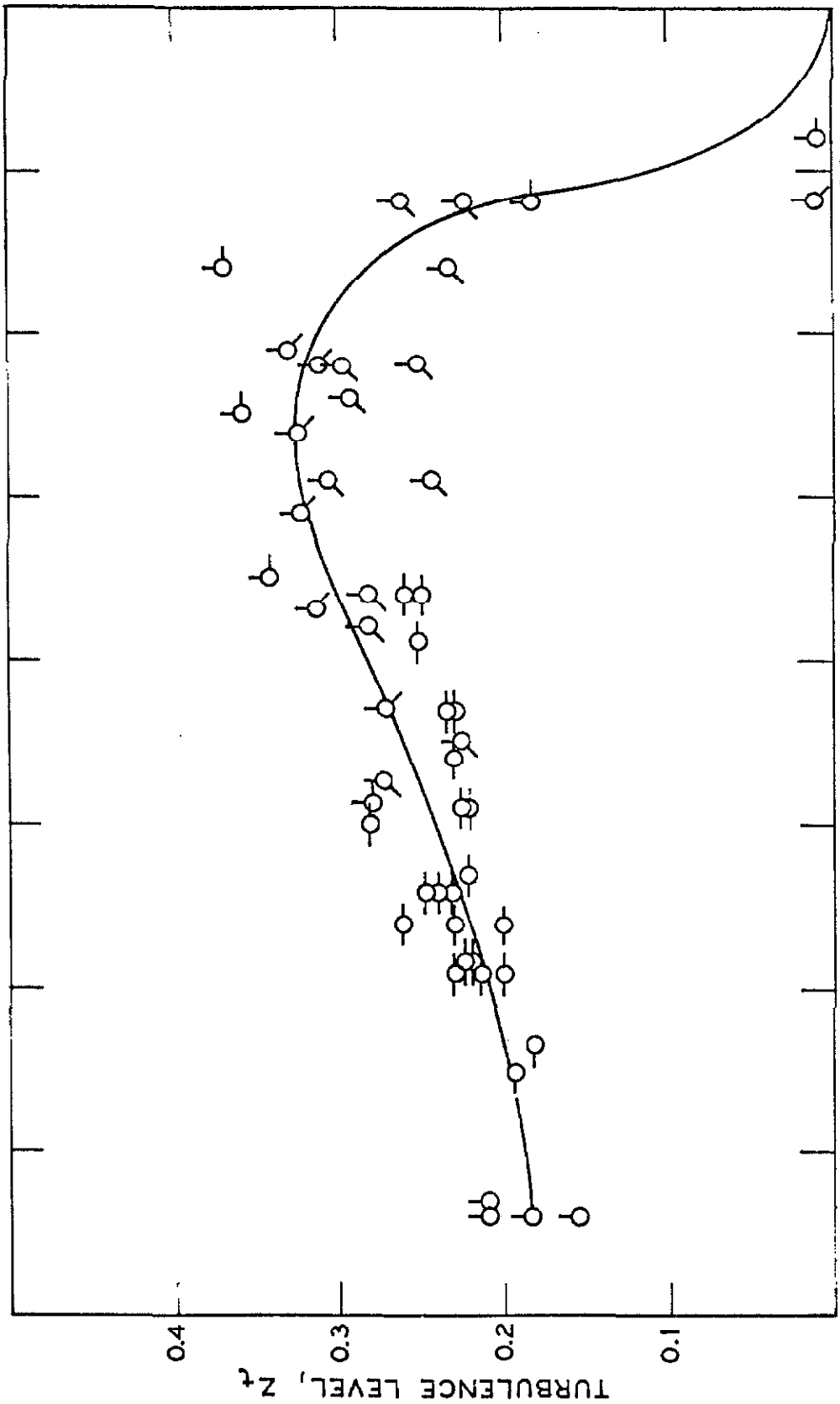

Figure 9. Fluidized Beds of Spheres -- Apparent Interstitial Turbulence.

show that increases in Sherwood number can be attributed to increasing turbulence. Handley et. al. (45) used a tracer method to measure the statistical motion of individual particles. The turbulent particle-velocity components they found achieved a maximum at a bed voidage of 0.70, which compares favorably with Figure 9. This random particle motion will not only generate turbulence which will then interact with the boundary layers about the particle, but will also subject individual particles to regions of quite different velocity. The overall transport that is being analyzed by this model is an average of all of these statistical effects.

MACROSCOPIC TRANSPORT IN FIXED AND FLUIDIZED BEDS:

The basis of this boundary layer model is that the local Frössling number is essentially independent of particle surface shape and bed configuration; consequently this model should apply equally well to beds of short cylinders and other commerical packing, such as Rashig and Partition rings and Beryl saddles. When the J-factors and heights of transfer units are converted to the appropriate Nusselt or Sherwood numbers and plotted against $Re_{\infty}^{1/2} Pr_{m,\infty}^{1/3}$ or $Re_{\infty}^{1/2} Sc_{m,\infty}^{1/3}$, the functional dependence is illustrated in Figure 10. The steady state conduction limit is in the region of two and the curvature upward is obvious. Although there is less data, the trends compare with those shown in Figures 3 and 4. By the same technique as before the parameters ε_b and the apparent interstitial turbulence, Z_t, were obtained from the data. These parameters together with the ranges of conditions are given in Table II.

Again using the local Frössling number and local Reynolds number, the data are shown in Figure 11. The solid curves are again predicted by

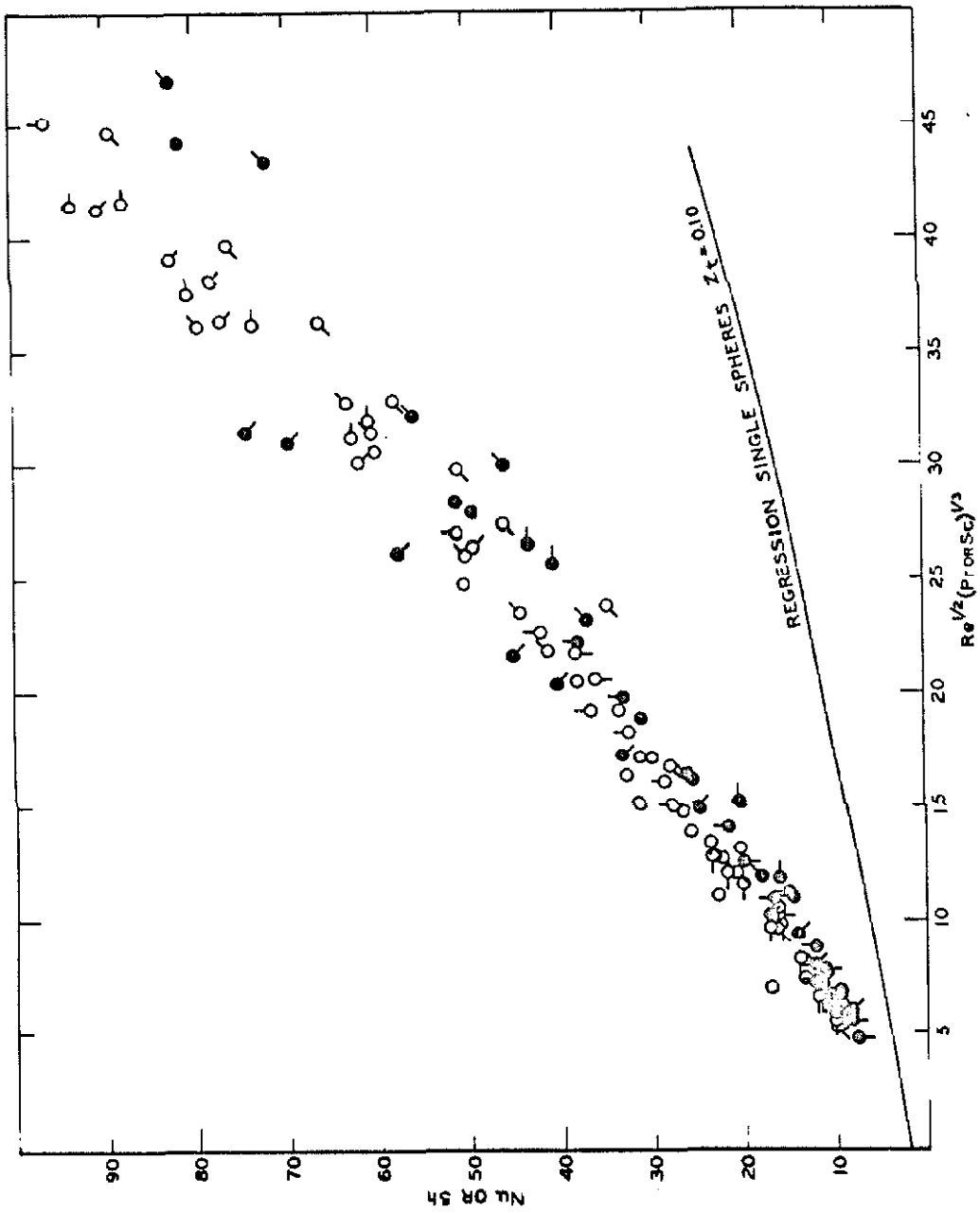

Figure 10. Heat and Mass Transfer in Beds of Cylinders and Commercial Packing.

LEGEND FOR FIGURE 10

SHORT CYLINDERS

○	Gamson, Thodos, & Hougan	=0.368	Pr=0.735	D_p=0.161"
○	Gamson, Thodos, & Hougan	0.370	Pr=0.735	0.268
○	Gamson, Thodos, & Hougan	0.410	Pr=0.735	0.387
○	Gamson, Thodos, & Hougan	0.390	Pr=0.735	0.552
○	Gamson, Thodos, & Hougan	0.357	Pr=0.735	0.740
○	Taecker, and Hougan	0.390	Pr=0.735	0.500
○	Glaser, and Thodos	0.477	Pr=0.710	0.250
○	Wilke, and Hougan	0.34-0.430	Sc=0.615	

COMMERCIAL PACKING

(Taecker and Hougan, Pr=0.7-5)

●	2" Rashig Rings	=0.74
●	1/2" Rashig Rings	0.63
●	1" Rashig Rings	0.73
●	2" Partition Rings	0.74
●	1/2" Beryl Saddles	0.63
●	1/4" Beryl Saddles	0.60

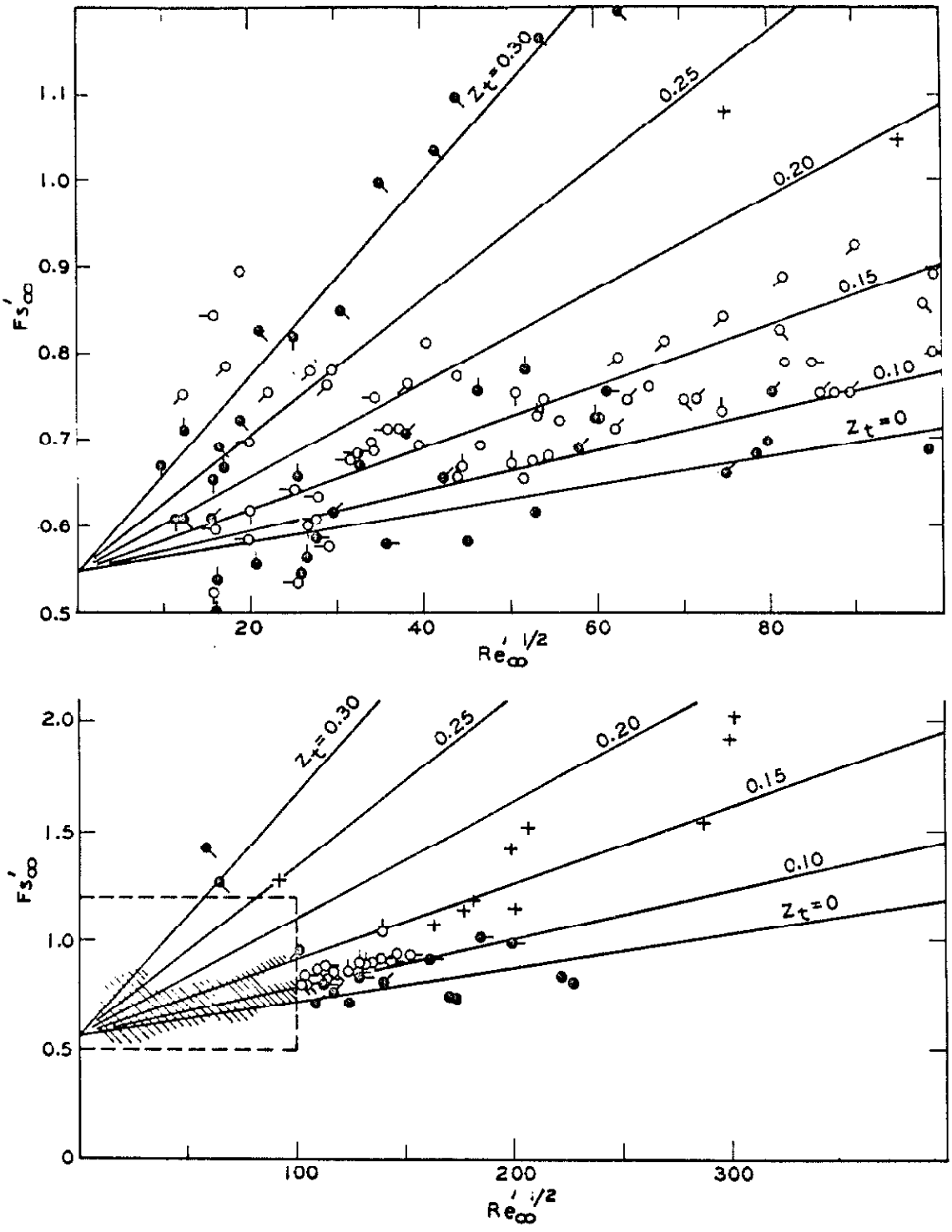

Figure 11. Heat and Mass Transfer in Beds of Cylinders and Commercial Packing.

TABLE 2

PACKED BEDS OF SHORT CYLINDERS AND COMMERCIAL PACKING

PACKING PARAMETERS AND RANGE OF CONDITIONS

Type of Packing	D_p (in.)	Pr or Sc	Re	ϵ	ϵ_b	Z_t
Cylinders (D_p=L)	0.161	0.735	62-3700	0.368	.196	.15
" " "	0.268	0.735	310-3200	0.370	.148	.12
" "	0.387	0.735	630-1600	0.410	.247	.12
" "	0.552	0.735	1200-3800	0.390	.226	.11
" "	0.740	0.735	860-2400	0.357	.184	.12
" "	0.500	≈.73	142-515	0.390	.188	.10
" "	0.250	0.710	35-2517	0.477	.233	.17
" "	0.20-.55	2.57	700-17,000	.32-.39	.200	.16
" "	0.12-.75	0.615	67-244	.34-.44	.200	.14
Rashig Rings	2.00	0.705	450-8270	0.74	.58	.05
Rashig Rings	1.00	0.705	675-2800	0.73	.528	.10
Rashig Rings	0.50	0.705	59-620	0.63	.399	.16
Partition Rings	2.00	0.705	176-7930	0.74	.509	.10
Beryl Saddles	0.25	0.705	29-195	0.60	.295	.28
Beryl Saddles	0.50	0.705	47.2-1784	0.63	.330	.30

Equation 7. In the beds of short cylinders the parameters ε_b and the interstitial turbulence compare very closely to the curves for random beds of spheres in Figures 6 and 7, respectively. For beds of commercial packing the values of ε_b are considerably higher than for either beds of spheres or short cylinders, and this can be attributed to the surface geometry of the particle. The commercial packing has hollow and various internal regions which may not contribute as an effective flow passage, and as a result may act as a stagnant region, unavailable for flow. In general the larger pieces of commercial packing possess higher values of ε_b and lower interstitial turbulence, however, more data are necessary before any geometrical conclusions can be drawn. When Equation 11 was used with the exponents determined as m=0.03 and n=0.16, a fractional deviation of 9.8% resulted when all of the data presented in Tables 1 and 2 were subjected to non-linear regression analysis.

The height of a transfer unit can be obtained directly from these results. For heat transfer one obtains:

$$a\,HTU = \frac{Re\ Pr}{Nu} = \frac{Re^{1/2}Pr^{2/3}}{Fs + 2/Re^{1/2}Pr^{1/3}} \qquad (12)$$

and for mass transfer:

$$a\,HTU = \frac{Re\ Sc}{Sh} = \frac{Re^{1/2}Sc^{2/3}}{Fs + 2/Re^{1/2}Sc^{1/3}} \qquad (13)$$

aHTU has been plotted in Figure 12. For data expressed as the J-factor or Stanton number, St, these are related as follows:

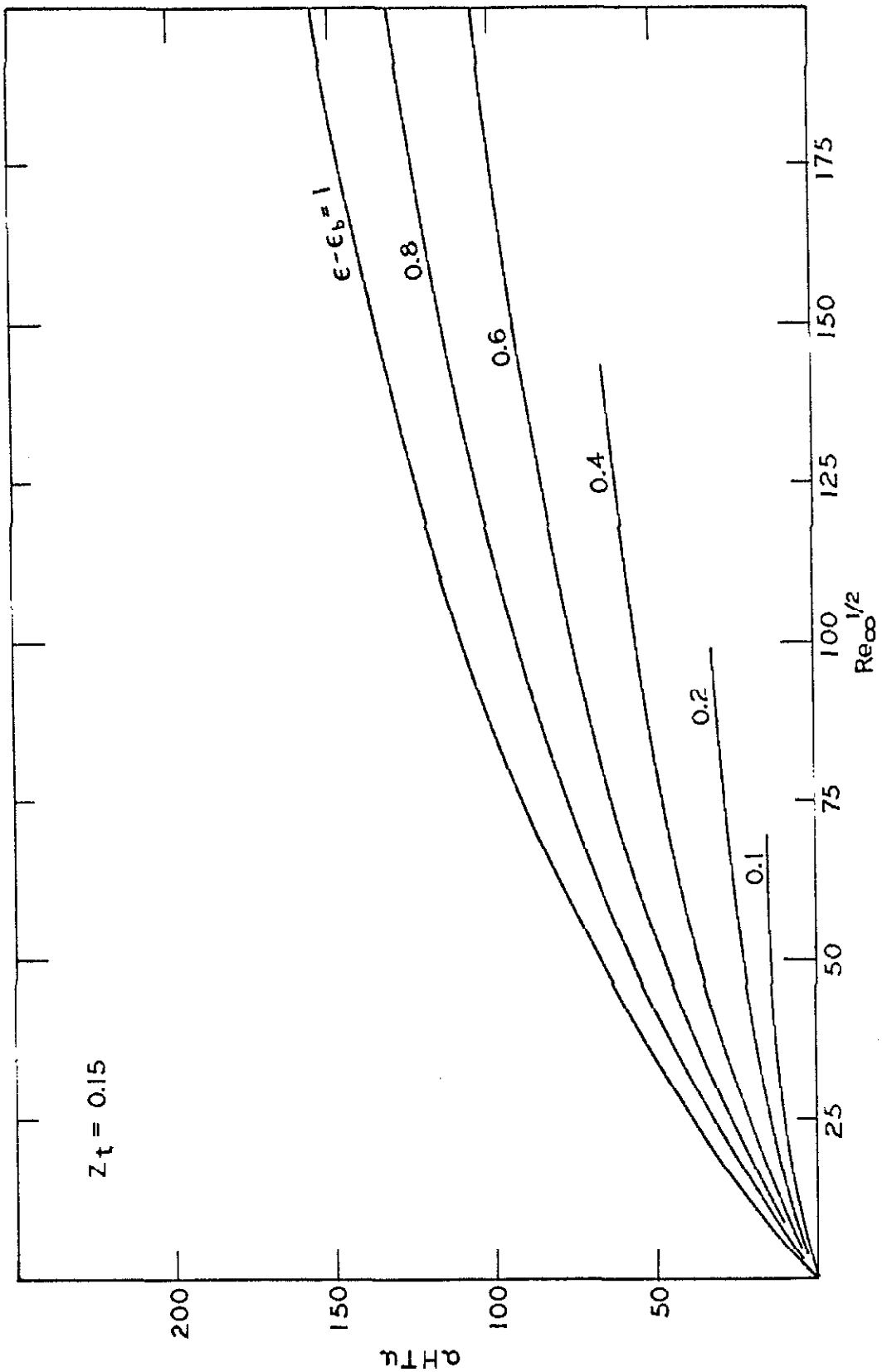

Figure 12. Height of a Transfer Unit at 15% Turbulence.

$$J_h = StPr^{2/3} = Nu/RePr^{1/3} = Pr^{2/3}/aHTU \qquad (14)$$

$$J_d = StSc^{2/3} = Sh/ReSc^{1/3} = Sc^{2/3}/aHTU \qquad (15)$$

The effective interfacial area, a, can be obtained from various empirical techniques such as that by Shulman, et. al. (46) and Yoshida and Koyanagi (47) for packed columns. This is expressed as the function of particle area actually wetted with liquid and participating in transport. This effective area of transfer depends on the nature of the transfer, such as absorption, vaporization, or distillation, and depends upon the properties of the liquid (i.e. viscosity, surface tension, etc.) and the liquid flow rate down the bed. For high liquid flow rates (i.e. region of loading) the parameter ϵ_b would probably increase slightly owing to gas flow passages being partially occupied by a liquid layer; however, this parameter was assumed as constant for prediction of commercial packed column transfer units. Twelve random conditions were chosen where data were available (46-49) covering vaporization and absorption where transport was either gas phase or liquid phase controlled. Using Equation 11 with the coefficients established from single sphere transport (27) together with Equations 12 and 13, the heights of the transfer unit were predicted within 12% on the average. The agreement was well within the experimental scatter in the raw HTU data, which may be as high as 20%. Prediction of transport in distillation operations can also be made by the same approach (47); however, considerably more good quality quantitative measurements must be carried out in distillation equipment before definite conclusions can be drawn. The concept of the effective interfacial area is fundamental and most useful in revealing the mechanism of irrigation of column packing for the purpose of utilizing known transport behavior in unirrigated columns.

LIST OF REFERENCES

1. Gamson, B. W., George Thodos, and O. A. Hougan, "Heat, Mass, and Momentum Transfer in the Flow of Gases Through Granular Solids," A. I. Ch. E. J. 39, 1-32 (1943).

2. Wilke, C. R., and O. A. Hougan, "Mass Transfer in the Flow of Gases Through Granular Solids Extended to Low Modified Reynolds Numbers," Trans. A. I. Ch. E. 41, 445-451 (1945).

3. McCune, L. K., and R. H. Wilhelm, "Mass and Momentum Transfer in Solid-Liquid Systems -- Fixed and Fluidized Beds," Ind. and Eng. Chem. 41, 1124-1134 (1949).

4. Taecker, R. G., and O. A. Hougan, "Heat, Mass Transfer of Gas Film in Flow of Gases Through Commerical Tower Packings," Chem. Eng. Progr. 45, 188-193 (1949).

5. Hobson, Merk, and George Thodos, "Mass Transfer in the Flow of Liquids Through Granular Solids," Chem. Eng. Progr. 45, 517-524 (1949).

6. Gaffney, B. J., and T. B. Drew, "Mass Transfer from Packing to Organic Solvents in Single Phase Flow Through a Column," Ind. and Eng. Chem. 42, 1120-1127 (1950).

7. Denton, W. H., "The Heat Transfer and Flow Resistance for Fluid Flow Through Randomly Packed Spheres," General Discussion on Heat Transfer," Inst. M. E. (London) and A. S. M. E., pp. 370-373 (1951).

8. Hobson, Merk, and George Thodos," Mass Transfer, Laminar Flow of Gases Through Granular Beds," Chem. Eng. Progr. 47, 370-375 (1951).

9. Gamson, B. W., "Heat and Mass Transfer, Fluid Solid Systems," Chem. Eng. Progr. 47, 19-28 (1951).

10. Eichhorn, Jacob, and R. R. White,"Particle-to-Fluid Heat Transfer in

Fixed and Fluidized Beds," Chem. Eng. Progr. Symp. Ser. 4, 48, 11-18 (1952).

11. Chu, J. C., James Kalil, and W. A. Wetteroth, "Mass Transfer in a Fluidized Bed," Chem. Eng. Progr. 49. 141-149 (1953).

12. Evans, G. C., and C. F. Gerald, "Mass Transfer from Benzoic Acid Granules to Water in Fixed and Fluidized Beds at Low Reynolds Numbers," Chem. Eng. Progr. 49, 135-140 (1953).

13. Galloway, L. R., W. Komarnicky, and N. Epstein, "Effect of Packing Configuration on Mass and Heat Transfer in Beds of Stacked Spheres," Canad. J. Chem. Eng. 35, 139-150 (1957).

14. Glaser, M. B., and George Thodos, "Heat and Momentum Transfer in the Flow of Gases Through Packed Beds," A. I. Ch. E. J. 4, 63-68 (1958).

15. Baumeister, E. B., and C. O. Bennett, "Fluid-Particle Heat Transfer in Packed Beds," A. I. Ch. E. J. 4, 69-74 (1958).

16. Thoenes, C., and H. Kramers, "Mass Transfer from Spheres in Various Regular Packings to a Flowing Fluid," Chem. Eng. Sci. 8, 271-283 (1958).

16.5 DeAcetis, James, and George Thodos, "Mass and Heat Transfer in Flow of Gases Through Spherical Packing" Ind. and Eng. Chem. 52, 1003-1006 (1960).

17. Gupta, A. S., and George Thodos, "Mass and Heat Transfer Through Fixed and Fluidized Beds," Chem. Eng. Progr. 58, 58-62 (1962).

18. Chukhanov, Z. F., "Heat and Mass Transfer Between Gas and Granular Material," Int J. Heat Mass Transfer 6, 690-701 (1963).

19. Meek, R. M. G., "The Measurement of Heat-Transfer Coefficients in Packed Beds by the Cyclic Method," A. S. M. E. Proc. 1961-1962, Heat Transfer Conf., 770-780 (1963).

20. Wadsworth, J., "An Experimental Investigation of the Local Packing and Heat Transfer Processes in Packed Beds of Homogeneous Spheres,"

A. S. M. E. Proc. 1961-1962, Heat Transfer Conf., 760-769 (1963).

21. McConnachie, J. T. L., and George Thodos, "Transfer Processes in the Flow of Gases Through Packed and Distended Beds of Spheres," A.I.Ch.E. J. 9, 60-64 (1963).

22. Rowe, P. N., and K. T. Claxton, "Heat and Mass Transfer from a Single Sphere to Fluid Flowing Through an Array," Trans. Inst. Chem. Eng. (London) 43, T321-31 (1965).

23. Rhodes, J. M., and F. N. Peebles, "Local Rates of Mass Transfer from Spheres in Ordered Arrays," A.I.Ch.E. J. 11, 481-487 (1965).

24. Mickley, H. S., K. A. Smith, E. I. Korchak, "Fluid Flow in Packed Beds," Chem. Eng. Sci. 20, 237-246 (1965).

25. Ziegler, E. N., and J. T. Holmes, "Mass Transfer from Fixed Surfaces to Gas Fluidized Beds," Chem. Eng. Sci. 21, 117-122 (1966).

26. Handley, P., A. Doraisamy, K. L. Butcher, and N. L. Franklin, "A Study of the Fluid and Particle Mechanics in Liquid-Fluidized Beds," Trans. Inst. Chem. Eng. (London) 44, T260-273 (1966).

27. Galloway, T. R., and B. H. Sage, "Thermal and Material Transport from Spheres. Prediction of Macroscopic Thermal and Material Transport," transmitted to Int. J. Heat Mass Transfer.

28. Galloway, T. R., and B. H. Sage, "Thermal and Material Transport From Spheres, Prediction of Local Transport", transmitted to Int. J. Heat Mass Transfer.

29. Galloway, T. R., B. H. Sage, "Local and Macroscopic Transport From a 1.5 inch Cylinder in a Turbulent Air Stream", accepted for publication by A.I.Ch.E. Journal.

30. Mickley, H. S., K. A. Smith, and E. I. Korchak, "Fluid Flow in Packed Beds," Chem. Eng. Sci. 20, 237-246 (1965).

31. Martin, J. J., and W. L. McCabe, and C. C. Monrad, "Pressure Drop Through Stacked Spheres," Chem. Eng. Progr. 47, 91-94 (1951).

33. Ergun, Sabri, "Fluid Flow Through Packed Columns," Chem. Eng. Progr. 48, 89-94 (1952).

34. Wentz, C. A., and George Thodos, "Total and Form Drag Friction Factors for the Turbulent Flow of Air Through Packed and Distended Beds of Spheres," A. I. Ch. E. J. 9, 358-361 (1963).

35. Ergun, Sabri, "Mass-Transfer Rate in Packed Columns. Its Analogy to Pressure Loss." Chem. Eng. Progr. 48, 227-236 (1952).

36. Ranz, W. E., "Friction and Transfer Coefficients for Single Particles and Packed Beds, " Chem. Eng. Progr. 48, 247-253 (1952).

37. Happel, John, "Viscous Flow in Multiparticle Systems: Slow Motion of Fluids Relative to Beds of Spherical Particles," A. I. Ch. E. J. 4, 197-201 (1958).

38. Pfeffer, Robert, and John Happel, "An Analytical Study of Heat and Mass Transfer in Multiparticle Systems at Low Reynolds Numbers," A. I. Ch. E. J. 10, 605-611 (1964).

39. Carberry, J. J., "A Boundary-Layer Model of Fluid-Particle Mass Transfer in Fixed Beds," A. I. Ch. E. J. 6, 460-463 (1960).

40. Kusik, C. L., and John Happel, "Boundary Layer Mass Transport with Heterogeneous Catalysis," Ind and Eng. Chem., Fundamentals 1, 163-172 (1962).

41. Zabrodsky, S. S., "Heat Transfer Between Solid Particles and a Gas in a Non-Uniform Aggregated Fluidized Bed," Int. J. Heat Mass Transfer 6, 23-31 (1963).

42. Rowe, P. N., "Comments on Heat Transfer Between Solid Particles and a Gas in a Non-Uniform Aggregated Fluidized Bed," Int. J. Heat Mass Transfer 6, 989-992 (1963).

43. Frantz, J. F., "Fluid-to-Particle Heat Transfer in Fluidized Beds," Chem. Eng. Progr. 57, No. 7, 35-42 (1961).

43.5 Baerns, Manfred, "The Effect of Interparticle Adhesive Forces on

Fluidization of Fine Particles," Ind. Eng. Chem., Fundamentals, 5, 508-516 (1966).

44. Cornish, A. R. H., "Note on Minimum Possible Rate of Heat Transfer from a Sphere When Other Spheres are Adjacent to It," Trans. Inst. Chem. Eng. (London) 43, T332-333 (1965).

45. Handley, D., A Doraisamu, K. L. Butcher, and N. L. Franklin, "A Study of the Fluid and Particle Mechanics in Liquid-Fluidized Beds." Trans. Inst. Chem. Eng. 44, T260-273 (1966).

46. Shulman, H. L., C. F. Ullrich, A. Z. Proulx, and J. O. Zimmerman, A.I.Ch. E. J. 1, 253 (1955)

47. Yoshida, Fumitake, and Tetsushi Koyanagi, "Mass Transfer and Effective Interfacial Areas in Packed Columns," A.I.Ch.E. J. 8, 309-316 (1962).

48. Sherwood, T. K., and R. L Pigford, Absorption and Extraction, (New York: McGraw-Hill Book Co., Inc., 1952) 478 pp.

49. Norman, W. S., Absorption, Distillation and Cooling Towers, (New York: John Wiley and Sons, Inc. m 1961) 477 pp.

APPENDIX A 7

The results of the earlier[1] analysis of the available data for packed beds of uniform spheres, cylinders, and commercial packing in regular geometric arrays are presented herein. As shown in Figure 1 in a plot of the product of the packing voidage, ϵ_p, and the Chilton-Colburn J-factor for mass transfer as a function of the superficial Reynolds number, the experimental data covering a range of Schmidt numbers from 0.62 to 10,600, Reynolds numbers from 0.4 to 30,000, and bed voidages from 0.37 to 1.00 are well represented by the solid curves for Schmidt numbers of 1, 100, and 1,000 and apparent interstitial turbulence levels of 0.04, 0.07, and 0.10. The model parameters of the interstitial turbulence as 0.10 and the voidage, ϵ_b, as 0.20 were found empirically to fit the data best. The form of the equation, it is noted, is based entirely upon results from single spheres[2]. A tremendous simplification in plotting this equation can be utilized when it is noted that for $\epsilon_b = 0.20$, $\epsilon_p - \epsilon_b$ can be represented to within $\pm 5\%$ by ϵ_p^2. The utility of this observation is that the solution can be multiplied through by ϵ_p, leaving the only variables as D_pG/μ and Sc. This technique puts a Schmidt group dependence in the steady state, molecular diffusion term which results in a family of curves at low Reynolds numbers that are strongly dependent on the Schmidt group but only weakly dependent on ϵ_p. At the

---

1. The early analysis was carried out in the Department of Chemical Engineering at the University of California at Berkeley during 1963 and was presented as a Research Report for Chemical Engineering Research (Ch. E. 250) March 24, 1964.

2. Galloway, T. R., and B. H. Sage, "Thermal and Material Transfer in Turbulent Gas Streams--A Method of Prediction for Spheres, Int, J. Heat and Mass Transfer 7, 283-291 (1964).

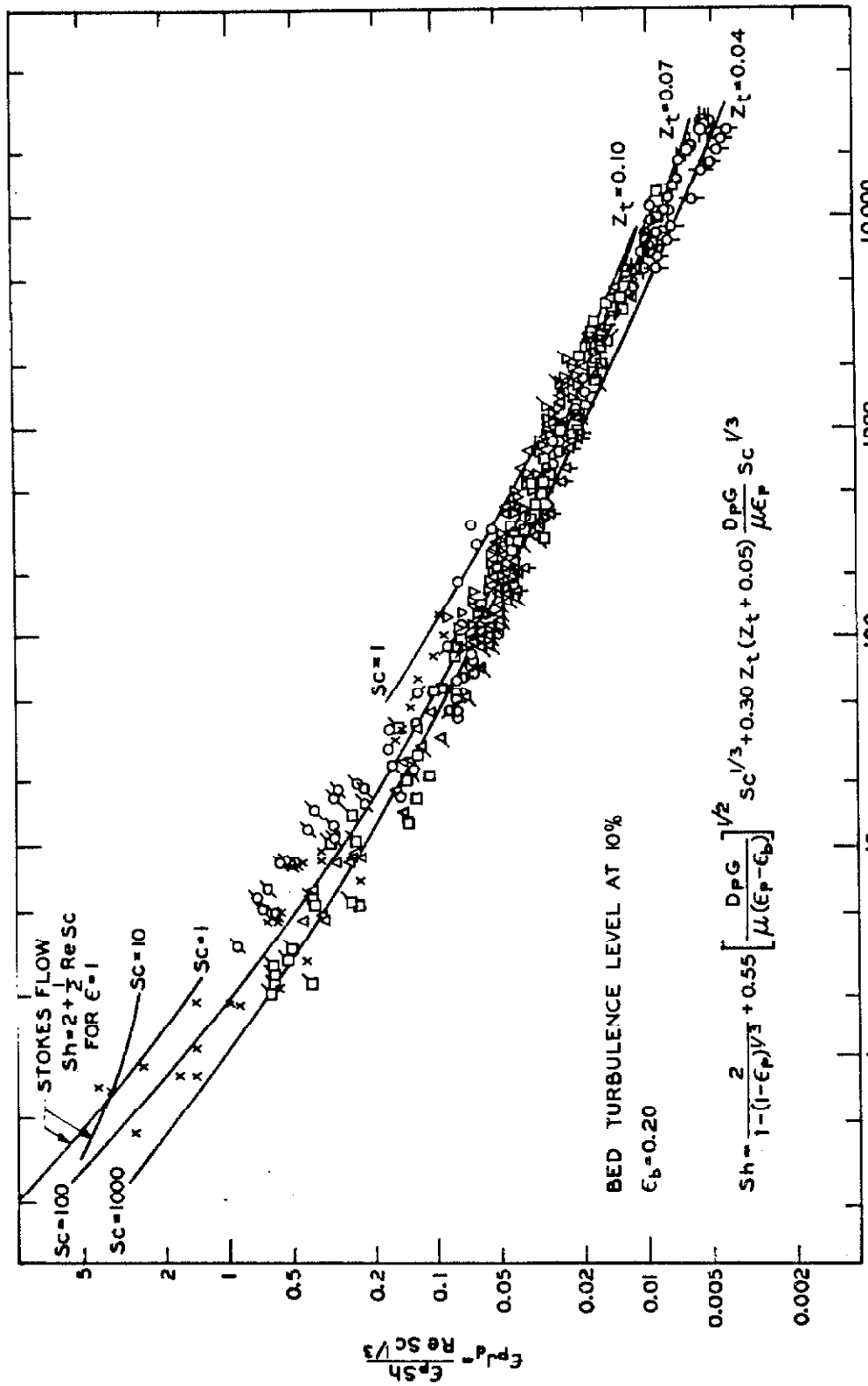

Figure 1. Heat and Mass Transfer in Beds of Spheres.

LEGEND FOR FIGURE 1

Symbol	ϵ_p	Sc	Author
+	0.493-.526	380.	Gaffney and Drew
×	0.372-.550	10,600	Gaffney and Drew
△	0.421-.621	170.	Gaffney and Drew
○	0.38 - .64	2.57	Chu, Kalil, & Wetteroth
□	0.482	0.607	DeAcetis and Thodos
▽	0.404-.430	0.615	Gamson, Thodos, & Hougan
⌀	0.475, 0.538	800.	Hobson and Thodos
◺	0.355-.375	1300.	McCune and Wilhelm
⊘	0.416	0.617	McConnachie and Thodos
▽	0.576	0.617	McConnachie and Thodos
▽	0.778	0.617	McConnachie and Thodos
◱	0.357-.410	0.615	Gamson, Thodos, & Hougan
⚲	1.000	0.620	Evnochides and Thodos
◱	1.000	1.850	Evnochides and Thodos
⊖	1.000	0.620	Maisel and Sherwood
⊕	1.000	1.70	Maisel and Sherwood
△	1.000	0.620	Pasternak and Gauvin
◱	1.000	0.620	Skelland and Cornish
⏃	0.476	0.620	Galloway, et. al.

higher flow rates numerous experimental data are available for single spheres (ϵ_p=1.00) and are correlated quite well by this form of equation. For consistent sets of data the prediction is within about 8% up to a Reynolds number of 1.3×10^6. These data at high Reynolds number need not be shown, as they are presented in Part II of this thesis.

Figure 2 shows the results of the same approach described above carried out for packed beds of cylindrical packing with a length approximately equal to its diameter. The comparison is made between the available experimental data for beds of cylinders and single cylinders. The form of the equation at this early time was taken as the form established from single sphere transport, but now is known to be of slightly different form.' At the higher Reynolds numbers the data for the packed tower with a turbulence level about 10% are significantly higher than those for single cylinders in streams of about 4% turbulence. Data for the lower Reynolds numbers were not available at this time.

For commercial packing a reasonable approximation to the form of the equation was based on the form established from the single sphere data. In Figure 3 data for various commercial packing are shown. A large portion of the bed was found to be occupied by relatively stagnant regions, such as boundary layers or wakes, and the value of ϵ_b was found to be 0.47. This indicated that the local velocity past the particle was many times larger than that past a single particle. These preliminary results were a foundation to the more exacting treatment presented as Part III.

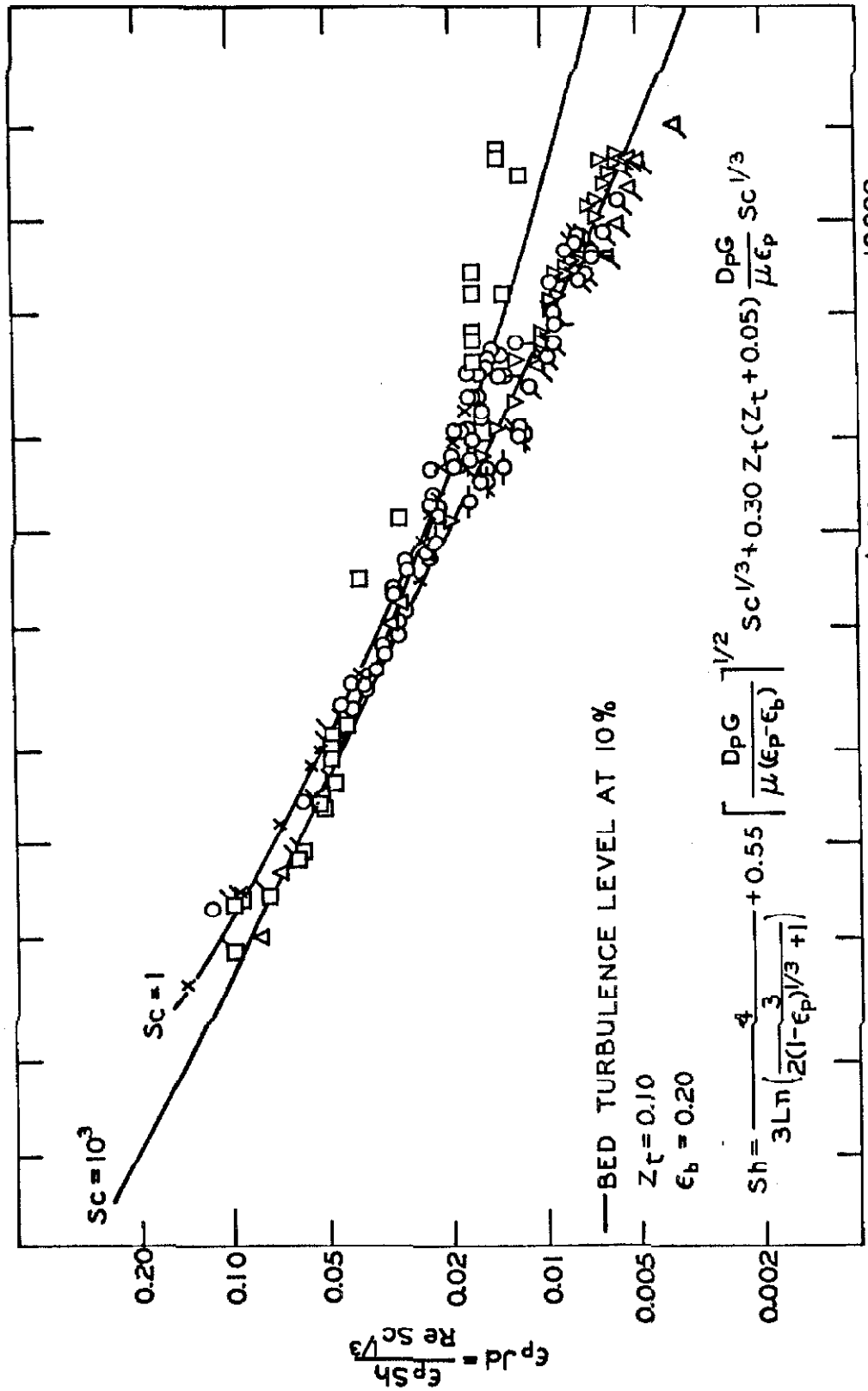

Figure 2. Heat and Mass Transfer in Beds of Short Cylinders.

LEGEND FOR FIGURE 2

Symbol	ε_p	Sc	Author
○	0.357-.410	0.615	Gamson, Thodos, & Hougan
□	0.322-.388	2.57	Chu, Kalil, & Wetteroth
△	0.390	0.617	Taecker and Hougan
◻́	0.342-.436		Wilke and Hougan
×	0.477		Glaser and Thodos
▽	1.000	0.62	Maisel and Sherwood
△	1.000	0.50	Maisel and Sherwood
⊖	1.000	1.20	Maisel and Sherwood
⌀	1.000	1.70	Maisel and Sherwood
♀	1.000	2.18	Maisel and Sherwood

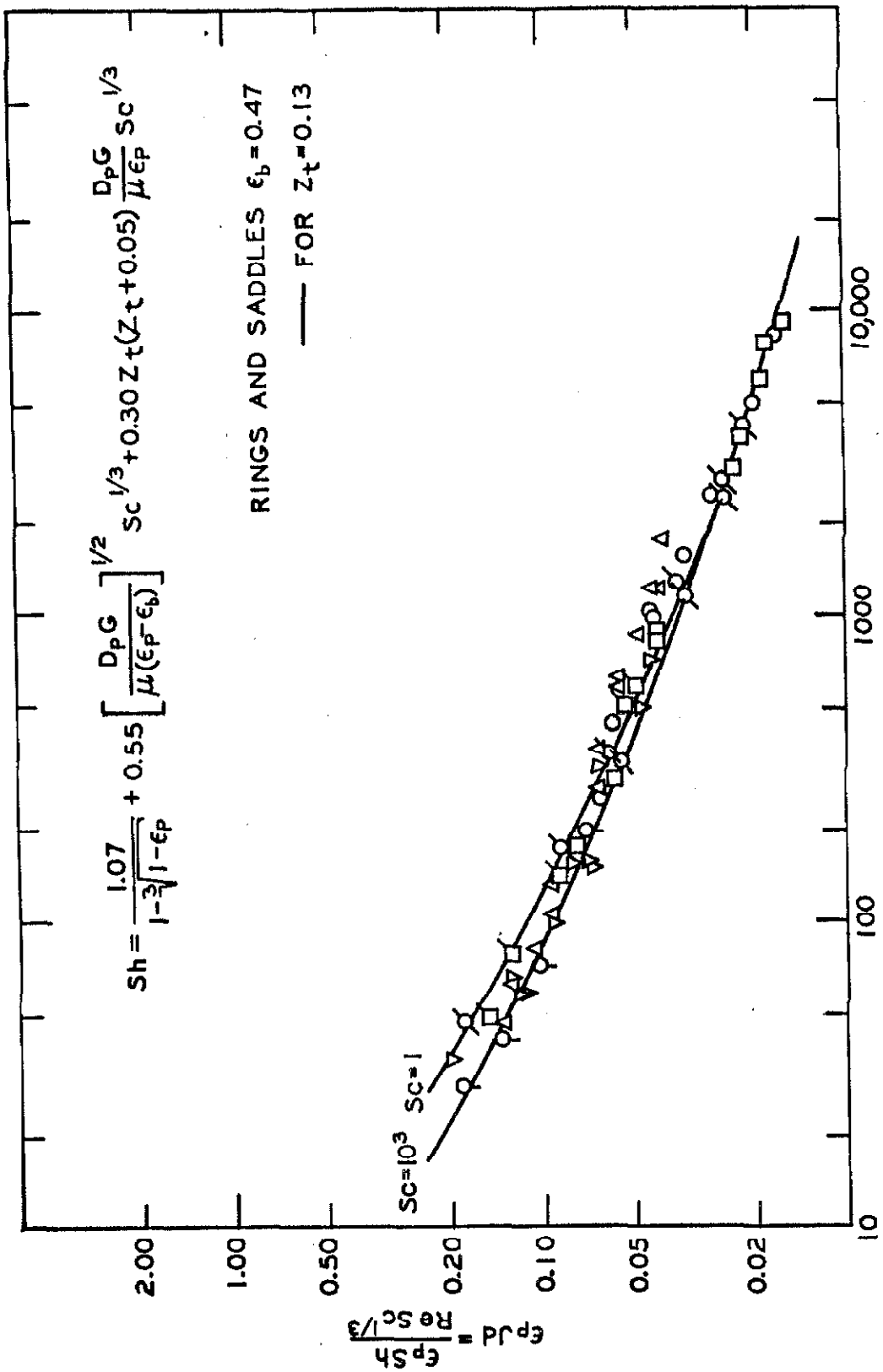

Figure 3. Heat and Mass Transfer in Beds of Commercial Packing.

LEGEND FOR FIGURE 3

ϵ_p	Packing	Symbol
0.74	2" Rashig Rings	○
0.73	1" Rashig Rings	⌀
0.63	1/2" Rashig Rings	▽
0.74	2" Partition Rings	□
0.63	1/2" Beryl Saddles	△
0.60	1/4" Beryl Saddles	♀
0.39	1/2" Cylinders	◻́

APPENDIX A 8

TABLE 1: OVERALL HEAT TRANSFER MEASUREMENTS IN THE ARRAY.

		Superficial				Interstitial						
Test	ν_∞/ν_o	U_∞	$\Delta P/L$	f_k	Re_∞	U'_∞	Re'_∞	$Re'^{1/2}_\infty$	Pr_∞	Nu_∞	Fs_∞	$Fs_\infty \nu_o/\nu_\infty$
664A	0.9833	1.3302	0.001380	1.764	874.5	14.6048	9635.7	98.162	.70482	70.331	0.80509	0.80727
664B	0.9843	1.3372	0.001412	1.786	878.1	14.6103	9632.6	98.146	.70482	74.264	0.85025	0.85240
664C	0.9843	1.3374	-	-	877.4	14.6110	9634.7	98.156	.70490	74.479	0.85259	0.85475
664D	0.9842	1.3349	-	-	885.8	15.1640	10118.0	100.588	.70486	74.103	0.82779	0.82990
664E	0.9847	1.3353	-	-	886.5	15.1643	10117.4	100.585	.70492	75.747	0.84615	0.84824
664F	0.9847	1.3312	-	-	882.7	15.1668	10122.5	100.611	.70506	75.345	0.84140	0.84348
665A	0.9846	2.7080	0.005294	1.633	1785.6	29.1433	19288.0	138.881	.70473	128.111	1.03657	1.03915
665B	0.9846	2.7027	0.005254	1.627	1782.1	29,1439	19281.0	138.856	.70473	128.437	1.03940	1.04198
665C	0.9844	2.7045	-	-	1779.4	29.0278	19174.7	138.473	.70478	125.899	1.02166	1.02473
665D	0.9845	2.7051	-	-	1773.8	29.0451	19153.3	138.395	.70478	127.194	1.03274	1.03532
666A	0.9845	5.5095	0.020028	1.492	3618.3	53.9356	35574.8	188.613	.70476	203.886	1.21470	1.21774
666B	0.9852	5.5074	-	-	3615.8	53.9404	35557.9	188.568	.70473	206.953	1.23328	1.23624
666C	0.9853	5.4998	-	-	3604.9	53.9943	35507.3	188.434	.70470	203.191	1.21174	1.21462
666D	0.9855	5.5119	-	-	3609.1	54.0146	35494.2	188.399	.70470	204.033	1.21699	1.21984

$\Delta P/L$ in units of psi/inch of packing.

U_∞ and U'_∞ in units of ft/sec.

f_k = Blake-type friction factor = $\frac{\Delta P}{L} \frac{g_c D_p}{\rho U^2} \frac{e^3}{1-e}$

Void fraction of the rhombohedral No. 6, blocked passage array = $e = 0.2595$

TABLE 2: LOCAL HEAT TRANSFER MEASUREMENTS IN THE ARRAY.

THE MODIFIED FRÖSSLING NUMBER, FS'_{∞}

Test	664	664	664	664	664	665	665	665	665	666	666	666	666
β=	30°	40°	60°	0°	-30°	0°	60°	30°	-30°	60°	-30°	0°	30°
$\cos\psi$													
1.0	1.7144	-	1.6943	-	-	1.8092	-	-	1.8117	-	-	-	1.9791
0.9	-	-	-	1.1071	1.2089	1.2853	-	-	1.3522	-	1.5289	1.4862	-
0.8	1.1436	-	-	0.5566	0.4207	0.6401	-	1.3475	0.3991	-	0.4093	0.7315	1.5351
0.7	1.2124	1.0353	-	0.6822	0.4007	0.7678	-	1.4453	0.5022	-	0.6126	0.9075	1.7285
0.6	1.3920	1.1918	-	1.0471	0.5218	1.1074	-	-	1.5354	-	0.7431	-	0.9997
0.5	1.4294	1.2880	1.2861	1.2422	0.6590	1.3563	1.5210	1.5544	0.9399	1.7111	1.1611	1.5305	1.7671
0.4	1.3735	1.2505	1.2518	1.2690	0.7934	1.4514	1.5023	1.5112	1.0577	1.7943	1.2523	1.6516	1.6763
0.3	1.3182	1.2505	1.2373	1.3042	0.8871	1.5220	1.4463	1.4438	1.1409	1.7572	1.3918	1.7340	1.6010
0.2	1.2542	1.2394	1.0327	1.3466	-	1.6424	1.2807	1.3629	1.1648	1.5669	1.4499	1.8789	1.5276
0.1	1.1848	1.1891	0.6878	1.0791	0.9302	1.3818	0.8023	1.2715	1.1525	0.9054	1.4502	1.8041	1.4228
0.0	1.0473	1.0168	0.4275	0.7100	-	0.8487	0.4163	1.1416	1.0696	0.4099	1.3347	1.1436	1.2786
-0.1	0.8754	0.7235	0.3152	0.4537	0.7668	0.5460	0.2809	0.9203	0.9238	0.2592	1.1855	0.6944	1.0226
-0.2	0.6400	0.4713	0.2909	0.4588	-	0.6787	0.3420	0.6716	0.7668	0.4443	1.0224	0.8107	0.7508
-0.3	0.4544	0.3409	0.3574	0.6596	0.5328	0.9672	0.5453	0.4988	0.7237	0.8265	0.9554	1.0163	0.6671
-0.4	0.3971	0.3082	0.4840	0.7859	0.5796	1.0696	0.7253	0.5374	0.7987	1.0179	1.0091	1.0453	0.8364
-0.5	0.4633	0.3404	0.5357	0.7513	0.7179	1.1188	0.7771	0.7075	0.8916	1.0346	1.0977	1.0350	1.0127
-0.6	0.7227	0.5345	0.5676	0.6636	0.7644	1.1191	0.8149	0.9447	0.8931	1.1149	1.1035	1.0197	1.2761
-0.7	1.0668	0.8883	0.5908	0.6907	0.7693	1.1848	0.8595	1.2451	0.8977	1.1258	1.0774	1.1054	1.6387
-0.8	1.0767	0.9512	0.5825	0.8323	0.7894	1.2492	0.8264	1.1695	0.9651	0.9976	1.1106	1.2037	1.5591
-0.9	0.5186	0.4710	0.4776	0.7879	0.7309	1.0696	0.7095	0.5525	0.9266	0.9436	1.1351	1.0540	0.6752
-1.0	-	0.5176	0.5226	-	-	0.7168	-	0.7165	-	-	0.8924	-	0.8880

PROPOSITIONS

PROPOSITION A

AN INEXPENSIVE ELECTROMECHANICAL INTEGRATOR FOR THE LABORATORY

A design is proposed for an inexpensive laboratory elctromechanical integrator that can be constructed without any great degree of precision and very little machine work. The principle of this instrument is based on the operating characteristics of a d.c. motor, which can be used as a tachometer. The integral is obtained by magnetically detecting the degree or rotation of the tachometer shaft (digitizing) and displaying the result as a digital output. The author has constructed such an integrator and found precisions better than one half of one percent were feasible.

INTRODUCTION

Recently, there has been an influx of fine compact, portable electronic laboratory instruments which are capable of measuring and displaying almost any laboratory signal. Since it is now possible to continuously monitor or instantaneously record these signals, there has been an increased demand for instantaneously performing various operations on these signals, such as differentiation or integration. These operations are the most difficult in terms of a useful analog, and instruments equipped with differentiators or integrators are therefore quite expensive.

Most commercial integrators use the mechanical analog of a ball riding at various radii on a synchronous spinning disk. Although this has proved quite useful despite large mechanical losses, expensive maching of high precision

is required. Various other analogs (1,2,3) have been suggested such as electrochemical deposition, the electronic tachometer, the charging of a capacitor, and voltage to frequency conversion. Each of these techniques are quite sophisticated and involve considerable electronics and proportionately greater expense. Of these analogs, the tachometer system (4) becomes most economical when the d.c. motor shaft rotation is magnetically digitized and the non-linear operating characteristics are corrected electronically.

DISCUSSION

The success of the analog in the electromechanical integrator depends on the linearity of speed of shaft rotation with respect to the voltage applied:

$$RPM = C_1 V(t) \tag{1}$$

Then the total number of turns that the shaft makes is merely the integral of the speed or rotation over the time interval taken:

$$N = C_1 \int_0^t V(t)\, dt \tag{2}$$

If the shaft rotation is further resolved by digitizing the angular variation, the integral can be expressed in terms of the total number of digital counts:

$$N = C_2 \int_0^t V(t) dt$$

Now if the laboratory signal is amplified to such an extent (eg. V(t)) so as to actuate this tachometer, the integral is thus directly obtained. In

practice the expense of a stabilized power d. c. amplifier with a high degree of amplification is prohibitive so it is desirable to utilize the output of the servo-amplifier of a laboratory recorder. A multi-turn slidewire resistor (eg. Helipot) is coupled to the servo-motor that actuates the recorder pen. This slidewire inturn varies the voltage that is then applied to the tachometer.

Unfortunately, in practice few d. c. motors possess a linear relation between the angular rotation and the voltage applied. The characteristics of one of the eight motors which the author has tested* and rejected are shown in Figure 1. This shows the angular rotation in counts per minute in terms of the varying rotor field at various stator field strengths. Linearity is evidenced only for very high field strengths. This fact has been exploited in the final design. Curvature is most marked for application of the signal to both the stator and rotor simultaneously and is therefore undesirable. Figure 1 also shows that a finite voltage must be applied before the tachometer can be actuated, thus the laboratory signal must be made proportional to the voltage applied in excess of this starting voltage. The integral relation of Equation 2 is useful only when C_2 (the ratio of counts per minute to this voltage excess) remains constant. Figure 2 illustrates this relationship for the data shown in Figure 1.

Now the circuitry required to correct solely for the effects of finite starting voltage is merely a bridge as shown in Figure 3. The retransmitting slidewire potentiometer shown is driven by the servo-motor of a laboratory recorder which the author has designed and constructed. Although the bridge circuit achieves the result, two complicating factors arise: the tachometer resistance tends to load down the bridge, and, further, the resistance that

---

* All of the data in this and the accompanying figures were obtained by the author.

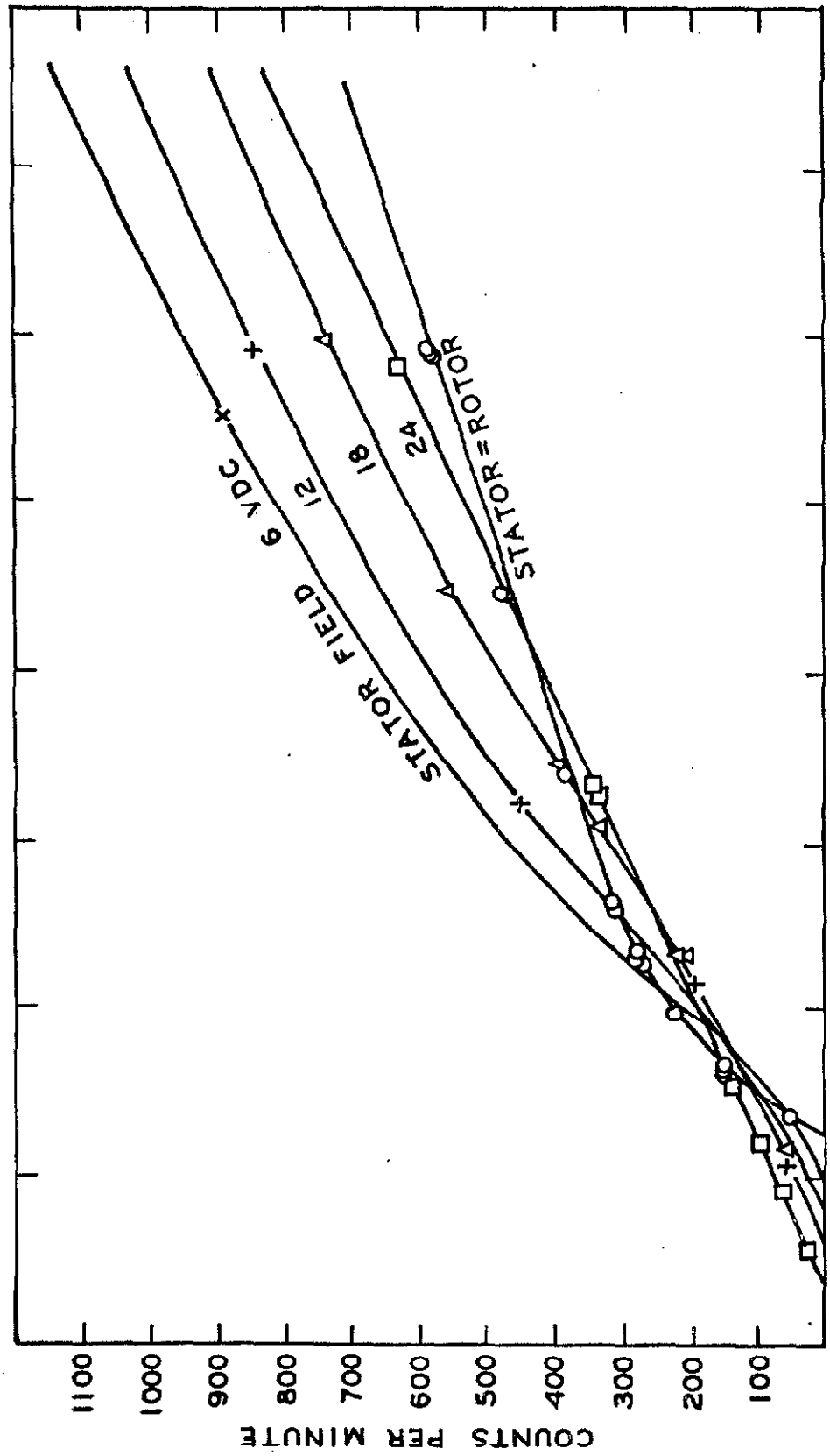

Figure 1. D. C. Motor Characteristics.

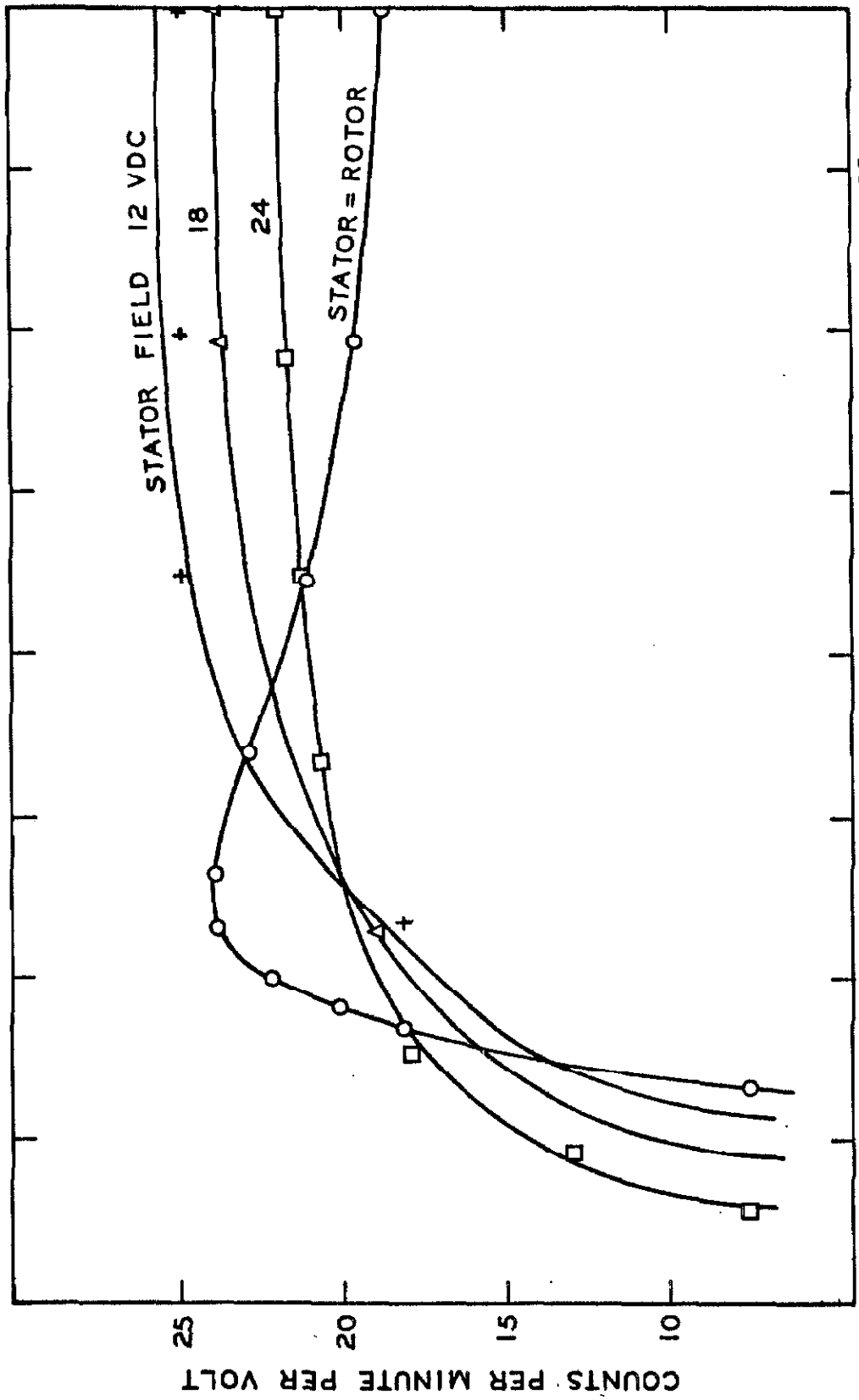

Figure 2. Linearity of D. C. Motor Characteristics.

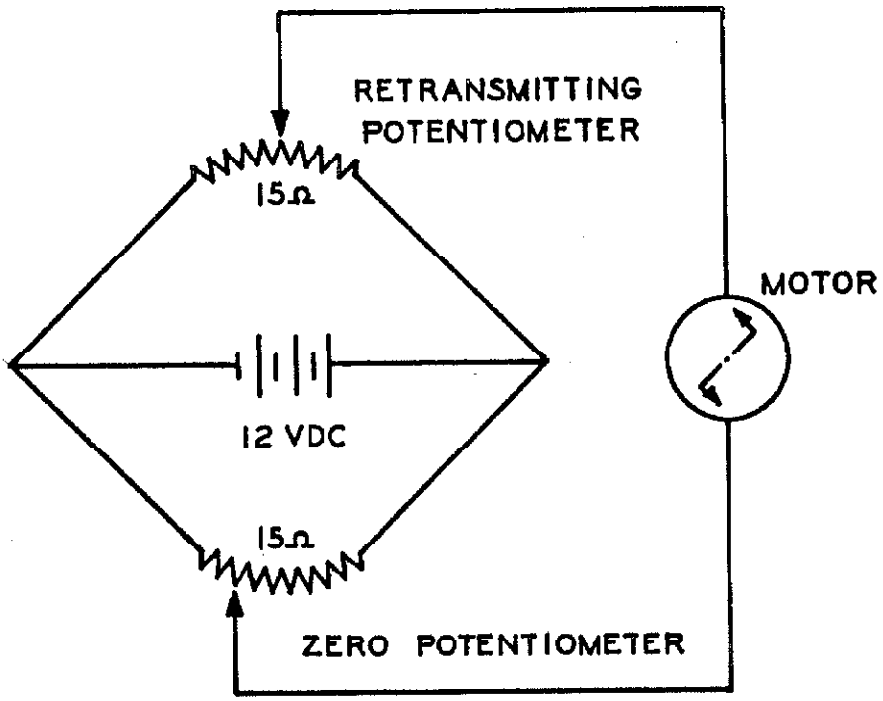

Figure 3. Bridge Circuit.

this tachometer presents to the bridge changes appreciably with the rate of angular rotation (proportional to the voltage applied) as shown in Figure 4. This effect can be substantially corrected by designing a correcting circuit; that is, to partially counteract the effects of the finite motor resistance by symmetrically loading the bridge circuit as shown in Figure 5. Here "d" represents the displacement of the servo-motor; R, the loading resistance, and R_m, the variable resistance of the motor. The voltage relationship is as follows:

$$\frac{V}{E} = \frac{1}{1 + \dfrac{\dfrac{1}{R} + \dfrac{1}{20\,d}}{\dfrac{1}{R_m} + \dfrac{1}{20(1-d)}}} \qquad (3)$$

The utility of this technique is two-fold -- to correct for the non-linear operating characteristics of the motor at the lower voltages and partially counteract the finite motor resistance. Figure 6 illustrates the results of symmetric loading. This shows the extent by which the voltage applied to the motor is increased over that from the input displacement, d. As shown for several values of the loading resistor, this parameter varies the degree of non-linear compensation.

When all of these features are encorporated into the final design the resulting circuit is as shown in Figure 7. Here the bridge has been refined somewhat with capabilities for fine zero adjustments and count rate scaling factor calibration. A motor shunt is provided to damp the counting between laboratory records varying rapidly with time. The problem of counting or resolving the angular rotation of the tachometer shaft with high precision yet while imposing a minimal torque to the tachometer was alleviated by utilizing

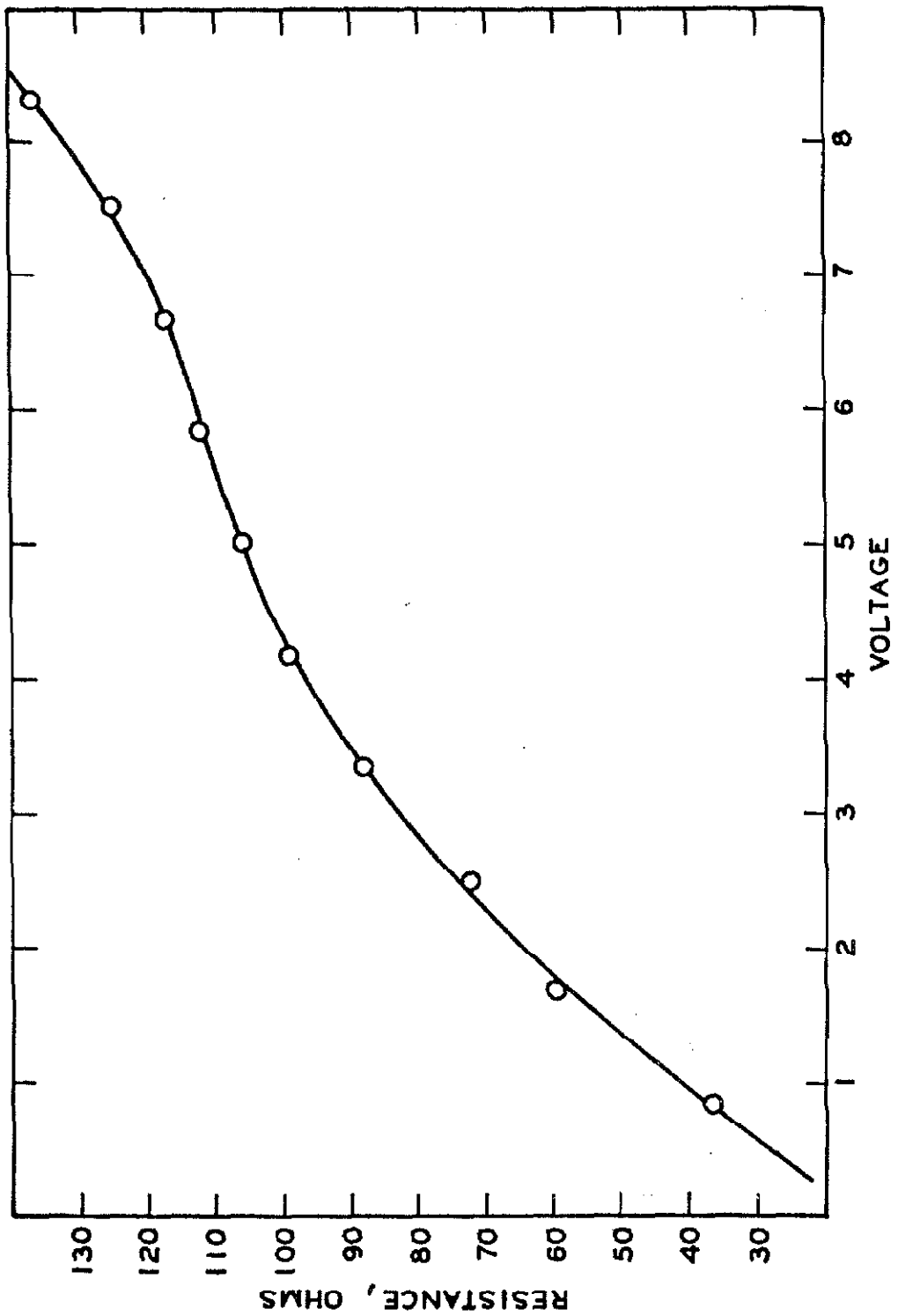

Figure 4. Variation of Motor Resistance.

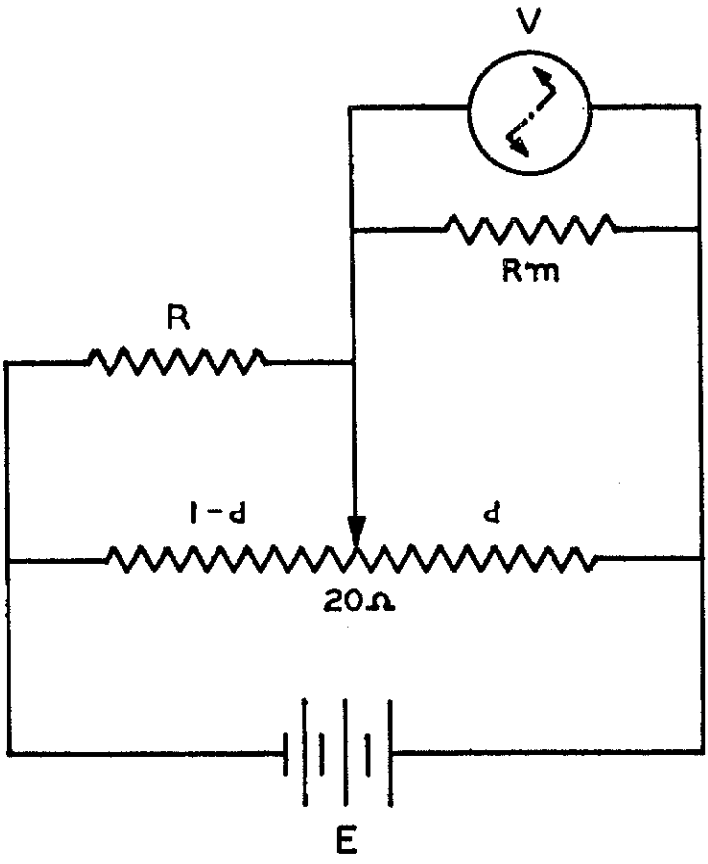

$$\frac{V}{E} = \frac{1}{1 + \frac{\frac{1}{R} + \frac{1}{20d}}{\frac{1}{Rm} + \frac{1}{20(1-d)}}}$$

Figure 5. Linear Compensating Modification.

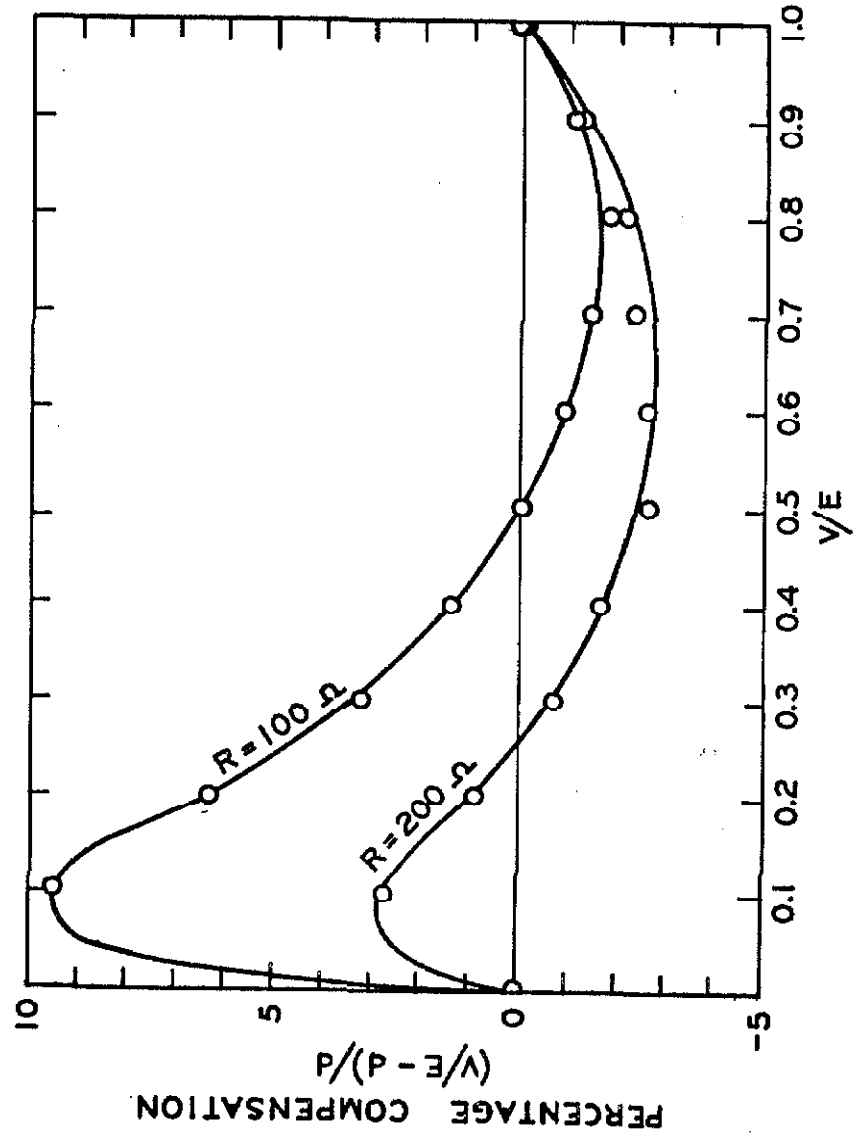

Figure 6. Compensating Characteristics.

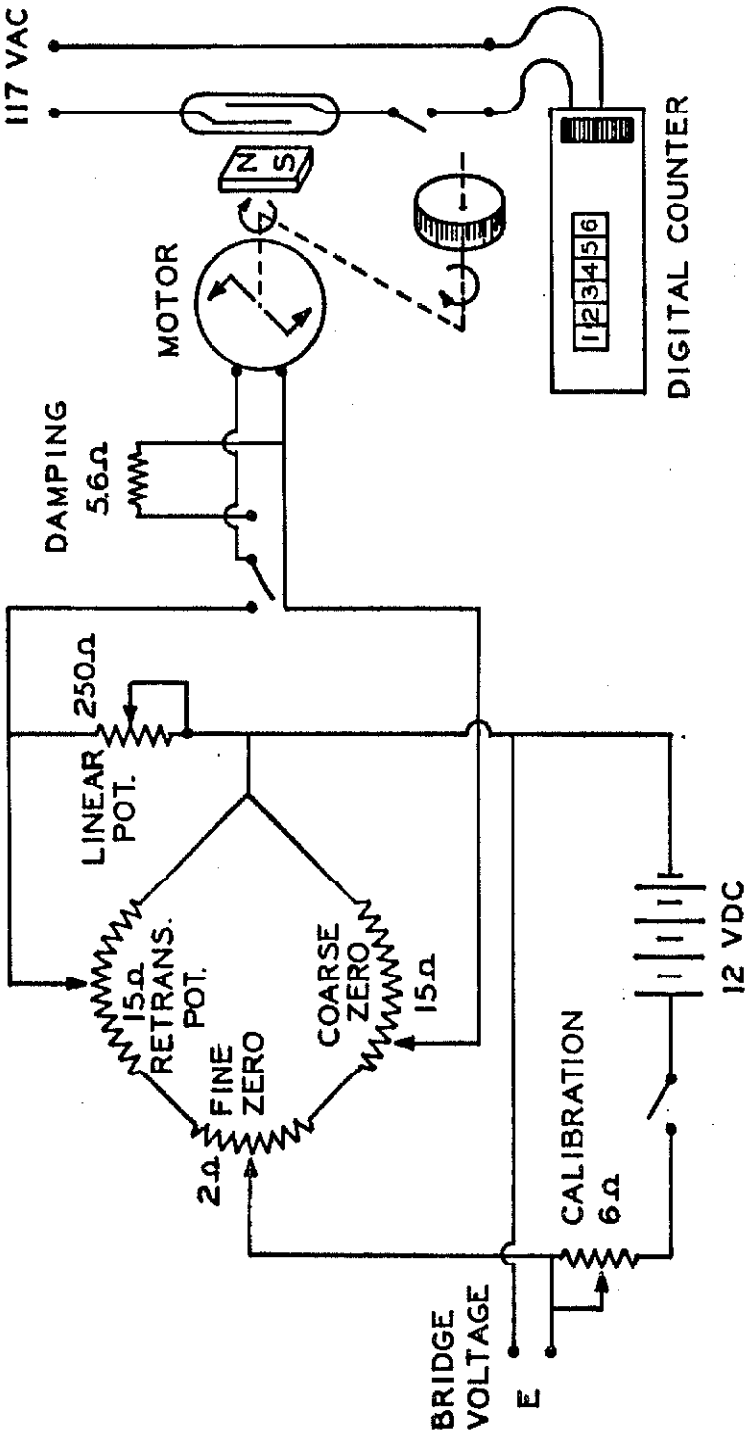

Figure 7. Complete Integrator Schematic.

a magnetically actuated dry reed switch.. A small Alnico magnet was mounted on the tachometer shaft and rotated in front of the reed switch. Whenever the poles of the magnet are parallel to the reed, the switch is actuated; thus, achieving two counts per revolution. This switch then actuates a electro-magnetically driven digital counter, as shown, or it could actuate a digital scaling circuit, which can inturn trigger a punch tape unit for computer input or process control. For signals which vary rapidly with time a high degree of angular revolution is required. Increasing the tachometer speed greatly, however, also magnifies the inertial effects which result in deterioration of the frequency response. A compromise must be made between high resolution and inertial effects. One solution is to greatly increase the angular resolution by the rotation of a very light weight, low inertial disk, marked off in 200 divisions on the circumference. The higher rate of the disk rotation is limited by the frequency response of economical digital counters (around 1 KHZ). This refinement is shown in the enlargement of Figure 8 together with the servo amplifier. In this way counting frequencies as high as 100,000 counts per second can be obtained, although for common practice 10,000 is most desirable.

The counting technique used for the integration of laboratory signals is important in obtaining the higher precision. Bridge voltage must be maintained before and after integration to guard against d.c. voltage fluctuations. Any variation in the initial bridge voltage varies the proportionality between the integral and the total counts. The maximum in the laboratory signal must be anticipated so that non-linear compensation can be made to increase the linearities of the characteristics in the operating region to be studied. Just before the signal is to be integrated the count rate must be zeroed at the same point on the scale as the initial value of the signal. The area under the curve will then be given by the difference in the counts before and after the event.

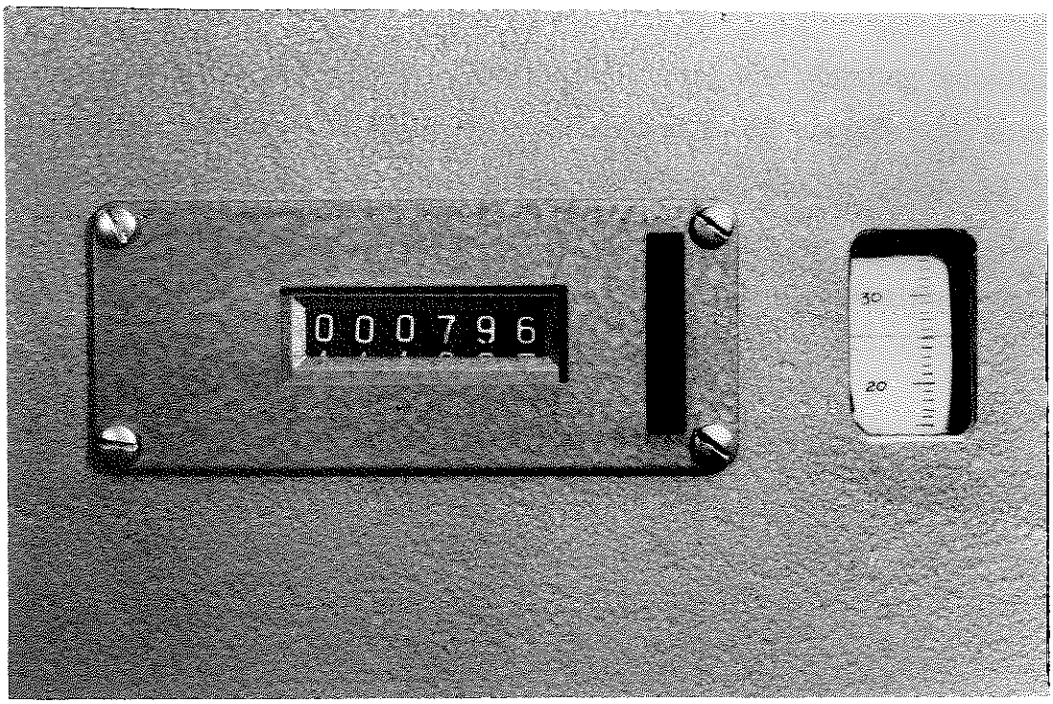

Integrator Digital Readout

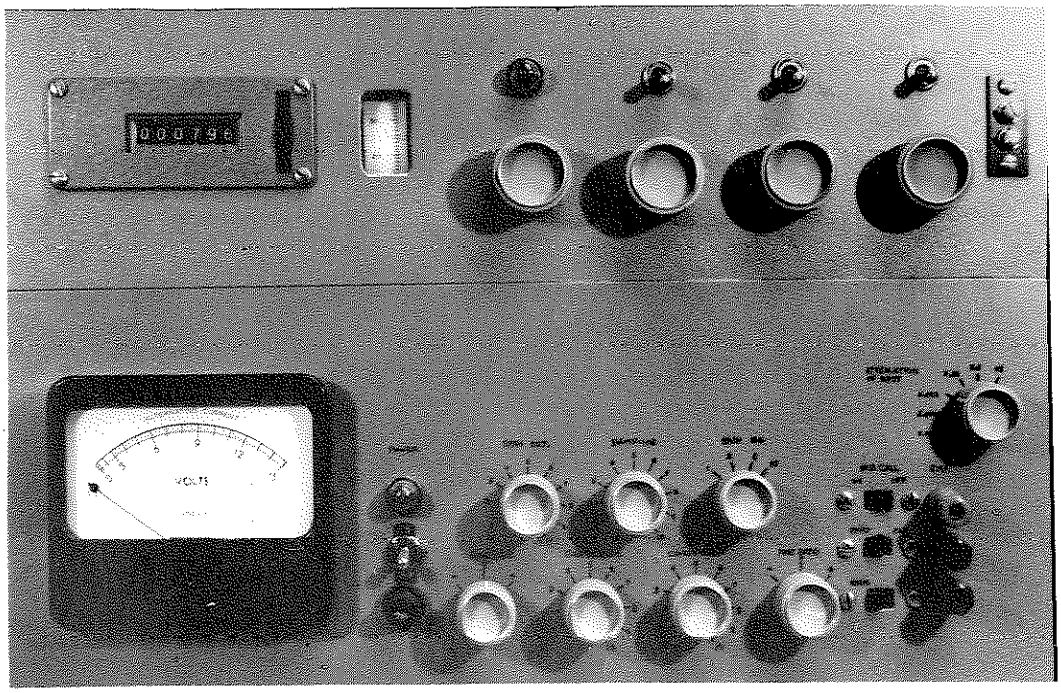

Figure 8. An Integrator Digital Readout and Servo Amp.

Tests for a square wave have been carried out using this counting technique and the results recorded in Figure 9. The necessity for considerably more non-linear compensation for higher bridge voltages is clearly seen. By judicious selection of these parameters (as shown in the lower curve) one can achieve integrations with precisions somewhat better then one-half of one percent.

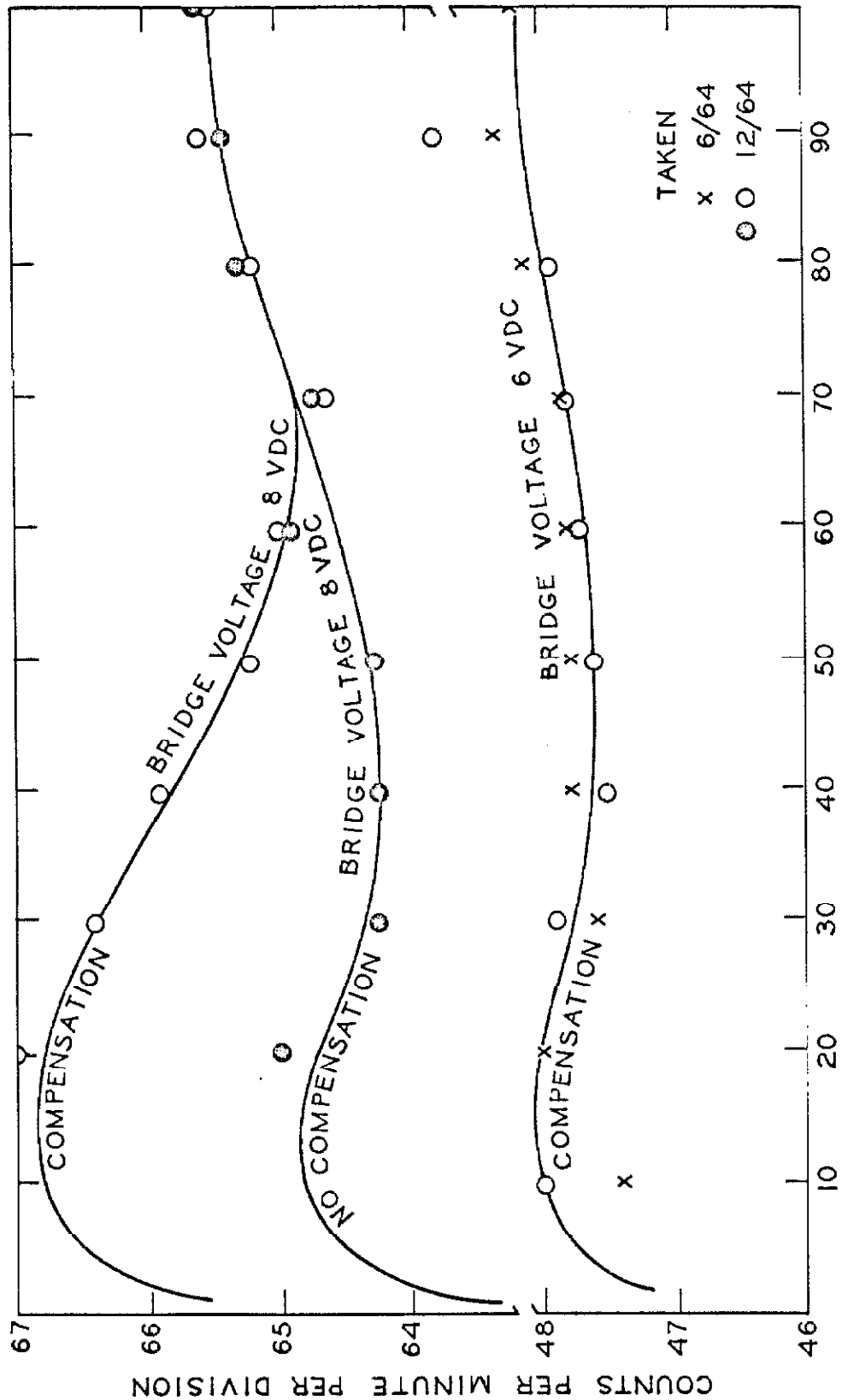

Figure 9. Integration of a Square-wave.

NOMENCLATURE

C_1 = Proportionality constant, Equation 1

C = Total number of digital counts

N = Total number of turns of tachometer

RPM = Rate of rotation of tachometer shaft (rpm)

t = Time elapsed during integration (sec)

V(t) = Time varying voltage signal (volts)

REFERENCES

1. Lion, K. S., "Instrumentation in Scientific Research," (New York: McGraw-Hill Book Co., 1959)
2. Partridge, G. R., "Principles of Electronic Instruments," (New Jersey: Prentice-Hall Inc., 1958)
3. Sawyer, D. T., and J. K. Barr, "Evaluation of Several Integrators for Use in Gas Chromatography," Anal. Chem. 34, 1213-1216 (1962)
4. Nogare, S. D., C. E. Bennett, and J. C. Herden, "A Simple Electro-mechanical Integrator," Instru. Soc. of America Proceedings, Int. Gas Chromatog. Symp. (1957)

PROPOSITION B

AUTOMATING THE PHOTOGRAPHIC REFRACTOR TELESCOPE FOR LONG FOCAL LENGTH PHOTOGRAPHY

An automated system is proposed which will consistently permit high resolution, long exposure time photographs to be made with a long focal length camera on a photographic refractor telescope. The essential part of the system is a solid state oscillator which ultimately drives a standard 115 volt synchronous Cramer control motor by means of a silicon control rectifier inverter. Telescope tracking during an exposure can be achieved at calibrated sidereal, solar, or lunar rates as well as variable rates.

INTRODUCTION

The problem of astronomical photography is to record the maximum amount of visual information possible from the available telescope system. The information content in a photographic record can be expressed as the maximum number of lines per millimeter just resolved. The resolution is a function entirely of the effective focal ratio, f, of the system:

$$\text{Lines/mm} = 1464/f$$

Owing to the low contrast of most astronomical objects, the resolution of the

---

* The author has instituted proceedings toward the procurement of a patent covering this device. The content of this proposition will be submitted to "Sky and Telescope" for publication.

film should be at least three times that of the photographic telescope system. Most sheet films will resolve 60 lines/mm. Consequently the optimum photographic record can be obtained with a photographic telescope of a focal ratio of f/76.

ASTRONOMICAL PHOTOGRAPHY

The problem arises when a record needs to be viewed by the human eye, which, in good operating condition, can only resolve 6 lines/mm. Enlarging the photographic record more than four times by available methods results in considerable loss in definition. A long focal length photographic system (capable of producing records of high magnification) requires faster film with a consequent loss in resolution owing to coarse grain size ans such a system also requires longer exposures. When an exposure is over about one minute the response of the film is no longer proportional to the photon count; this is known as "reciprocity failure". Very long exposure times demand extremely accurate tracking of the telescope in order to maintain a steady image on the photographic plate, and the length of exposure is limited by friction in the mount, minute gear error, atmospheric refraction, etc.. Therefore, an optimum is sought between extreme enlargement of a small, high resolution image and the long exposure times required for a highly magnified image.

Figure 1a illustrates the effects of tracking error of about 40 seconds of arc during an exposure of ten minutes. The single disk is that of Jupiter. The cloud belts can be made out as well as the oblate nature of the planet; however, a tracking error of less than one second of arc would greatly improve the resulting record. The enlargement of the original negative for the positive is about two times, and the grain size cannot be seen on the original positive (i.e. better than 6 lines/mm). Figure 1b is a photograph of Saturn

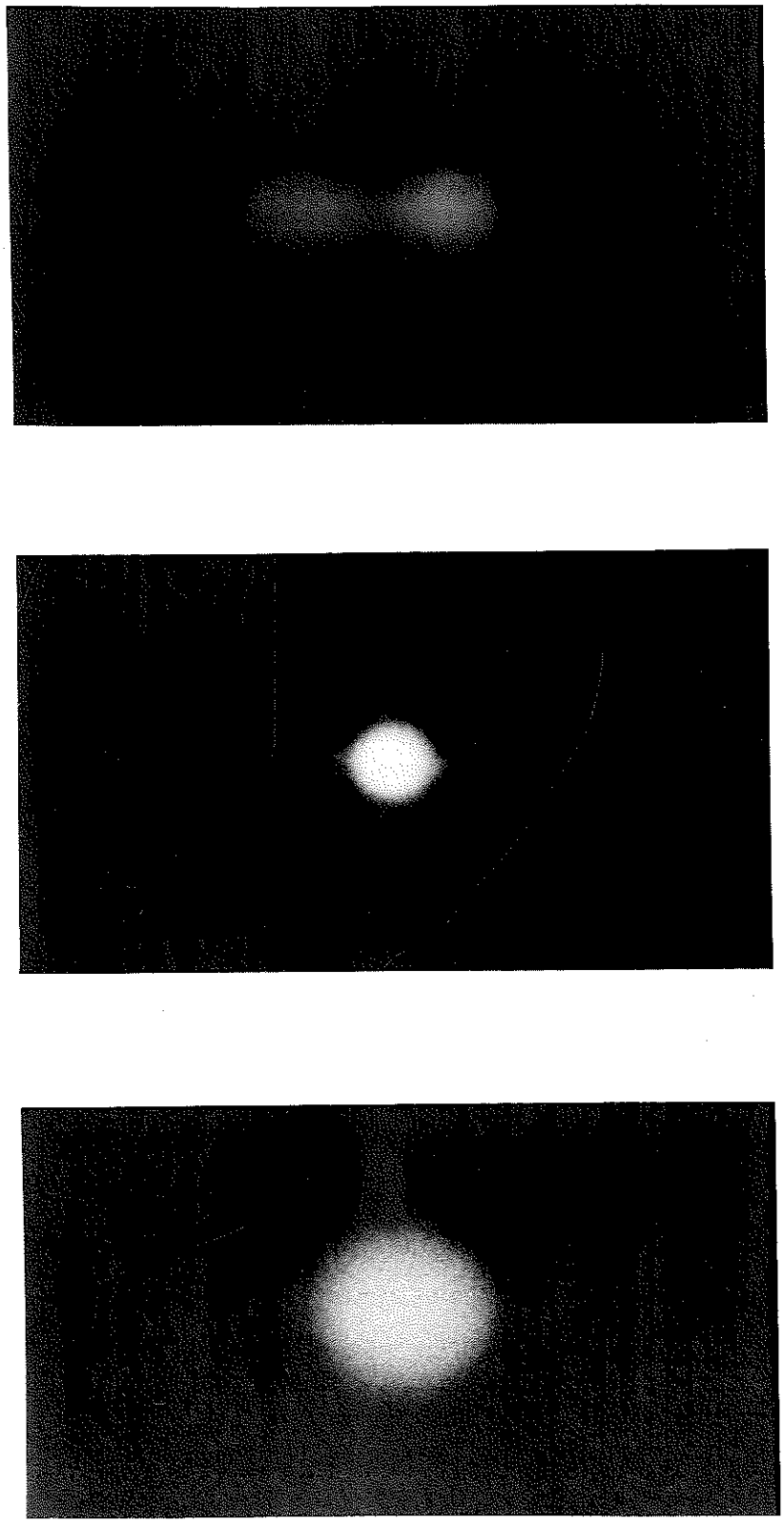

Figure 1. Photograph of Jupiter and Saturn

taken with a f/50 camera and the resulting negative has been enlarged about six times for this positive. The grain size is pronounced and seriously reduces the higher resolution of the original. The exposure has been made for the disk and not the rings. Figure 1c is the result of another exposure of Saturn made with the long focal length camera (f/131). The grain size is about one third of a millimeter and comparable to the resolution of the camera. The negative image has been enlarged about three times which is taken to be the optimum. The photography of Saturn is a harsh test for the telescope tracking system as well as the camera since the planet is only about 18 seconds of arc in diameter and requires very long exposures.

Figure 2 shows a long focal length photograph of the lunar surface which is illuminated by the sun at a low angle, enhancing the features in relief. The lunar coordinates for the center of the photograph are +30°, -10°. The large crater at the lower left of center is Theophilus, a ring plane. It has been extensively studied for its typical center peak and peculiar ridge normal to the crater walls.

The bright crater immediately beneath Theophilus is Mädler, also extensively studied as a newly formed crater. The older crater at the lower right of center partially hidden in the mare is Fracastorius. The visible definition in all these features illustrates that the design limits of the telescope system have been achieved. Theophilus is 64 miles in diameter. Features 1.5 miles in diameter can be resolved in the original positive which corresponds to 1.2 seconds of arc -- comparable to the limit of resolution of the telescope main objective (the Dawes limit being 0.8 seconds). The grain size in the enlarged positive is about one-third smaller than this limit of resolution; illustrating that the properties of the emulsion have not interferred with the optimum resolution of the optics.

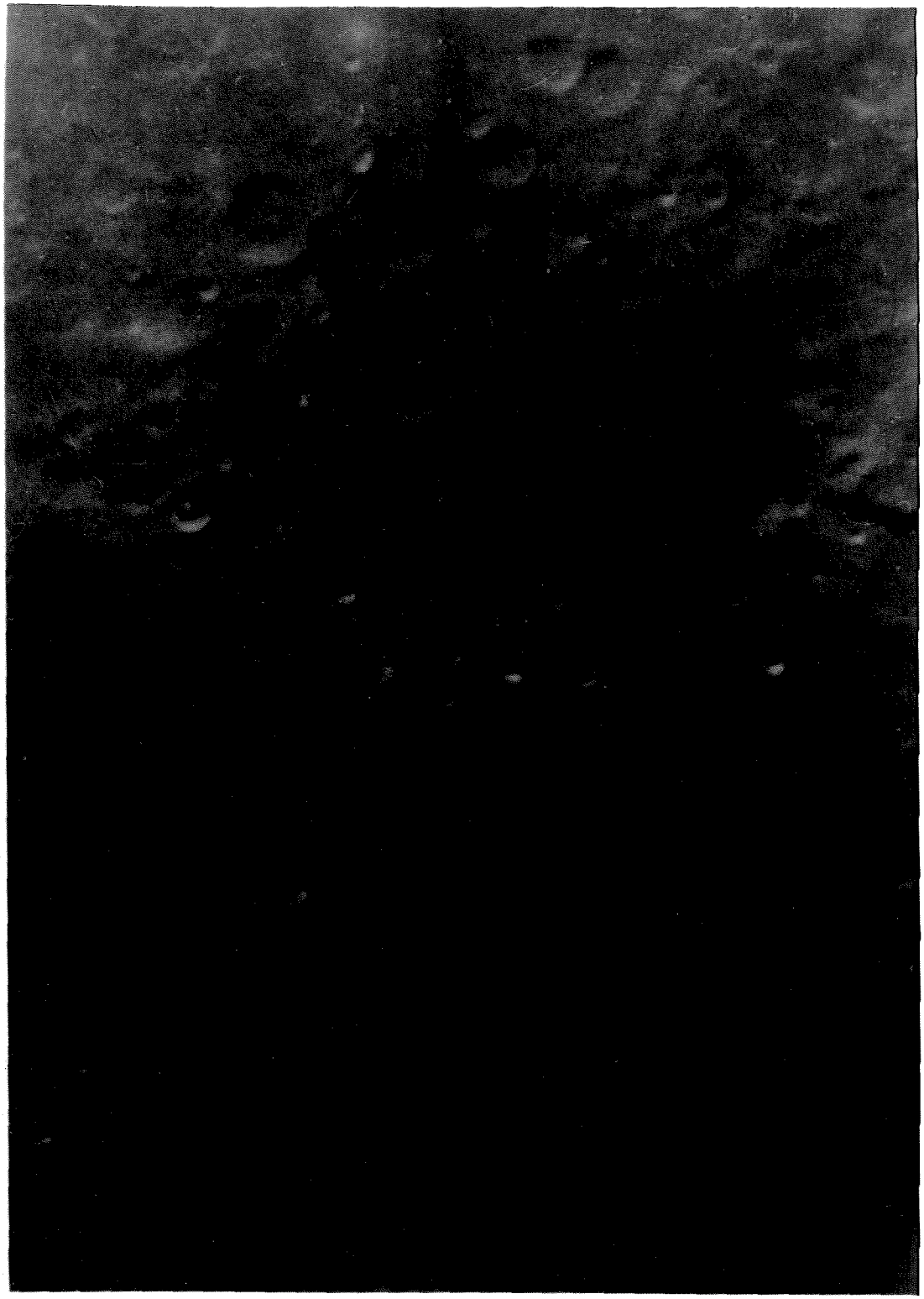

Figure 2. Photograph of Lunar Surface.

OPTICAL DESIGN

Current sheet film characteristics dictate the optimum. The system that has been selected is a refractor telescope photographic system with an equivalent focal length of 525" (43 feet 9 inches) and an effective focal ratio of f/131. The camera system itself provides an 8.75 magnification of the primary image, illuminating a 6 inch film diagonal. A number of differing optical designs were tried before the final configuration was selected, as shown in Figure 3.

This camera is a combination of a positive and negative projection system. A type G, deep yellow, wratten filter has been used to filter out those wavelengths, to which the photographic film is sensitive, that are not properly focused by a visual achromatic objective. This common type objective is corrected for the yellow portion of the spectrum to which the human eye is most sensitive. Most photographic panchromatic films are responsive to a wider range of wavelength than is the eye; thus, these must be filtered out. The four element, positive, air-spaced, coated achromat is the primary portion of the projection system enlarging the primary image four times. The coated negative achromat then functions as Barlow lens again magnifying the image more than twice in a very short distance; thus, achieving a magnification of 8.74x. The back of the camera is equipped with a housing into which can be slipped a 4x5 inch ground glass for focusing or a 4x5 inch dual sheet film holder as shown in Figure 4a. The camera lens tube is replaced with others with smaller focal ratios and permit photographing objects of larger angular field. The lens tube of the camera slides into the focusing tube of the refractor as shown in Figure 4b. The refractor telescope itself is of conventional design, being equipped with an equatorial mount and both right ascension and declination slewing servos on the axes

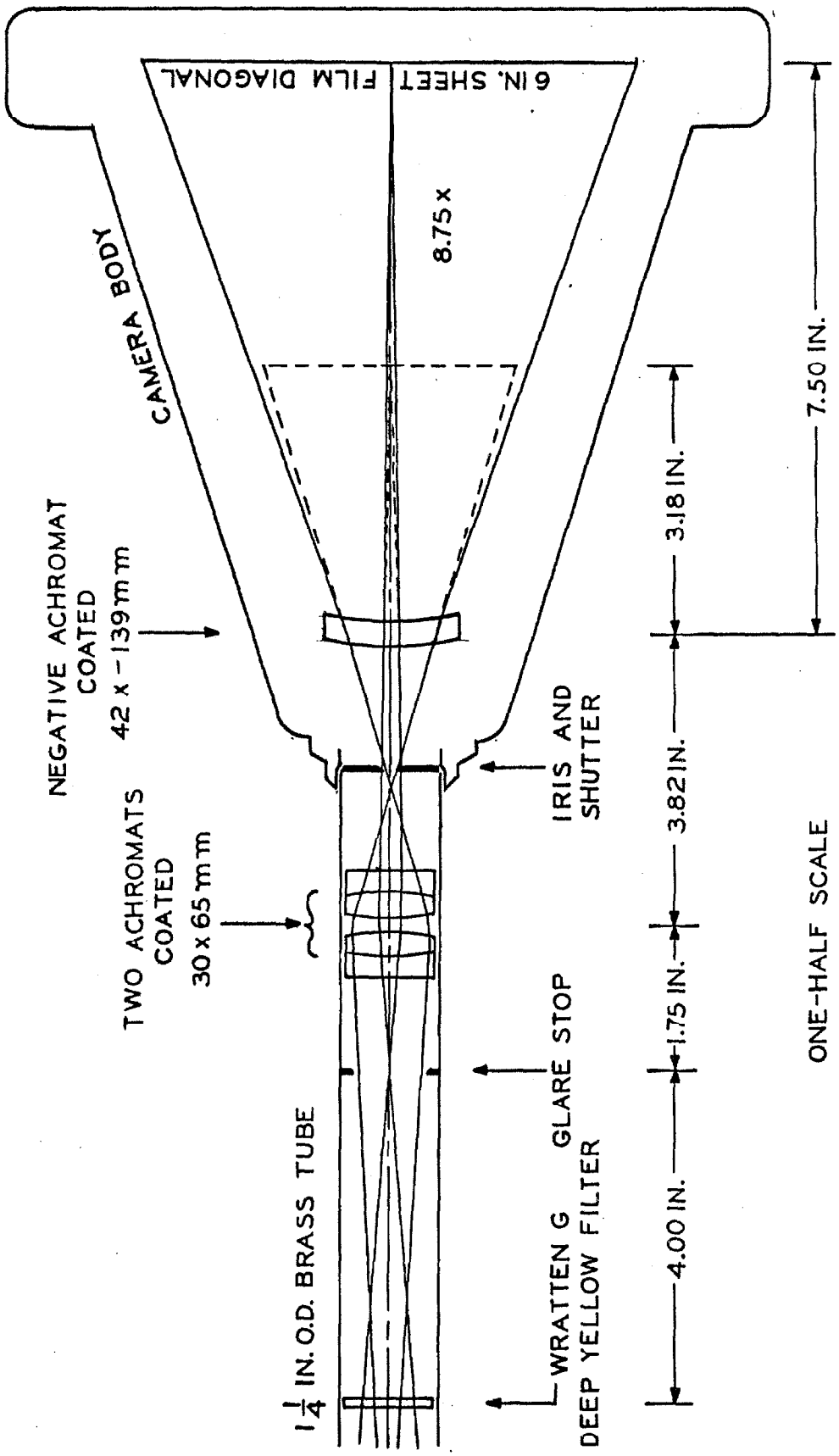

Figure 3. Diagram of Refractor 4 x 5 Plate Camera.

a

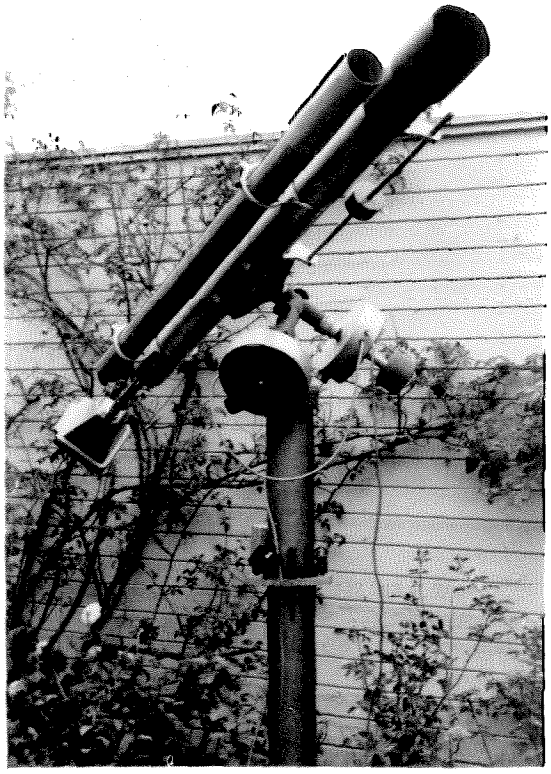

b

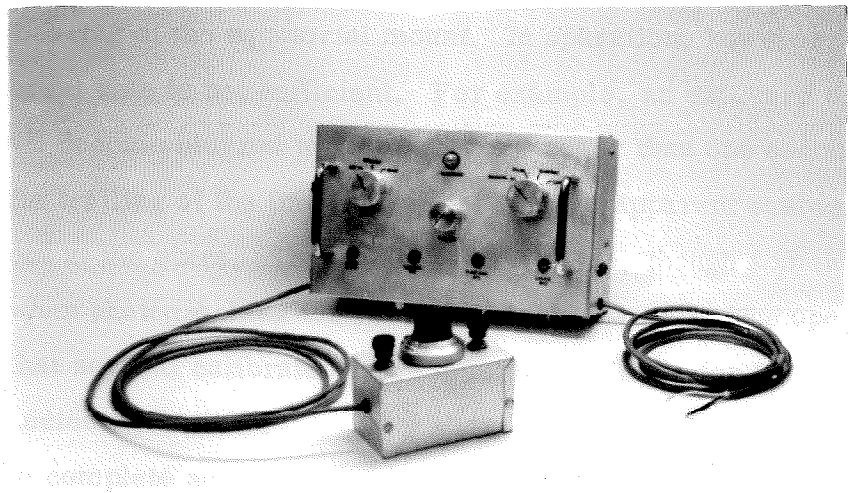

c

Figure 4. Final Installation.

(continuously variable forward and reverse). Mounted outside the servo enclosures there are large eight inch setting circles which allow one to set the celestial coordinates to which the system is to control.

TELESCOPE TRACKING SYSTEM

Such long focal length astronomical photography demands a very accurate tracking system, in order to fully utilize the optimum selection of the various optical parameters. The intimate part of this system is the unique solid state drive.

A stable variable frequency solid state oscillator circuit has been designed which will maintain the right ascension coordinate on the set point with an accuracy of better than 0.05%. The completed system is shown in Figure 4c. Remote push-button coarse tracking rate and fine vernier adjustments are necessary from the eyepiece. The vernier adjustments are made by visually sighting through the reticle eyepiece of a 2.25 inch refractor finder telescope. The main electronics housing is normally located beneath the north bearing of the equatorial mount. In operation, however, tracking at the sidereal rate is not sufficient. For example, an exposure of the lunar surface will become blurred when exposures longer than one second are made, owing to the trailing of the image from the moon's apparent eastward motion with respect to the stars. The same result is true, though somewhat less serious, when photographing the sun, planets or comets. The operation, then, demands that several calibrated rates must be available for tracking the full variety of celestial objects.

The complete schematic circuit has been shown in Figure 5. Although the circuit is unique in design the individual component functions follow current design methods. The circuit can be broken down into six basic functions, reading from left to right. On the left is a zener diode (1N4747A)

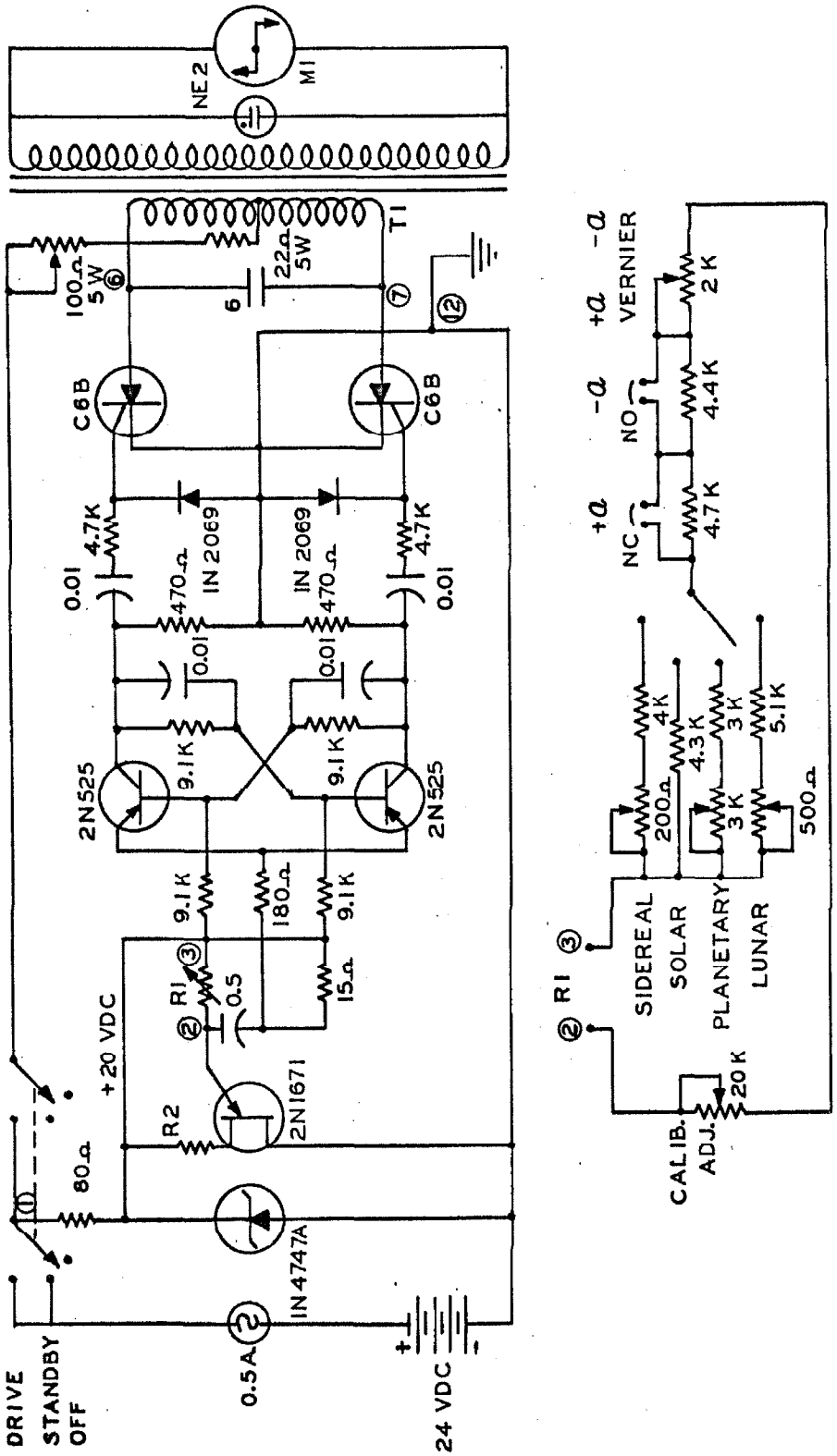

Figure 5. Schematic of Oscillator-Inverter.

voltage regulator maintaining a +20 vdc supply to the next two sections over a relatively wide load variation and component temperature variation. The second function is the solid state unijunction relaxation oscillator (2N1671) which provides an extremely stable but still continuously variable frequency. The variable resistor R1 controls the frequency of the oscillator. The third function is the binary flip-flop which is triggered by the very stable voltage spikes of the unijunction relaxation oscillator. The flip-flop generates two very symmetric positive-going 15 piv square waves out of phase by 180° as in Figure 6a and 6b. The waveforms shown in Figure 6 are those recorded from an oscilloscope under typical operating conditions. This square wave is then differentiated in the fourth section and the smaller negative-going spike is suppressed by diode action (1N2069). The alternate positive-going pulses are then fed to the fifth section as a gating pulse to a silicon control rectifier (SCR) inverter, as shown in Figure 6c and 6d. It is through this fifth section that the necessary current amplification is achieved. The operation of the SCR inverter will be discussed in more detail later. In the unijunction oscillator a current of only 4 ma is capable of operating each SCR at a level of 1.6 amps -- a current amplification of 400. The sixth section merely transforms the RMS, 30 vac signal up to 115 vac, capable of actuating a synchronous control motor typically of 2.7 watts, with a torque of 60 in-oz. This servo motor then moves the entire telescope about its main polar axis.

The unijunction relaxation oscillator was chosen for its extremely stable operation and extensively studied characteristics (1). Two important factors affect the frequency stability of the oscillator -- supply voltage and ambient temperature variation. The effects of varying the supply voltage to the unijunction oscillator and flip-flop in the actual circuit configuration are shown in Figure 7. The maximum change in frequency over the entire operating range of the components was less than 7%. With a 3 volt variation above

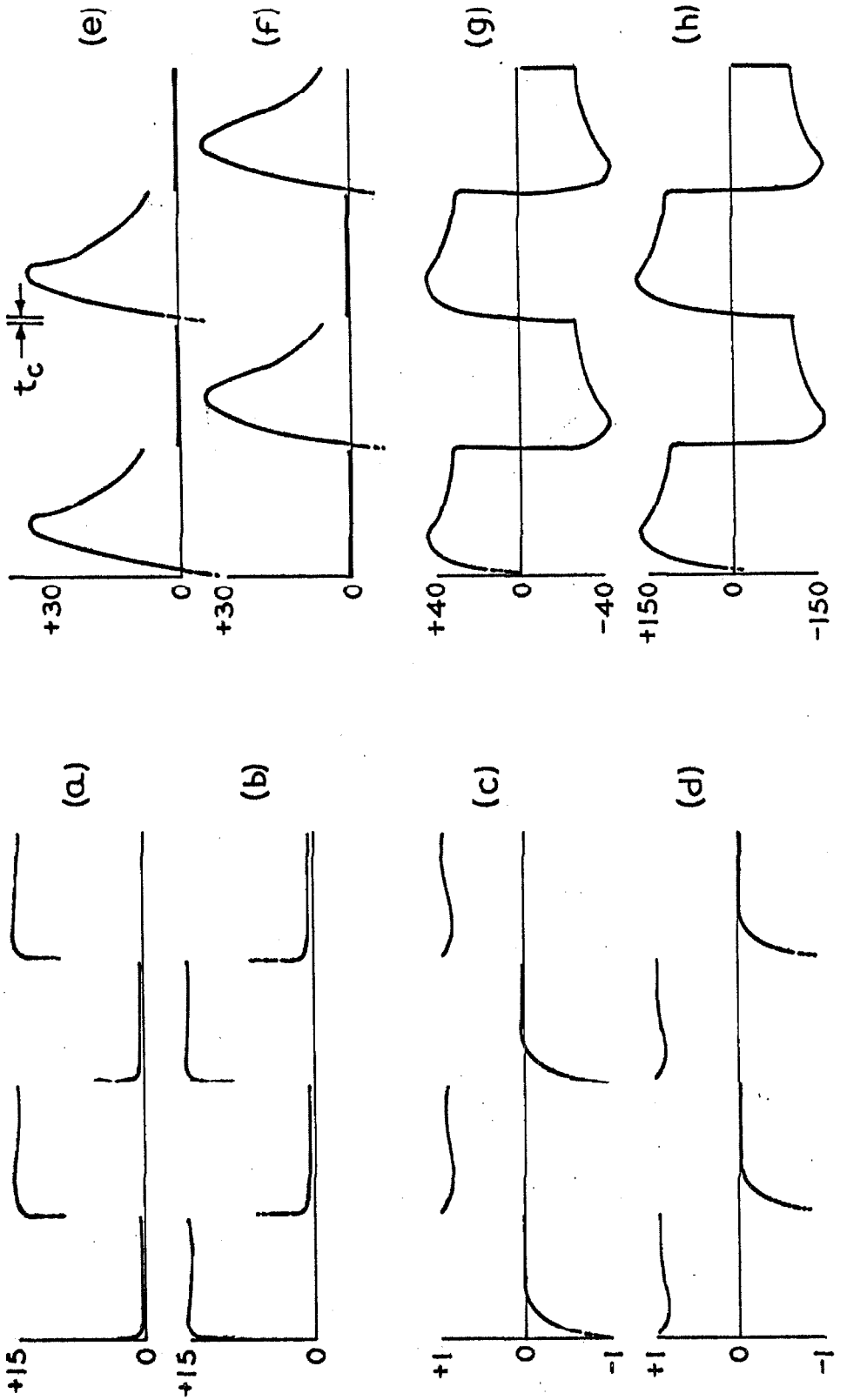

Figure 6. Waveforms of Tests Points in the Oscillator-Inverter Circuit.

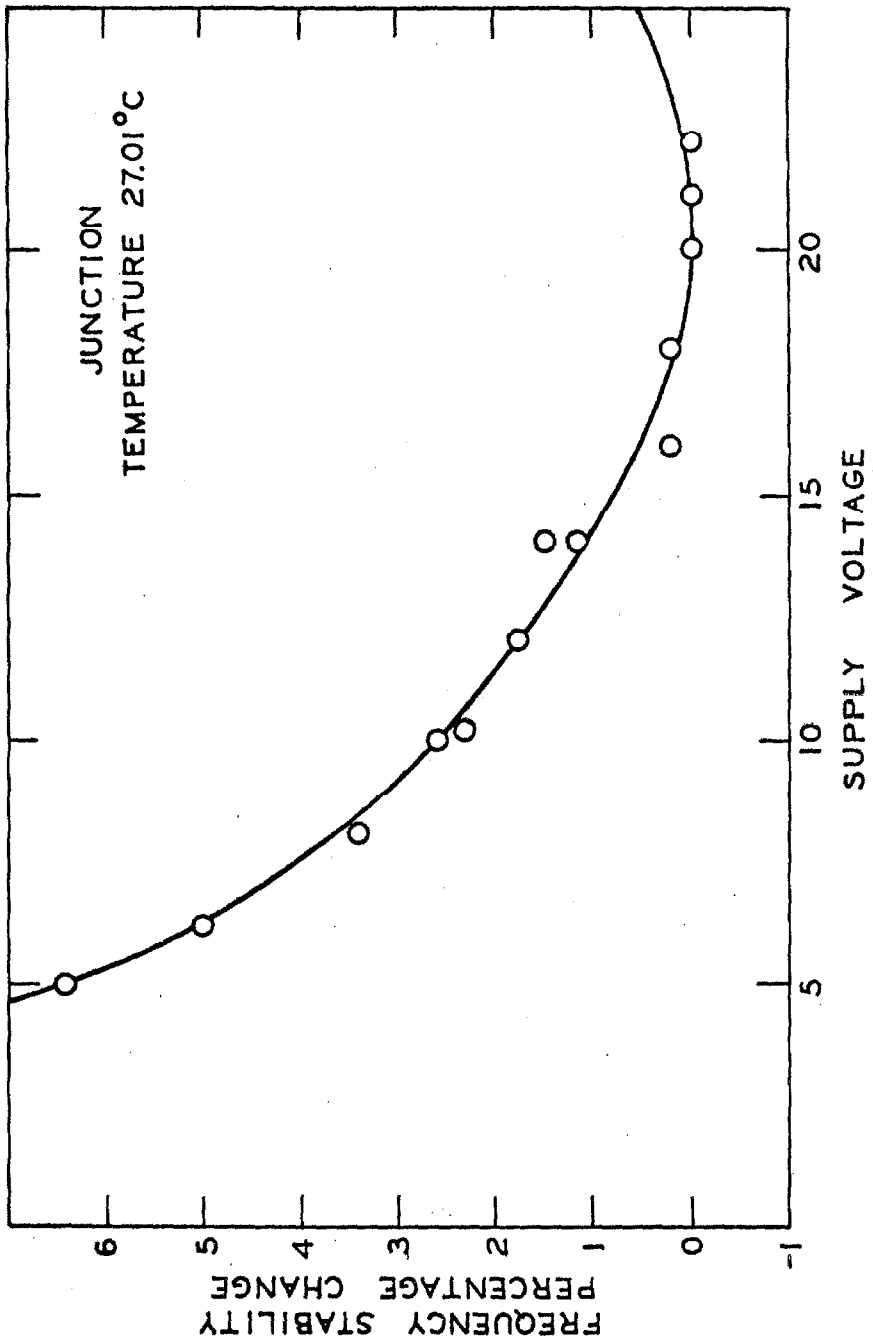

Figure 7. Frequency Stability.

and below 20 vdc there was a 0.3% change. Since the curve is flat at about 20 vdc, any measurable frequency variation with variations in supply voltage can be completely eliminated by regulating the voltage to 20 vdc with a zener diode.

The effects of temperature are much less severe. A 10° F. variation resulted in a 0.2% change in frequency. Since during even a very long exposure (maximum of 60 seconds) a 10° F. change in temperature of the circuit enclosed in a box is not likely, the effects of temperature are negligible. The temperature characteristic curve (1) is very flat around 20° C. and the position of the minimum is lowered when the value of R2 is decreased. It is possible to experimentally establish the optimum value of R2 which results in the minimum temperature variation in regions of the operating temperatures. The unijunction transistor (1) when this is done, will vary in frequency less than 0.25% when the temperature varies 200° F. With the effects of temperature and supply voltage removed frequency stabilities of better than 0.05% can be expected. This allows exposures to be made slightly over one minute with resolutions of 0.8 seconds of arc.

The application of a binary flip-flop for direct derivative mode coupling to the SCR gates is unique. This portion of the circuit required the most experimentation. To trigger an SCR properly through the gate requires a specific shape pulse of a small time duration. The SCR GE# C6B is basically the same as the C5 (2N2322-29) with more relaxed specification standards and a greatly reduced cost (under $2.00). The minimum gate voltage required to trigger all SCR units within the specification is about 0.8 vdc while the maximum allowed is 6 vdc. The peak gate power which the unit can handle is 100 mw, and the average is 10 mw, so with a 2 microsecond pulse about 5 volts would be more than ample. In operation the SCR in the conduction state reduces this voltage to slightly above 1.0 vdc which is within design limits. The 0.01 mfd capacitor and the 4.7 K resistor form the derivative of the

leading edge of the square wave from the flip-flop (Figure 6a and 6b). The trailing edge is less sharp and produces a smaller derivative; however, to prevent a severe negative-going pulse from appearing at the SCR gate it is shunted out by the reverse diode (1N2069) to a value less than 1 piv. The resulting waveform applied to the gate is shown in Figure 6c and 6d. When the SCR is in the conducting state, the sharp positive-going pulse is attenuated to a steady 1 vdc as the result of the gate current. The two curves in Figures 6c and 6d are out of phase by 180° following the flip-flop square wave; thus, the two SCR units are alternately triggered.

The operation of the SCR self-commutating class C inverter (2), in essence, is a resonating circuit. Referring to the schematic in Figure 5, when the upper SCR is conducting and the lower blocking, the 24 volt battery applies current through the upper half of the primary transformer (f91x) winding, which produces a potential difference between points 6 and 7 of about 48 volts, charging the capacitor. When the bottom SCR is triggered with the first portion of the waveform of Figure 6d, point 7 is immediately brought to ground potential and in the process point 6 has remained negative for about 25 microseconds, the upper SCR will stop conducting (turned off) and the capacitor will become charged in opposite polarity with point 7 at about +48 vdc. The cycle is repeated by triggering the lower SCR. The rise time of this voltage from being negative to ground is referred to as the "commutating time", t_c. This turn-off time increases with increasing values of the capacitor, which also decreases the peak voltage of Figure 6e and 6f. A 7 mfd capacitor drops the peak voltage from 32 piv to 29 piv. The history of the potential difference between points 6 and 7 is shown in Figure 6g. This non-linear square wave is then transformed up to 150 ppv or 115 vac which is then applied to the control motor. Although the SCR's are rated at 1.6 amps each only 0.6 amps is required to start the 2.7 watt, 60 in-oz control motor. The current is then reduced to about 0.2 amp with the vari-

able 100Ω potentiometer, which provides just enough power to maintain the control motor in synchronous operation.

The completed circuit is shown in Figure 8. The components have been mounted on a "vector board" in miniature style. This breadboard is then plugged directly into the main portion of the circuit which is then, in turn, all contained in the unit shown in Figure 4c.

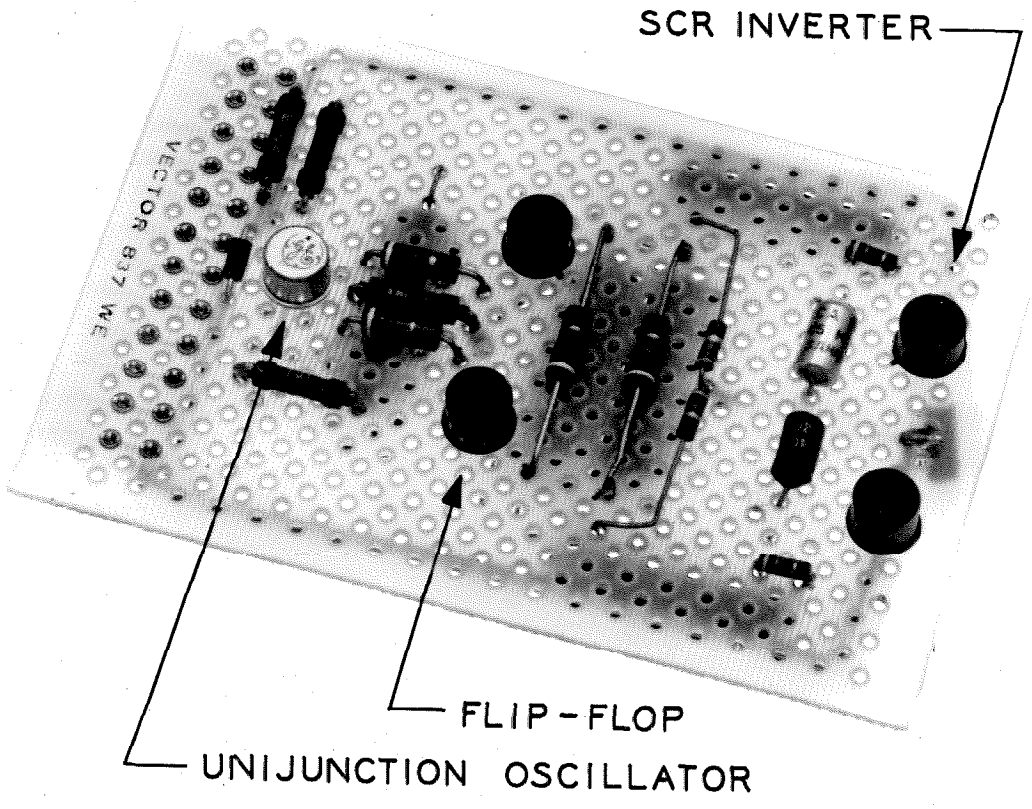

Figure 8. Finished Oscillator Vector-Board Circuit.

LIST OF REFERENCES

1. Cleary, J. F. (editor), Transistor Manual, (New York: General Electric Company, 1964) 648 pp.
2. Gutzwitler, F. W., (editor), Silicon Controlled Rectifier Manual, 3rd edition, (New York: General Electric Company, 1964) 409 pp.

PROPOSITION C

THE STUDY OF INTERMOLECULAR POTENTIAL MODELS FOR POLYATOMIC GASES USING VISCOSITY DATA

It is not sufficient to seek more adequate potential models for representing polyatomic gas phase viscosities. A formal kinetic theory for polyatomic molecules must be used as opposed to the well established Chapman-Enskög theory. Actual viscosity data for the normal paraffins through decane was used as a basis for these recommendations.

INTRODUCTION

An insight into the capabilities and inadequacies of the intermolecular pair potential and the very nature of the collisional process appears to be one of the more rewarding as well as difficult problems of our time. Recently there has been a rather wide diversity of well conceived experimental approaches designed to reveal the very fundamental nature of the intermolecular forces. It appears to be a formidable task to accurately measure and tabulate all the variable properties and characteristics of the various molecules which occur in nature. Current technological developments have led to the largest diversity of fields of study that has ever been known; currently there appears to be a reversal in this trend. A more unifying approach to science, and specifically chemical engineering, must be undertaken. Generalized approached to property prediction of very large classes and homologous series of molecules are critically needed. Once a correct description of intermolecular forces results there emerge equations of state for the gaseous molecules and the associated thermodynamic properties as well as the gaseous molecular transport properties of viscosity, thermal conductivity, mass diffusivity and the thermal diffusion ratio.

FAILURES OF POTENTIAL MODELS

It is most disturbing that the more detailed and sophisticated the research the more inadequate current intermolecular potentials models tend to become. The Lennard-Jones 12-6 potential model has, for over forty years, been the most successful model. Now it is known that it is not even adequate for the inert gases (1). Recently there has been rash of different potential models -- each slightly more exotic than its predecessors and, ironically as a result, also more clumsy to use. Each of these models is a product of the finite capacities of man. Man can only develop models in terms of concepts which are direct products of the environment in which he has developed and grown. Hence, models of rigid spheres were first used; then soft spheres with various attractive and repulsive forces, soft spheres withhard cores, ellipsoids, cylinders, etc.

These potentials are used in the Chapman-Enskög kinetic theory of gases which is valid for monatomic gases, which are spherically symmetric and possess no internal degrees of freedom. Although mass and momentum are still strictly conserved in the collisional process of a polyatomic gas, with the viscosity and diffusivity still adequately predictable, it is when the molecules no longer are spherically symmetric that the Chapman-Enskög kinetic theory itself is in question. Spherical asymmetry greatly complicates the collision process. That energy is not conserved in the kinetic sense in the inelastic collision of polyatomic molecules, owing to internal degrees of freedom, leads to the fact that there is exchange between the internal modes of relaxation (such as vibration and rotation) and translation. Thus, the very nature of the translational kinetic collision process is indeed affected by the presence of internal degrees of freedom and asymmetry.

Current kinetic theories of polyatomic gases (2,3) make to use of potential models but use angular transition probabilities. Applying potential models to polyatomic gases is in effect averaging the result of the action of all possible collisions in various angular orientations and then expecting them to predict the behavior of all the individual cases which were just averaged out. Recently (4) the homologous series of the normal paraffins through decane was used to investigate the applicability of a variety of intermolecular pair potential models. No single potential model was at all adequate in describing the viscosity data, although the Kihara spherical core model was the best, predicting within about 9%. Analysis of thermal conductivity data indicated the necessity of recognising internal degrees of freedom. The use of what little relaxation times which are available for the rotational modes did predict the data accurately (0.3%). This immediately brings to mind that the very idea of using a potential model for viscosity is not consistent with the findings for thermal conductivity. In other words, using angularly independent potentials and ignoring internal degrees of freedom, the temperature dependency of viscosity cannot be predicted accurately. The findings (4) indicate that it is the incorrect temperature dependence of the viscosity which is the largest source of error.

These facts suggest that it is futile to propose exotic varieties of potential models in order to predict the gas phase viscosity data accurately for polyatomic molecules. But instead emphasis must be placed on understanding the very nature of the collision process of polyatomic molecules and the phenomena of energy exchange, relaxation of internal modes of vibration and rotation, and effects of spherical asymmetry. Considerably more experimental work is needed concerning the transition probabilities of polyatomic molecules more complex than triatomic. The kinetic theory of polyatomic molecules (2,3) can be most effectively used when there is a technique to obtain the individual energies of the internal quantum states and

differential scattering cross sections. To date (5) no differential cross sections have even been calculated from any molecular model.

CONCLUSIONS

The solution to this transport problem, short of empiricizing the theory, is to carry through the statistical mechanics for polyatomic gases with a kinetic theory applicable to molecules possessing internal degrees of freedom and a symmetry which is not spherical. This undoubtedly would be a frontier and a breakthrough in the field of chemical engineering. To have a theory accurate enough to predict the PVT relationships, thermodynamic properties, and transport properties of gases (and with great hope, liquids) better than could be measured by conventional laboratory techniques would make the dream[1] of most chemical and petroleum companies come true -- to calculate all necessary properties with the digital computer

---

1. Most companies at the present time have very limited but nevertheless operational systems of this kind now. However, the accuracy of the results for polyatomic species is especially limited.

LIST OF REFERENCES

1. Rowlinson, J. S., "A Test of Kihara's Intermolecular Potential," Molec. Phys. 9, 197-198 (1965)
2. Wang Chang, C. S., and G. E. Uhlenbeck, "Transport Properties in Polyatomic Gases," CM-681, Project NOrd 7924, University of Michigan (1951)
3. De Boer, J. and G. E. Uhlenbeck, "Studies in Statistical Mechanics," North Holland Pub. Co., Amsterdam, 1964.
4. Galloway, T. R., and B. H. Sage, "Prediction of the Transport Properties of Paraffin Hydrocarbons," accepted for publication by Chem. Eng. Sci. 1966
5. Hirschfelder, J. O., and C. F. Curtiss, and R. B. Bird, "Molecular Theory of Gases and Liquids," John Wiley and Sons, Inc. 1965.

PROPOSITION D

TURBULENT EDDY PERTURBATION MODEL FOR EFFECTS OF FREE STREAM TURBULENCE ON THE TRANSPORT FROM SPHERES

A qualitative development of a physical model for prediction of the influence of free stream turbulence on a laminar boundary layer on a sphere is presented. In essence this model illustrates an idealized mechanism for the free stream perturbation and penetration of eddies into the laminar boundary layer and the consequent net effect on the local transport. From this model a non-linear theory is developed to explain this phenomenon.

INTRODUCTION

When there is subcritical flow over the surface of a sphere, a three dimensional stagnation point occurs at the foremost point on the surface, and after steady state is reached, a laminar boundary layer is formed which grows in thickness up to the point of separation; after which free (wake) flow results. Now if the free stream is turbulent or in a state of unsteady induced turbulence, as for example generated behind a grid, the free stream eddies interact with the laminar boundary layer in such a way as to substantially increase the heat transfer. The greater the extent of eddy motion in the mainstream the more significant the effect on the laminar layer. It is now becoming well established that the influence of this free stream turbulence is greatest in the region of stagnation and decreases in a smooth fashion up to separation. This phenomenon will be analyzed. It is also known that free-

stream turbulence effects the position of the point of separation as well as the transition Reynolds number, but these effects will not be treated further here.

DISCUSSION

These eddies adjacent to a laminar thermal or concentration boundary layer evidently possess a spectra of kinetic energies with sufficient magnitude, dependent on mainstream turbulence, so that a number of the higher energy eddies are capable of penetrating into the laminar layer on the forward hemisphere. These higher energy eddies, it is supposed, are capable of penetrating deep enough into the laminar boundary layer so as to alter the thermal or concentration profiles before the energy of the eddy is dissipated. The eddy, by its very nature, carries with it properties of the free stream; thus, it is a pure mixing effect. As the eddy penetrates into this laminar layer its energy is dissipated through a long stepwise process of degradation into smaller eddies (Kolmogoroff's Principle). As these eddies become smaller their motion is more rapidly damped out by viscous dissipation. The effect of this penetration is to instanteously alter the thermal or concentration profile up to the depth of penetration. If the Prandtl or Schmidt groups within this layer are small; thus, high diffusivities, unsteady thermal or molecular diffusion occurs quickly in the direction of the steepest local gradient. This, then, steepens the profile between the depth of penetration at the surface, increasing the gradient at the wall, and accomplishing an increase in the flux at this point. This unsteady process is shown schematically in Figure 1.

When the Prandtl or Schmidt groups are large (such as with liquids) the profile is steep and the boundary layer thinner; therefore, less kinetic

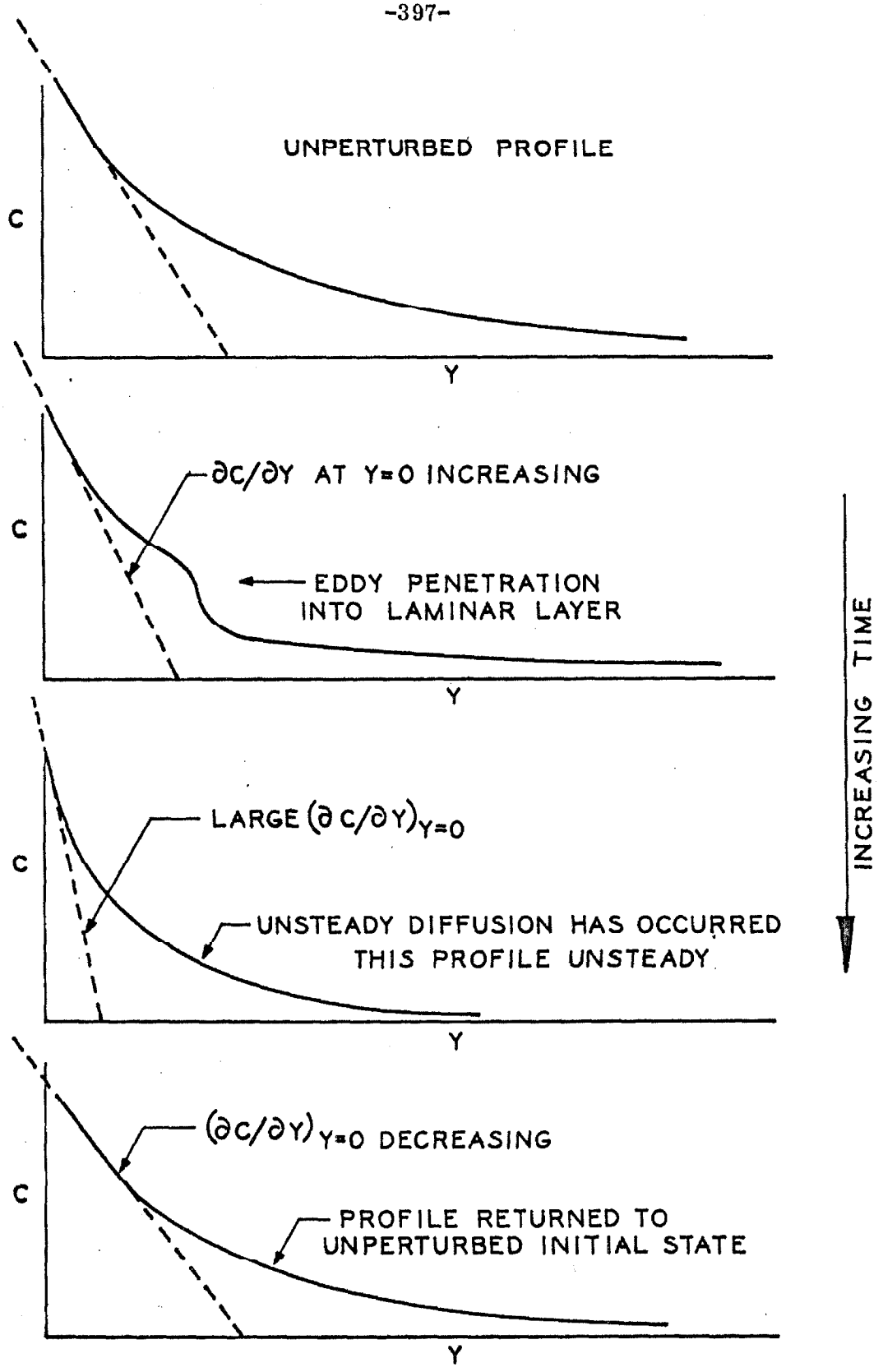

Figure 1. The Effect of an Eddy on the Concentration Profile.

energy is needed for an eddy to penetrate deeply into the layer. Also the lower diffusivities retard the unsteady restoration process; thus, leaving large gradients near the surface for longer times, greatly increasing the transfer. This illustrates that the influence of the free-stream turbulence should be many times greater for systems of lower diffusivity.

Now as we proceed away from the stagnation point the boundary layer thickness increases and a smaller portion of this layer is being penetrated by the free-stream turbulence. Therefore, the effect of turbulence consequently should decrease from the stagnation. This result has been verified experimentally as enumerated in Part II of this thesis.

The problem now is to use these concepts in this idealized model in order to establish the non-linear dependence of the convective transfer coefficient on the flow rate and turbulence level. Since these phenomena are truly of an unsteady random nature, the solution more correctly must come simultaneously from the continuity and the unsteady momentum and energy or species equations. This is a formidable task*. One well known technique is to time average the equations and use the instantaneous parameters as the sum of a time averaged component plus a fluctuating component:

$$u = U + u'$$

$$t = T + t'$$

$$c = C + c'$$

The equations in axially, rotationally symmetric coordinates become:

---

* It appears very likely that a stochastic approach using the unsteady nature of the phenomena and neglecting possibly convective terms may, indeed, be realistic.

$$\frac{\partial Ur}{\partial x} + \frac{\partial Vr}{\partial y} = 0 \tag{1}$$

$$U\frac{\partial U}{\partial x} + V\frac{\partial U}{\partial y} = -\frac{1}{\rho}\frac{dP}{dx} + \nu\frac{\partial^2 U}{\partial y^2} - \frac{\partial}{\partial y}(\overline{u'v'}) \tag{2}$$

$$U\frac{\partial t}{\partial x} + V\frac{\partial t}{\partial y} = \alpha\frac{\partial^2 t}{\partial y^2} - \frac{\partial}{\partial y}(\overline{v't'}) - \frac{\overline{u'v'}}{C_P}\frac{\partial U}{\partial y} + \frac{\nu}{C_P}\left(\frac{\partial U}{\partial y}\right)^2 \tag{3}$$

$$U\frac{\partial C}{\partial x} + V\frac{\partial C}{\partial y} = \mathfrak{D}_{AB}\frac{\partial^2 C}{\partial y^2} - \frac{\partial \overline{v'c'}}{\partial y} \tag{4}$$

These equations have been written neglecting all of the other secondary effects, except viscous dissipation and the longitudinal pressure gradient. It is only logical at this point to define a resistance to the transport of the eddy fluxes as the flux per unit local driving force:

$$\varepsilon_m(y, Re) = -\frac{\overline{u'v'}}{\partial U/\partial y} \tag{5}$$

$$\varepsilon_c(y, Re) = -\frac{\overline{v't'}}{\partial t/\partial y} \tag{6}$$

$$\varepsilon_d(y, Re) = -\frac{\overline{v'c'}}{\partial c/\partial y} \tag{7}$$

Using these definitions in Equations 2, 3, and 4, there results:

$$U\frac{\partial U}{\partial x} + V\frac{\partial U}{\partial y} = -\frac{1}{\rho}\frac{dP}{dx} + \frac{\partial}{\partial y}\left[(\nu + \varepsilon_m)\frac{\partial U}{\partial y}\right] \tag{8}$$

$$U\frac{\partial T}{\partial x} + V\frac{\partial T}{\partial y} = \frac{\partial}{\partial y}\left[(\alpha + \epsilon_c)\frac{\partial T}{\partial y}\right] + \frac{\nu + \epsilon_m}{C_p}\left(\frac{\partial U}{\partial y}\right)^2 \tag{9}$$

$$U\frac{\partial C_k}{\partial x} + V\frac{\partial C_k}{\partial y} = \frac{\partial}{\partial y}\left[(\mathcal{D}_{kj} + \epsilon_d)\frac{\partial C_k}{\partial y}\right] \tag{10}$$

It is seen that each of the bracketed terms represent the gradient of the respective fluxes:

$$\frac{\tau}{\rho} = -(\nu + \epsilon_m)\frac{\partial U}{\partial y} \tag{11}$$

$$q = -(\alpha + \epsilon_c)\rho C_p \frac{\partial T}{\partial y} \tag{12}$$

$$\dot{m}_k = -(\mathcal{D}_{kj} + \epsilon_d)\frac{\partial C_k}{\partial y} \tag{13}$$

Now at low flow rates in the region of the stagnation point the remaining analogy defeats; viscous dissipation and the longitudinal pressure gradient will be neglected. Although this is somewhat indefensible, a tremendous simplification results:

$$\frac{\tau}{\rho} = \text{constant}$$

$$\frac{T}{\dot{m}} = \text{constant}$$

That is, there is a complete analogy. From this analogy there results:

$$\frac{\tau}{q} = \frac{\tau_w}{q_w} = \frac{(\upsilon + \epsilon_m)}{(\alpha + \epsilon_c)} \frac{1}{C_p} \frac{\partial U}{\partial T} \tag{14}$$

which uses the assumption in the model that eddies can penetrate very near to the surface. The temperature driving force between the surface and the free stream can then be obtained:

$$t_\infty - t_w = \frac{1}{C_p} \frac{q_w}{\tau_w} \int_0^{U_\infty} \frac{\upsilon + \epsilon_m}{\alpha + \epsilon_c} \, dU \tag{15}$$

The thermal transport coefficient is then defined by:

$$q_w = h(t_\infty - t_w)$$

Thus,

$$q_w = \frac{Nu-2}{RePr} \rho C_p U_\infty (t_\infty - t_w) \tag{16}$$

The stagnant limit of 2 for the Nusselt number is easily justified. Substituting Equation 15 into 16 and defining $\xi = U/U_\infty$; there results:

$$\frac{Nu-2}{RePr} = \frac{\tau_w}{\rho U_\infty^2} \frac{1}{\int_0^1 \frac{\upsilon + \epsilon_m}{\alpha + \epsilon_c} \, d\xi} \tag{17}$$

There is enough pointwise local experimental data available to predict the Reynolds number dependence of the skin friction coefficient (1):

$$\frac{C_f}{2} = \frac{\tau_w}{\rho U_\infty^2} = A Re^{-1/2}$$

Using this relationship, the Frössling number for spheres is then obtained directly from Equation 17:

$$Fs_{\infty} = \frac{Nu - 2}{Re_{\infty}^{1/2} Pr_{m,\infty}^{1/3}} = A \Big/ \int_0^1 \frac{\nu + \epsilon_m}{\alpha + \epsilon_c} Pr_m^{-2/3} d\xi \tag{18}$$

The integrand can easily be rewritten as:

$$1 + \frac{Pr_m^{1/3} - 1) - \frac{\epsilon_c}{\alpha}(1 - Pr_t/Pr_m^{2/3})}{1 + \frac{\epsilon_c}{\alpha}} \tag{19}$$

Now the term $Pr_m^{1/3}-1$ is quite negligible even for high molecular Prandtl number, since the term ϵ_c/α depends linearly on Pr_m as will be developed later. So that Equation 18 becomes:

$$Fs = \frac{A}{1 - \int_0^1 \frac{\frac{\epsilon_c}{\alpha}(1-Pr_t/Pr_n^{2/3})}{1 + \epsilon_c/\alpha} d\xi} \tag{20}$$

Expanding in a series, Equation 20 simplifies to:

$$Fs = A\left\{ 1 + \int_0^1 \left[\frac{\frac{\epsilon_c}{\alpha}(1-Pr_t/Pr_m^{2/3})}{1 + \epsilon_c/\alpha} d\xi\right] + \left[\int_0^1 \frac{\epsilon_c/\alpha}{1+\epsilon_c/\alpha}(1-Pr_t/Pr_m^{2/3}) d\xi\right]^2 + \ldots \right\} \tag{21}$$

This is the non-linear result in the most general form. It can be seen that for laminar flow with eddy perturbations adjacent to the laminar layer, the Frössling number, in general, will not be a constant, as expected from well known linear theory.

A useful engineering solution to this complex problem is possible, if the higher order terms of Equation 21 are neglected and effective averages used for the eddy conductivity and turbulent Prandtl number:

c
$$Fs = A + \frac{A\overline{\epsilon_c}/\alpha}{1 + \overline{\epsilon_c}/\alpha}\left(1 - Pr_t/Pr_m^{2/3}\right) \tag{22}$$

Unfortunately, there is evidently little alternative since profiles of these eddy coefficients are not available and cannot be measured for a aphere by methods other than the very tedious detection of the fluctuating components.

Now since these eddies and the corresponding fluctuating components penetrate into the laminar layer from the turbulent free stream, and are not generated within, the effective average eddy coefficients in the layer are expected to be proportional to the external free-stream turbulence and flow conditions. This result can be developed from the definition of the eddy viscosity:

$$\epsilon_m = \frac{\overline{u'v'}}{\partial U/\partial y} = \frac{\epsilon_m}{\epsilon_c}\epsilon_c = Pr_t\,\epsilon_c \tag{23}$$

For isotropic, homogeneous turbulence, the level of turbulence can be expressed as:

$$Z_t^2 = Z_{tx}^2 = \frac{\overline{u'^2}}{U^2} = Z_{ty}^2 = \frac{\overline{v'^2}}{U^2} = \frac{\overline{u'v'}}{U^2} \tag{24}$$

Substituting this result into Equation 23, the eddy conductivity can be obtained as:

$$\epsilon_c = \frac{\overline{u'v'}}{Pr_t\frac{\partial U}{\partial y}} = \frac{Z_t^2}{Pr_t}\frac{U^2}{\partial U/\partial y} \tag{25}$$

Note that:

$$\frac{\tau}{\rho U^2} = \frac{(\nu+\epsilon_m)}{U^2}\frac{\partial U}{\partial y} \approx A_2 \, Re^{-1/2}$$

This approximation can be used in Equation 25:

$$\frac{\epsilon_c}{\alpha} = \frac{Z_t^2}{Pr_t}\left(\frac{\nu+\epsilon_m}{\alpha}\right)\frac{Re^{1/2}}{A_2}$$

$$\frac{\epsilon_c}{\alpha} = \frac{Z_t^2}{Pr_t}\left[Pr_m + Pr_t\left(\frac{\epsilon_c}{\alpha}\right)\right]\frac{Re^{1/2}}{A_2}$$

$$\frac{\overline{\epsilon_c}}{\alpha} = f\,\frac{\epsilon_c}{\alpha} = f\,\frac{Z_t^2\, Pr_m/Pr_t}{\frac{A_2}{Re^{1/2}} - Z_t^2} \qquad (27)$$

where f is taken as some numerical constant. Substituting this result into Equation 22, the Frössling number becomes:

$$Fs = A + \frac{fAZ_t^2 Re^{1/2} Pr_m/Pr_t (1-Pr_t/Pr_m^{2/3})}{A_2 + Z_t^2(fPr_m/Pr_t - 1)Re^{1/2}}$$

The coefficient A_2 has a minimum of about 0.5 at stagnation and for most gases in subcritical laminar layers Pr_t=0.7, while in wake flow Pr_t=0.5; thus, a fair approximation for the Frössling number may be:

$$Fs = A + BZ_t^2 Re^{1/2} \Phi(Pr_m, Pr_t)$$

Similarly there obtains for mass transport:

$$Fs = A + BZ_t^2 Re^{1/2} \Phi(Sc_m, Sc_t)$$

These then are the final results for this non-linear theory based on the turbulent eddy perturbation model.

NOMENCLATURE

A = Coefficient of correlation, see text

A_2 = Coefficient of Equation 26

B = Coefficient of correlation, see text

C = Coefficient of correlation, see text

c' = Turbulent fluctuating concentration (lbmoles/ft^3)

c = Instantaneous concentration (lbmoles/ft^3)

C = Time averaged concentration (lbmoles/ ft^3)

C_P = Heat capacity (Btu/lbm-° F.)

d = Sphere diameter (ft)

$\mathscr{D}_{jk}$ = Binary diffusion coefficient of component k in fluid at x,y (ft^2/sec)

D = Coefficient of correlation, see text

f = Numerical constant

Fs = Frössling number, $(Nu-2)/Re^{1/2}Pr^{1/3}$ or $(Sh-2)/Re^{1/2}Sc^{1/3}$

h = Heat transfer coefficient (BTu/hr-ft-° F.)

k = Thermal conductivity (Btu/hr-ft-° F.)

$\dot{m}$ = Mass flux (lbmoles/hr-ft^2)

Nu = Nusselt number, hd/k

Pr_m = Molecular Prandtl number, ν/α

Pr_t = Turbulent Prandtl number, ϵ_m/ϵ_c

q = Heat flux (Btu/hr-ft^2)

Re = Reynolds number, Ud/ν

r = Radial distance to point in question measured from axis of symmetry of sphere passing through stagnation point and sphere center (ft.)

Sc = Schmidt number, $\nu/\mathscr{D}_{jk}$

Sh = Sherwood number, same as Nusselt only for mass transfer

t' = Turbulent fluctuating temperature (° F)

t = Instantaneous temperature (° F.)

T = Time averaged temperature (° F.)

u' = Turbulent fluctuating velocity in x direction (ft/sec)

u = Instanteous velocity in x direction (ft/sec)

U = Time averaged velocity in x direction (ft/sec)

U_1 = Time averaged velocity at edge of boundary layer (ft/sec)

v' = Turbulent fluctuating velocity in y direction (ft/sec)

v = Instanteous velocity in y direction (ft/sec)

V = Time averaged velocity in y direction (ft/sec)

x = Distance along surface of sphere from stagnation point (ft.)

y = Distance perpendicular to sphere surface (ft.)

Z_t = Level of free-stream turbulence obtained by hot wire methods

Z_{tx} = as above but in x direction

Z_{ty} = as above but in y direction

GREEK SYMBOLS

α = Thermal diffusivity, $k/\rho C_p$ (ft^2/sec)

α_t = Apparent level of turbulence of free stream (based on Davis' work, discussed in Part II)

ϵ = Eddy coefficient, defined in Equations 5 - 7.

υ = Kinematic viscosity at point x,y (ft^2/sec)

ρ = Density of fluid at point x,y (lbm/ft^3)

Φ = Functional relation, see text

ψ = Polar angle measured from sphere stagnation (degree)

τ = Shear (lbf/ft^2)

ξ = Dimensionless velocity, U/U_∞

SUBSCRIPTS

c = for conductivity of heat

d = for diffusivity of mass

i = for interfacial conditions

k = for component k

m = denotes molecular property, or for viscosity of momentum

t = denotes turbulent property

w = for solid surface condition

∞ = for free-stream cnnditions

SUPERSCRIPTS

* = denotes average over surface

REFERENCES

1. Giedt, W. H., "Effect of Turbulence Level of Incident Air Stream on Local Heat Transfer and Skin Friction on a Cylinder," J. Aero. Sci., 18, 725-730, 766 (1951)
2. Eckert, E. R. G., and E. M. Drake, "Heat and Mass Transfer," (New York, McGraw-Hill Book Co., 1959) pg. 220.

PROPOSITION E

CORRECTION OF ERROR FOR THERMAL CONDUCTIVITY OF A POLYATOMIC FLUID

The thermal conductivity of a polyatomic fluid at elevated pressures has been developed from the Enskög theory taking into account the effects of the internal structure of the molecule. The previous treatment presented by Hirshfelder, Curtiss, and Bird was found to be in error.

INTRODUCTION

The Enskög theory (1,2) was developed to describe the transport properties of dense fluids using kinetic theory of gases and applying two significant dense gas corrections. Enskög considered the effects of finite molecular size in comparison to the intermolecular distances prevailing at conditions of elevated pressure. Enskög corrected for the collisional transfer of momentum and energy when gas molecules are in close proximity and for the increase in the rate of collision from the reduction in free space. The results express the additional contribution to the thermal conductivity from effects of elevated density as compared to the conductivity at low pressure.

DEVELOPMENT

The contribution to the thermal conductivity of a dense fluid over and above that for a rarified fluid was presented by Enskög as:

$$\frac{k}{k_o} = \frac{1}{Y}\left[1+\frac{6}{5}\rho^*Y+0.755(\rho^*Y)^2\right] \qquad (1)$$

where:

$$Y = 1 + 0.6250\rho^* + 0.2869\rho^{*2} + 0.115\rho^{*3}$$

and

$$\rho^* = \frac{2}{3}\pi N_o \sigma^3 \rho$$

In Ensk$\ddot{o}$g's development k_o represents the thermal conductivity of the gas at low pressure.

This expression has been extended to the case of polyatomic molecules by Hirschfelder, Curtiss, and Bird (2) through the use of the Eucken correction, and their result as Equation 9.3-37a is:

$$k = \frac{1}{Y}\left(\frac{C_{v,o}}{R} + \frac{9}{4}\right)\frac{R}{M}\eta_o + \frac{15}{4}\rho^*\left[\frac{6}{5} + 0.755\rho^* Y\right]\frac{R}{M}\eta_o \qquad (2)$$

This result is incorrect.

The monatomic limit of the thermal conductivity is well established since the thermal conductivity at low pressure is simply related to the viscosity at low pressure:

$$k_o^{(o)} = \frac{15}{4}\frac{R}{M}\eta_o \qquad (3)$$

When this is used in Equation 1 for a monatomic gas ($k_o = k_o^{(o)}$) the resulting expression becomes:

$$k^{(o)} = \frac{1}{Y}\frac{15}{4}\frac{R}{M}\eta_o + \frac{15}{4}\rho^*\left[\frac{6}{5} + 0.755\rho^* Y\right]\frac{R}{M}\eta_o \qquad (4)$$

Note that this expression for the monatomic gas does not compare to Equation 2 as presented by Hirschfelder, Curtiss, and Bird (2). When the Eucken correction is made from the relation:

$$k_o = \left(\frac{C_v}{R} + \frac{9}{4}\right)\frac{R}{M}\eta_o \qquad (5)$$

then Equation 1 becomes:

$$k = \left[\frac{1}{Y} + \frac{15}{4}\rho^*\left(\frac{6}{5} + 0.755\rho^*Y\right)\right]\left(\frac{C_v}{R} + \frac{9}{4}\right)\frac{R}{M}\eta_o \qquad (6)$$

This relation also does not compare to Equation 2, since the relation which they have presented is a hybrid between the monatomic and polyatomic limits.

A more correct relation for the effects of density on the thermal conductivity can be obtained from the result (3):

$$\frac{k_o - k_o^{(o)}}{k_o^{(o)}} = 0.3267\left(\frac{C_{P,O}}{R} - \frac{5}{2}\right) \qquad (7)$$

where $k_o^{(o)}$ is given by Equation 3. Equation 7 can be rearranged as:

$$k_o = \frac{15}{4}\frac{R}{M}\left[1 + 0.3267\left(\frac{C_{P,0}}{R} - \frac{5}{2}\right)\right]\eta_o \qquad (8)$$

Equation 8 can be substituted into Equation 1 to obtain the result:

$$k = \frac{15}{4}\frac{R}{M}\left[\frac{1}{Y} + \frac{15}{4}\rho^*\left(\frac{6}{5} + 0.755\rho^*Y\right)\right]\left[1 + 0.3267\left(\frac{C_{P,0}}{R} - \frac{5}{2}\right)\right]\eta_o$$

For a typical hydrocarbon such as n-pentane at a reduced density of 0.3 this relation predicted a thermal conductivity more than twice that predicted by Equation 1.

REFERENCES

1. Chapman, Sydney and T. G. Cowling, Mathematical Theory of Non-Uniform Gases, (New York: Cambridge Univ. Press, 1939)
2. Hirschfelder, J. O., C. F. Curtiss, and R. B. Bird, "Molecular Theory of Gases and Liquids", second printing (New York: John Wiley and Sons, Inc., 1964)
3. Galloway, T. R. and B. H. Sage, "Molecular Transport Properties of the Normal Paraffins," accepted by Chemical Engineering Science for publication.

NOMENCLATURE

See Part I of this thesis.